UNIVERSITÀ DI SIENA 1240

Department of Physical, Earth and Environmental Sciences

PhD in Earth, Environmental and Polar Sciences

29° Cycle

Coordinator: Prof. Roberto Bargagli

PASSIVE METHOD FOR DYNAMIC CHARACTERIZATION OF SOIL AND BUILDINGS

Scientific field: GEO/10 (Geofisica della terra solida)

PhD Candidate:

Eng. ELONA XHIXHA
CGT-Centro di GeoTecnologie, Università di Siena,
Via Vetri Vecchi 34 - 52027 San Giovanni Valdarno

Università degli studi di Siena,
Via Laterina 8 - 53100 Siena

Thesis Coordinator:

Prof. LUIGI CARMIGNANI
Università degli studi di Siena, Sezione di
Scienze della Terra, Via Laterina 8 - 53100 Siena

Thesis Advisor:

Prof. DARIO ALBARELLO
Università degli studi di Siena, Sezione di
Scienze della Terra, Via Laterina 8 - 53100 Siena

Academic year of achieving the title of Doctor of Research

2013/2016

Università degli Studi di Siena

Dottorato in Scienze della Terra, ambientali e polari

29° Ciclo

Componenti del Collegio dei docenti

Personale di ruolo nelle università italiane	***Personale non accademico dipendente di altri enti e di università straniere***
Bargagli Roberto, Università di Siena	Brugnoli Enrico, CNR – Dip. Terra Ambiente
Boscato Paolo, Università di Siena	Calamandrei Gemma, Istituto Superiore di Sanità
Carmignani Luigi, Università di Siena	Depledge Michael H., Universities of Exeter and Plymouth, Plymouth UK
Casini Silvia, Università di Siena	Frezzotti Massimo, ENEA Roma
Corsi Ilaria, Università di Siena	Gambi Maria Cristina, Stazione Zoologica Anton Dohrn, Napoli
Corsolini Simonetta, Università di Siena	Matranga Valeria, IBIM CNR Palermo
Delmonte Barbara, Università di Milano Bicocca	Meloni Antonio, INGV Roma
Foresi Luca Maria, Università di Siena	Mehlum Fritjof, Natural History Museum (Norvegia)
Fossi Maria Cristina, Università di Siena	Ranalli Giorgio, Carleton University Ottawa Canada
Leonzio Claudio, Università di Siena	
Manganelli Giuseppe, Università di Siena	
Mantovani Enzo, Università di Siena	
Marchettini Nadia, Università di Siena	
Masini Maria Angela, Università di Genova	
Monaci Fabrizio, Università di Siena	
Moroni Adriana, Università di Siena	
Pieruccini Pierluigi, Università di Siena	
Protano Giuseppe, Università di Siena	
Pugliese Nevio, Università di Trieste	
Ricci Carlo Alberto, Università di Siena	
Sandrelli Fabio, Università di Siena	
Talarico Franco, Università di Siena	
Tavarnelli Enrico, Università di Siena	
Viti Cecilia, Università di Siena	

Data dell'esame finale:

4 Luglio 2017

Commissione giudicatrice:

- Riccardo Salvini, Università di Siena, DSFTA (ricercatore) <riccardo.salvini@unisi.it>;
- Giacomo Alfredo D'Amato Avanzi, Università di Pisa, Dip. Scienze della Terra (ricercatore) <giacomo.damato@unipi.it>;
- Roberto Giannecchini, Università di Pisa, Dip. Scienze della Terra, (professore associato) <roberto.giannecchini@unipi.it>.

Esperto:

- Enzo Mantovani, Università di Siena <enzo.mantovani@unisi.it>.

Supplenti:

- Paolo Conti, Università di Siena, DSFTA (ricercatore) <paolo.conti@unisi.it>;
- Giancarlo Molli, Università di Pisa, Dip. Scienze della Terra (ricercatore) <giancarlo.molli@unipi.it>.

ABSTRACT

Dynamic characterization of soil and building, by using ambient vibration measures, is the main objective of this study. Passive methods have been implemented in local seismic response of the construction site and in calibration of finite element model of the building. Structural verifications are then realized for the building using response spectrum estimated both from standard (NTC08-DM 14/01/2008) and from local seismic response of the construction site.

Passive methods use ambient vibrations as natural load excitation, which contain all frequency band useful to excite natural frequencies of structures and soil. This lead to a wider use of ambient vibration measures for dynamic characterization of buildings and soil. For this purpose, ambient noise measures have been acquired in the free field near the construction area and inside the building, by the help of three components portable seismographs called Tromino™, by Micromed S.p.a.

The building under examination is a prefabricated reinforced concrete structure consisting of five floors above ground and one underground, located in Sanremo, province of Imperia in Italy. It has a strategic interest of regional competence, being a hospital, whose functionality during seismic events is of fundamental importance for the purposes of civil protection. Therefore, local seismic response of the construction site and dynamic characterization of building have a great importance in the future for building monitoring after an important seismic event.

The study area belongs to Helminthoid Flysch of the Western Liguria Alps and continues below with the tectonic unit of Sanremo-Monte Saccarello Flysch. The area of interest is located on the geological formation known as ‘Flysch of Sanremo’ with arenaceous clayey component in its lithofacies. This formation is characterized by an alternation of materials with rigid behavior (sandstones and siltstones) and by a small levels of plastic clayey-marl. During the project design of the building Vs data were deduced from penetrometric surveys by the use of empirical correlations, to evaluate the local seismic response. These, however, have dubious validity and thus, a more effective analysis is required to constrain the local Vs profile. An innovative technique has been applied on purpose. It is based on the analysis of ambient vibration measurements performed by two portable seismographs only (each composed by three directional geophones), placed at a distance of 50-70 m and synchronized by the GPS signal. These measurements allow the retrieval of the local Rayleigh waves dispersion curve and Horizontal to Vertical Spectral Ratios. These pieces of information are jointly inverted to determine the local Vs profile. Decay curves of each soil layer, stratigraphic profile and layer properties were identified from the bibliography and geologic report which was realized before the construction of the building and several seismic surveys carried out by the Municipality of Sanremo for different study purposes.

By considering this information, one-dimensional equivalent-linear analyses has been performed, to estimate the response spectrum of site. To this purpose and to account for uncertainty affecting available data, the effect of stochastic variation of the site properties have been evaluated by a suitable software. Finally, V_{s30} has been estimated to identify the soil class due to standards classifications.

The seismic response of the building to this seismic input has been evaluated. In particular, the dynamic behavior of the building has been identified by a Finite Element Modeling (Sap2000 software). The calibration of this model has been performed by a trial and error procedure aiming at fitting numerical outcomes (in the linear domain) to the dynamic properties of the building (natural frequencies and mode shapes) deduced empirically from ambient vibration measures. Experimental and operational methods (EMA and OMA) have been implemented aiming at evaluating the most efficient method to infer dynamic features from measurements. Passive seismic measurements have been performed in several verticals near the corners of the structure, in two different ways: first leaving the fixed instruments on

the top floor and second leaving the fixed one in free field. Two portable seismographs have been synchronized and then velocimetric measurements have been performed at all floors of the buildings. Furthermore, the ambient vibrations inside the building have been acquired in two different measurement sessions to evaluate the influence of the mass and stiffness added to the structure during its construction. Internal walls, floors layers, mechanical ventilation plant with associated machinery on the terrace have been added to the building when performed the ambient vibration measurements about 8 months later from the initial ones.

The method with iterative parameter has been used for the calibration of finite element model, by using the sensitivity of parameters that directly affect the dynamic properties. Best fitting between model outcomes and observations has been obtained by modeling the rigidity of external wall panels. These elements have shown to have an elevated influence on the complex stiffness of the structure. The concrete class has been set as described in the executive project for each structural elements, differently from the initial finite element model in which was put the same concrete class for all structural elements. Since this analysis is performed in the elastic range, the elastic modulus of concrete has been increased 25%, to match experimental and theoretical frequencies. Moreover, various elements and loads which weren't taken into account before, have been modeled. Finally, structural verification have been realized with calibrated FE model by using response spectrum estimated both from local seismic response and standard NTC08.

Furthermore, experimental and operational modal analysis have been also applied in historic masonry constructions (three historic Tower of San Marino) to estimate modal parameters. The lack of the project design in this case (material properties, dimensions and distribution of structural elements etc.), makes more difficult the calibration of finite element model (FEM). The calibration of the model has been realized only for the 'Montale' Tower, in collaboration with the University of San Marino which created first FEM by using 3D laser scanner technology for a complete survey of the building in 2D (floor plants and section) and in 3D data (point cloud of the tower).

The calibrated FE model can be used in the future in various structural engineering applications: health monitoring, structural monitoring, damage detection after an important seismic event etc.

RIASSUNTO

Lo studio consiste principalmente nella caratterizzazione dinamica del suolo e dell'edificio impiegando le misure di microtremore ambientale. I metodi passivi sono stati implementati nello studio della risposta sismica locale del sito e nell’identificazione dei parametri modali dell'edificio ubicato nello stesso sito. In ultimo, vengono eseguite delle verifiche strutturali utilizzando sia lo spettro di risposta sismica locale del sito che quello fornito dalle norme tecniche per le costruzioni (NTC08-DM 14/01/2008).

I metodi passivi utilizzano le vibrazioni ambientali come carico naturale di eccitazione, il quale contiene tutto l’intervallo delle frequenze utile per eccitare le frequenze naturali dell’edificio e del terreno. Quest’ultimo ha portato ad una ampio utilizzo delle misure di vibrazioni ambientali nella caratterizzazione dinamica dell’edificio e del terreno. A tale scopo, le misure di rumore ambiente sono state acquisite in campo libero vicino alla zona della costruzione e all'interno dell'edificio, con l'aiuto dei sismografi portatili chiamati Tromino™, da Micromed S.p.a.

L'edificio preso in esame è una struttura in calcestruzzo armato prefabbricata costituita da quattro piani, piano terra seminterrato ed un piano completamente interrato. La struttura è il Nuovo Palazzo della Salute del comune di Sanremo in Provincia di Imperia in Italia. Essendo un ospedale ha un interesse strategico di competenza regionale la cui funzionalità durante gli eventi sismici è di fondamentale importanza ai fini della protezione civile. Pertanto, la risposta sismica locale del sito e la caratterizzazione dinamica dell’edificio hanno un importanza rilevata nel monitoraggio della struttura in un futuro dopo un importante evento sismico.

L’area di interesse appartiene alla Falda dei Flysch ad Elmintoidi delle Alpi Liguri Occidentali e in sottordine all'unità tettonica del Flysch di Sanremo-Monte Saccarello. L’area della costruzione risulta appoggiata alla Flysch di Sanremo, nella sua litofacies a componente arenaceo argillosa. Questa formazione è caratterizzata dalla fitta alternanza di materiali a comportamento rigido (arenarie e siltiti) e da livelletti argillo-marnosi plastici. Durante la fase di progettazione dell'edificio, i dati delle Vs, per stimare la risposta sismica locale, sono stati dedotti da dati penetrometrici per mezzo di correlazioni empiriche. Queste ultime, tuttavia, hanno una validità dubbia e pertanto è necessaria un'analisi più efficace per ottenere il profilo delle Vs locale. A tale proposito, è stata appositamente applicata una tecnica innovativa che si basa sull'analisi delle misure di vibrazioni ambientali acquisite da due sismografi portatili (ciascuno composto da tre geofoni direzionali), posizionati ad una distanza di 50-75 m e sincronizzati tra di loro tramite il segnale GPS. Tale misure consentono di ottenere la curva di dispersione locale delle onde di Rayleigh e quella dei rapporti spettrali tra la componente orizzontale e quella verticale del moto del suolo. Queste informazioni vengono invertite congiuntamente per determinare la variazione in profondità delle velocità di propagazione delle onde di taglio (Vs). Questa informazione è necessaria per la stima dei possibili effetti di amplificazione del moto del suolo in occasione di futuri terremoti. Altre grandezze necessarie a questo genere di stima (curve di decadimento per i materiali presenti, profilo lito-stratigrafico) sono state dedotte dalla bibliografia, dalla relazione geologica che fu realizzata prima della costruzione dell'edificio e da diverse indagini sismiche effettuate dal Comune di Sanremo per vari motivi di studio.

Successivamente sono state utilizzate tali informazioni per effettuare l'analisi lineare equivalente uni dimensionale della risposta sismica locale allo scopo di stimare lo spettro di risposta caratteristico del sito analizzato. A tal fine e per tenere conto dell'incertezza dei dati disponibili, è stato valutato l'effetto della variazione stocastica delle proprietà del sito con l'aiuto di un software adeguato. Infine, è stato stimato il valore medio della velocità di propagazione delle onde nei primi 30 metri di sottosuolo (V_{s30}) per identificare la classe di appartenenza del terreno secondo la classificazione delle norme tecniche per le costruzioni.

La risposta sismica dell'edificio è stata stimata utilizzando come input sismico lo spettro di

risposta locale. In particolare, il comportamento dinamico dell'edificio è stato valutato con l'utilizzo del modello degli elementi finiti (software Sap2000). La calibrazione di questo modello è stata effettuata tramite una procedura ‘per tentativi ed errori’ che ha avuto l'obiettivo di adattare i risultati numerici (nel dominio lineare) con le proprietà dinamiche dell'edificio (frequenze naturali e forme di modo) dedotte empiricamente dalle misure di vibrazioni ambientali. Sono stati implementati due metodi sperimentali ed operativi (EMA e OMA) allo scopo di definire quello più efficiente nella stima delle caratteristiche dinamiche dalle misure di vibrazioni ambientali. A tale proposito, le misure di sismica passive sono state acquisite nelle diverse verticali vicino agli spigoli della struttura, con due modalità differenti: prima lasciando uno degli strumenti fisso all'ultimo piano e spostando l'altro strumento ai vari piani della struttura e il secondo lasciando lo strumento fisso in campo libero e spostando l'altro strumento ai vari piani dell'edificio. I due sismografi portatili sono stati sincronizzati tra di loro in modo tale da acquisire contestualmente misure di velocità di scuotimento su tutti i piani dell'edificio. Inoltre, le vibrazioni ambientali all'interno dell'edificio sono state acquisite in due periodi diversi durante la costruzione dell'edificio e questo ha permesso di valutare l'influenza della massa e della rigidità aggiunta alla struttura (pareti interne, gli strati dei pavimenti, l’impianto di ventilazione meccanica con il relativo impianto posto all’ultimo piano dell’edificio).

Il metodo con parametro iterativo è stato utilizzato per la calibrazione del modello degli elementi finiti. Il metodo utilizza allo scopo la sensibilità dei parametri che influenzano direttamente sulle proprietà dinamiche della struttura. Il migliore accordo tra i risultati del modello FE e le osservazioni è stato ottenuto modellando la rigidezza delle mura esterne. Questi elementi hanno dimostrato di avere un'influenza elevata sulla complessa rigidezza della struttura. La classe del calcestruzzo è stata impostata come descritto nel progetto esecutivo per ogni elemento strutturale, diversamente da come era impostata nel modello FEM iniziale: la stessa classe per tutti gli elementi strutturali. Tenendo conto che l'analisi sperimentale è stata eseguita in campo elastico, il modulo elastico del calcestruzzo è stato aumentato fino al 25%, in modo tale da poter confrontare le frequenze sperimentali con quelle teoriche. Inoltre, sono state modellati vari elementi e carichi che non erano prima presi in considerazione. Infine, sono state realizzate verifiche strutturali con il FEM calibrato, utilizzando lo spettro di risposta stimato sia dalla risposta sismica locale che dalle norme tecniche per le costruzioni NTC08.

La procedura di analisi utilizzata per Sanremo è stata applicata anche allo studio di tre costruzioni storiche di muratura nel territorio della Repubblica di San Marino per stimare i parametri modali. La mancanza del progetto di calcolo e/o esecutivo in questo caso (le proprietà dei materiali, le dimensioni e la distribuzione degli elementi strutturali, ecc.), ha reso più difficile la calibrazione del modello agli elementi finiti (FEM). Questa è stata realizzata esclusivamente per uno dei tre edifici (la Torre 'Montale'), in collaborazione con l'Università di San Marino che ha creato il modello ad elementi finiti iniziale utilizzando la tecnologia 3D laser scanner che ha permesso di avere un'indagine completa della torre in 2D (piante e sezioni) e 3D (nuvola di punti).

Il modello agli elementi finiti così calibrato potrà essere utilizzato in un futuro in varie applicazioni di ingegneria strutturale: monitoraggio della salute, controlli strutturali, rilevamento dei danni e conformità strutturale dopo un importante evento sismico ecc.

INDEX

List of abbreviations

DM	Ministerial decree
EMA	Experimental modal analysis
EC8	Eurocode 8
ESAC	Extended spatial auto-correlation
FEM	Finite element model
FFT	Fast Fourier transform
FRF	Frequency response function
GA	Genetic algorithms
HVSR	Horizontal to vertical spectral ratio
MDOF	Multiple degree of freedom
NASW	Noise analysis of surface waves
NTC08	Technical standard for the construction, 2008
OPCM	Order of the president of the council of ministers
OMA	Operational modal analysis
PSD	Power spectral density
PSHA	Probabilistic seismic hazard analysis
RSL	Local seismic response
RC	Reinforced concrete
SVD	Singular value decomposition
SPAC	Spatial Autocorrelation method
SDOF	Single degree of freedom

I. INTRODUCTION

The identification of dynamic characteristics such as natural frequencies, mode shapes, and modal damping, is an important task during seismic design of civil engineering structures. Furthermore, the local seismic response is another important task in the identification of seismic input for the construction area, which can be used then for seismic structural verifications of the building, in the presence of earthquakes. Solving both tasks by using ambient vibration tests, leads to economic and faster solutions from the traditional ones, which are briefly described below.

The most popular methods for the identification of seismic-stratigraphic profile of Vs consist on surface wave tests, seismic borehole surveys and array measurements of ambient seismic noise (Albarello et al., 2011; Foti et al., 2011; Ali et al., 2006; Adel et al., 2013; Di Giulio et al., 2014; Shapiro et al., 2005; Mucciarelli et al., 2007; Mucciarelli et al., 2008). The shallow S-wave velocity is very important for the seismic design of engineered structures and facilities, seismic hazard evaluation of a region, comprehensive earthquake preparedness, development of the national seismic hazard map, and seismic-resistant design of buildings. The use of ambient vibration wavefield for the characterization of the shallow subsurface has become of growing interest to geotechnical engineers and geophysicists in the frequency range of engineering interest between 0.5-20 Hz. Furthermore, the V_S profile is of paramount importance for seismic site response, soil-structure interaction and seismic microzonation studies. In particular, it allows to assess the dynamic characteristics and to derive a quantitative analysis of seismic amplification of the investigated site. This amplification effect is often based on the average shear wave velocity estimated in the first 30 m of subsoil; this parameter, object of several scientific disputes (e.g., Gallipoli and Mucciarelli, 2009), is commonly defined as V_{S30} (Eurocode 8). Horizontal to Vertical Spectral Ratios (HVSR) and Rayleigh wave dispersion curves are strictly related to the V_S profile of the site, which can be extracted from these measurements by means of an inversion procedure which provide detailed quantitative information about the dynamic characteristics of the subsoil.

Several authors studied efficiency of passive methods by comparing their outcomes with the ones of other methods. For example, Foti (2000, 2003) compared the results from surface wave tests (SWM) and borehole tests (cross-hole test, CHT), which show the reliability of both methods (see Figure 1.1). With respect to the evaluation of seismic site response, it is worth noting the affinity between the model used for the interpretation of surface wave tests and the model adopted for most site responses study. The application of equivalent linear elastic methods is often associated with layered models, (see, e.g., the code SHAKE by Schnabel et al., 1972). This affinity is also particularly important in the light of equivalence problems, which arise because of the non-uniqueness of the solution in inverse problems. Indeed, profiles which are equivalent in terms of Rayleigh wave propagation are also equivalent in terms of seismic amplification (Foti et al., 2009).

Many seismic building codes introduce the weighted average of the shear wave velocity profile in the shallowest 30 m to discriminate classes of soil where similar site amplification effect can be associated. $V_{S,30}$ can also be evaluated very efficiently with surface wave methods because its average nature does not require the high resolution provided by seismic borehole methods, such as Cross-Hole tests and Down-Hole tests (Moss, 2008; Comina et al., 2011).

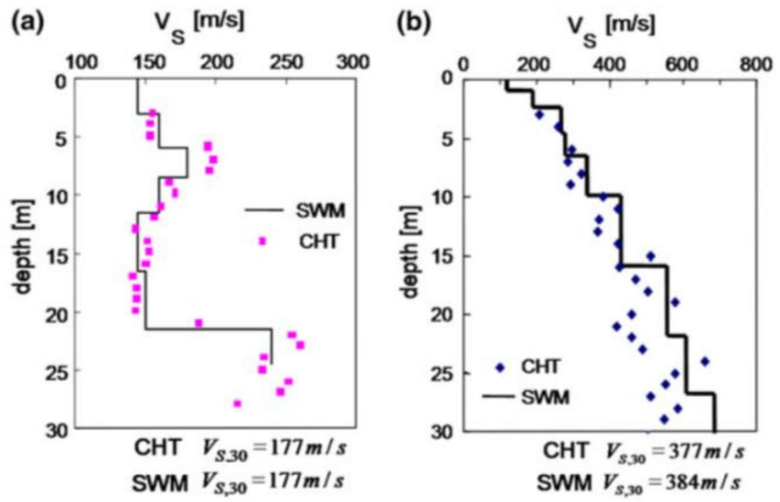

Figure 1.1 *Shear wave velocity profiles and the equivalent $V_{S,30}$ value: a) Leaning Tower of Pisa site (data from Foti 2003); b) Saluggia site (data from Foti 2000)*

The main type of surveys used to achieve dynamic behavior of engineering structures, rely on ambient vibration tests, forced vibration tests and earthquake response measurement. Among these field procedures, ambient vibration tests are the most commonly used as they are economic, non-destructive, fast and easy to be performed, and also can be carried out during the normal functionality of buildings. However, as the input excitation in ambient vibration tests is usually weak, these tests are not as effective in obtaining an accurate estimation of the higher modes data, and uncertainties remain as to whether the modal information applies in the higher strain ranges (Ventura et al., 2002). Forced vibration tests overcome these problems by providing higher input forces, but have other restrictions: are substantially more expensive, necessitate more time for their performance and often require special permissions as there is an increased likelihood of damaging the structure. As ambient vibration testing is output driven, it is highly cost effective and is regarded as being harmless to the integrity of the structure (Endrun et al., 2010; Celebi, 2009; Celebi et al., 2010). Several Authors, have studied the reliability of ambient vibrations measurements for dynamic identification of structures by comparing relevant outcomes with structure response achieved from forcing measures (Beskhyroun et al., 2013; Lamarche et al., 2008; Taleb at al., 2012). Strong correlation between modal parameters from both implemented methods have been found. For example, the Lamarche et al. (2008) studied the dynamic behavior of a 13-story reinforced concrete building under forced vibration, ambient vibration and distal earthquake excitation. An eccentric mass shaker located on the upper floor of the building was used to excite the building, while ambient vibrations were recorded over a period of two weeks utilizing over 40 tri-axial accelerometers. During this period the building was also excited by a M6.5 earthquake roughly 350 km away and high quality acceleration data was recorded. A good agreement were obtained between modal parameters identified through ambient vibrations and the forced vibration analyses, providing so that ambient vibration testing can be as effective as forced vibration testing in determining modal parameters for similar structures.

Generally, civil engineering structures can be adequately excited by wind, traffic, and human activities and the resulting motions can be readily measured with highly sensitive instruments. Expensive and cumbersome devices to excite the structure are therefore not needed. Consequently, the overall cost of the measurements conducted on a large structure is reduced (Ventura et al., 2000; Ventura et al., 2002).

Output-only method is generally used to identify modal parameters, as in ambient vibration measurements, the input force is unknown. Some researchers suggest that output-only analysis is superior with multiple-input data and the distribution of the input forces across the structure may affect the quality of the identified modal parameters (Au et al., 2012; Brownjohn, 2003). Researchers also emphasize that for output-only analysis to be successful it is important to have sufficient quality data with good signal-to-noise ratio (Brincker et al., 2003; Brincker et al., 2000). Another important issue that needs further investigation is whether output-only analysis can work well in both the time and frequency domains.

In this Thesis, ambient vibration measurements have been utilized to perform the LSR (Vs profile of local shear-wave velocity profile and the local response spectrum) of the construction site, and to identify the modal parameter of the reinforced concrete building (modal frequencies and mode shapes) which is constructed at the same area, in Sanremo, Northern Italy. This study consisted mainly on three steps: the estimation of the response spectrum of site, the calibration of finite element model of the building and structural verifications by using both the response spectrum estimated on site and from NTC2008. The first two steps have been realized by passive methods that use ambient vibrations acquired by the help of two seismic portable geophones.

The use of only two sensors, which acquired simultaneously ambient vibration measures in the free field or inside the building, is the newness of this study, when using passive methods for dynamic characterization of soil and buildings. Therefore, the Rayleigh phase velocity dispersion curve, has been estimated by comparing ambient vibrations measures at two stations (SPAC zero crossing method). Seismic-stratigraphic profile of Vs waves has been obtained then from the inversion of the phase velocity of surface waves, and subsequently the spectrum response of the site on the surface has been determined by the equivalent linear analysis.

In case of the dynamic characterization of the building, modal frequencies and mode shapes have been estimated by synchronized pairs of ambient vibration measures acquired to the various floors of the structure in two different procedures: first leaving the fixed instrument on the top floor and moving the other one in the other floors, and second, leaving the fixed seismograph in free field and moving the other one inside the building. Therefore, experimental and operational modal analysis (EMA, OMA) have been performed to identify modal parameters. Finally, the calibrated finite element model, achieved by comparing experimental and theoretical responses, has been used to seismic structural verifications.

1.1 General overview of the study

The use of ambient vibrations in the dynamic characterization of the subsoil starts from 1979, while their application in dynamic characterization of buildings is extended in the last decade thanks to their propriety to contain a wide frequency band useful to excite natural frequencies of structures. This leads to a wider use of ambient noise as are natural excitation reducing so the costs of analysis.

The application of passive methods on the dynamic characterization of soil and building is the main objective of this dissertation. The study is structured on three main steps, which consist of:

- Local seismic response of site when the building is constructed;
- Calibration of FEM of building;
- Structure verification of the building by using the response spectrum estimated.

Ambient vibration measures, acquired in the free field and inside the building by two portable seismographs, have been exploited. The dispersion curves of soil and mode shapes of building have been estimated experimentally. ESAC2015 code based on the SPatial AutoCorrelation zero crossing method has been used to achieve the Rayleigh phase velocity dispersion curve between two sensors (two synchronized portable seismographs). This method is based on the spatial autocorrelation analysis and derived from SPAC method. Seismic stratigraphic profile (1D model) has been estimated then by the inversion procedure with

'GAinvers6 code'. Finally, the response spectra and 1D-Vs model have been estimated performing one-dimensional equivalent linear analysis on 'STRATA' software.

Experimental and operational modal analysis (EMA and OMA) have been applied to estimate the dynamic behavior of building. Confronts between OMA and EMA methods have been realized at the aim to estimate their applicability in the identification of the modal parameters At this aim, two case study have been taken into account. The first case study is a reinforced concrete structure in Sanremo, while the second one are the three historic towers in San Marino.

1.2 Research methodology

The research methodology consists mainly in the use of synchronized pairs of ambient vibration measures for the estimation of the dispersion curves of soil and mode shapes of the building.

Dispersion curve has been estimated from experimental data, acquiring pairs of synchronized ambient vibration measures with two portable seismographs. The vertical profile of Vs has been then identified by solving the inverse problem and successively, the response spectrum of site by an equivalent linear analysis. Local seismic response of construction site has been estimated by the help of ambient vibration measurements acquired with two synchronized portable seismographs, each one equipped with three directional geophones. Geophones, synchronized with GPS signal, have been placed at a distance of about 75 m and have acquired for 30 minutes.

The directionality of the signal may be a problem when using two-station method. Therefore, the knowledge of the location, using previous investigations and detailed stratigraphic sections are important parameter, to identify the correct dispersion curve.

The response spectrum estimated on site is then considered for estimating the seismic response of the building.

Mode shapes of the building have been identified thanks to the use of synchronized ambient vibration measures. Experimental and operational modal analysis (EMA and OMA) have been applied to estimate the dynamic behavior of building. These two procedures have been compared to identify the most effective one when two single stations are considered for measuring structural response to ambient vibrations. Furthermore, another method has been applied by analyzing separately each synchronized pair of measures at the aim to evaluate the influence in modal parameter results of the non-simultaneously acquisition of measures in all floors.

Iterative parameter method has been used for the calibration of the finite element model, by varying parameters that directly affect the dynamic properties. The finite element model has been calibrated by comparing the dynamic response experimentally identified with those from theoretical dynamic response (finite element model, Sap2000).

Structural verifications have been then realized, using the estimated response spectrum and the calibrated FE model.

II. AMBIENT VIBRATIONS

Ambient vibrations, also called 'seismic noise' or 'microtremors', are small vibrations always present at the surface of the Earth even in absence of the earthquakes. The term ‘seismic noise’ derived from seismology, which considers it as a continuous noise with weak intensity that can significantly disturb earthquake recordings. Seismologists define as 'microseisms' the natural vibrations with frequencies lower than 1 Hz. Instead, in earthquake engineering the term ‘microtremors’ is used for signals with frequencies greater than about 1 Hz. Recently, the term ‘ambient vibrations’ has been adopted in several disciplines (geology, applied geophysics, oil exploration and earthquake engineering) where this phenomenon can be used as an input signal in different analysis. The ambient noise is ubiquitous and includes both natural and anthropic small vibrations, without distinctions about their spectral content. Its displacement amplitude is generally very small in the order of 10^{-4} to 10^{-2} mm (Okada, 2003), much lower than human sensitivity, and varies greatly between different sites and different frequencies.
The use of ambient vibrations in the dynamic characterization of the subsoil starts from 1979, while their application in the Seismic Microzonation studies from 1990 (Pilz et al., 2015). In the last decade, their use is extended also in the dynamic characterization of buildings, structural monitoring, damage detection etc. This is possible as ambient vibrations can adequately excite natural frequencies of structures (Ventura et al., 2002), which leads to a wider use of them as are natural excitation reducing so the costs of analysis.

2.1 Origin of ambient vibrations

The origin of ambient vibrations may be natural or anthropic (Gutenberg, 1958; Asten, 1978; Shearer, 1999; Bonnefoy-Claudet, 2006 a), therefore, they are generated by natural sources (ocean currents, tides, waves striking the coasts, wind, atmospheric pressure variations, water flow in rivers etc.) and anthropic sources (power plants, factories, cars, human footsteps, trains) which contribute in the different spectral domains (Table 2.1):

- at frequencies below 0.5 Hz, the sources are essentially natural, defined as *microseisms* from various authors;
- in the frequency range between 0.5 Hz and 1 Hz (f_{nh}) (see Table 2.2), the sources are both natural and anthropic;
- at frequencies higher than 1 Hz, the origin is predominantly related to human activities (traffic, machinery) (Shearer, 1999) and may also be associated with wind and water flows (Okada, 2003). These waves are generally called *microtremors* by engineers. Their sources are mostly located at the surface of the earth (except some sources like metros), and often exhibit a strong day/night and week/weekend variability.

Table 2.1 *Summary of ambient vibrations sources according to frequency (Gutenberg, 1958; Asten, 1978; Asten and Henstridge, 1984 (from Bennefoy-Claudet, 2006 a))*

	Gutenberg (1958)	Asten (1978 - 1984)
Waves striking the coast	0.05 - 0.1 Hz	0.5 - 1.2 Hz
Moonson/large scale meteorological perturbations	0.1 - 0.25 Hz	0.16 - 0.5 Hz
Cyclones over the ocean	0.3 - 1.0 Hz	0.5 - 3.0 Hz
Local meteorological conditions	1.4 - 5 Hz	
Volcanic tremor	2 - 10 Hz	
Urban	1 - 100 Hz	1.4 - 3.0 Hz

Various authors have studied over the years the ambient vibration characteristics which are summarized in the Table 2.2 (Pei, 2007). Generally, lower frequency waves (< 0.1 Hz) are often associated to atmospheric movements or excitation by oceans (Rhie and Romanowicz, 2004). Extracting information from microseisms is easier on islands than in the heart of continental areas because the energy at frequencies between 0.1 Hz and 1.0 Hz decreases with increasing distance from oceans (SESAME, 2004). High frequency waves generally have much closer sources, which most of the time are located very close to the surface. Furthermore, the wavefield in the immediate vicinity (less than a few hundred meters) includes both body and surface waves, while at longer distances surface waves become predominant (Lay and Wallace, 1995). Only little information is available on the quantitative proportions between body and surface waves, and the different kinds of surface waves that may exist. Few available results, reviewed in Bonnefoy-Claudet et al. (2006 a), report that low frequency microseisms predominantly consist of fundamental mode Rayleigh waves, while there is no real consensus for higher frequencies (> 1 Hz). Some investigations on the relative proportion of Rayleigh and Love waves shows a slight trend toward a slightly higher energy carried by Love waves (around 60% - 40%) (SESAME, 2004).

Table 2.2 *Summary of seismic noise characteristics (Pei, 2007; Shearer, 1999; SESAME, 2004; Lay and Wallace, 1995; Okada, 2003; Bonnefoy-Claudet et al., 2006 a)*

	Natural	Human
Name	Microseism	Microtremor
Frequency	0.1 - f_{nh}	f_{nh} - 10 Hz
Origin	Ocean	Traffic, Industry, Human activity
Incident wavefield	Surface waves	Surface and body waves
Amplitude variability	Related to oceanic storms	Day - Night
Rayleigh, Love issue	Incident wavefield predominantly Rayleigh	Comparable amplitude – slight indication that Love waves carry a little more energy
Fundamental, Higher mode issue	Mainly Fundamental	Possibility of higher modes at high frequencies (at least for 2-layer case)
Further Comments	Local wavefield may be different from incident wavefield	Some monochromatic waves related to machines and engines. The proximity of sources, as well as the short wavelength, probably limits the quantitative importance of waves generated by diffraction at depth
Note: f_{nh} = 0.5 - 1.0 Hz		

2.2 Ambient vibrations

In general, ambient vibrations are constituted by different seismic phases, including Body waves (propagating within the Earth) and Surface Waves (propagating along the Earth's surface). In general, propagation velocities of seismic phases depend on the mechanical properties of the subsoil (bulk density, rigidity and incompressibility). The presence of interfaces where significant variations in the mechanical properties of the subsoil exist, significantly affect the propagation of seismic phases.

All the four seismic phases (P, S, R and L waves) are non-dispersive in a homogeneous medium. (i.e., their propagation velocity does not depend of their frequency). *P* wave speed is the highest, typically 400 m/s to 800 m/s for soft outcropping soils. The *S* wave is somewhat slower than the *P* wave and only slightly faster than the surface waves (200-300 m/s for soft outcropping soils). In the ideal case, when the ground is homogenous, the longitudinal and shear waves propagate in all directions away from the source, and hence suffer substantial geometric attenuation, as well as losses due to the damping properties of the ground. Surface waves do not suffer the same geometric attenuation (they propagate along the Earth's surface) but are still subject to loss by damping.

P and *S* waves spread with hemispherical wave fronts in the ground, their decay rate is inversely proportional to the distance from the source. *R* and *L* waves spread on a circular wave front with a decay rate inversely proportional to the square root of distance from the source. This reduction in amplitude with distance is called geometric decay. Material damping will also influence the rate at which energy decays with distance from the excitation point. In practice, the ground is far from being homogenous and mechanical heterogeneities existing along all the directions. In this situation, surface waves exhibit dispersion and several propagation modes come into the play. Depending on subsoil configuration, the vibration energy is not shared equally among the modes. Because of different geometric attenuations, the Rayleigh wave carries most of the vibration energy far from the source. Due to material damping, high frequencies are attenuated much more rapidly than low frequencies, so that low frequencies dominate the spectrum at distances of more than a few meters from the source (Chung and Bernreuter, 1981; Suhairy, 2000).

2.2.1 Body waves

The first kind of body wave is the *P wave or primary wave*. This is the fastest kind of ground wave. *P* waves travel at speeds between 1 km/s and 14 km/s within the Earth, which depend on the rock type. The motion produced by a *P* wave is an alternating compression and expansion of the material as illustrated in the Figure 2.1, left. Studying the equation of motion of an element can be determined the parameters and properties of baby waves.

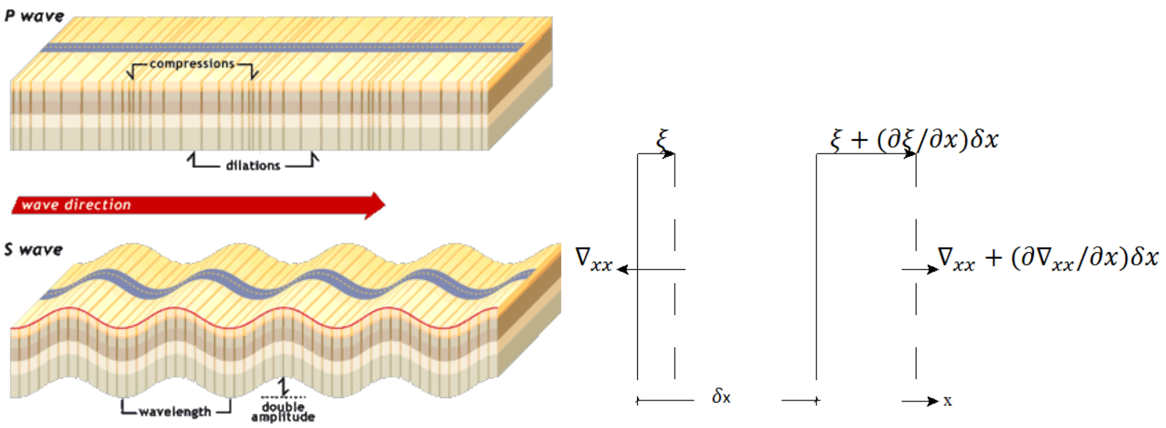

Figure 2.1 *Body wave representation (left), scheme of motion of a ground soil element (right)*

Heaving a pure longitudinal wave motion, the waves can propagate in large volume of solids. Two parallel planes of an undisturbed solid elastics medium, which are separated by a small distance δ_x, may be moved by different amounts during the passage of a longitudinal wave (see Figure 2.1, right). The element may undergo a strain ε_{xx} given by:

$$\varepsilon_{xx} = \frac{\partial\xi}{\partial x} \qquad \text{(Eq. 2.1)}$$

which is proportional to the longitudinal stress σ_{xx} according to Hook's law. In cases that one dimensional longitudinal wave propagates in a solid medium, there can be no lateral strain because all material elements move purely in the direction of the propagation. The ratio $\sigma_{xx}/\varepsilon_{xx}$ is not equal to *E* (Young's modulus), as the complete behavior of a uniform elastic medium shows that the ratio of longitudinal stress to longitudinal strain depend by *E* and Poisson ratio:

$$\sigma_{xx} = B\frac{\partial \xi}{\partial x} \quad \text{(Eq. 2.2)}$$

where $B = \frac{E(1-\upsilon)}{(1+\nu)(1-2\nu)}$

The equation of motion of an element in this case is:

$$(\rho \cdot A \cdot \delta x)\frac{\partial^2 \xi}{\partial t^2} = \left(\sigma_{xx} + \left(\frac{\partial \sigma_{xx}}{\partial x}\right)\delta x - \sigma_{xx}\right) \cdot A = \left(\frac{\partial \sigma_{xx}}{\partial x}\right)\delta x \cdot A \quad \text{(Eq. 2.3)}$$

where ρ is the material mean density (the earth density).

Equation 2.2 and 2.3 can be combined into the wave equation:

$$\frac{\partial^2 \xi}{\partial t^2} = \left(\frac{\rho}{B}\right)\frac{\partial^2 \xi}{\partial t^2} \quad \text{(Eq. 2.4)}$$

The general solution of Equation 2.4, which has the same form as the equation of one dimension acoustic wave, shows that the phase speed C_l:

$$C_l = \left(\frac{B}{\rho}\right)^{1/2} \quad \text{(Eq. 2.5)}$$

is independent of frequency. The compression waves velocity can also written in the form:

$$c_p = \sqrt{\frac{\lambda+2\mu}{\rho}} \quad \text{(Eq. 2.6)}$$

where μ=G

$$\lambda = \frac{E\upsilon}{(1+\nu)(1-2\nu)}$$

where λ is the Lame's elastic constant of the medium, *G* is the shear stiffness, *E* is the Young's modulus, υ is the Poisson's coefficient, ρ is the mass density.

The second type of body wave is the *S wave or secondary wave* (Shear waves), which is slower than *P* wave and can only move through solid rock. This wave moves rock up and down, or side-to-side (see Figure 2.1). Shear waves travel with a speed c_s equal to:

$$c_s = \sqrt{\frac{\mu}{\rho}} \quad \text{(Eq. 2.7)}$$

The shear modulus *G* is related to Young's modulus *E* by:

$$G = \left(\frac{E}{2(1+\nu)}\right) \quad \text{(Eq. 2.8)}$$

2.2.2 Surface waves

In an infinite homogeneous isotropic medium, only body waves exist and instead at least one interface (e.g., the Earth's surface) is necessary for the surface wave existence (Aki and Richards, 2002). However, when the medium does not extend to infinity in all directions, surface waves (known in seismic exploration as 'ground roll') can be generated (Figure 2.2, left).

The primary type of surface waves is the *Rayleigh wave* named from Lord Rayleigh (John William Strutt), who mathematically predicted the existence of this kind of wave in 1885. This wave travels along the surface of the Earth and involves an interference of *P* wave and *S* wave. Amplitude of Rayleigh wave motion decreases exponentially with depth (Figure 2.2, right). Rayleigh waves velocity varies with wavelength (called dispersion curves), because of the existence of vertical medium-velocity gradients: longer period waves propagate faster when rigidity increases with depth.

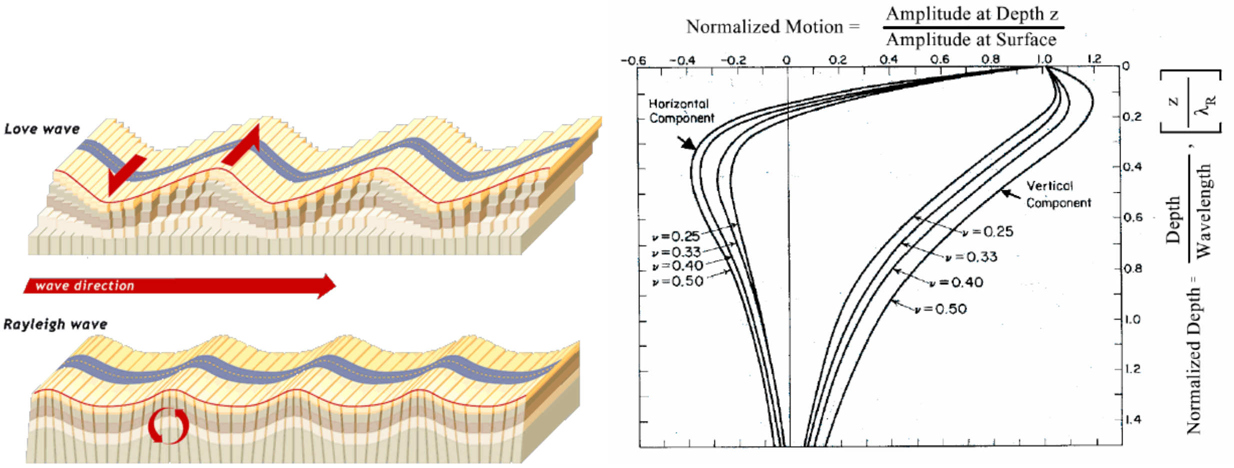

Figure 2.2 *Surface waves (left), Variation of horizontal and vertical normalized components of displacements induced by Rayleigh waves with normalized depth in a homogeneous isotropic, elastic half-space (right) (Richart et al.,1970)*

Rayleigh wave is a result of the interaction of *P* and *S* waves under the following particular conditions:

- the wave motion associated with the Rayleigh waves rapidly attenuates with depth;
- no stresses exists at the free interface.

The propagation velocity of the Rayleigh wave c_R, on the free surface of the homogeneous half-space, is slightly lower than the speed of the shear waves c_s (from 0.862 c_s to 0.955 c_s) and depends on the Poisson coefficient ν (Achenbach, 1999):

$$c_R = \frac{0.862+1.14\nu}{1+\nu} c_S \qquad \text{(Eq. 2.9)}$$

Into a homogeneous half-space the phase velocity of Rayleigh wave does not depend on the frequency or on the wave number k, hence dispersion does not happen. Horizontal and vertical components are 90° out of phase and generate an ellipse during their propagation (Figure 2.2, right). The major axis of the ellipse is parallel to the free surface down to a depth of about 0.2 λ (λ is the wavelength), where the horizontal displacement changes its sign and the orientation of the axes.

The second type of surface wave is the *Love wave* named after A.E.H. Love (Augustus Edward Hough Love), a British mathematician who worked out the mathematical model for this kind of wave in 1911. These phases exist only in the case that at least one interface exists in the ground below the Earth's surface. Love waves are formed through the constructive interference of high order *SH* multiples. The particle motion are linearly polarized in the direction of *SH* waves (i.e., *S* waves polarized in the horizontal plane). The amplitude of this wave motion decreases exponentially with depth. They exhibit dispersion as well. It is the fastest surface wave. Love waves are dispersive, therefore, the phase velocity depends on the frequency associated to the wave.

Geometrical spreading for surface waves is proportional to $r^{-0.5}$ (see Figure 2.5) in contrast to the body wave where it is proportional to r^{-1}, being r the distance from the source (Anderson, 1991). The amplitude of surface waves decreases exponentially with depth. In a *homogeneous medium*, the wavelengths have the same velocity. In other words, Rayleigh waves are non-dispersive and Love waves do not exist in a homogeneous medium. The propagation of surface waves in a *vertically heterogeneous medium* shows a dispersive behavior. Dispersion means that different frequencies have different phase velocities. Each wavelength propagates at a phase velocity depending on the mechanical properties of the layers involved in the propagation. So the surface wave does not have a single velocity, but a phase velocity that is a function of frequency. This relation between frequency and phase velocity is called a *dispersion curve* and depends on the geology underneath.

Generally, longer wavelengths penetrate deeper than shorter wavelengths for a given mode and are more sensitive to the elastic properties of the deeper layers. Thus, for a profile where *S* wave velocity increases with depth, a normal dispersion curve (phase velocities decrease with frequency) will be observed. For a profile where *S* wave velocity decreases with depth, a reverse dispersion curve (phase velocities increase with frequency) will be observed. In an irregular *S* wave velocity profile, the phase velocities show a complex relation with frequency (Figure 2.3). In reality, the *S* wave velocities increase with depth in most geological structures.

The surface wave propagation in vertically heterogeneous media is actually a multi-modal phenomenon. For a given geology, at each frequency different wavelengths can exist (Figure 2.4, left). Hence different phase velocities are possible at each frequency, each one corresponding to a mode of propagation. Different modes can exist simultaneously (Figure 2.4, right). Except the first one, modes exist only above their cut-off frequency, which is the lowest limit frequency at which the mode can exist (Aki and Richards, 2002).

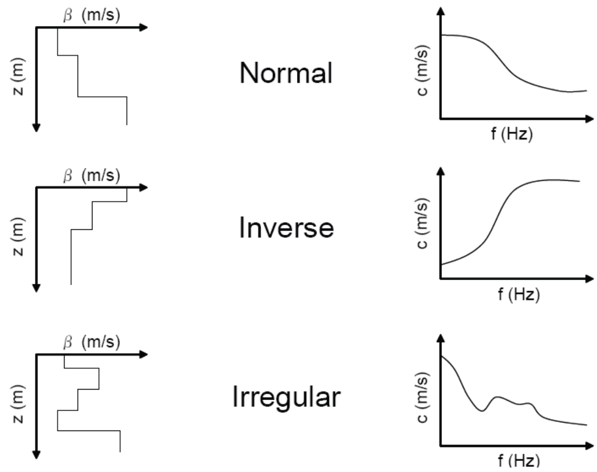

Figure 2.3 *Phase velocities versus frequencies*

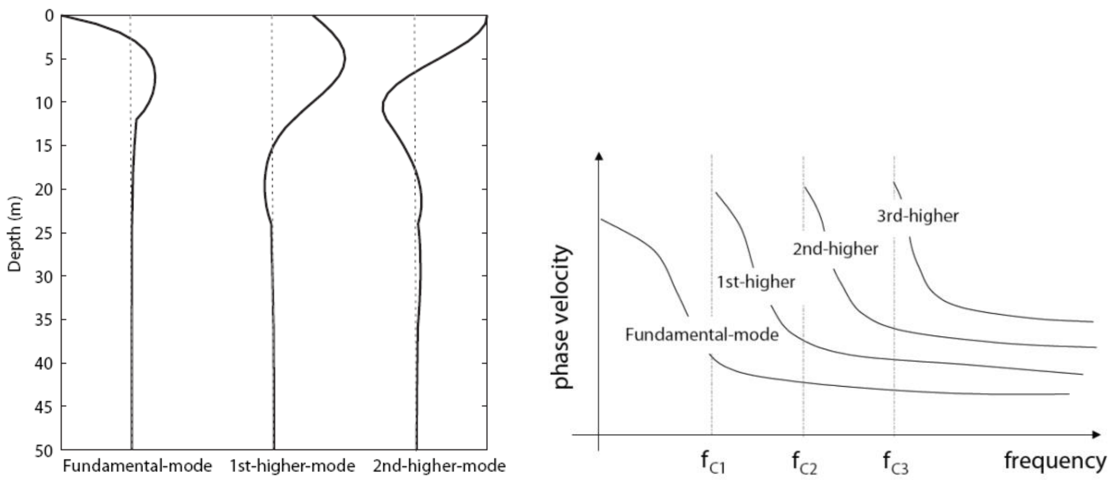

Figure 2.4 *Modes of surface waves for the same frequency (left), Dispersion curves of higher-mode surface waves (right) (Aki and Richards, 2002)*

Modes are not just theory or mathematically possible solutions; they are often observed in experimental data, also in the frequency range of interest for engineering purposes. The energy associated to each different modes depends on many factors: the seismic properties of subsoil materials, the depth of layers and the kind of source. The first mode is sometimes dominant over a wide frequency range, but in many common situations higher modes play important roles and are dominant in energy. Also, the modal superposition should be considered.

2.2.3 The contribution of seismic phases to ambient vibrations

The distribution of energy between the different kinds of waves have been estimated by Miller and Pursey (1955), for an elastic half space model excited by a vertically oscillation (see Figure 2.5). The total input energy is radiated 67% as *R* waves, 27% as *S* waves, and 7% as *P* waves.

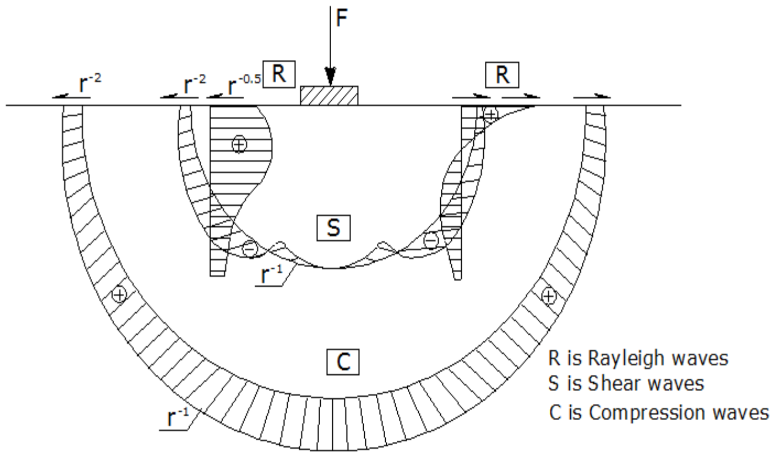

Wave type	Total energy (%)
Rayleigh	67
Shear	27
Compression	7

Figure 2.5 *Waves generated by a vertical harmonic load on a homogeneous half-space and energy distribution among them for a Poisson ratio of 0.25 (Richart et al., 1970; Miller and Pursey, 1955)*

The surface waves (R waves and Love waves) are of main interest for the present study. Various authors studied the quantitative proportions between body and surface waves. Kohler et al. (2007) suggest a composition of 90% Love waves and 10% Rayleigh waves, while Bonnefoy-Claudet et al. (2007) suggest at least 50% Love waves. At the same time, theoretical arguments suggest that that the Love waves should play a minor role with respect to Rayleigh ones (Campillo and Paul, 2003; Shapiro and Campillo, 2004) since they are not sufficiently excited. More details about the characteristics of body and surface waves are shortly outlined in the following paragraphs.

2.3 Stochastic properties of ambient vibration

Ambient vibrations wavefield, formed by body and surface waves, varies spatially and temporally as are generated by different kinds of sources, randomly distributed both in space and in time. These characteristics and geological conditions in which the waves propagate make complex the form of the recorded signal, which shows an evident randomness in terms of amplitude.

The temporal and the spatial stationary character of seismic noise were studies by several authors (Okada, 2003; Chatfield, 1996) which performed data at different times and places. A time series is defined stationary if there is no systematic increase or decrease in the mean (i.e. no trend) and no systematic change in variance (namely, no turbulence).

In view of this, the seismic noise amplitude can be defined as a stochastic phenomenon, that is a process characterized by undetermined and unrepeatable features at a certain place and time. The study of this kind of processes requires statistical approaches able to reduce the complexity of the analysis: in particular, if the amplitude of the ambient vibrations is considered a

stochastic variable, it is possible to define a probability density function to describe it (Okada, 2003).
Nogoshi and Igarashi (1970) and Sakaji (1998) showed that the probability density function of the amplitude of the ambient vibrations approximates a normal distribution. Furthermore, they showed that the average, the standard deviation and the autocorrelation function of the microtremors amplitude are characterized by very little variations. These results prove that the ambient vibrations satisfy the properties of a stochastic and temporally stationary process. However, this is not always true when the acquisition exceed the length of few hours (Okada, 2003).
Moreover, as demonstrated by Groos and Ritter (2009), considerable deviations from a Gaussian distribution can be due to large amplitude transient and sinusoidal signals (cars, footsteps, industrial machinery, etc...) that can interfere during the recording time. In view of what described above and considering that the spatial stationarity of the microtremors is strictly related with the geological characteristics of the subsoil, it is evident that the ambient vibrations can be considered a stochastic and stationary process for a suitable spatial extent and for a time length of few hours. This assumption is of paramount relevance for the analysis techniques based on the seismic noise wavefield acquisition.

III. DYNAMIC CHARACTERIZATION OF SOIL AND SEISMIC RESPONSE ANALYSIS BY USING AMBIENT VIBRATIONS

Dynamic behavior of soil is characterized by its mechanical properties such as shear wave velocity, shear modulus, damping ratio and Poisson's ratio. In particular, the Vs profile plays a major role in the assessment of the local seismic response. In the present study, Shear wave velocity profile has been estimated by passive seismic surveys. In particular, in the investigations considered in the present thesis, NASW and HVSR passive methods have been considered.

NASW (Noise Analysis of Surface Waves) and HVSR method use seismic noise or "microtremor" as the source of surface waves, differently from the MASW and SASW method which use an artificial seismic energization of the ground (Nazarian and Stokoe, 1984; Park et al., 1999). Experimental analysis of microtremor has evidenced that the seismic noise has, in general, spectral characteristics particularly suitable to the exploration of the first subsurface depth (significant density of energy in the band 0.05-25 Hz). The use of "natural seismic sources" makes passive method suitable for investigations in noisy urban areas, where the use of the effective seismic sources would increase the geophysical survey costs. Those passive methods use specific physical-mathematical laws that govern the propagation of seismic surface waves in stratified media (one-dimensional). In such conditions, both Love and Rayleigh waves have dispersive character and also the propagation velocity has a strong dependence from the frequency of seismic motion. Using ambient vibration as an input allows to estimate the vertical profile of shear waves. Assuming a layered medium, the characteristics of the "dispersion curve" are closely related to the stratigraphic characteristics of the investigated area: the structure of the dispersion curve depends almost exclusively from the vertical profile of the propagation velocity of the shear waves. The diagram of surface wave dispersion analysis and the schematic graphics of results from each step, are show in the Figure 3.1. In a stratified medium characterized by increasing stiffness, hence shear-wave velocity increase with depth, the high frequency Rayleigh wave travelling in the top layer will have a velocity of propagation slightly lower than the velocity of a shear wave in the first layer. On the other hand, a low frequency wave will travel at a higher velocity because it is influenced also by the underlying stiffer materials. The phase velocity wavelength plot will hence show an increasing trend for longer wavelengths. Considering the relationship between wavelength and frequency, this information can be represented as a phase velocity versus frequency plot (dispersion curve). For a given vertically heterogeneous medium, the dispersion curve will be associated with the variation of medium parameters with depth. This explain the difficulties and problems of the method. It is important, however, to recognize the multimodal nature of surface waves in vertically heterogeneous media, i.e., several modes of propagation exist and higher modes can play a relevant role in several situations. Generally, only the fundamental mode dispersion curve is considered.

In this thesis, the dispersion curve has been estimated from experimental data, acquiring pairs of synchronized measures with two portable seismographs. The vertical profile of Vs has been then identified by solving the inverse problem.

The procedure followed to estimate the seismic stratigraphic profile and the response spectrum, using ambient vibrations as input, consist mainly in:

- Acquisition of synchronized experimental data;
- Signal processing to obtain the experimental dispersion curve;
- Inversion process to estimate the shear wave velocity profile;
- Equivalent linear analysis to estimate 1D-model (final Vs profile) and the response spectrum of site.

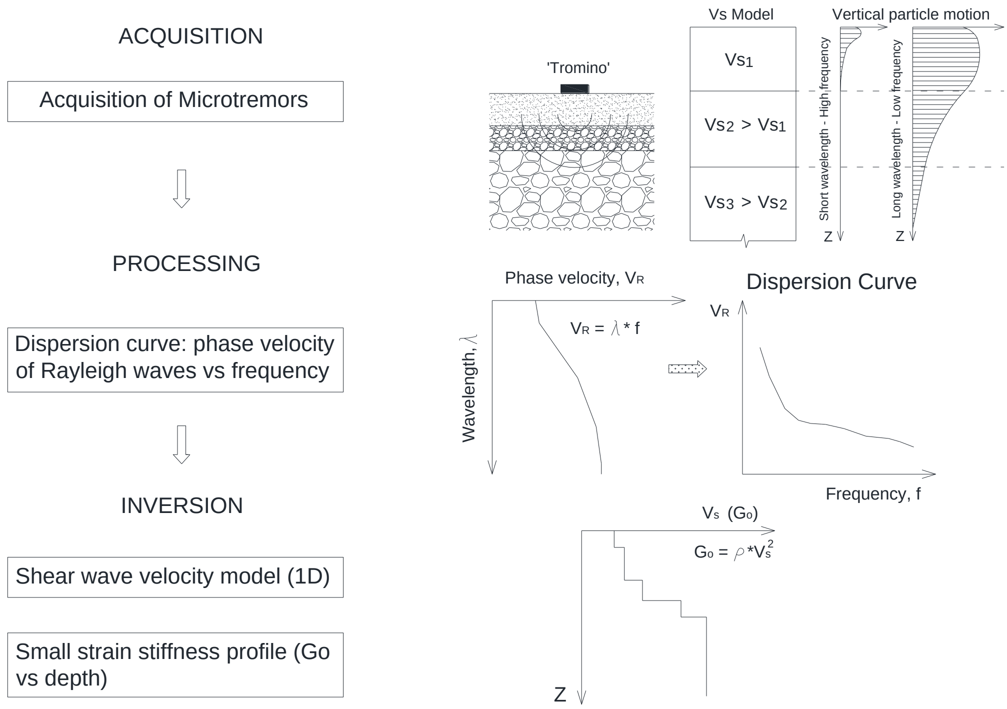

***Figure 3.1** Schematic phases of surface wave dispersion analysis (left), graphics of results from each step (right)*

3.1 Extracting S-Waves profile from ambient vibrations measurements

In order to constrain the Vs profile from ambient vibrations a two steps approach is considered. The first step aims at defining two experimental curves potentially informative about the Vs profile: the horizontal to vertical spectral ratios of ambient vibrations as a function of frequency (HVSR curve) and the Rayeligh waves dispersion curve. The second step is jointly inverting these two pieces of information to retrieve the local Vs profile in the assumption that subsoil is constituted by a stack of homogeneous layers, each characterized by a suite of seism-mechanical parameters (Vs, Vp, thickness and damping). The following major interpretative aspects relative to HVSR and dispersion curves are shortly outlined. Then the adopted inversion procedure will be analyzed.

3.1.1 Basic principles of HVSR method

Horizontal to Vertical Spectral Ratio (HVSR) technique was first introduced by Nogoshi and Igarashi (1971), and later revised by Nakamura (1989, 1996, 2000). These authors have highlighted the correlation between the frequency value of the HVSR peak and the fundamental resonance frequency of site, thus suggesting the capability of this technique to provide information on the dynamic characteristics of the subsoil.

This method simply consist in normalizing the average spectral amplitudes recorded on the horizontal components by the vertical one, with the aim to minimize the eventual source effects. In practice, the method of HVSR curve estimation consist of: merging the average spectral amplitudes of the two horizontal components of motion (H_1 and H_2) to obtain a single combined horizontal component (H') and then compute the ratio between this horizontal component and the vertical one. The modulus of the H' combined spectra can be computed both by the geometrical average:

$$H'(f) = \sqrt{H_1(f) \cdot H_2(f)} \qquad \text{(Eq. 3.1)}$$

or as root mean square average (r.m.s.):

$$H'(f) = \sqrt{\frac{H^2{}_1(f)+H^2{}_2(f)}{2}} \qquad \text{(Eq. 3.2)}$$

The function of the spectral ratio HVSR, is estimated as the ratio between the average of the amplitudes of the horizontal components $H'(f)$ and the amplitude of the vertical component $V(f)$ computed over a number of time windows in the form:

$$HVSR(f) = \frac{H'(f)}{V(f)} \qquad \text{(Eq. 3.3)}$$

The HVSR theory is characterized by some controversial aspects. These issues concern the exact physical interpretation of the HVSR curve and most of them are related with the nature of the ambient vibration wavefield and of its sources. In fact, in order to exploit the HVSR curve to infer the dynamic characteristics of the subsoil, theoretical models are needed to relate this curve with the mechanical and geological properties beneath the investigated site. Nowadays, several theoretical models of the ambient vibration wavefield exist. In particular, they are mainly divided in:

- models based on body waves theory, where it is assumed that body waves coming from the depth play a dominant role in the ambient vibration wavefield;
- models where it is assumed a dominant role of the surface waves and where the HVSR ratio is interpreted in terms of ellipticity of Rayleigh waves;
- models where no ex ante assumption is required about the seismic phases present in the expected wavefield; in this case, the HVSR curve is provided by full wavefield simulations.

The differences in the HVSR curve modeling can affect significantly the outcomes of inversion procedures used to retrieve the V_S profile from the experimental data.
Nowadays HVSR is widely used tool for a quick detection and evaluation of seismic-amplification effects in terms of *S* wave resonance frequency by using a single-station measurements carried out on the Earth's surface. This technique requires the acquisition of the three components of the ground motion and consists in performing the ratio between the horizontal and vertical Fourier spectrum. This ratio, which is expressed as a function of the frequency, is called the HVSR (or HVSR) curve (or function). In the last twenty years, many studies based on experimental and theoretical approach (Lermo and Chavez-Garcia, 1993; Lachet and Bard, 1994; Fäh, 1997) have shown that the HVSR method can be successful applied for identifying the fundamental *S* wave resonance frequency of sedimentary deposits when a sharp impedance contrast occurs between the soft materials and the underlying stiffer formations. However, some disputes concerning the applicability of this technique to evaluating the site amplification are ongoing. In particular, many authors consider the HVSR peak as a good estimate of the fundamental resonance frequency of the site, but unable to estimate the site amplification factor (Kudo, 1995; Konno and Omachi, 1998; Mucciarelli, 1998; Fäh et al., 2001): in this case, the HVSR peak amplitude and the site amplification would be connected only by a qualitative relationship.

In general, in a single layer 1-D stratigraphic the analysis of the HVSR of microtremor allows to estimate with reasonable accuracy the principal *S* wave resonant frequency (f_0) of the sedimentary coulters overlaying an infinite bedrock as well as its thickness *h* (Lermo and Chavez- Garcia, 1993, 1994; Bard, 1998; Fah et al., 2001) simply by relationship:

$$f_0 = V_s/4h \qquad \text{(Eq. 3.4)}$$

where Vs is the average *S* wave velocity in the sediment layers.

The existence of a single layer of sediments is almost never encountered in practice over substantial depths. In general, there are several alternated layers of different lithology and these produce a HVSR curve with several peaks and humps and troughs. Assuming an appropriate model for the wave field and for the medium, a theoretical HVSR curve can be fitted to the experimental one to infer a subsoil model.

HVSR curve should be cleaned before analysis and also time windows (for example 20 s) must be used to obtain the average HVSR and its subintervals (Castellaro et al., 2005). Sometimes no HVSR peak can be associated to a shallow stratigraphic horizon especially when the recorded is performed on perfectly homogeneous rock without any cover/alteration layer. The later gives a truly flat HVSR curve and is of little interest, since no particular amplification exists. The artificial soil (pavements, asphalts and similar) should be avoided during the acquisition since these can include velocity inversions which force the HVSR curve to amplitudes below 1 Hz even down to 1 Hz.

3.1.1.1 Interpretation of HVSR in terms of ellipticity of Rayleigh waves

Empirical evidences indicate that surface waves are the most coherent seismic phase into the ambient vibration wavefield. As an indirect proof of this fact, surface-wave dispersion curves can be estimated from the seismic noise exactly because they are more coherent than other seismic phases. This implies that surface waves should play a major role in the explanation of HVSR results. Several authors (Tuan et al., 2011; Lachet and Bard, 1994; Tokimatsu, 1997; Konno and Ohmachi, 1998; Fäh et al., 2001; Wathelet et al., 2004) agree on the close relation existing between the HVSR spectral ratio and the ellipticity of Rayleigh waves. This relation is justified by the simple consideration that Rayleigh waves are generally energetically predominant in the vertical component of ambient vibration wavefield.

Konno and Ohmachi (1998), show that the HVSR peak by ambient vibrations could be explained by the ellipticity of the fundamental Raylegh mode as well as by the Airy phase of the fundamental Love mode. In particular, these authors investigate the particle motion related to fundamental Rayleigh mode as a function of the fundamental period T of the subsoil profile and, in particular, of the velocity contrast between the single layer and the half-space. They showed that only in presence of very high impedance contrasts, for increasing period the HVSR curve corresponds to the presence of horizontal motion only (i.e., vanishing of the vertical one). It is worth noting how this frequency dependent particle motion simply can explain the presence of peaks and troughs in the HVSR curves. Moreover, in numerical simulations performed by these authors, the HVSR-peak amplitude roughly approximates the S wave amplification factor, providing that a specific proportion between Rayleigh and Love waves exists; this mimics the Nakamura’s statement, but in terms of surface waves instead that of body waves (Lunedei and Malischewsky, 2015). Fäh et al. (2001) explore two ways to generate HVSR synthetic curves. The first one is a numerical simulation made by a finite difference technique, where both superficial and buried ambient vibration sources are considered. These sources, with positions, depths and time-dependences chosen randomly, are distributed around a receiver. The second technique focuses on Rayleigh wave ellipticity of fundamental and higher modes, to explain the HVSR-peak frequency: in fact, only this element is considered reliable in the HVSR curve by the authors, in that the peak amplitude and other features of the curve also depend on other parameters besides than the S-wave velocity profile. Moreover, they identify parts of the HVSR ratio that are independent on the sources distance and are dominated by the ellipticity of the fundamental Rayleigh mode, in the frequency band between the HVSR-peak frequency (which they check to be close to the site S-wave fundamental resonance-frequency) and the first minimum of the HVSR curve (Lunedei and Malischewsky, 2015).

Bonnefoy-Claudet et al. (2004, 2006a, 2008) carry out a systematic study of the HVSR curve by numerical simulations, in which ambient vibrations are generated by a multitude of point-like forces, randomly oriented in the space and located relatively near to the observation point. By using several simple stratigraphical profiles, Bonnefoy-Claudet et al. (2008) check the good correspondence between the HVSR-peak frequency and the S-wave resonance one. Moreover, they shows that the interpretation of the HVSR main peak in terms of Rayleigh ellipticity seems limited to profiles characterized by high impedance contrast (more than 4). Overall, this work highlighted the importance of all surface wave phases propagating in the subsoil in constructing a suitable HVSR model, as well as the paramount role of the impedance contrast in computing the HVSR peak.

3.1.1.2 HVSR curve by full wavefield simulations

The recent theories based on full wavefield simulations assume that both body and surface waves play a significant role in the ambient vibration wavefield. As described previously all seismic phases should be taken into account to provide a reliable interpretation of the HVSR curves.

Different type of models (full wavefield model, DSS-Distributed Surface Sources and DFA-Diffuse Field Approach) were developed in the past years to interpret the HVSR curves properties and information derived from. DSS developed a model considering the case of a continuous distribution of random independent point sources, which are active at the surface of a flat, viscoelastic layered Earth. A limit of this model, is that it does not regard the presence of unavoidable deep scattering, because sources are only superficial, but it has to be said that the hypothesis of a stratified Earth presumes that the discontinuities due to layer-interfaces are more relevant than any other inhomogeneity (included the deep scattering generators) (Albarello and Lunedei, 2009, 2010, 2011; Lunedei and Malischewsky, 2015).

'Diffused field' approach model assumed that ambient vibrations constitute a diffuse wavefield. In this assumption, the seismic waves propagate in every (three-dimensional) spatial direction in a uniform and isotropic way. Moreover, a specific energetic proportion between P and S waves exists, which is always the same, both spatially and temporally (Sánchez-Sesma et al., 2006, 2011 and Kawase et al., 2011).

In order to study the differences and similarities between DSS and DFA models, a set of synthetic tests were performed considering stratigraphical profiles showed in the Table 3.1.

Generally, three frequency ranges can be identified. For example, in case of the stratigraphical profile M2* (Lunedei and Malischewsky, 2015) the frequency range are:

- low-frequency domain (below the *S* wave resonance frequency value, f_S), where the spectral powers of the ambient vibrations are relatively low;
- high-frequency domain (above $\max\{f_P, 2f_S\}$, where f_P is the *P* wave resonance frequency), where the surface waves (both Love and Rayleigh, in their fundamental and higher modes) dominate the wavefield;
- intermediate frequency domain (at and in-between f_S and $\max\{f_P, 2f_S\}$), where most of the seismic energy of the ambient vibrations is concentrated. Horizontal ground motion is dominated by surface waves, with a varying combination of Love (in the fundamental mode) and Rayleigh waves, that depends on the Poisson’s ratio. In the vertical component, Rayleigh and other phases play different roles, both depending on the dimension of the source-free area and of V_P and V_S depth profiles.

The peak frequency in the HVSR curves is generally very near to f_S, regardless to the Poisson’s ratio and the dimension of the source-free area. Furthermore, HVSR peak-frequency is a good estimate of f_S (Lunedei and Malischewsky, 2015).

For the profile M2, DSS model shows a significant contributions of body waves for frequencies around and below the *S* wave resonance frequency f_S (2 Hz in this case), and a clear surface-wave dominance for frequencies larger than the P wave one f_P (4 Hz in this case). This characteristic causes the amplitude differences between the blue HVSR curve (full wavefield, FW) and the green one (surface waves, SW) in the Figure 3.2a around the peak frequency. Instead, when a source-free area with a radius of 10 m is inserted in the simulations (Figure 3.2b), the FW produces an HVSR peak very similar to the one of the SW. Regarding the DFA model, the HVSR curves generated by its simulations show no difference between FW and SW; moreover, the HVSR peak amplitudes are less that the DSS ones.

Table 3.1 *Stratigraphic profiles used in the numerical testing. The symbols h, V_S, V_P, ν, ρ , D_P and D_S represent, respectively, the values of thickness, S wave velocity, P wave velocity, Poisson's ratio, density, damping for P wave and damping for S wave (from Lunedei and Malischewsky, 2015).*

		M2			
h **(m)**	V_S **(m/s)**	ν	ρ **(g/cm³)**	D_P	D_S
25	200	0.333	1.9	0.001	0.001
5000	1000	0.333	2.5	0.001	0.001
∞	2000	0.257	2.5	0.001	0.001
		M2*			
h **(m)**	V_S **(m/s)**	ν	ρ **(g/cm³)**	D_P	D_S
25	200	0.01-0.49	1.9	0.001	0.001
5000	228-1520	0.333	2.5	0.001	0.001
∞	2000	0.257	2.5	0.001	0.001
		M3			
h **(m)**	V_S **(m/s)**	V_P **(m/s)**	ρ/ρ_4	D_P	D_S
5	30	500	1	0.001	0.001
25	100	500	1	0.001	0.001
50	150	500	1	0.001	0.001
∞	500	1500	1	0.001	0.001

The profile M3 is characterized by two strong and one weak impedance contrasts and, therefore, presents more complicated configuration with main and secondary impedance contrasts. The HVSR trends computed with DFA and DSS are characterized by more remarkable differences. The elastic DFA computation presents two maxima at about 0.4 Hz and 1.5 Hz (probably associated with the two subsoil principal interfaces), both for the FW (black lines in Figure 3.3) and the SW (red lines in Figure 3.3). For the DSS-FW model (blue line in Figure 3.3), it is possible to note that a more strictly correspondence with the DFA-FW curve exists only removing the close sources from the simulations (Figure 3.3b): in this way, the surface waves play a predominant role respect to the body waves. Differently, the SW models show very similar results in all investigated cases.

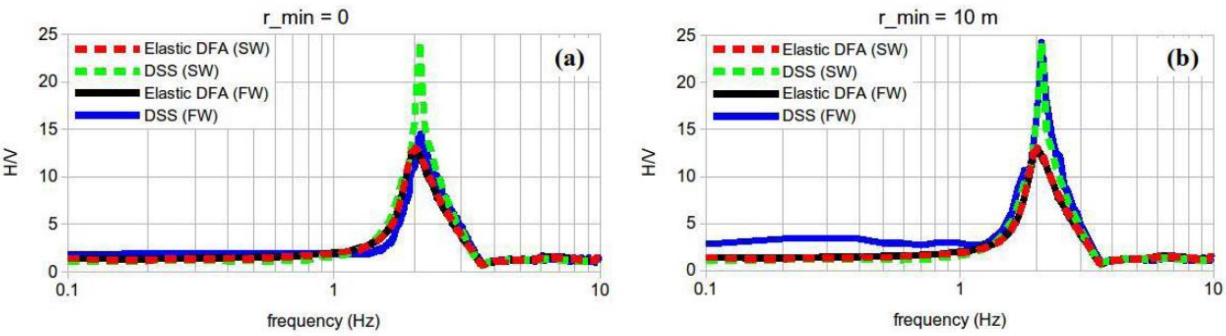

Figure 3.2 *HVSR curves for the stratigraphy M2 obtained by the DSS for the full-wavefield (blue) and the surface-wave component (green), as well as by the DFA for the full-wavefield (black) and the surface-wave component (red); a: no source-free area is considered; b: a source-free area with radius 10 m is set in the DSS (From Lunedei and Malischewsky, 2015).*

Both the DSS and the DFA provide reasonable full-wavefield and surface-wave synthetics of HVSR spectral ratios, in particular for stratigraphic profiles with a dominant impedance contrast (profile M2). Moreover, the results relative to DSS can depend on the source distribution around the receiver.

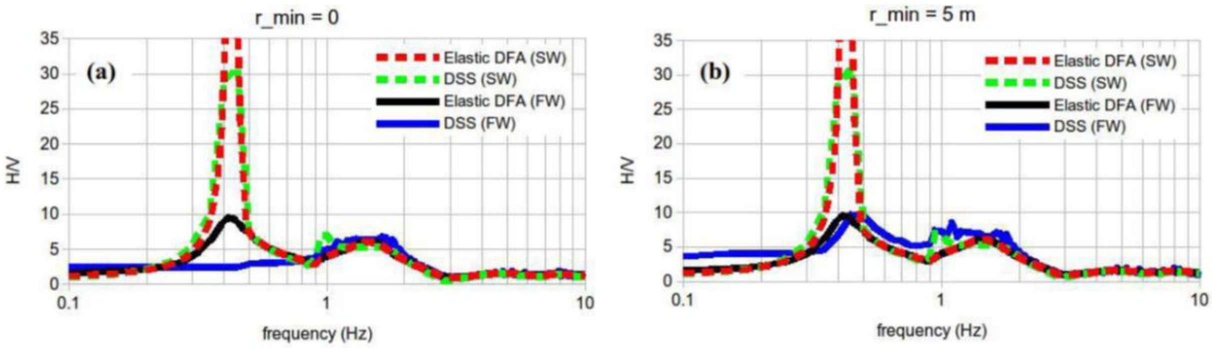

Figure 3.3 *HVSR curves from DFA and DSS method for the profile M3; a: sources are allowed on the whole Earth's surface; b: near sources are removed from around the receiver up to the distance of 5 m (from Lunedei and Malischewsky, 2015).*

3.1.1.3 Experimental assessment of the HVSR curve

The computation of HVSR function is related to the procedure which provide a stable HVSR curve as well as an estimate of its confidence interval.
HVSR curves estimate in this study are retrieved from ambient vibration recordings, using the following procedure:

- recordings are divided into windows of 20 seconds length (suitable time interval to ensure a good spectral resolution), each of which is analyzed separately. The number of temporal windows required, i.e. the recording duration of 30 minutes, ensure the statistical stabilization of the signal;
- within each window, for each of the three ground motion components, are performed the following analyses:
  - linear trend removal (detrend) and tapering of the signal ends with a Hann cosine function (to avoid leakage phenomena);
  - spectral amplitudes computation by using Fast Fourier Transform (Cooley and Turkey, 1965);
  - the smoothing of spectra with triangular moving window with frequency dependent half-width (5% of central frequency). This is a mandatory operation to avoid the presence of spurious peaks and excessive irregularities in the HVSR curve (Bindi et al., 2000; Picozzi et al., 2005a);
- the geometrical mean H' of the two horizontal components (H_1 and H_2) spectral amplitudes are computed through the Equation 3.1. After this, the HVSR curves in each time window are obtained by the spectral ratio between H' and the vertical component spectral amplitude (Equation 3.3);
- the final HVSR function and the corresponding 95% confidence interval (Figure 3.5, a) are achieved by averaging the HVSR ratios obtained for each time window, thus identifying the frequency value for which the HVSR ratio is maximum (resonance frequency f_0).

Experimental HVSR spectral ratio values depend strongly on the processing strategy adopted for their estimate and that eventual inversion and testing procedures should account for these differences (Albarello and Lunedei, 2013).

3.1.1.4 Quality criteria of HVSR curve

The quality of HVSR measure is depend on the time stability of the HVSR function during the acquisition (temporal stationarity) and the possible presence of directional phenomena that can produce spatial heterogeneities in the ambient vibration wavefield. Two analyses should be realized to check these phenomena:

- to assess the stationarity assumption: the HVSR spectral ratios obtained in the different time windows as a function of the recording time (Figure 3.4, left), allow to identify and remove the possible strong transient signals (e.g., cars or people passing too near the sensor) that can significantly affect the outcomes of the whole analysis (Parolai et al., 2004);
- to check the directionality of the recorded signal: the horizontal components are rotated at regular intervals in the 0°-180° degree range in order to highlight the presence of significant spatial heterogeneity in the ambient vibration wavefield (Figure 3.4, right). A wavefield characterized by a single dominant source may excessively affect the spectral characteristics of the signal, so that the relevant HVSR ratio would no longer dependent only by the site physical properties.

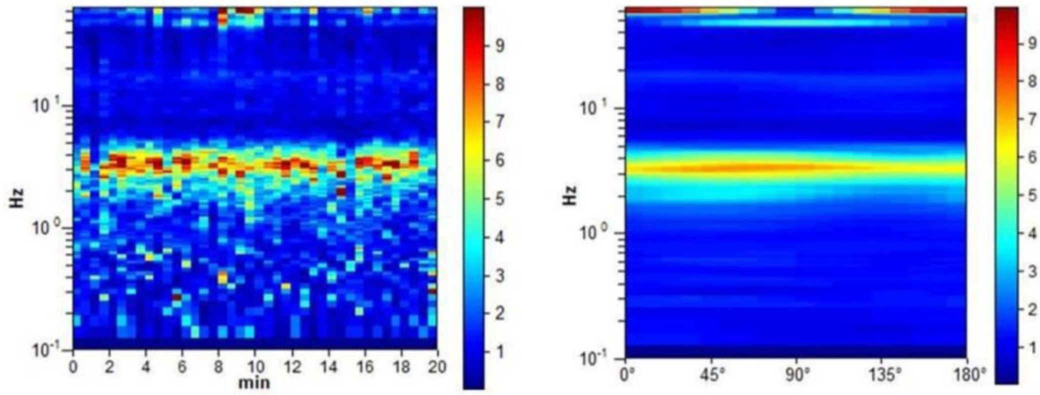

Figure 3.4 *Contour plot of the HVSR curves computed for each time window. The scale-bar on the right indicates HVSR amplitudes (left). Contour plot of HVSR curves obtained by the rotation and combination of the horizontal components of motions. The scale-bar on the right indicates HVSR amplitudes (right).*

Various authors set several criteria for the reliability and the clearness of the HVSR function maxima, to achieve optimal applications of HVSR prospecting techniques and to provide comparable measurements among themselves. The framework of the European research project SESAME (Site Effects Assessment Using Ambient Excitations), set some criteria for the peaks quality; in fact, an unsatisfactory statistical quality of the measure can be produced spurious peaks that can hamper a correct identification of resonance effects. However, these statistical norms cannot be considered exhaustive in all cases. Recently, Albarello et al. (2011) proposed some classification criteria including a larger number of elements, turns out to be more complete than that proposed by the SESAME group (SESAME, 2004b). In order to provide an immediate indication about the quality of single HVSR measure and preventing over-interpretation of bad experimental results, the authors have developed the following classification scheme with three classes (Albarello et al., 2011):

- class A: trustworthy and interpretable HVSR curve, which represents a reference measurement, that can be considered representative of the dynamical behavior of the subsoil at the site of concern by itself;

- class B: suspicious HVSR curve, which should be used with caution and only if it is coherent with other measurements performed nearby;
- class C: bad HVSR curve (it is hardly interpretable), to be discarded.

To classify a single measurement as of class A are used the following criteria:

- stationarity: the HVSR curve included in the frequency range of interest must show a persistent shape for at least 30% of the measurement duration;
- isotropy: the azimuthal amplitude variations do not exceed 30% of the maximum;
- absence of artifacts: there are not symptoms of electromagnetic noise or peaks of industrial origin into the frequency range of interest;
- physical plausibility: HVSR maxima are characterized by a localized lowering of the vertical amplitude spectral component, forming an "eye-shaped" structure (Figure 3.5, b);
- statistical robustness: SESAME criteria for a reliable HVSR curve are fulfilled;
- representative sampling: the measurement took place for at least 15 minutes.

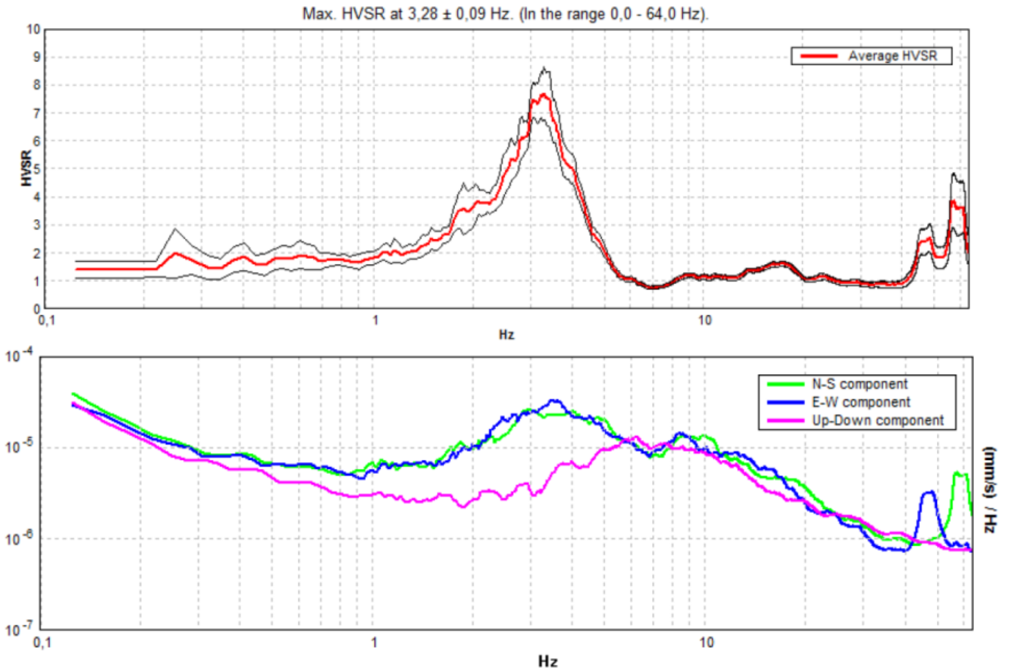

Figure 3.5 *Experimental average HVSR curve (red line) and confidence intervals 95% (black lines) (a). Amplitude spectra of the three components of the ground motion: presence of a lowering of the vertical amplitude spectral component 'eye shape' located in correspondence of the HVSR curve peak frequency (b).*

The measurement should fall in the class B if one or more of the previous conditions are not fulfilled. But a measurements of class B become of class C if; a rising drift exists from low to high frequencies, that indicates a movement of the instrument during the acquisition (Forbriger, 2006), or if the electromagnetic or industrial disturbances affect several frequencies in the frequency range of interest.

The SESAME conditions for "peak clearness" are taken also into account as it is difficult to provide a physical interpretation of the curve in terms of "absence/presence" of resonance phenomena. At this aim, two sub-classes (type) were introduced:

- type 1: the HVSR curve presents at least one clear peak in the frequency range of interest (possible resonance);

- type 2: the HVSR curve does not present any clear peak in the frequency range of interest (absence of resonance).

3.1.1.5 Role of HVSR in local seismic response

HVSR curve has an important role in local seismic response since its makes possible to achieve a preliminary information on the shallow subsoil structure, by estimating directly the resonance frequency f_0 and exploiting the approximate relationship (Equation 3.4) between f_0, the thickness h and the average S wave velocity Vs of the sedimentary cover. Using the Equation 3.4 it is possible to estimate the resonant interface depth, by estimating first the f_0 value as the HVSR peak and known the Vs value. In absence of S wave information for the shallow materials, Albarello et al. (2011) proposed a simple abacus (Table 3.2) in order to obtain a very rough estimate of the latter parameter.

Table 3.2 *Approximate summary relationship between HVSR peak frequency (f_0) and resonant interface depth (h) (from Albarello et al., 2011)*

fo (Hz)	h (m)
< 1	> 100
1 ÷ 2	50 ÷ 100
2 ÷ 3	30 ÷ 50
3 ÷ 5	20 ÷ 30
5 ÷ 8	10 ÷ 20
8÷ 20	5 ÷ 10
> 20	< 5

Gallipoli et al., 2011listed the piece of information that can be obtained from HVSR analysis, useful in seismic microzonation and in emergency earthquake contexts:

- provide an estimate, at least qualitatively and comparatively, of the possible seismic impedance contrast taking into account the peak amplitude;
- define the lithologies and the geological formations that can constitute the sedimentary cover and the bedrock;
- provide a map of the resonance frequency of sedimentary covers, helping geologists to refine on formation limits and for identification of the areas with a danger of soil-structure resonance.

Recent studies (Yamanaka et al., 1994; Ibs-von Seht and Wohlenberg, 1999; Delgado et al., 2000a, b; Parolai et al., 2001; D'Amico et al., 2008) showed that noise measurements can be used to map the thickness of soft sediments.

The cheapness, the robustness and the quickness that characterize the HVSR deduced by single station measurements (specially using very portable instruments) makes this analysis a very attractive tool in the first level of Seismic Microzonation studies and in the phases immediately following major damaging earthquakes (Albarello et al., 2011; Gallipoli et al., 2011; Priolo et al., 2012). Furthermore, in the emergency post-earthquake phases, it is of paramount importance to quickly identify the sites where provisory recovery area could be safely emplaced due to lack of significant local amplification effects during the seismic sequence.

3.1.2 Retrieving the Rayleigh waves Dispersion curve from ambient vibrations - SPAC zero crossing method

SPatial AutoCorrelation zero crossing method can be used to achieve the Rayleigh phase velocity dispersion curve between two sensors (two synchronized portable seismographs). This method is based on the spatial autocorrelation analysis and derived from SPAC method (Paolucci, 2016). As it is known, the phase velocity of surface waves is a function of frequency (called dispersion curves), in a vertically heterogeneous medium. This curve is a function of shear wave (S wave) velocity, layer thickness, density, and compression wave (P wave) velocity of each geological layer, listed in a decreasing order of priority according to Xia et al. (1999).

In this thesis, the dispersion curves have been measured experimentally, making possible to obtain the mechanical parameters of the medium from the dispersion curves.

SPAC zero crossing method differ from SPAC method from two main aspects: first, considering sensor disposition in array and non in circular as SPAC method and second, using the locations of the zero crossings in the spatial correlation spectra as the dispersion observables. In the following paragraphs are described briefly those aspects.

SPatial AutoCorrelation method (SPAC) was proposed by Aki (1957, 1965) which analyzed the ambient vibration recordings to estimate the Rayleigh wave phase velocity using a statistical approach. Practically, considering the ambient vibration wavefield as a stochastic and stationary process in time and space, the author assumed that this signal represents the sum of waves propagating without attenuation in a horizontal plane in different directions with different powers, but with the same phase velocity for a given frequency. Moreover, he supposed that waves with different propagation directions and different frequencies are statistically independent. The spatial correlation function between two receivers can be defined as:

$$\phi(r,\varphi)= \langle u(x,y,t)u(x+r\cos\varphi,y+r\sin\varphi,t)\rangle \qquad \text{(Eq. 3.5)}$$

where $u(x,y,t)$ and $u(x+r\cos\varphi,y+r\sin\varphi,t)$ is the signal measured at the first receiver (with coordinates (x,y)) and at the second receiver (with coordinates $(x+r\cos\varphi,y+r\sin\varphi)$) at time t, r is the inter-station distance, φ is the azimuth of the two receivers measured from the direction of the x axis and the angle brackets $\langle\ \rangle$ denote the temporal averaging.

Using a circular disposition of sensor, the azimuthal average of the spatial correlation function $\bar{\phi}(r)$, between each of them and a sensor placed in the circumference center, can be computed. This function is related to the temporal power spectrum $\Phi(\omega)$, for single-mode scalar wave with Rayleigh phase velocity $c(\omega)$, by:

$$\bar{\phi}(r)=1/\pi\int_0^{\infty} \Phi(\omega)\, J_0\left[\frac{\omega_o}{c(\omega_o)} r\right] d\omega \qquad \text{(Eq. 3.6)}$$

where J_0 is the Bessel function of zero-th order.

This equation can also be written as:

$$\bar{\rho}(r,\omega_0)= J_0\left[\frac{\omega_o}{c(\omega_o)} r\right] \qquad \text{(Eq. 3.7)}$$

This equation shows that the phase velocity $c(\omega_0)$ of the waves can be derived by fitting the experimental values of $\bar{\rho}(r,\omega_0)$ (calculated for a series of receivers set in a circular pattern around a central reference receiver) with the theoretical ones computed by the Bessel function J_0 at different tentative combinations of parameters r, ω_0 and $c(\omega_0)$.

SPAC method use sensors disposed on a circumference of radius r and regularly spaced among themselves while SPAC zero method used linear stringing. Ekstrom at al. (2009) justify the application of the SPAC formulation considering separately each station pairs relying on the Aki (1957) work. The authors argue that the azimuthally averaged spatial correlation spectrum $\bar{\rho}(r,\omega 0)$ (Equation 3.7) can be replaced in the analysis by the spectrum obtained for a single station pair. Moreover, Aki's (1957) states that this assumption can be exploited only if that the stochastic ambient vibration wavefield is sufficiently isotropic. In the Figure 3.6 is shown the spatial correlation spectra for two station pairs belonging USArray, located in Washington State and separated by 282 km and 145 km, respectively. The real parts of the spectra (dark blue lines) resemble a Bessel function in their oscillatory character, but the amplitudes of the peaks do not decrease monotonically with frequency as for Bessel function (J_0). This amplitude behavior depends on the background noise and non-linear effects of the data processing as well as the azimuthally non-uniform power of the ambient vibration witnessed by the non-vanishing imaginary part of the spatial correlation spectrum (Cox, 1973). It is evident that dispersion information cannot readily be deciphered from the detailed shape of the spectrum.

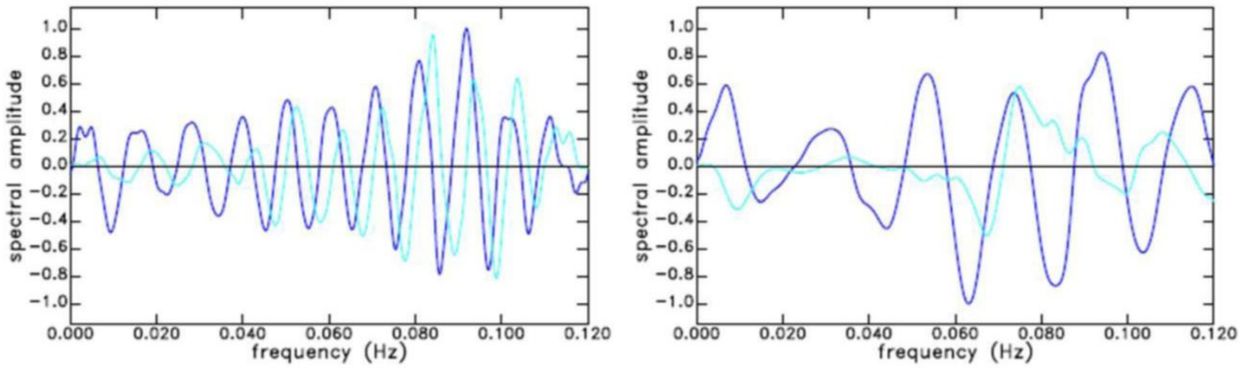

Figure 3.6 *Spatial correlation spectra for two station pairs belonging to USArray; the stations are separated by 282 km (left) and 145 Km (right). Dark blue lines show the real parts of the spectra and light blue lines show the imaginary parts (from Ekstrom et al., 2009).*

In view of this, the authors decided to use the locations of the zero crossings as the dispersion observables, assuming that these points in the spectrum should be insensitive to variations in the spectral power of the background noise. In particular, if ω_n denotes the frequency of the nth observed zero crossing and z_n denotes the *n-th* zero of J_0 (namely the argument value that makes null the J_0 value), it is possible to determine the corresponding phase velocity $c(\omega_n)$ as:

$$c(\omega_n) = \frac{\omega_n\, r}{z_n} \qquad \text{(Eq. 3.8)}$$

following the Aki's (1957) approach. In observed spatial correlation spectra, association of a given zero with a particular zero crossing of J_0 may be difficult because background noise in the spectrum can cause missed or extra zero crossings. To overcome this problem, the authors developed a set of phase velocity estimates $c_m(\omega_n)$, where m takes the values 0, ±1, ±2, etc., indicating the number of missed or extra zero crossings. Following the Equation 3.8, this relationship can be expressed as:

$$c_m(\omega_n) = \frac{\omega_n\, r}{z_{n+2m}} \qquad \text{(Eq. 3.9)}$$

In the Figure 3.7 are shown the dispersion curves obtained by the spectra showed in the Figure 3.6. The connection of the $c_m(\omega_n)$ values computed by Equation 3.9 by considering the positive-to-negative zero crossings (downward triangles in Figure 3.7) and of the ones computed by the negative-to-positive zero crossings (upward triangles in Figure 3.7) generates two dispersion curves that can be assessed for consistency. It is also evident that several dispersion curves are derived from the phase-velocity measurements resulting from different possible choices of m for each zero. At low frequencies, the authors discard all the curves that do not fall within a realistic range (dashed lines in Figure 3.7), while at higher frequencies they do not consider the dispersion curves characterized by step-like velocity changes (namely evaluating the curve smoothness).

The remaining dispersion curve is evaluated by considering two sub-dispersion curves (one connecting up-crossing zeros and one connecting down-crossing zeros) as a quality criterion: in

particular, the dispersion curve is not included in the subsequent analysis if the phase velocity values of the two sub-dispersion curves at considered frequency differ than more a defined threshold.
The reliability of the SPAC zero crossing method in retrieving the Rayleigh phase velocity (V_R) dispersion curve between two sensors was tested from several authors, which show a reliability validation of this method. Recently, Pilz et al. (2012) and Pilz et al. (2013) explored the use of the SPAC zero crossing method to retrieve the Rayleigh wave phase velocity values between each pair of sensors belonging to a small scale array, with maximum inter-station distance of the order of 100 m, only the case where m=0 (no extra or missing zero crossing).

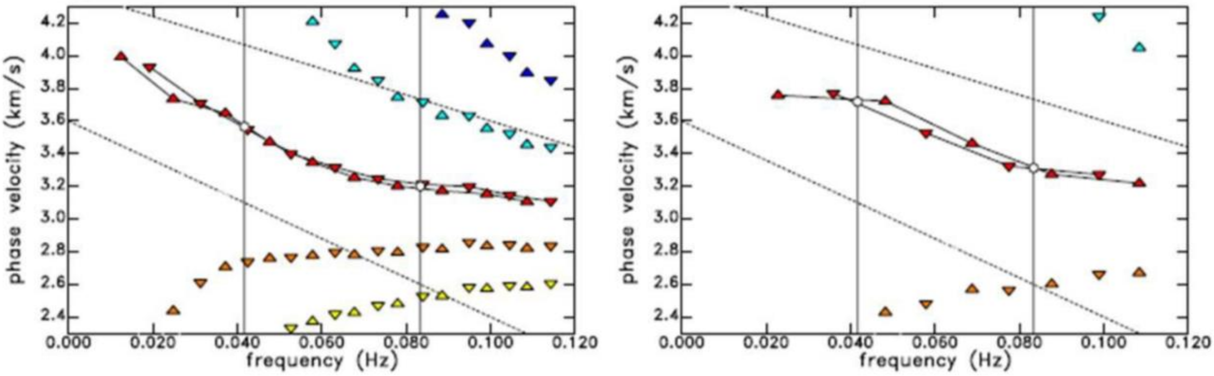

Figure 3.7 Dispersion diagrams showing the phase-velocity values derived from the zero crossings of the spectra in Figure 3.8. (Downward triangles show zero crossings from positive to negative, upward triangles show crossings from negative to positive. Red for m = 0, with no missing or extra zeros; orange for m = 1; yellow for m = 2; light blue for m = -1; and dark blue for m = -2. Dashed lines outline the region used to define acceptable phase velocities at each frequency. Black lines connect upward- and downward-pointing triangles to define the dispersion curves that are sampled at discrete frequencies for the subsequent analysis. Thin vertical lines and white dots show the frequencies and phase velocities values taken into account to accomplish the tomographic Rayleigh wave velocity maps at 12 s and 24 s) (from Ekstrom et al., 2009).

3.1.3 Seismic stratigraphic profile - Inversion procedure

Seismic stratigraphic profile (1D model) can be estimated by the inversion process, using as input the dispersion curve and the HVSR curve estimated from ambient vibration measures (Paolucci, 2016).
The aim of the inversion procedure is to retrieve its underlying causes, i.e., the variation with the depth of the subsoil dynamic properties. Such causes can be studied on the basis of the appropriate choice of different types of effects (e.g., the Rayleigh-wave velocity dispersion curve or the HVSR function) defined as output response.
Inverting experimental data is a normal and fundamental procedure used in geophysics, and its aim is to return to a given physical structure. In other words, starting from the consequences of physical phenomenon (outputs or effects), you can go back to its underlying causes, i.e., the variation with the depth of elastic constants. Such causes can be studied on the basis of the appropriate choice of different types of effects (e.g., the Rayleigh-wave or Love-wave dispersion curve or the Horizontal-to-Vertical Spectral Ratio, HVSR curve), defined as output response.

S wave velocity structure below a site have been studies by various authors in the last decade. Fah et al. (2001) retrieve Vs profile the from single station measurements based on noise horizontal to vertical spectra ratio computation. The inversion was based on a genetic algorithm (GA) (Fah et al., 2001, 2003), furthermore, was carried out for a fixed number of layers and a priori defined ranges of the geophysical properties (*S* wave, *P* wave, density and thickness) of the layers. Tanimoto and Alvizuri (2006) and Hobiger et al. (2009) proposed to extract the ellipticity of Rayleigh waves from NHV curves by a random decrement technique. This might in turn be used as input for the inversion analyses to estimate the *S* wave velocity profiles. The inversion was carried out by fixing the total thickness of the sedimentary cover in order to avoid problems of trade-off between the total thickness and the *S* wave velocity (Scherbaum et al., 2003; Arai and Tokimatsu, 2004). Three different values for the total thickness of the sediments were considered: the average value from an empirical relation between velocity versus depth calculated for the investigated area, and the maximum and minimum values considering the standard errors in that relationship. Finally, the derived *S* wave velocity profiles have been compared with those obtained by array techniques (Parolai et al., 2006) and an excellent agreement was found.

The "inverse problem" in geophysics (like in general) is neither linear nor unambiguous. This means that inversion procedure does not lead to identify a single Vs profile (there is no uniqueness in the solution) or rather, each elaboration of data leads to the identification of alternative Vs profiles, partially different between one another, but equally compatible with the experimental data. Generally speaking, the lack of a single solution to an inverse problem can be directly attributed to; paucity of information in the data (few output-effects) and intrinsic nature of the problem itself.
In order to deal with this difficulty and make the result of the inversion procedures informative to all intents and purposes, the following two strategies are usually employed:

- maximizing the available information;
- adding limitations to the possible solutions.

As concerns the Rayleigh wave inversion, the first point can be pursued reducing the number of parameters to be inverted, adding possible available a priori information (e.g., *P* wave velocity) or jointly inverting a different output response function (i.e., adding another set of experimental data, although dependent on the same subsoil parameters). The second point can be pursued fixing the solution limits of some parameters (e.g., constraining between a minimum and a maximum the possible V_S and/or V_P values), blocking the ratio between some of them (e.g., setting the Poisson's coefficient value) or adopting restrictions on the overall trend of the solution (the V_S profile) making sure that this one does not present sharp irregularities.
From the above, it is clear that a preliminary knowledge of the subsoil characteristics from the pre-existing surveys (e.g., borehole, geological map) is a fundamental prerequisite in the successive stages linked to the process of data inversion.

The successful outcome of an inversion procedure can be obtained by solving an optimization problem, i.e., the research of the minimum points of a function defined in a multi-dimensional space that can be subject to constraints (Parker, 1994). In particular, the simplest approach for the solution of an inverse problem consists in minimizing the squared Euclidean norm of the difference between the observed (d_i) and theoretical (f_i) data:

$$M = \sum_{i=1}^{N} (d_i - f_i)^2 \qquad \text{(Eq. 3.10)}$$

The function *M* is defined as "objective", "cost", "loss", or "misfit" function. In order to define this function, it is evident that it is needed to solve the problem of the forward modeling. In particular, once that all the physic laws and the parameters of the process under study are known and well modeled, the deduction of the theoretical values of the interested output response function is a computational task only. Hence, the forward modeling is a fundamental part of the inversion procedure (Figure 3.8).

The strategies aimed to perform the research of the misfit function minimum are divided in two main classes: Local Search Method and Global Search Method. This difference is due to the fact that, in general, in nonlinear problems the misfit function is characterized by multiple minima: among these, there will be an absolute minimum, called the global minimum, that is related to the best model. Nevertheless, there will be also several other relative minima in *M* function, called local minima, related to models more or less similar to the best one.

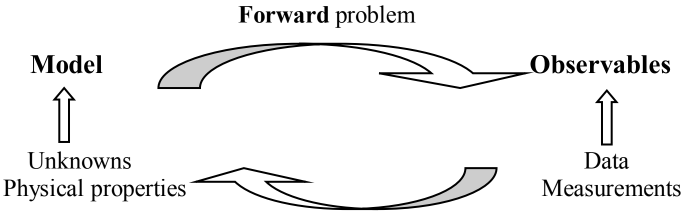

Figure 3.8 *Definition of an inversion problem (from Wathelet, 2005)*

Starting from an assumption of initial model, the local search methods are iterative schemes which implement a sequence of perturbations to the parameters that allow to converge to a minimum point. In nonlinear cases these techniques advance by successive linearization and are defined as linearized Methods (Menke, 1989; Tarantola, 2005). These methods require a smooth misfit function such as to be differentiable with respect to the various parameters of the model. However, even if this condition is accomplished, the convergence to the minimum occurs only if the initial model is close enough to the solution. Moreover, even when these procedures are able to converge to a minimum point, it is not possible to realize if it is the absolute minimum. This limitation is coped by the Global Search Methods, where the whole solutions space is explored. These procedures are more robust and stable than the local ones, but more troublesome from the computational point of view. One of the most widespread global procedures is the Monte Carlo method, developed in the 50s (Metropolis and Ulam, 1949; Press, 1968; Tarantola, 2005).

Sambridge and Mosegaard (2002) proposed to classify different Local and Global Search Methods on the base of the trade-off between "exploration" and "exploitation" criteria. "Exploration" means that one tries to minimize the objective function by looking (randomly) in different regions of the parameter space, without considering what has been already learned from previous samples (Picozzi, 2005). "Exploitation" criterion has the opposite meaning: in fact, it means that one decides where to sample next by using the previous samples or the current best fitting sample only (Picozzi, 2005). Both methods were compared by Sambridge and Mosegaard (2002): the more explorative methods (e.g., Uniform Search, Genetic Algorithms, Simulated Annealing, Neighbourhood Algorithm, Importance Sampling) are less efficient to converge on a solution, but is less likely that they fall into local minima; the exploitative algorithms (e.g., Steepest Descent, Newton-Raphson, Amoeba Search) are generally more efficient at converging, but are inclined to be entrapped in local minima.

Different procedures are used by several authors to invert the Rayleigh wave velocity dispersion curve (obtained both by active and passive measurements):

- *LIN* methods: e.g. Dorman and Ewing, 1962; Horike, 1985; Tokimatsu et al., 1992; Tokimatsu, 1997; Lai, 1998; Xia et al., 1999; Herrmann, 2002; Ohori et al., 2002; Arai and Tokimatsu, 2005.
- *MC* methods:
  - Simulated Annealing: e.g. Martinez et al., 1999, 2000;
  - Genetic Algorithm: e.g. Yamanaka and Ishida, 1996; Parolai et al., 2005; Picozzi et al., 2005b;
  - Neighbourhood Algorithm: e.g. Wathelet et al. 2004, Wathelet, 2005; Wathelet et al., 2005; Di Giulio et al., 2012; Hobiger et al., 2013.

- Hybrid strategy (MC and LIN methods). These strategies can be useful to face highly nonlinear problems. In particular, the use of global method allows an inversion analysis that does not depend upon an explicit starting model; the best-fitting model of MC is then used as the starting model for the LIN procedure that is able to drive the inversion to the global optimal minimum of the cost function. Two kinds of strategies has been used:
  - Simulated Annealing and LIN: Liu et al., 2005;
  - Genetic Algorithm and LIN: Picozzi and Albarello, 2007.

The knowledge of the nature and complexity of the data-model relationship of the problem (i.e., the degree of non-linearity), the number of unknowns, and the computational resources available, should help us to choose the most suitable inversion technique. Nevertheless, for highly non-linear problems with multiple minima/maxima in the objective function, like for example the inversion of surface wave dispersion curves where various models might explain the data set with equal misfit, a combination of exploration and exploitation should be more appropriate (Picozzi, 2005).

3.1.3.1 Genetic algorithms (GA)

Genetic Algorithms (GA) were originally devised by Holland (1975) as a model of adaptation in artificial systems. *GA* use random numbers to control the characteristics of the search process: this feature is typical of *MC* techniques. Several strategies were proposed to perform the inversion process with *GA* and, in general, an ensemble of specific operators is created for each particular application. The basic idea of *GA* is to mimic the natural optimization process of biological evolution. Indeed, processes based on evolution are particularly suitable for solving computational problems, and especially those that require to find a best solution among a huge number of possible alternatives. Moreover, *GA* require only the computation of the objective function to be minimized: for this reason, they are inherently stable and robust procedures. In seismology field, several papers dealing with *GA* have been produced in the early 1990s (Goldberg, 1989; Stoffa and Sen, 1991; Sambridge and Drijkoningen, 1992). Starting from this period, these inversion algorithms have been applied widely.
The basic structure of *GA* is summarized in Figure 3.9. The authors use stochastic processes to produce an initial population of models from a defined search area (parameter space) and then, those able to satisfy some particular criteria (objective function) are selected (selection operation) and used as parents for the generation of offspring (a new population of models). This generation stage happens generally by means of crossover and mutation operations (Picozzi, 2005). Finally, the process described is iterated until a suitable model or group of models evolve and the optimization criteria are satisfied.

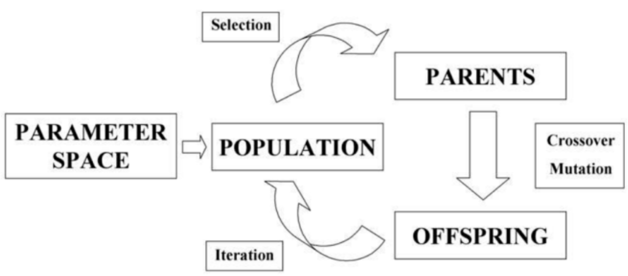

Figure 3.9 *The basic structure of genetic algorithms*

The first stage of building any evolutionary algorithm is to define a suitable genetic representation of a candidate solution to the problem. Several approaches have been proposed for this step of the algorithm. One of the most common one is to adopt the binary representation, where each parameter in the search area is digitized with a n-bit binary string of 2n. In particular, parameters at the lower and upper limits of the search area become (00…0) and (11…1), respectively and any other parameter to be examined is transferred to a binary string between these two limit strings (Picozzi, 2005). Subsequently, similarly again to the genetic operation, the binary strings relevant to all the parameters forming the model are concatenated in order to generate a "chromosome" to be used in the genetic operation. After this first step, a set of models (Q) has been randomly extracted from the parameter space in order to assess their ability to explain the observed data. However, it is not merely sufficient to define which the better models are, but it is necessary to quantify how much one model is better than another. Thus, a fitness function (f_j) must be evaluated for each model j. To this purpose, the differences between observed (d_0) and theoretical (dt) data are evaluated by the misfit function (ϕ) (Yamanaka and Ishida, 1996):

$$\emptyset_j = \frac{1}{N}\sum_{i=1}^{N}[\frac{(d_0)_i-(d_0)_i}{\sigma\,(d_0)_i}]^2 \qquad \text{(Eq. 3.11)}$$

where N is the number of data and $\sigma(d_0)_i$ is the standard deviation associated to the observed data $(d_0)_i$.

The fitness function f_j, is defined from Yamanaka and Ishida, 1996, $f_j = 1 / \emptyset_j$.
After this estimation, the parent selection operation is carried out in order to define which model should produce the offspring of the new population. In particular, models with higher values of f_j (or equivalently lower ϕ_j) have higher probability of proceeding to the next generation producing a set of Q new models (Gallagher and Sambridge, 1994). This stage is performed by means of the roulette rule (Goldberg, 1989): roughly speaking, it can be seen as the spinning of a one-armed roulette wheel where the sizes of holes are proportional to the probability of each model of being reproduced (Eiben and Smith, 2003). Using this approach, the population size does not change and multiple copies of models with higher fit will survive at the expense of those with lower fit, which could be extinguished completely. In conclusion, this operator introduces the element of survival of the fittest into the algorithm (Sambridge and Mosegaard, 2002). These reproduced models were modulated by the crossover and mutation operations. The crossover process allows merging the chromosome structure relevant to the parents, by the exchange and recombination of each parent structure (Gallagher and Sambridge, 1994). In other words, the offspring obtained are a combination of the parents' characteristics and might develop some different features. Usually, this operator starts from two parents and creates two offspring, although in the case of specific applications any number of parents can be used (Eiben and Smith, 2003). In practice, a threshold called "crossover probability", p_c, is determined. Then, all the Q parent strings are randomly paired and a random number ranging from 0.0 to 1.0 is generated. At this stage, if the random number is smaller than p_c, one of the forms of crossover takes place and the parents interchange a part of each bit string creating two new offspring (Figure 3.10). Otherwise, if the random number is greater than p_c, the two individuals in the original pair remain in the next generation (Picozzi, 2005). Mutation is instead a random process that allows the introduction of new characteristics unrelated to the parents into the offspring. It is a particular operator that considers each gene separately and has been introduced in *GA* with the aim to maintain a degree of diversity in the population. Also in this case a threshold value of mutation probability, p_m, is defined. Then, a series of random numbers ranging from 0.0 to 1.0 is generated and assigned to each gene: if these numbers are smaller than p_m, a bit in an individual string will flip from 0 to 1 and vice versa (Figure 3.10) (Picozzi, 2005). In general the selected value of p_m is relatively low.

Yamanaka and Ishida (1996) observed that using the simple *GA* an individual with the lowest misfit could not be selected for the next generation. Moreover, with this inversion scheme the crossover might also destroy the chromosome of the best individual. Therefore, to overcome these problems these authors proposed a modified version of *GA* taking advantage of two further operators: the elite selection and the dynamic mutation. The elite selection operator has been introduced in *GA* with the goal to ensure that the best model of a generation will be present also in the next one. For that reason, it simply replaces the worst model in the current generation with the best individual of the previous generation (Goldberg, 1989). Despite the advantages, the use of the elite selection might cause a premature convergence towards the model introduced by this operator that has a local minimum of the misfit. To avoid the risk of a bias in the inversion procedure, a new kind of mutation operator was introduced. It is called dynamic mutation, and is a generation-variant mutation probability that may help the inversion avoiding premature convergence (Sen and Stoffa, 1992).

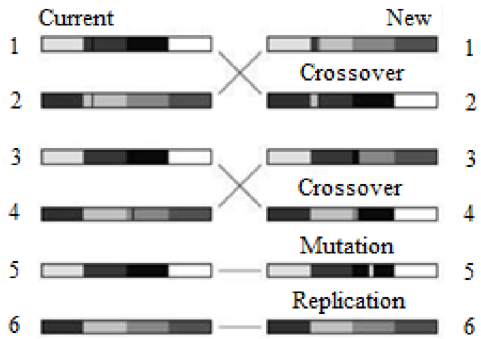

Figure 3.10 *The effect of crossover and mutation operators in a genetic algorithm. In cases 1–4, the crossover operator cuts, swaps, and rejoins pairs of strings. In case 5, mutation changes a single bit. In case 6 a whole string is replicated. The shading represents the values of four different variables encoded into the bit string (from Sambridge and Mosegaard, 2002).*

In practice, when most of the models in the current population have a similar fit and chromosome patterns, the parameter p_m is increased. After the variety of the chromosomes in the population is assured, pm assumes again the initial value (Picozzi, 2005). The average coefficient of variation (γ) is evaluated for all parameters in all individuals of each generation as:

$$\gamma = \frac{1}{M}\sum_{i=1}^{M}\frac{\sigma_i}{\bar{x}i} \qquad \text{(Eq. 3.12)}$$

where M is the number of parameters, $\bar{x_i}$ is the average of the i^th parameter, and σ_i is the standard deviation (Yamanaka and Ishida, 1996).

According to γ, the mutation probability p_m is defined as:

$$p_m = \begin{cases} p_i, \ \gamma > 0.1 \\ 0.1, \ 0.02 < \gamma < 0.1\,, \\ 0.2, \ \gamma < 0.02 \end{cases} \qquad \text{(Eq. 3.13)}$$

where p_i is the initial mutation probability.

After these adaptations, Yamanaka and Ishida (1996) showed that the modified *GA* found a better solution than the simple *GA*, as indicated by the lower misfit value at the end of the inversion process.

Despite the conceptual simplicity of the general *GA* structure, several aspects have to be considered for their implementation. The main reason for such difficulties is that each of the basic operations used must be properly adapted, bearing in mind the nature of the particular optimization problem of interest.

3.1.4 Equivalent linear analysis - Response spectrum

One-dimensional equivalent-linear site response analyses can be performed, to estimate the response spectrum of site and *S* wave velocity profile.

Generally, *S* wave velocity profile and response spectrum are estimated by seismic methods that requires specific apparatuses and, for some active methods also drilling, which influence in survey time and operative costs. A fast an inexpensive technique has been used in this thesis to estimate Vs profile (also V_{s30}). This method is based on HVSR of microtremors recorded at two single station by the help of two synchronized seismographs.

Ambient vibration measures have been acquired in the free field near the construction area to estimate the dispersion curve and the HVSR curve of site. The dispersion curves have been estimated from vertical components of a pair of synchronized ambient vibration measures acquired with two portable seismographs. The directionality of the signal may be a problem when using two-station method. Therefore, the knowledge of the location, using previous investigations and detailed stratigraphic sections are important parameter to identify the correct dispersion curve. ESAC2015 code, based on the SPatial AutoCorrelation zero crossing method, has been used to achieve the Rayleigh phase velocity dispersion curve between two sensors (two synchronized portable seismographs). Vertical components of pairs of synchronized ambient vibration measures, have been used as input to estimate those curves.

Seismic stratigraphic profile (1D model) has been estimated then by the inversion procedure with 'GAinvers6 code', which use as input the dispersion curve estimated first and the respective HVSR curve of ambient vibration measures. Finally, the response spectra and 1D-Vs model have been estimated performing an one-dimensional equivalent linear soil response analysis on 'STRATA' software. Seismic stratigraphic profile has been estimated first by the inversion procedure and then from equivalent linear analysis. The decay curves are taken from the bibliography for each soil layer. Stratigraphic profile and layer properties are identified by the geologic report which was realized before the construction of the hospital and several seismic surveys carried out by the Municipality of Sanremo for different study purposes. Stochastic variation of site properties, including shear-wave velocity, layer thicknesses, depth to bedrock, and shear modulus reduction and material damping curves have been taken into account on STRATA software.

Selected input data for equivalent linear numerical analyses concerning the soil stratigraphic profile, the geotechnical layer properties and seismic inputs can be summarized in:

- Seismic input: 7 input accelerograms selected for site class A, SLV limit state, 7 input accelerograms selected for site class A, SLD limit state, selected in Rexel v3.5 database;
- Dispersion curves of soil: from SPatial AutoCorrelation zero crossing method using ambient vibration measures acquired on site;
- Input Seismic Stratigraphic profile: defined from the Inversion analysis of dispersion curve and HVSR curve;
- Stratigraphic profile and layers properties (geology description and unit weight): geologic report achieved from the project design;
- Decay curve of layers: selected from bibliography.

Reference accelerograms of site have been identified from 'REXEL v3.5' database which select natural spectra recorded in Europe. REXEL v.3.5 software allows to build design spectra according to Eurocode 8, Italian seismic code (NTC2008) or completely user-defined. Horizontal and/or vertical components can be selected simultaneously or separately, depending on the number of components desired to be included in the ground motion, by using European, Italian or SIMBAD database. Two orthogonal independent components that describe the horizontal motion are characterized by the same elastic response spectrum as for the considered codes, while the component that describes the vertical motion is characterized by a specific spectrum.

The methodology applied in this thesis is summarized in the diagram at the Figure 3.11.

The outputs achieved from this analysis, seismic stratigraphic profile and the response spectra, have been used for V_{s30} estimation of and for several building verifications. V_{s30} estimated can be used to identify the subsoil class of the construction site. In the Table 5.13 are shown the subsoil category due to Italian and Eurocode standards classification. Estimation of V_{s30} for subsoil is required not only at large scale for regional Microzonation, but also at the single building for designing of its foundations and for future verification during its operability.

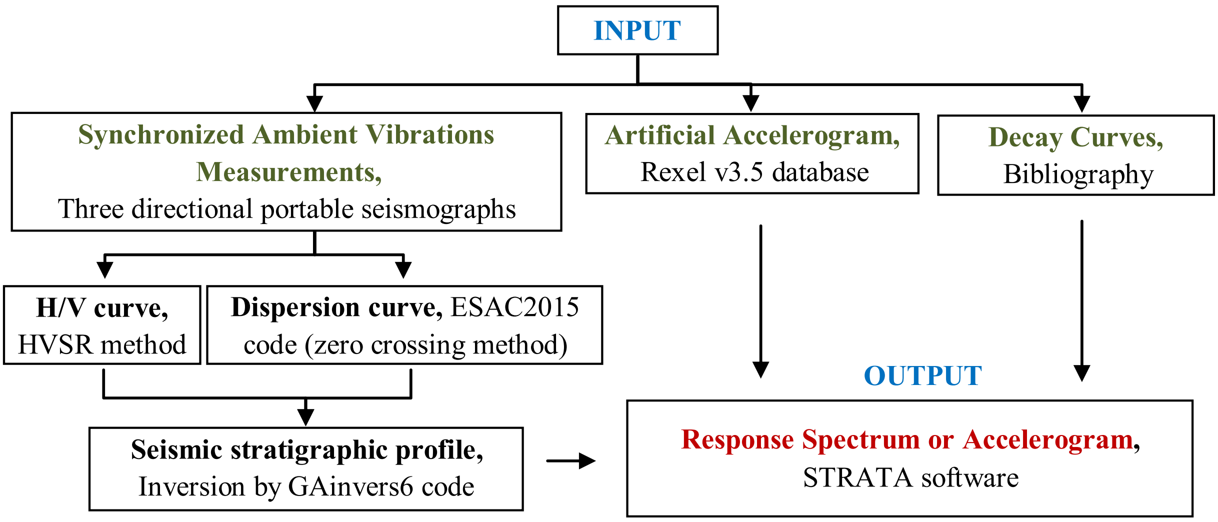

Figure 3.11 *Diagram of the steps performed for the equivalent linear analysis*

IV. DYNAMIC BEHAVIOR OF BUILDING - PASSIVE METHODS

In civil engineering, the understanding of structural dynamics is important in the design and retrofit of structures to withstand severe dynamic loading from earthquakes, hurricanes, and strong winds, or to identify the occurrence and location of damage within an existing structure. Structural dynamics, therefore, is a type of analysis that covers its behavior subjected to dynamic loads which include people, wind, waves, traffic, earthquakes, and blasts.

Modal analysis is a fundamental tool for understanding the dynamic behavior of a building and provides very useful information about the structure response to a dynamic load (e.g. an earthquake) in elastic field. Modal parameters of existing structures can be estimated experimentally and can be useful information for uploading Finite Element Model (FEM) for future structural verifications after an important earthquake, and Structural Health Monitoring (SHM), etc. Modes are inherent properties of a structure determined by the material properties (mass, damping and stiffness) and boundary conditions. Each mode is defined by a natural frequency (modal or resonant), a modal damping, and a mode shape, i.e. the so-called "modal parameters". If either the material properties or the boundary conditions of a structure change, its modes will change. For instance, if mass is added to a structure, it will vibrate differently. The natural frequencies and the mode shapes can be determined both from damped and no damped models. We have to do with real mode shapes in the case of no damped models and with complex mode shapes in case of damped model. Obviously in the case of experimental measurements it is always present a dissipation of energy, so, the measured fundamental modes are complex.

Techniques that enable the dynamic characterization of structures can be classified as either input output methods or output only methods. Input-output methods involve applying a known input, such as an impulse load, to the structure and measuring its output vibration response. Output only methods (OMA) involve measuring the output vibration of the structure in response to ambient vibrations which include loadings that may occur from wind, micro-earthquakes, vehicular and pedestrian traffic, and ocean waves (Farrar and Sohn, 2001). The ambient excitation is assumed to be a stationary random process containing a flat frequency spectrum (Salawu and Williams, 1995). Input-output methods have the advantage of suppressing noise effects on the structural response, which output-only methods do not have. However, input-output solutions tend to be more expensive than output-only solutions and usually create a disruption in the regular use of the structure. Output-only methods allow continuous uninterrupted acquisition or Structural Health Monitoring (SHM), because the structural response can be measured under operational conditions. Nonetheless, output only methods have the disadvantage that excitation forces are unknown and are not always able to excite the higher frequency modes of the structure.

The most commonly used data acquisition instruments for vibration-based damage detection are acceleration and displacement transducers. Recently, velocimeters also are used to structure monitoring of buildings. For civil structures, accelerometers tend to be the most widely used data acquisition instruments. This is due to their ability to operate over a large range of frequency responses, their ease of installment and high measurement accuracy (Green, 1995).

Modal parameters (modal frequencies and mode shapes) can be extracted from a dynamic analysis of a structures which are useful for structural verifications, uploading of Finite Element Model (FEM), SHM and damage detection, etc.

4.1 Dynamics of structures

The dynamic identification of a structure comprises the estimation of natural frequency, mode shapes and damping rations. Modal analysis is a fundamental tool for understanding the dynamic behavior of a building and provides very useful information about the structure response to a dynamic load (e.g. an earthquake) in elastic field. Modal parameters depend mainly by the material properties (mass, damping and stiffness) and boundary conditions. The natural frequencies and the mode shapes can be determined both from damped and undamped models having respectively complex mode shapes and real mode shapes. To understand these concepts, the basics of single and multiple degree of freedom systems are described in the following paragraphs.

4.1.1 Single degree of freedom system

Single-degree-of-freedom (SDOF) system is a system whose motion is defined just by a single independent co-ordinate which is a function of time. The behavior of SDOF systems is probably the most important topic in structural dynamics to be understood because the behavior of more complex systems, whose motion needs to be described by several coordinates, are simply collection of several SDOF systems. The prototype of a single degree of freedom system is a spring-mass-damper system in which the spring has no damping or mass, the mass has no stiffness or damping and the damper has no stiffness or mass. Furthermore, the mass is allowed to move in only one direction. The response of a free damped SDOF system and the response of a forced damped SDOF systems are described below.

4.1.1.1 Dynamics of a free SDOF system

The aim of developing a SDOF mathematical model is to use it in order to find the position u(t) of the moving mass m at any instant of time and therefore also its velocity u'(t) and acceleration u''(t). A *free damped SDOF systems* vibrate freely, after being released from an initial displacement. So, a SDOF oscillators require a restoring force on the mass that increases as displacement increases. The initial force is applied at the beginning of vibration at time t = 0, when initial displacement is $u(0) \neq 0$ or initial velocity is $u'(0) \neq 0$ or both applied simultaneously. An idealized undamped SDOF system does not have a mechanism for removing energy from the vibrating system. This energy consists of the potential energy stored in the spring:

$$U_s(t) = 0.5\ k\ u^2(t) \qquad \text{(Eq. 4.1)}$$

and kinetic energy stored in the moving mass:

$$U_m(t) = 0.5\ m\ u'^2(t)$$

The undamped SDOF system (see Figure 4.1, left), set in motion by an initial disturbance and in the absence of the energy dissipation, would continue to oscillate indefinitely. During this ideal process there is an exchange between the potential and kinetic energies, but the total energy initially supplied to the system remains constant.

In a damped system (see Figure 4.1, right) the total vibration energy supplied to the system decreases over time, so, the oscillations diminish and eventually cease. Some form of damping is always present in real vibrating systems. Essentially, damping has the ability to reduce to total vibration energy within the system by some means of energy dissipation, such as heating, radiation, etc. The damping, that produces a damping force proportional to the mass velocity, is commonly referred to as "viscous damping" and is denoted graphically by a dashpot. The structure response is described by the horizontal displacement *u(t)* of the oscillator with respect to the soil which can undergo by itself a displacement u_g (see Figure 4.2).

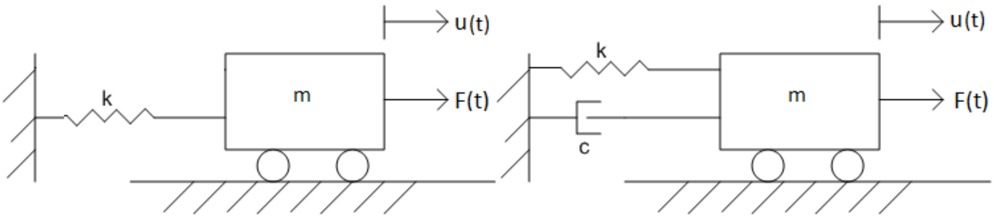

Figure 4.1 *Undamped SDOF system (left), damped SDOF system*

The equation of motion of an elementary oscillator presents the equilibrium of all forces acting on the system:

$f_I(t) + f_D(t) + f_S(t) = F(t)$ (Eq. 4.2)

where:

$f_I(t) = m\, u_i''(t)$ are inertia forces, $u_i''(t) = u''(t) + u_g''(t)$;

$f_D(t) = c\, u'(t)$ are damping forces;

$f_S(t) = k\, u(t)$ are strain forces;

and F(t) is the applied load which is 0 for free oscillations.

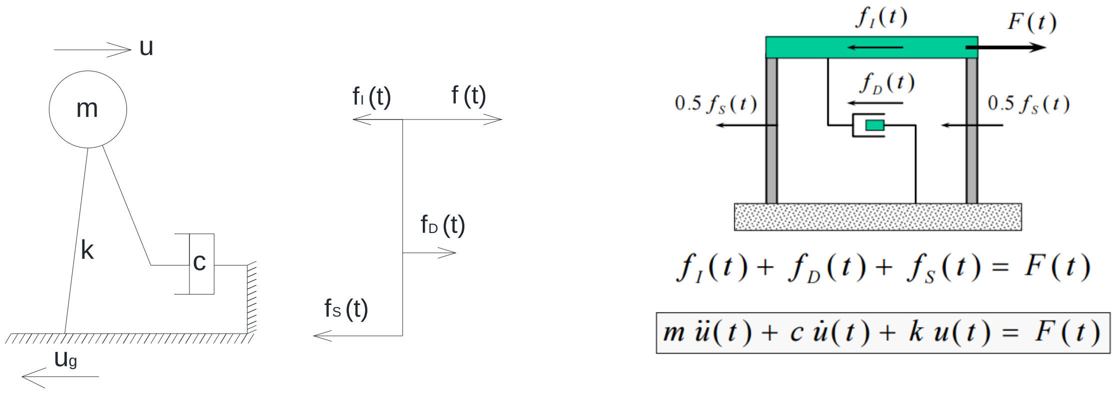

Figure 4.2 *Energy dissipation mechanisms of an elementary oscillator (left), equation of dynamic equilibrium (right)*

Substituting the above expressions to Equation 4.2, the equation of motion of a free damped SDOF system can be written in the form:

$mu''(t) + cu'(t) + ku(t) = 0$ (Eq. 4.3)

with the initial conditions: $u(t{=}0) = u_0$; $u'(t{=}0) = v_0$

in which *m* is the mass, *k* is the stiffness, *c* is the damping, *u(t)* is the displacement, *u'(t)* is the speed and *u''(t)* is the acceleration.

Dividing both sites of the above equation by *m* (Eq. 4.4) the canonical form of the equation of motion (Eq. 4.5) can be received:

$u''(t) + \frac{c}{m}u'(t) + \frac{k}{m}u(t) = 0$ (Eq. 4.4)

$u''(t) + 2\xi\omega_n u'(t) + \omega_n^2 u(t) = 0$

where $\omega_n = \sqrt{\frac{k}{m}} = \frac{2\pi}{T}$ is the angular speed of motion, and $\xi = \frac{c}{c_{cr}}$ is the damping coefficient that measure the capacity to dissipate energy during oscillations.

Assuming a solution form u(t) = C e^{st} and substituting it in the above equation,

$$s^2 + 2\xi\omega_n s + \omega_n^2 = 0 \qquad \text{(Eq. 4.5)}$$

we get the solution (Eq. 4.6):

$$s = \frac{-2\xi\omega_n \pm \sqrt{4\xi^2\omega_n^2 - 4\omega_n^2}}{2} = \left(-\xi \pm \sqrt{\xi^2 - 1}\right)\omega_n \qquad \text{(Eq. 4.6)}$$

Depending on the value of damping coefficient ξ and nature of solution *s* the corresponding *u(t)* will be determined as described in the following three cases (underdamped, critically damped and overdamped system).

As one can see, the equation of motion is a second order, homogeneous, ordinary differential equation (ODE). If all parameters (mass, spring stiffness, and viscous damping) are constants, the equation becomes a linear ODE with constant coefficients and can be solved by the characteristic equation method. The characteristic equation has two independent roots for the damped vibration problem. Those roots can fall into one of the following cases:

- If (c^2 - 4mk) < 0, the system is termed underdamped. The roots of the characteristic equation are complex conjugates, corresponding to oscillatory motion with an exponential decay in amplitude;
- If (c^2 - 4mk) = 0, the system is termed critically-damped. The roots of the characteristic equation are repeated, corresponding to simple decaying motion with at most one overshoot of the system's resting position;
- If (c^2 - 4mk) > 0, the system is termed overdamped. The roots of the characteristic equation are purely real and distinct, corresponding to simple exponentially decaying motion.

To simplify those solutions, the critical damping c_c, the damping ratio ξ and the damped vibration frequency ω_d are defined as:

$$c_{cr} = 2m\sqrt{(k/m)} = 2m\omega_n \qquad \text{(Eq. 4.7)}$$

$$\xi = \frac{c}{c_{cr}} = \frac{c}{2m\omega_n}$$

$$\omega_d = \sqrt{1-\xi^2\omega_n}$$

in which the ω_n is the natural frequency of the system.

The time solutions for the free SDOF system is presented below for each of the three case specified above.

In the case of *an underdamped system* (c^2 - 4mk < 0, equivalent to c < c_c or ξ< 1) the characteristic equation has a pair of complex conjugate roots (Eq. 4.8). The displacement solution for this kind of system has the form:

$$u(t) = c_1 e^{\left(-\xi + i\sqrt{1-\xi^2}\right)\omega_n t} + c_2 e^{\left(-\xi - i\sqrt{1-\xi^2}\right)\omega_n t} = e^{-\xi\omega_n t}[d_1\cos(\omega_d t) + d_2\sin(\omega_d t)] \qquad \text{(Eq.4.8)}$$

$$u(t) = \underbrace{e^{-\xi\omega_n t}}_{\text{Exponentially decay}}\left[\underbrace{u_0\cos(\omega_d t) + \frac{v_0 + \xi\omega_n u_0}{\omega_d}\sin(\omega_d t)}_{\text{Periodic motion}}\right]$$

while an equivalent solution must be:

$$u(t) = A_0{}^{-\xi\omega_n t}\cos(\omega_d t - \varphi_0)$$

The displacement-period graphic of an underdamped system is shown in Figure 4.3, the graphic on the left.

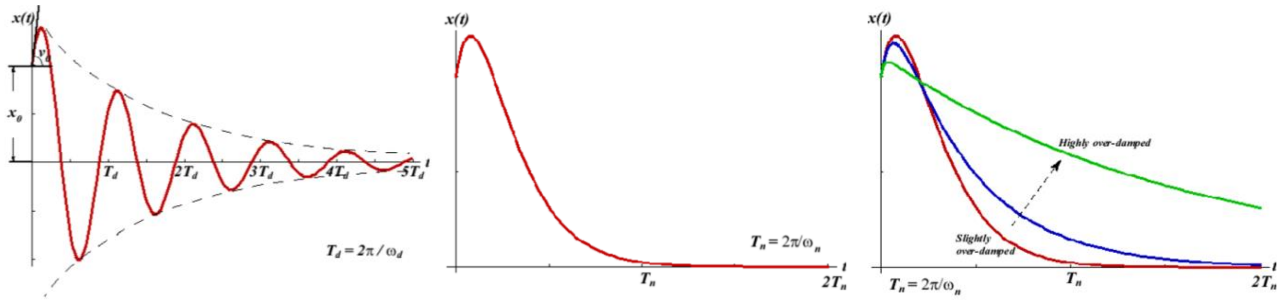

Figure 4.3 *The displacement-period graphics: an underdamped system (left), a critically damped system (center), an overdamped system (right)*

As one can see, from the equation above the displacement amplitude decays exponentially, so, the natural logarithm of the amplitude ratio for any two displacements separated in time by a constant ratio is a constant.

$$\frac{A_k}{A_{k+1}} = \frac{A_0 e^{-\xi\omega_n(kT_d)}\cos(\varphi_0)}{A_0 e^{-\xi\omega_n[(k+1)T_d]}\cos(\varphi_0)} = \frac{e^{-\xi\omega_n(kT_d)}}{e^{-\xi\omega_n[(k+1)T_d]}} = e^{\xi\omega_n T_d} \qquad \text{(Eq. 4. 9)}$$

$$\ln\left(\frac{A_k}{A_{k+1}}\right) = \xi\omega_n T_d = \xi\omega_n\frac{2\pi}{\omega_d} = \frac{2\pi\xi}{\sqrt{1-\xi^2}}$$

where $T_d = \frac{1}{f_d} = 2\pi/\omega_d$ is the period of the damped system.

In the case of *a critically damped system* (c^2 - 4mk = 0, equivalent to c = c_c or ξ=1) the characteristic equation has repeated real roots. The displacement solution for this kind of system is:

$$u(t) = (c_1 + c_2 t)e^{-\omega_n t} \qquad \text{(Eq. 4.10)}$$

$$u(t) = e^{-\omega_n t}[u_0 + (v_0 + \omega_n u_0)t]$$

The critical damping factor c_c can be interpreted as the minimum damping that results in a non-periodic motion. The displacement plot of a critically damped system is shown in the Figure 4.3 (the central plot). As can be seen from the figure, the displacement decrease level is negligible after a natural period T_n. Note that if the initial velocity v_0 is negative while the initial displacement x_0 is positive, there will exist one overshoot of the resting position in the displacement plot.

In the case of *an overdamped system* (c^2 - 4mk > 0, equivalent to c > c_c or ξ>1) the characteristic equation has repeated real roots. The displacement solution for this kind of system is:

$$u(t) = c_1 e^{\left(-\xi+\sqrt{\xi^2-1}\right)\omega_n t} + c_2 e^{\left(-\xi-\sqrt{\xi^2-1}\right)\omega_n t} \qquad \text{(Eq. 4.11)}$$

$$u(t) = \frac{u_0\omega_n\left(\xi+\sqrt{\xi^2-1}\right)+v_0}{2\omega_n\sqrt{\xi^2-1}}e^{\left(-\xi+\sqrt{\xi^2-1}\right)\omega_n t} + \frac{-u_0\omega_n\left(\xi-\sqrt{\xi^2-1}\right)-v_0}{2\omega_n\sqrt{\xi^2-1}}e^{\left(-\xi-\sqrt{\xi^2-1}\right)\omega_n t}$$

The displacement plot of an overdamped system is shown in the Figure 4.3 (plot on the right). The motion of an overdamped system is non-periodic, regardless of the initial conditions. The larger the damping, the longer is the time to decay from an initial disturbance. If the system is heavily damped, ξ>>1, the displacement solution takes the approximate form:

$$u(t) \approx u_0 + \frac{v_0}{2\xi\omega_n}(1 - e^{-2\xi\omega_n t}) \qquad \text{(Eq. 4.12)}$$

4.1.1.2 Dynamic of a forced SDOF system

In the Figure 4.3 (right) is shown the scheme of a forced damped SDOF system. When a SDOF system is forced by *f(t)*, the solution for the displacement *x(t)* consists of two parts: the complimentary solution, and the particular solution. The complimentary solution of the problem, is given by the free vibration discussed before while the particular solution depends on the nature of the forcing function. The forced system response is described by the following equation:

$$m\,u''(t) + c\,u'(t) + k\,u(t) = F(t) \qquad \text{(Eq. 4.13)}$$

where *m* is the mass, *c* is the damping, *k* is the stiffness, *u(t)* is the displacement, *u'(t)* is the speed and *u''(t)* is the acceleration.

Let's consider that SDOF system is forced by a sinusoidal load. In this case, the equation of motion has the following form:

$$m\,u''(t) + c\,u'(t) + k\,u(t) = r_0\,\mathrm{sen}(\omega_f\,t) \qquad \text{(Eq. 4.14)}$$

Using the dynamic parameters ξ and ω_n the equation of motion can be written as:

$$u''(t) + 2\xi\omega_n\,u'(t) + \omega_n^2\,u(t) = r'_0\,\mathrm{sen}(\omega_f\,t) \qquad \text{(Eq. 4.15)}$$

where $r'_0 = r_0/m$.

The ration β between the angular velocity of forcing and the angular velocity of oscillator measure the dynamic effect that the sinusoidal force produce.

$$\beta = \omega_f/\omega \qquad \text{(Eq. 4.16)}$$

In all cases in which $\beta \neq 0$ the equilibrium must be considered in dynamic terms with greater force of inertia as much β is near to one. A forcing is slower, i.e. modeled statically, when its angular velocity is different from the angular velocity of the free vibration of the oscillator, so as when β is different from one.

The oscillation are composed by a transitory term, which depend by the oscillatory characteristics (decrease with the increase of time t), and a stationary term which depends on the characteristics of forcing (doesn't change vs. time):

$$u(t) = Ae^{-\xi\omega t}\cos(\omega_D t - \varphi) + R\,U_{st}\mathrm{sen}(\omega_f t - \varphi_f) \qquad \text{(Eq. 4.17)}$$

where $R = [(2\beta\xi)^2 - (1-\beta^2)^2]^{-0.5} = \frac{u_{max}}{u_{st}}$ is the amplification factor of the dynamic resonance with respect to the static response, so is the static response calculated assuming none the inertia and viscosity forces $u_{st} = r_0/k$, $\varphi_f = f(\beta,\xi) = \tan^{-1}\left(\frac{2\xi\beta}{1-\beta^2}\right)$ is the phase angle to which it is associated the delay time between the forcing and the particular solution, $A = f(\beta,\xi)$ is the amplitude of the oscillation and *R* is the factor by which the displacement responses are amplified due to the fact that the external forcing is dynamic, not static.

In the Figure 4.4 is shown the relationship between the amplification factor *R* and β ration, from which we can identify three different areas of structure behavior: in the first one the frequency of forcing is too small compared to the frequency of the oscillator so the force can't excite the oscillator; the second part lies to the field of resonance, where the frequency of forcing is equal to that of oscillator, so as we have to do with the maximum of dynamic amplification; in the third area the frequency of forcing is too much compared to the frequency of the oscillator so the force varies rapidly and can't excite the oscillator.

In the case of a SDOF system forced by a harmonic function *F(t)*:

$$F(t) = f_0\,e^{i\omega f\,t} = a\cos(\omega_f\,t) + b\sin(\omega_f\,t) \qquad \text{(Eq. 4.18)}$$

where ω_f is the frequency of the forcing, in radians per second, the particular solution is:

$$u_p(t) = \frac{f_0}{(k - m\omega_f^2) + ic\omega_f} e^{i\omega_f t} \qquad \text{(Eq. 4.19)}$$

The general solution is given by the sum of the complimentary and the particular solutions multiplied by two weighting constants c_1 and c_2:

$$u(t) = c_1 u_c(t) + c_2 u_p(t) \qquad \text{(Eq. 4.20)}$$

where $u_c(t)$ is the complementary solution described for the free vibration case, the values of c_1 and c_2 are found by the initial conditions.

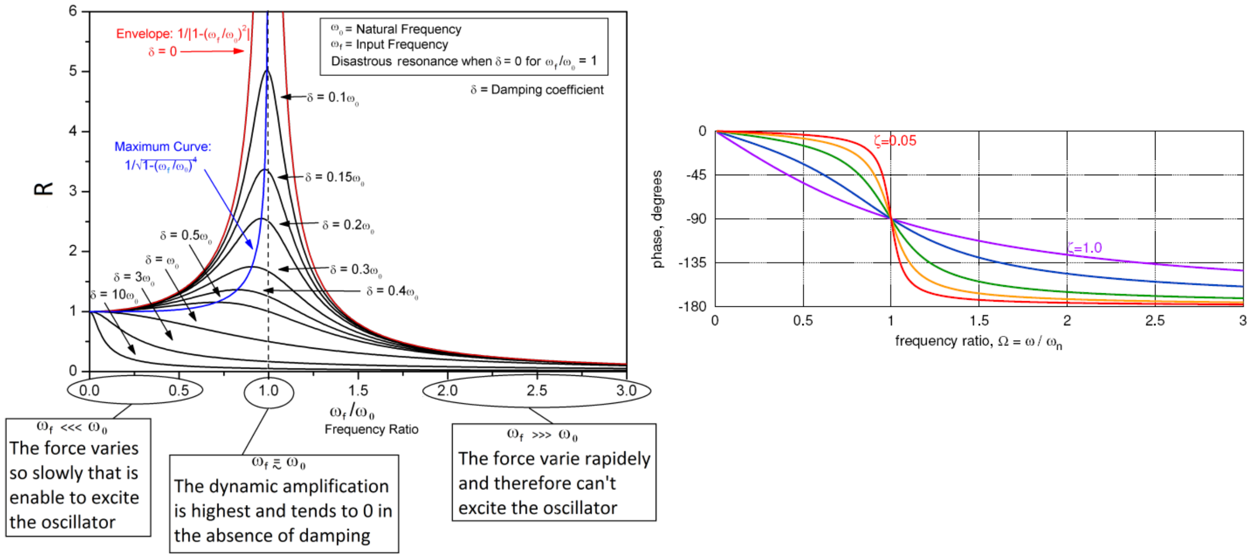

Figure 4.4 *Graphic of dynamic amplification factor for external forcing*

4.1.2 Multiple degree of freedom systems

A complex system cannot be described by a model with only one degree of freedom. Therefore, the multiple degree of freedom system need to be discretized in a system with N-degree of freedom, i.e. N-SDOF systems. The discretization of a frame structure plan is shown in the Figure 4.5. The nodes of the structure are the intersections of structural elements (beams and columns, in this case) while their degree of freedom (u, v, θ) corresponding to the displacement components (see Figure 4.5, plot on the left). The system can be considered as a combination of three components related to the mass (m), to the stiffness (k) and to the damping (c) (see Figure 4.5, plot on the right). The state of a system at a generic instant t, on which acting external forces variable in time, is described by displacements, velocities and accelerations. Therefore, the movement of N-degrees of freedom system is defined by the displacement of nodes at the variation of time. Discretization of kinematics through Lagrangian coordinates (degree of freedom of the system) is shown in the Figure 4.6 for pillars and beams deformable axially (plot on the left) and for pillars and beams not deformable axially (plot on the right).

'Coefficients of influence' of stiffness (k_{ij}), damping (c_{ij}) and mass (m_{ij}) must be defined to estimate respectively forces related to the elasticity, to the ability to dissipate energy and to the inertia of the system (Equation 4.2).

The elastic forces (f_{Si}) which act on the components of the stiffness are correlated with the displacements $\{u_j\}$. Applying a unit displacement of the degree of freedom j and blocking all the other degrees of freedom, it is necessary to apply forces (k_{ij}) along the other degrees of freedom i, to maintain the deformed configuration (see Figure 4.7, plot on the right).

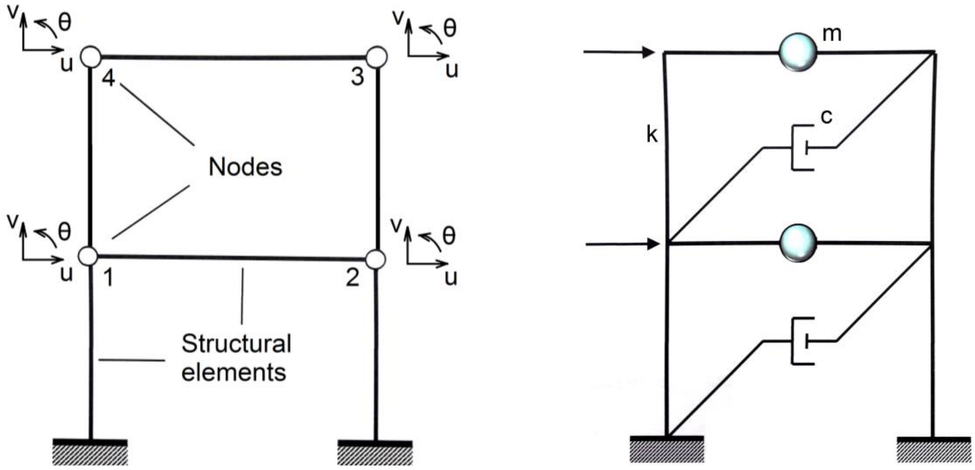

Figure 4.5 *Discretization of a frame structure plan*

Therefore, k_{ij} is the force required along the degree of freedom i by the effect of a unitary displacement along the degree of freedom j. In case of a system with N-degree of freedom, the elastic force (f_{Si}) along the degree of freedom i, is expressed as a function of displacements u_j (j=1...N) by the relationship:

$$f_{si} = k_{i1} \cdot u_1 + k_{i2} \cdot u_2 + ... + k_{ij} \cdot u_j + ... + k_{iN} \cdot u_N \qquad \text{(Eq. 4.21)}$$

For each j=1...N exist an analog equation with the one above and the set of those equations can be written in the matrix form as:

$$\begin{Bmatrix} f_{S1} \\ f_{S2} \\ . \\ . \\ . \\ f_{SN} \end{Bmatrix} = \begin{bmatrix} k_{11} & k_{12} \ldots k_{1j} \ldots & k_{1N} \\ k_{21} & k_{22} \ldots k_{2j} \ldots & k_{2N} \\ & \ldots & \\ & \ldots & \\ & \ldots & \\ k_{N1} & k_{N2} \ldots k_{Nj} \ldots & k_{NN} \end{bmatrix} \begin{Bmatrix} u_1 \\ u_2 \\ . \\ . \\ . \\ u_N \end{Bmatrix} \Longrightarrow \{f_S\} = [K]\{u\} \qquad \text{(Eq. 4.22)}$$

Mechanisms that dissipate the energy of vibrations are usually assimilated to a viscous equivalent damping. Therefore, the external forces of damping (c_{ij}) are correlated with the velocities $\{u_j'\}$. Each of unit velocities applied at the degree of freedom j, by keeping null the velocity along the other degrees of freedom, generate internal damping forces that will be balanced by the external forces. The 'coefficients of influence' of damping c_{ij} are the external forces along the degree of freedom i due to unit velocity applied along the j degree. In this case, the equation in matrix form is:

$$\begin{Bmatrix} f_{D1} \\ f_{D2} \\ . \\ . \\ . \\ f_{DN} \end{Bmatrix} = \begin{bmatrix} c_{11} & c_{12} \ldots c_{1j} \ldots & c_{1N} \\ c_{21} & c_{22} \ldots c_{2j} \ldots & c_{2N} \\ & \ldots & \\ & \ldots & \\ & \ldots & \\ c_{N1} & c_{N2} \ldots c_{Nj} \ldots & c_{NN} \end{bmatrix} \begin{Bmatrix} u'_1 \\ u'_2 \\ . \\ . \\ . \\ u'_N \end{Bmatrix} \Longrightarrow \{f_D\} = [C]\{u'\} \qquad \text{(Eq. 4.23)}$$

The same reasoning applies also to external forces, acting on the mass components of the structure, which are correlated to the accelerations $\{u_j''\}$. The fictitious forces of inertia oppose these accelerations (due to D'Alembert principle), therefore, external forces (m_{ij}) are needed to equilibrate those inertia forces. The 'coefficients of influence' of mass m_{ij} are the external forces along the degree of freedom i due to unit acceleration applied along the j degree.

The equation of inertia forces in matrix form is:

$$\begin{Bmatrix} f_{I1} \\ f_{I2} \\ . \\ . \\ . \\ f_{IN} \end{Bmatrix} = \begin{bmatrix} m_{11} & m_{12} \dots m_{1j} \dots & m_{1N} \\ m_{21} & m_{22} \dots m_{2j} \dots & m_{2N} \\ & \dots & \\ & \dots & \\ & \dots & \\ m_{N1} & m_{N2} \dots m_{Nj} \dots & m_{NN} \end{bmatrix} \begin{Bmatrix} u''_1 \\ u''_2 \\ . \\ . \\ . \\ u''_N \end{Bmatrix} \Longrightarrow \{f_I\} = [M]\{u''\} \quad \text{(Eq. 4.24)}$$

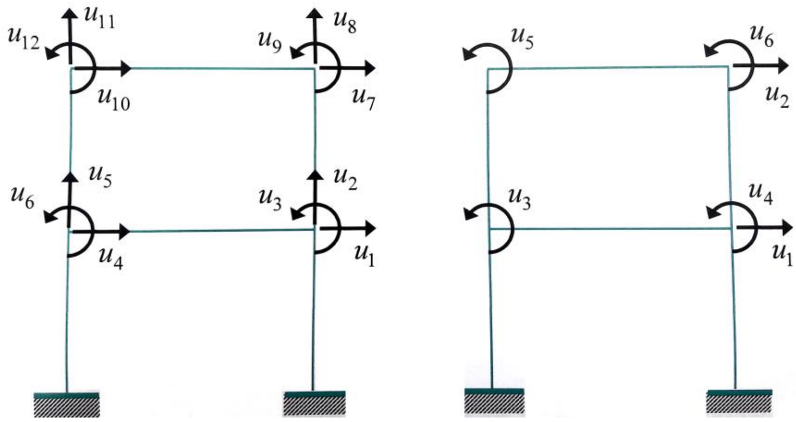

Figure 4.6 *Discretization of kinematics through Lagrangian coordinates for pillars and beams deformable axially (plot on the left) and for pillars and beams not deformable axially (plot on the right)*

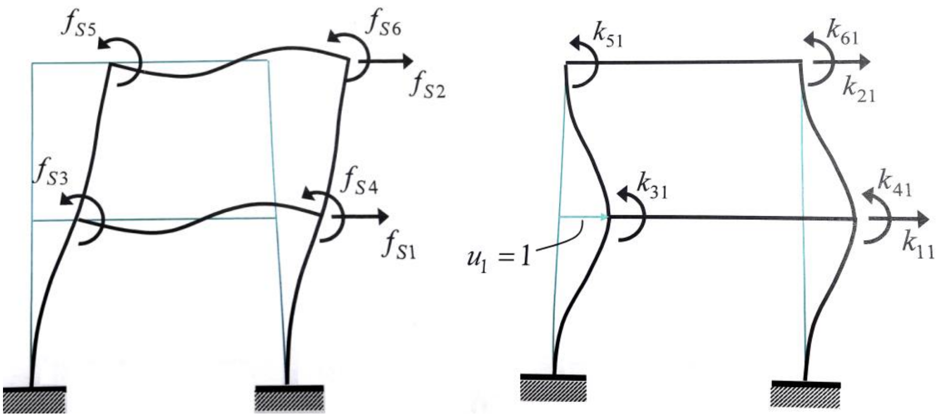

Figure 4.7 *Elastic forces which acts on the components of the stiffness (plot on the left). The influence coefficients by applying a unity displacement of the degree of freedom u_1 and blocking all the other degrees of freedom (plot on the right).*

The equations of motion of a multi degree of freedom (MDOF) system has the same form as the equation of the single degree of freedom (SDOF) elementary oscillator. Summarizing the above conclusions, the equation of the free vibration can be written in the form:

$$[M]\{u''(t)\} + [C]\{u'(t)\} + [K]\{u(t)\} = 0 \quad \text{(Eq. 4.25)}$$

in which [M] is the mass matrix, [C] is the damping matrix, [K] is the stiffness matrix,$\{u(t)\}$ is the vector of nodal displacements relative to not deformed structure, $\{u'(t)\}$ is the vector of nodal speed (du(t)/dt), and $\{u''(t)\}$ is the vector of nodal accelerations ($d^2u(t)/dt^2$). [M], [C] and [K] are N order square symmetric and positive matrices.

In the presence of a stress at the base, given by horizontal acceleration (seismic action) and defined as the second derivative of the soil displacement $\{u_s(t)\}$, the system suffers an external force equal to:

$$F_s(t) = [M]\{I\}\{u''_S(t)\} \qquad \text{(Eq. 4. 26)}$$

being I a vector of *N* element equal to 1, for which the equation of the motion becomes:

$$[M]\{u''^{(t)}\} + [C]\{u'(t)\} + [K]\{u(t)\} = \{F_s(t)\} \qquad \text{(Eq. 4. 27)}$$

The solution is searched in the form:

$$\{u(t)\} = \sum_{n=1}^{N} \Psi_n(t) \cdot \emptyset_n = [\phi] \cdot \{\Psi(t)\} \qquad \text{(Eq. 4. 28)}$$

by separating time dependent components $\Psi(t)$ from a shape function $[\phi]$ (the 'modal matrix'). If one assumes that:

$$\Psi(t) = e^{i\omega t}$$

Equation 4.25 becomes:

$$[M]\{\phi\}\,\omega^2 + [C]\{\phi\}\,\omega + [K]\{\phi\} = 0$$

That, for undamped systems reduces to:

$$[M]\{\phi\}\,\omega^2 + [K]\{\phi\} = 0 \qquad \text{(Eq. 4. 29)}$$

or

$$([M]\omega^2 + [K])\{\phi\} = 0$$

Representing the characteristic equation of the system.
To solve the equation one must have:

$$det([M]\omega^2 + [K]) = 0 \qquad \text{(Eq. 4. 30)}$$

In this way, *N* solutions are found for ω (the eigenvalues of the characteristic equation). Corresponding to these solutions one can find the values of $\{\phi\}$ satisfying the characteristic equation (the eigenvectors).

The Equation 4.30 represents a homogeneous linear system whose generic solution $\phi_i$is defined at less than a constant of proportionality. All eigenvectors corresponding to the N-roots ω_i^2 of the characteristic equation, can be obtained by repeating N-times this procedure. Calculating the j-th eigenvector by one of rules (normalization rule of the scalar and vector part: separation from shape and scale; unit normalization due to mass, which is implemented in software Sap2000), it can be normalized by decomposed it into shape and scale. This is an important aspects to be known, when identifying mode shapes from operational modal analysis using ambient vibrations, which can be achieved in different scale from theoretical results (Sap2000), due to the diverse normalization processes realized.

Modal superposition is a powerful idea of obtaining solutions from Equation 4.29. It is applicable to both free vibration and forced vibration problems. The uncoupled equations are in terms of variables called the modal coordinates. Solution for the modal coordinates can be obtained by solving each equation independently. A superposition of modal coordinates then gives solution of the original equations.
The orthogonality property of the natural modes of vibration can be used to uncouple the equations of motion of a viscous linear system to N-degrees of freedom. Considering a free-vibration equation, the modal angular velocity (eigenvalue) and the generic modal vector (eigenvector) can be defined solving the problem related to the eigenvalues of equation:

$$[K]\{\phi\} = \omega^2[M]\{\phi\} \qquad \text{(Eq. 4. 31)}$$

but there are *N*-values of ω and corresponding $\{\phi\}$,

$\omega_i; \phi_i \equiv \{\phi\}_i \qquad 1 \le i \le N$

Thus,

$$[K]\,\{\phi_i\} = \omega_i{}^2 [M]\,\{\phi_i\} \qquad 1 \le i \le N \qquad \text{(Eq. 4. 32)}$$

The eigenvectors have the fundamental property of being orthogonal with respect to [M] and [K] (see Equation 4.34). Consider the j-th mode (ω_j, ϕ_j) and premultiply both sides of Equation 4.32 by $\{\phi_j^T\}$ we have:

$$\omega_i{}^2\,\{\phi_j^T\}\,[M]\,\{\phi_i\} = \{\phi_j^T\}\,[K]\,\{\phi_i\} \qquad \text{(Eq. 4. 33)}$$

$$\{\phi_j^T\}\,[M]\,\{\phi_i\} = \{0\} \qquad \text{for } j \neq i \qquad \text{(Eq. 4. 34)}$$

$$\{\phi_j^T\}[K]\,\{\phi_i\} = \{0\} \qquad \text{for } j \neq i$$

or $[\Psi]^T[M]\,[\Psi] = [M_r]$

or $[\Psi]^T[K]\,[\Psi] = [K_r]$

where the *r* symbol indicate diagonal matrix and the elements, different from 0, in the diagonal, indicate the generalized mass or stiffness $([M_r],[K_r])$ of the r-th mode. $[\Psi]$ is one of eigenvectors matrixes. From ∞ solution of $[\Psi]$ is chosen $[\emptyset] = \alpha\,[\Psi]$, normalized with respect to [M].

Assuming that the vectors $\{\phi_i\}$ are normalized to [M], we can write the following relations:

$$\{M_i\} = \{\phi_i^T\}\,[M]\,\{\phi_i\} = \{1\} \qquad \text{(Eq. 4. 35)}$$

$$\{K_i\} = \{\phi_i^T\}[K]\,\{\phi_i\} = \{\omega_i^2\}$$

or $[\emptyset]^T\,[M]\,[\emptyset] = [I]$

or $[\emptyset]^T\,[K]\,[\emptyset] = [\omega_r^2]$

in which [I] is the unit diagonal matrix, and $[\omega_r^2]$ is the only one diagonal matrix solution of eigenvectors.

Also, it is supposed that the eigenvectors, as well as being orthogonal with respect to [M] and [K], are also orthogonal with respect to [C]:

$$\{\phi_j^T\}\,[C]\,\{\phi_i\} = \{0\} \qquad \text{for } j \neq i \qquad \text{(Eq. 4. 36)}$$

$$\{C_i\} = \{\phi_j^T\}\,[C]\,\{\phi_i\} = 2\,\{\xi_i\}\,\{\omega_i\}$$

where ξ_i is the modal ratio of viscous damping which is a positive number much smaller than one for the civil structures ($0 \le \xi_i << 1$) and is determined as:

$$\xi_i = \frac{C_i}{2\cdot\omega_i\cdot M_i} = \frac{1}{2}\left(\frac{\alpha}{\omega_i} + \beta\cdot\omega_i\right) \qquad \text{(Eq. 4. 37)}$$

The system is defined as classically damped if the Equations 4.36 are verified. This happens when [C] matrix satisfies the relation $[C][M]^{-1}[K] = [K][M]^{-1}[C]$. Referred to Equations 4.34, 4.35 and 4.36, the Equation of motion 4.27, for a system with N uncoupled modal equation, can be written as:

$$[M_i]\,\{\Psi_i''(t)\} + [C_i]\,\{\Psi_i'(t)\} + [K_i]\,\{\Psi_i(t)\} = \{F_i(t)\} \qquad \text{(Eq. 4.38)}$$

$$\{F_i(t)\} = [\emptyset_i^T]\,\{F_s(t)\} = [\emptyset_i^T]\,[M]\,[I]\,\{x_S''(t)\} = \Lambda_i\,\{x_S''(t)\} \qquad 1 \le i \le N$$

where Λ_i is the modal factor of the seismic action, and $\Psi_i(t)$ are the unknowns (modal coordinates, or principal coordinates, or amplitude of mode shapes).

Those functions $\Psi_i(t)$ define a transformation of coordinate for which the displacement vector {u(t)} is equal to the sum of *N* modal responses $u_i(t)$, relating to the *N* modes of vibration given by the expressions:

$$u_i(t) = \Psi_i(t) \cdot \phi_i \qquad \text{(Eq. 4.39)}$$

$$\{u(t)\} = \sum_{i=1}^{N} u_i(t) = \sum_{i=1}^{N} \Psi_i(t) \cdot \phi_i = [\phi] \cdot \{\Psi(t)\}$$

where $[\phi]$ is the modal matrix (which has the eigenvectors ϕ_i for columns); $\{\Psi(t)\}$ is the vector which has as elements the *N*-functions $\Psi_i(t)$.

It is therefore concluded that if the system is classically damped, the modal matrix makes possible to uncouple the Equation of motion 4.27 since $[\phi]$ makes simultaneously [M], [C] and [K] diagonal matrices. The damping matrix [C] can be written in the form (proportional dissipation):

$$[C] = \alpha\,[M] + \beta\,[K] \qquad \text{(Eq. 4.40)}$$

In which the α and β are real numbers.

The equations (4.38) have the same form as for a damped SDOF system subject to external forcing. For this reason the quantities M_i, C_i and K_i respectively defined by equations 4.35 and 4.36 are the generalized properties (mass, damping and stiffness) of the system associated to i-th mode of vibration, while $F_i(t)$ represents the generalized forcing. The coefficient of modal participation ratio is estimated by the expression:

$$L_i = \frac{\Lambda_i}{M_i} = \frac{\phi_i^T [M]\, I}{\phi_i^T [M]\, \phi_i} \qquad \text{(Eq. 4.41)}$$

and has an importance in structural analysis since it determines the influence that has the i-th mode of vibration in the calculation of displacements and forces for the seismic action $d^2x_S(t)/dt^2$. The equation 4.38 can be written in the form:

$$\Psi_i''(t) + 2\,\xi_i\,\omega_i\,\Psi_i'(t) + \omega_i^2\,\Psi_i(t) = L_i\,x_s''(t) \qquad \text{(Eq. 4.42)}$$

and have a solution of the type such as:

$$\Psi_i(t) = \frac{L_i}{\omega_{Di}} \cdot X_i(t) \qquad \text{(Eq. 4.43)}$$

In which the $X_i(t)$ is the convolution integral (or integral of Duhamel) given by the expression:

$$X_i(t) = \int_0^t x_s''(\tau) \cdot \sin(\omega_{Di}(t-\tau)) \cdot \exp(-\xi_i \cdot \omega_i (t-\tau))\,d\tau \qquad \text{(Eq. 4.44)}$$

$$\omega_{Di} = \omega_i \sqrt{1-\xi_i^2}$$

The integral function $X_i(t)$ depends on the mode of vibration through the damping ratio ξ_i and the angular velocity ω_i. The modal response of the system relative to the i-th mode is given by:

$$u_i(t) = \frac{L_i}{\omega_{Di}} \cdot X_i(t) \cdot \phi_i \qquad \text{(Eq. 4.45)}$$

So, the displacement vector {u(t)} of the system, obtained by the Equation 4.39, is the sum of all these answers:

$$u(t) = \sum_{i=1}^{N} \frac{L_i}{\omega_{Di}} \cdot X_i(t) \cdot \phi_i \qquad \text{(Eq. 4.46)}$$

4.1.2.1 Modal analysis of a free undamped 2-DOF system

The estimation of frequencies and mode shapes of a free 2-DOF undamped system are described. The steady state vibration at any resonant frequencies ω_i takes place in the form of a special oscillatory shape, known as the corresponding mode shape ϕ_i. The mode shapes (ϕ_1, ϕ_2) define the relative amplitudes of motion of the different degree of freedom. The equation of motion in matrix form of a two degree of freedom system is:

$[m] \{u''(t)\} + [k] \{u(t)\} = 0$

$$\begin{bmatrix} m_1 & 0 \\ 0 & m_2 \end{bmatrix} \begin{Bmatrix} u''_1 \\ u''_2 \end{Bmatrix} + \begin{bmatrix} (k_1 + k_2) & -k_2 \\ -k_2 & k_2 \end{bmatrix} \begin{Bmatrix} u_1 \\ u_2 \end{Bmatrix} = \begin{Bmatrix} 0 \\ 0 \end{Bmatrix}$$

In this case $k_{11} = (k_1 + k_2)$, $k_{12} = k_{21} = - k_2$ and $k_{22} = k_2$, referred to the Equation 4.22.

The two equations of motion can also be written as:

$m_1 u''_1(t) + (k_1+k_2)\, u_1(t) – k_2\, u_2(t) = 0$ with solution form $u_1(t) = X_1 \cos(\omega t + \varphi)$,

$m_2 u''_2(t) – k_2\, u_1(t) + k_2\, u_2(t) = 0$ with the solution form $u_2(t) = X_2 \cos(\omega t + \varphi)$.

in which X_1 and X_2 are the maximum amplitude of $u_1(t)$ and $u_2(t)$ and φ is the phase angle.

For 2-DOF system roots are found by solving the characteristic equation $(([k]-\omega^2[m]) \{u\} = 0)$, from which are defined ω_1, ω_2 (the natural frequencies of this system). At this aim, the determinant of the characteristic equation must be defined:

$$det\begin{bmatrix} -m_1\omega^2 + (k_1 + k_2) & -k_2 \\ -k_2 & -m_2\omega^2 + k_2 \end{bmatrix} = 0$$

or $((k_1+k_2) - \lambda m_1)(k_2 - \lambda m_2) - (-k_2)(-k_2) = 0$, in which $\lambda = \omega^2$

or $(m_1\, m_2)\, \lambda^2 - (m_2\, k_2 + m_1\, k_2 + m_2\, k_1)\, \lambda + k_1\, k_2 = 0$

The standard approach can be used to solve those equation:

$a\, \lambda^2 + b\, \lambda + c = 0$

where general solution is: $\lambda_{1,2} = \frac{-b \pm \sqrt{b^2 - 4ac}}{2a}$

Therefore, the natural frequencies of the system are defined as:

$$\omega_1^2, \omega_2^2 = \frac{(k_1 + k_2)m_2 + k_2\, m_1}{2(m_1 m_2)} \pm [(\frac{(k_1 + k_2)m_2 + k_2\, m_1}{m_1 m_2})^2 - 4(\frac{(k_1 + k_2)\, k_2 - k_2^2}{m_1 m_2})]^{1/2}$$

To define the mode shapes (one for each identified ω_i) the value of ω_i must be substitute in the characteristic equation):

$([k]-\omega_i^2[m]) \{\phi_i\} = 0$

and solve it for the vector $\{u\}$ which will define the corresponding mode shape ϕ_i.

The frequency ratio are:

$$r_1 = \frac{u_2{}^{(1)}}{u_1{}^{(1)}} = \frac{-m_1\omega^2{}_1 + (k_1 + k_2)}{k_2} = \frac{k_2}{-m_2\omega^2{}_1 + k_2}$$

$$r_2 = \frac{u_2{}^{(2)}}{u_1{}^{(2)}} = \frac{-m_1\omega^2{}_2 + (k_1 + k_2)}{k_2} = \frac{k_2}{-m_2\omega^2{}_2 + k_2}$$

The normal mode of vibration (the modal vectors) are:

$$U^{(1)} = \begin{Bmatrix} u_1{}^{(1)} \\ u_2{}^{(1)} \end{Bmatrix} = \begin{Bmatrix} u_1{}^{(1)} \\ r_1\, u_1{}^{(1)} \end{Bmatrix} \quad \text{first mode;} \qquad U^{(2)} = \begin{Bmatrix} u_1{}^{(2)} \\ u_2{}^{(2)} \end{Bmatrix} = \begin{Bmatrix} u_1{}^{(2)} \\ r_2\, u_1{}^{(2)} \end{Bmatrix} \quad \text{second mode}$$

The free vibration solution is:

$$u^{(1)}(t) = \begin{Bmatrix} u_1{}^{(1)} cos(\omega_1 t + \varphi_1) \\ r_1\, u_1{}^{(1)} cos(\omega_1 t + \varphi_1) \end{Bmatrix} \text{ first mode; } u^{(2)}(t) = \begin{Bmatrix} u_1{}^{(2)} cos(\omega_2 t + \varphi_2) \\ r_2\, u_1{}^{(2)} cos(\omega_2 t + \varphi_2) \end{Bmatrix} \text{ second mode}$$

The unknown constant $(u_1{}^{(1)}, u_1{}^{(2)}, \varphi_1,\ \varphi_2)$ can be determined from the initial conditions at time 0. Therefore, the eigenvector are determined:

$$\phi_1 = \begin{bmatrix} \phi_{11} \\ \phi_{21} \end{bmatrix};\quad \phi_2 = \begin{bmatrix} \phi_{12} \\ \phi_{22} \end{bmatrix}$$

The mode shapes of 2-DOF system are shown in the Figure 4.8.

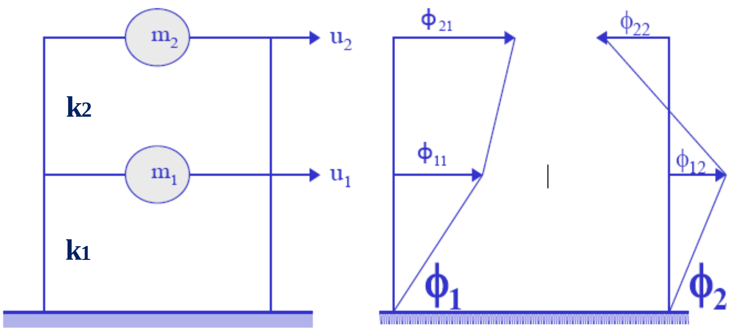

Figure 4.8 *Mode shapes of a 2-DOF system*

4.2 Dynamic identification methods

Dynamic identification methods of systems acts as interface between the physics of dynamical systems and their idealization by means of mathematical models. Mathematical models of dynamic systems are creating by a series of experimental data measured which can be input-output systems or output-only systems where input are forcing and output is the response. In addition, the dynamical systems are often subject to noise disturbances, which usually are not measured.

Dynamic identification methods provide as results the modal parameters of the structure, such as the natural frequencies, the mode shapes and the damping ratios, which can be used in civil engineering for:

- Estimation of structural response;
- Structural health monitoring and damage identification;
- FEM model updating;
- Sensitivity analysis etc.

Two type of modal analysis are considered within this thesis: the Operational Modal Analysis (OMA) and the Experimental Modal analysis (EMA). In the last few years OMA has acquired a broad application in structural and mechanical engineering fields because it measures the response of the structure without interrupting its functionality. In fact, using OMA method does not need to perform shaker tests or impact tests. This technique extracts the modal properties of the building by analyzing its dynamic output response to its operational input excitation. OMA can be used for structural monitoring which offers a series of applications in the field of civil engineering, such as design, damage evaluation, maintenance and reinforcement of the existing structures.

Experimental modal analysis (EMA) is an effective instrument for describing, understanding

and modeling the dynamic behavior of a structure. It can be carried out to determine the natural frequencies and mode shapes of a structure and to verify accuracy and calibrate a finite element model (FEM). Also combined EMA/OMA method can be used.
Before starting with the description of those two methods, used for dynamic characterization of structures, let's see briefly the signal processing.

4.2.1 Signal processing

Usually, the accelerometers or velocimeters are utilized for dynamic characterization and structure monitoring. In this study the velocimeters sensor were employed to calibrate the finite element model of the project. The signal processing consist on various steps which has their importance in the quality of results. To define the modal parameter from passive seismic measurement carried out inside the building, the signals should first be integrated, filtered if necessary, pass in frequency domain using the fast Fourier transform, estimate the frequency response function, estimate the cross/auto power spectral density and then perform frequency domain decomposition. It is important to know those processes to evaluate the reliability of outcomes.
The measurements carried out can contain noise which sources can be caused by:

- *noise from measurement* that depends on electrical deviations, sensitivity variations due to the temperature and the humidity, aging and other phenomena that are related to instrumentation;
- *computational* noise that comes from the use of discrete data that describe continuous phenomena (ex. truncation of signal, aliasing, leakage, etc.).

The choice of the *sample frequency* has an important role in the natural frequency estimation. The sample frequency f_s is the frequency by which the Analog/Digital conversion is realized. An analog signal, whose frequency band is limited by the frequency f_M, can be uniquely reconstructed from its samples taken at frequency f_s, if $f_s > 2f_M$. This is the content of the Nyquist sampling theorem that is fundamental in digital signal processing as establishes a sufficient condition for a sample rate that permits to capture all the information from a continuous-time signal of finite bandwidth, so as, to pass from continuous-time signals (often called "analog signals") to discrete-time signals (often called "digital signals") without aliasing error. The frequency $f_N = 2\ f_M$ is called the Nyquist frequency. In cases when the f_s is greater than f_N we are oversampling, while when the f_s is lower than f_N we are under-sampling which can cause the *aliasing* phenomenon. In the Figure 4.9, the effects of the aliasing error in the frequency results, are shown. The aliasing frequency (A_2, A_3, in the graphic) are calculated by the expression: Aliasing frequency = abs (integer multiple of f_s - frequency of signal). In this way the frequency F_2 = 50 Hz of the original signal is 30 Hz due to aliasing error and also for the F_3= 260 Hz which is 20 Hz in the sampled signal.
A_2 = abs(80-50) = 30 Hz; A_3 = abs(3*80-260) = 20 Hz.

An antialiasing filter should be used to eliminate the errors. The most common way to avoid the aliasing is to filter the input signal (before passing from analog to digital) using a low pass filter with a cutoff frequency equal to half the sampling frequency. This filter takes the name of anti-aliasing filter and is implemented on all modern acquisition systems. Those filters show a gradual attenuation of the signal therefore, the cutoff frequency is not perfectly equal to the half of the *fs*. In the measurement carried out for this study, the sampling frequency is chosen correctly so, there isn't applied any antialiasing filter in the signals.
The *leakage effect* is another problem derived by the signal processing when calculating the discrete Fourier transform or truncate the signals. The discrete/fast Fourier transform utilizes a discrete number of cycles of the signal, but in real cases is difficult to obtain a whole number of oscillations. This cause the leakage error and to reduced it a windowing function (Hanning

window) must by applied.
The correction of *spurious trend* should be realized when the signal measured does not have a zero mean, or has a linear or parabolic trend etc. In these cases the signal must be filtering by using the polynomial of degree n, to eliminate problems in case of signal integration.

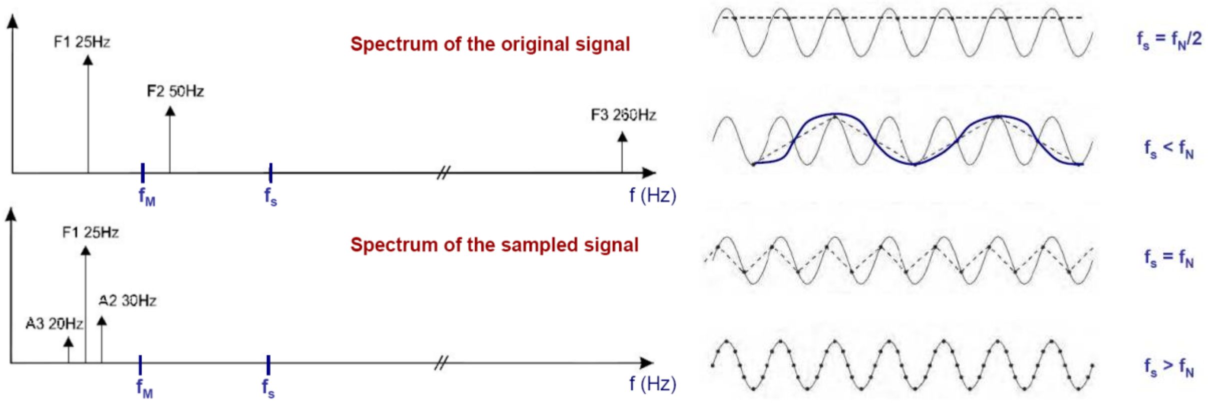

Figure 4.9 *Aliasing error effects on frequency results*

Spectral smoothing can be realized for a better resolution in frequency. This process consist of dividing the signal in segment and applying the discrete Fourier transform to each windowed and mediated segments. In this way the frequency resolution of the discrete Fourier transform is reduced. Practically, an overlapping of the signal, to increase the spectrum estimate as a result of the windowing, is realized.

The numerous kinds of *filters* can be classified in three types: low pass filter, high pass filter and band pass filter. A *low-pass filter* is an electronic filter that passes low-frequency signals but attenuates (reduces the amplitude of signals) the signal segment with frequencies higher than the cutoff frequency. The actual amount of attenuation for each frequency varies from filter to filter. A low-pass filter is the opposite of a high-pass filter. A *high-pass filter* is an electronic filter that passes high-frequency signals but attenuates (reduces the amplitude of signals) the signal with frequencies lower than the cutoff frequency. The actual amount of attenuation for each frequency varies from filter to filter. A band-pass filter is a device that passes frequencies within a certain range and rejects (attenuates) frequencies outside that range. A band-pass filter is a combination of a low-pass and a high-pass filter. Schematically those filters are presented in the Figure 4.10.

The *Butterworth filter* constitute a family of filters that satisfied well the requirements on the pass-band gain and less well in the transition band. It is also referred to as a maximally flat magnitude filter. A Butterworth filter is characterized by two parameters: the order N and the cutoff frequency ω_c. The general form of the transfer function module of a Butterworth filter of N-order and cutoff frequency ω_c is:

$$|H(j\omega)| = \frac{\mathrm{Go}}{\sqrt{(1+\frac{j\omega}{\mathrm{j}\omega_c})^{2N}}} \qquad \text{(Eq. 4.47)}$$

where G_o is the *DC* gain (gain at zero frequency), *N* is the order of filter, while ω/ω_c denotes the normalized frequency to the cutoff frequency.

The transfer function H(s) where s = $\sigma + j\omega$ (from Laplace transform) is determined by the expression:

$$H(s)H(-s) = \frac{G^2o}{(1+\frac{-s^2}{\omega^2 c})^N} \quad \text{(Eq. 4.48)}$$

where the denominator is a *N*-th polynomial of Butterworth in s. If *N* is even, the polynomial is given by the product of *N/2* second-degree polynomials of type (s^2 + b s + s) with b> 0, while if *N* is odd then there is also present the factor (s+1).

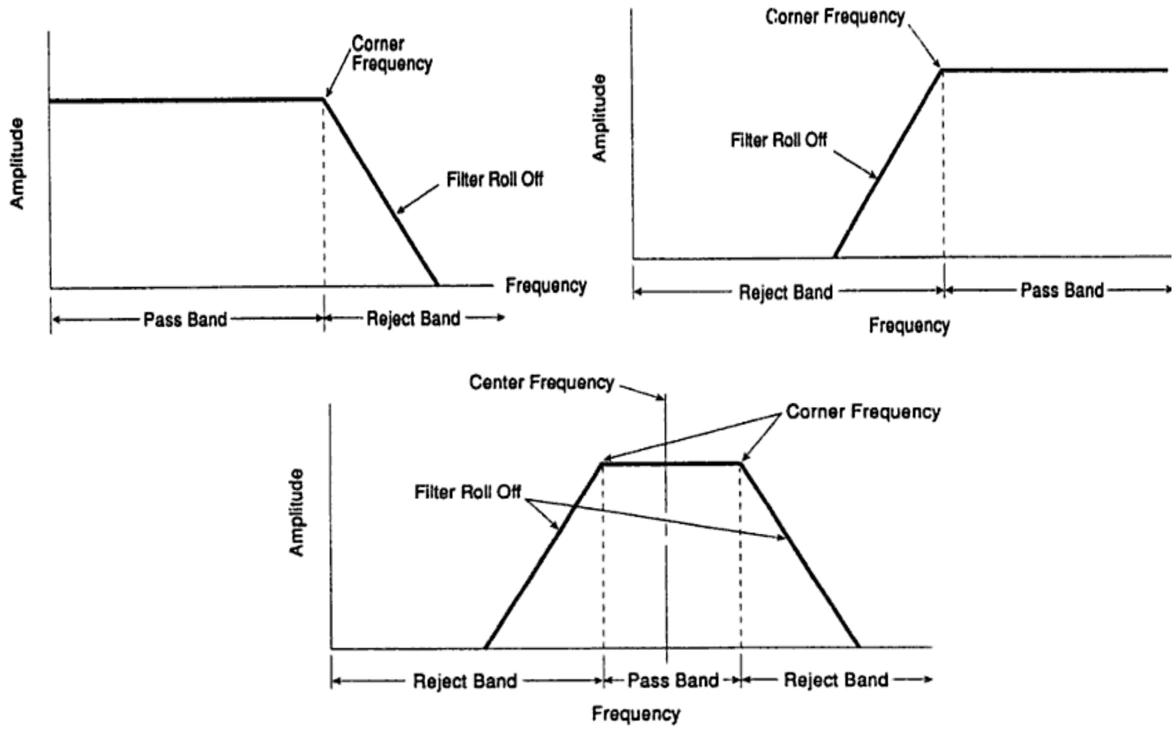

Figure 4.10 *Filter types: low pass filter, high pass filter and band pass filter*

An interesting property is that all polynomials have roots that lie on the unit circle.

B1 (s) = s + 1 (Eq. 4.49)
B2 (s) = s^2 + 1.414s + 1
B3 (s) = (s + 1)(s^2 + s + 1)
B4 (s) = (s^2 + 0.765s + 1)(s^2 + 1.848s + 1)

The frequency response of some Butterworth filters with different order number is shown in the Figure 4.11 in which we can do the following observations:
- the cutoff frequency of 3dB ω_c, is independent of the filter order N;
- the attenuation in the non-pass band depends critically on N;
- there are no oscillations in pass band and in the prohibited band.

The Butterworth filter has the largest "flatness" in pass band compared to the other filter types. In a typical design situation, the cutting desired frequency ω_c is fixed, while the order *N* is chosen so as to satisfy the demand for the attenuation in the prohibited band.

The measure of ambient vibration can be used either by position, velocity, or acceleration, depending on the type of instruments used to perform the measurement. The three quantities are interrelated through integrals and derivatives. As it is known, any vibration occurring at a given frequency can be described at a sinusoidal motion (simple sine wave) and its acceleration can be written as:

a = -A sin(2πft)

in which *A* is the peak acceleration (the amplitude) and *f* is the frequency.

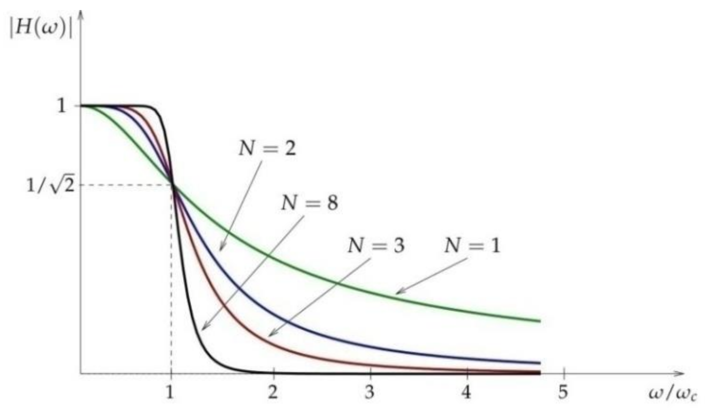

Figure 4.11 *Butterworth filter for different N-order*

The signal in velocity derives from integration of acceleration:

$$v = -\int A\sin(2\pi ft)\,dt = \frac{A}{2\pi f}\cos(2\pi ft) \qquad \text{(Eq. 4.50)}$$

The peak or the root means square value of the motion can be written as $v = \frac{A}{2\pi f}$ and doesn't vary with time.

In the like manner the equation of displacements is:

$$x = -\iint \sin(2\pi ft)dt\ ; \quad x = (\frac{A}{2\pi f})^2 \sin(2\pi ft) \qquad \text{(Eq. 4.51)}$$

The methods of integration that exist in practice are two: digital and analog integration. The *digital integration* can be performed by many spectrum analyzers. The analyzer after reads the time domain acceleration signal generates the frequency domain spectra via a FFT calculation. To receive the velocity data are used 400-line analyzer that are divided of a corresponding 400 center frequencies multiplied by 2π. The advantage of this system is that either the acceleration and velocity spectra may be viewed at any time. The disadvantage is that the precision of each of the 400 calculations is a function of the bandwidth of each of the filter bins. When used digital integration of an accelerometer signal to get velocity or displacement, a calibration correction must be made by either the analyzer or by hand. The correction consist in changes the calibration from mV/g (at a single integration or g-sec at a double integration) to mV/in/sec/sec (mV/g/(386 in/sec/sec/g) = mV/g · 0.00259 = mV/in/sec/sec).

Analog integration uses the fact that the equation that relates acceleration and velocity is equivalent with passing the acceleration signal through an analog low pass filter whose roll off is 6 dB/octave. The advantage is that the acceleration signal is converted to velocity as a continuous function of frequency. There are no bandwidth errors. In the like manner, we can obtain displacement from an accelerometer by passing the signal through a low pass 12 dB/octave filter. The spectrum analyzer never sees an acceleration signal in either the time or frequency domain.

Signal integration can be realized in time domain (numeric method) or in frequency domain to obtain signals in displacement as the measurements carried out in this study are in velocity.

After filtering and integration of the signal, the cross covariance, power spectrum density, frequency response function and singular value decomposition can be estimated to achieve the natural frequencies and mode shapes. Those function are explained briefly in the following section.

4.2.2 Experimental modal analysis, EMA

The experimental modal analysis can be defined as the "inverse problem" in which it is note the response and the cause (input) and needs to be study the structure, in analogy with the "direct problem" in which the inputs and the structure are known and the response is unknown. Experimental modal analysis is a process whereby the modal properties of a structure are extracted. Since the modal properties can be used to model or characterize a structure, damage detection algorithms can use these features to determine and monitor the condition of said structure.

EMA makes use of a forced input excitation as well as the measured dynamic response of the structure. The input forcing function is typically created using impact hammers, shakers or drop weights. The output dynamic response is usually measured using transducers that measure position, velocity or acceleration. Compared to other technologies used in generating forced structural input excitation, the impact hammer tends to be more cost effective, more portable and easier to operate. However, the impact hammer also tends to have a poor signal to noise ratio. Another commonly used technology for generating forced input excitation is a drop weight. The drop weight allows for control of the amplitude of the input forcing function and for low frequencies to be excited but, like the impact hammer, also has poor signal to noise ratio and cannot be used for continuous monitoring. Lastly, the shaker can excite higher modal frequencies (up to 100 Hz), as the impact hammer or drop weight technologies, but is more expensive and difficult to install (Vistasp and Farhad, 2009).

A large number of EMA algorithms have been developed in both time domain and frequency domain. Most of these algorithms implement single-input-single-output (SISO), single-input-multiple-output (SIMO), or multiple-input-multiple-output (MIMO) techniques. The technique of EMA has been widely used for mechanical and aerospace applications, as well as civil applications.

Acquiring ambient noise vibration and considered it as an input this method can also be applied in our case when synchronized pairs of measures are taken by living one of seismographs fixed in the free field and moving the other one inside the building.

The dynamic behavior of a structure depends only on its intrinsic characteristics (mass, stiffness, damping, degree of constraint, etc...) and not by the entity and/or the type of applied load; therefore, if they are not internal modifications (such as structural damage) the behavior of the structure remains unchanged, otherwise, a variation of the frequencies and of their modes of vibration may be noted. Furthermore, structural identification is a non-destructive technique, as it can be applied to both new structures, for example in the testing phase, and to existing or historical structures for their monitoring.

The experimental dynamic identification methods (Table 4.1) differ mainly from:

- the domain in which they operate (time or frequency);
- the reference model SDOF or MDOF;
- estimation field (local or global);
- single or multiple input and output.

The EMA method consist on the determination of the frequency response function (FRF) which allow to characterize the response of a system excited by a forcing. At this aim, the matrix of frequency response function (FRF) should be constructed to identify the modal parameter. The elements of this matrix are estimated by the ratio between the output signal X and the input signal F (the forcing):

$$FRF_{ij}(\omega) = H_{ij}(\omega) = \frac{X_i(\omega)}{F_j(\omega)} = \frac{FFT(X_i)}{FFT(F_j)} \qquad \text{(Eq. 4. 52)}$$

where X_i and F_i are respectively the fast Fourier transform of the output and the input signals.

Table 4.1 *Methods of experimental dynamic identification*

EMA	**Method**	**SDOF/MDOF**	**Field estimation**	**Input/Output**
Frequency domain	Peak Picking	SDOF	Local	SISO
	Circle - fit			
	Inverse			
	Dobson			SISO/SIMO
	Nonlinear LSFD	MDOF	Local/Global	SIMO/MIMO
	Orthogonal Polynomial			
Time domain	Logarithmic Decrement	SDOF	Local	SISO
	LSCE	MDOF	Global	SIMO/MIMO
	Ibrahim			MIMO
	ERA			
	ARMA			

Also, the estimator of frequency response function can be used, at the aim to minimize the noise present in input or output signals. The noise contained in the input signal, ambient vibration in our case, can be minimized by the ratio:

$$H_1(\omega) = \frac{S_{XX}}{S_{XF}} \qquad \text{(Eq. 4. 53)}$$

while the noise on the output signal can be minimized by the ratio:

$$H_2(\omega) = \frac{S_{FX}}{S_{FF}} \qquad \text{(Eq. 4. 54)}$$

where S_{XX}, and S_{FF} are respectively the auto-spectrum of the output and the input signals, while S_{XF} and S_{FX} are the cross spectrum which can be calculated as follows:

$$S_{XX} = X(\omega) \cdot X^*(\omega) \qquad \text{(Eq. 4. 55)}$$

$$S_{FF} = F(\omega) \cdot F^*(\omega)$$

$$S_{XF} = X(\omega) \cdot F^*(\omega)$$

$$S_{FX} = F(\omega) \cdot X^*(\omega)$$

where * marks the complex conjugate of the signal.

In the case of a *forced damped SDOF system*, the equation of motion and its canonic form, after the division with mass m on both sites of the equation and considering an exponential forcing ($f=Fe^{i\omega t}$), can be written as follows:

$$u''(t) + 2\xi\omega_n u'(t) + \omega_n^2 u(t) = (Fe^{i\omega t})/m \qquad \text{(Eq. 4. 56)}$$

The general solution as the form; $u(t)=Xe^{i\omega t}$

$$(\omega_n^2 + 2i\xi\omega_n \omega - \omega^2) X e^{i\omega t} = (Fe^{i\omega t})/m \qquad \text{(Eq. 4. 57)}$$

The frequency response function is:

$$H_{ij}(\omega) = \frac{X_i(\omega)}{F_j(\omega)} = \frac{1}{m} \frac{1}{(\omega_n{}^2 - \omega^2) + 2i\xi\omega_n\omega} = \frac{1}{(k - m\omega^2) + i\omega c} \qquad \text{(Eq. 4. 58)}$$

where $c = 2\xi\sqrt{k\,m}$, $\omega_n = \sqrt{k/m}$, ω is the angular velocity of the forcing f, k is the stiffness of the system, m is the mass of the system, c is the damping, ξ is the viscous damping ratio, i is the imaginary number.

The mobility and the inheritance (acceleration) of this SDOF system can be estimated respectively by the integration of the frequency response function (Equation 4.58) and by the integration of the mobility equation (Equation 4.59):

$$V_{ij}(\omega) = \frac{V_i(\omega)}{F_j(\omega)} = \frac{1}{m}\frac{i\,\omega}{({\omega_n}^2-\omega^2)+2i\xi\omega_n\omega} = \frac{i\,\omega}{(k-m\omega^2)+i\omega c} \qquad \text{(Eq. 4. 59)}$$

$$A_{ij}(\omega) = \frac{A_i(\omega)}{F_j(\omega)} = \frac{1}{m}\frac{-\omega^2}{({\omega_n}^2-\omega^2)+2i\xi\omega_n\omega} = \frac{-\omega^2}{(k-m\omega^2)+i\omega c} \qquad \text{(Eq. 4. 60)}$$

where $c = 2\xi\sqrt{k\,m}$; $\omega_n = \sqrt{k/m}$, ω is the angular velocity of the forcing *f*, *k* is the stiffness of the system, *m* is the mass of the system, *c* is the damping, ξ is the viscous damping ratio, *i* is the imaginary number.

In the Figure 4.12 are shown the graphic of amplitude vs. frequencies (real and imaginary part) of frequency response, mobility and inheritance functions.

In a *free damping SDOF system*, the general solution of the equation of motion can be written in the sequent form (considering a solution type $u(t) = X\,e^{st}$ with *s* complex number):

$$u(t) = e^{-\omega_0\xi t}(c_1e^{+i\omega_D t} + c_2e^{-i\omega_D t})$$

where $\omega_D = \omega_0\sqrt{1-\xi^2}$ is the damped angular frequency.

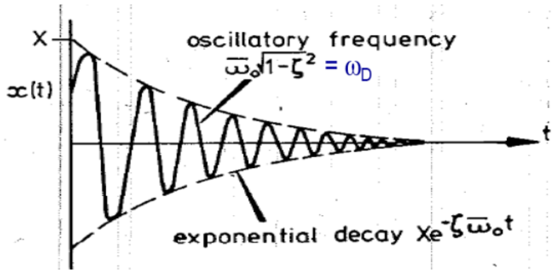

$$u(t) = \underbrace{Xe^{-\omega_0\xi t}}_{\text{Exponential component}}\underbrace{(c'_1 cos\omega_D t + c'_2 sen\omega_D t)}_{\text{Oscillatory component}}$$

Considering a solution type $u(t) = X\,e^{i\omega t}$ and an exponential forcing $f(t) = F\,e^{i\omega t}$, in the equation of a *forced damped MDOF* system, the frequency response function can be written in the form:

$$[H(\omega)] = \frac{\{X(\omega)\}}{\{F(\omega)\}} = ([K] + i\omega[C] - \omega^2[M])^{-1} \qquad \text{(Eq. 4. 61)}$$

Its elements, $H_{ij}(\omega) = \frac{X_i(\omega)}{F_j(\omega)}$ indicate the response in *j*-node as a results of a forcing on *i*-node.

Pre-multiply by ϕ^T and post-multiply by ϕ both sides of the Equation 4.61:

$$\phi^T[H(\omega)]^{-1}\phi = \phi^T([K] + i\omega[C] - \omega^2[M])\,\phi$$

so,

$$[H(\omega)] = \phi\,([\omega_r^2] + i\omega[C_r]/[M_r] - \omega^2)^{-1}\,\phi^T$$

$$H_{ij}(\omega) = H_{ij}(\omega) = \sum_{r=1}^{N}\frac{(\varphi_{ir})(\varphi_{jr})}{({\omega_r}^2-\omega^2)+i\omega c_r/m_r} \qquad \text{(Eq. 4. 62)}$$

where $[C_r] = [\Psi]^T[C]\,[\Psi] = \beta[K_r]$, $H_{ij}(\omega) = H_{ij}(\omega)$ as the matrix $[H(\omega)]$ is symmetric.

See Paragraph 4.1.2 for the significance of the other symbols.

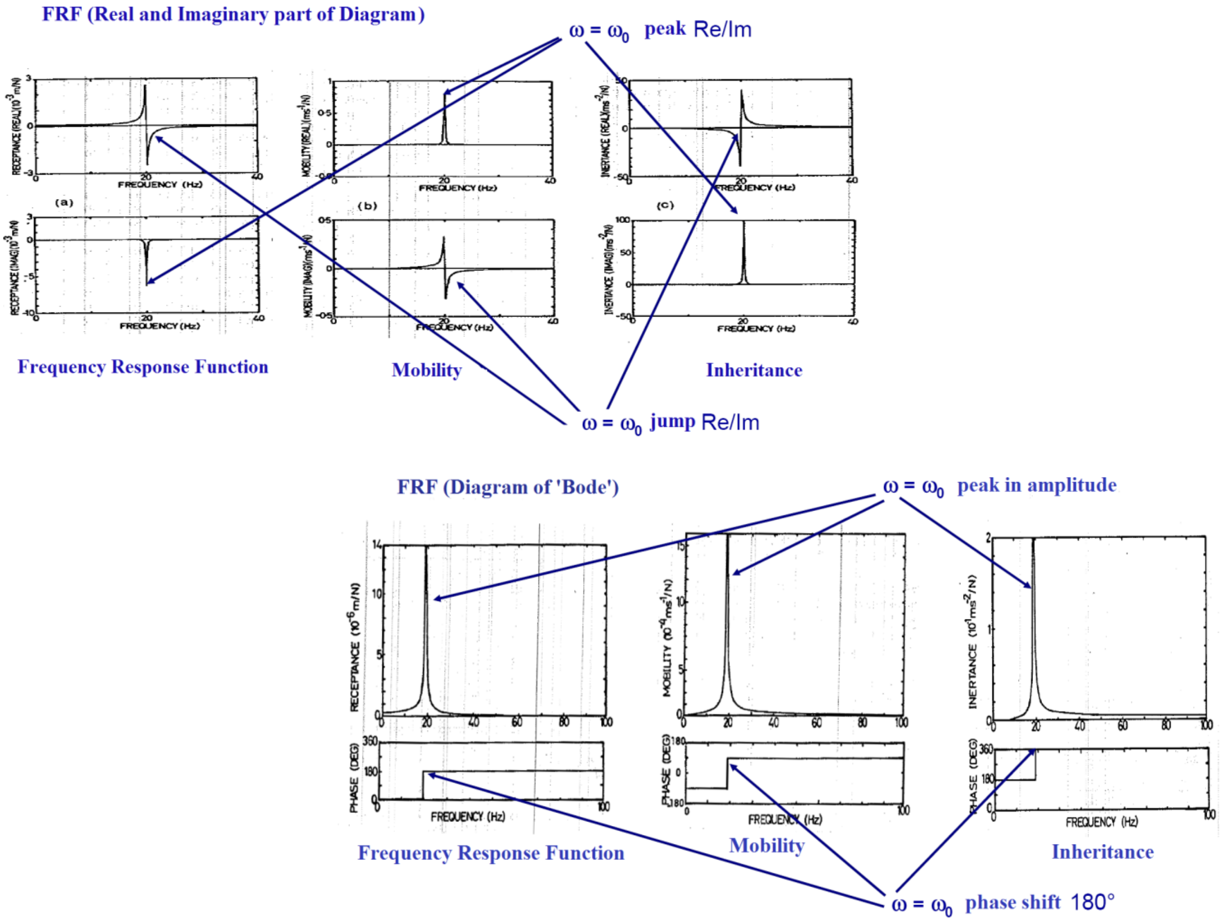

Figure 4.12 *Graphic representation: Amplitude-frequency (left), Real and imaginary part (right)*

The numerator of the Equation 4.62 is the residual while the denominator is the pole.

In the case of a viscous damping ($\omega \approx \omega_r, so\ 2i\xi_r = \eta_r$) the equation is:

$$H_{ij}(\omega) = \sum_{r=1}^{N} \frac{(\varphi_{ir})(\varphi_{jr})}{(\omega_r{}^2-\omega^2)+2i\xi_r\omega\omega_r} \qquad \text{(Eq. 4. 63)}$$

while in the case of structural damping the equation has the form:

$$H_{ij}(\omega) = \sum_{r=1}^{N} \frac{(\varphi_{ir})(\varphi_{jr})}{(\omega_r{}^2-\omega^2)+i\eta_r\omega_r{}^2} \qquad \text{(Eq. 4. 64)}$$

In both cases the matrix of the frequency response function of the system can be written in the form:

$$H_{ij}(\omega) = \begin{bmatrix} H_{11} & H_{12} & \dots & & H_{1n} \\ . & & . & & . \\ . & & & . & . \\ . & & & . & . \\ H_{n1} & H_{n2} & \dots & & H_{nn} \end{bmatrix} \qquad \text{(Eq. 4. 65)}$$

where H_{ij} are the FRF (Frequency Response Function) in *i* node caused by the effect of the input in the *j* node of the structures and *n* is the number of measurement carried out.

The matrix of the frequency response function is a three dimensional matrix as a function of *i*, *j* and ω. The measurements can be carried out in two ways (Figure 4.13) for identification of FRF matrix elements.

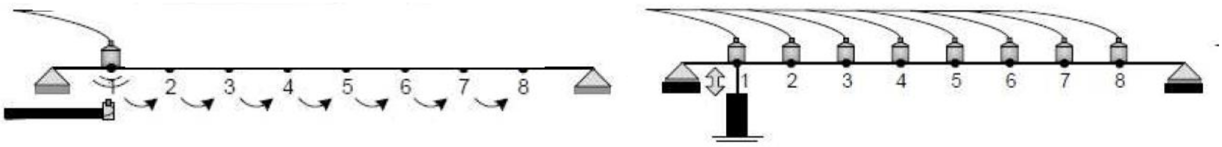

Figure 4.13 *Movable input - fixed output (left), Fixed input - movable output (right)*

The first way consist on taking fixed the output (the sensor, accelerometer or velocimeter) and moving the input (forcing) to the different nodes of the structure to be analyzed. The first line (H_{11}, H_{12}, ...H_{1n} elements) of the FRF matrix are measured. Due to Maxwell's rule of reciprocity for linear systems ($H_{ij}=H_{ji}$) also the first column is estimated.

$$H_{ij}(\omega) = \begin{bmatrix} H_{11} & H_{12} & \dots & H_{1n} \\ H_{21} & H_{22} & & \\ . & & . & \\ . & & & . \\ H_{n1} & H_{n2} & \dots & H_{nn} \end{bmatrix} \xrightarrow{\text{Maxwell rule}} H_{ij}(\omega) = \begin{bmatrix} H_{11} & H_{12} & \dots & H_{1n} \\ H_{21} & H_{22} & & \\ . & & . & \\ . & & & . \\ H_{n1} & H_{n2} & \dots & H_{nn} \end{bmatrix} \quad \text{(Eq. 4. 66)}$$

The second schemes of measurements has the input fixed and the output (the response) movable. In this case the elements of the first column of the FRF matrix are measured. Applying the Maxwell rule even in this case the first line of the matrix is estimated. Knowing the elements of a line and a column in the FRF matrix we can determine the other elements by the expression:

$$H_{ij}(\omega) = \frac{X_i}{F_j} \Longrightarrow \frac{H_{ik} \cdot H_{kj}}{H_{kk}} = \frac{X_i}{F_k}\frac{X_k}{F_j}\frac{F_k}{X_k} = \frac{X_i}{F_j} \quad \text{(Eq. 4. 67)}$$

where k is a line or e column measured.

A delay time is present in the signal moving the forcing from the output. So, ideal would be to position the sensors in all nodes.

4.2.2.1 Frequency and time domain methods, EMA

Let's analyze the most commonly used frequency domain methods in civil engineering.
Peak picking method gives accurate results when the vibration modes of the structure are well separated. Modal parameters can be estimated as follows:
- the natural frequency is identify by selecting the pick on FRF (Frequency response function) graphic;
- damping ratio is obtained using the half-power bandwidth method (see Figure 4.14);
- the mode shapes are identify as a function of FRF amplitude, damping ratio and angular frequency.

Natural frequencies:

$$f_r = \frac{\omega_r}{2\pi} = \frac{\omega(max|H|)}{2\pi}$$

Damping ratio can be estimated by using half-power bandwidth method (George et al, 2011):

$$\xi_r = \frac{\omega_b{}^2 - \omega_a{}^2}{4\omega_r{}^2} \cong \frac{\omega_b - \omega_a}{2\omega_r}, \text{ for small values of } \xi$$

$$also, \ \xi_r \cong \frac{f_b - f_a}{2 f_r}$$

$$\omega_b, \omega_a = \omega(|H| = \frac{|H|(\omega = \omega_r)}{\sqrt{2}})$$

Mode shapes can be identified by the relationship:

$$\varphi_{ir}\varphi_{jr} = \left|H_{ij}(\omega = \omega_r)\right| \cdot 2\xi {\omega_r}^2$$

$$\varphi_{ir}\varphi_{ir} = \left|H_{ii}(\omega = \omega_r)\right| \cdot 2\xi {\omega_r}^2$$

where H_{ij} is the frequency response function in the i-th node for effect of a forcing in j-th node,
H_{ii} is the frequency response function in the i-th node for effect of a forcing in i-th node.

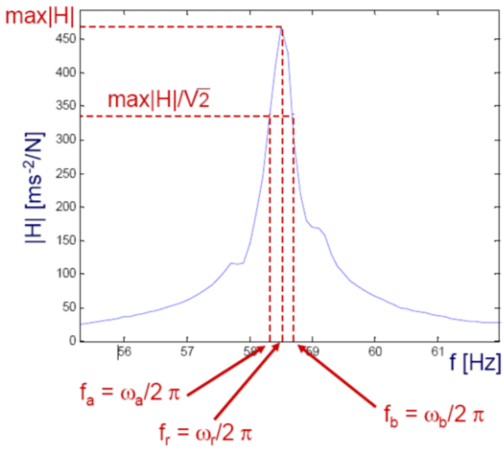

Figure 4.14 *Half-power bandwidth method*

The frequency response function can be estimated as the spectral ratio between the input signal x_i (the forcing) and the output signal F_i:

$$H_{ij} = \frac{x_i}{F_j} = \frac{FFT(x_i)}{FFT(F_j)}$$

Cycle-fit method, which fit the FRF in the Nyquist diagram (real - imaginary part) by a circle (see Figure 4.15). The modal parameter are defined as a function of diameter of the cycle. The natural frequency is estimated by the spacing technique, i.e. each resonant frequencies can be plot by a circle, therefore, the maximum space of data (more concentrated) is at the point where there is present the resonance (Clarence, 2007). The mobility transfer function (velocity/force) of a SDOF system with linear viscous damping when plotted on the Nyquist plane of real axis and imaginary axis for the frequency transfer function, is a circle. The receptance function (FRF, displacement/force) of a SDOF system with hysteretic damping when plotted on the Nyquist plane, is also a circle (Clarence, 2007). Therefore, the Nyquist diagram of FRF and mobility function is a circle. This information is used when plot experimental data in the Nyquist diagram, to identify modal parameters. The damping (ξ_r) and the mode shapes (eigenvector, φ_{ij}) can be defined by the sequent expressions:

Damping ratio:

$$\xi_r = \frac{\omega_b - \omega_a}{{\omega_r}^2} \frac{1}{\tan(\Delta\theta_a) + \tan(\Delta\theta_b)}$$

Mode shapes:

$$\varphi_{ir}\varphi_{jr} = D_r \xi_r {\omega_r}^2$$

It is not recommended to use this method when modes are close to each other.

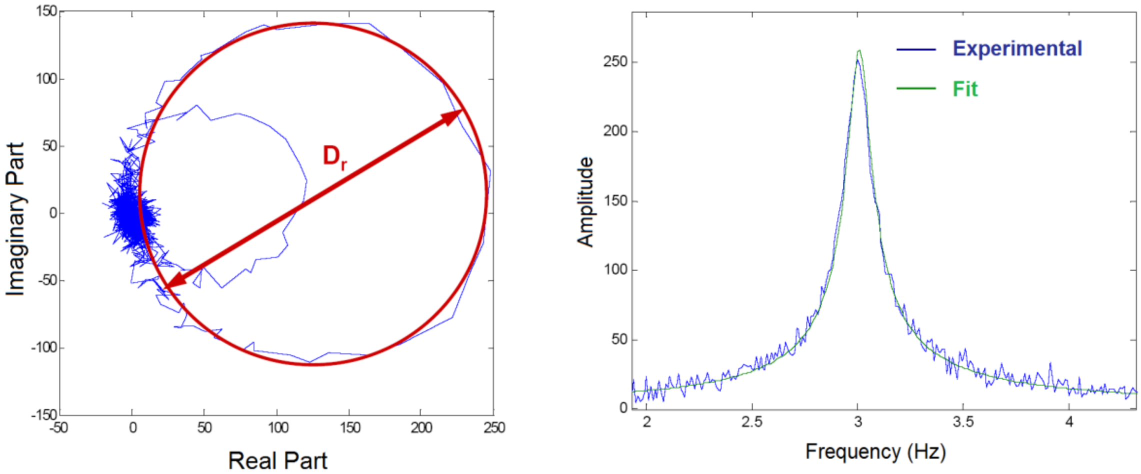

Figure 4.15 *Cycle fit method (left), Experimental fit (right)*

Fit of experimental FRF is realized by means of the analytical formulation for SDOF. This method presents better results in the estimation of the damping ratio as it is determined by fit more than one point (not just 3 as in the Peak Picking and Circle Fit methods).

The analytic representation of SDOF is:

$$H_{jk}(\omega) = \sum_{r=1}^{l} \frac{\varphi_{jr}\varphi_{kr}}{(\omega_r{}^2 - \omega^2) + 2i\xi_r\omega\omega_r}$$

where ω_r, ξ_r, ϕ_r are the unknown.
The parameters are identified by minimizing an error function.

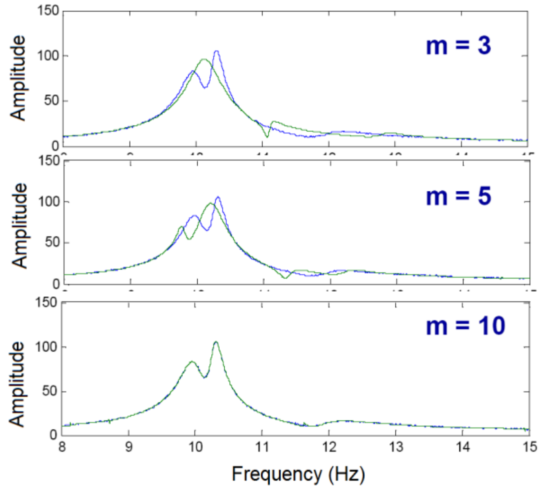

Figure 4.16 *RFP method*

Rational Fraction Polynomials (RFP) is a global method which takes into account all modes simultaneously (MDOF). This method fit the FRF in the form of polynomials fraction. Is a very useful to be utilized when modes are close to each other for a better estimation. The number of modes to be analyzed can be chosen by the help of the number of stabilization diagram (see Figure 4.16).
The rational fraction form of the analytic expression of MDOF is:

$$H(\omega) = \frac{\sum_{r=0}^{m} a_r i\omega^r}{\sum_{r=0}^{m} b_r i\omega^r}$$

The partial fraction form of the analytic expression of MDOF is:

$$H(\omega) = \sum_{r=1}^{n/2} \frac{r_r}{i\omega - \rho_r} + \frac{r_r{}^*}{i\omega - \rho_r}$$

Time domain, EMA

Fit with band pass filter in the neighborhood of each natural frequency. To get a more accurate estimate of damping ratio ξ_r, the fit (with a line) of the peaks of the frequency structure response graph, in semi-logarithmic scale, should be realized (see Figure 4.17).

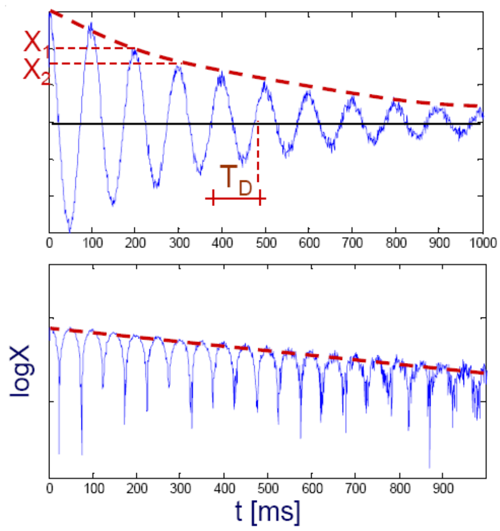

Figure 4.17 *Fit with band pass filter*

The frequency is determined as a function of times between consecutive peaks:

$f_r \approx \frac{1}{T_D}$,

if the damping is relative small than $\omega_r \approx \omega_r \sqrt{1-\xi^2)}$

The damping is a function of the decrement logarithmic δ, defined as a ratio between two consecutive peaks amplitude:

$$\delta = ln \frac{x_i}{x_{i+1}} = \xi \omega_r T_D \qquad where\ \xi = \frac{\delta}{2\pi}$$

or, $\delta = ln \frac{x_i}{x_{i+n}}$; $\xi = \frac{\delta}{2\pi n}$

where n is the number of peaks taken in consideration, δ is the logarithmic decrement.

In the case of a MDOF system, the ratio FRF/FFT graphic should be used to estimate the natural frequency and then to define the frequency band of the filter.
Modal shapes can be defined by the following expression:

$$x(t) = Xe^{-\omega_r \xi t}\ e^{i(\omega_r \sqrt{1-\xi^2})t}$$

4.2.2.2 Algorithm used for EMA

Two synchronized seismographs (equipped by three directional geophones) have been used to measure the environmental seismic noise. The ambient noise measurements have been acquired in different verticals of the building once leaving the fixed instrument on the top floor and once in the free field. The second one has been used for experimental modal analysis. All measurements carried out inside the building have been first synchronized with the measure in the free field, which is considered as the forcing, and then the FRF (Frequency Response Function) has been estimated.
Generally, modal parameter can be determined by using one of the following estimator:

- FRF, estimated by the ratio of FFT between output and input;
- the real part of FFT;
- the ration $H_{input}(\omega) = \frac{S_{XX}}{S_{XF}}$, to minimize the noise in the input.

The experimental modal analysis has been applied in this study by using two algorithm which differ between them mainly on the use of FFT or power spectral density (PSD) (see Figure 4.18). This last, is estimated as a function of fast Fourier transform in Matlab software (see Appendix, 'Script code for Power spectral density function').
FFT gives a high resolution in *df* and a slightly smooth spectrum of the signal making so difficult the final resolution in frequency. Using PSD, the spectrum has been calculated on the segments whose length affect the frequency resolution of the final spectrum. Those segments have been averaged to obtain a more smooth spectrum, so as to see all frequencies. Furthermore, those segments have been windowed and overlap to eliminate the leakage error and to increase the resolution. As seen from the diagram below, those algorithm are named EMA 1 and EMA 2 to identify between one another.

Maxwell rule for the reciprocity of linear system has been used then to estimate the cross power spectrum density (CPSD) or the FRF matrix. The first line (H_{11}, H_{12}, ...H_{1n} elements) of the FRF/PSD matrix have been calculated from ambient noise measures while the first column has been estimated due to Maxwell's rule (H_{ij}=H_{ji}). Knowing the elements of a line and a column in the FRF/PSD matrix we can determine the other elements by the Equation 4.67.
The constructed matrix of frequency response function (FRF) is useful for modal parameter

estimation. The elements of this matrix have been estimated by the ratio between the fast Fourier transform (FFT) of the output signal x (the forcing) and the FFT of the input signal F (forcing):

$$H_{ij} = \frac{x_i}{F_j} = \frac{FFT(x_i)}{FFT(F_j)}$$

EMA2 algorithm calculate the cross power spectrum density by using in Matlab software the function [Pxypt,F]=cpsd(x,y,window,noverlap,nfft,fs). Periodic Hamming window has been used to obtain 8 equal segments of both signals x and y. An overlap of 50%, the number of the fast Fourier transform 256 and the sampling frequency 128 Hz, have been used. P_{xy} is a complex vector which is useful to compute the phase.

In the diagram below are shown the steps done to estimate the modal parameter of the structure. The peak-picking method has been used to identify the natural frequencies by selecting manually the peaks in the singular value decomposition (SVD) of FRF or PSD graphics. The damping ratio can be estimated by half-power bandwidth method.

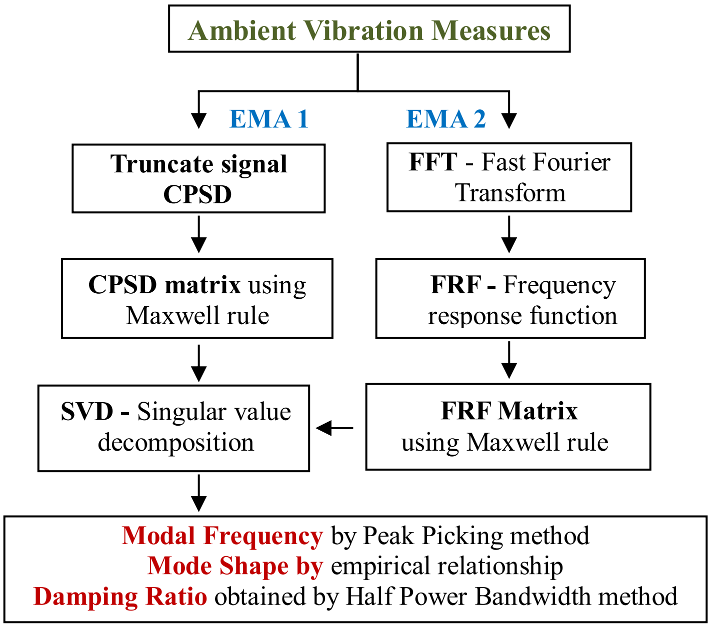

Figure 4.18 *Diagram of EMA methods used*

4.2.3 Operational modal analysis OMA

Similar to EMA, operational modal analysis (OMA) is a technique whereby the modal properties of a structure are extracted. The OMA technique extracts the modal properties of a structure by analyzing its dynamic output response to its operational input excitation. In other words, OMA analyzes a structure's response based solely on ambient vibrations that it is exposed to (Karbhari and Ansari, 2009). For civil applications, OMA has become a very appealing technique for the extraction of modal parameters to be used in long term vibration-based Structural Health Monitoring studies.

OMA is an input only technique in which it is only possible to measure the response of the dynamic system while forcing (input) remains unknown. The input used is commonly known as environmental excitation and the vibrations produced in the structures are said environmental vibrations. Civil structures are subjected continuously to excitations present in the environment (ex. wind, traffic, micro tremors etc.). The environmental vibration has the energy distributed over a wide range of frequencies, and accordingly, is able to excite many structural mode. This type of excitement is not deterministic and can be characterized only by means of statistical parameters, such as the mean and covariance. If excitement is a Gaussian noise, with zero mean value, the response of the structure directly reflects the characteristics of the structural system:

$$H_1(\omega) = \frac{S_{XX}}{S_{FF}} = \frac{S_{XX}}{constant}$$

The use of environmental vibrations is much less expensive methodology, and also in some cases it allows to excite large structures that otherwise would be excited by powerful excitatory not always available. Sensors (accelerometer or velocimeters) must be acquired simultaneously as the input (the microtremor) is note measured. Therefore, OMA method requires many sensors to identify the modal parameter identification. OMA techniques are usually classified as frequency domain OMA or time domain OMA.

***Table 4.2** Output Only Methods for dynamic identification*

OMA	**Method**	**SDOF/MDOF**	**Field estimation**	**Input/Output**
Frequency domain	Peak Picking	SDOF	Local	SISO
	ANPSD (Averaged normalized power spectral density)			
	FDD/EFDD (Frequency domain decomposition, Enhanced frequency domain decomposition)			
	LSCF (Least square complex frequency)	MDOF	Global	MIMO
	Random decrement	SDOF	Local	SISO
	LSCE (Least square complex exponential)	MDOF	Global	SIMO/MIMO
Time domain	Ibrahim			SISO
	ARMA			SISO
	SSI - Date - SSI - Cov			MIMO

4.2.3.1 Frequency and time domain methods, OMA

There exist a large number of frequency domain OMA techniques in the technical literature. The simplest technique, called peak-picking (Maia at al., 1997), extracts the natural frequencies of a structure by finding the peaks of the power spectrum response plot. In theory, each peak corresponds to a natural mode of the structure. The major limitation to this technique is its inability to differentiate between modal frequencies that are very close in value. Furthermore, it also requires the structure to have low damping values.

A second group of frequency domain OMA techniques utilizes the singular value decomposition of the matrix containing the cross spectrum of the structure's output response. Typically, these methods are called frequency domain decomposition (FDD) (Brincker at al., 2000). After singular value decomposition is performed, the modal shapes and scaled frequencies are obtained. FDD type methods also allow for modal damping to be extracted. These methods have an advantage over peak-picking methods in that neither fairly spaced natural frequency values nor low damping values are required. However, the major drawback of FDD-type techniques is that the values of damping obtained may be biased. A third group of frequency based OMA methods that allow for the extraction of modal shapes and frequencies use an approximation called the least squares complex frequency (LSCF) domain approximation (Karbhari and Ansari, 2009).

Averaged Normalized Power Spectral Density (ANPSD) synthesizes the information of power spectral density contained in the various measuring points.

Analysis consist in those steps:

- Estimation of PSD for y_i signal:

$G_{yy}(\omega)=\frac{FFT^T[y_i]\cdot FFT[y_i]}{\Delta f}$

- Normalizzation of PSD:

$$NSPD_I(\omega) = \frac{\mathrm{Gyy}(\omega)}{\sum_{n=1}^{N/2} \mathrm{Gyy}(\omega_n)}$$

- Average of PSD:

$$ANPSD_i(\omega) = \frac{1}{nNPSD} \sum_{m=1}^{nNPSD} NPSD(\omega_m)$$

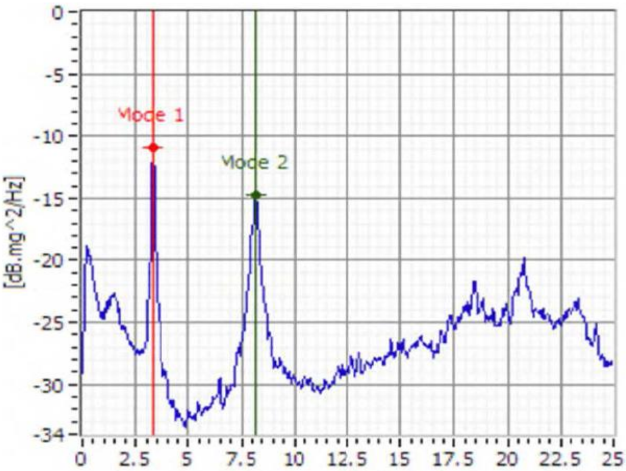

Figure 4.19 *PSD - Frequency (Hz)*

The principle of algorithm can be illustrated by writing the system response using modal coordinates:

$$y(t) = \sum_{r=1}^{n} \varphi_r q_r(t) = \phi q(t)$$

The covariance matrix of the response is:

$C_{yy}(\tau)$=E $[y(t+\tau)y(t)^T]$

Substituting the above equation we have:

$C_{yy}(\tau)$=E $[\phi q(t+\tau)\ q(t)^H\phi^H] = \phi C_{qq}(\tau)\ \phi^H$

Covariance of output and modal coordinates are correlated by Matrix mode shapes. If we pass in the frequency domain:

$G_{yy}(\omega)=\phi\ G_{qq}(\omega)\ \phi^H$

Furthermore, the power spectral density are correlated with the matrix of mode shapes. The spectral density can be estimated using the FFT (Fast Fourier Transform) and then the matrix of response can be defined as:

$$G_{yy}(\omega) = \begin{bmatrix} G_{11}(\omega) & \dots & G_{1r}(\omega) \\ . & . & . \\ . & . & . \\ . & . & . \\ G_{r1}(\omega) & \dots & G_{rr}(\omega) \end{bmatrix}$$

The G_{qq} matrix is diagonal if the modal coordinate aren't correlated. If the mode shapes are orthogonal then the singular value decomposition (SVD) must be used to define mode shapes:

$\phi G_{qq}(\omega)\ \phi^H = \mathrm{SVD}(G_{yy}(\omega))$

In this case the natural frequency are defined as the peaks in singular value decomposition graphic.

EFDD (Enhanced frequency domain decomposition) method is an evolution of the FDD and it makes possible:

- the estimation of natural frequencies with more accuracy, since it uses a curve fitting rather than the peaks of the SVD;
- obtaining the estimated damping through the logarithmic decrement of autocorrelation function.

The modal parameter can be identify following the sequent steps:
- select the useful band of SVD using modal assurance criterion between modal forms in the vicinity of a frequency;
- estimation of correlation function by means of IFFT (inverse fast fourier transform) of power spectral density near the frequency (peaks);
- use Curve-Fitting to estimate modal parameter (or of the zero crossing times and logarithmic decrement).

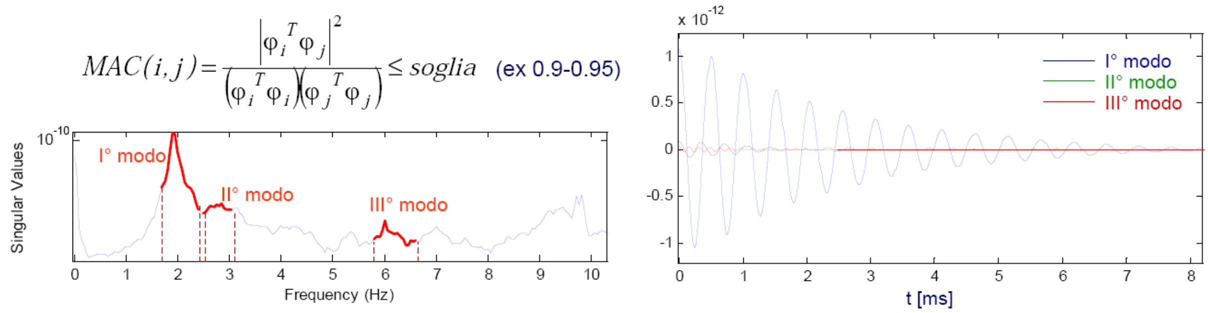

Figure 4.20 *First three mode shapes*

Similar to frequency domain OMA, numerous time domain OMA techniques are present in the technical literature. One of the most popular techniques is the natural excitation technique (NExT). The NExT approach assumes that the operational excitation that the structure is exposed to can be modeled as a white noise process. This method establishes the cross correlation between two random dynamic response measurements in the structure and expresses these signals as summations of decaying sinusoidal functions (James at al., 1993). Once the decaying sinusoidal functions are created, time domain modal identification algorithms such as the Eigen-system realization algorithm (ERA) or the polyreference complex exponential technique (PRCE) can be applied in order to obtain the modal parameters.
Other commonly used time domain OMA methods are the autoregressive moving average (ARMA) and stochastic space identification (SSI) methods. The major drawback to time domain OMA methods is that under noisy conditions, the number of vibration modes cannot be estimated accurately. This is due to the fact that since the order of natural modes is unknown, it is difficult to determine the real structural modes from those created by noise effects. Furthermore, due to this mode estimation inaccuracy, many time domain methods are not appropriate for long term monitoring as the algorithms must rely on a user to determine the number of modes manually (Karbhari and Ansari, 2009).

4.2.3.2 Algorithm used for OMA

The ambient noise measurements acquired in different verticals of the building by leaving the fixed instrument on the top floor and moving the other one to the various floors have been used for operational modal analysis. In the diagram below (see Figure 4.21) are shown the steps used for both OMA 1 and OMA 2 algorithm which differ between them mainly for the truncated signal in the OMA 2. The theorem of Wiener and Khinchin has been used to calculate the PSD from the FFT of the cross covariance of the signal (see OMA 2 method). The cross covariance function has been realized after truncate the signal and then the mean of cross covariance of all segments to reduce the noise effect in the frequency resolution. The matrix of PSD has been created by using the Maxwell rule and finally the singular decomposition of PSD matrix has been realized. The peak-picking method has been used to identify the natural frequency by selecting manually the peaks in the SVD (singular value decomposition) of PSD graphics. The damping ratio can be estimated by the help of decrement logarithmic method, as described in the above paragraph.

Furthermore, this method has been applied by analyzing separately each synchronized pair of measures (see diagram plot on the right of the Figure 4.21) at the aim to evaluate the influence in modal parameter results of the non-simultaneously acquisition of measures in all floors.

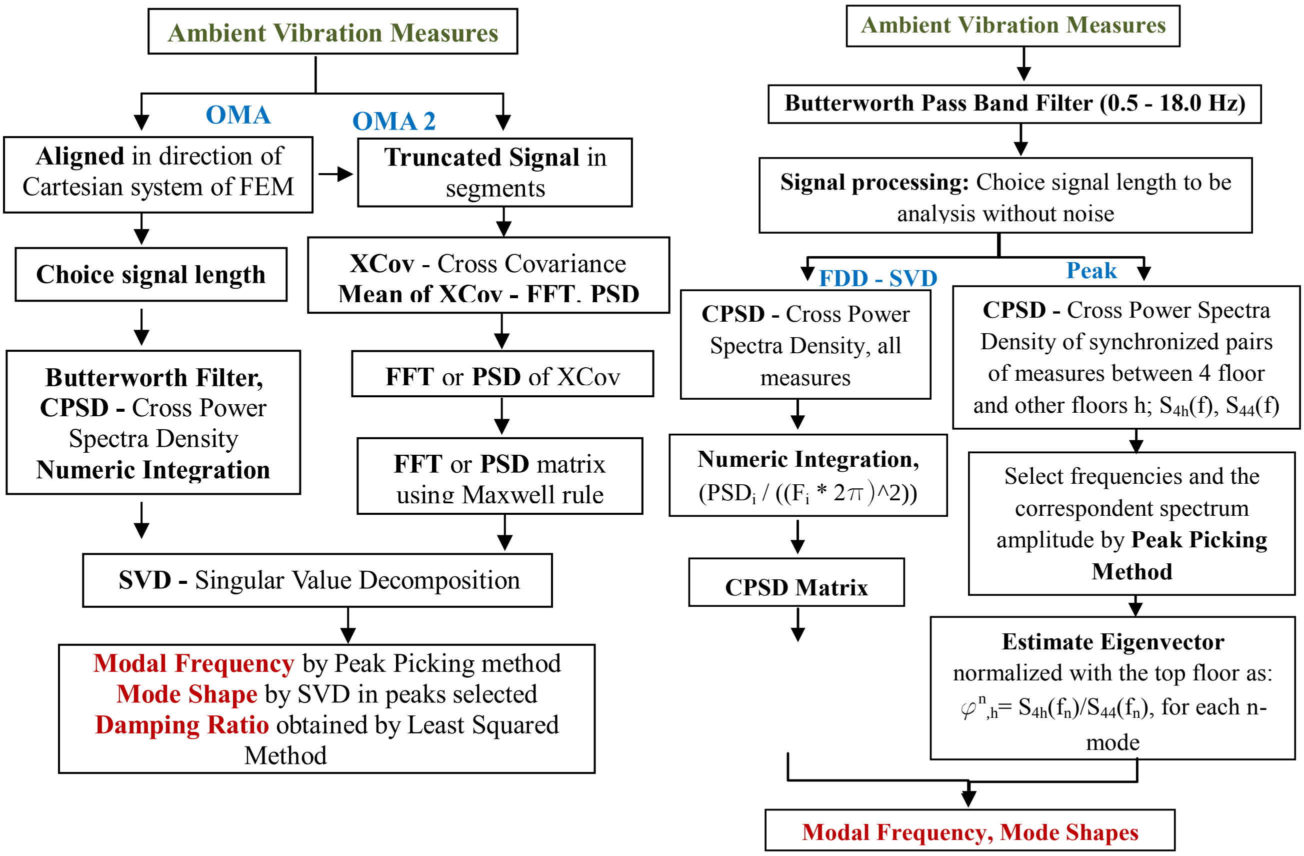

Figure 4.21 *Diagram of OMA methods used*

V. Case study 1 - LOCAL SEISMIC RESPONSE 1D

Estimate the seismic hazard of soil means formulating a prediction about the seismic shaking expected at a given point of the territory in a future set time interval also called exposure time. The term "seismic hazard" in engineering practice can refer specifically to strong ground motions produced by earthquakes that could affect constructions, therefore seismic hazard analysis often refers to the estimation of earthquake induced ground motions having specific probabilities over a given time period. Generally, the procedure suggested to characterize the local seismic hazard of a given area is based on a multidisciplinary approach implying: the knowledge of the seismic history of the area; geological surveys; seismic noise measurements and/or geophysical surveys; simulations of earthquake scenarios. Real seismic records, which are often recommended by seismic design code, will be used as an input for linear equivalent analysis. On the other hand, international seismic guidelines, concerning this issue, have been found hardly applicable by practitioners. This is related to both the difficulty in rationally relating the ground motions to the hazard at the site and the required selection criteria, which do not favor the use of real records, but rather various types of spectrum matching signals. REXEL v3.5 database, developed for code-based real records selection, helps to overcome some of these obstacles. REXEL allows to define the design spectra according to the Eurocode 8, the new Italian Building Code or completely user-defined. Based on these spectra, the software allows to search for sets of 1, 7, or 30 records compatible, in the average, with them. Records may also reflect the seismogenetic features of the sources (in terms of magnitude and epicentral distance), ground motion intensity measures, and soil conditions appropriate to the site. The datasets contained in REXEL are the European Strong-motion Database (ESD), the Italian Accelerometric Archive (ITACA) (for a table of matching between ITACA records and the accelerograms IDs in REXEL see here), and the Selected Input Motions for displacement-Based Assessment and Design (SIMBAD). The search of waveforms from the European strong-motion database, compatible to reference spectra being either user-defined or automatically generated according to EC8 and Italian seismic code, can be realized.

One of the key issues in Seismic structural verification (linear dynamic analysis of building) of the building is the selection of appropriate seismic input, which should allow for an accurate estimation of the seismic performance based on the seismic hazard at the site where the structures is located. If the probabilistic risk assessment of structures is concerned, procedures have been recently developed to properly select the seismic input.
The building under consideration is a prefabricated reinforced concrete construction destined for sanitary use, i.e. a strategic building as being a hospital. In this case, the study of seismic microzoning becomes even more important to be realized for the seismic prevention, being an ordinary construction.

Guidelines for seismic microzoning suggest, for new or existing strategic building, levels of knowledge comparable with those of seismic microzoning Level 3 at least in low (zone 3), medium (zone 2) or high-seismicity zones (zone 1). For very low-seismicity zones (zone 4), the criteria for the use of seismic microzoning studies are those in connection with new ordinary buildings or structures.

First level seismic Microzonation map of Sanremo has been downloaded from the website of The Regional Environmental Information System of Liguria (SIRAL) which is the set of databases and information (http://www.cartografiarl.regione.liguria.it/SiraMicroZonazioneSismica/Comuni3s.asp).

Sanremo falls in the class of seismic hazard 3S, referred to the seismic classification realized in 2014 (OPCM n. 3274, 2003) taking into account also the level of hazard. The cognitive preparatory mapping of scale 1:10000 for the seismic microzoning of Level 1 is shown in the Figure 5.1.

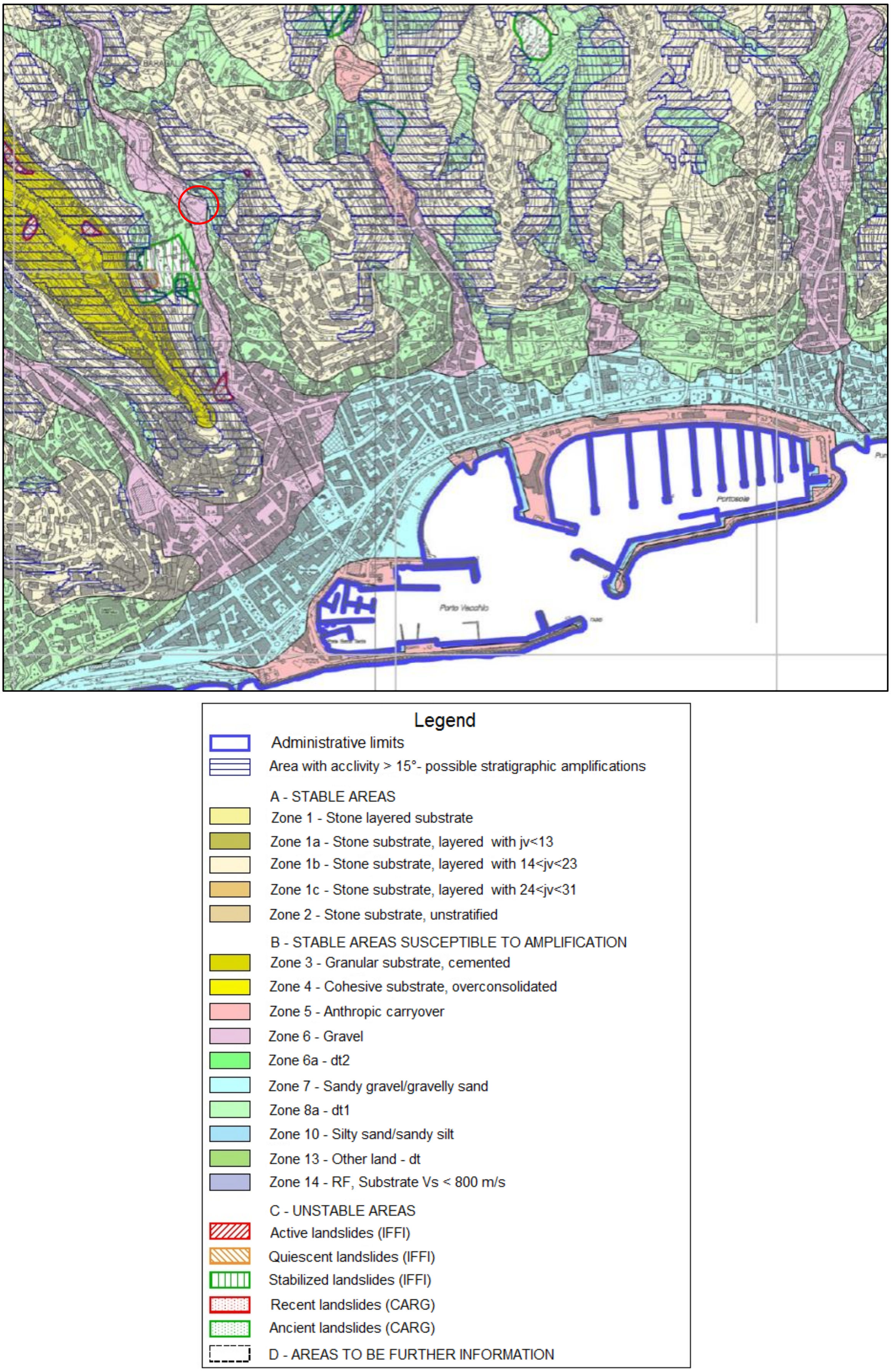

Figure 5.1 *First level seismic Microzonation map of Sanremo of scale 1:10.000, 2012 (Sanremo, 258140)*

Seismic surveys were carried out near the area of interest, referred to corresponding map with the location and type of investigations carried out. The area of interest (red cycle) falls in Zone 6 characterized by gravels.

Local seismic response has been realized in the free field near the building under exam, and in one-dimensional conditions, assumption justified by the horizontal alignment of soil layers. The dispersion curves have been estimated by spatial autocorrelation analysis which is based on zero crossing method. Vertical components of synchronized ambient vibration measures, have been used as input to estimate the dispersion curves. Seismic stratigraphic profile has been identified by the inversion procedure which use as input the dispersion curve and the respective HVSR curve of ambient vibration measures, both estimated in the free field near the construction area. For the definition of seismic input, 7 spectrum compatible accelerograms have been selected using the software 'REXEL v3.5 beta'. Horizontal accelerograms have been extracted from European database, selecting a set of input data for Sanremo at a given return period (100 years), for different limit states (SLV and SLD). Equivalent linear analysis of the subsoil has been executed using STRATA software, where the subsoil model consisted of a finite number of flat and parallel layers equivalent to an elastic material placed on a viscous-elastic half-space representing the bedrock. Each layer has been considered homogeneous and isotropic, with thickness, density, stiffness modulus and transverse damping factor defined from the bibliography and existent geological report. For each layer, the profiles of the normalized shear modulus *G* and the damping ratio *D*, as a function of the level of deformation, have been determined from the bibliography as described in the section 5.2.4. Stochastic variation of the site properties: shear-wave velocity, layer thicknesses, depth to bedrock, shear modulus reduction and material damping curves have been taken into account on STRATA software. Finally, V_{s30} has been estimated to identify the soil class due to standards classifications.

5.1 Soil and subsoil description

Stratigraphic profile and physical-mechanical properties of layers are important parameters to be known for the local seismic response analysis. At this aim, geological report which was realized before the construction of the building by Geologist Marco Abbi, and bibliographic data have been utilized to achieve information about the stratigraphic profile, physical and mechanical properties of layers. The decay curves have been selected from the bibliography as described in the section 5.2.4.

5.1.1 Geological description

The data used for geological and stratigraphic description, achieved from the project design and municipality of Sanremo, consist of:
- Geological maps of Sanremo of scale 1:10.000 and of scale 1:50.000;
- Geological report used for the project design which contain several geologic surveys (penetration tests, a continuous core, seismic surveys, NASW survey).

The area under exam belongs to Helminthoid Flysch of the Western Liguria Alps and continues below with the tectonic unit of Sanremo-Monte Saccarello Flysch. Inside the tectonic unit of Sanremo-Monte Saccarello Flysch are distinguished the sequent formation, starting from the bottom:
- Pelitic "base complex";
- Sandstone body;
- Flysch of Sanremo, mainly consisting of marl-sandstones turbidities which are generally in thick layers.

The interest area is supported by the Flysch of Sanremo with arenaceous clayey component in its lithofacies. This formation is characterized by a high alternation of materials with rigid

behavior (sandstones and siltstones) and by a small levels of plastic clayey-marl. The first can be fractured under the "new-tectonic" stress field, while the second can be deformed plastically developing often a dense family of lamination subparallel to the stratification (without presenting a dense grid of fracture), as well as to develop a schistosity equally oriented to swelling and alteration in contact with the air and with the changes in temperature. This involves the rapid breakdown of the top layer exposed to these small levels and consequently put in relief the less erodible material as arenaceous-silty, which result jutting in steep slopes or emerging in relief as "ribs" of the mountainside.
The layers are averagely plunging towards S-SE with a variable inclination of about 35°, but in realty the rock mass has most often a variable disposition of layers as the geological structure is disturbed by the tectonic deformations present in the area. The substrate is located at an average depth variable between 1.0-4.0 m, with a variable thickness as a function of the anthropic terracing and the superficial morphology that reaches the maximum values behind edge of terracing.

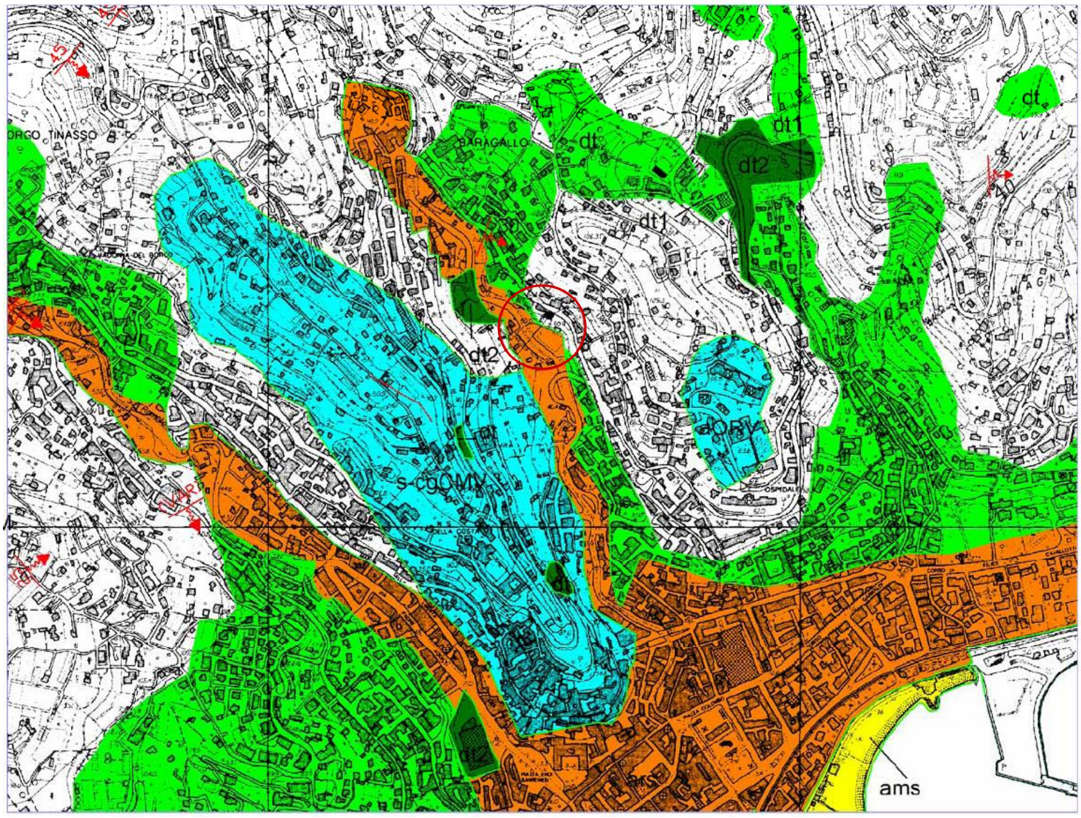

Legend:

Massive detrital covers of over 3 m in thickness

dt	Indistinct grain size
dt2	Coarse and medium grained

Alluvial deposits (Quaternary)

ams	Currently moving alluvia, mainly sand-silt grain sized
ars	Recent alluvia, occasionally terraced, mainly sand-silt grain sized

Pliocene

s-cgCMV	*Conglomerates of Monte Villa*, polygenic conglomerates with coarse stratification alternated with sands, usually ordinate and stratified and sometimes channeled

Sanremo - Saccarello Mountain

maELM	*Flysch of Sanremo.* Marl turbidities with or without calcareous - arenaceous base, thin to thick silty-arenaceous turbidities layered (mainly quartz micaceous), generally fine or medium, in layers and benches; clay marl and marl argillites; micritic limestone, thin and medium layered (Eocene-Cretaceous)

Scale 1:10000

***Figure 5.2** Geolithological map of scale 1:10000*

As can see in the Geolithological map of Sanremo of scale 1:10.000 (Figure 5.2) the area of study (red circle) falls in the recent terraced floods with sandy-silty predominantly particle size (arm) which are alluvial deposits of the quaternary. Also, the Flysch of Sanremo (maELM) is present in the construction area.

The area of interest falls in terraced alluvial deposits (bn1) and blanket eluvio colluvial (b2) both quaternary continental formation, referred to the geologic map of Sanremo of scale 1:50000 (Figure 5.3). Furthermore, the area near the building falls in Flysch of Sanremo (FSM4); argillites-arenaceous layers intercalated with calcilutites and rare sandstone marl layers (Member 'San Lorenzo').

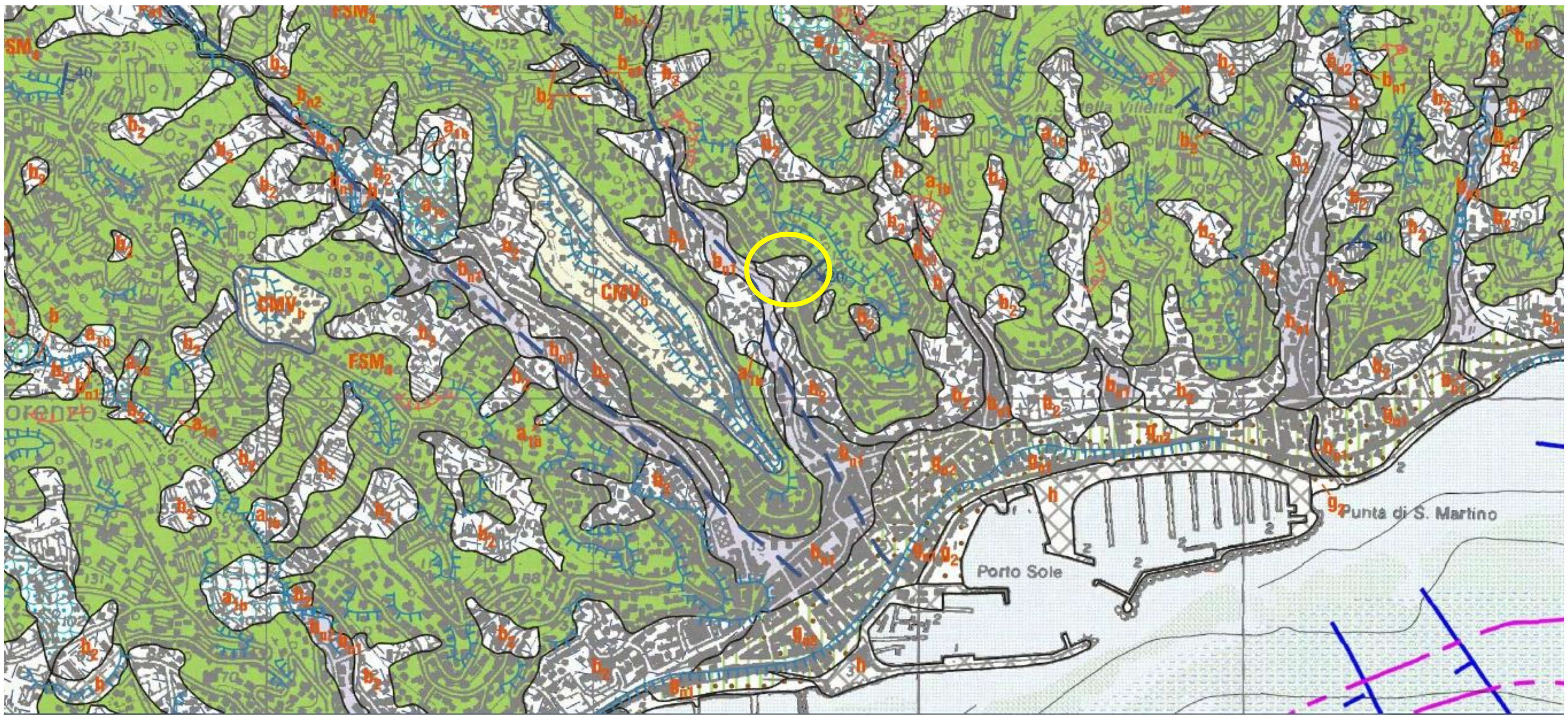

Legend:

QUATERNARIO

CONTINENTALE

Detriti di versante

a — Depositi di origine gravitativa di spessore variabile costituiti da materiali eterometrici spigolosi con prevalenza di granulometria grossolana, non cementati, con scarsa matrice, talora con prevalenza di grossi blocchi.
OLOCENE

Depositi di frana recente

a_{1a} — Accumuli gravitativi di materiale eterogeneo ed eterometrico con e senza segni di riattivazione.
OLOCENE

Depositi di frana antica

a_{1b} — Accumuli gravitativi di materiale eterogeneo ed eterometrico, antichi, talvolta coinvolgenti porzioni di substrato.
PLEISTOCENE-OLOCENE

Detriti di falda

a_3 — Depositi di origine gravitativa costituiti da materiali eterometrici con prevalenza di granulometrie grossolane e ciclopiche, spigolosi, in gran parte non cementati, privi di matrice, senza copertura pedogenetica, al piede di pareti rocciose.
OLOCENE

Coltre eluvio colluviale

b_2 — Coperture detritiche dovute ad alterazione in situ e, in seguito, mobilizzate da processi di versante, costituita da clasti eterometrici di varia litologia in matrice pelitica e/o sabbiosa.
OLOCENE

Depositi alluvionali

b — Coperture detritiche dovute ad alterazione in situ e, in seguito, mobilizzate da processi di versante, costituita da clasti eterometrici di varia litologia in matrice pelitica e/o sabbiosa.
OLOCENE

Depositi alluvionali terrazzati

b_{n1-4} — Depositi ghiaiosi, sabbiosi e limosi. I terrazzi sono numerati in ordine crescente a partire dal più recente (b_{n1}). I depositi dei terrazzi più vecchi (b_{n3} - b_{n4}) presentano una marcata ferretizzazione e un accenno di cementazione.
PLEISTOCENE MEDIO SUP. - OLOCENE?

Depositi di spiaggia

g_2 — Depositi ghiaiosi e sabbioso - ghiaiosi di spiaggia emersa.
OLOCENE

Depositi marini terrazzati

g_{n1-2} — Depositi sabbioso - ghiaiosi, talvolta ciottolosi di ambiente di transizione marino - continentale e sospesi. Due le superfici terrazzate: la più bassa e recente (g_{n1}), la più alta e antica (g_{n2}).
PLEISTOCENE?

UNITA' TETTONICA SAN REMO - M. SACCARELLO

FLYSCH DI SAN REMO

FSM_4, FSM_3, FSM_2, FSM_1 — Strati arenaceo-argillitici, con intercalazioni di calcilutiti e rari strati marnoso-arenacei (FSM_4: membro "San Lorenzo");
strati arenaceo-argillitici e calcilutitici nei quali si intercalano, ad intervalli regolari, "megaritmi" costituiti da megatorbiditi marnoso-arenacee (FSM_3: membro "San Michele");
marne ed arenarie calcaree costituenti strati torbiditici, con spessori inferiori rispetto a quelli della FSM_1 di cui rappresenta la parte distale e superiore, sono inoltre presenti livelli calcilutitici passanti a strati marnoso-arenacei e strati arenaceo-argillitici (FSM_2: membro "Villa Faraldi" - Foglio n. 259 "Imperia");
marne ed arenarie calcaree costituenti spessi strati torbiditici, organizzati in sequenze positive, con la porzione terminale costituita da calcilutiti, sono inoltre presenti scarsi strati arenaceo-argillitici (FSM_1: membro "Capo Mele" - Foglio n. 259 "Imperia").
FSM_4 è attribuito al *MAASTRICHTIANO SUP. (Zona a Micula murus)*
FSM_3 al *MAASTRICHTIANO SUP. (Zona a Micula murus)*
FSM_2 al *CAMPANIANO SUP. - MAASTRICHTIANO SUP. (Zona a Quadrum trifidum - Zona a Micula murus)*
FSM_1 al *CAMPANIANO SUP. - MAASTRICHTIANO MEDIO (Zona a Quadrum trifidum - Zona a Arkhangelskiella cynbiformis)*

ARENARIE DI BORDIGHERA

ABG — Arenarie torbiditiche spesso grossolane, sino a conglomeratiche, in strati spessi, localmente amalgamati. Sono inoltre presenti, nelle facies di lobo, anche livelletti di argille siltose e straterelli calcarenitici e marnosi, oltre ad arenarie calcaree e calcareniti fini e rare calcilutiti con al tetto argilliti scure.
CAMPANIANO SUP. - MAASTRICHTIANO MEDIO - SUP. (Zona a Quadrum trifidum - Zona a Lithraphidites quadratus)

FORMAZIONE DI SAN BARTOLOMEO

SBA_e, SBA_d, SBA_c, SBA_b, SBA_a — Sottili strati calcarei: successione di sottili strati calcarei alternati con livelli marnoso-argillosi, nella parte alta della serie prevalgono strati di calcisiltiti di color nocciola chiaro con più o meno significativi livelli pelitici grigi, nei quali compaiono sempre più significativi livelli e strati medi di arenarie arcosiche sviluppate in sequenze di Bouma (SBA_e); quarzoareniti: strati arenaceo-quarzosi a grana media e fine gradati con al tetto argilliti verdi e rosse; nella parte superiore della serie si hanno intercalazioni di straterelli di calcisiltiti nocciola chiaro (SBA_d); peliti varicolori: argilliti a colorazione vivace, oltre al grigio si hanno colorazioni verdi chiare e rosso vinato, sono presenti livelli arenacei grigio-chiari e rossastri a granulometria media (SBA_c); peliti manganesifere: alternanze ritmiche di argilliti grigio-verdastre e subordinate siltiti in strati sottili, con diffuse spalmature di ossidi metallici, sostituite da areniti fini e finissime, sono presenti, in modo molto subordinato, sottili strati centimetrici rossi e grigi a grana molto fine siliceo-argillosi (SBA_b); calcari tipo "palombino": calcisiltiti e calcilutiti con strati di spessore metrico e submetrico (SBA_a).
HAUTERIVIANO SUP. - CAMPANIANO SUP. (Zona a Calcicalathina oblongata - Zona a Quadrum gothicum)

Figure 5.3 *Zoom from geologic map of Sanremo of scale 1:50.000 (258 sheet)*

The area near the building is intensely urbanized which made difficult finding the rock outcropping in the neighborhood area except along the San Francesco torrent where the river itself has not manhole before the construction (Figure 5.4). Geognostic surveys, core drilling and dynamic penetration tests, were carried out before the construction of the hospital. Continuous core drilling survey was performed by the Municipality of Sanremo, near the area of interest and adjacent to the expansion tank of the San Francesco torrent for the construction of an access ramp at the torrent.

Figure 5.4 *Google map view (left), photo of rock outcropping along the San Francesco torrent (right)*

Continuous core drilling survey shows that the bedrock is located at the base of the manhole. Also, viewing the photo on the right bank, the bedrock outcropping practically at the San Francesco street. Lithological description identified from the core drilling is presented in the Table 5.1. Nine penetration tests were carried out in the area between 'San Francesco' street and 'Dante Strada San Pietro' street. All tests confirm that the mountainside is constituted by the sub-outcrops rock below the existing terracing. In the Figure 5.5 is shown the location of the continuous core survey (see blue circle) and the penetration tests position in the construction area.

Table 5.1 *Lithological description from core drilling survey*

Depth (m)	Lithology
from 0,00 to -3,00 m	Carryovers coarse composed from the mixed areated ground to the very loose inert S.P.T. 11/10/17 (-2.70, -3.00)
from -3,00 to -3,20 m	Calcareous-arenaceous
from -3,20 to -4,10 m	Carryovers rich in inert and little constipated
from -4,10 to -5,20 m	Mixed carryovers to reworked floods in sandy-silty matrix with rounded clasts
from -5,20 to -5,50 m	Capping of alteration of disarticulated and very altered (R.Q.D. 10-20) flysch
from -5,50 to -10,00 m	Flysch (Marl of Sanremo formation) consists of marl and marly limestone in thick layers with frequently diaclase with reddened edges, ricalcificate only partially, R.Q.D. 50-60

The penetration tests were realized by a lightweight dynamic penetrometer DL-30 of ‘Pagani’, around the area covered by the project. Such tests nominated from DP1 to DP9 were performed respectively at 1.9, 5.2, 1.3, 1.8, 2.8, 1.1, 1.2, 0.8, 1.2 m from the ground level. In the Figure 5.6 are shown the photo of some DP tests carried out. Also, the position of the geologic sections is shown in the Figure 5.6.
The maximum excavations during the construction of the hospital were approximately 11-12 m

deep behind the building and at the level with the existing electrical box of the transformation. Excavations of about 8 m were realized in the southern part of the building, located to about 3.5 m from the retaining wall on 'Street Dante' at the existing manhole of the San Francesco torrent. Furthermore, the foundations of building are supported by flysch of Sanremo.

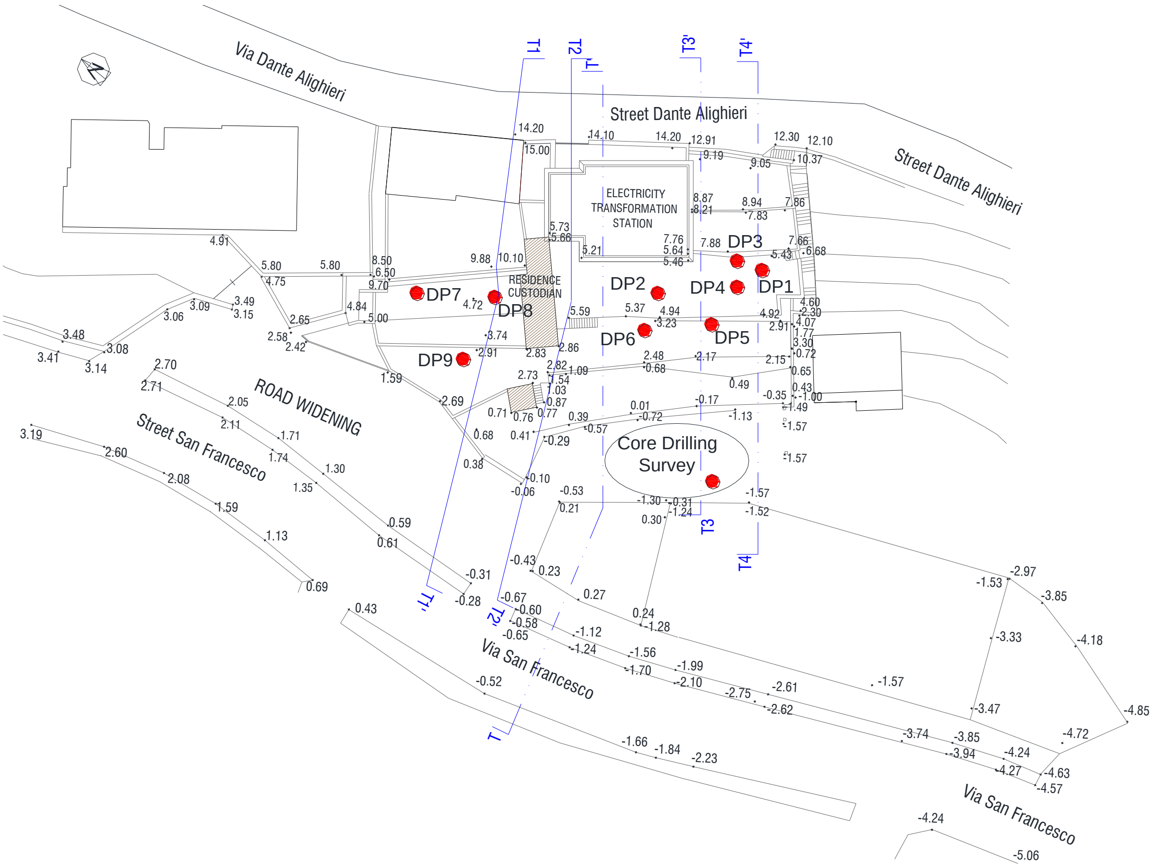

Figure 5.5 *Position of the dynamic penetration tests and the continuous core drilling survey (circle)*

Figure 5.6 *Photo of three dynamic penetration test, respectively DP3, DP8 and DP9*

The measurements and tests carried out on site allow the reconstruction of the *geological section* below the sediments of the construction site.

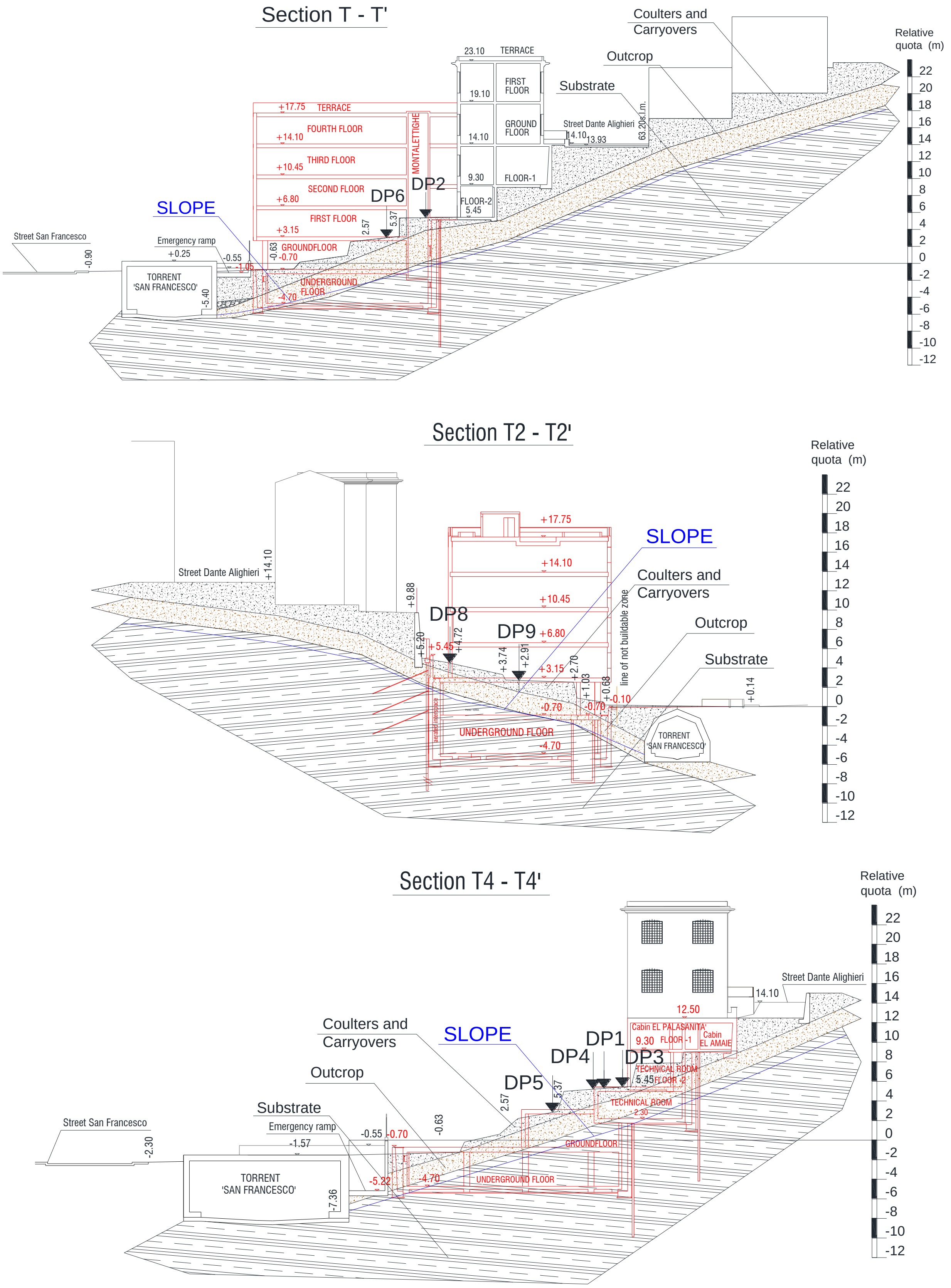

Figure 5.7 *Geological sections T-T', T2-T2' and T4-T4'*

The first few meters of rock substrate are characterized by poor geo-mechanics properties, corresponding to the most altered surface layer of the rock substrate (capping of alteration) in which the presence of rigid layers, even if disarticulated, can cause the interrupt of the DP test. The most significant geological sections (T-T', T2-T2' and T4-T4') are shown in the Figure 5.7. The presence of the water table wasn’t identified, it is assumed within the rock mass. This assumption is conservative but coherent with possible large rise of aquifer inside the discontinuity of the rock mass, in conjunction with the high aquifer recharges for significant weather events.

5.1.2 Geotechnical and geo-mechanical aspects

Mechanical parameters for the substrate were estimated (Geologist Marco Abbi) before the construction of the building, useful for analysis of stability and for calculation of bearing capacity. For the study under exam the layers formation, their deep and the unit weight have been taken from the geological report.

Geotechnical problems, during the construction of the building, essentially derived from the need to support an extended excavation front constituted almost by Flysch of Sanremo, since a thin coverage coulters detritus mostly arranged in terraces were observed. The presence of significant circulations of water underground, being in absence of sources and catchments phenomena, can be assumed only during the maximum recharging of water in the rock. The circulation of water along the discontinuity of Flysch rock mass can generate local concentration phenomena of the outflows in gaping fractures or discontinuities particularly persistent, often associated with phenomena of microkarst. Referred to the hydrogeological characteristics of the sediment layer and the discrete morphological slopes, it is considered unlikely the complete saturation of the surface blanked levels, which do not allow the deep percolation of water. This makes possible the use of effective parameters for the characterization of the sediment and the substrate.

Flysch formation affected by the project is a rock mass lithologically heterogeneous; to each separate level (sandstone, calcilutites, marl and argillites) associable with a specific geo-mechanical behavior. In the Table 5.2 are reported the mean values estimated by bibliographic data and from a significant number of tests in laboratory carried out for the excavation of Gallery of St. Giacomo.

Table 5.2 *Mechanical parameters value of rock mass*

Parameters	Sandstone	Marl and clayey marl	Calcilutites	Argillites
Unit weight (t/m3)	2,58 - 2,68	2,48 - 2,72	2,61 - 2,72	2,2 - 2,5
Cohesion (t/m3)	51,7 - 61,5	32 - 48		2
Angle of shear strength (°)	33° - 34°	17° - 20°		25°
Residual cohesion (t/m3)		11 - 17		1
Angle of residual shear resistance (°)		12° - 14°		16°
Uniaxial compression resistance (MPa)	107	1,6 - 100		0,28 - 5,74
Uniaxial compression resistance (sclerometric test, MPa)	77	35	128	
Uniaxial compression resistance (Point load test, MPa)		18	65	
Longitudinal wave velocity (intact specimen, Km/sec)	5,5	3,7	5,6	
Elastic module (GPa)	23		13,5	
Content of CaCO3 (%)		15 - 50	88 - 90	0 - 6

Proceeding as indicated by Marinos et al. (2005, 2007), can be identify an representative G.S.I. index between 24-36 for the rock. According to the observations made on natural outcrops can be identified the average parameters of rock mass, due to its natural heterogeneity. The geo-mechanical parameters are estimated as provided by the nonlinear failure criterion for fractured rock mass.

Anthropogenic carryover materials consist mostly of blankets detritus of old terracing derived from Flysch of Sanremo. The material has mostly a preponderant part of silts sandy clay, in which it adds a small proportion of fine gravel and small boulders. The particle size analysis always presents a considerable heterogeneity, with particle size classes well-distributed compared to the grains dimension, which leads to classify the sediment as *sandy clay weakly gravelly* with medium-low plasticity (Table 5.3):

Table 5.3 *Characteristics of anthropogenic carryover materials*

Parameters	**Value**
Unit weight (t/m3)	1,9 -2,1
Cohesion, from shear test (kPa)	0 - 85
Angle of friction from shear test (°)	16 - 23
Liquid limit (%)	45 - 51
Plastic limit (%)	22 - 26
Plastic index (%)	20 - 28
Uniaxial compression resistance (kPa)	300 - 420
Longitudinal wave velocity (Km/sec)	0,3 - 0,9
Transversal wave velocity (Km/sec)	0,2 - 0,4
Elastic dynamic module (Mpa)	1000 - 5000
Content of CaCO3 (g/kg)	200 - 300
Poisson coefficient	0,29 - 0,38

Cohesion and angle of friction relative to the coulter detritus, obtained from the shear test in laboratory on reconstructed specimens disturbed during sampling, are highly conservative with respect to the stability of the slopes observable in the area and also with respect to the real behavior of the excavation. Even the uniaxial compressive strength values are influenced by the same disturbing conditions of the samples and are slightly lower than the values obtained with pocket penetrometer test directly on site. Despite this, the theoretical value of uniaxial compression resistance, obtained from the maximum values of cohesion and angle of friction, is 256 kPa, compared to 320-420 kPa actually measured on disturbed samples.
It is recommend the adoption of the maximum parameters in the ranges above proposed, considering the hydrogeological conditions (the diffusion of superficial landslide events caused by lubrication of the sliding surface by infiltrating water at the bedrock-blanket interface) occurred during the last floods. Therefore the parameters can be: unit weight, γ = 1,9 -2,0 t/m^3; cohesion, c' = 0 t/m^2 and angle of friction, φ' = 34° - 36°.

Several penetrometric test were carried out on site to characterize the carryover material. In the Table 5.4 are shown the results of those tests.

The altered and deep rock substrate has those parameters:

- *Altered rock substrate:* unit weight, γ = 2,65 t/m^3; cohesion, c' = 40 kPa; angle of friction, φ' = 31,6°.
- *Deep rock substrate:* unit weight, γ = 2,65 t/m^3; cohesion, c' = 80 kPa; angle of friction, φ' = 42°.

Table 5.4 *Penetrometric test results*

DP Test	**Angle of shear strength (Meyerhof (1965)**
DP1	35,89
DP2	35,83
DP3	35,97
DP4	35,41
DP5	34,02
DP6	34,91
DP7	34,79
DP8	36,25
DP9	34,99
Mean value	35,34
Dev. Standard	0,72
Coeff. of variation	0,02
Characteristic value	34,16

5.1.3 Hydrogeological setting

The area is characterized by an impermeable bedrock that can present a secondary low permeability for water circulation along the fractures of the rock mass that are very discontinuous and variable as a function of the degree of fracturing, faulting and alteration of the rock mass, as well as to the degree of micro-karst which develops in more calcareous horizons of Flysch. The fracturing is present in a systematic and lateral continuity way, only in more rigid horizons of Flysch (limestone and calcilutites), while it is virtually absent in most plastic horizons (marl and argillites). An alternation of substantially impermeable levels, that can reach an equivalent permeability of about 9.4^{-7} cm/sec in case of continuous fractures with 40 cm spacing, is observed. The total permeability is therefore strongly conditioned by the degree of "communication" between these horizons generated by fault planes and/or fold fault (from tectonization of rock mass). The surface materials and the alteration layers have an primary permeability from discreet to poor ($k=10^{-5}$ - 10^{-6} cm/sec). The complete imbibitions of the detrital thin layer appears quite unlikely as the regime of annual average rainfall can saturate only the minimum thickness ground (less than 0.5 m, according to studies conducted by the model Pradel and Raad (1993). It must also highlights the strong erosive action that results from the surface runoff of almost all the precipitated water.
Penetrometric tests carried out on site did not identify the ground floor while the survey realized near the expansion tank of the San Francesco torrent shows the presence of a stable water table to a depth of about 7 m from the ground level.

5.1.4 Geomorphological setting

The area of the project is located along the versant on the left site of the San Francesco torrent and in the vicinity of the expansion tanks of the torrent, placed at an altitude between 50 and 60 m above sea level. This versant is placed on terraces, used mainly for residential purposes, and has an average gradient of about 21°-22°. As shown in the geomorphologic map (see Figure 5.8), some marine terraces near the ridge line of the slope, are present. The area of interest falls in the detrital covers deposits and in the recent alluvia, occasionally terraced, mainly sand-silt grain sized (see blue circle). In the versant of interest for the study aren't find morphological terraces of fluvial origin, probably identifiable on the opposite side where the slope are much softened. The area in question is located in the extrados of the original course of the river, in the area of erosion.

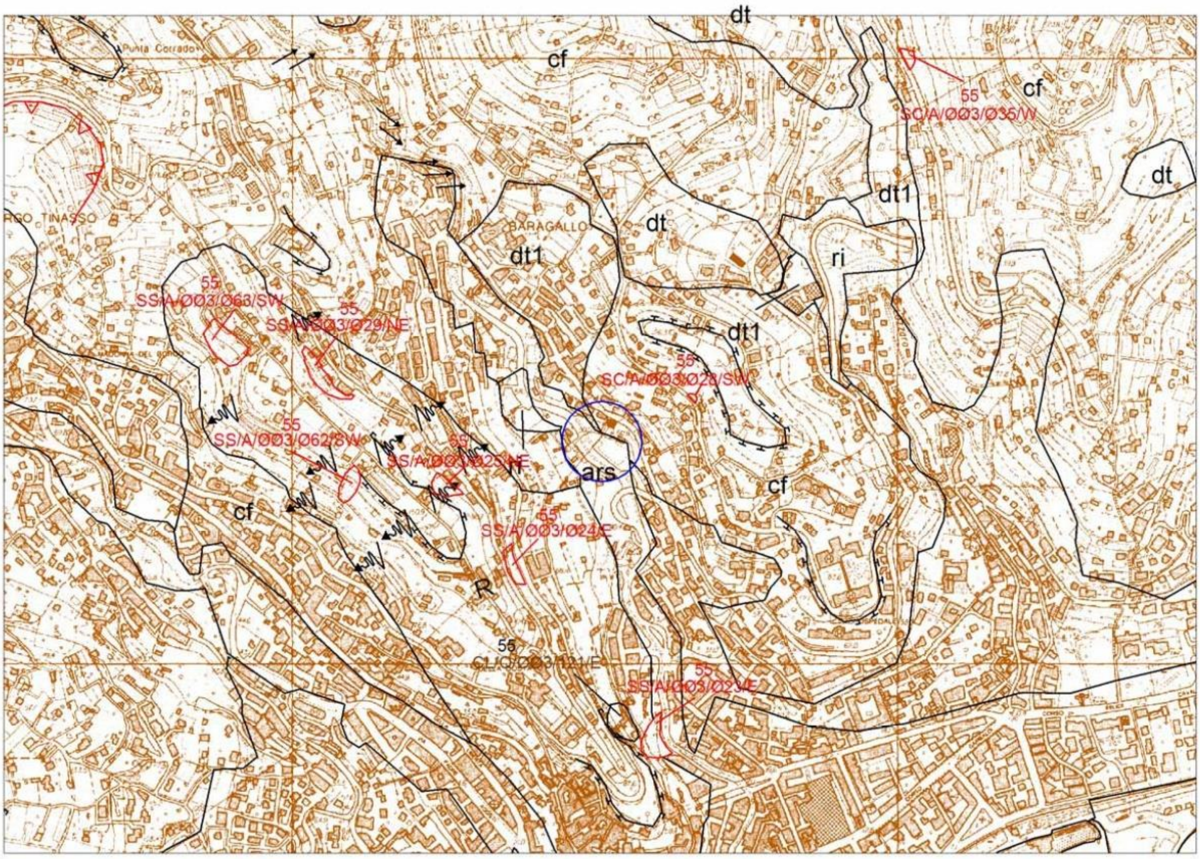

Legend:

Rocky outcrops and sub-outcrops with detritus covers up to 1m thick

- R — in good conditions of perseverance and/or inclination of the structures to the slope
- RS — in good conditions of perseverance with inclination of the structures opposed to the slope
- RF — in poor conditions of perseverance, altered and/or fractured in respect of the slope

Detrital covers and colluvial eluvial deposits from 1 to 3 m

- cf — fine-grained
- cg — coarse- and average-grained

Detrital massive covers with the thickness greater than 3 m

- dt — indistinct grain size
- dt1 — fine-grained
- dt2 — coarse- and average-grained

Alluvial deposits

- ams — Currently moving alluvia, mainly sand-silt grain sized
- ars — Recent alluvia, occasionally terraced, mainly sand-silt grain sized

Landslides

- SS — superficial landslide (of flow or soil slip): active A, quiescent Q
- SC — sliding or slipping landslide: active A, quiescent Q
- FC — complex landslide: active A, quiescent Q
- CL — collapse landslide: active A, quiescent Q
- P — paleo-landslide
- edge of active landslide
- edge of quiescent landslide
- Basin limits

Erosion forms

- bank erosion
- diffused surface runoff

Morphological elements

- rims of marine terraces
- quiescent slope failure

Anthropical forms

- large carryovers
- active quarries
- abandoned quarries
- quarry front
- landfill

Scale 1:10000

Figure 5.8 *Geomorphologic map of Sanremo of scale 1:10.000*

This versant falls in topographic category T2: slope with an average inclination higher than 15°. However, being the building near the valley floor and considering the depth reached by the excavation, a topographic category T1 can be consider, that have a topographical amplification coefficient S_t equal to 1 (Table 5.5).

Table 5.5 *Topographical amplification coefficient S_t, NTC08*

Topographical category	**Location of construction or intervention**	S_t
T1	–	1,0
T2	In correspondence to the top of the slope	1,2
T3	In correspondence with the crest of the relief	1,2
T4	In correspondence with the crest of the relief	1,4

5.2 Local seismic response procedure

The procedure followed to estimate the local seismic response (reference spectrum), on the basis of the design parameters (provided by the designer) and geological-technical properties (related to the campaign of exploration of the subsoil) has been realized through the use of some specific software and codes: 'Rexel v.3.5' database (Iervolino et al., 2010) for the extraction of the input motions, STRATA software (Kottke and Rathje, 2008) for linear equivalent analysis to estimate seismic response 1D, 'ESAC2015 code' and 'GAinvers6 code' to estimate respectively the dispersion curves and seismic stratigraphic profile by soling the inverse problem. This procedure is described in the diagram of the Figure 3.11 and consist mainly in the following steps:

- Select reference accelerograms of site by using 'Rexel v3.5' database;
- Identify stratigraphic profile from geologic report realized before the construction of the hospital (core drilling survey, geologic map of scale 1:10.000, penetrometric test, information from the excavation realized during the construction, NASW survey and seismic stringing survey in the vicinity of area of interest);
- Estimate dispersion curves from synchronized pairs of ambient vibration measures;
- Estimate seismic-stratigraphic profile of site by solving the inverse problem;
- Identify decay curves of layers: modulus of rigidity and damping as a function of deformations identified from bibliography (relationship of various authors, geophysical and seismic surveys, or laboratory test);
- Compute linear equivalent analysis with STRATA software to estimate response spectrum of site and/or accelerogram in surface;
- Estimate seismic stratigraphic of subsoil -1D model from linear equivalent analysis;
- Estimate V_{s30} of subsoil.

Those steps are described in the following sections. Pairs of synchronized ambient noise measurement were acquired to apply the methodology described above.

5.2.1 Select reference accelerogram

The reference accelerogram or spectrum of the area of interest has been selected from Rexel v3.5 database which contain natural accelerograms recorded in the word. Being a freely available software, in the website of the Italian Laboratories University Network of seismic engineering, ReLUIS can be used by everyone.
(*http://www.reluis.it/index.php?option=com_content&view=article&id=118&Itemid=105&lang=en*).
Recordings contained in the database derived from European Strong Motion Database (ESD), Italian Accelerometric Archive (ITACA) or from around the world (Select Input Motions for

Displacement-Based Assessment and Design, SIMBAD). Accelerograms selected from 'Rexel v3.5' have been used as input in the local seismic response analysis. This database allows the search for natural accelerograms combinations compatible with the spectrum in acceleration defined from Technical Standards for Construction (NTC 2008) in our case, Eurocode 8 or arbitrarily defined by the user. In the first case it is necessary to enter the geographical coordinates of the site (applicable to Italy only), longitude and latitude in decimal degrees, and to specify the site class (A, B, C, D or E of EC8), the topographic category, nominal life of the structure, functional type of the structure and the limit state of interest (to define the return period of the seismic action). Then the software automatically generates the spectrum accordingly. In case of EC8, it is necessary to specify only the anchoring value of the spectrum, a_g, and the site class. The value of a_g can be defined manually by the user or, in the case of sites on the Italian territory, can be obtained automatically from the geographical coordinates of the site. In the first two cases, if the spectrum is to be obtained automatically after the geographical coordinates, the software has built-in the official hazard data of the Italian seismic code (derived from the INGV study). In the third case (user-defined spectral shape), the spectral acceleration ordinates corresponding to123 periods between 0 and 4 s have to be entered by the user. Finally, it is necessary to specify the component of the spectrum to consider; i.e., horizontal and/or vertical. The two orthogonal independent components that describe the horizontal motion are characterized by the same elastic response spectrum as for the considered codes, while the component that describes the vertical motion is characterized by a specific spectrum. It is possible to select horizontal or vertical components separately or contemporarily, depending on the number of components desired to be included in the ground motion.
The accelerograms may also reflect the characteristics of source in terms of magnitude, epicentral distance and intensity of the earthquake measures.
Seismic hazard of construction site should be identified before check the reference accelerograms on the area of interest for the study. This is possible on the National Institute of Geophysics and Volcanology website (*http://esse1-gis.mi.ingv.it/)* where can be identified the interactive seismic hazard map of the area. In the Figure 5.9 are shown the disaggregation of a(g) values, near the area of interest, with probability of exceedance 10% in 50 years. As one can see, the magnitude of events is between 4 and 6.5 Richter happened in an epicentral distance between 0 km and 30 km. Those parameters have been used as input data when checking the reference accelerograms of site in 'Rexel v3.5' database.

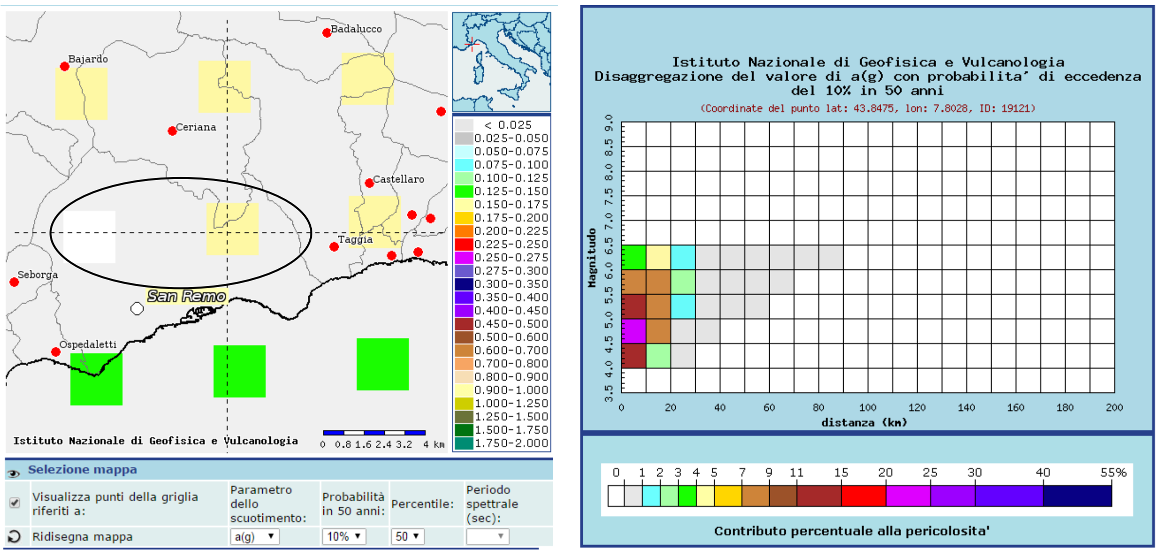

Figure 5.9 *Disaggregation of a(g) value with probability of exceedance 10% in 50 years near the area of interest*

Data input on 'Rexel v3.5' consist of:

- Site coordinate, Latitude and Longitude of hospital in Sanremo: 43.825 x 7.774 (43°49'30.26"N, 7°46'26.57"E);
- Code spectrum due to NTC2008: Site class A, Topographic category T_1, nominal life (V_n) 100 years, SLV and SLD limit state;
- Select horizontal or vertical component separately;
- Preliminary database research based on M, R and epsilon: M_{min} - M_{max} are respectively 4 and 6.5 Richter, R_{min}-R_{max} are respectively 0-30 km, ε_{min}-ε_{max} are respectively -1.5 and +1.5;
- Database search: European Strong-motion Database;
- Spectrum matching: Upper-lower tolerance of 10-30%, T_1-T_2 are respectively 0.10 and 2s;
- Set size: 7 records, 1 component, 1 number of compatible sets and 1 mean scale factor.

Accelerograms identified for SLV and SLD for horizontal components for different nominal life (50 and 100 years) are shown in the Figure 5.10 and in the Figure 5.11.

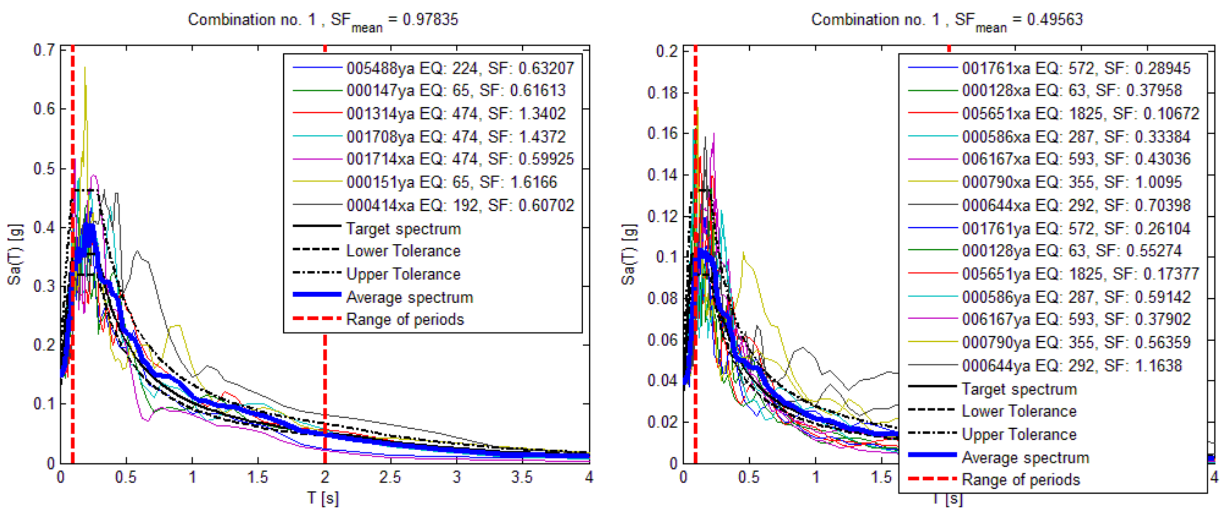

Figure 5.10 *Accelerograms identified for SLV limit state (graphic on the left) and SLD (graphic on the right), for horizontal components, for nominal life 50 years*

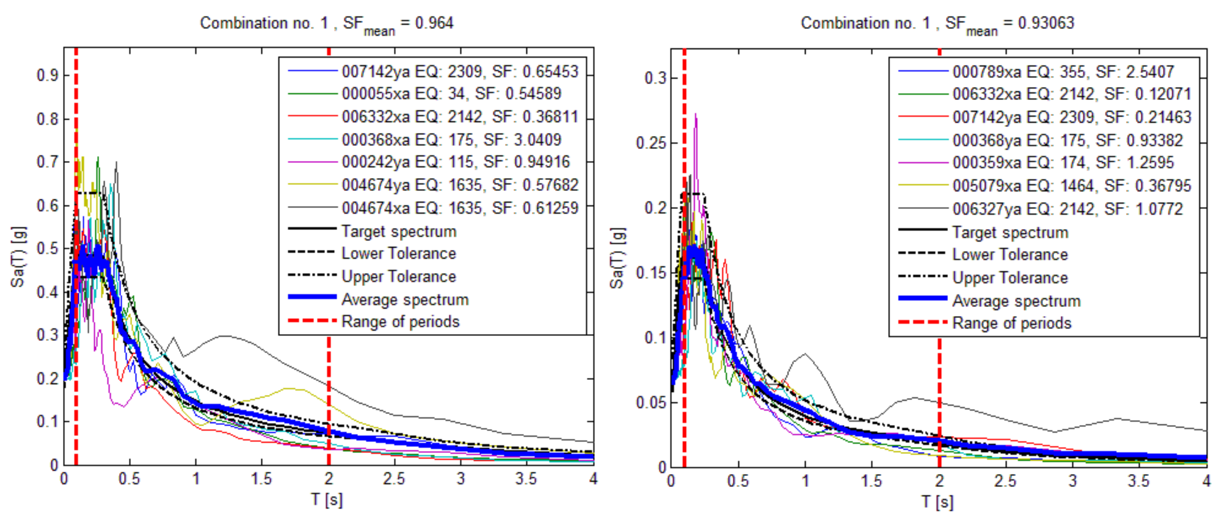

Figure 5.11 *Accelerograms identified for SLV limit state (graphic on the left) and SLD (graphic on the right), for horizontal components, for nominal life100 years*

5.2.2 Stratigraphic profile and decay curves

Stratigraphic profile of the area under exam has been identified from the available geological data: core drilling survey, laboratory test, geological report carried out by the geologist Marco Abbi before the construction of the building. Those results are summarized in the Table 5.6.

Table 5.6 *Stratigraphic profile and soil properties from core drilling and laboratory test*

Depth (m)	Lithology
from 0,00 to -3,00 m	Overs coarse composed from the mixed areated ground to the very loose inert S.P.T. 11/10/17 (-2.70, -3.00)
from -3,00 to -3,20 m	Calcareous-arenaceous
from -3,20 to -4,10 m	Overs rich in inert and little constipated
from -4,10 to -5,20 m	Mixed carryovers to reworked floods in sandy-silty matrix with rounded clasts
from -5,20 to -5,50 m	Capping of alteration of disarticulated and very altered (R.Q.D. 10-20) flysch
from -5,50 to -10,00 m	Flysch (Marl of Sanremo formation) consists of marl and marly limestone in thick layers with frequently diaclase with reddened edges, ricalcificate only partially, R.Q.D. 50-60

Depth (m)	Description	Unit weight (kN/m3)	Cohesion, c' (kPa)	Angle of friction, φ' (°)
from 0,00 to -3,00 m	Sandy clay weakly clayey	19	–	16-23
from 4,10 to -5,20 m	Carryover with silty sandy matrix with rounded clasts	20	0	35
from 5,20 to -5,50 m	Capping of alteration of flysch	26,5	40	31,6
from 5,50 to -10,00 m	Flysch	26,5	80	42
> 10 m	Flysch	26,5	–	–

Referred to the existing data, four type of soil have been created in the STRATA software which consist of:

- Sandy clay weakly clayey: unit weight19 kN/m3, decay curve for 'Sandy clay' estimated from Pergalani F. et al (2000), Idriss (1990) 'clay' from STRATA database;
- Carryovers with silty sandy matrix: unit weight 20 kN/m^3, decay curve for 'Sandy clay' estimated from Pergalani F. et al (2000), Idriss (1990) 'sand' from STRATA database;
- Altered Flysch: unit weight 26.5 kN/m^3, decay curve for 'Clayey Flysch' estimated from Lo Presti D.C.F. et al (2000), from STRATA database;
- Flysch: unit weight 26.5 kN/m^3, decay curve for 'Marl clayey Flysch' estimated from National Seismic Service.

The decay curves have been chosen from the bibliography for each soil type (Table 5.8). In the Table 5.7 are presented the G/Gmax model and damping model value. The last points on those graphics have been added to reach a valid analysis in STRATA. Also, the decay curves presented in bibliography of STRATA have been used to estimate the influence of the decay curve in the response spectrum estimation.

The uncertainty of nonlinear soil properties (G/Gmax and D) have been taken into consideration during the analysis by varying those parameters due to the Darendeli (2001) model. Nonlinear soil properties variation (shear modulus reduction curve, damping ratio curve and damping of the bedrock) has been realized to all layers described before.

***Table 5.7** Values of normalized shear modulus G and damping in percentage*

Sandy clay weakly clayey		
Strain (%)	G/Gmax	Damping (%)
0,000	1,00	5,20
0,001	0,97	5,50
0,010	0,75	8,30
0,100	0,17	25,00
0,150	0,10	26,00
0,200	0,09	27,00
0,300	0,08	28,00
0,400	0,07	29,00
0,500	0,06	30,00
0,600	0,05	31,00
0,700	0,04	32,00
0,800	0,03	33,00
0,900	0,02	34,00
1,000	0,02	34,00

Carryover - Gravelly Sand		
Strain (%)	G/Gmax	Damping (%)
0,000	1,00	1,00
0,001	0,98	2,00
0,010	0,75	7,00
0,100	0,30	17,00
0,200	0,25	17,00
0,300	0,20	18,00
0,400	0,15	18,50
0,500	0,14	19,00
0,600	0,13	20,00
0,700	0,12	21,00
0,800	0,11	22,00
0,900	0,10	23,00
1,000	0,10	24,00

Clayey Flysch		
Strain (%)	G/Gmax	Damping (%)
0,000	1,00	0,05
0,001	1,00	0,05
0,002	0,95	0,05
0,005	0,83	0,10
0,010	0,77	2,00
0,020	0,67	4,00
0,050	0,53	6,00
0,100	0,35	8,00
0,300	0,18	12,00
0,500	0,18	12,00
0,600	0,17	12,00
0,650	0,17	13,00
0,700	0,17	13,00
0,900	0,15	14,00
1,000	0,15	15,00

Marl clay Flysch		
Strain (%)	G/Gmax	Damping (%)
0,000	1,00	3,29
0,001	1,00	3,42
0,002	1,00	3,44
0,010	0,88	4,66
0,020	0,69	7,84
0,050	0,50	11,27
0,100	0,29	18,00
0,200	0,19	25,95
0,500	0,19	25,95
0,700	0,18	27,00
1,000	0,18	27,00

***Table 5.8** References for the decay curve of layers*

Authors	Litology	SITO	Deep_Sample	GAMMA	Vs	Test
Servizio Sismico Nazionale (2003) - Microzonazione sismica di S. Giuliano Servizio Sismico Nazionale	Marl clay Flysch	S. Giuliano (CB)	6.80 - 7.50	2,15		CR
Lo Presti D.C.F. et al (2000) – Definizione del modello di sottosuolo per le analisi di risposta sismica: il caso di Castelnuovo Garfagnana. Corso CISM 2000.	Clayey Flysch	Garfagnana	16,6	2,59	530 - 550	CR
Pergalani F. et al (2000) – Definizione delle istruzioni tecniche e valutazione quantitativa degli effetti locali di alcune località della Garfagnana. Corso CISM 2000.	Sandy clay	Garfagnana	-	21	380 - 800	-
Pergalani F. et al (1999) - Seismic microzoning of the area struck by Umbria - Marche (Central Italy) Ms 5.9 earthquake of 26 September 1997 - Soil Dynamics and Earth. Engineer. 18 (1999) 279 - 296.	Gravelly Sand	Umbria-Marche	-	19,6	400 - 700	-

5.2.3 Passive seismic field surveys

Synchronized HVSR measures have been carried out near the area of interest. Dispersion curve has been estimated from synchronized ambient vibration measures placed at a distance of 50 m and 75 m from each other.

Also, seismic surveys which were realized near the area of interest for the construction of the S. Giacomo tunnel, have been taken into consideration to identify the bedrock category. The longitudinal wave velocity of anthropic carryovers and detrital blankets was estimated from penetrometric tests and from bibliographic data. Furthermore, a NASW survey was carried out before the construction of the building.

Referred to the bibliography data and to the penetrometric tests carried out in the area under exam, the Vs of anthropic carryovers and detrital blankets (estimated by the empirical relationships provided by various authors, see references in the table below) is about 180 m/s (Table 5.9).

As it is known, the seismic action of the project is defined starting from "base seismic hazard" of the construction site (NTC 2008). This constitutes the element of primary knowledge for the determination of seismic actions, under which can be verified the limit states considered. The seismic hazard is defined in terms of expected maximum horizontal acceleration a_g in free field conditions over a rigid reference site with horizontal topographic surface (National Institute of Geophysics and Volcanology website *http://esse1-gis.mi.ingv.it/*). The seismic hazard is defined by an approach "dependent area" in NTC 2008 and not anymore as "depended zone" as in O.P.C.M of 20/03/03 and the subsequent O.P.C.M. 3519/2006.

***Table 5.9** Vs calculated from empirical relationships*

DP Test	Nspt	Prof. layer (m)	Nspt corrected for the presence of acquifer	Unit weight (kg/m3)	Vs (m/s), Seed (1983), note 2	Vs (m/s), Otha and Goto (1978), note 1	Vs (m/s), Yoshida (1988), note 3	Vs (m/s), Imai (1982), note 4	Vs (m/s), Sykora (1983), note 4	Vs (m/s), Muzzi (1984), note 4	Vs (m/s), Oshaka (1973), note 4
DP1	16,3	1,3	16,26	1,8	222	139	117	233	231	203	226
DP2	14,3	1,5	14,31	1,8	208	140	111	224	222	194	212
DP2a	19,4	5,2	19,36	1,8	242	187	100	246	243	215	246
DP3	16,5	1,1	16,51	1,8	223	135	120	234	232	204	228
DP4	14,8	1,7	14,83	1,8	212	144	110	226	225	197	216
DP5	10,9	2,7	10,93	1,8	182	149	95	206	205	178	185
DP6	13,4	1,0	13,39	1,8	201	128	115	219	218	190	205
DP7	13,1	0,6	13,05	1,8	199	115	123	217	216	189	202
DP8	17,4	0,6	17,36	1,8	229	121	132	238	235	207	233
DP9	13,6	0,5	13,62	1,8	203	112	127	220	219	191	207
Mean	15,0		15,0		212,1	137	115	226,3	224,6	196,8	216
Maximum	19,4		19,4		242	187	132	246	243	215	246
Minimum	10,9		10,9		182	112	95	206	205	178	185
Standard deviation	2,6		2,6		18,3	20,9	9,5	12,3	11,6	11,3	18,6

Note 1: the empirical equation tends to underestimate the Vs for increasing of gravel, silt and age of the deposit, so, values of Vs > 300 m/s is valid for sands and gravel. Note 2: for sand and gravel. Note 3: for all sandy and gravelly soil type. Note 4: for all sandy soil type.

The subsoil category can be identify by estimating the equivalent value of longitudinal wave velocity normalized on 30 m by the following equation:

$$V_{s30}; N_{30}; C_{u30} = \frac{\sum_{i=1}^{n} d_i}{\sum_{i=1}^{n} \frac{d_i}{V_{si}}; \frac{d_i}{N_i}; \frac{d_i}{C_{ui}}} \qquad \text{(Eq. 5.1)}$$

where n is the number of homogeneous layers in which it is possible to divide the soil, d_i is the thickness layer, V_{si} is the shear wave velocity of the layer i, N_i is the number of shots of SPT test (N_{SPT}) of i-th layer, $\sum_{i=1}^{n} d_i = 30$ m.

In cases where the vertical stratigraphy investigated is higher than 30 m the sequence is truncates while when is inferior of 30 m than the thickness of the last layer is increased.

Subsoil categories, referred to the V_{s30}, N_{spt30} and undrained cohesion values, are shown in the Table 5.10.

***Table 5.10** Subsoil category description referred to V_{s30}, N_{spt30} and undrained cohesion values*

Category of subsoil	$V_{s,30}$ (m/s)	$N_{SPT,30}$	Plastic index	Undrained cohesion, $c_{u,30}$ (kPa)	Description
A	> 800				Lithoid formations/very rigid (with max. 5.0 m gossan)
B	360 - 800	> 50		> 250	Sands, densified gravels, consistent clays
C	180 - 360	15 - 50		70 - 250	Sands and gravels averagely densified and clays with an average consistency
D	< 180	< 15		< 70	5 - 20 m thickness, floods, Vs of bedrock > 800 m/s
E	< 180; 180 - 360				
S1	< 100		> 40	10 - 20	Clay/silt with thickness > 8 m
S2					Sensible clay and/or liquefiable soils

5.2.3.1 NASW and seismic refraction from bibliography

NASW survey and seismic refraction stringing were carried out in years, from the Municipality of Sanremo, for different purposes. Also, a NASW survey was carried out from the geologist Marco Abbi, near the area of interest, in the vicinity of the existent Hospital which is located on the top of the slope that underlies the area of interest (see Figure 5.12). Through the NASW surveys is identified the presence of Flysch rock mass with values of Vs comprised between 860-1150 m/sec in the first 30 m from the surface. 'Abem Terraloc Mk6' seismometer, with 24 channels and 24 geophones with a characteristic frequency of 4.5 Hz spaced by 2 m for a total length of stringing 46 m, were used to acquire the data. The processing steps of data acquired consisted of:

- Pre-processing of seismic noise records: the average characteristics of the "noise" have been analyzed to check the space-time stationarity and spectral coherence. In particular, statistical analysis of the coherence allowed the identification of the frequency range from 3.5 Hz to 25 Hz to be used in the subsequent phases of the processing;
- Processing of seismic noise records: transformation from 'time - distance' to 'time intercepts, tau - slowness or apparent velocity, p' domain and transformation from 'time intercepts - slowness' (tau-p) to 'frequency - slowness' (f-p) domain;
- Statistical processing of all records in p-f domain and normalization procedure, to obtain the diagram indicated as "p-f Image" diagram which represents the normalized power spectrum as a function of the frequency *f* and of the apparent velocity *p*;
- The dispersion curve V_R (f) was subsequently used to estimate the vertical profile of the shear waves velocity propagation using a direct modeling method, which allows to obtain Vs as a function of *z*, such as to minimize the misfit between the theoretical dispersion curve and the observed one.

The vertical profile of the propagation of the shear waves velocity as a function of the depth is shown in the Figure 5.13. Soil classification referred to V_{s30} value, as indicated by OPCM 3274 (Ordinance of President of the Council of Ministers, 20 March 2003 "The first items regarding the general criteria for seismic classification of the national territory and technical standards for construction in seismic zone") and by Eurocode 8 (see Table 5.13), indicate a soil Type B with V_{s30} of about 488 m/s.

Furthermore, the longitudinal wave velocity of the bedrock was estimated from a series of seismic stringing carried out along the excavation section (1560 m long) for the exploratory tunnel S. Giacomo in Sanremo. Seismic geophone string with 24 channels with vertical and horizontal geophones (EG&G Geometrics Strata View) spaces varying among 1-2-4-5-8 m, were used to record the signals. In particular, the entire gallery was measured by spacing equal to 5 m between the geophones (in 1994), while some specific segments were investigated through the use of different geometry of geophones (1, 2, 4, 8 m in 1992 and in 1997). The measurements were also repeated in years in order to highlight the possible presence of the geo-mechanical decay properties of marl and clay materials as the rock mass is direct exposure inside the pilot tunnel. The measures in 1994 show an average value of Vs equal to 2171m/sec, with standard deviation 191 m/sec. This value doesn't change significantly in years, taking into account the changing of operators and purposes of measures.

The collection of such data leads to choice a mean value of Vs for the rock substrate equal to1000 m/sec. Knowing the Vs of coulters 180 m/s (and Poisson ratio equal to 0.32) and of flysch bedrock 1000 m/s, the Vs30 is about 813 m/s, which corresponds to soil **Type A** (see Table 5.13).

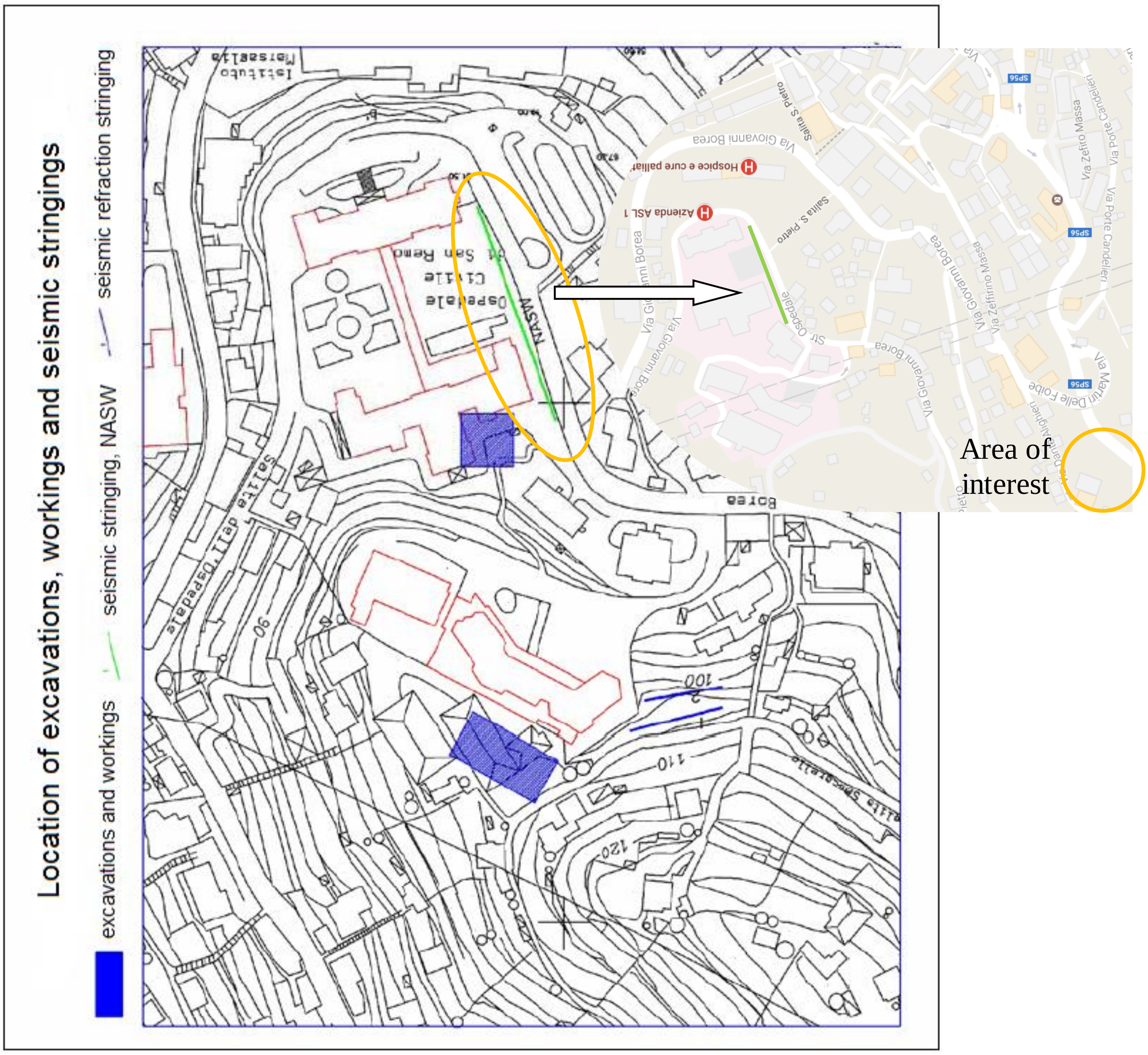

***Figure 5.12** Location of NASW and Seismic refraction stringing*

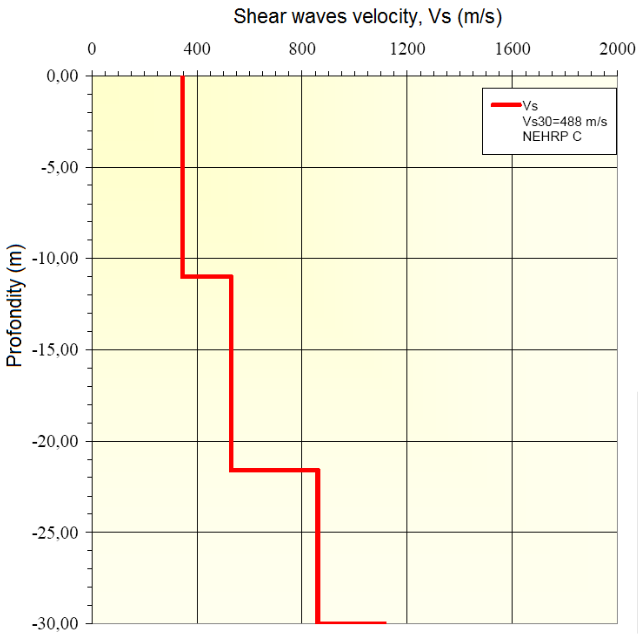

Depth (m)	Vs (m/s)
0,00	346
-11,00	346
-11,00	530
-21,60	530
-21,60	860
-30,00	860
-30,00	1112

***Figure 5.13** The vertical profile of the shear wave velocity propagation from NASW survey*

5.2.3.2 In field HVSR test

Pairs of synchronized ambient vibration measures have been acquired near the area of interest. Several measurements in the vicinity of the hospital, have been acquired as the site around the hospital is trafficked and build up area. The maximum accessible distance found in the free field was about 75 m. Pairs of synchronized ambient vibration measures have been recorded by two portable seismographs called Tromino™, spaced at 50 m and about 75 m with sampling frequency 512 Hz and with a duration of 30 minutes. Seismographs have been synchronized by GPS signal. Measures position, with reference to the new hospital (yellow circle), is shown in the Figure 5.14. Ambient vibration measures evidenced with blue circle in the figure below, have been demonstrate better results, having a higher distance between sensors (of about 75 m). In the Figure 5.15 is shown a photo of one pairs of measures acquired in the garden of 'Caritas', which gave better results being in a quite area.

Figure 5.14 *Position of ambient vibration measures carried out in the free field*

Figure 5.15 *Photo of a pair of synchronized ambient vibrations in the free field, acquired with 'Tromino'*

The main properties of data recorded are summarized in the Table 5.11, indicating with slave and master the individual acquisition of each pair of synchronized ambient vibration measures.

***Table 5.11** Summarize of data recorded properties*

Measure 'Caritas'	Start time recording	Latitude (N)	Longitude (E)	Altitude above mean sea level (m)	Sampling frequency, f (Hz)	Duration (min)	Distance master - Slave (m)
Master 1	07:44:48	43°49'18.32"N	7°46'45.39"E	54,6	512 Hz	30	50
Slave 1	07:47:16	43°49'17.87"N	7°46'43.04"E	81,7	512 Hz	30	
Master 2	08:39:58	43°49'18.32"N	7°46'45.39"E	54,6	512 Hz	30	75
Slave 2	08:26:16	43°49'17.69"N	7°46'42.39"E	64,9	512 Hz	30	

Measure 'Hospital - ASL1'	Start time recording	Latitude (N)	Longitude (E)	Altitude above mean sea level (m)	Sampling frequency, f (Hz)	Duration (min)	Distance master - Slave (m)
Master	10:21:17	43°49'28.04"N	7°46'39.46"E	103,3	512 Hz	30	35
Slave	10:22:19	43°49'28.46"N	7°46'41.57"E	111,4	512 Hz	30	

Measure 'New Hospital'	Start time recording	Latitude (N)	Longitude (E)	Altitude above mean sea level (m)	Sampling frequency, f (Hz)	Duration (min)	Distance master - Slave (m)
Master	08:28:47	43°49'26.96"N	7°46'27.45"E	53,0	512 Hz	30	16
Slave	08:26:48	43°49'27.89"N	7°46'27.42"E	55,8	512 Hz	30	

Measure 'New Hospital'	Start time recording	Latitude (N)	Longitude (E)	Altitude above mean sea level (m)	Sampling frequency, f (Hz)	Duration (min)	Distance master - Slave (m)
Master	08:28:47	43°49'26.96"N	7°46'27.45"E	53,0	512 Hz	30	16
Slave	08:26:48	43°49'27.89"N	7°46'27.42"E	55,8	512 Hz	30	

In the Geologic map of scale 1:10.000 (Figure 5.16) are overlapped the position of ambient vibration measurements, at the aim to evaluate the geologic formation of sites (letters in blue) where those records were acquired. As one can see, the building under exam (New hospital) is constructed in Flysch of Sanremo (maELM), massive detrital covers (dt) and alluvial deposits (ars). Ambient vibration measures acquired near 'Caritas' is located in Flysch of Sanremo, near 'ASL 1' in Pliocene while in 'Garden' in massive detrital covers (dt).

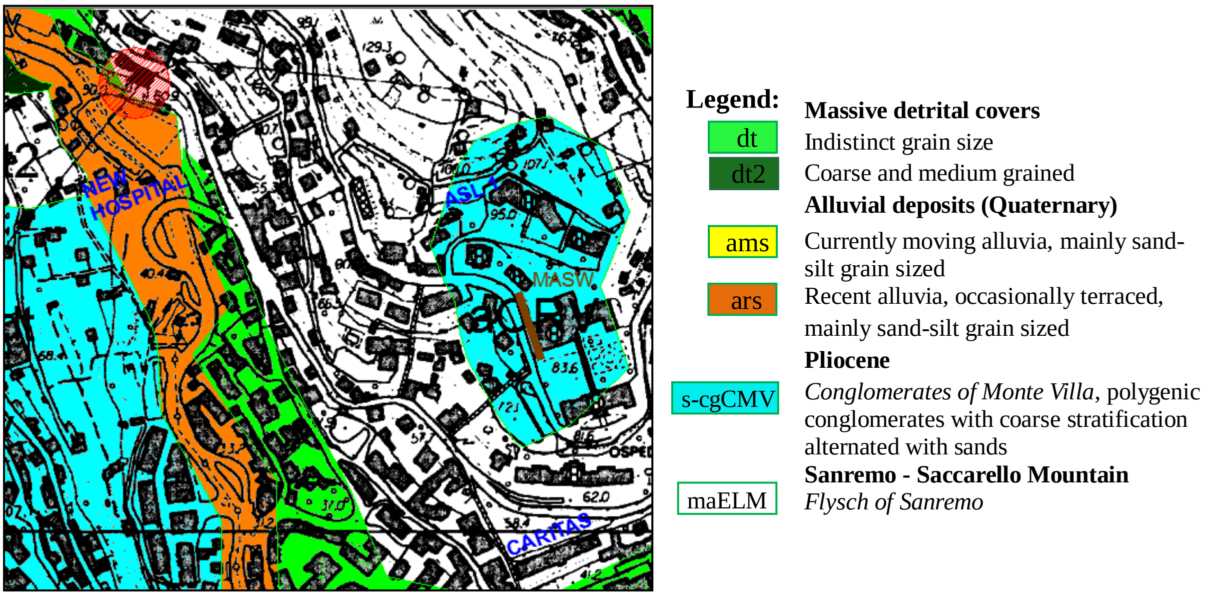

***Figure 5.16** Position of ambient seismic noise measures in Geologic map of scale 1:10.000*

Synchronized pairs of measurements needed to estimate the dispersion curve. Those ambient vibration measurement have been acquired in the vicinity of the building as it was impossible

to find free area (not build up) near the building. Furthermore, ambient noise measures acquired in the vicinity of the interest area have been confronted with those acquired outside the building under exam, at the aim to evaluate their comparability in the interval of interest frequencies from 0 Hz to 10 Hz. HVSR curve chosen to estimate the dispersion curve, shows a discrete equality with HVSR curve of the construction site. In the Figure 5.17 are shown some of HVSR curve estimated from ambient vibration measurements acquired. The measures named 'Punto 1' has been acquired outside the building while the other one in its vicinity due to the difficulty to find free area for the acquisition of synchronized measures by two seismographs, which should be placed at a distance higher than 50 m to reach good results on the dispersion curves.
HVSR curve chosen for analysis is shown in the Figure 5.19. A peak in frequency around 3.8 Hz, present in all HVSR curve, can be considered as a natural frequency of site.

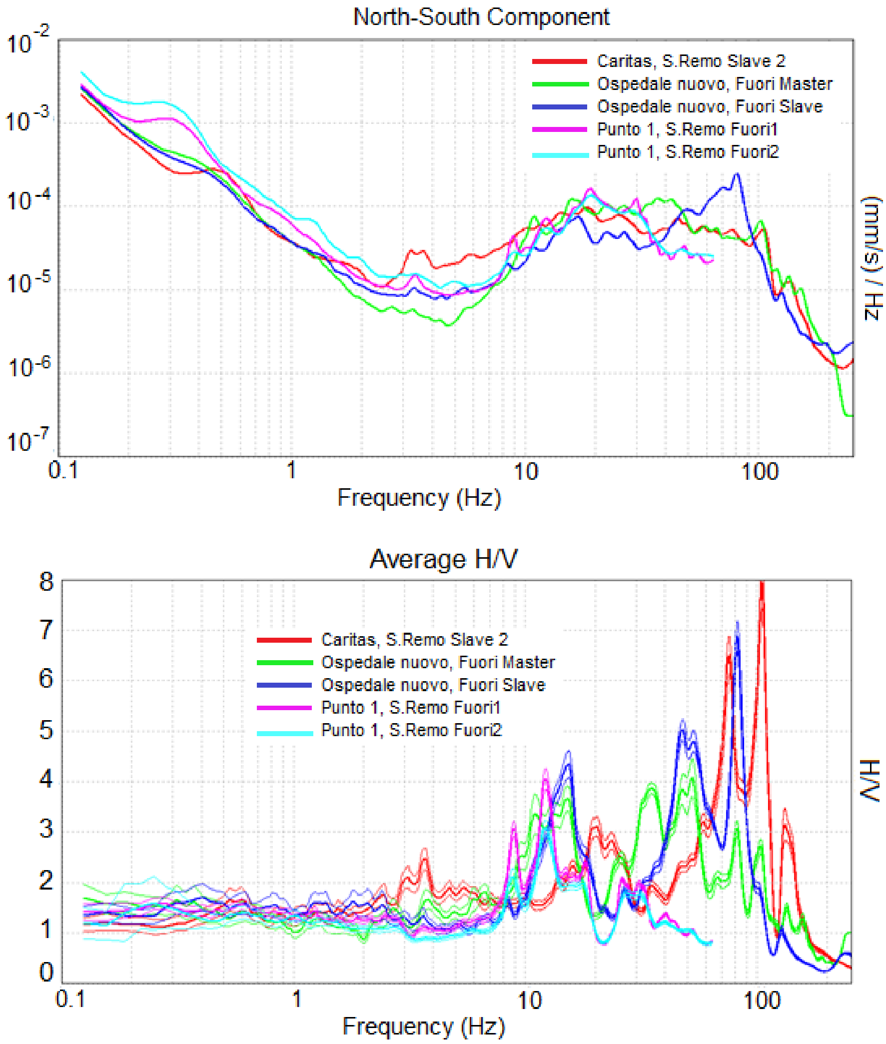

Figure 5.17 *HVSR curve of ambient noise measurement acquired in the free field near the construction area*

5.2.4 Dispersion curve estimated

SPAC zero crossing method (ESAC 2015 code) has been used in the framework of this dissertation to estimate the Rayleigh phase velocity (VR) dispersion curve by comparing ambient vibrations measured at two sensors. Ambient vibrations have been acquired for 30 minutes with two synchronized three-directional sensors with a sampling frequency of 512 Hz.

Two acquisitions with different inter-sensor distances *D* have been performed: 50 m and 75 m. Vertical components of a pair of synchronized ambient vibration measures, pleased at a distance of 75 m (or of 50 m) between each other, have been used as input to estimate the dispersion curves (Figure 5.18). SPAC zero crossing analysis has been carried out for two vertical component of the recorded signals, considering positive and negative zero crossing (values equal to -2, -1, 0, 1, 2) in the Equation 3.9.

Graphic of dispersion curves estimated from synchronized ambient vibration measures placed at a distance of 50 m or 75 m from each other shows similarities in their results, (see third graphic in the Figure 5.18). Dispersion curves for m=0 presents better results, referred to the bibliography surveys executed near the area of construction (see Paragraph 5.2.3.1).

The dispersion curve estimated on site, has been subsequently used to identify the vertical profile of the shear waves velocity propagation using a direct modeling method, which allows to obtain Vs as a function of z, such as to minimize the misfit between the theoretical dispersion curve and the observed one.

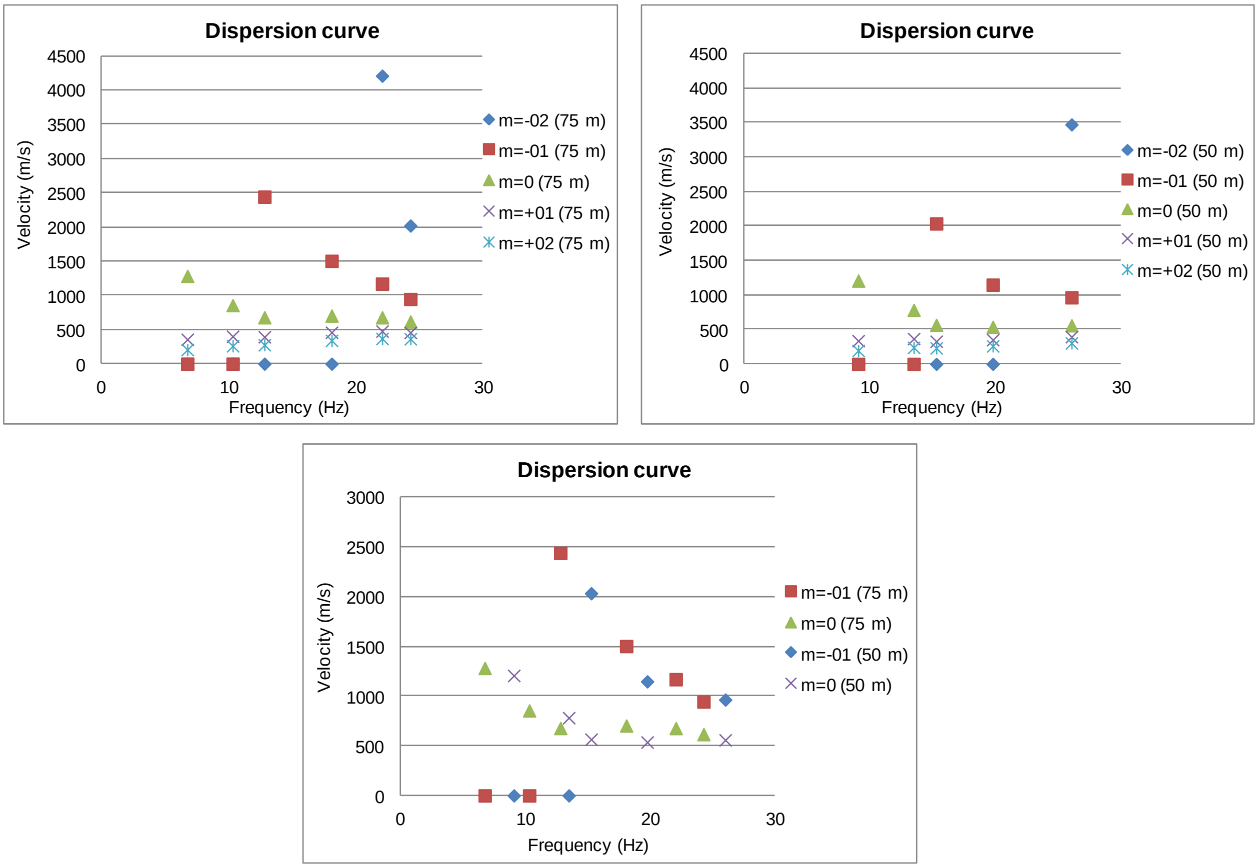

Figure 5.18 *Dispersion curves from synchronized ambient vibration measures placed at a distance of 50 m or 75 m from each other*

5.2.5 Seismic stratigraphic profile – 1D model

One-dimensional equivalent linear soil response analysis has been performed in the selected site by using STRATA software. Inversion process has been first realized by GAinvers6 code to identify seismic stratigraphic profile using as input the dispersion curve $V_R(f)$ (Figure 5.18) and HVSR curve (see Figure 5.19).

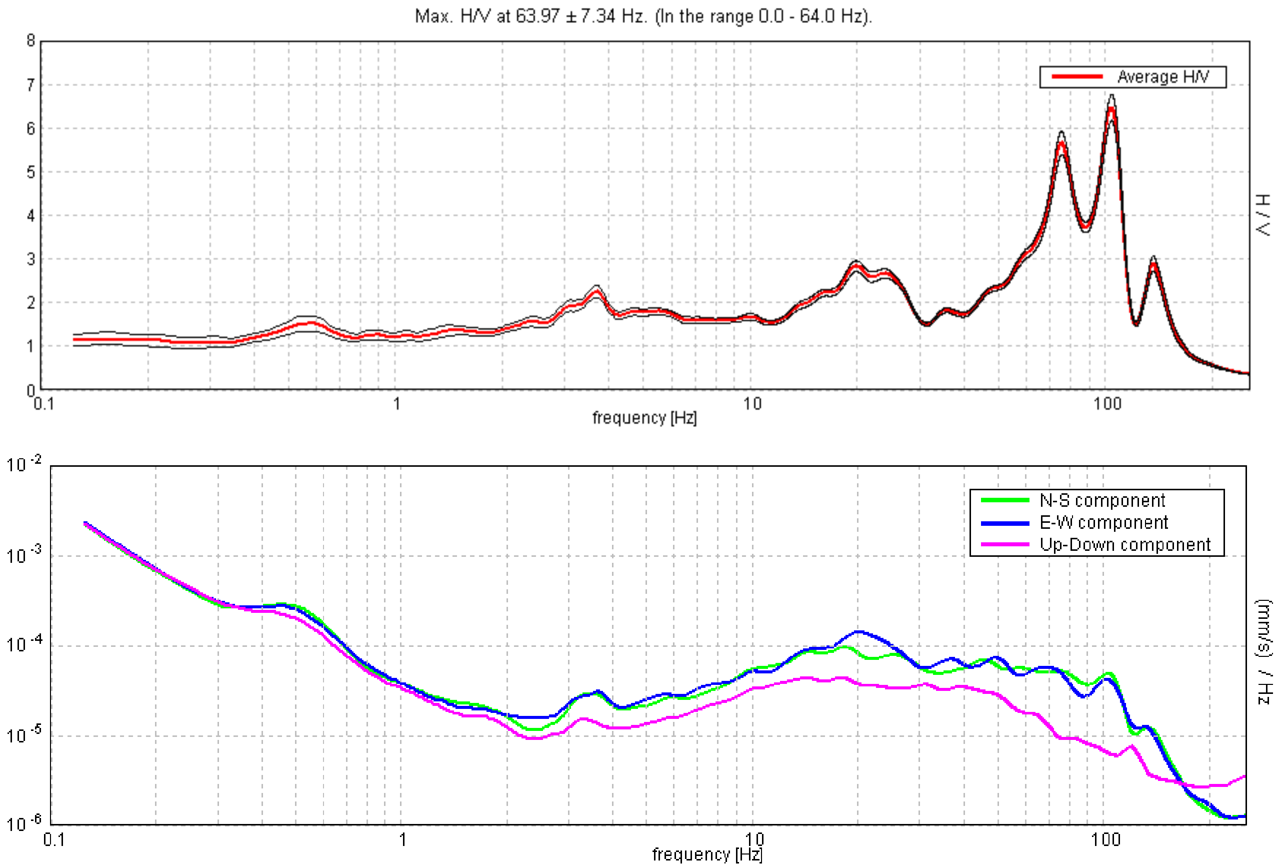

Figure 5.19 *Horizontal to vertical average spectral ratio and spectral component graphics*

The input (derived from dispersion curves) and the output seismic stratigraphic profiles are presented in the Table 5.12.

Table 5.12 *Results from the dispersion curve (left table), final seismic stratigraphic profile (right table)*

Hmin (m)	Hmax (m)	Vpmin (m/s)	Vpmax (m/s)	Vsmin (m/s)	Vsmax (m/s)
1	5	100	1500	200	600
1	5	200	1500	300	800
5	10	200	2000	400	1000
10	50	400	2000	600	1200
30	80	500	2500	700	1500
50	100	500	2500	800	1800
100	1000	1000	3000	1000	2000
0	0	1100	3000	1000	2000

h (m)	Vp (m/s)	Vs (m/s)	ro (kg/m^3)	Dp (-)	Ds (-)
1,3	1484,8	225,0	1504,4	0,005	0,006
2,3	910,9	343,5	1934,5	0,010	0,011
9,1	1911,0	632,3	1845,8	0,003	0,013
20,0	1992,5	678,0	2094,8	0,006	0,006
45,2	2397,9	1121,5	1965,8	0,023	0,050
80,6	2698,5	1298,5	2430,1	0,004	0,007
450,1	2982,4	1376,3	2087,0	0,003	0,017
0,0	3300,0	1828,2	2673,1	0,003	0,048

Seismic stratigraphic profile which has the lower misfit have been selected. In the Figure 5.20 is shown the best Vs seismic stratigraphic profile estimated by varying some parameters (limits of Vs, HVSR and V_R percentage participation on analysis, i.e. their weights) up to reach available result.

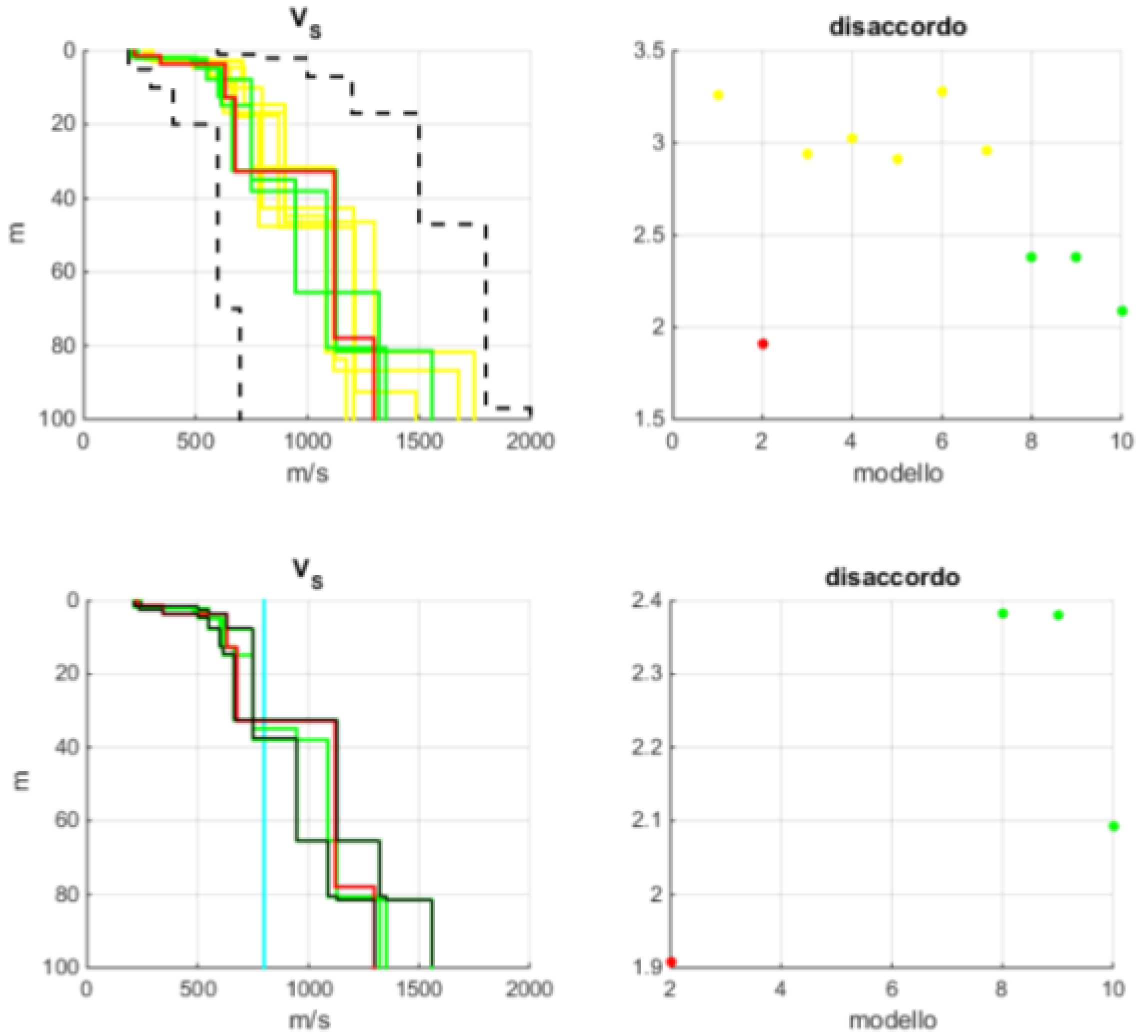

Figure 5.20 *Seismic stratigraphic profile estimated by ESAC code*

5.3 Response spectrum estimated

Soil stratigraphic profile, geotechnical layer properties and seismic inputs assumed for the equivalent linear numerical analyses, consist of:

- Input accelerograms selected from 'Rexel v3.5' database, are shown in the Figure 5.11;
- Input Seismic stratigraphic profile (Figure 5.20 estimated from the inversion of dispersion curve V_R estimated from ambient vibration measures (Figure 5.18);
- Layers properties (the depth, the unite weight and geologic description) Table 5.6;
- Decay curves of layers identify from the bibliography (see Paragraph 5.2.2);

Surface elastic response spectra numerically obtained for soils class B, compared to the corresponding spectra prescribed by NTC2008 (5% of critical damping ratio), have been estimated on Strata software by using equivalent linear analysis. Acceleration response spectra estimated are shown in the Figure 5.21 and in the Figure 5.22 respectively for SLV and SLD limit state also for different nominal life (50 years and 100 years). Variation of the nonlinear dynamic properties of layers, and also different decay curve (G/Gmax and D), have been utilized to estimate their impact in the selection of the response spectrum. Spectrum amplitude doesn't vary significantly (see blue and red line in the Figure 5.21 and in the Figure 5.22) when have been used diverse decay curves of layers selected from different bibliography as described in the Paragraph 5.2.2.

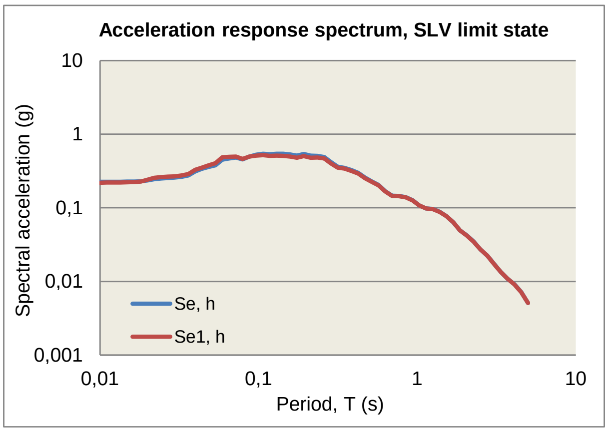

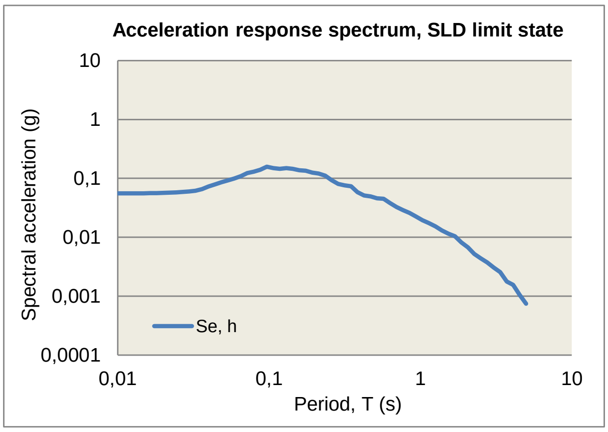

Figure 5.21 *Horizontal components of Acceleration Response Spectrum of site, for SLV and SLD limit state, 50 years nominal life*

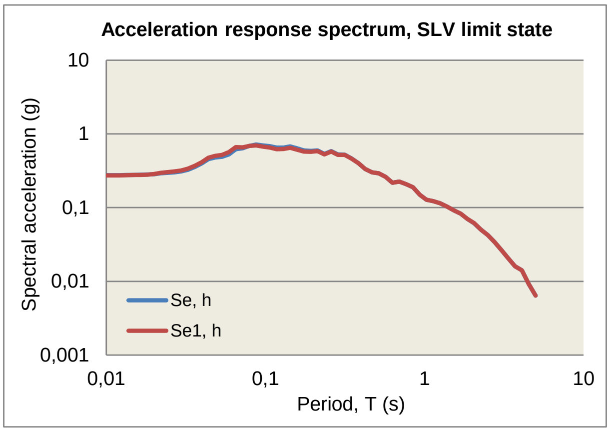

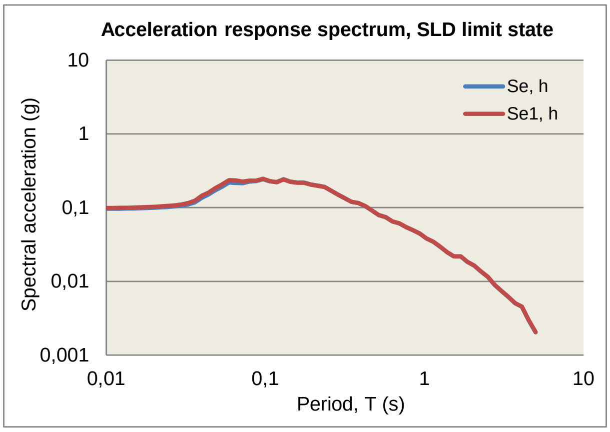

Figure 5.22 *Horizontal components of the Acceleration Response Spectrum of site, for SLV and SLD limit state, 100 years nominal life*

Horizontal spectral acceleration components generated from 7 accelerograms (selected for SLV limit state) by varying nonlinear properties of layers (shear modulus, damping ration curves, damping of the bedrock) and site profile parameters (shear wave velocity, layer thickness, depth to bedrock) are shown in the Figure 5.23. The mean values of those results (graphics with continue blue line) have been taken into consideration to realize verifications of the building.

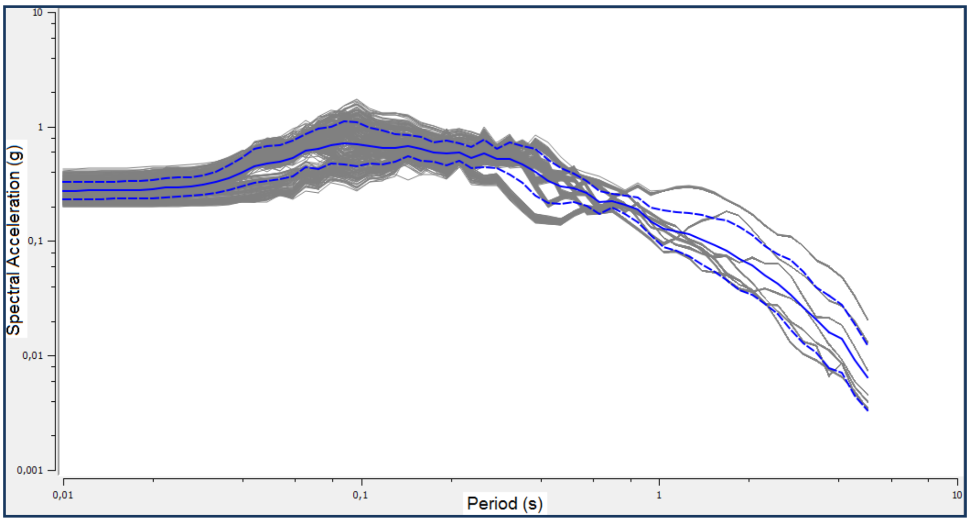

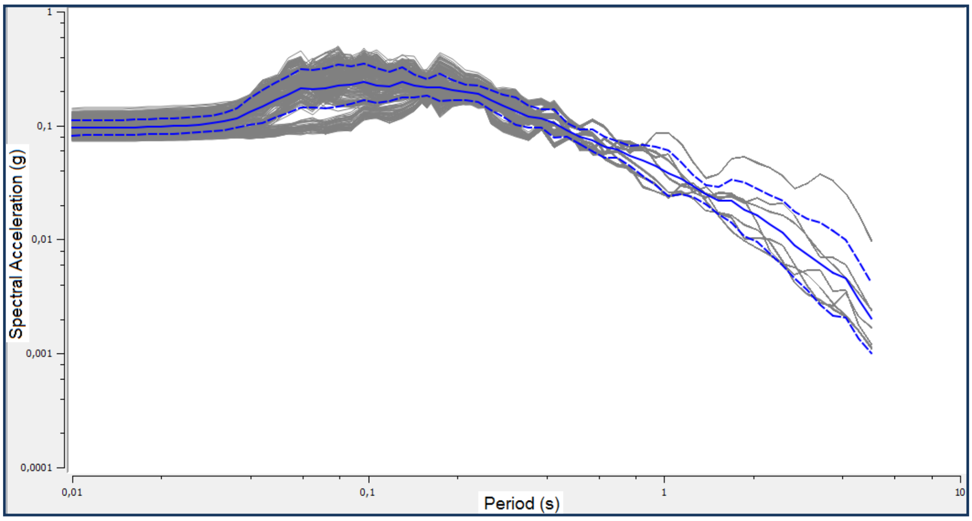

Figure 5.23 *Horizontal Spectral Accelerations generated from 7 accelerograms by varying nonlinear properties of layers and site profile, for SLV and SLD limit state*

Deformed and not deformed Vs subsoil model (final and initial seismic stratigraphic profile) are shown in the Figure 5.24.

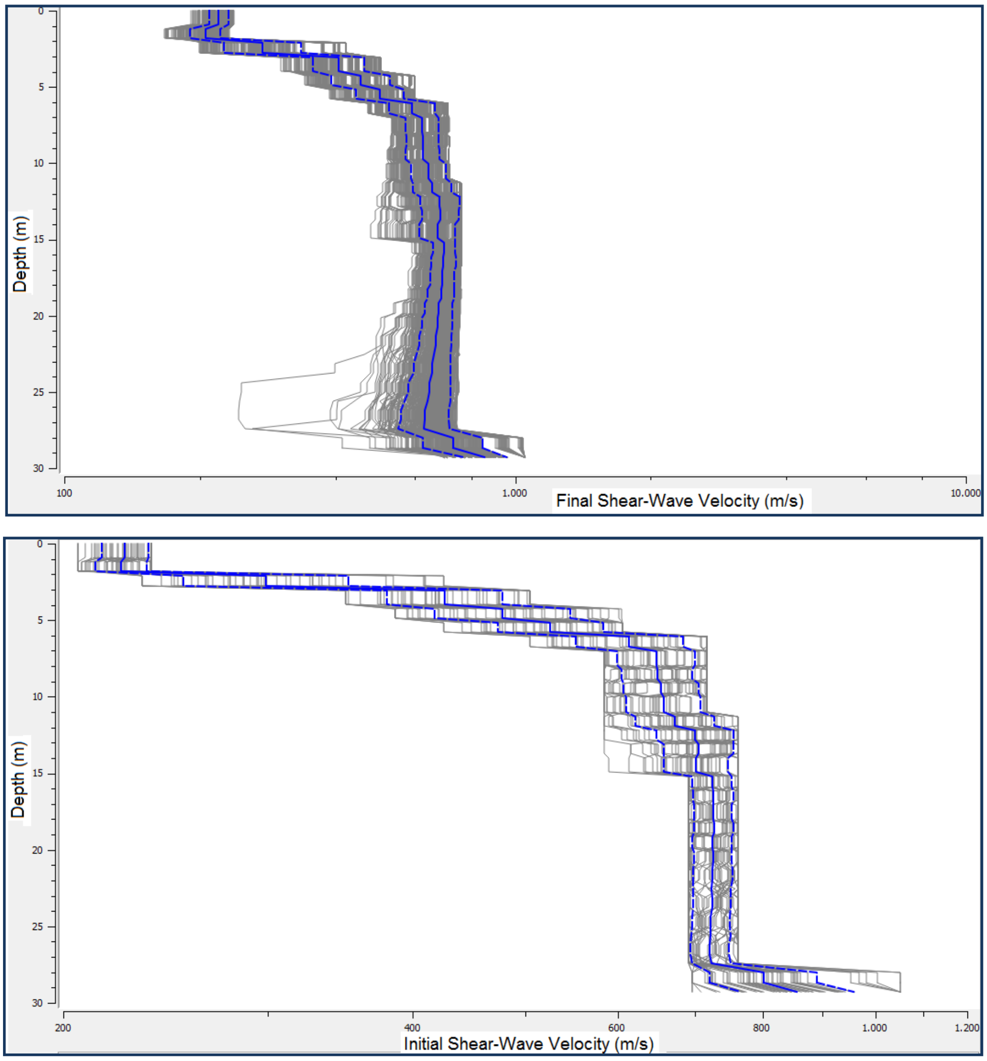

Figure 5.24 *Initial and Final Seismic stratigraphic profile, SLV limit state*

V_{s30} estimated from the seismic stratigraphic profile is about 577 m/s. Therefore, the subsoil has a class B referred to the standards (Table 5.13).

5.4 Soil classification for engineering purposes

The seismic classification of soils, referred to Italian and European standards and passive methods, are described in this chapter. The importance is underlined of the alternative geotechnical methods of investigations, which should be considered as complementary each other's.

The Italian seismic code OPCM 3274 (Ordinance of President of the Council of Ministers, 20 March 2003) "The first items regarding the general criteria for seismic classification of the national territory and technical standards for construction in seismic zone", as well as the DM 14/09/2005 (Ministerial decree) "Technical standards for construction, NTC 2008", when no other specific analyses are available, defines the seismic load for design on the basis of the seismic zone and the seismic class of the site where the structure is expected to be constructed.

Table 5.13 *Seismic classification of soil according to OPCM 3274, NTC2008 and Eurocode 8*

Category of subsoil	Description of stratigraphic profile (Eurocode 8)	Description of stratigraphic profile (NTC 2008)	Parameters		
			V_{s30} (m/s)	$N_{SPT,30}$	Cu (kPa)
A	Rock or other rock-like geological formation, including at most 5 m of weaker material at the surface.	Rock masses or very rigid soils, including at most 3 m of an alteration layer at the surface.	> 800	-	-
B	Deposits of very dense sand, gravel, or very stiff clay, at least several tens of meters in thickness, characterised by a gradual increase of mechanical properties with depth.	Soft rocks and deposits of densified coarse-grained soils or very consistent fine-grained soils with thicknesses greater than 30 m, characterized by a gradual improvement of the mechanical properties with depth ($N_{SPT,30}$> 50 in coarse-graned soils and $c_{u,30}$> 250 kPa in fine-grained soils).	360 - 800	> 50	> 250
C	Deep deposits of dense or medium dense sand, gravel or stiff clay with thickness from several tens to many hundreds of meters.	Deposits of coarse-grained soils averagely densified or averagely consistent fine-grained soils with thicknesses greater than 30 m, characterized by a gradual improvement of the mechanical properties with depth (15 < $N_{SPT,30}$ < 50 in coarse-graned soils and 70 < $c_{u,30}$ < 250 kPa in fine-grained soils).	180 - 360	15 - 50	70 - 250
D	Deposits of loose to medium cohesionless soil (with or without some soft cohesive layers), or of predominantly soft to firm cohesive soil.	Deposits of coarse-grained soils sparsely densified or sparsely consistent fine-grained soils with thicknesses greater than 30 m, characterized by a gradual improvement of the mechanical properties with depth ($N_{SPT,30}$ < 15 in coarse-graned soils and $c_{u,30}$ < 70 kPa in fine-grained soils).	< 180	< 15	< 70
E	A soil profil consisting of a surface alluvium layer with Vs values of type C or D and thickness varying between about 5 m and 20 m, underlain by stiffer material with Vs > 800 m/s.	Lands of subsoils of type C or D to a thickness not exceeding 20 m, places on the reference substrate (with Vs > 800 m/s).			
S1	Deposits consisting, or containing a layer at least 10 m thick, of soft clays/silts with a high platicity index (PI > 40) and high water content.	Deposits of soils characterized by values of $V_{s,30}$ of less than 100 m/s (or 10 <$c_{u,30}$ <20 kPa), which include a layer of at least 8 m in fine-grained soils of low consistency, or that include at least 3 m of peat or highly organic clays.	< 100	-	10 - 20
S2	Deposits of liquefiable soils, of sensitive clays, or any other soil profile not included in types from A to E or S1.	Deposits of soils susceptible to liquefaction, of sensitive clays or any other category of subsoil not classified in the previous types.			

In the Table 5.13 are shown the soil categories according to NTC and OPCM seismic Italian and Eurocode 8 codes. As can be seen the soil classification according to Italy and European standards differ between them essentially by the description of stratigraphic profile.

Four seismic zones have been identified until now, in Italy. To each zone a value a_g of the peak ground acceleration normalized to the gravity has been assigned. The conventional values a_g of the 4 different seismic zones refer to the peak acceleration on the free surface of site of type A, that is rock or very stiff soil (see Table 5.14), where seismic motion does not vary significantly propagating from the bedrock to the free surface. When dealing with sites of type B, C, D, E, S1, S2 the seismic motion varies passing from the bedrock to the free surface, depending on the amplitude and the frequency content of the motion and the seismic and geotechnical and geometrical characteristics of the soils above the bedrock.

Table 5.14 *Seismic zones in Italy*

Seismic zone	**Description**	**Acceleration with probability of exceeding equal to 10% in 50 years (a_g)**
1	Is the most dangerous area, where major earthquakes may occur.	$a_g > 0,25$
2	Municipalities in this area may be affected by quite strong earthquakes.	$0,15 < a_g < 0,25$
3	Municipalities in this area may be subject to modest shocks.	$0,05 < a_g < 0,15$
4	It is the least dangerous. Municipalities of this area have a low probability of seismic damages.	$a_g \leq 0,05$

When a specific analysis of the local seismic effects at the site is not available, for sites B, C, D, E the code recommends the amplification factor S, to evaluate the seismic spectral acceleration, as well as the characteristic periods that define the spectral response of a simple oscillator with 5% damping. When dealing with sites of type S1 or S2 the code recommends a specific analysis of the local seismic effects at the site, particularly in cases where the presence of soils susceptible to liquefaction and/or clays with high sensitivity which can lead to collapse of the soil.

The seismic classification of the site is conventionally performed on the basis of the averaged equivalent propagation velocity of the shear waves within the first 30 m of the site:

$$V_{s30} = \frac{30}{\sum_{i=1}^{n}(\frac{h_i}{V_{si}})} \qquad \text{(Eq. 5.2)}$$

The equivalent dynamic penetrometer resistance is defined by the expression:

$$N_{SPT,30} = \frac{\sum_{i=1}^{m} h_i}{\sum_{i=1}^{m}(\frac{h_i}{N_{SPT,i}})} \qquad \text{(Eq. 5.3)}$$

The equivalent undrained shear resistance is defined by the expression:

$$c_{u,30} = \frac{\sum_{i=1}^{k} h_i}{\sum_{i=1}^{k}(\frac{h_i}{c_{u,i}})} \qquad \text{(Eq. 5.4)}$$

where V_{si} is the shear wave velocity in the i-th layer, h_i is the thickness of the i-th layer within the first 30 m, $N_{SPT,i}$ is the number of strokes in the i-th layer, $c_{u,i}$ is undrained shear resistance in the i-th layer, n is the number of layers within the first 30 m of depth, m is the number of coarse-grained layers within the first 30m deep, k is the number of fine-grained layers within the first 30 m deep.

When the subsoil consist of coarse-grained or fine-grained soils distributed with thicknesses within first 30 m of depth (falling under categories A to E) we can proceed as follows, in luck of direct measurements of shear waves velocity:
- Determine $N_{SPT,30}$ only at coarse-grained soils coarse included within the first 30 m deep;
- Determine $c_{u,30}$ only at fine-grained soils comprised within the first 30 m deep;
- Identify the categories corresponding individually to N_{SPT} and c_u parameters;
- Refer to the subsoil of the worst category identified above.

It should be observed that:
- Even if it is not explicitly said, the vertically propagating shear waves must be considered;
- The velocity V_{s30} is not a simple arithmetic average of the shear wave velocities V_{si} of the different layers, but it is the "equivalent" velocity in terms of time within the first 30 m of site;
- When the velocity V_{s30} is not available, the code allows the use of the N_{SPT} (for granular soils) or the use of the undrained shear resistance c_u (for cohesive soils). This option is discouraging since it is not appropriate. In fact the SPT (Standard Penetration Test) and the c_u are only indirectly linked to the wave propagation characteristics of the ground; also the use of N_{SPT} or c_u may be difficult in several situations: when both granular and cohesive layers exist; failure of the SPT test due to the presence of blocks; value of c_u depending on deformation level and on the method of investigation;
- The seismic classification of the site cannot be performed by knowledge of only the velocity V_{s30}, in fact additional information are required for sites of type S1 and S2. The geotechnical classification of a site can be done by means of different types of geotechnical investigations, which should be considered complementary each other's.

In the Table 5.15 are shown the topographic category that must be used for simple surface configurations. For complex topography shall be necessary to provide specific analysis of local seismic response.

Table 5.15 *Topographic category*

Category	**Characteristics of topographic surface**
T1	Level surface, slopes and isolated reliefs with an average inclination i ≤ 15°
T2	Slopes with an average inclination i > 15°
T3	Reliefs with a much smaller crest width that the base and with an average inclination 15°≤ i ≤ 30°
T4	Reliefs with a much smaller crest width that the base and with an average inclination i > 30°

The above topographic categories refer predominantly to the two-dimensional geometric configurations, elongated ridges or crests, and must be considered in the seismic action if have a height greater than 30 m.

The classification of soils according to European standards (Eurocode 8) is presented in the Table 5.13 and differ from Italian standards essentially by the description of stratigraphic profile.

VI. Case study 1 – REINFORCED CONCRETE BUILDING

6.1 Building description

The building under consideration is a prefabricated reinforced concrete construction consisting of five floors above ground and one underground (Figure 6.1), with a total height of about 18.5 m in view, and about 23 m in elevation considering the basement. Given its considerable dimensions in plan of about 60 m and 23 m, the mobility inside building is guaranteed by two different vertical blocks which consist of traditional stairs with two flights, lifts and service elevator. This building is located in the municipality of Sanremo, province of Imperia in Italy, and has a sanitary use. The hospital extends horizontally in a single flat roof block, oriented in the direction northwest-southeast that prospect to Street San Francesco.

Figure 6.1 *Photo of building*

In order to reduce the period of the construction and at the same time to realize a more resistance structure from the point of view of the durability and the seismic response, the reinforced concrete structure cast in situ was substituted with a prefabricated skeleton. Therefore, the prefabrication technology substitute the traditional one provided first by the tender. Structural elements of the building consists of:

- *prefabricated pillars* in reinforced concrete (vibrated reinforced concrete prefabricated pillar), with rectangular section, C45/55 concrete class and mild steel reinforcement of class B450C anchored to the foundation (cast in situ) by HSCF3 connections which are realized by a mixed system composed of Peikko anchor bolts and corrugated pipes. The Peikko connection is useful for the positioning of elements before the final grouting of the resistant rebar. The pillars are equipped with shelves and holes which are useful respectively for the support or anchoring of the beams and for efficient connection with the slab;
- *rectilinear beams* in pre-stressed reinforced concrete, with L or T section for the support of slabs, C45/55 concrete class, harmonic steel (f_{ptk}=18600 daN/cm^2) and mild steel reinforcement of class B450C, and are equipped with a special HYBRID beams for the support of slabs and cantilever cast on site;
- *slabs* realized by the self-supporting twin-wall sheets in pre-stressed reinforced concrete with a total thickness of 16 cm or 20 cm and a reinforced slab thickness of 4 cm or 5 cm which justify the consideration of the slab as a rigid diaphragm at various levels. Concrete class C45/55 and C28/35, respectively for plates and for completion jets, and B450C class for mild steel reinforcement, were used;

- *stairwells and lift shaft* realized by semi-prefabricated technology through double plate elements by lattice connection (5cm+15cm+5cm) with a total thickness of 25 cm. The concrete class C28/35 and mild steel reinforcement of class B450C, were used. The anchoring technology of foundations was similar to that for the pillars;
- *stairs and rampant slabs* built with prefabricated elements supported and/or anchored to walls and other elements cast on site;
- *external walls* realized by wall panels in vibrated reinforced concrete with a total thickness equal to 16 cm, with a double layer of reinforced concrete and interposed elements of polystyrene. Those are anchored in correspondence of the pillars and at the ends of the protruding elements allocated at the external facade;
- overhangs in correspondence of the main facade are realized with metal shelves coated of concrete on which are supported the slabs to create the perimeter areas of the floor.

The prefabricated structure are anchored to a ribbed slab of foundation, inserted and contained in the excavated basin which was first confined by micropiles tie rods and by supporting reinforced concrete walls.

The building consists of the ground floor, four floors above ground and one completely underground. The mainly destination of use of these floors are described below:

- underground floor: changing rooms and toilets for doctors, nurses, maintenance staff, housekeeping and other staff; archive; inventory deposits; cleaning deposit; depot of maintenance etc.;
- ground floor: first aid station; methadone distribution and preservation place; conventional radiology block, mammography, ultrasonography, magnetic resonance; atrium and porch etc.;
- first floor: surgical operations rooms on an outpatient basis with local technical annexes (rooms for patients preparation and for physical recovery after surgery, storage for surgical instruments, washing and sterilization chamber, deposits of clean and dirty material); pharmacy etc.;
- second floor: rehabilitation wards; echography wards; ambulatory etc.;
- third floor: mental health center (secretary, rooms for single and group therapy, offices of social workers and doctors); SERT services (reception, back office, operative and meeting rooms, social worker, doctors and psychologists offices etc.);
- fourth floor: department prevention area-veterinary (offices, deposits/warehouses with refrigerators); counseling (reception, back office, ambulatory, different offices of the staff, gyms for physical exercises for pregnant women and children);
- terrace: garden, mechanical ventilation system with relevant machinery, photovoltaic and solar plants with attached panels for production of electricity and hot water.

The building was under construction during the passive seismic measurements. At this aim, the ambient noise measurements have been carried out in two different periods with a distance between them of about eight months. The internal walls in all floors, the pavement layers, the external wall panels, the mechanical ventilation system with relevant machinery, were finished during the second measurements. Therefore, mass and stiffness was added to the structure. The equipment, plants, elevators and loading capacity etc. weren't installed during ambient vibration measurements that helps in the reduction of the noise level.

The influence of external walls rigidity in the dynamic structure response has been studied by modeling those as frame element. Therefore, two FE models have been created, with and without wall panels, which have been calibrated by using ambient noise measurements acquired in two different periods during the construction of the building.

6.1.1 Material characteristics

Different classes of concrete were used for the construction of the building. Pillars, beams and twin-wall sheets slabs were realized with concrete C45/55 that has an exposure class XC3 referred to UNI 11104, a consistency class S4, the maximum aggregate size 20 mm and a chloride content class of about 0,40 (EN 206-1, 2006). The stairwells and lift shaft were constructed with concrete C28/35 while the external infill panels with concrete C32/40. All prefabricated or semi-prefabricated elements guarantee a fire resistance REI 120'.

The general characteristics of concretes utilized for the construction of the hospital are shown in the Table 6.1.

Table 6.1 *General characteristics of concrete*

Concrete Class	f_{ck} (N/mm^2)	R_{ck} (N/mm^2)	f_{cm} (N/mm^2)	f_{ctm} (N/mm^2)	f_{ctk} (N/mm^2)	f_{ctd} (N/mm^2)	f_{cd} (N/mm^2)	E_{cm} (N/mm^2)	Coefficient of Poisson
C25/30	25	30	33	2,6	1,8	1,2	14,2	31475,81	0,2
C28/35	28	35	36	2,8	1,9	1,3	15,9	32308,25	0,2
C32/40	32	40	40	3,0	2,1	1,4	18,1	33345,76	0,2
C45/55	45	55	53	3,8	2,7	1,8	25,5	36283,19	0,2

The design compressive strength of concrete, f_{cd}, is estimate by the equation:

$$f_{cd} = \frac{\alpha_{cc}}{f_{ck} \cdot \gamma_c}$$

where f_{ck} is the characteristic cylinder compressive strength of concrete at 28 days, γ_c is the safety partial factor of concrete while α_{cc} is a coefficient taking account of the long-term effects on the compressive strength (which is reduced under sustained load) and the unfavorable effects resulting from the way in which the load is applied.

The design tensile strength of concrete, f_{ctd}, is estimated by the equation:

$$f_{ctd} = \frac{f_{ctk}}{\gamma_c}$$

where $f_{ctk} = 0.70 \cdot f_{ctm}$ is the characteristic tensile strength of concrete while $f_{ctm} = 0.3 \cdot f_{ck}^{2/3}$ is the average tensile strength calculated as a function of the characteristic cylindrical compression strength of concrete f_{ck}.

The average cylindrical strength, f_{cm}, is calculate by the expression:

$$f_{cm} = f_{ck} + 8$$

The modulus of elasticity, E_{cm}, is calculated by the above equation:

$$E_{cm} = 22000(\frac{f_{cm}}{10})^{0.3}$$

The loose and pre-stressing reinforcement was used. The loose reinforcement of B450C steel class has the following properties:

- Characteristic yield strength $f_{yk} = 450.0$ N/mm^2
- Characteristic rupture strength $f_{tk} = 540.0$ N/mm^2
- Design yield strength $f_{yd} = f_{yd} / \gamma_s = 391.3$ N/mm^2
- Characteristic ultimate deformation $\varepsilon_{uk} = (A_{gt})_k = 0.075$
- Characteristic ultimate deformation $\varepsilon_{ud} = 0.9\ \varepsilon_{uk} = 0.068$
- Modulus of elasticity $E_f = 200000$ N/mm^2
- Partial safety coefficient $\gamma_s = 1.15$

while the pre-stressing reinforcement has the following properties:

- Characteristic tensile strength at1% of total deformation $f_{pk} \geq 1670$ N/mm^2
- Characteristic tensile strength of rupture $f_{ptk} \geq 1860$ N/mm^2
- Design yield strength $f_{yd} \geq 1409$ N/mm^2
- Elongation $A_{gt} \geq 3.5$ %
- Partial safety coefficient $\gamma_s = 1.15$

6.1.2 Typical floor plan

The hospital has five floors above ground and one completely underground. The building extends horizontally in a single flat roof block and has two scale and lift cores. The pillars has rectangular section with dimensions of the cross section 50x40cm, 50x50cm and 50x60cm while the beams has rectangular, L or T sections (see Figure 6.5, Figure 6.2, Figure 6.6 and Figure 6.7).

Referred to the set-backs in plan and dimension of structural elements, fourth different plan of structural elements are presented: the ground floor, the first floor, the terrace and the 'typical floor' of the other levels which have more similarities among them. The distribution in plan of structural elements on the typical floor and on the first floor is show in the Figure 6.2 and in the Figure 6.3. In the Figure 6.4 is shown the vertical section of a pillar with dimension 50x40cm. The dimension of structural elements are shown in the Figure 6.5, Figure 6.2, in the Figure 6.6 and in the Figure 6.7 respectively for the first floor, the ground floor and the typical floor.

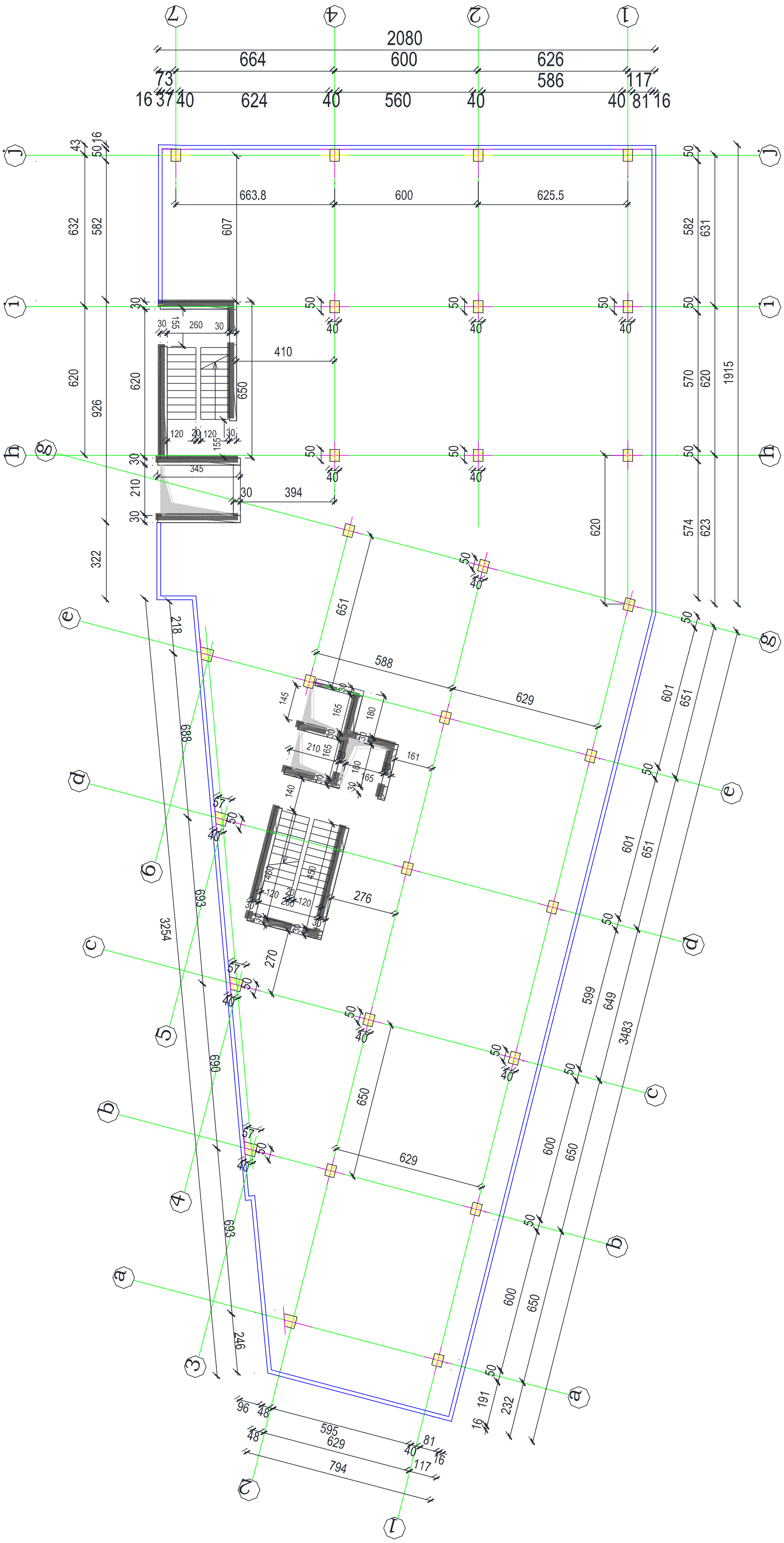

Figure 6.2 *Plan of the typical floor*

The plan of the first floor has a set-back which start from the J axis.

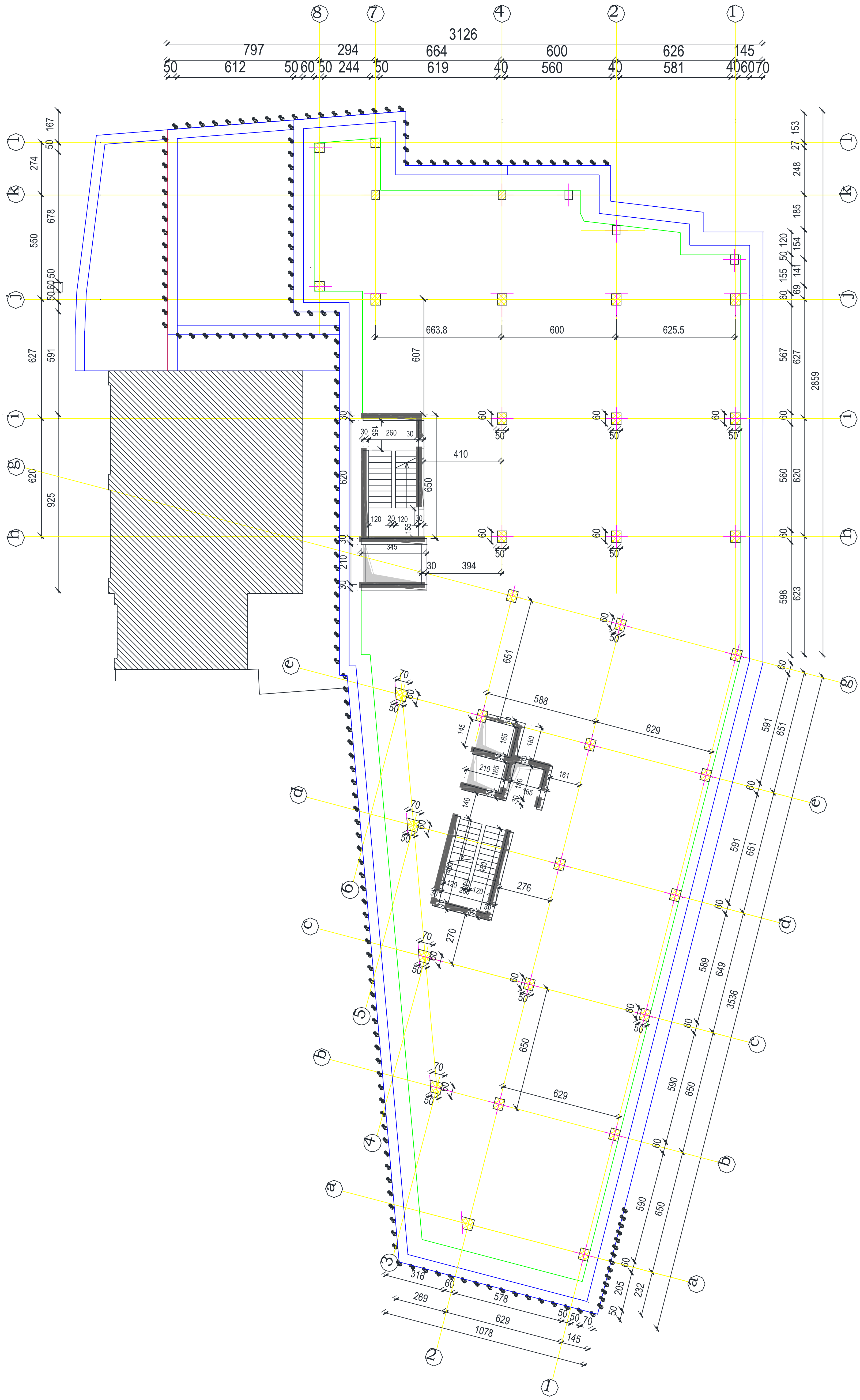

Figure 6.3 *Plan of the first floor*

The vertical section of a typical pillar is shown in the Figure 6.4 below.

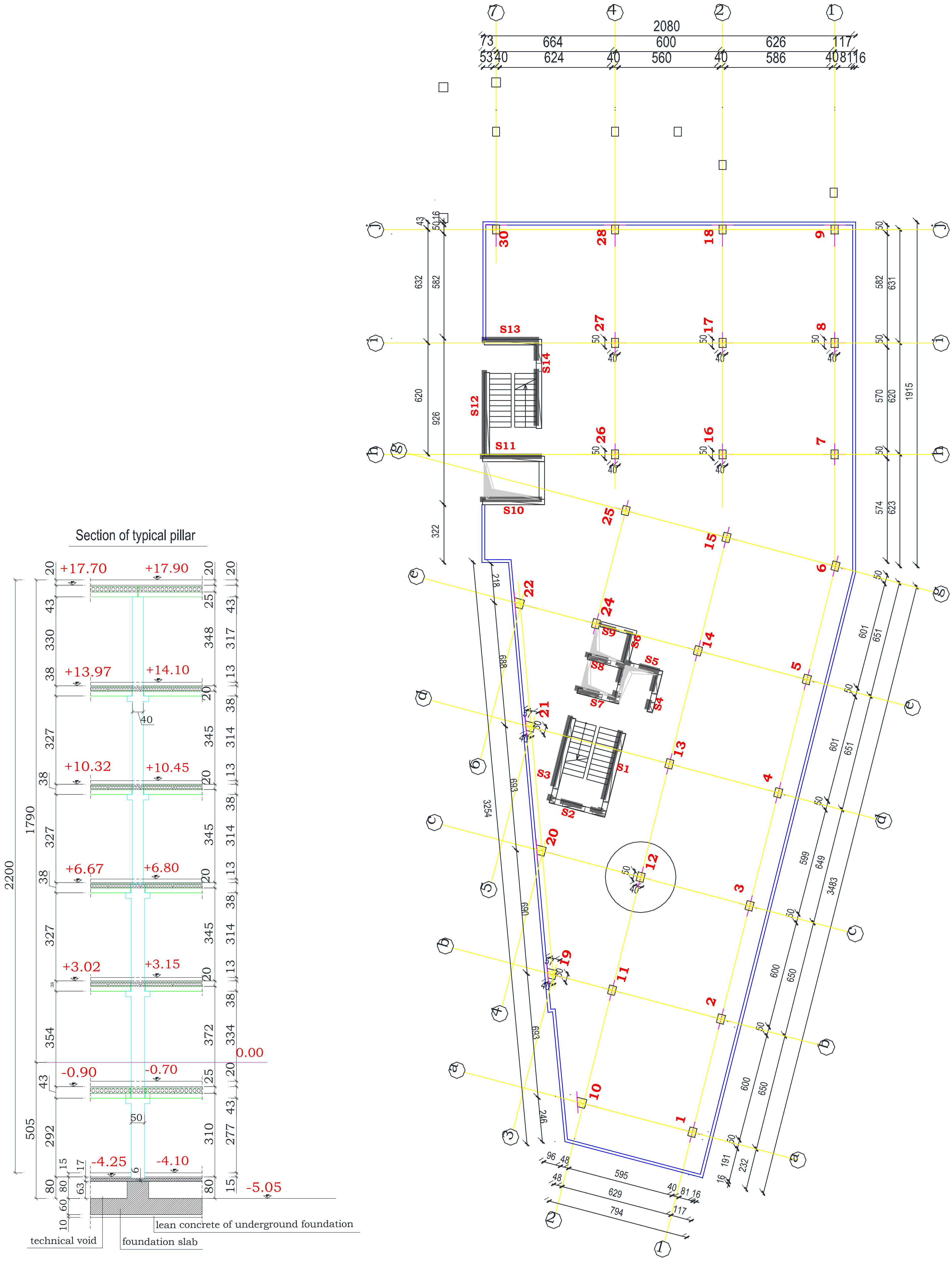

Figure 6.4 *The vertical section of a pillar 50x40cm and its position in plan*

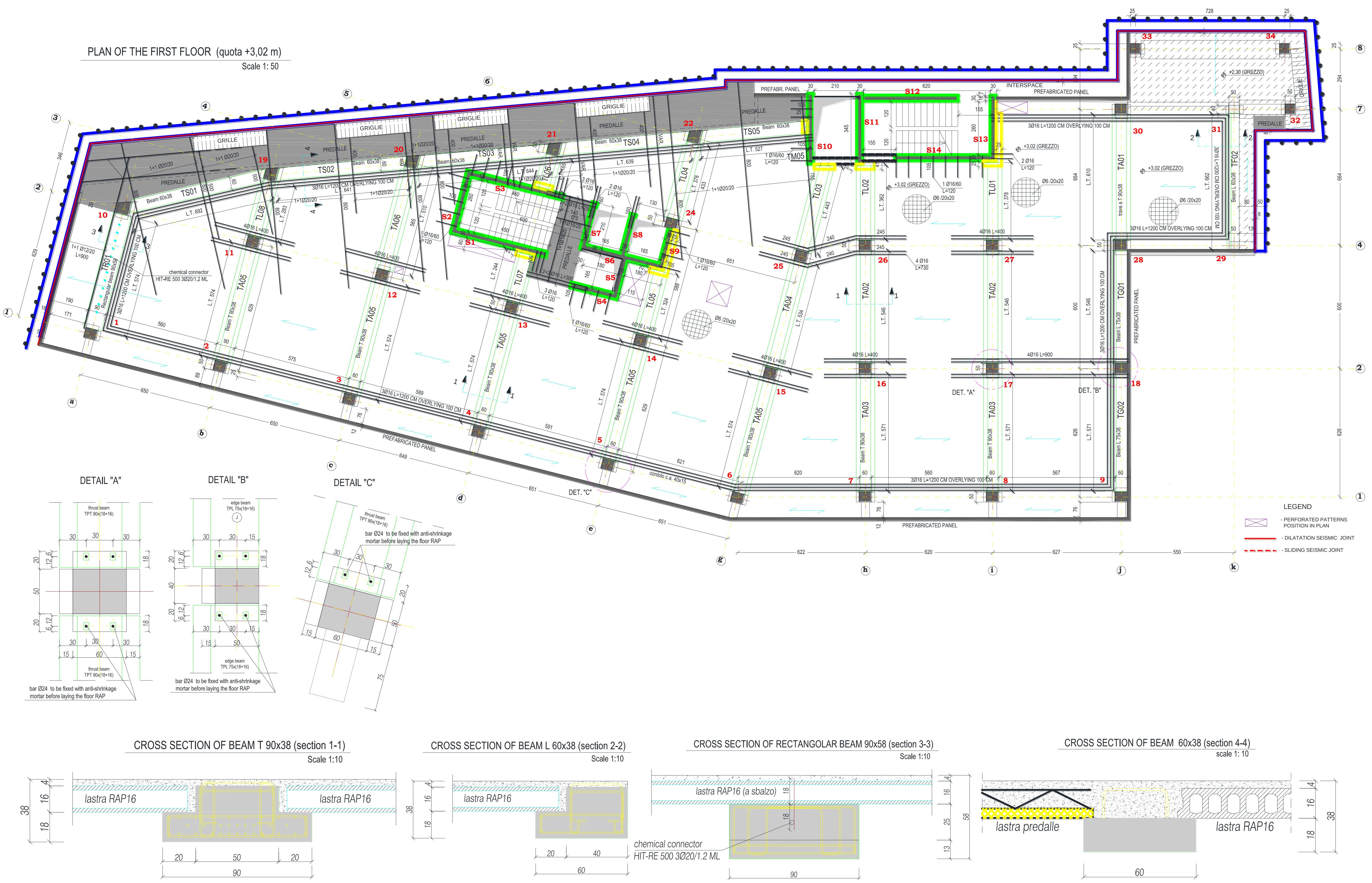

Figure 6.5 *Structural plan of the first floor and relative details*

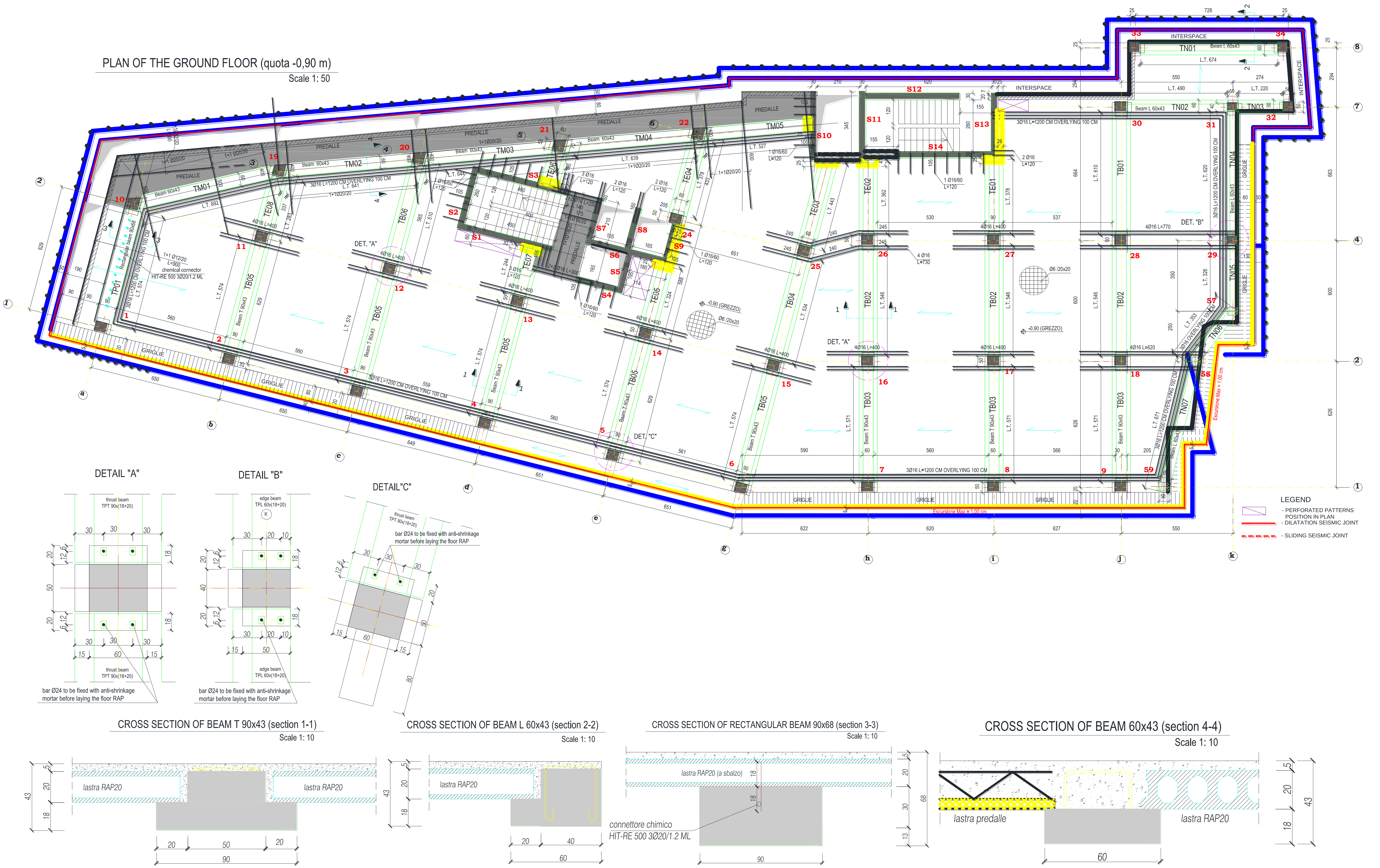

Figure 6.6 *The ground floor of structural elements and relative details*

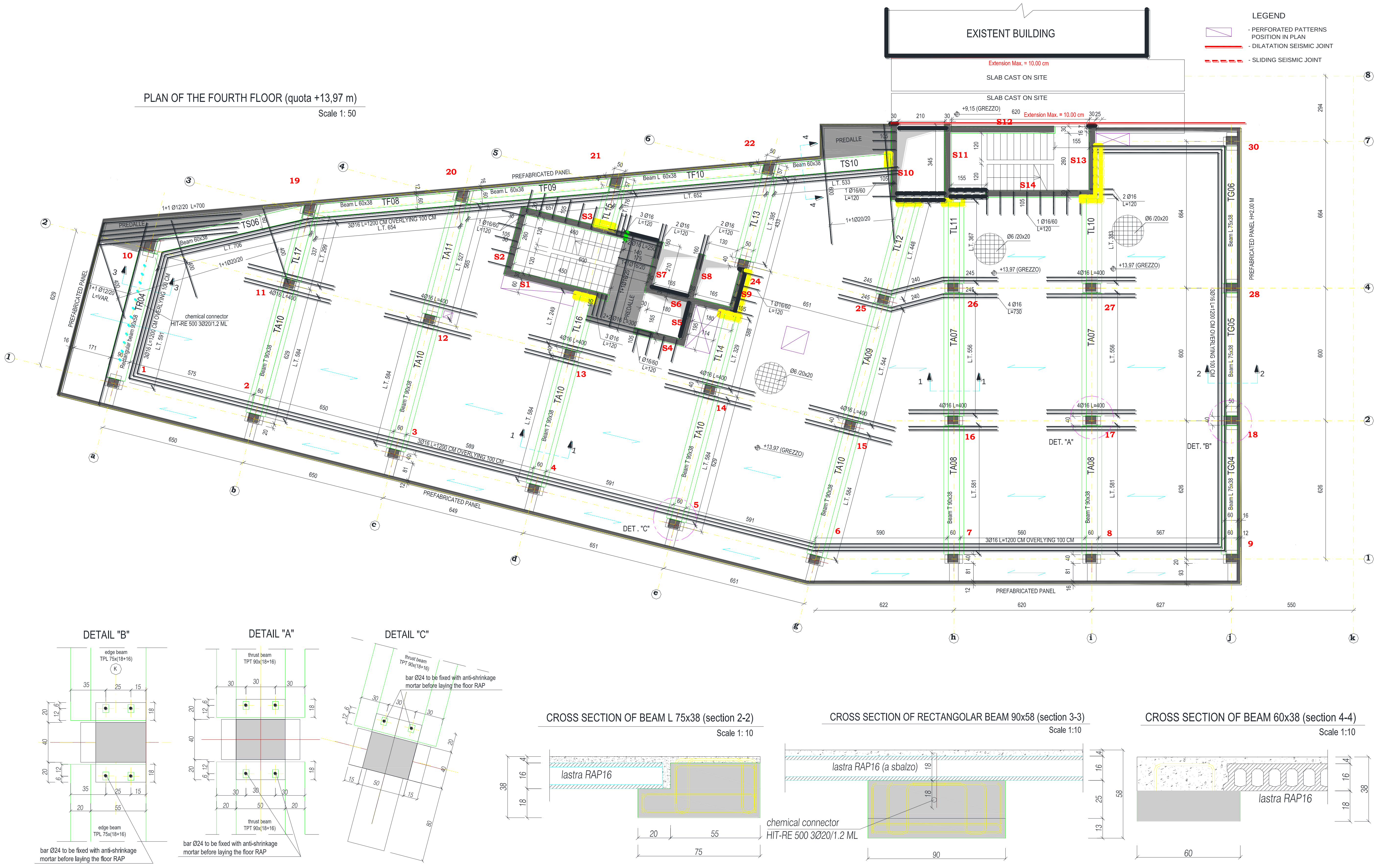

***Figure 6.7** The typical floor of structural elements and relative details*

6.1.3 Regularity in plan and in elevation

The building is considered regular in plan as the following conditions are fulfilled:

- The building is approximately symmetrical in plan with respect to the stiffness and mass distribution, referred to the orthogonal directions;
- The plan configuration is compact, therefore each floor is delimited by a polygonal convex line. The set-backs present in plan do not affect significantly the floor in-plan stiffness as for the set-back, the area between the outline of the floor and a convex polygonal line enveloping the floor does not exceed 5% of the floor area;
- The 'in-plane stiffness' of the floors is sufficiently large in comparison with the lateral stiffness of the vertical structural elements, so that the deformation of the floor has a small effect on the distribution of the forces among the vertical structural elements. In this respect, the horizontal elements can be considered infinitely rigid in their plane with respect to vertical and sufficiently resistant elements. The plan shapes satisfy the rigid diaphragm condition;
- The ratio between two sides of the rectangle in which the construction is inscribed is less than 4;
- At each level and for each direction of analysis x or y, the structural eccentricity e_o and the torsional radius r verify the two conditions below, which are expressed for the direction of analysis y:

$e_o \leq 0.30\, r_x$; $r_x \geq l_s$

where e_{ox} is the distance between the center of stiffness and the center of mass, measured along the x direction, which is normal to the direction of analysis considered; r_x square root of the ratio between torsional stiffness and lateral stiffness in the y direction; l_s radius of rotation of the floor in plan (square root of the ratio between the polar moment of inertia of the floor in plan with respect to the center of mass of the floor and the floor plan area).

The building is regular in elevation as:

- The lateral load resisting systems, like cores, structural walls or frames, are extended without interruption from their foundations to the top of the building. The setbacks present at the first floor respect the second condition (b) of the general ones, that should be satisfy in the presence of the different setbacks types (see Figure 6.8):
    a) for gradual setbacks preserving axial symmetry, the setback at any floor is not greater than 20% of the previous plan dimension in the direction of the setback;
    b) for a single setback within the lower 15% of the total height of the main structural system, the setback is not greater than 20% of the previous plan dimension;
    c) for a single setback within the lower 15% of the total height of the main structural system, the setback is not greater than 50% of the previous plan dimension;
    d) if the setbacks do not preserve symmetry, in each face the sum of the setbacks at all floors is not greater than 30% of the plan dimension at the first storey, and the individual setbacks are not greater than 10% of the previous plan dimension;
- both lateral stiffness and mass of individual levels reduce gradually, without abrupt changes, from the base to the top.

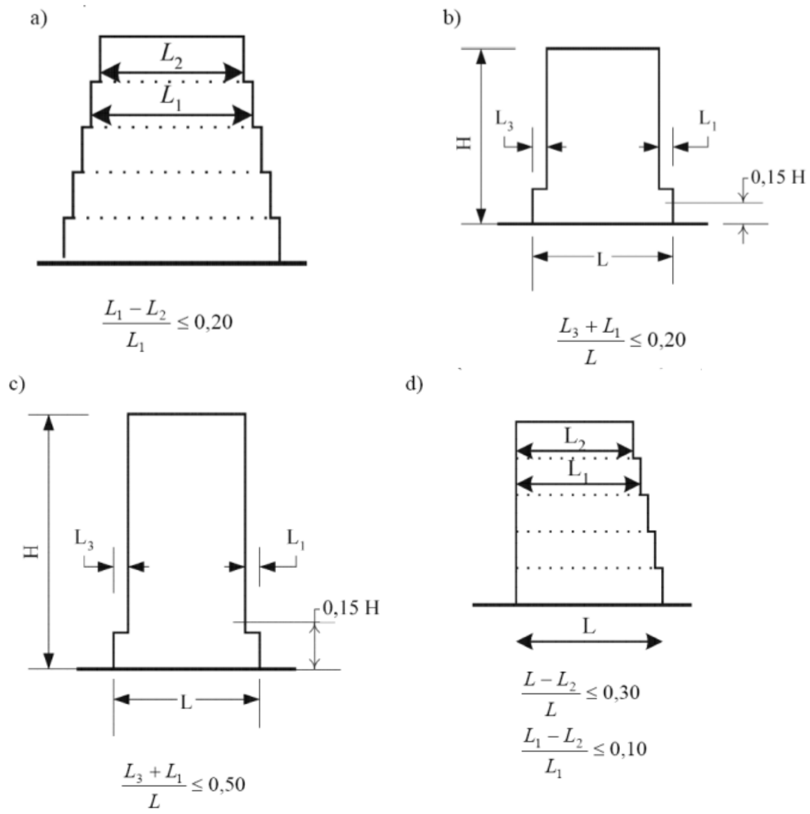

Figure 6.8 *Criteria for regularity of buildings with setbacks*

6.1.4 Load analysis

Referred to the original project design the loads for different levels consist of:

- for the slab at the level from +3.15 m up to13.97 m: dead load of 385 daN/m^2; permanent load of 200 daN/m^2; accidental load of 300 daN/m^2;
- for the slab at the -0.90 m level: dead load of 410 daN/m^2; permanent load of 250 daN/m^2; accidental load of 800 daN/m^2;
- for the slab at the -4.25 m level: dead load of 325 daN/m^2; permanent load of 200 daN/m^2; accidental load of 600 daN/m^2;
- for the slab at the +17.70 m level: dead load of 410 daN/m^2; permanent load of 500 daN/m^2; accidental load of 200 daN/m^2;
- the load of external walls, 860 daN/m.

In the Table 6.2 is presented load analysis for the typical floor of the structure.

Table 6.2 *Load analysis at the typical floor*

Beam between Pillar 1 and 10	**L (m)**		**Load (kN/m2)**	**Load (kN/m)**
Structural dead load	6,25	2,16	3,9	**20,35**
Non structural dead load	6,25	2,16	2,0	**10,57**
Accidental load	6,25	2,16	3,0	**15,86**
External wall panel				**8,58**

Beam near Pillar 1	**L (m)**		**Load (kN/m2)**	**Load (kN/m)**	**Concentraded load (kN)**
Structural dead load	6,25	2,16	3,9	**20,35**	
Non structural dead load	6,25	2,16	2,0	**10,57**	
Accidental load	6,25	2,16	3,0	**15,86**	
External wall panel	6,5	2,16		**8,58**	**46,4178**

Beam between Pillar 2 and 11	**L (m)**		**Load (kN/m2)**	**Load (kN/m)**
Structural dead load	6,25	6,00	3,9	**23,58**
Non structural dead load	6,25	6,00	2,0	**12,25**
Accidental load	6,25	6,00	3,0	**18,38**
External wall panel				**8,58**

Beam near Pillar 2	**L (m)**		**Load (kN/m2)**	**Load (kN/m)**	**Concentraded load (kN)**
Structural dead load	6,25	6,00	3,9	**23,58**	
Non structural dead load	6,25	6,00	2,0	**12,25**	
Accidental load	6,25	6,00	3,0	**18,38**	
External wall panel	6,50	6,50			**55,77**

Beam between Pillar 3 and 12	**L (m)**		**Load (kN/m2)**	**Load (kN/m)**
Structural dead load	6,00	5,99	3,9	**23,08**
Non structural dead load	6,00	5,99	2,0	**11,99**
Accidental load	6,00	5,99	3,0	**17,99**
External wall panel				

Beam near Pillar 3	**L (m)**		**Load (kN/m2)**	**Load (kN/m)**	**Concentraded load (kN)**
Structural dead load	6,00	5,99	3,9	**23,08**	
Non structural dead load	6,00	5,99	2,0	**11,99**	
Accidental load	6,00	5,99	3,0	**17,99**	
External wall panel	6,5	6,49			**55,7271**

Beam between Pillar 4 and 13	**L (m)**		**Load (kN/m2)**	**Load (kN/m)**
Structural dead load	5,99	6,01	3,9	**23,10**
Non structural dead load	5,99	6,01	2,0	**12,00**
Accidental load	5,99	6,01	3,0	**18,00**
External wall panel				

Beam near Pillar 4	**L (m)**		**Load (kN/m2)**	**Load (kN/m)**	**Concentraded load (kN)**
Structural dead load	5,99	6,01	3,9	**23,10**	
Non structural dead load	5,99	6,01	2,0	**12,00**	
Accidental load	5,99	6,01	3,0	**18,00**	
External wall panel	6,51	6,49			**55,77**

Beam between Pillar 5 and 14	**L (m)**		**Load (kN/m2)**	**Load (kN/m)**
Structural dead load	6,01	6,01	3,9	**23,14**
Non structural dead load	6,01	6,01	2,0	**12,02**
Accidental load	6,01	6,01	3,0	**18,03**
External wall panel				

Beam near Pillar 5	**L (m)**		**Load (kN/m2)**	**Load (kN/m)**	**Concentraded load (kN)**
Structural dead load	6,01	6,01	3,9	**23,14**	
Non structural dead load	6,01	6,01	2,0	**12,02**	
Accidental load	6,01	6,01	3,0	**18,03**	
External wall panel	6,51	6,51			**55,8558**

Beam between Pillar 6 and 15	**L (m)**		**Load (kN/m2)**	**Load (kN/m)**
Structural dead load	6,01	4,94	3,9	**21,07**
Non structural dead load	6,01	4,94	2,0	**10,95**
Accidental load	6,01	4,94	3,0	**16,42**
External wall panel				

Beam near Pillar 6	**L (m)**		**Load (kN/m2)**	**Load (kN/m)**	**Concentraded load (kN)**
Structural dead load	6,01	5,86	3,9	**22,84**	
Non structural dead load	6,01	5,86	2,0	**11,87**	
Accidental load	6,01	5,86	3,0	**17,80**	
External wall panel	6,52	6,51			**55,8987**

Beam between Pillar 7 and 16	**L (m)**		**Load (kN/m2)**	**Load (kN/m)**
Structural dead load	4,94	5,70	3,9	**20,47**
Non structural dead load	4,94	5,70	2,0	**10,64**
Accidental load	4,94	5,70	3,0	**15,95**
External wall panel				

Beam near Pillar 7	**L (m)**		**Load (kN/m2)**	**Load (kN/m)**	**Concentraded load (kN)**
Structural dead load	5,86	5,70	3,9	**22,24**	
Non structural dead load	5,86	5,70	2,0	**11,56**	
Accidental load	5,86	5,70	3,0	**17,33**	
External wall panel	6,52	6,2			**54,5688**

Beam between Pillar 8 and 17	**L (m)**		**Load (kN/m2)**	**Load (kN/m)**
Structural dead load	5,70	5,77	3,9	**22,08**
Non structural dead load	5,70	5,77	2,0	**11,47**
Accidental load	5,70	5,77	3,0	**17,21**
External wall panel				

Beam near Pillar 8	**L (m)**		**Load (kN/m2)**	**Load (kN/m)**	**Concentraded load (kN)**
Structural dead load	5,70	5,77	3,9	**22,08**	
Non structural dead load	5,70	5,77	2,0	**11,47**	
Accidental load	5,70	5,77	3,0	**17,21**	
External wall panel	6,2	6,56			**54,7404**

Beam between Pillar 9 and 18	**L (m)**		**Load (kN/m2)**	**Load (kN/m)**
Structural dead load	5,77		3,9	**11,11**
Non structural dead load	5,77		2,0	**5,77**
Accidental load	5,77		3,0	**8,66**
External wall panel				**8,58**

Beam near Pillar 9	**L (m)**		**Load (kN/m2)**	**Load (kN/m)**	**Concentraded load (kN)**
Structural dead load	5,77		3,9	**11,11**	
Non structural dead load	5,77		2,0	**5,77**	
Accidental load	5,77		3,0	**8,66**	
External wall panel		6,56		**8,58**	**28,1424**

Beam between Pillar 10 and 19	L (m)		Load (kN/m2)	Load (kN/m)
Structural dead load	3,13	3,42	3,9	**19,19**
Non structural dead load	3,13	3,42	2,0	**9,97**
Accidental load	3,13	3,42	3,0	**14,96**
External wall panel				**8,58**

Beam between Pillar 11 and 19	L (m)		Load (kN/m2)	Load (kN/m)
Structural dead load	3,13	6,00	3,9	**17,58**
Non structural dead load	3,13	6,00	2,0	**9,13**
Accidental load	3,13	6,00	3,0	**13,70**
External wall panel				

Beam between Pillar 12 and 20	L (m)		Load (kN/m2)	Load (kN/m)
Structural dead load	6,00	5,99	3,9	**23,08**
Non structural dead load	6,00	5,99	2,0	**11,99**
Accidental load	6,00	5,99	3,0	**17,99**
External wall panel				

Beam between Pillar 12 and 20	L (m)		Load (kN/m2)	Load (kN/m)
Structural dead load	6,00	2,45	3,9	**20,98**
Non structural dead load	6,00	2,45	2,0	**10,90**
Accidental load	6,00	2,45	3,0	**16,35**
External wall panel				

Beam between Pillar S3 and 21	L (m)		Load (kN/m2)	Load (kN/m)
Structural dead load	1,79	6,01	3,9	**18,46**
Non structural dead load	1,79	6,01	2,0	**7,80**
Accidental load	1,79	6,01	3,0	**11,70**
External wall panel				

Beam between Pillar 26 and S1	L (m)		Load (kN/m2)	Load (kN/m)
Structural dead load	2,08	5,70	3,9	**14,98**
Non structural dead load	2,08	5,70	2,0	**7,78**
Accidental load	2,08	5,70	3,0	**11,67**
External wall panel				

Beam between Pillar 27 and S14;17 and 27	L (m)		Load (kN/m2)	Load (kN/m)
Structural dead load	5,77	5,70	3,9	**22,08**
Non structural dead load	5,77	5,70	2,0	**11,47**
Accidental load	5,77	5,70	3,0	**17,21**
External wall panel				

Beam between Pillar 26 and 16	L (m)		Load (kN/m2)	Load (kN/m)
Structural dead load	3,41	5,70	3,9	**17,54**
Non structural dead load	3,41	5,70	2,0	**9,11**
Accidental load	3,41	5,70	3,0	**13,67**
External wall panel				

Beam between Pillar 18-9; 18-28;28-30	L (m)		Load (kN/m2)	Load (kN/m)
Structural dead load		5,70	3,9	**10,97**
Non structural dead load		5,70	2,0	**5,70**
Accidental load		5,70	3,0	**8,55**
External wall panel				**8,58**

Beam between Pillar 19-20; 20-21;21-22	L (m)		Load (kN/m2)	Load (kN/m)
Structural dead load		1,86	3,9	**7,16**
Non structural dead load		1,86	2,0	**3,72**
Accidental load		1,86	3,0	**5,58**
External wall panel				**8,58**

Beam between Pillar S1 and 13	L (m)		Load (kN/m2)	Load (kN/m)
Structural dead load	5,99	6,01	3,9	**23,10**
Non structural dead load	5,99	6,01	2,0	**12,00**
Accidental load	5,99	6,01	3,0	**18,00**
External wall panel				

Beam between Pillar S6 and 14	L (m)		Load (kN/m2)	Load (kN/m)
Structural dead load	6,01	4,98	3,9	**21,16**
Non structural dead load	6,01	4,98	2,0	**10,99**
Accidental load	6,01	4,98	3,0	**16,49**
External wall panel				

Beam between Pillar 24 and 22	L (m)		Load (kN/m2)	Load (kN/m)
Structural dead load	6,01	6,01	3,9	**23,14**
Non structural dead load	6,01	6,01	2,0	**12,02**
Accidental load	6,01	6,01	3,0	**18,03**
External wall panel				

Beam between Pillar 25 and S10	L (m)		Load (kN/m2)	Load (kN/m)
Structural dead load	2,08	6,01	3,9	**15,56**
Non structural dead load	2,08	6,01	2,0	**8,09**
Accidental load	2,08	6,01	3,0	**12,13**
External wall panel				

Beam between Pillar 25 and 15	L (m)		Load (kN/m2)	Load (kN/m)
Structural dead load	4,98	3,41	3,9	**16,15**
Non structural dead load	4,98	3,41	2,0	**8,39**
Accidental load	4,98	3,41	3,0	**12,59**
External wall panel				

Beam between Pillar 22 and S10	L (m)		Load (kN/m2)	Load (kN/m)
Structural dead load		1,30	3,9	**5,01**
Non structural dead load		1,30	2,0	**2,60**
Accidental load		1,30	3,0	**3,90**
External wall panel				**8,58**

Beam between Pillar 31 and 29	L (m)		Load (kN/m2)	Load (kN/m)
Structural dead load		5,10	3,9	**9,81**
Non structural dead load		5,10	2,0	**5,10**
Accidental load		5,10	3,0	**7,64**
External wall panel				**8,58**

Beam between Pillar 30 and 28	L (m)		Load (kN/m2)	Load (kN/m)
Structural dead load	5,77	5,10	3,9	**20,92**
Non structural dead load	5,77	5,10	2,0	**10,87**
Accidental load	5,77	5,10	3,0	**16,31**
External wall panel				

Beam between Pillar 31-30;31-32;33-34	L (m)		Load (kN/m2)	Load (kN/m)
Structural dead load		2,64	3,9	**5,09**
Non structural dead load		2,64	2,0	**2,64**
Accidental load		2,64	3,0	**3,97**
External wall panel				

Those loads have been put on beams that discharge on the slab, in the finite element models created. During the first measurements of ambient noise the mechanical plant of ventilation and

the garden planed in the terrace weren't constructed, therefore, the permanent load implied in the FEM (permanent load of 2 kN/m^2) is lower than the permanent load of the project (permanent load of 5 kN/m^2). Also, the internal walls weren't constructed all, so as their load of 3,5 kN/m was put in the beams where the wall existed.
The load from the external wall panels is 8,58 kN/m. The window opening has been considered in the FEM in two different ways: first by reducing the load applied on the beams by the difference in weight between wall panel and rods, and second by reducing the rod width of the frame elements used to model the external walls (by the reduction factor, see Table 6.20). The concrete class used to model the external wall panels by frame element is C32/40, equal to the concrete class used to construct the external cover panels.

6.1.4.1 Seismic action due to NTC08

The seismic action of the project is defined starting from the seismic hazard of the construction site, referred to NTC 2008. This constitutes the element of primary knowledge for the determination of seismic actions, under which can be estimated the satisfy of limit states considered. The seismic hazard is defined in terms of expected maximum horizontal acceleration a_g in the free field over a rigid reference site with horizontal topographic surface (Category A), as well as the ordinates of the elastic response spectrum in acceleration Se(T) referred to predetermined exceeding probability (P_{VR}) in the reference period V_R.
The spectral shapes for each exceeded probability in reference period V_R, are defined from the following parameters values of horizontal rigid reference site, referred to the Italian standard:

- ag maximum horizontal acceleration of site;
- Fo maximum value of the amplification factor of the spectrum in horizontal acceleration;
- T^*_C period at the beginning of the segment with constant velocity of the horizontal acceleration spectrum.

Those value are given by the standard for each soil type. Ultimate and serviceability limit states, in respect of seismic actions, are identified referring to the performance of the construction in its entirety including the structural and not structural elements. The probability of exceedance in the reference period, which is the point of reference for identifying the seismic action agent in each of the considered limit state, are presented in the Table 6.3.

Table 6.3 *Probability of exceeding P_{VR}, to different limit state (Table 3.2.I, NTC 2008)*

Limit states		P_{VR}, probability of being exceeded in reference period V_R
Serviceability limit states	SLO	81%
	SLD	63%
Ultimate limit states	SLV	10%
	SLC	5%

For the purposes of estimating the design seismic action, it is necessary to evaluate the seismic local response by specific analyzes, as indicated in § 7.11.3. In the absence of such analysis, the seismic action may be defined refer to a simplified approach which is based on the identification of reference subsoil categories (Table 3.2.II and 3.2.III, NTC2008). The subsoil categories, using longitudinal wave velocity V_{s30}, are shown in the Table 5.14 and in the Table 6.4. The class of the site can be calculated using the information given previously, as proposed by the ministerial decree. The equivalent value of longitudinal wave velocity normalized on 30 m can be estimated by the following equation:

$$V_{s30}; N_{30}; C_{u30} = \frac{\sum_{i=1}^{n} d_i}{\sum_{i=1}^{n} \frac{d_i}{V_{si}}; \frac{d_i}{N_i}; \frac{d_i}{C_{ui}}}$$

where n is the number of homogeneous layers in which it is possible to divide the subsoil, d_i is the thickness layer, V_{si} is the shear wave velocity of the layer i, N_i is the number of shots of SPT test (N_{SPT}) of i-th layer; $\sum_{i=1}^{n} d_i = 0$ m.

In cases where the vertical stratigraphic investigated is higher than 30 m the sequence is truncates while when is inferior of 30 m, than the thickness of the last layer is increased.

Table 6.4 *Subsoil category*

Category of subsoil	Vs30 (m/s)	Nspt30	Plastic index	Undrained cohesion (kPa)	Description
A	> 800				Lithoid formations/very rigid (with max. 5.0 m gossan)
B	360 - 800	> 50		> 250	Sands, densified gravels, consistent clays
C	180 - 360	15 - 50		70 - 250	Sands and gravels averagely densified and clays with an average consistency
D	< 180	< 15		< 70	5 - 20 m thickness, floods, Vs of bedrock > 800 m/s
E	< 180; 180 - 360				
S1	< 100		> 40	10 - 20	Clay/silt with thickness > 8 m
S2					Sensible clay and/or liquefiable soils

The seismic action is characterized by three translational components, two horizontal (x and y direction) and one vertical (z direction). The vertical direction should be considered in cases when the construction site falls in Zone 3 or Zone 4, when the structure has horizontal elements with dimension exceeding 20 m, pre-stressed elements (excluding floors with dimension less than 8 m), cantilever elements with dimension greater than 4 m, buildings with suspended floors, bridges etc. as described in standard (see 7.2.1). The components can be described by means of the maximum acceleration waiting at the surface, relative response spectrum at the surface or by accelerograms, chosen all in function of the type of analysis to be performed.

The spectral shapes for the two horizontal orthogonal components $\mathrm{S_a(T)}$ and the vertical component $\mathrm{S_{va}(T)}$ of the seismic action are given by the following relationships:

$$\mathrm{S_a(T)} = \mathrm{a_g}\,\mathrm{S}\,\eta\,F_o\left[\frac{\mathrm{T}}{\mathrm{T_B}} + \frac{1}{\eta\,F_o}\left(1 - \frac{\mathrm{T}}{\mathrm{T_B}}\right)\right] \quad \text{for } 0 \le \mathrm{T} < \mathrm{T_B}$$
$$\mathrm{S_a(T)} = \mathrm{a_g}\,\mathrm{S}\,\eta\,F_o \quad \text{for } \mathrm{T_B} \le \mathrm{T} < \mathrm{T_C}$$
$$\mathrm{S_a(T)} = \mathrm{a_g}\,\mathrm{S}\,\eta\,F_o\left(\frac{T_C}{T}\right) \quad \text{for } \mathrm{T_C} \le \mathrm{T} < \mathrm{T_D}$$
$$\mathrm{S_a(T)} = \mathrm{a_g}\,\mathrm{S}\,\eta\,F_o\left(\frac{T_C\,T_D}{T^2}\right) \quad \text{for } \mathrm{T_D} \le \mathrm{T} < 4s$$

$$\mathrm{S_{va}(T)} = \mathrm{a_g}\,\mathrm{S}\,\eta\,F_v\left[\frac{\mathrm{T}}{\mathrm{T_B}} + \frac{1}{\eta\,F_o}\left(1 - \frac{\mathrm{T}}{\mathrm{T_B}}\right)\right] \quad \text{for } 0 \le \mathrm{T} < \mathrm{T_B}$$
$$\mathrm{S_{va}(T)} = \mathrm{a_g}\,\mathrm{S}\,\eta\,F_v \quad \text{for } \mathrm{T_B} \le \mathrm{T} < \mathrm{T_C}$$
$$\mathrm{S_{va}(T)} = \mathrm{a_g}\,\mathrm{S}\,\eta\,F_v\left(\frac{T_C}{T}\right) \quad \text{for } \mathrm{T_C} \le \mathrm{T} < \mathrm{T_D}$$
$$\mathrm{S_{va}(T)} = \mathrm{a_g}\,\mathrm{S}\,\eta\,F_v\left(\frac{T_C\,T_D}{T^2}\right) \quad \text{for } \mathrm{T_D} \le \mathrm{T} < 4s$$

where T is the vibration period of a linear single-degree-of-freedom (SDOF) system or vertical vibration in case of vertical spectra, a_g is the design ground acceleration on type A site class, S is the product of the stratigraphic factor S_S and the topographic amplification factor S_T, T_B and T_C are the limit periods of the constant segment of the spectrum, T_D is the lowest period of the constant displacement spectral portion, η is the damping correction factor ($\eta = 1$ for 5% viscous damping) estimated by the viscous damping ratio of the structure ξ ($\eta = \sqrt{10/(5+\xi)} \ge 0{,}55$), F_o is an amplification factor (equal to the ratio between the maximum spectral ordinate and the ag value) and F_v is the vertical amplification factor related to F_o as $F_v = 1.35\ F_o\ (a_g/g)^{0.5}$.

The ordinates and shapes (i.e., T_B, T_C, T_D and S) of horizontal components depend on the seismic hazard and site class, and are calculated by the relationship proposed by the standard. T_B, T_C and T_D values for the vertical response spectrum are given in the Table 6.5.

Table 6.5 *Recommended values for parameters describing the vertical elastic response spectra*

Ground type	Ss	T_B (s)	T_C (s)	T_D (s)
A, B, C, D, E	1,00	0,05	0,15	1,00

The building under consideration is a prefabricated reinforced concrete construction destined for sanitary use, i.e. a strategic building as being a hospital. It consists of five floors above ground and one underground with a total height of about 23 m, considering the basement. The building falls in the class of use IV (with coefficient C_U equal to 2), according to Eurocode 8 and NTC 2008: buildings which provides normal crowds, without dangerous content for the environment and without essential public and social functions. The nominal life V_N is higher than 100 years and consequently the reference period V_R is 100 year for the seismic action (see Table 6.6). Being an ordinary construction the study of seismic microzoning becomes even more important to be realized for the seismic prevention of the building.

Table 6.6 *Reference period of seismic action (referred to the Table 2.4.1 of NTC 2008)*

Reference period of seismic action $V_R = V_N\ C_U$ (year)						
Class of use			I	II	III	IV
Coeff. C_U			0,7	1,0	1,5	2,0
Construction type		V_N	V_R			
1	Provisional structures, structures in construction phase	≤ 10	35	35	35	35
2	Ordinary building, bridge, infrastructure and dams construction of normal importance and dimention	≥ 50	35	50	75	100
3	Great construction, bridges, infrastructure and larg dams or of strategic importance	≥ 100	70	100	150	200

The seismic action has been calculated by the free sheet ‘Spettri-NTC ver.1.0.3' in which have been implemented the relationship described above. The building under exam is located in the Municipality of Sanremo (longitude 7.7622°, latitude 43.8192°), province of Imperia, Liguria region in Italy. The seismic actions have been evaluated in relation to the reference period V_R, which is obtained by multiplying the nominal life V_N with the user coefficient C_U. The class of use C_U of the building is equal to 2, while the nominal life V_N is higher than 100 years. The building falls in the subsoil Category B with topographic category T_2.

The spectrum of the project to SLU/SLV, SLE/SLD and SLE/SLO limit states have been estimate for structural verification of the building. The structure factor q value used for each direction of the horizontal seismic action, depends on the construction type, the degree of its hyperstaticity and the design criteria adopted and also, takes into account the non-linearity of the material. The structure factor q, can be calculated as the product of the maximum structure factor value q_o with the reductive factor K_R ($q = q_0\ K_R$), which is 1 for structures regular in elevation. The value of q_o depend on the class of ductility of the building (CD "B" in our case) and on the type of the building (Table 7.4.I of NTC2008). This factor, assumes a value 2 for torsional deformable structures. Furthermore, the structure factor q for vertical component of seismic action is assumed 1.5.

In the Figure 6.9 are shown the response spectrum from SLV and SLD limit state and for both horizontal and vertical components.

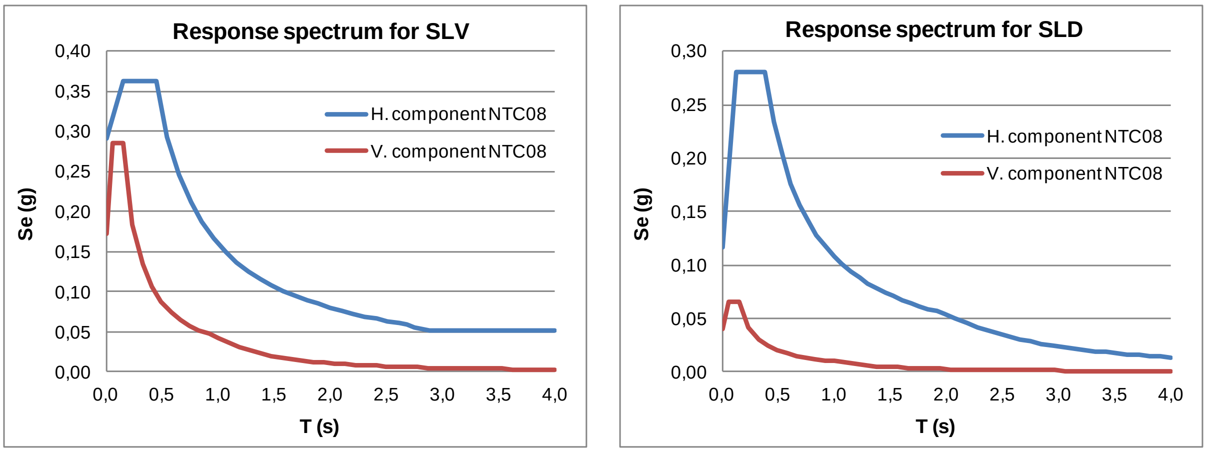

Figure 6.9 *Response spectrum for SLV and SLD limit state due to NTC08*

6.1.5 Load combinations

For verification of the limit states are defined different combinations of actions.
The *fundamental combination*, generally used for ultimate limit state SLU, is estimated by the relationship:

$$\gamma_{G1}\times G_1 + \gamma_{G2}\times G_2 + \gamma_P\times P + \gamma_{Q1}\times Q_{k1} + \gamma_{Q2}\times\Psi_{02}\times Q_{k2} + \gamma_{Q3}\times\Psi_{03}\times Q_{k3} + \ldots$$

where γ_{G1} is partial coefficient of the own weight of the structure, as well as of its own weight soil and water when relevant, γ_{G2} is partial coefficient of own weight of nonstructural elements, γ_{Qi} is partial coefficient of variable actions.
For verification of structural ultimate limit state (STR) those coefficient can be taken in the Table 2.6.I of the standard (1.3 for γ_{G1} and 1.5 for γ_{G2} and γ_{Qi}). The value of partial safety coefficients γ_{Gi} and γ_{Qj} are presented in the Table 2.6.I of the standard.
Seismic combination with other actions to be used for ultimate limit state and serviceability limit state, related to the seismic action *E* defined in the paragraph v. § 3.2 of the standard, is defined as:

$$E + G_1 + G_2 + P + \sum_j \Psi_{2j} \times Q_{kj}$$

The value of the coefficient of combinations Ψ_{2j} are given in the Table 2.5.I of the standard NTC08.
The horizontal (Ex, Ey) and vertical (Ez) components of the seismic action, estimated as described in the paragraph 6.1.4.1, must be combined with each other by changing the sign and 30 percent of the value:

$$E = \pm Ex \pm 0.3\ Ey \pm 0.3\ Ez$$

Generally, 32 combination must be used for linear dynamic or static analysis (Table 6.7). In our case, we used only 8 combination using only horizontal spectrum components and taking into account that Sap2000 software consider the sign of actions.

Table 6.7 *Number of seismic combination for different type of analysis*

Type of analysis	NTC 2008		EC8 - 2005	
	Comb. dir.	Comb. Total	Comb. dir.	Comb. Total
Linear Analysis (static or dynamic)	±Ex ± 0.3Ey	32	±Ex ± 0.3Ey	32
	±0.3Ex ± Ey		±0.3Ex ± Ey	
Linear Static Analysis	±Ex	8	±Ex ± 0.3Ey	32
	±Ey		±0.3Ex ± Ey	
Linear Dynamic Analysis	min 3 bidirectional accelerograms	min 12	min 3 bidirectional accelerograms	min 12

6.2 Finite element model of the building, FEM

Four main finite element models have been realized in this thesis with software SAP2000. The first one is the FEM of the project 'FE Model 0' realized by using the computing project data and verifying in site the presence and dimension of structural elements. This finite element model has been calibrated twice 'FE Model 1' and 'FE Model 2', by using respectively the structural response estimated from ambient noise measurements acquired in two different periods during the construction of the building. As described in the above paragraphs, the ambient vibration measures have been acquired in two different periods to evaluate the influence of added mass and rigidity during the construction of the hospital. The latest model 'FE Model 3' is the calibrated one 'FE Model 2' without modeling the external walls. Being in the field of environmental measures the rigidity of external walls panels influence significantly in the dynamic response of the structure but they are not designed to withstand the earthquake. Therefore, the calibrated model without modeling the wall panels have been used for seismic response controls of the structure.
In all finite element models the pillars and beams have been modeled with frame elements while the staircase and lift cores with shell elements. The horizontal structures at all levels have been modeled as rigid diaphragms (by the help of joint constraints), considering the stiffening effect of the completion reinforced slab of 5 cm thick. The pillars are wedge in the base while beams are stuck with the pillars. Also, the staircase and lift cores are wedge in the base. The mass has been defined from elements and loads which are applied in beams referred to the direction of slabs. Different classes of concrete have been used as described by the computing project (see Table 6.1). The equivalent connecting rod theory has been used to dimension the frame elements used to model external walls in the calibrated FE model. In the Figure 6.10 is shown the FEM of the project, the staircase and elevator cores.

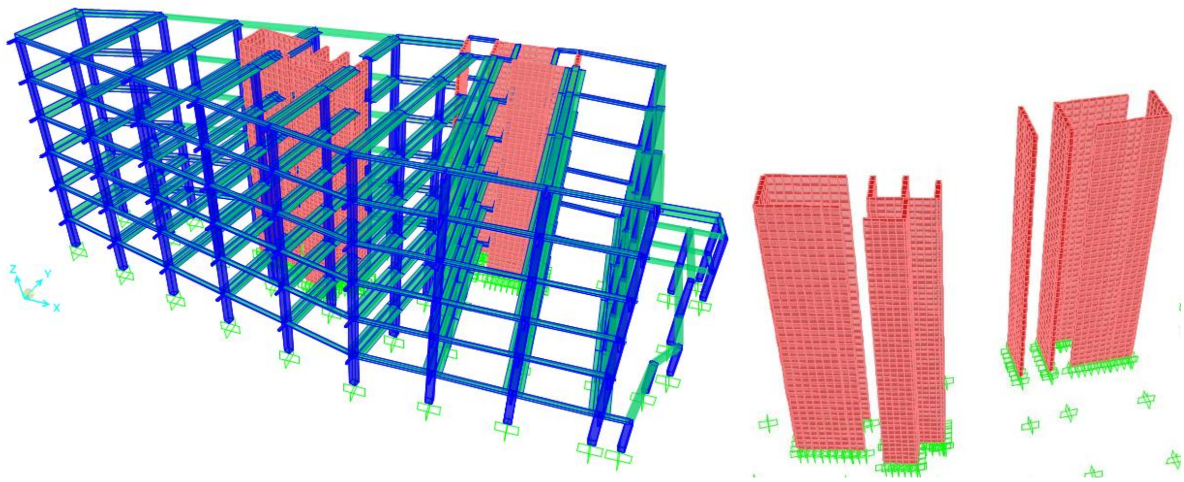

Figure 6.10 *FEM of building 'Model 0' (left), staircase and lift cores (right)*

6.2.1 Modal parameters

The modal parameters of 'FE Model 0' are presented in this paragraph. The frequencies and the modal participation mass ration are shown in the Table 6.8.

__Table 6.8__ Periods and modal participating mass ratios of 'FE Model 0'

TABLE: Modal Participating Mass Ratios									
Mode		Period	Frequency	UX	UY	RZ	SumUX	SumUY	SumRZ
	No	Sec	Cyc/sec	Unitless	Unitless	Unitless	Unitless	Unitless	Unitless
Mode	1	0,865595	1,1553	0,06537	0,00534	**0,11154**	0,06537	0,00534	0,11154
Mode	2	0,629794	1,5878	0,08071	**0,55487**	**0,48434**	0,14609	0,56021	0,59589
Mode	3	0,48788	2,0497	**0,48141**	0,07906	0,01082	0,6275	0,63926	0,60671
Mode	4	0,219259	4,5608	0,01514	0,00158	0,04228	0,64264	0,64085	0,64898
Mode	5	0,140307	7,1272	0,00853	**0,20827**	0,16799	0,65118	0,84912	0,81697
Mode	6	0,10712	9,3353	0,1681	0,00494	0,02736	0,81928	0,85406	0,84433
Mode	7	0,103967	9,6184	0,04928	0,00325	0,00721	**0,86856**	**0,85731**	**0,85153**

The first mode shape is a rotational mode with modal participating mass ratio of about 11% and has a contribution of the translational mode in the x direction higher than 5% (mass ratio of about 7%). The second mode is a combined translational in the *y* direction with rotational mode respectively with a modal participating mass ratio of about 55% and 48%. The third mode is a translational mode in the *x* direction (with participation mass ration of about 48%) and has a contribution of the translational mode in the *y* direction higher than 5% (participation mass of about 8%). The frequency of the first three mode shapes are respectively 1.16 Hz, 1.59 Hz and 2.05 Hz. The third mode can be considered as a first translational mode shape in *x* direction while the second mode shape as a first translational mode shape in the *y* direction. In the Figure 6.11 are presented the first fourth mode shapes. The first three mode shapes has a form as a first mode while the fourth mode shape has a form as a second mode shape. The damping ratio has been set 5% for all cases.

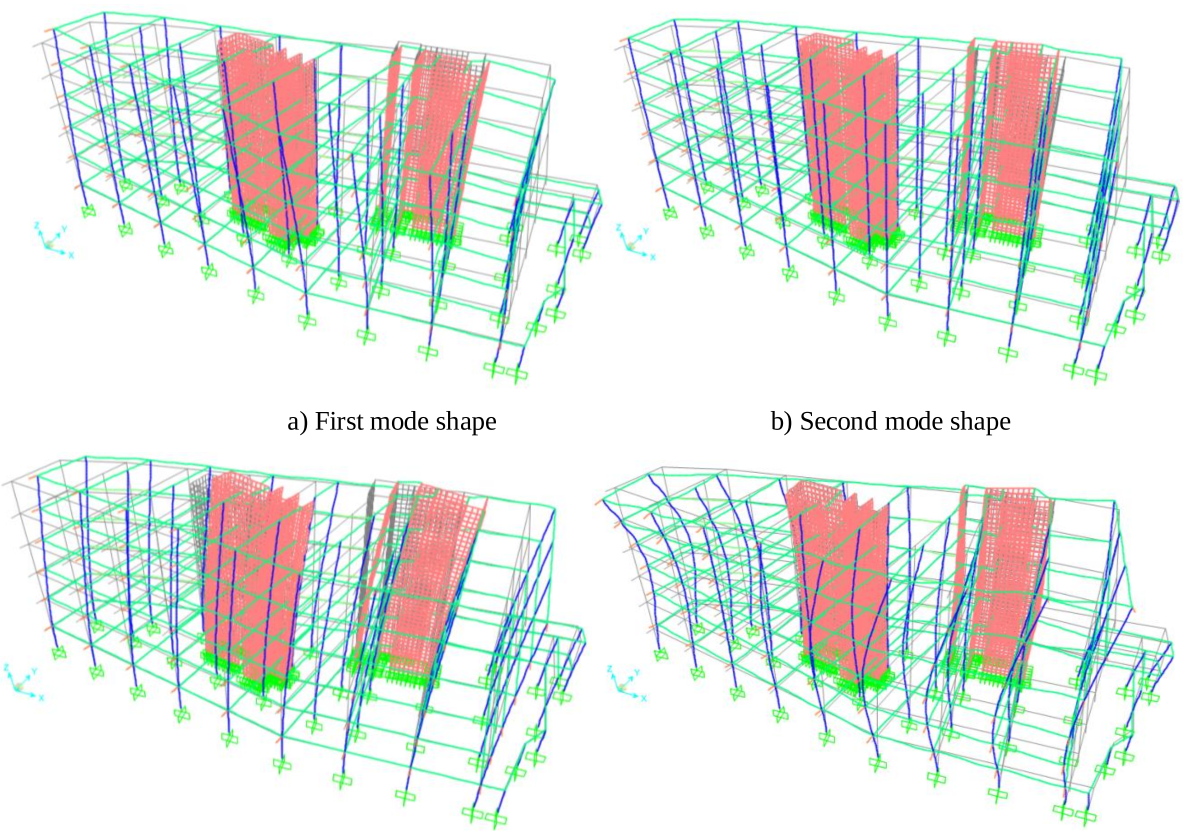

a) First mode shape b) Second mode shape

c) Third mode shape d) Fourth mode shape

***Figure 6.11** Mode shapes of 'FE Model 0': a) first mode, b) second mode, c) third mode and d) fourth mode shape*

The initial FEM of the project design is shown in the Figure 6.12. The mode shape number which achieve 85% of cumulative modal participation mass ratio is 47. Some elements and loads were not modeled. Also, the same class of concrete for all structures elements was used. The first period 1.42 s is higher than the bibliography value (see paragraph 6.2.2). Therefore, this model has been created again due to the computing project. The initial model has a first rotational mode with the frequency of about 0.70 Hz (period 1.42 s) and the mass ratio of about 21%. The second mode has a modal frequency of about 1.13 Hz and is a combined translational mode in the *y* direction (mass ratio 56%) with a rotational mode (mass ratio 36%), while the third mode is a translational mode in the *x* direction (mass ratio of about 57%) and has a modal frequency of about 1.61Hz.

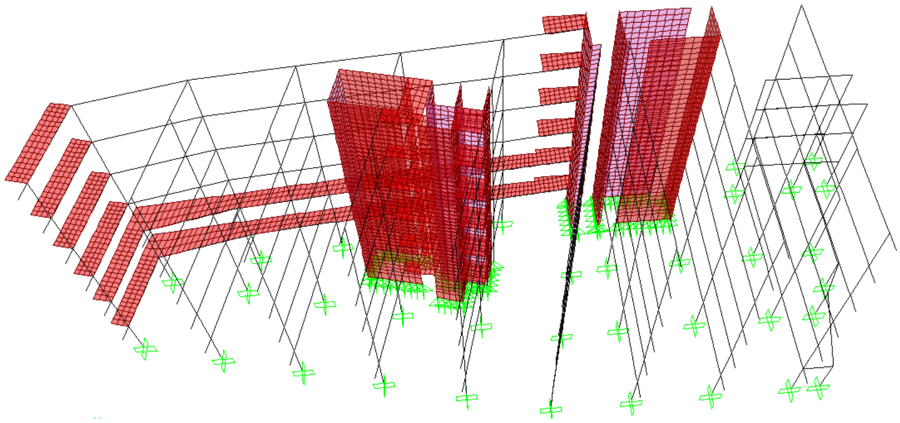

Figure 6.12 *FEM of the computing project*

6.2.2 Natural frequency from the bibliography

The natural frequency, estimated from the project and from ambient noise measurement carried out inside the building, have been compared with bibliographic values obtained by various studies using seismic noise, empirical relationships of numerous authors and technical standard. The height of the building taken in this study is about 22 m and has a first period of about 0.8 s referred to the FEM of the project 'FE Model 0', 1.4 s referred to the initial FEM of the project, and a period 0.43 s referred to the ambient noise measurement results. As can see from the reported studies the value of periods estimated theoretically (0.76 s referred to the Italian and European standards and 0.8 s by the FEM) is overestimated comparing to experimental data results (0.40 s, see paragraph 6.4) which is compatible with values estimated from various authors for similar structures height and reinforced concrete building.

The natural frequency of the building can be estimated as function of its height or floor numbers and building type, referring to Italian and European technical standards (NTC and Eurocode). In the Table 6.9 are presented different empirical relationship of several authors, between the frequency and the high or the floor numbers of the building. Those results are shown in the Figure 6.13 (see graphic on the left).

The relationship of the first period T_1(s) for the building heights up to 40 m, is approximated by the following expression given by the Italian 'NTC 2008' and European 'Eurocode 8' standard:

$T_1 = C_t \cdot H^{3/4}$

where C_t is 0.085 for moment resistant space steel frames, 0.075 for moment resistant space concrete frames and for eccentrically braced steel frames, 0.050 for all other structures, *H* is the height of the building in m, from the foundation or from the top of a rigid basement.

The graphic of the period as a function of building height is shown in the Figure 6.13 (see green line Eurocode 8). As can see from this graphic the values estimated experimentally using ambient noise measurements (Potenza and Senigallia, Gallipoli) remain below the standards values. Furthermore the relationship of some authors present higher period values referred to the standards. In general, the theoretical period values are overestimated in comparison with experimental ones.

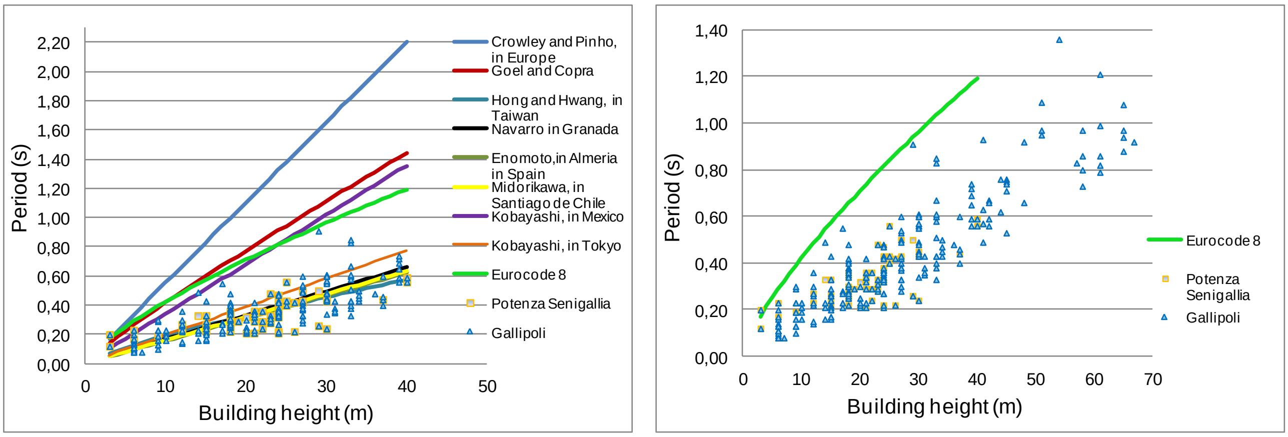

Figure 6.13 *Graphic of the period as a function of its high or floor numbers and construction type*

Two studies who used the ambient noise measurements to evaluate the dynamic structure response are reported. The first was realized by Gallipoli at all (2009) which acquired several hundred ambient noise measurements, at least 10 min sampled at 128 Hz, in RC (reinforced concrete) buildings with height in the range 1–20 floors. The ambient noise measurements were performed in 65 buildings in Italy, 47 buildings in Slovenia, 62 buildings in Croatia and in 70 buildings in Republic of Macedonia (see Table 6.10). For all buildings the fundamental period on the two orthogonal components, was determined (Figure 6.13, right). The height-period scatter plot for all the 244 RC buildings is presented in the Figure 6.14. The empirical relationship between the period and the building height was defined by using the best fit line on the height-period graphic.

$T_1 = 0.016\ H$

when *H* is the building height from the foundation at the top floor.

Also, a bootstrap procedure returned the 95% confidence limits for the parameter a, equal to 0.0150 and 0.0175. For European buildings, this result are very similar to that obtained by Navarro et al. (2007) for Spanish RC buildings, who proposed the relationship T = 0.049N, with N equal to the number of floors (assuming 3 m as the inter-storey height).
The damping was associated to the fundamental period and confirm the findings from Gallipoli et al. (2008). The standard assumption of an average 5% damping is justified for this set of buildings. The empirical distribution of the observed damping is fit by a log-normal distribution whose mean is 4.8%.

The results demonstrate the similarity of the height-period relationships in the four countries, which allowed the treatment of all measurements as a single database. The relationship height-period found is very different from European code provisions. Also, the values of periods estimated by Eurocode 8 results higher than those estimated from ambient noise measurements. Instead, the average observed damping 4.8% justifying the standard assumption 5%, while its distribution is well fit by a log normal distribution.
The second study realized from Gallipoli at all (2008) presents the translational frequencies in orthogonal directions and their relative damping for 80 buildings in the urban areas of Potenza and Senigallia in Italy (Figure 6.13, graphic on the right). The comparison of the results obtained through microtremor measurements with those obtained from earthquake recordings, were realized. This shows an agreement between the results obtained with microtremors and earthquakes that encouraged extending ambient noise measurements to a large number of buildings (see Table 6.12).

Table 6.9 *Periods calculated from empirical relationship of various authors and from Eurocode 8*

Height (m)	Eurocode 8 T (s)	European RC Tgross = 0,038 H (Uncracked infilled building) T (s)	Crowley and Pinho (yield stiffness-bare frames) T = 0,1 H T (s)	European RC Tgross = 0,055 H (Cracked infilled building) T (s)	Goel and Copra (best fit) T = 0,052 H^0,9 T (s)	Hong and Hwang (RC building in Taiwan) T = 0,0294 H^0,804 T (s)	Navarro (RC building in Granada) T=0,051 N T (s)	Enomoto (in Almeria, Spain) T = 0,048 N T (s)	Midorikawa (Santiago de Chile, Chile) T = 0,049 N T (s)	Kobayashi (Mexico) T = 0,105 N T (s)	Kobayashi (Tokyo, Japan) T = 0,06 N T (s)
3	0,17	0,11	0,30	0,17	0,14	0,07	0,05	0,05	0,05	0,10	0,06
4	0,21	0,15	0,40	0,22	0,18	0,09	0,07	0,06	0,06	0,14	0,08
5	0,25	0,19	0,50	0,28	0,22	0,11	0,08	0,08	0,08	0,17	0,10
6	0,29	0,23	0,60	0,33	0,26	0,12	0,10	0,09	0,09	0,20	0,12
7	0,32	0,27	0,70	0,39	0,30	0,14	0,12	0,11	0,11	0,24	0,14
8	0,36	0,30	0,80	0,44	0,34	0,16	0,13	0,12	0,13	0,27	0,15
9	0,39	0,34	0,90	0,50	0,38	0,17	0,15	0,14	0,14	0,30	0,17
10	0,42	0,38	1,00	0,55	0,41	0,19	0,16	0,15	0,16	0,34	0,19
11	0,45	0,42	1,10	0,61	0,45	0,20	0,18	0,17	0,17	0,37	0,21
12	0,48	0,46	1,20	0,66	0,49	0,22	0,20	0,19	0,19	0,41	0,23
13	0,51	0,49	1,30	0,72	0,52	0,23	0,21	0,20	0,21	0,44	0,25
14	0,54	0,53	1,40	0,77	0,56	0,25	0,23	0,22	0,22	0,47	0,27
15	0,57	0,57	1,50	0,83	0,59	0,26	0,25	0,23	0,24	0,51	0,29
16	0,60	0,61	1,60	0,88	0,63	0,27	0,26	0,25	0,25	0,54	0,31
17	0,63	0,65	1,70	0,94	0,67	0,29	0,28	0,26	0,27	0,58	0,33
18	0,66	0,68	1,80	0,99	0,70	0,30	0,30	0,28	0,28	0,61	0,35
19	0,68	0,72	1,90	1,05	0,74	0,31	0,31	0,29	0,30	0,64	0,37
20	0,71	0,76	2,00	1,10	0,77	0,33	0,33	0,31	0,32	0,68	0,39
21	0,74	0,80	2,10	1,16	0,81	0,34	0,35	0,33	0,33	0,71	0,41
22	0,76	0,84	2,20	1,21	0,84	0,35	0,36	0,34	0,35	0,75	0,43
23	0,79	0,87	2,30	1,27	0,87	0,37	0,38	0,36	0,36	0,78	0,45
24	0,81	0,91	2,40	1,32	0,91	0,38	0,39	0,37	0,38	0,81	0,46
25	0,84	0,95	2,50	1,38	0,94	0,39	0,41	0,39	0,40	0,85	0,48
26	0,86	0,99	2,60	1,43	0,98	0,40	0,43	0,40	0,41	0,88	0,50
27	0,89	1,03	2,70	1,49	1,01	0,42	0,44	0,42	0,43	0,91	0,52
28	0,91	1,06	2,80	1,54	1,04	0,43	0,46	0,43	0,44	0,95	0,54
29	0,94	1,10	2,90	1,60	1,08	0,44	0,48	0,45	0,46	0,98	0,56
30	0,96	1,14	3,00	1,65	1,11	0,45	0,49	0,46	0,47	1,02	0,58
31	0,99	1,18	3,10	1,71	1,14	0,46	0,51	0,48	0,49	1,05	0,60
32	1,01	1,22	3,20	1,76	1,18	0,48	0,53	0,50	0,51	1,08	0,62
33	1,03	1,25	3,30	1,82	1,21	0,49	0,54	0,51	0,52	1,12	0,64
34	1,06	1,29	3,40	1,87	1,24	0,50	0,56	0,53	0,54	1,15	0,66
35	1,08	1,33	3,50	1,93	1,28	0,51	0,58	0,54	0,55	1,19	0,68
36	1,10	1,37	3,60	1,98	1,31	0,52	0,59	0,56	0,57	1,22	0,70
37	1,13	1,41	3,70	2,04	1,34	0,54	0,61	0,57	0,58	1,25	0,72
38	1,15	1,44	3,80	2,09	1,37	0,55	0,63	0,59	0,60	1,29	0,74
39	1,17	1,48	3,90	2,15	1,41	0,56	0,64	0,60	0,62	1,32	0,75
40	1,19	1,52	4,00	2,20	1,44	0,57	0,66	0,62	0,63	1,35	0,77

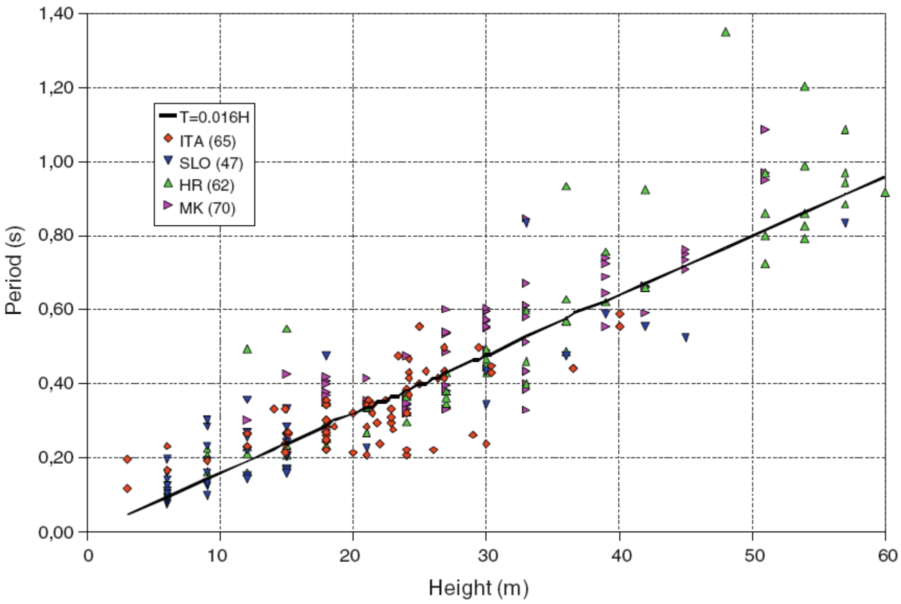

Figure 6.14 *Height-period scatter plot for all the 244 RC buildings surveyed with the best fit line*

Table 6.10 Periods value of 244 buildings, Gallipoli et al. (2009)

Country	Height (m)	Year	Type	T (s)
ITA	3		frame	0,20
ITA	3		frame	0,12
SLO	6	1970	r.c.	0,16
SLO	6	1975	r.c.	0,20
SLO	6	1976	r.c.	0,09
SLO	6	1976	r.c.	0,11
SLO	6	1977	r.c.	0,13
SLO	6	1980	r.c.	0,14
SLO	6	1981	r.c.	0,11
SLO	6	1983	r.c.	0,11
SLO	6	1988	r.c.	0,08
SLO	6	1993	r.c.	0,10
SLO	6	2000	r.c.	0,08
SLO	6	2001	r.c.	0,11
SLO	6	2001	r.c.	0,13
ITA	6		frame	0,23
SLO	6		r.c.	0,11
ITA	6		frame	0,17
HR	7		r.c.	0,08
SLO	9	1959	r.c.	0,29
SLO	9	1963	r.c.	0,23
SLO	9	1980	r.c.	0,19
SLO	9	1980	r.c.	0,30
SLO	9	1984	r.c.	0,16
SLO	9	1986	r.c.	0,10
SLO	9	1990	r.c.	0,13
SLO	9	2000	r.c.	0,13
SLO	9		r.c.	0,23
ITA	9		frame	0,19
HR	10		r.c.	0,21
HR	10		r.c.	0,19
HR	10		r.c.	0,23
HR	10		r.c.	0,16
SLO	12	1960	r.c.	0,22
SLO	12	1964	r.c.	0,26
SLO	12	1978	r.c.	0,27
SLO	12	2000	r.c.	0,36
SLO	12	2003	r.c.	0,14
ITA	12		frame	0,23
ITA	12		frame	0,27
MK	12		frame	0,30
SLO	12		r.c.	0,15
HR	14		r.c.	0,49
HR	14		r.c.	0,16
HR	14		r.c.	0,21
HR	14		r.c.	0,23
MK	15	1958	frame	0,43
ITA	15	1965	frame	0,27
ITA	15	1965	frame	0,24
ITA	15	1965	frame	0,22
ITA	15	1965	frame	0,26
SLO	15	1965	r.c.	0,26
SLO	15	1967	r.c.	0,17
SLO	15	1976	r.c.	0,33
SLO	15	1978	r.c.	0,21
SLO	15	1979	r.c.	0,24
SLO	15	1980	r.c.	0,16
SLO	15	1980	r.c.	0,17
SLO	15	1998	r.c.	0,20
SLO	15	2000	r.c.	0,29
ITA	15	2000	frame	0,33
HR	17		r.c.	0,28
HR	17		r.c.	0,55
HR	17		r.c.	0,21
HR	17		r.c.	0,23
HR	17		r.c.	0,27
MK	18	1958	frame	0,41
MK	18	1958	frame	0,38
MK	18	1958	frame	0,38
MK	18	1958	frame	0,42
MK	18	1969	frame	0,40
MK	18	1970	frame	0,35
ITA	18	1975	frame	0,25
ITA	18	1975	frame	0,25
ITA	18	1975	frame	0,26
ITA	18	1979	frame	0,22
SLO	18	1980	r.c.	0,48
MK	18	1990	frame	0,37
MK	18	1991	frame	0,28

Country	Height (m)	Year	Type	T (s)
ITA	18	1995	frame	0,36
ITA	18	1995	frame	0,30
ITA	18	1995	frame	0,34
ITA	18	2000	frame	0,30
ITA	18		frame	0,27
ITA	18		frame	0,31
ITA	19	1965	frame	0,29
ITA	20	1975	frame	0,21
HR	20		r.c.	0,22
HR	20		r.c.	0,30
HR	20		r.c.	0,25
HR	20		r.c.	0,23
MK	21	1959	frame	0,42
ITA	21	1975	frame	0,36
ITA	21	1975	frame	0,32
ITA	21	1975	frame	0,21
ITA	21	1975	frame	0,34
SLO	21	1982	r.c.	0,23
MK	21	1993	frame	0,36
MK	21	1993	frame	0,36
ITA	21	1995	frame	0,29
ITA	21	1995	frame	0,34
MK	21	2004	frame	0,34
ITA	22	1965	frame	0,36
ITA	22	1975	frame	0,29
ITA	22	1975	frame	0,24
ITA	23	1965	frame	0,48
ITA	23	1975	frame	0,33
ITA	23	1975	frame	0,28
ITA	23	1975	frame	0,29
ITA	23	1975	frame	0,31
ITA	24	1965	frame	0,43
ITA	24	1965	frame	0,42
MK	24	1973	frame	0,48
ITA	24	1975	frame	0,21
ITA	24	1975	frame	0,37
ITA	24	1975	frame	0,47
ITA	24	1975	frame	0,22
MK	24	1982	shear walls	0,33
MK	24	1984	shear walls	0,35
MK	24	1984	shear walls	0,34
MK	24	1989	frame	0,36
MK	24	1989	frame	0,36
MK	24	1990	frame	0,37
MK	24	1990	frame	0,37
MK	24	1991	frame	0,32
ITA	24	1995	frame	0,32
ITA	24	1995	frame	0,32
HR	24		r.c.	0,34
ITA	24		frame	0,38
HR	24		r.c.	0,27
HR	24		r.c.	0,36
HR	24		r.c.	0,27
HR	24		r.c.	0,33
ITA	25	1975	frame	0,40
ITA	25	1975	frame	0,56
ITA	25	1975	frame	0,43
ITA	26	1975	frame	0,42
ITA	26	1975	frame	0,22
MK	27	1970	frame	0,60
ITA	27	1975	frame	0,50
ITA	27	1975	frame	0,42
ITA	27	1975	frame	0,43
MK	27	1978	shear walls	0,40
MK	27	1979	shear walls	0,33
MK	27	1979	frame	0,53
MK	27	1980	frame	0,54
MK	27	1981	frame	0,49
MK	27	1991	frame	0,38
HR	27		r.c.	0,37
HR	27		r.c.	0,33
HR	27		r.c.	0,28
HR	27		r.c.	0,38
HR	27		r.c.	0,30
ITA	29	1965	frame	0,91
ITA	29	1975	frame	0,26
MK	30	1965	frame	0,49
MK	30	1965	frame	0,44
SLO	30	1965	r.c.	0,34

Country	Height (m)	Year	Type	T (s)
MK	30	1965	frame	0,48
ITA	30	1965	frame	0,45
MK	30	1968	frame	0,56
MK	30	1968	frame	0,56
MK	30	1968	frame	0,56
MK	30	1968	frame	0,55
SLO	30	1970	r.c.	0,43
MK	30	1970	frame	0,57
MK	30	1970	frame	0,57
MK	30	1972	frame	0,61
MK	30	1972	frame	0,60
MK	30	1972	frame	0,60
ITA	30	1975	frame	0,43
ITA	30	1984	frame	0,24
MK	30	1984	shear walls	0,44
HR	31		r.c.	0,43
HR	31		r.c.	0,35
HR	31		r.c.	0,38
HR	31		r.c.	0,36
SLO	33	1967	r.c.	0,83
MK	33	1970	frame	0,60
MK	33	1970	frame	0,60
MK	33	1970	frame	0,67
MK	33	1970	frame	0,58
MK	33	1970	frame	0,61
MK	33	1980	shear walls	0,85
MK	33	1982	shear walls	0,43
MK	33	1982	shear walls	0,38
MK	33	1982	shear walls	0,40
MK	33	1982	shear walls	0,51
MK	33	1982	shear walls	0,43
MK	33	1982	shear walls	0,33
HR	34		r.c.	0,50
HR	34		r.c.	0,43
HR	34		r.c.	0,45
HR	34		r.c.	0,47
SLO	36	1968	r.c.	0,48
ITA	37	1950	frame	0,44
HR	37		r.c.	0,46
HR	37		r.c.	0,60
HR	37		r.c.	0,40
SLO	39	1975	r.c.	0,59
MK	39	1979	frame	0,69
MK	39	1980	frame	0,72
MK	39	1982	shear walls	0,56
MK	39	1990	frame	0,65
MK	39	2000	frame	0,74
ITA	40	1975	frame	0,56
ITA	40	1975	frame	0,59
HR	41		r.c.	0,93
HR	41		r.c.	0,57
HR	41		r.c.	0,63
HR	41		r.c.	0,57
HR	41		r.c.	0,49
MK	42	1982	shear walls	0,67
MK	42	1988	frame	0,66
MK	42	1988	frame	0,59
SLO	42		r.c.	0,56
HR	44		r.c.	0,76
HR	44		r.c.	0,62
SLO	45	1969	r.c.	0,53
MK	45	1970	shear walls	0,71
MK	45	1971	shear walls	0,76
MK	45	1971	shear walls	0,75
MK	45	1971	shear walls	0,74
HR	48		r.c.	0,66
HR	48		r.c.	0,92
MK	51	1979	frame	0,97
MK	51	1979	frame	1,09
MK	51	1980	shear walls	0,95
HR	54		r.c.	1,36
SLO	57	1971	r.c.	0,83
HR	58		r.c.	0,73
HR	58		r.c.	0,86
HR	58		r.c.	0,80
HR	58		r.c.	0,97
HR	61		r.c.	0,82
HR	61		r.c.	0,86
HR	61		r.c.	0,79
HR	61		r.c.	1,21
HR	61		r.c.	0,99
HR	65		r.c.	0,88
HR	65		r.c.	1,08
HR	65		r.c.	0,97
HR	65		r.c.	0,94
HR	66,8		r.c.	0,92

The empirical frequency estimates from ambient vibration data for RC buildings are very similar to those obtained in other countries, and shows the big difference from technical standards. Among the possible causes of the observed discrepancy, the soil–structure interaction has to be ruled out, because the measurements already include the whole soil-building system. Another reason may be the design of the old buildings without anti-seismic rules that behave differently than expected by the code because the stiffness of the infills overwhelms the poor quality of the frame. The fundamental period of the 65 reinforced concrete surveyed building are shown in the Table 6.11.

***Table 6.11** Periods of reinforce concrete buildings, Gallipoli at all 2008*

Town	Building address	Age	Type	Height (m)	T (s)
Senigallia	Mercantini	1970	r.c.	3	0,20
Senigallia	Venezia	1950	r.c.	3	0,12
Senigallia	Capannone	1980	r.c.	6	0,23
Senigallia	Rovereto	1980	r.c.	6	0,17
Senigallia	Podesti	1950	r.c.	9	0,19
Senigallia	Bologna	1970	r.c.	12	0,23
Senigallia	Celafonia	1970	r.c.	12	0,27
Potenza	Firenze 44	1960	r.c.	14	0,33
Potenza	Firenze 41	1960	r.c.	15	0,24
Potenza	Firenze 55	1960	r.c.	15	0,22
Potenza	Oscar Romeo 7	1990	r.c.	15	0,33
Potenza	Cagliari	1960	r.c.	15	0,26
Potenza	Milano 57	1960	r.c.	15	0,27
Melfi	ATER B2	1970	r.c.	18	0,25
Potenza	Consolini 27	1990	r.c.	18	0,3
Potenza	Di Giura 247	1970	r.c.	18	0,26
Potenza	Gandhi 52	1990	r.c.	18	0,3
Potenza	Giovanni XXIII 28	1990	r.c.	18	0,34
Potenza	Giovanni XXIII 52	1990	r.c.	18	0,36
Potenza	Livorno 115	1970	r.c.	18	0,22
Potenza	Livorno 77	1970	r.c.	18	0,25
Senigallia	Baroccio	1970	r.c.	18	0,27
Senigallia	Hotel Excelsior	1970	r.c.	18	0,29
Potenza	Torino 80	1960	r.c.	19	0,29
Potenza	Appia 30	1970	r.c.	20	0,32
Potenza	Di Giura 6	1970	r.c.	20	0,21
Potenza	De Coubertin	1990	r.c.	21	0,29
Potenza	Gandhi 9	1990	r.c.	21	0,34
Potenza	San Remo 73	1970	r.c.	21	0,21
Potenza	Oleandri Murate	1970	r.c.	21	0,36
Potenza	Pienza 3	1970	r.c.	21	0,34
Potenza	Pienza 54	1970	r.c.	21	0,32
Potenza	Bertazzoni 24	1970	r.c.	22	0,29
Potenza	Livorno 58	1970	r.c.	22	0,24
Potenza	Nicola Sole 2	1960	r.c.	22	0,36
Potenza	Bertazzoni 1	1970	r.c.	23	0,31
Potenza	Bertazzoni 2	1970	r.c.	23	0,29
Potenza	Livorno 35	1970	r.c.	23	0,33
Potenza	Livorno 31	1970	r.c.	23	0,28
Potenza	XVIII Agosto	1960	r.c.	23	0,48
Potenza	Consolini 52	1990	r.c.	24	0,32
Potenza	Oscar Romero 13	1990	r.c.	24	0,32
Potenza	San Remo 154	1970	r.c.	24	0,22
Potenza	San Remo 67	1970	r.c.	24	0,21
Senigallia	Gerani	1980	r.c.	24	0,38
Potenza	Dante Benz	1970	r.c.	24	0,47
Potenza	Mazzini 51	1960	r.c.	24	0,43
Potenza	Nicola Sole 6	1960	r.c.	24	0,42
Potenza	Nitti	1970	r.c.	24	0,37
Potenza	Grippo 2	1970	r.c.	25	0,4
Potenza	Sofia 28	1970	r.c.	25	0,56
Potenza	Grippo 1	1970	r.c.	25	0,43
Potenza	Livorno 131	1970	r.c.	26	0,22
Potenza	Baracca	1970	r.c.	26	0,42
Potenza	Bratislava 75	1970	r.c.	27	0,42
Potenza	Vilnius 61	1970	r.c.	27	0,43
Potenza	Zagabria	1970	r.c.	27	0,5
Potenza	Di Giura 209	1970	r.c.	29	0,26
Potenza	Due Torri	1960	r.c.	29	0,5
Potenza	Ordina Valla 3	1980	r.c.	30	0,24
Potenza	Filzi	1970	r.c.	30	0,43
Potenza	Mazzini 57	1960	r.c.	30	0,45
Potenza	IV Novembre	1950	r.c.	37	0,44
Potenza	Bratislava 69	1970	r.c.	40	0,59
Potenza	Vilnius 53	1970	r.c.	40	0,56

The ECDFs (Empirical cumulative distribution function) of pseudo-damping obtained with NonPaDAn along the longitudinal direction from the strongest earthquake and from noise, were compared (Figure 6.15). As expected, there is a small damping increase in the earthquake with the median damping shifting from about 3% to more than 3.5%. However, the difference between ECDFs is not significant.

Table 6.12 *Comparison between the orthogonal fundamental frequencies obtained applying ambient noise and the average of earthquake recordings for the test building*

Component	Method	Frequency determined from earthquakes (Hz)	Frequency determined from noise (Hz)	var %
Longitudinal	HVSR	3.4	3.7	−8.8
	SSR	3.9	4.1	−5.1
	NonPaDAn	3.7	3.9	−5.4
	HBW	3.8	4.0	−5.3
Transversal	HVSR	3.4	3.5	−2.9
	SSR	3.7	4.0	−8.1
	NonPaDAn	3.6	3.7	−2.8
	HBW	3.7	3.9	−5.4

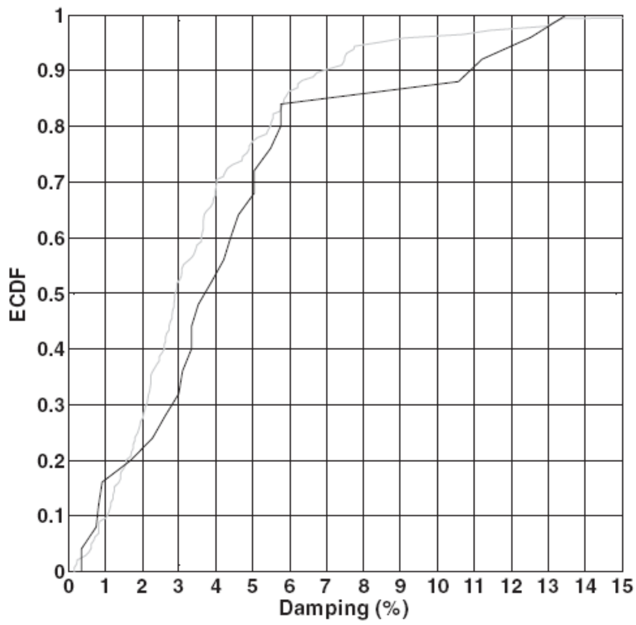

Figure 6.15 *Empirical cumulative distribution function of damping obtained applying the NonPaDAn technique to noise (grey) and to the strongest quake (black) record atop the test building (longitudinal direction).*

6.3 HV field measurements

The environmental seismic noise have been acquired in different verticals inside the building by using two seismographs called 'Tromino' which were synchronized between them. The major measures have an acquisition length of about 20 min and a sampling frequency 128 Hz.

The choice of measure position in the free field was difficult as the area around the hospital is constructed (roads and buildings) and moreover the San Francesco torrent it is located underground the free space outside the building (see yellow circle in the Figure 6.16, right). Ambient noise measures outside the building, have been recorded in the free space found where were not underground parking and cavities (Figure 6.16, left).

The microtremor measurements have been recorded out in two different ways: first leaving one seismograph fixed outside in the free field and moving the other one to the various levels inside the building; second living one seismograph fixed at the top floor and moving the other one to the various levels of the building. In this way, EMA and OMA techniques have been applied to evaluate their use in the estimation of modal parameters. The modal frequencies found through different methods have been compared with one another. The identification of mode shapes has been possible thanks to the use of two synchronized seismographs.

The ambient noise measurements inside the building have been also carried out in to different periods during its construction to evaluate the influence of added mass and rigidity in the response of the structure. As can be seen in the Figure 6.17, the external panels were finished all during the second ambient noise measurements. Also, the internal walls, the pavement layers in all floors and the plans in the terrace were completed, and were all taken into consideration during the calibration of the finite element model.

Figure 6.16 *'Tromino' fixed in the free field (left) and San Francesco torrent (right)*

Figure 6.17 *Photo of the Hospital in two different periods, before and after eight months*

6.3.1 Instrumentation

Three components portable seismographs called Tromino™, by Micromed S.p.a., have been used (see Figure 6.18) to acquire the ambient vibrations in the free field and inside the building. The digital tromometer measure the microtremor in a range of frequencies comprised between 0.1 Hz and 200 Hz. This instruments is composed by three electrodynamics velocimeter channels with high resolution for measurements of ambient seismic microtremor up to ± 1.5 mm/s. The sensors, positioned in three directions (x, y, z), transmit signal to a digital acquisition system with low noise and with a resolution of not less than 23 bits. In addition, an analog channel is predisposed for acquiring data from the integrated GPS receiver (receiver / antenna system) and a radio module which allows the synchronization between different instruments. The ambient vibration measurements acquired have been synchronized with an internal GPS antenna.

Figure 6.18 *Photo of portable seismographs 'Tromino' used*

The sampling frequency of the measures is 128 Hz which allows to define dynamic structure properties up to 64 Hz, sufficient for the RC buildings. The synchronization of two portable seismographs with GPS antenna facilitated the movement to the various levels of the building. The length of the acquisition signal is 20 min.

6.3.2 Measurement position in free field and inside the building

The synchronized ambient noise measurements have been acquired in different nodes of the structure both in plane and in elevation, with a duration of 20 min and a sampling frequency of 128 Hz. Two different distribution in elevation of synchronized environmental seismic noise measurements, have been realized. The first consist on living one seismograph fixed in the free field and moving the other one to the various floor of the building. The second distribution consist on positioning an instrument in the top floor and moving the other one into the building at the same verticals measured before. In the Figure 6.19 and in the Figure 6.20 is shown the measurement position respectively in plan and in elevation.

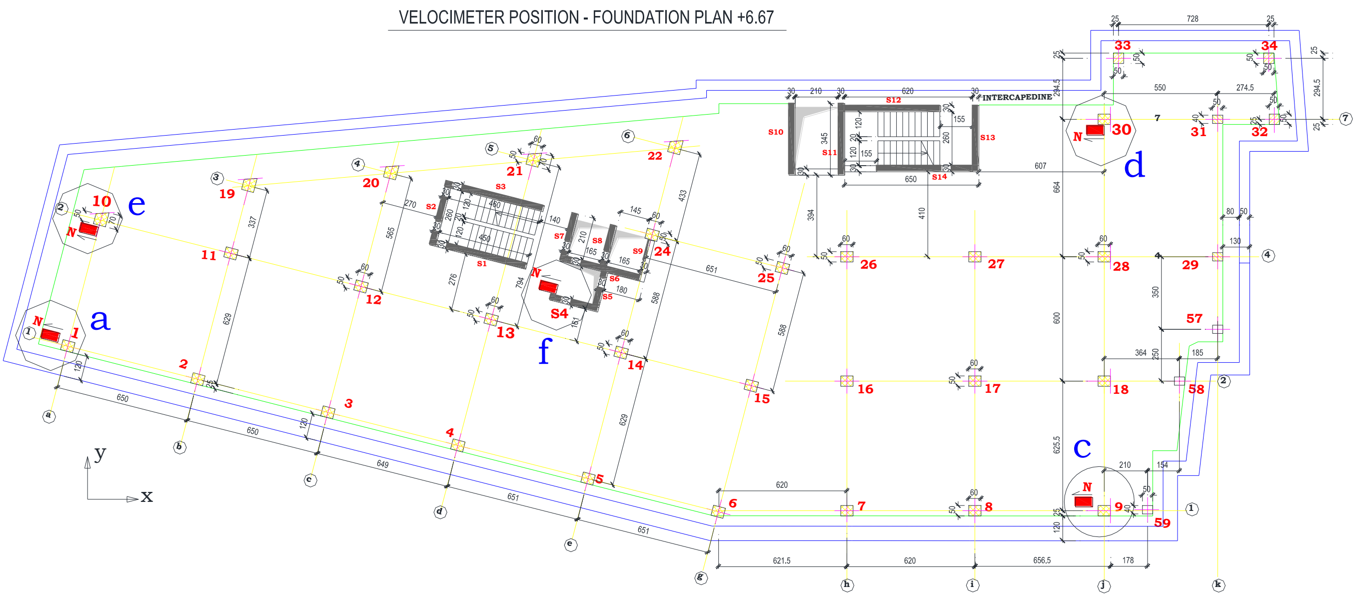

Figure 6.19 *Location of measurements in plan*

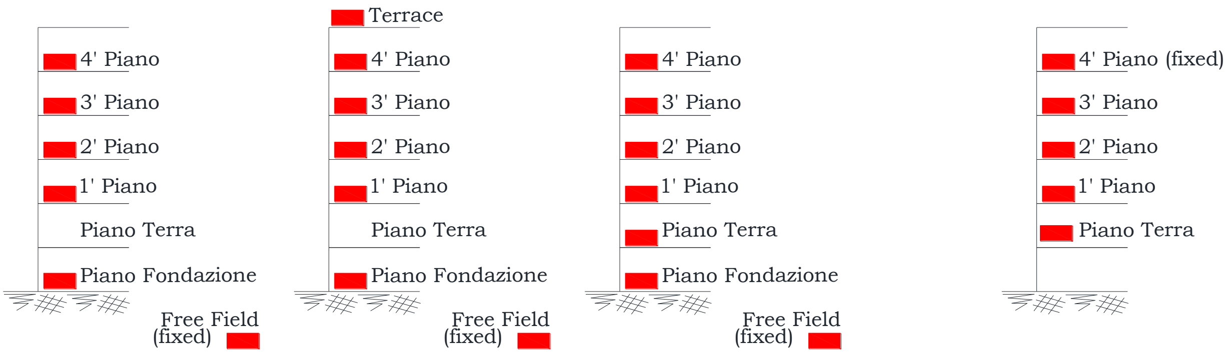

Figure 6.20 Location of measures in elevation: 'Vertical a', 'Vertical f' and 'Vertical d' from the first measures (first three figures) and in all verticals from the second measures (fourth figure)

The measurements in the 'Verticals a', in the 'Vertical d' and in the 'Vertical f' have been recorded by positioning the portable seismographs as described before with both methods. The mode shapes have been estimated utilizing the synchronized couples of measures in elevation by living in the top floor one instrument and moving the other one inside the building to the various floors.

6.4 Structure response due to environmental seismic noise

Modal parameters of the building have been estimated using ambient noise measurements acquired in different verticals of the building once leaving the fixed instrument on the top floor and once in the free field. The script code written in Matlab (see Appendix) has been used to identify the frequency and the mode shapes. The signals in velocity acquired have been first filtered around the interested frequency and then integrated to have the measures in displacement. This process doesn't influence significantly the final results. The frequency spectrum has been calculated by using the Fast Fourier Transform (FFT) or Power Spectral Density (PSD).

The singular value decomposition (SVD) of the cross power spectral density PSD matrix has been performed to identify the natural frequency and the mode shapes of the building. By the help of the peak picking method have been identified the natural frequencies and also the relative mode shapes. Therefore, the peaks in frequency identified first from the spectrum, have been used to estimate the relative mode shapes with peak picking method on the SVD graphic.

The diagram below (Figure 6.21) shows methods and procedures followed to determine the dynamics properties of the structure. Also, the method which analyze separately each synchronized pair of measures (see diagram on the right in the Figure 4.21) have been implemented, at the aim to evaluate the influence in modal parameter results of the non-simultaneously acquisition of measures in all floors.

The ambient vibration measurements have been acquired in two different ways: by leaving one instrument fixed in the free field or in the top floor of the building. Therefore, the use of EMA and OMA methods has been possible to evaluate their applicability in the dynamic structure response. Those algorithm are described in the paragraphs 4.2.2.2 and 4.2.3.2.

Ambient vibration measures have been aligned due to x, y Cartesian System directions of FEM, as some sides of the building have an angle of 14.2° with x direction.

Cross power density or frequency response function of signals have been estimated to define first the peaks in frequency. The singular value decomposition of the cross power density matrix or frequency response function matrix has been computed then to define the modal frequencies and the mode shapes.

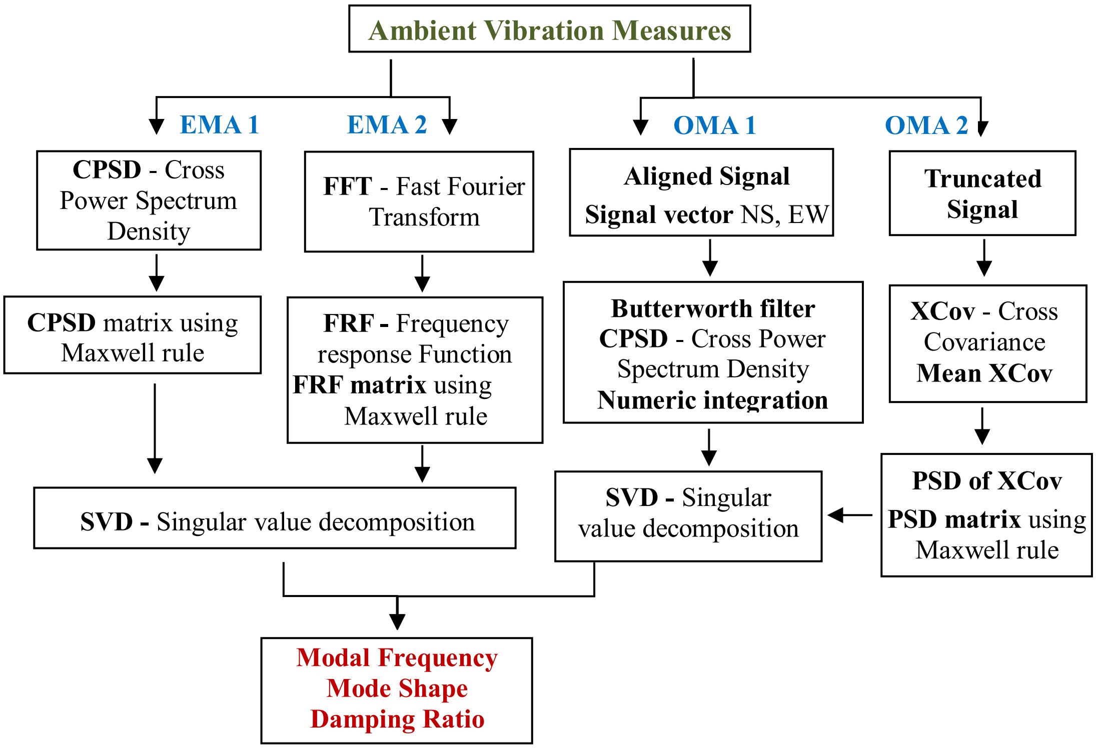

Figure 6.21 *Diagram of methods used*

6.4.1 Results from the first ambient vibration measurements

The structure response results, due to the ambient noise measurements acquired with the fixed portable seismographs in the free field and the other one movable to the various floors of the building, are presented in this paragraph. Those measurements have been acquired in various verticals of the building with a duration of 20 min and a sampling frequency of 128 Hz. These pairs of measurements have been synchronized with one another by GPS signal.

EMA and OMA methods have been used to identify the modal parameter of the structure.

The quality of signals acquired has been checked before starting the analysis. At this aim, the cross covariance graphics and the signals in function of time have been plotted first to check the presence of the noise. Some of signals present noise at the beginning of the acquisition probably caused by the operator during the start process of the acquisition. For example the signal at 'Vertical a' (on the four floor) contain noise so, the first 30 seconds of the signal on the fourth floor and in the free field (the correspondent synchronized measure), have been removed (see Figure 6.22). Furthermore, the frequency content of signals acquired inside the building has been confronted with frequency content of the measure outside in the free field.

The elaboration of measures acquired in three verticals of the building is shown in the sequent figures. The 'FE Model 1' is the calibrated model from the first measures acquired inside the building. The rigidity of external walls has been modeled by frame element dimensioned due to the equivalent connecting rod theory (see paragraph 6.5.1).

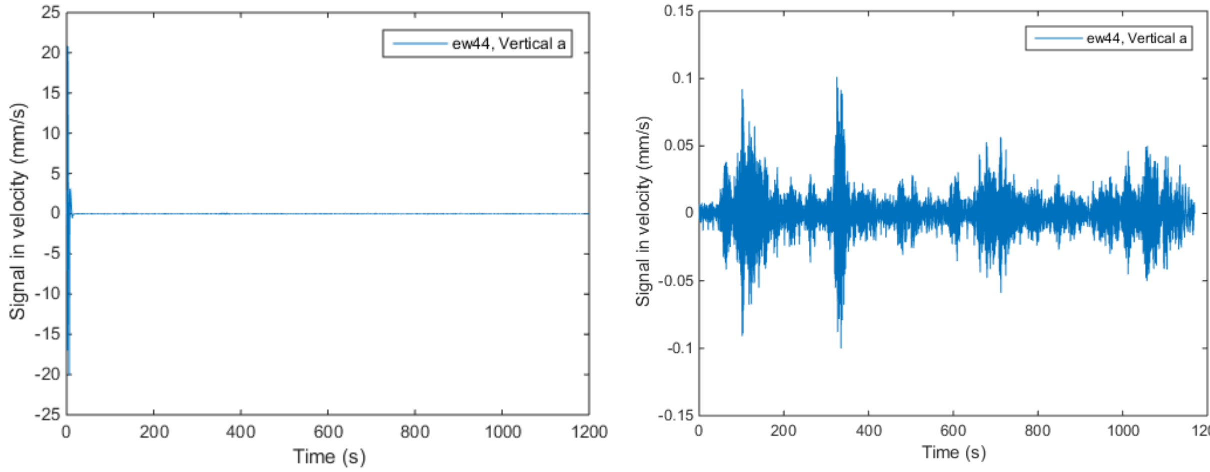

Figure 6.22 *Signal-time graphic with noise on the fourth floor (left), signal without noise at the beginning of the acquisition (right), at 'Vertical a'*

Cross covariance graphics of signals in the 'Vertical a' are shown in the Figure 6.23. Those signals were zoomed to check the symmetry of signals around zero (see Figure 6.24).

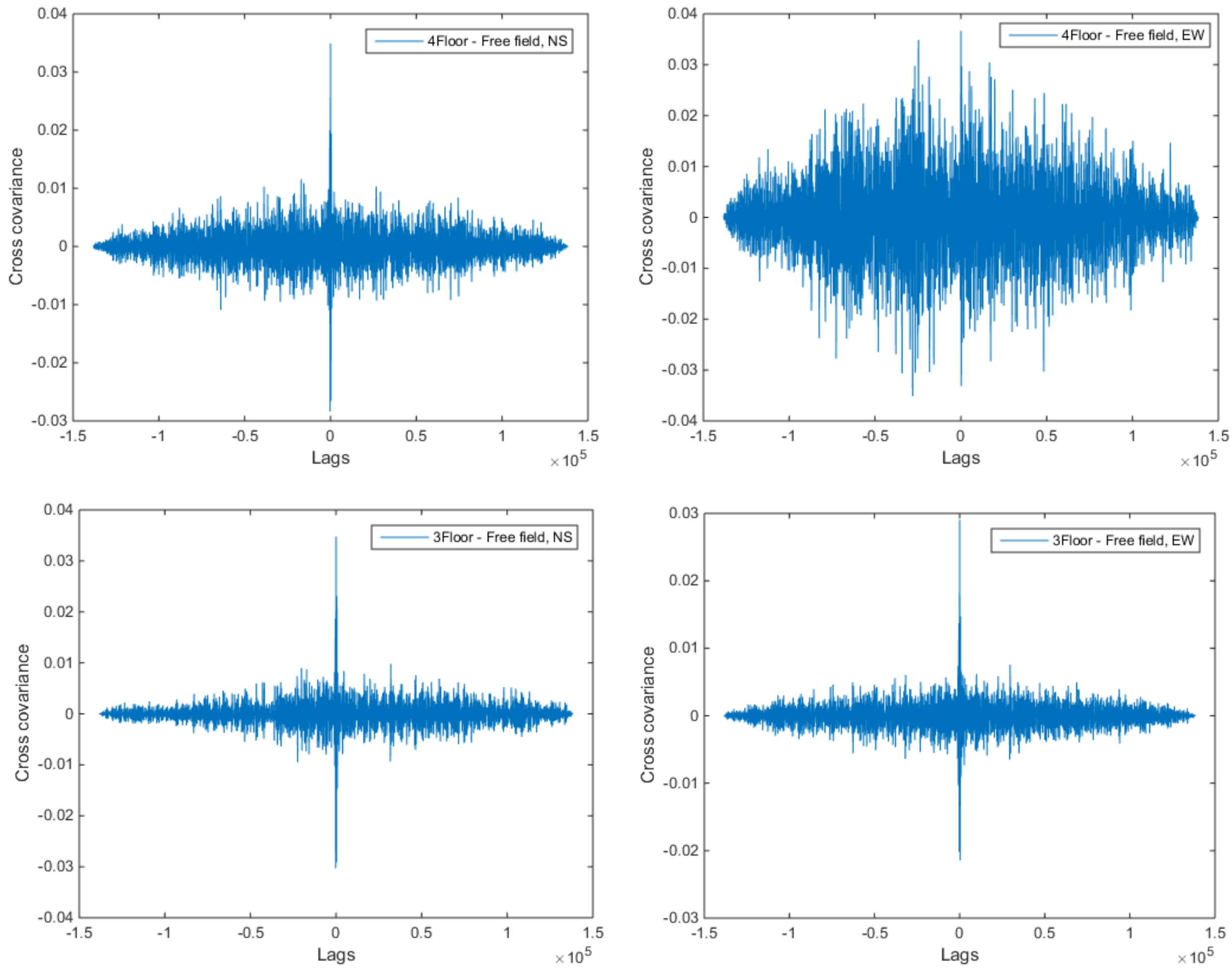

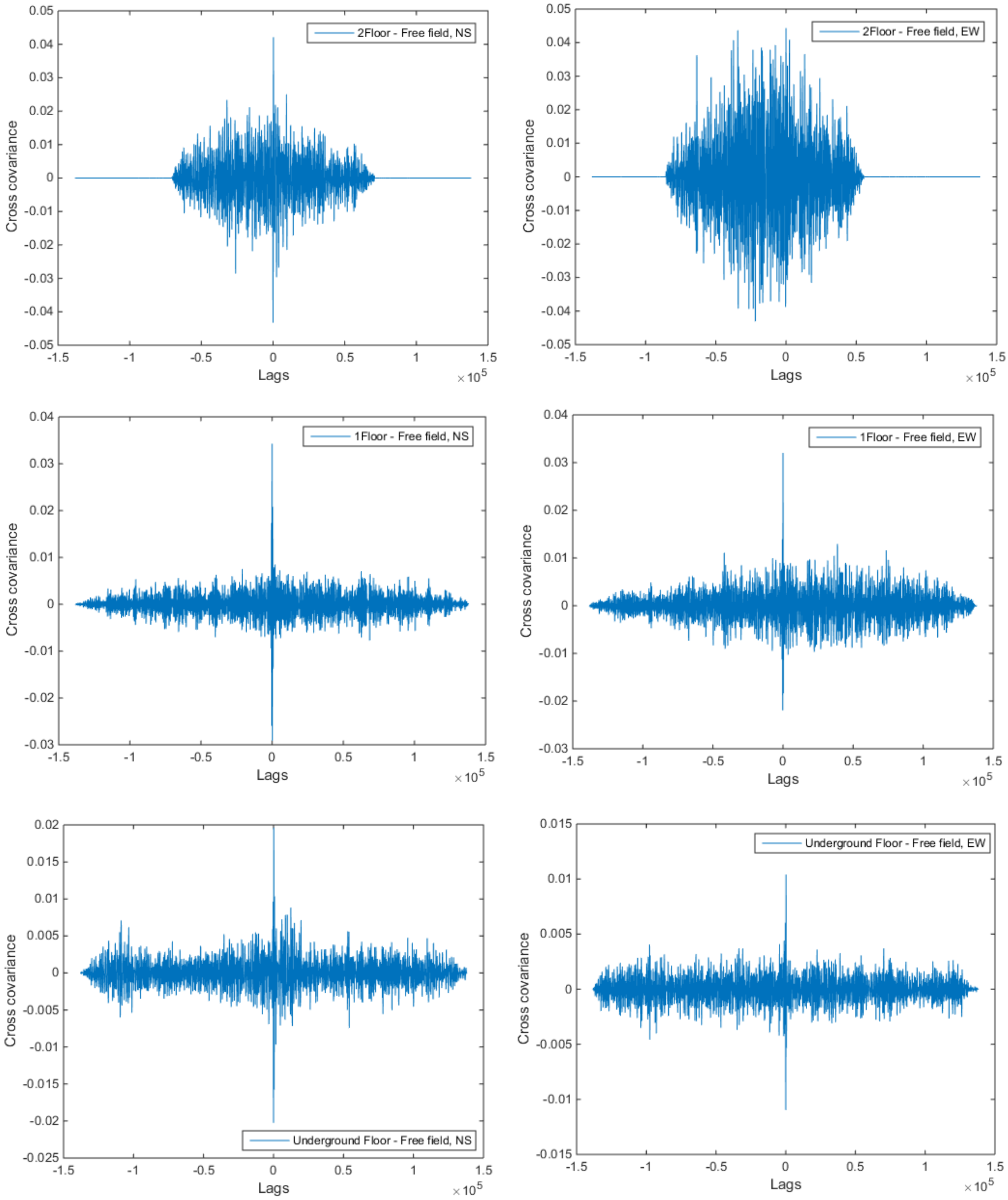

Figure 6.23 *Cross covariance graphics of measures at 'Vertical a' of both components EW and NS*

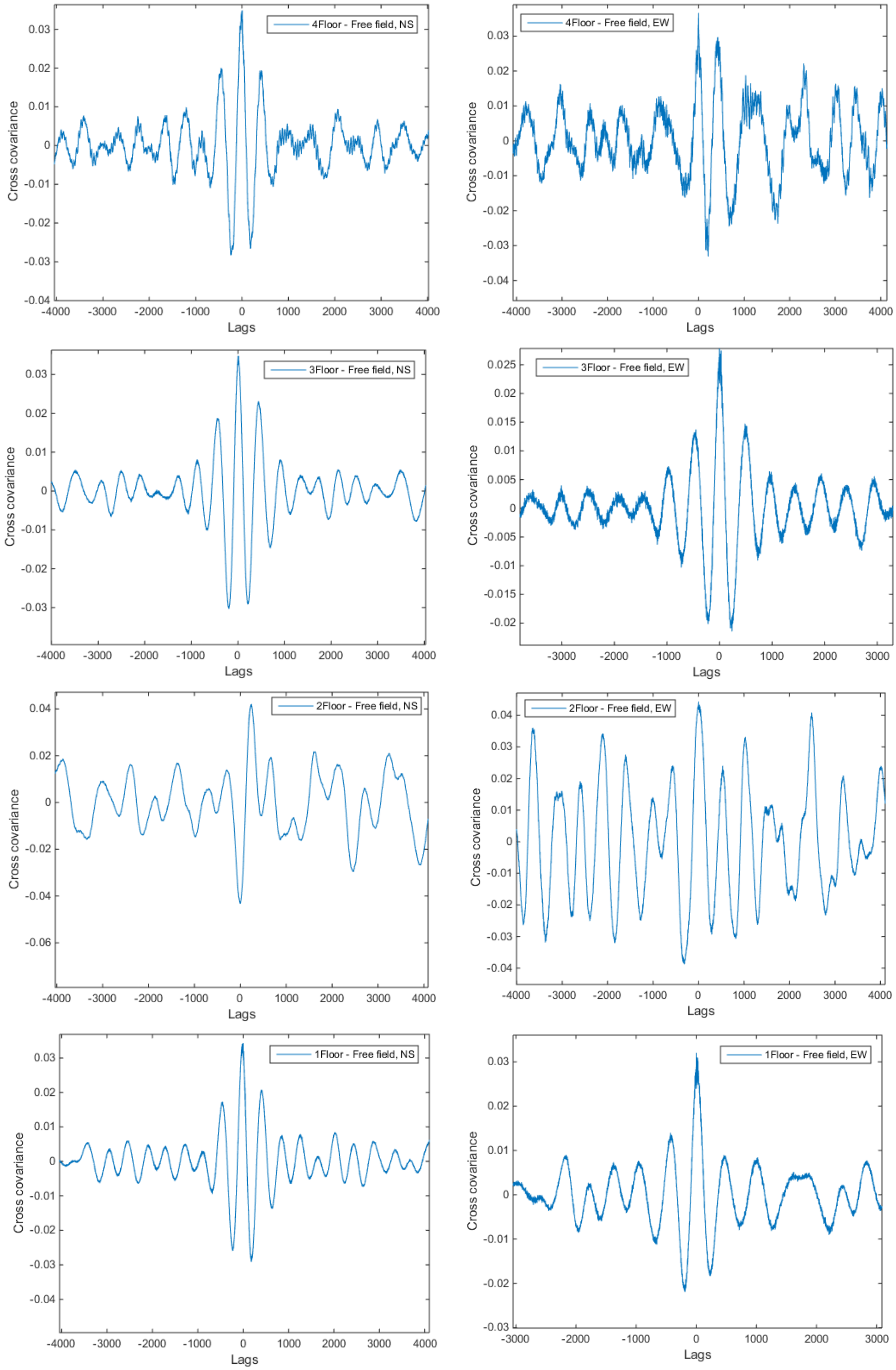
4Floor - Free field, NS
4Floor - Free field, EW
3Floor - Free field, NS
3Floor - Free field, EW
2Floor - Free field, NS
2Floor - Free field, EW
1Floor - Free field, NS
1Floor - Free field, EW
Cross covariance
Lags

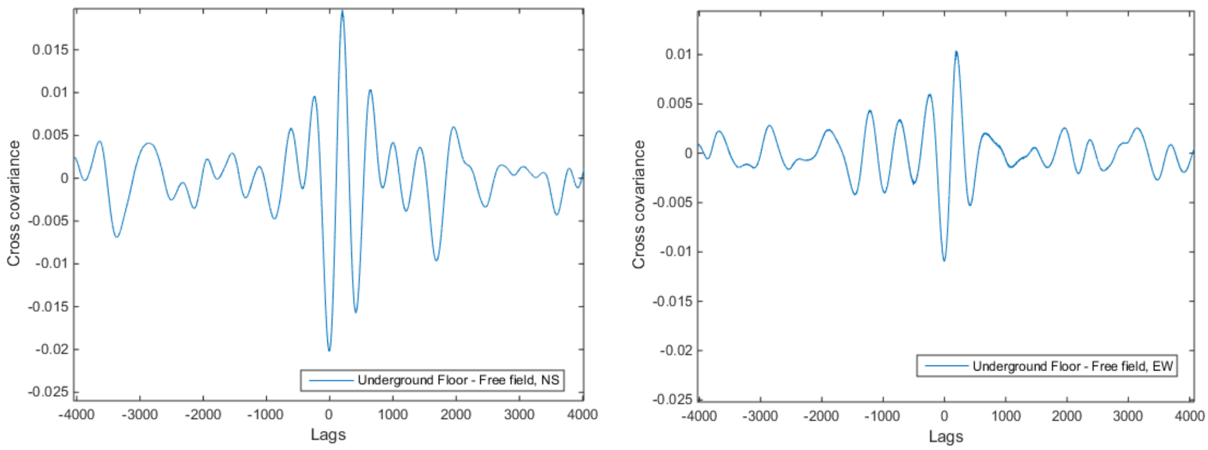

Figure 6.24 *Zoom of the Cross covariance graphics around zero of measures in the 'Vertical a' of both components EW and NS*

Cross covariance graphics and their zoom around zero of signals in the 'Vertical d' are shown respectively in the Figure 6.25 and Figure 6.26. One measure (in the fourth floor) has a problem during the acquisition therefore has e lower length. In this measure were added zeros to have the same length with the other signals.

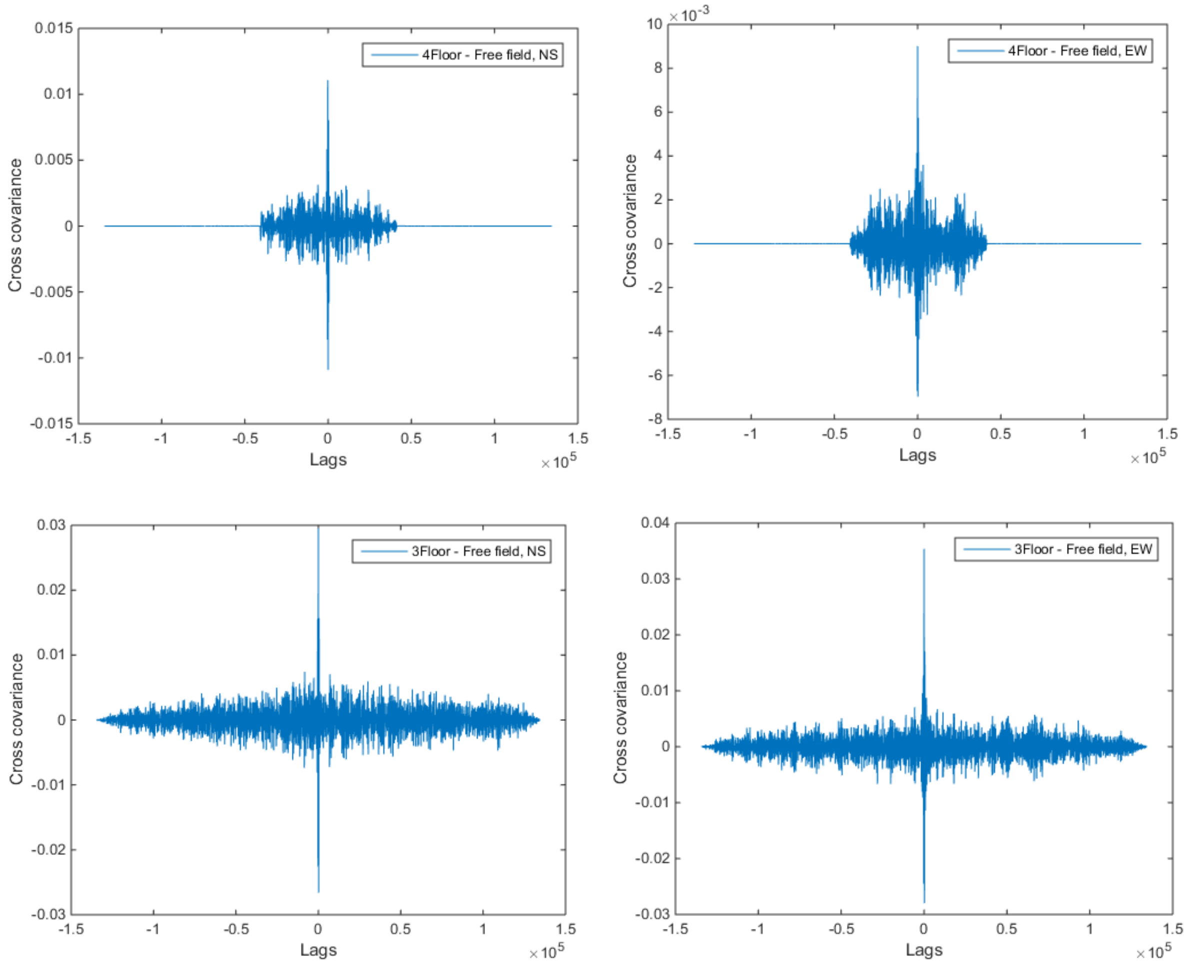

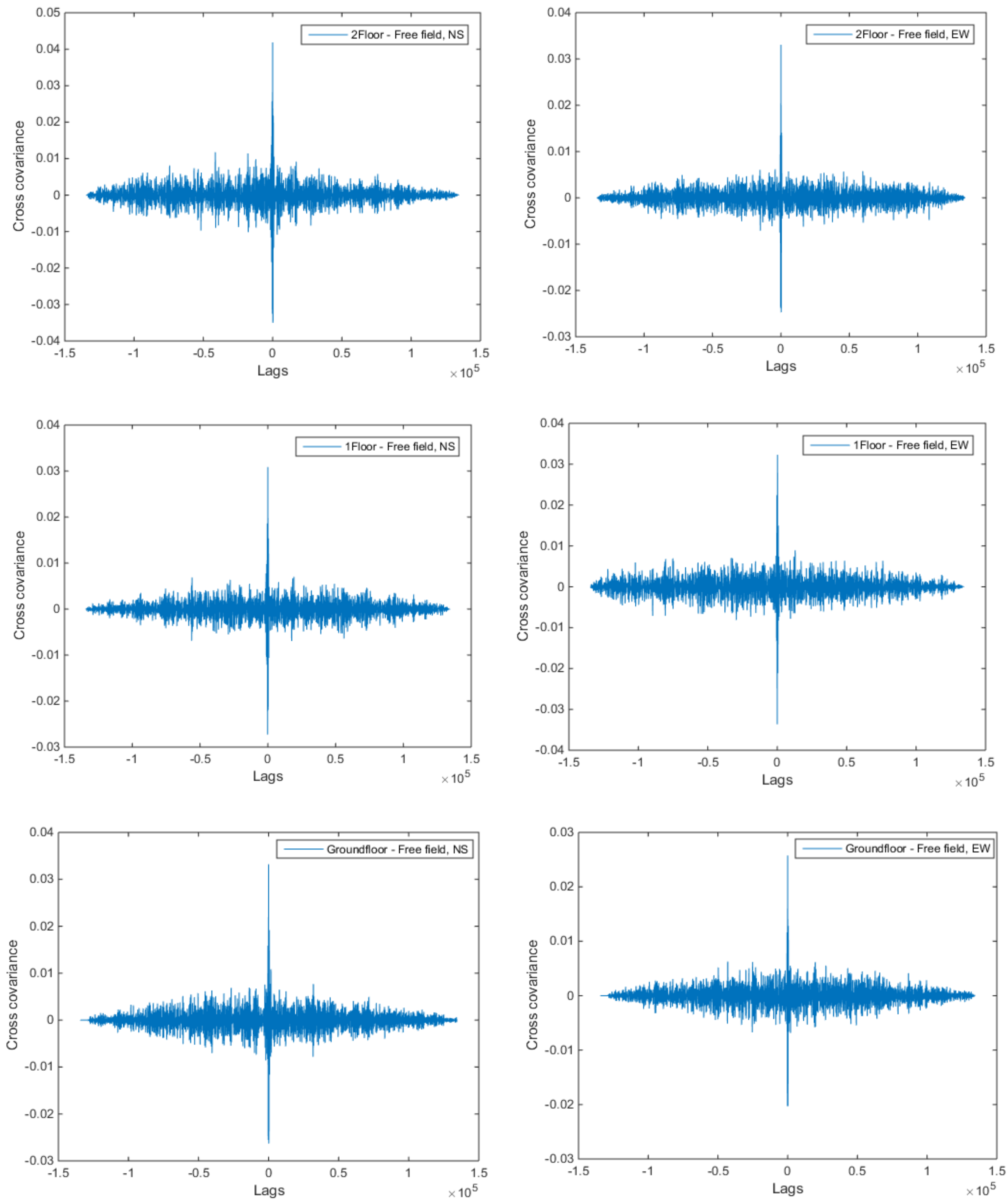

Figure 6.25 *Cross covariance graphics of measures in the 'Vertical d' of both components EW and NS*

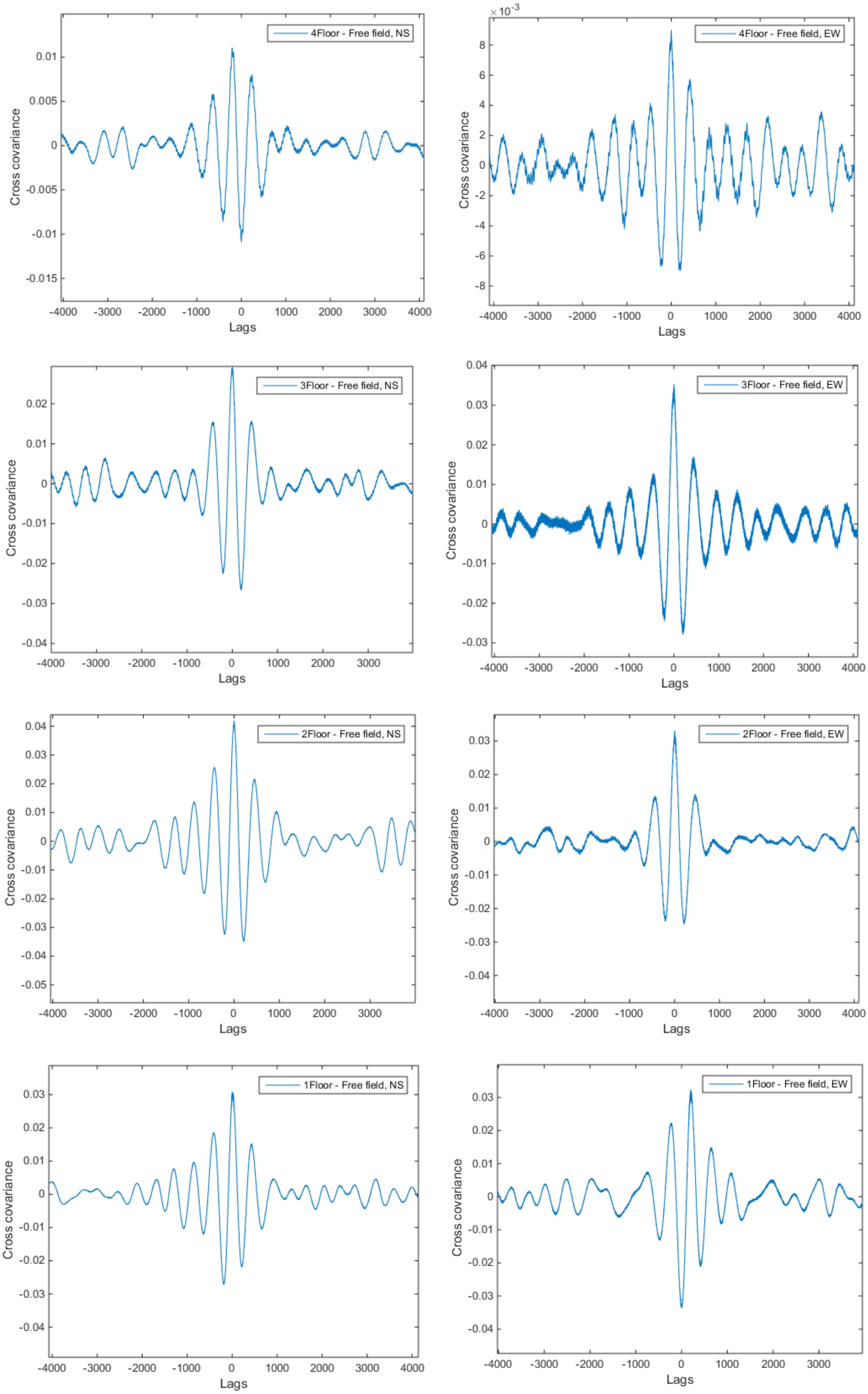
4Floor - Free field, NS
4Floor - Free field, EW
× 10^-3
3Floor - Free field, NS
3Floor - Free field, EW
2Floor - Free field, NS
2Floor - Free field, EW
1Floor - Free field, NS
1Floor - Free field, EW
Cross covariance
Lags

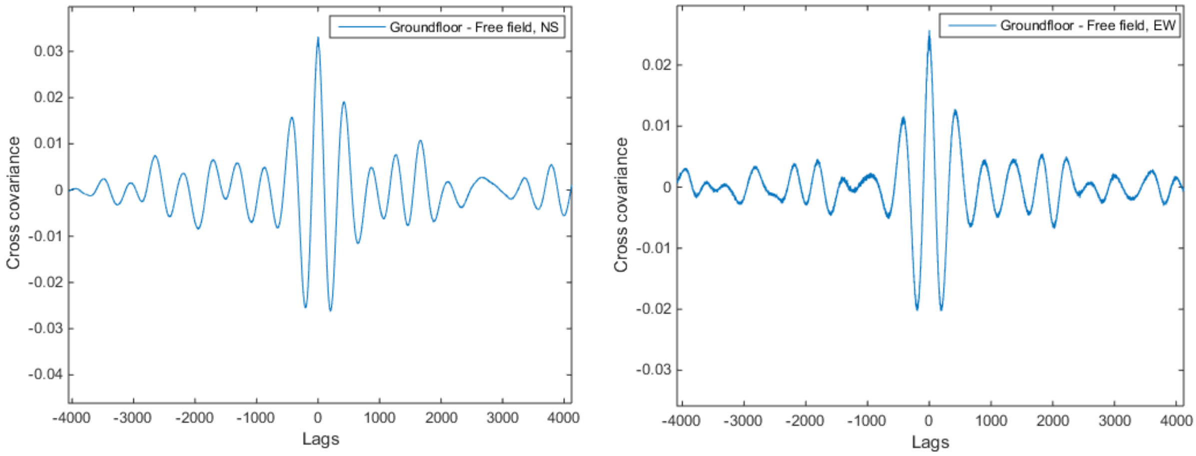

Figure 6.26 *Zoom of the Cross covariance graphics around zero of measures in the 'Vertical d' of both components EW and NS*

The cross covariance graphics and their zoom around zero of signals in the 'Vertical f' are shown respectively in the Figure 6.27 and Figure 6.28.

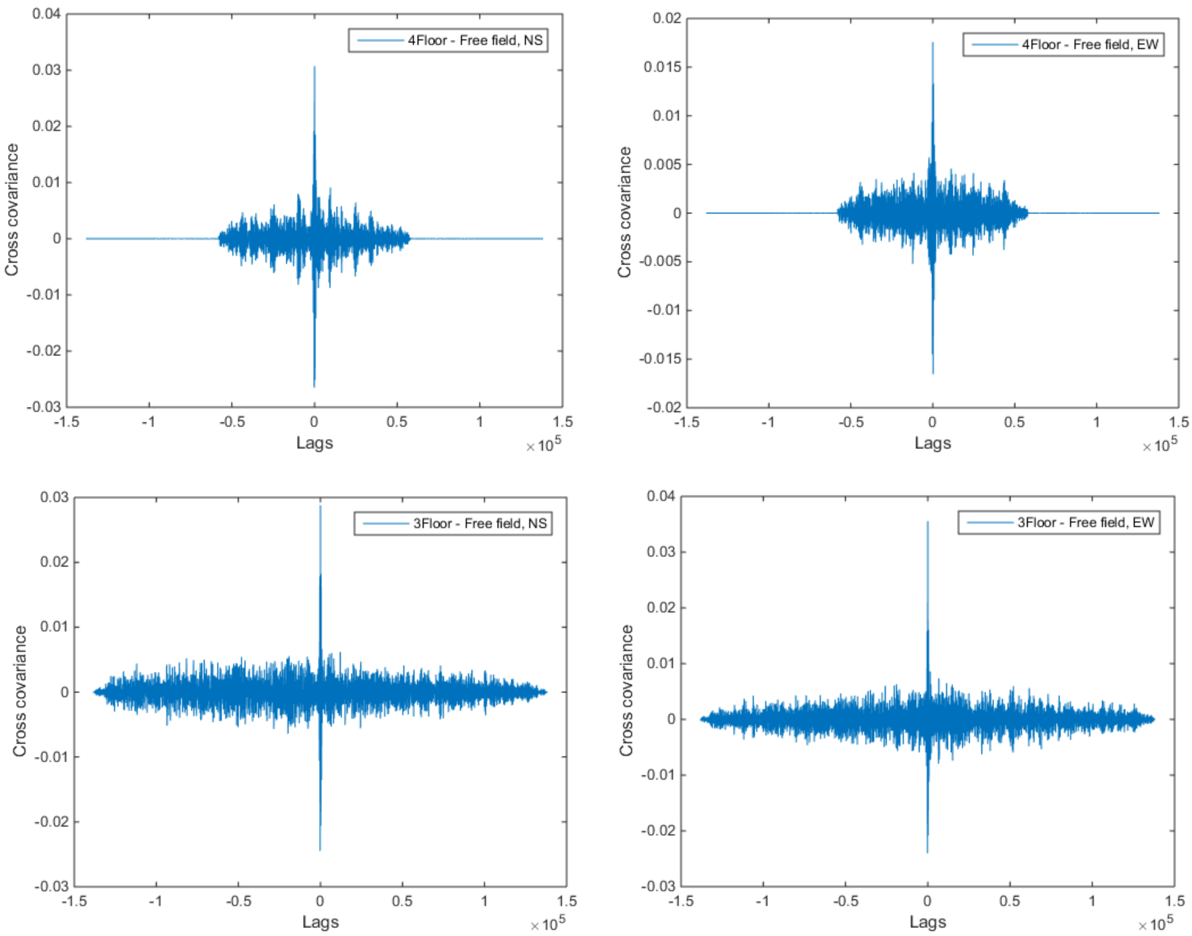

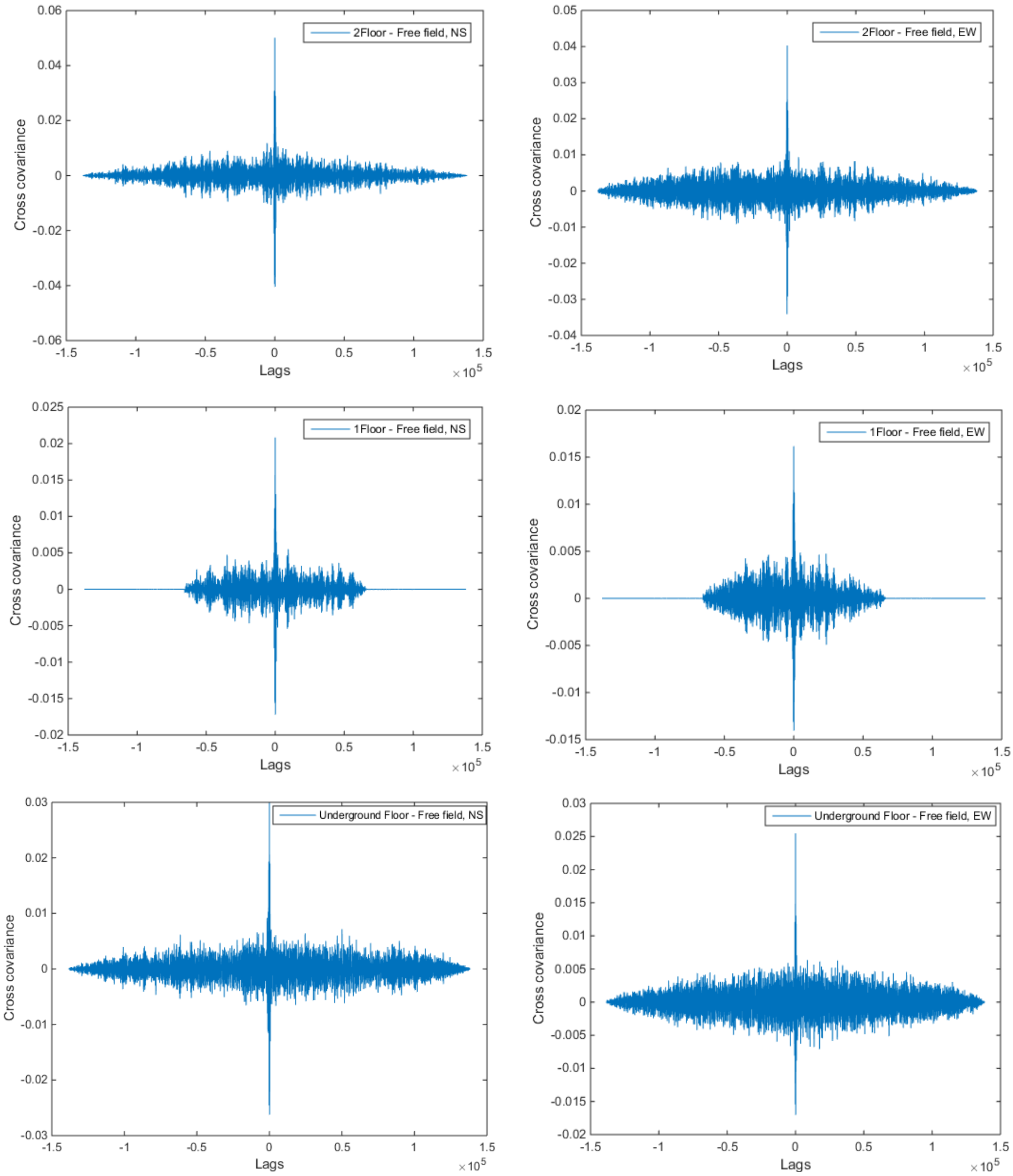

Figure 6.27 *Cross covariance graphics of measures in the 'Vertical f' of both components EW and NS*

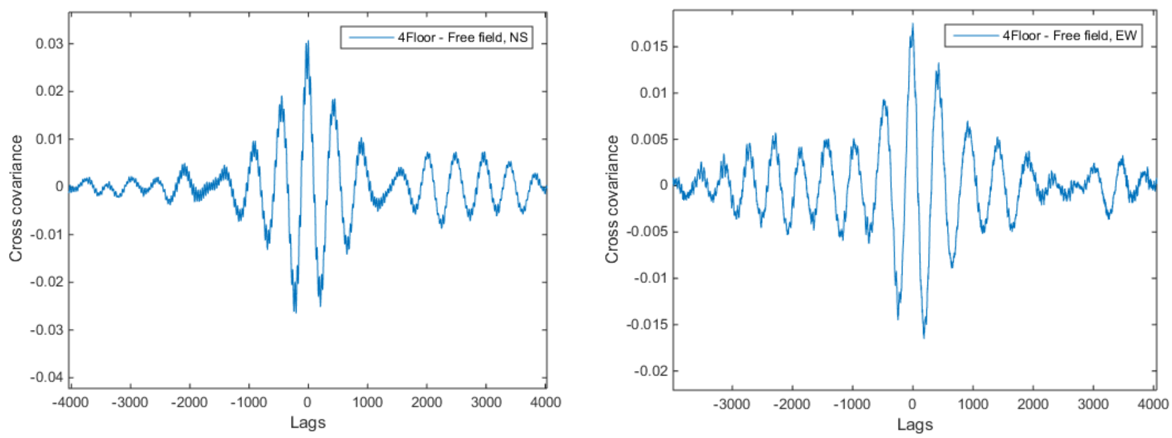

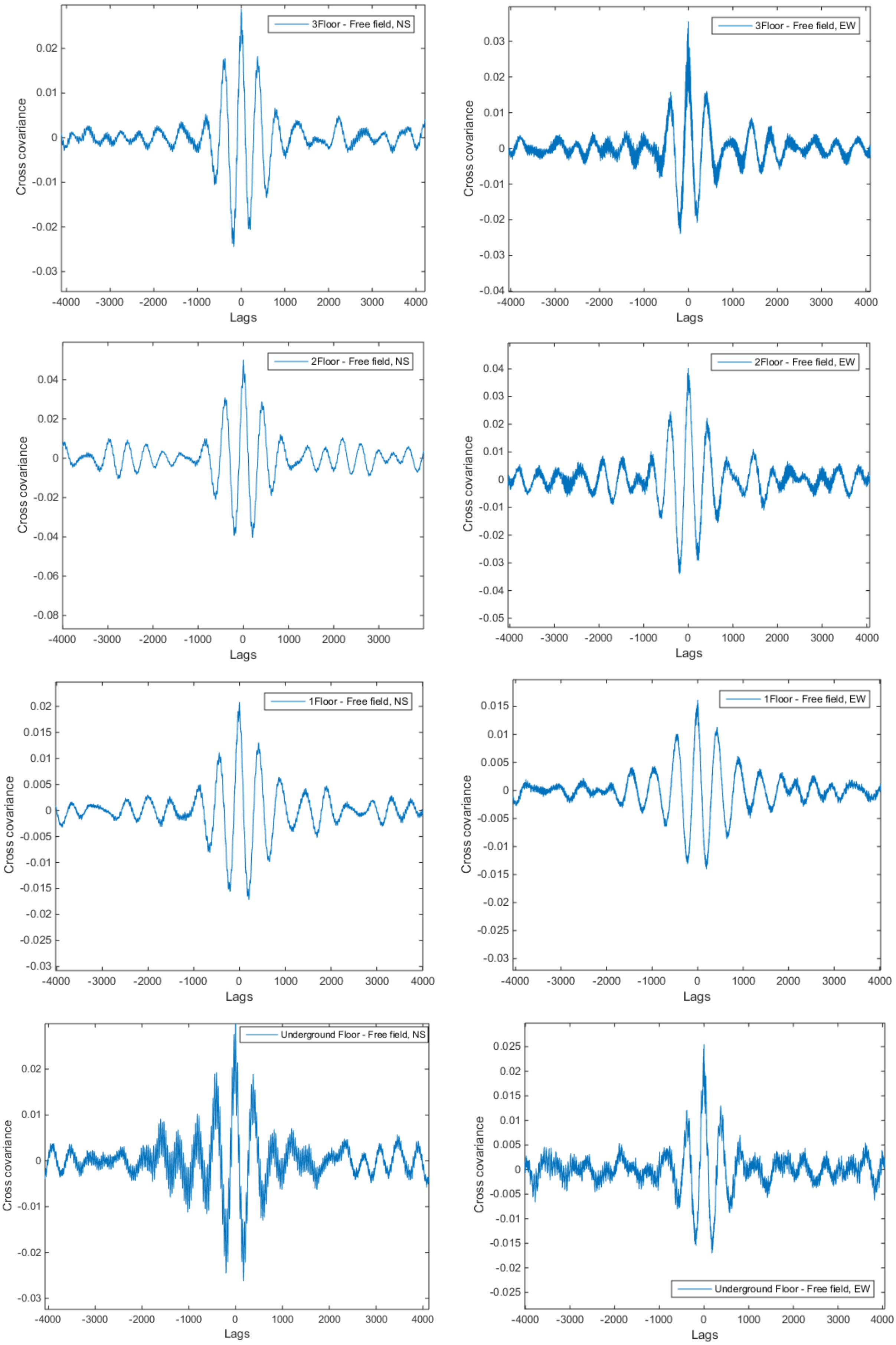

Figure 6.28 *Zoom of the Cross covariance graphics around zero of measures in the 'Vertical f' of both components EW and NS*

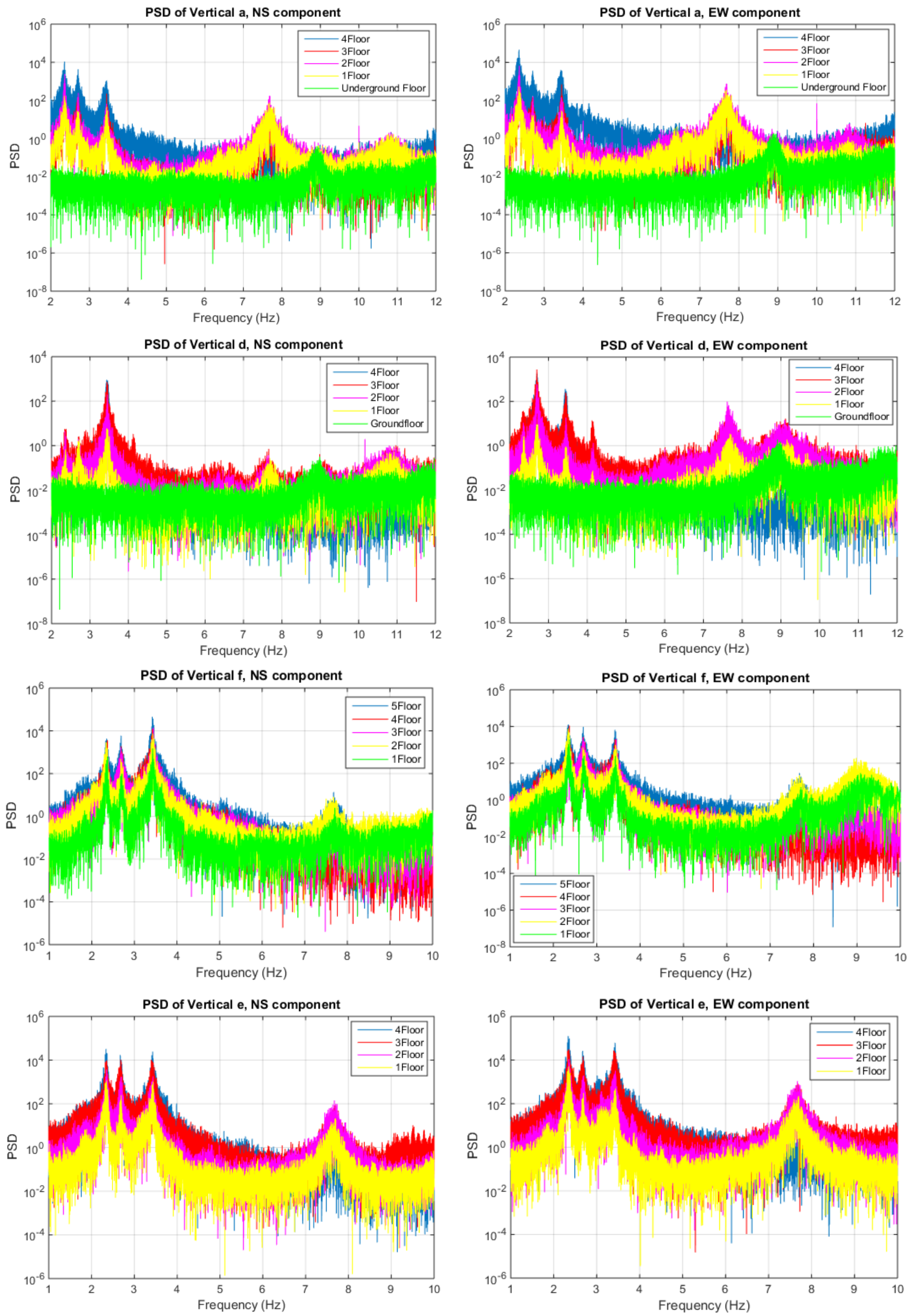

Figure 6.29 *PSD-frequency graphics of measures in some verticals of the building*

The spectrum in frequency of measures in verticals and in both direction EW and NS are shown in the Figure 6.29. The amplitude of the spectrum in the frequency peaks of the first mode shapes decrease when passing from the top floor to the ground floor measures. Furthermore, we can see from the spectrum that the peaks in amplitude have different frequency value for diverse verticals. The measure in 'Vertical a', 'Vertical f' and in 'Vertical e' has a peak amplitude at 2.34 Hz while the measures in the 'Vertical d' at 2.71Hz.

The peak in frequency for all verticals referred to spectrum graphics are presented in the Table 6.13. The first three modal frequency, present in all verticals, are respectively at 2.3 Hz, 2.7 Hz and 3.4 Hz which corresponds to the modal frequency of the first three mode shapes.

Table 6.13 *Frequency values from PSD spectrum and SVD graphics*

Frequency (Hz)	Vertical a			Vertical d			Vertical f			Vertical e		
	Spectrum		SVD	Spectrum		SVD	Spectrum		SVD	Spectrum		SVD
	ns	ew		ns	ew		ns	ew		ns	ew	
Mode 1	**2,36**	**2,36**	**2,35**	**2,35**	**2,35**	**2,33**	**2,35**	**2,34**	**2,34**	**2,34**	**2,34**	**2,35**
Mode 2	**2,71**	**2,71**	**2,70**	**2,70**	**2,7**	**2,71**	**2,69**	**2,69**	**2,69**	**2,67**	**2,67**	**2,67**
Mode 3	**3,45**	**3,43**	**3,45**	**3,44**	**3,43**	**3,44**	**3,42**	**3,42**	**3,43**	**3,43**	**3,43**	**3,41**
Mode 4	7,69	7,68	7,68	7,66	7,61	7,61	7,68	7,68	7,68	7,67	7,67	7,68

blue - first peak in amplitude; red - second peak in amplitude; black - third peak in amplitude.

Graphics of singular value decomposition are show in the Figure 6.30.

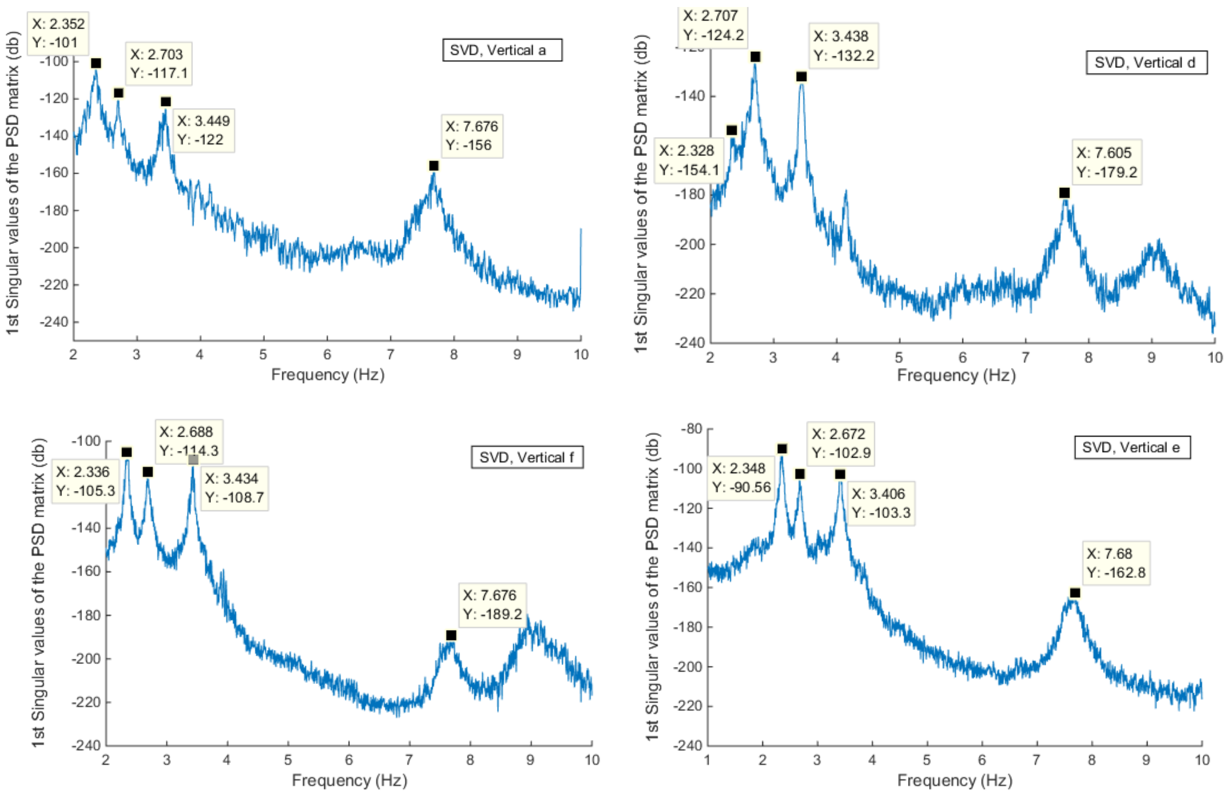

Figure 6.30 *Graphics of Singular Value Decomposition of PSD matrix for 'Vertical a', 'Vertical d', 'Vertical f' and 'Vertical e'*

The first three mode shapes in the 'Vertical a', 'Vertical d', 'Vertical f' and 'Vertical e' due to OMA1 method and 'FE Model 1', are show in the Figure 6.31, Figure 6.32 and Figure 6.33. 'FE Model 1' is the calibrated FEM from the first ambient noise measures (see paragraph 6.5). As one can see, mode shapes estimated from experimental and theoretical analysis are similar.

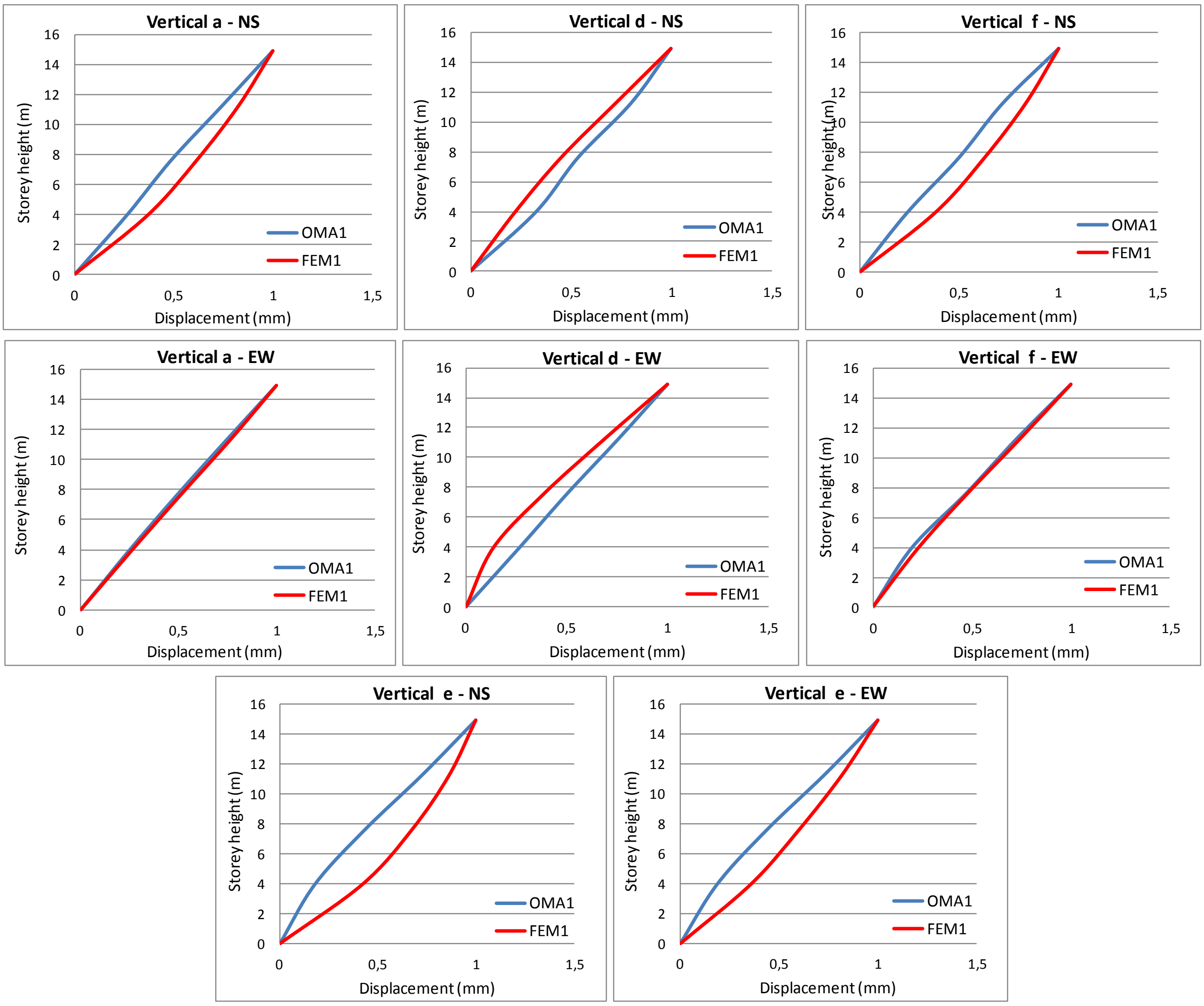

Figure 6.31 *The first mode shape in 'Vertical a', in 'Vertical d', in 'Vertical f' and in 'Vertical e' due to OMA1 method and 'FE Model 1'*

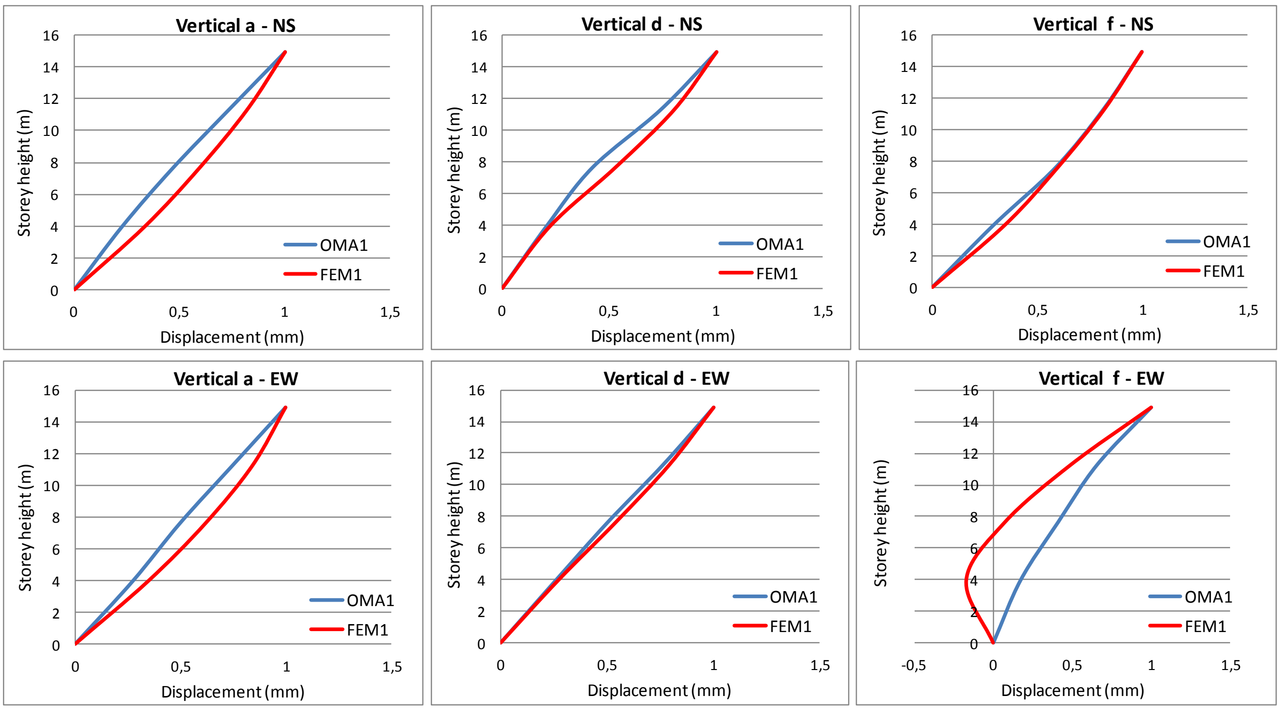

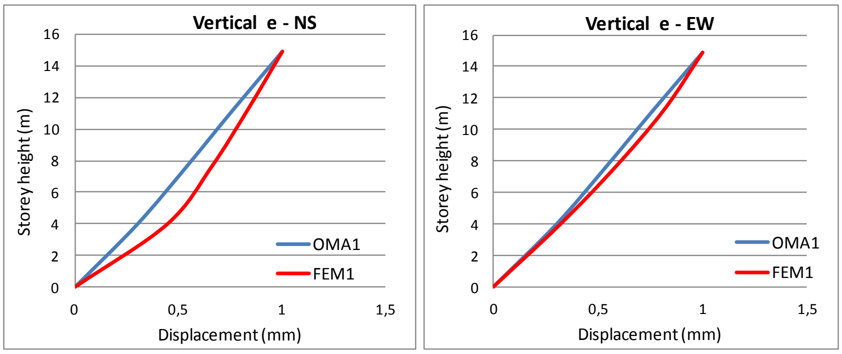

Figure 6.32 *The second mode shape in 'Vertical a', in 'Vertical d', in 'Vertical f' and in 'Vertical e' due to OMA1 method and 'FE Model 1'*

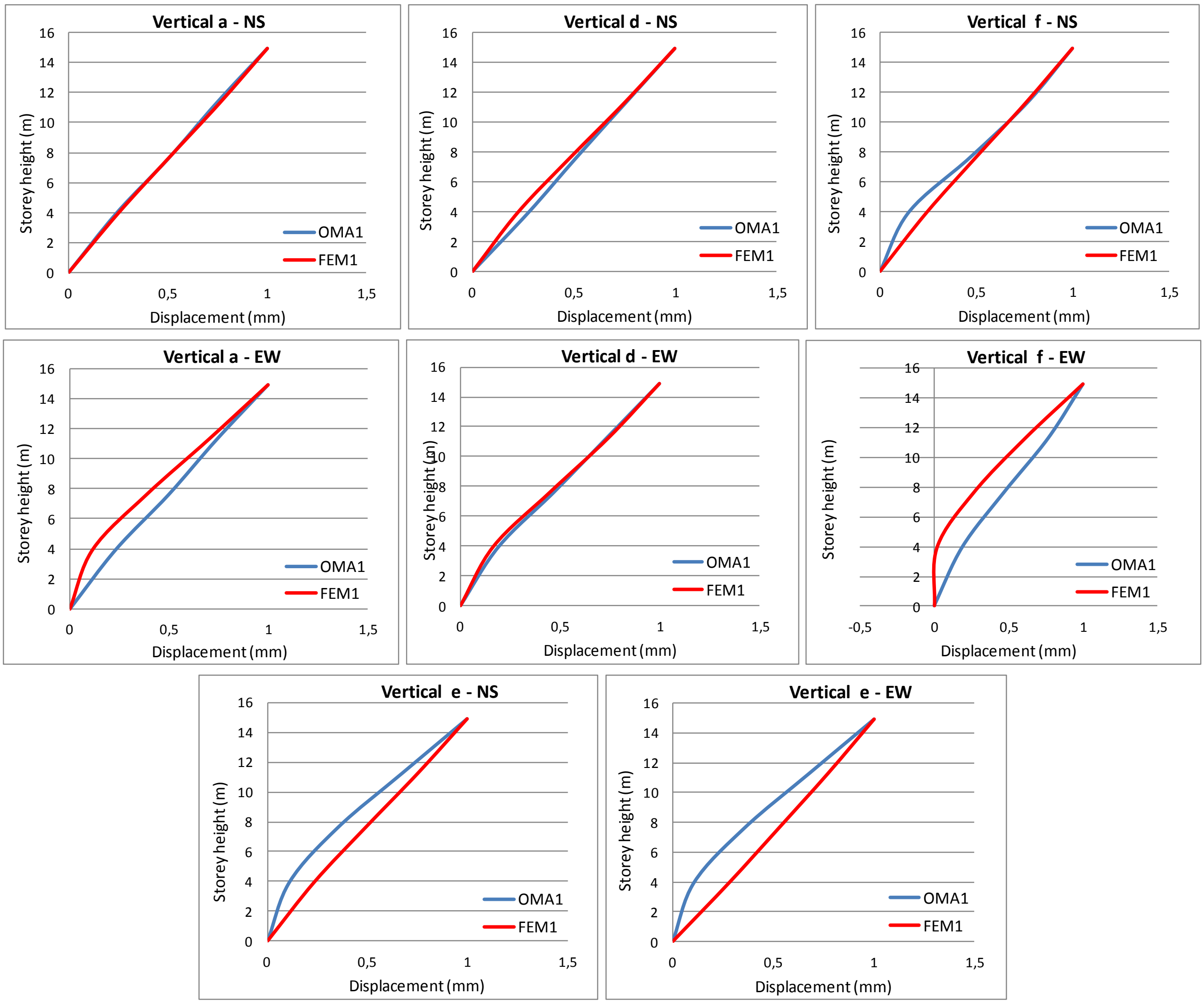

Figure 6.33 *The third mode shape in 'Vertical a', in 'Vertical d', in 'Vertical f' and in 'Vertical e' due to OMA1 method and 'FE Model 1'*

Modal frequencies estimated from different methods, described in the Figure 6.21, are summarized in the Table 6.14. Frequencies values estimated from OMA and EMA methods doesn't differ significantly. As can be seen, the frequency values variation is lower than 1.5% referred to the different methods used for elaboration of the ambient noise measurements. The experimental frequencies estimated (EMA/OMA methods) are different from the theoretical ones (FEM) which leads to the calibration of the initial finite element model ('FE Model 1' or FEM1).

__Table 6.14__ Modal frequencies from different methods in verticals of the building

Frequency (Hz), in 'Vertical a'	OMA		EMA		FE Model 0
	Method OMA1	Method OMA2	Method EMA1	Method EMA2	
Mode 1	2,35	2,38	2,35	2,33	1,16
Mode 2	2,70	2,71	2,69	2,68	1,59
Mode 3	3,45	3,45	3,47	3,45	2,05
Mode 4	7,68	7,70	7,64	7,65	4,56

Frequency (Hz), in 'Vertical d'	OMA		EMA		FE Model 0
	Method OMA1	Method OMA2	Method EMA1	Method EMA2	
Mode 1	2,33	2,37	2,35	-	1,16
Mode 2	2,71	2,72	2,68	2,67	1,59
Mode 3	3,44	3,45	3,47	3,44	2,05
Mode 4	7,61	7,66	7,64	7,62	4,56

Frequency (Hz), in 'Vertical f'	OMA		EMA		FE Model 0
	Method OMA1	Method OMA2	Method EMA1	Method EMA2	
Mode 1	2,34	2,37	2,35	2,36	1,16
Mode 2	2,69	2,69	2,68	2,66	1,59
Mode 3	3,43	3,45	3,46	3,44	2,05
Mode 4	7,68	7,65	7,61	7,62	4,56

Frequency (Hz), in 'Vertical e'	OMA		EMA		FE Model 0
	Method OMA1	Method OMA2	Method EMA1	Method EMA2	
Mode 1	2,35	2,37	2,38	2,39	1,16
Mode 2	2,67	2,69	2,73	2,74	1,59
Mode 3	3,41	3,45	3,48	3,50	2,05
Mode 4	7,68	7,65	7,69	7,71	4,56

The mode shapes in the 'Vertical a' and in the 'Vertical f', referred to EMA2 method and calibrated finite element model 'FE Model 1' (FEM1) by modeling the rigidity of external walls, are shown in the Figure 6.34. Also, in this case the mode shapes are similar.

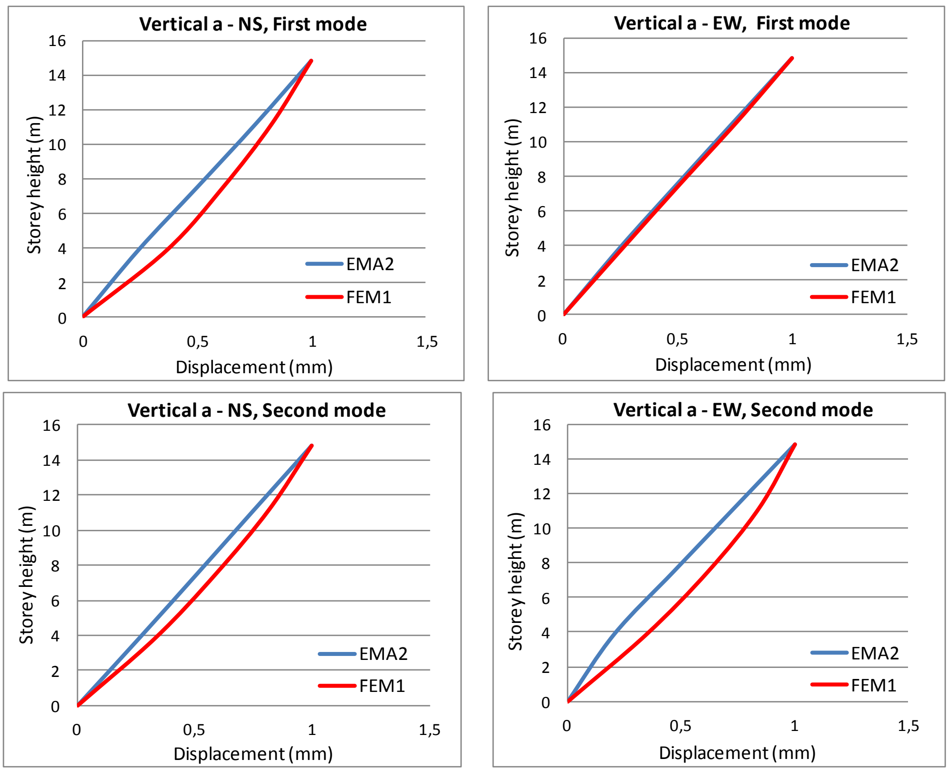

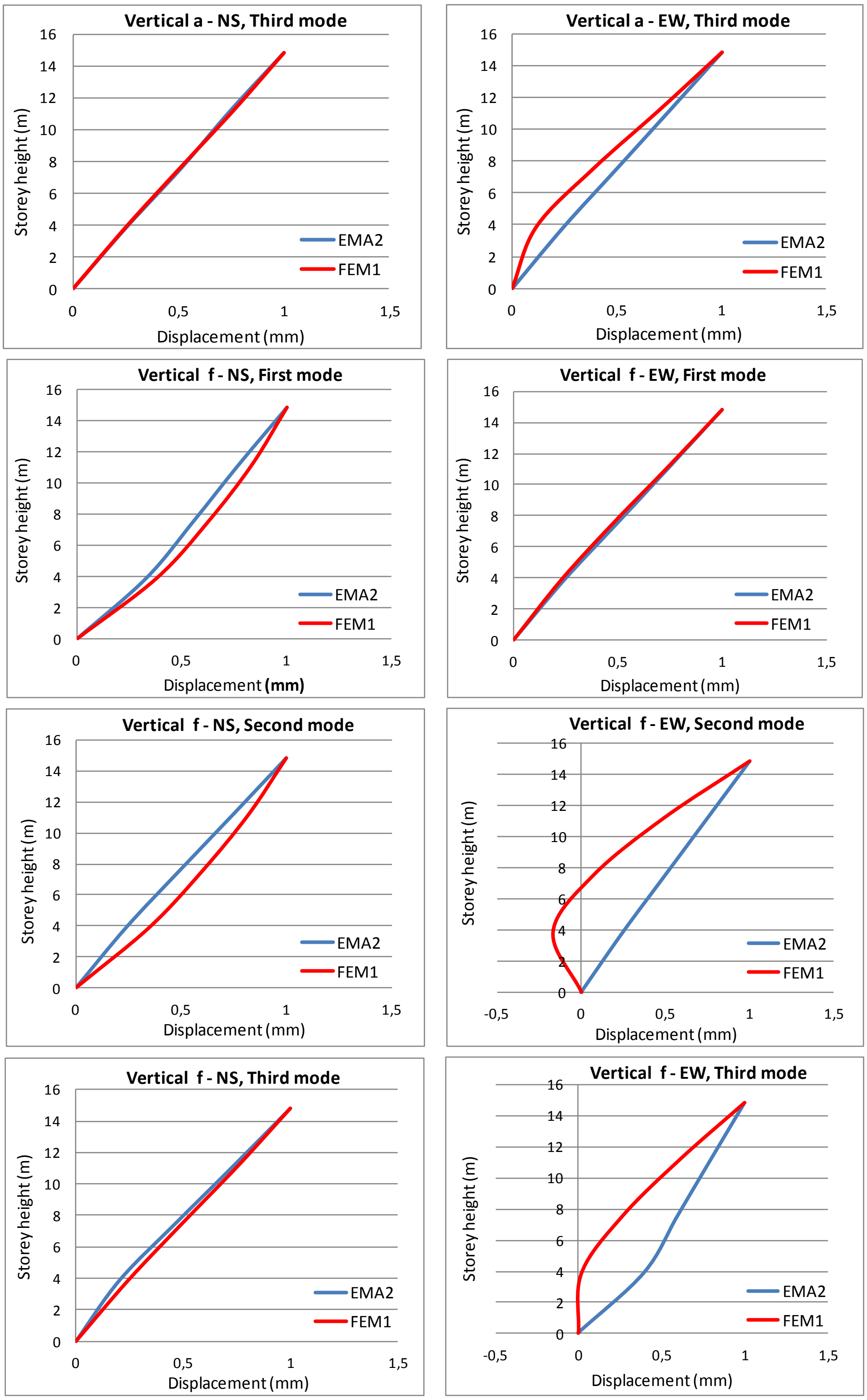

Figure 6.34 *Three mode shapes in the 'Vertical a' and in the 'Vertical f' due to EMA2 method and calibrated 'FE Model 1' model*

The mode shapes identified from the initial 'FE Model 0' (without modeling the external wall panels) and the calibrated finite element model 'FE Model 1', using the first ambient vibration measures acquired in the 'Vertical a', 'Vertical d' and 'Vertical f', are plotted in the Figure 6.35, Figure 6.36 and Figure 6.37. Modeling the rigidity of external walls doesn't influence significantly the mode shapes.

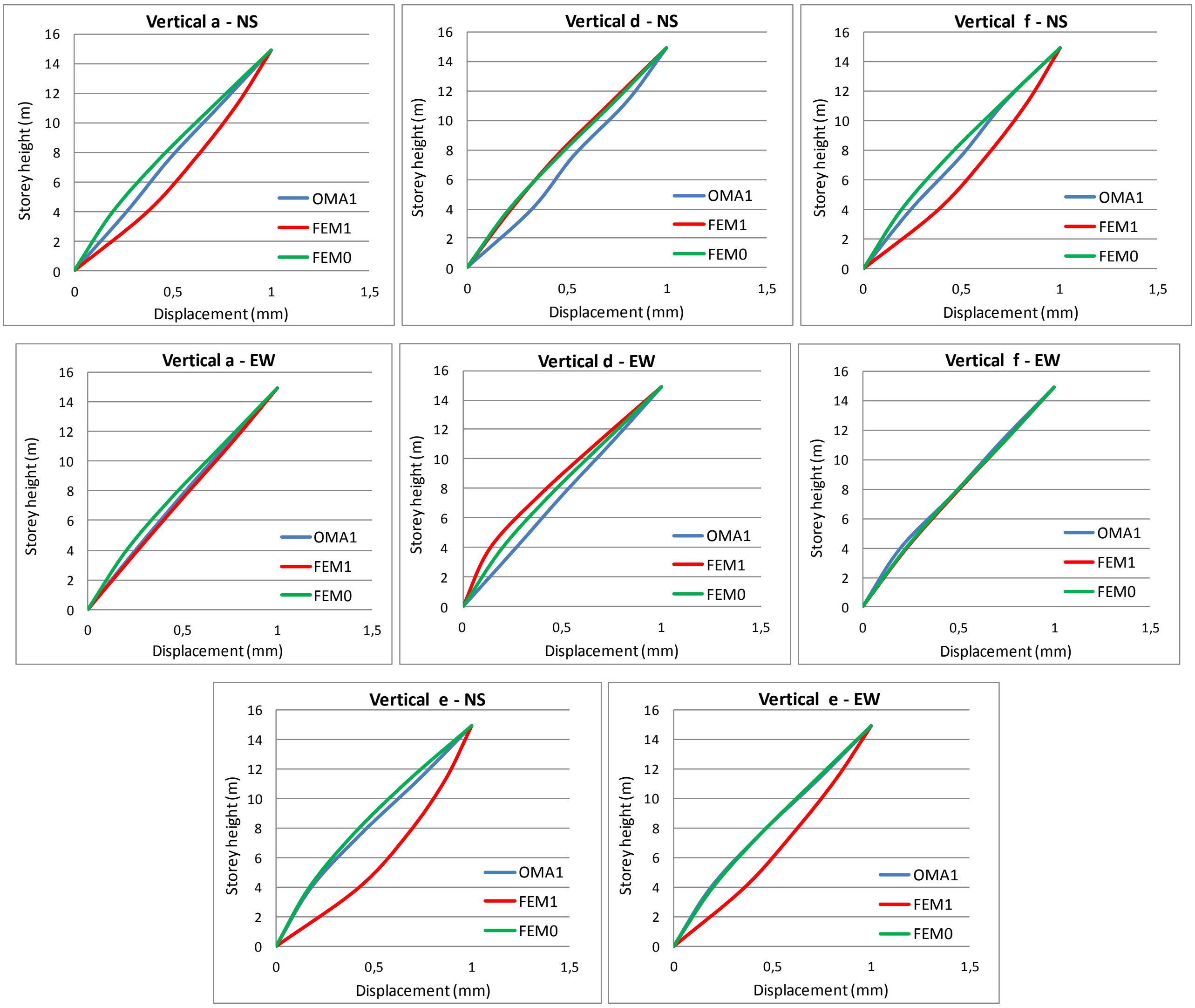

Figure 6.35 *The first mode shape in 'Vertical a', in 'Vertical d', in 'Vertical f' and in 'Vertical e' due to OMA1 method 'FE Model 0' and 'FE Model 1'*

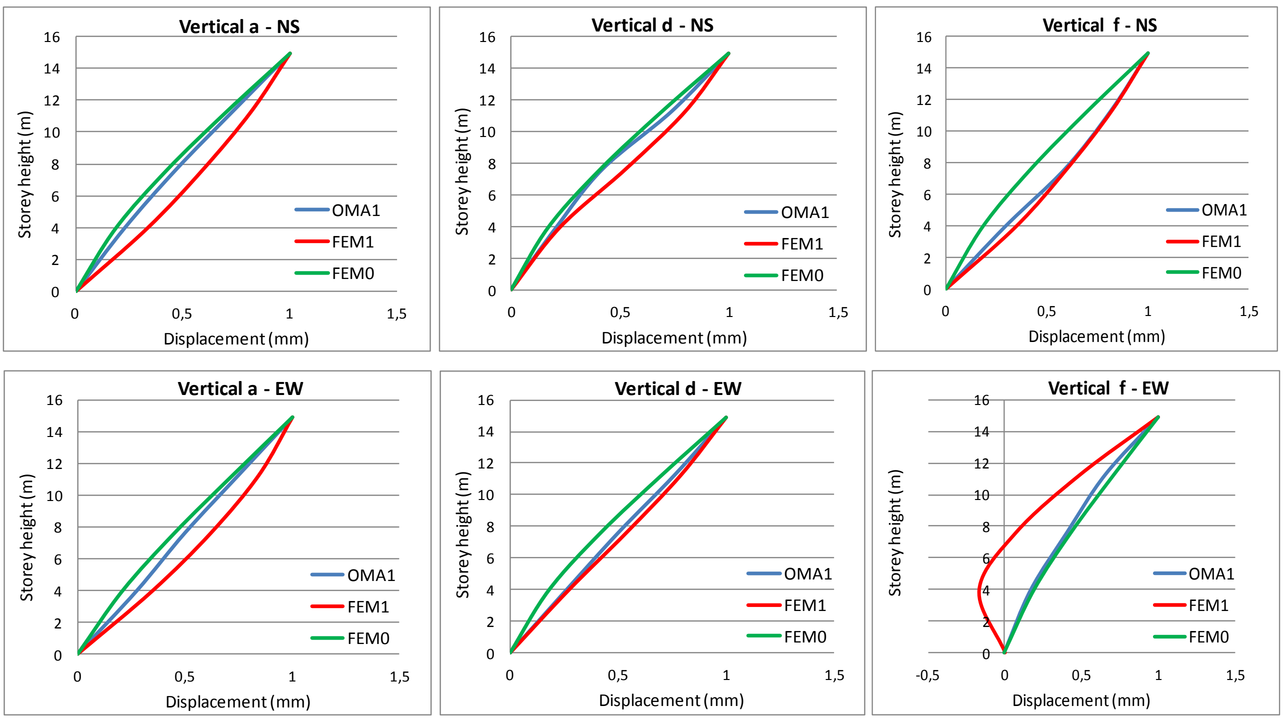

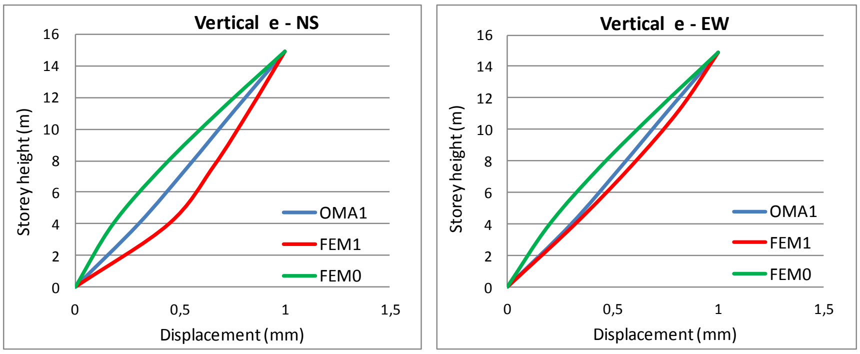

Figure 6.36 *The second mode shape in 'Vertical a', in 'Vertical d', in 'Vertical f' and in 'Vertical e' due to OMA1 method 'FE Model 0' and 'FE Model 1'*

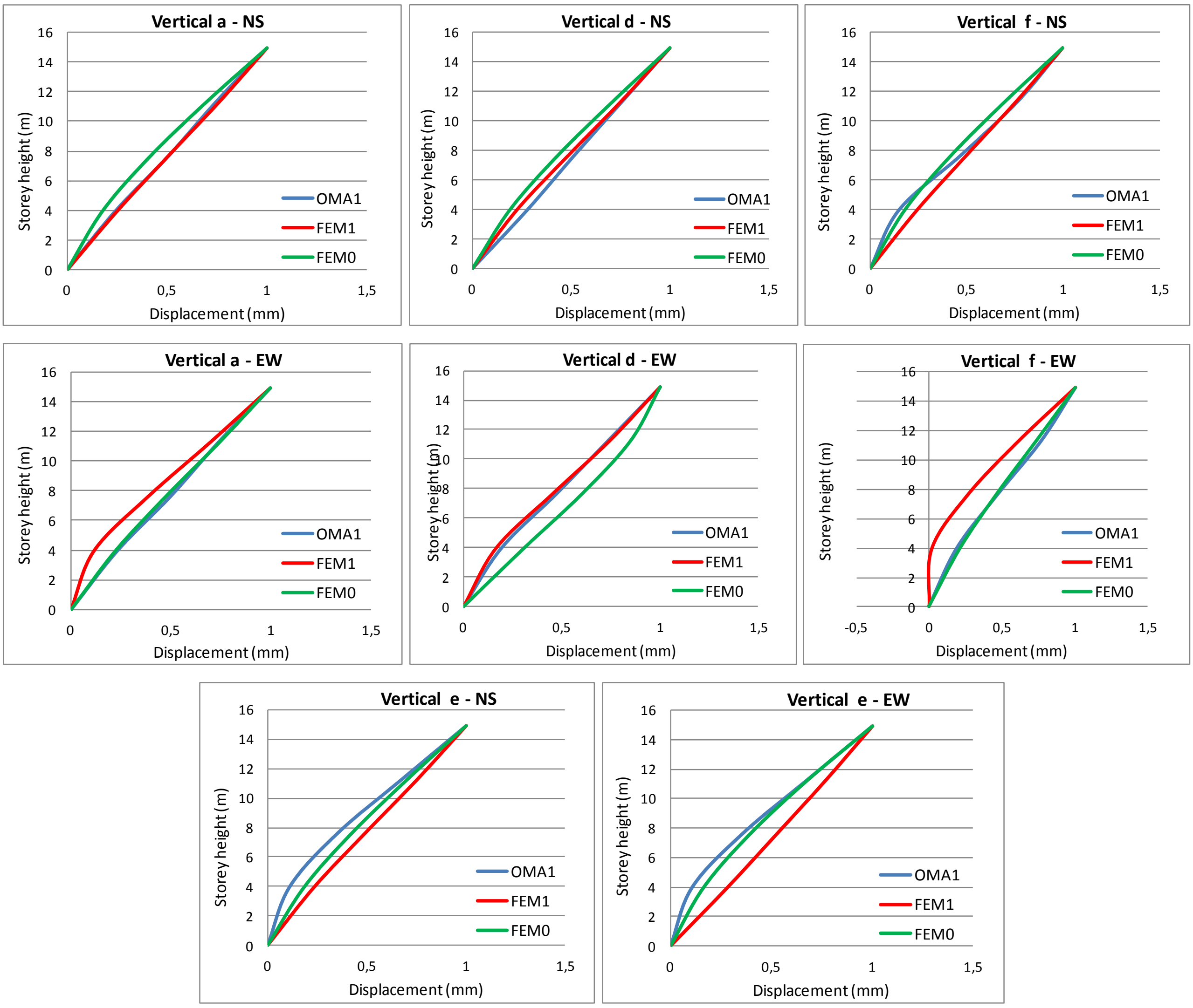

Figure 6.37 *The third mode shape in 'Vertical a', in 'Vertical d', in 'Vertical f' and in 'Vertical e' due to OMA1 method 'FE Model 0' and 'FE Model 1'*

6.4.2 Results from the second ambient vibration measurements

The result of ambient noise measures, acquired with one seismograph fixed in the top floor and the other one moved to the various floors, are presented in this paragraph. Those measurements have been acquired in different vertical of the building named 'Vertical a', 'Vertical d' and

'Vertical f' (see Figure 6.19 and Figure 6.20), with a duration of 20 min and a sampling frequency of 128 Hz. These pairs of measurements have been synchronized by GPS signal.

OMA methods have been used to identify the modal parameter of the structure. Operational modal analysis OMA1 presents better results for the mode shapes. Truncating the signal does not give a higher resolution in frequency and mode shapes identification as was expected from OMA2 method.

The quality of signals acquired has been checked before starting the analysis. At this aim, the cross covariance graphics and the signals in function of time have been plotted first to check the presence of the noise. It has been observed that some of signals present noise at the beginning of the acquisition or at the end, probably caused by the operator during the start or the end process of the acquisition. Therefore, the segments with noise have been removed from the signals.

Cross covariance graphics of synchronized couples of ambient noise measures in the 'Vertical a', 'Vertical d' and 'Vertical f', are shown in the Figure 6.38, Figure 6.39 and Figure 6.40. The copies of measurements are centered at 0 value so, are all aligned. Also, the signals are almost symmetrical referred to the maximum value and to the zero value. The same length, starting from the center of signals, it was chosen for analysis to reduce the noise which may be present at the beginning and at the end of the acquisition. The instrumental noise level has been reduced applying a Butterworth band pass filter at all measurements with a band passing frequency from 0.5 Hz to 12 Hz.

Another method has been used to identify the mode shapes of the building (see the diagram on the right in the Figure 4.21), which consist on the estimation of eigenvectors by analyzing the synchronized pairs of measures separately from each other. For each pair of synchronized measures has been calculated the cross-power spectral or/e auto-spectrum density: for example; S44(f), S40(f) and S00(f) for the pair of synchronized measures in the fourth floor and in the underground floor; S44(f), S41(f) and S11(f) for the pair of synchronized measures in the fourth floor and in the first floor; S44(f), S42(f) and S22(f) for the pair of synchronized measures in the fourth floor and in the second floor; S44(f), S43(f) and S33(f) for the pair of synchronized measures in the fourth floor and in the third floor. After this operation, the peaks in frequency have been selected, using peak picking method, and consequently the correspondent spectrum ordinate values. The ratio between the cross-spectrum ordinate of the fourth floor with one of the other n-floors, and the auto-spectrum ordinate of the fourth floor gives the eigenvector values of the n-floor normalized with the fourth floor, in the selected peaks in frequency. Those steps can be summarized as:

- Estimation of the cross-spectrum and auto-spectrum of each pears of synchronized measures; S_{hh}, S_{4h}, S_{44} ;
- Identification/selection of the peaks in frequency by ‘peak picking method’ in the $S_{hh}(f)$, $S_{4h}(f)$, S_{44} (f) graphics and their respective spectrum value $S_{hh}(fi)$, $S_{4h}(fi)$, S_{44} (fi);
- Estimation of the ratio $\varphi_{h,i} = S_{4h}(fi)/ S_{44} (fi)$, when *i* is the mode shape number and *h* is the floor number.

The elaboration of measures acquired in several verticals of the building is shown in the sequent figures. The 'FE Model 2' is the calibrated model from the second measures acquired inside the building. The rigidity of external walls has been modeled by frame elements, which has been dimensioned due to the equivalent connecting rod theory. Furthermore, other elements have been added to the model and also the Young modulus of the concrete have been modified (see paragraph 6.5.1).

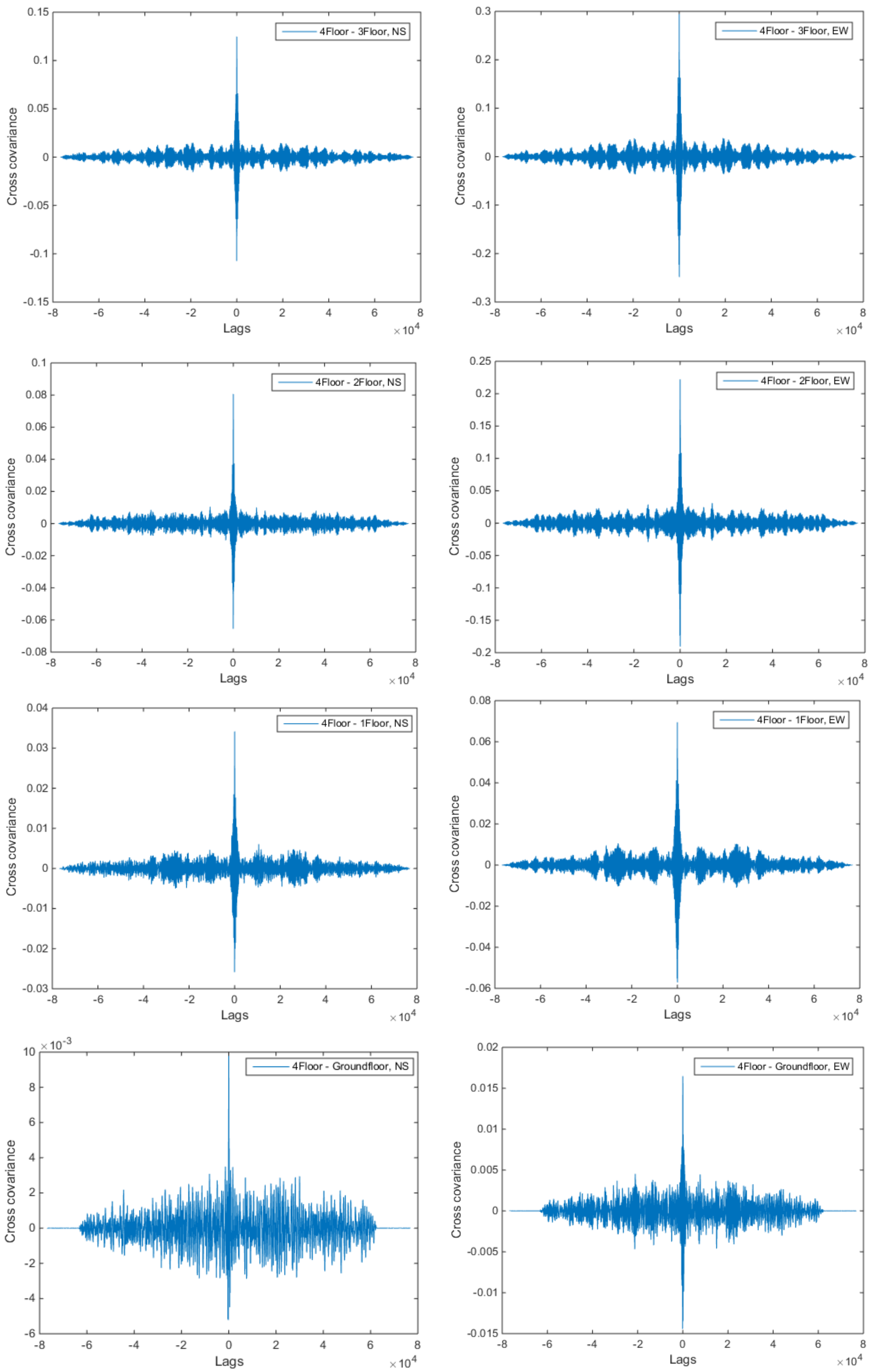

Figure 6.38 *Cross covariance graphics of measures in the 'Vertical a' of both components EW and NS*

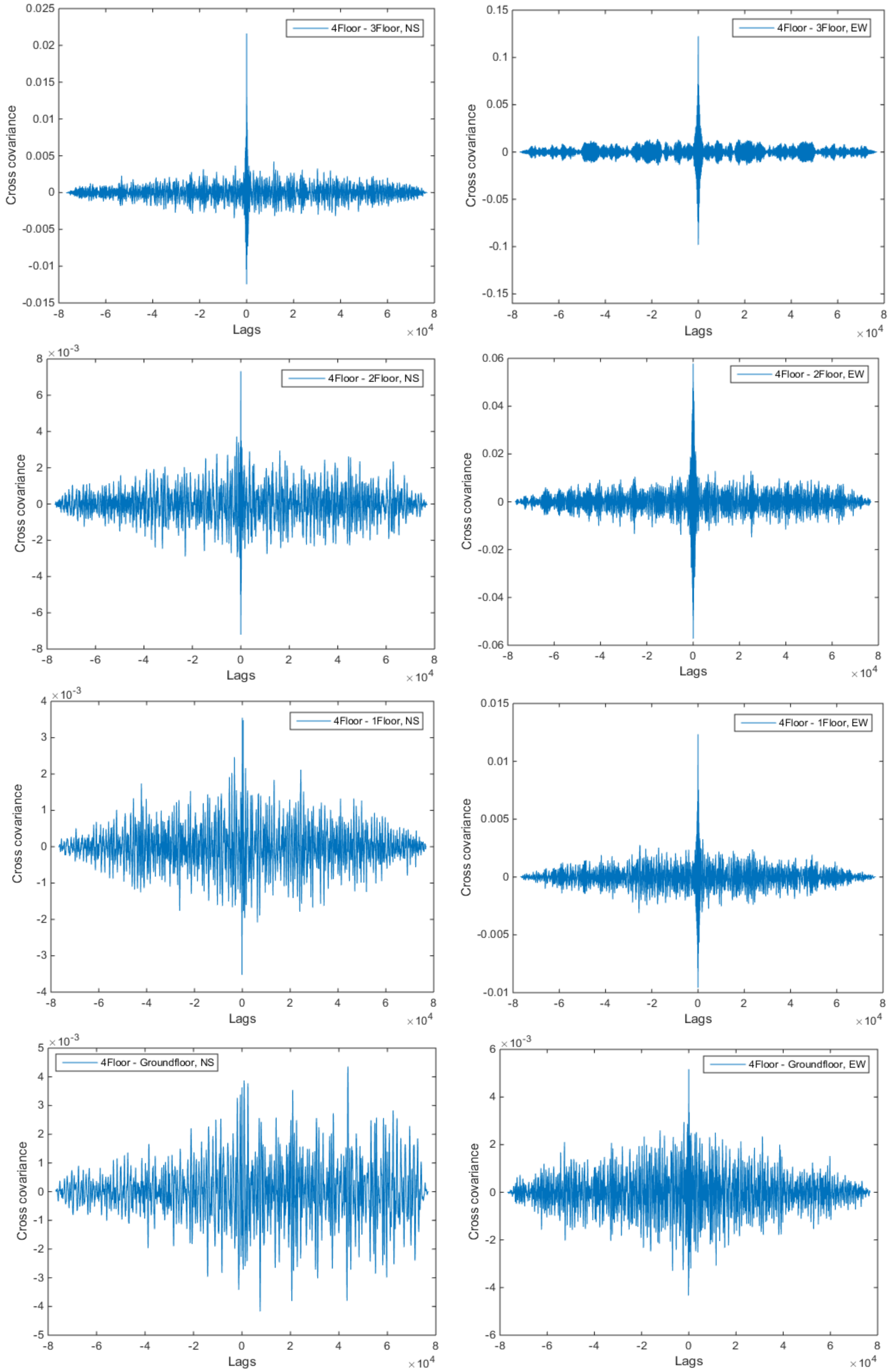

Figure 6.39 *Cross covariance graphics of measures in the 'Vertical d' of both components EW and NS*

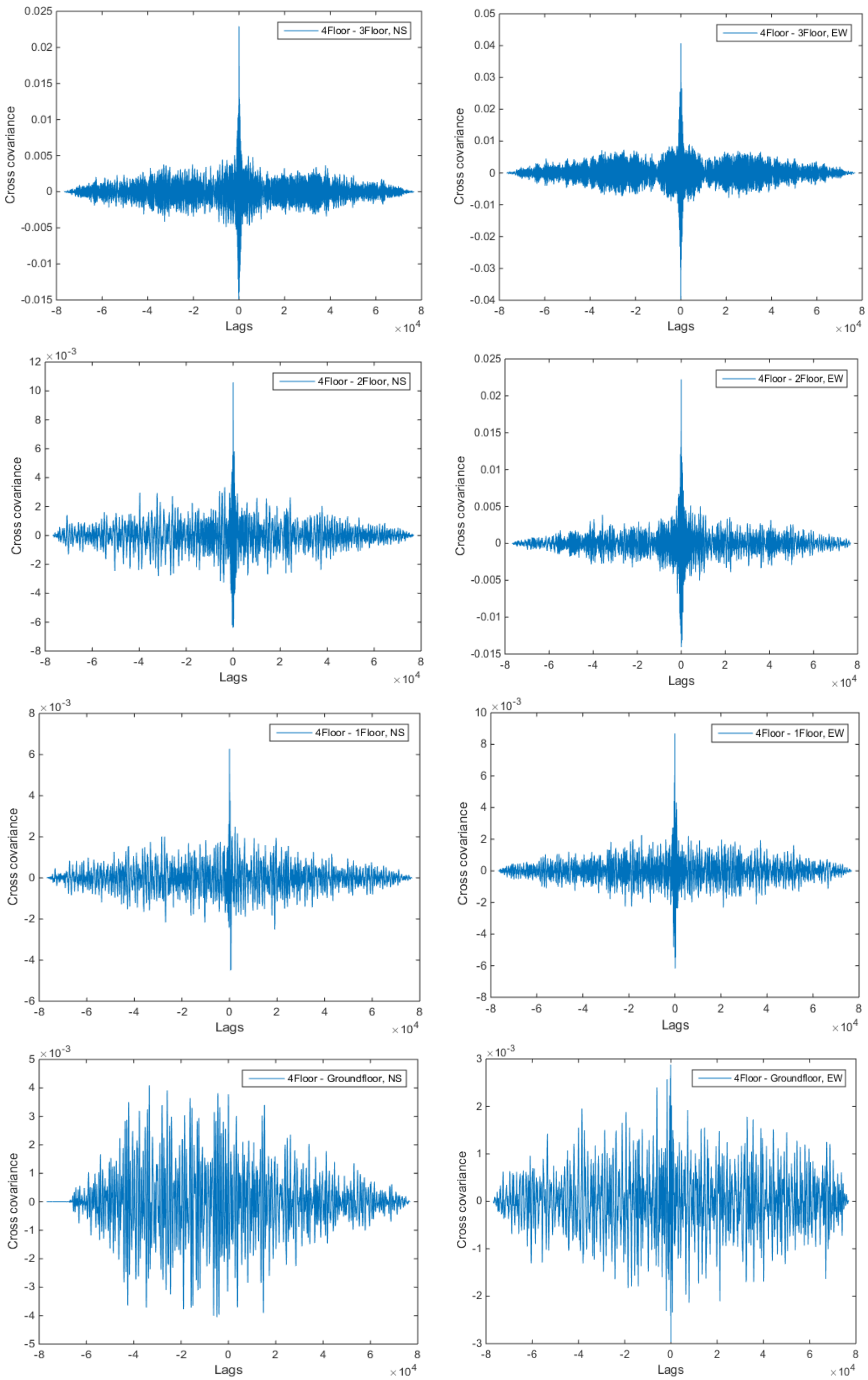

Figure 6.40 *Cross covariance graphics of measures in the 'Vertical f' of both components EW and NS*

The spectrum in frequency of measures on three verticals and in both direction EW and NS are shown in the Figure 6.41. As expected, the amplitude of PSD in frequency peaks of the first mode shapes decrease when passing from the top floor to the ground floor measures. Furthermore, we can see from the spectrum that the peaks in amplitude have different frequency value for diverse verticals. The 'Vertical a' and 'Vertical f' has a peak amplitude at 2.3 Hz while the 'Vertical d' at 3.0 Hz.

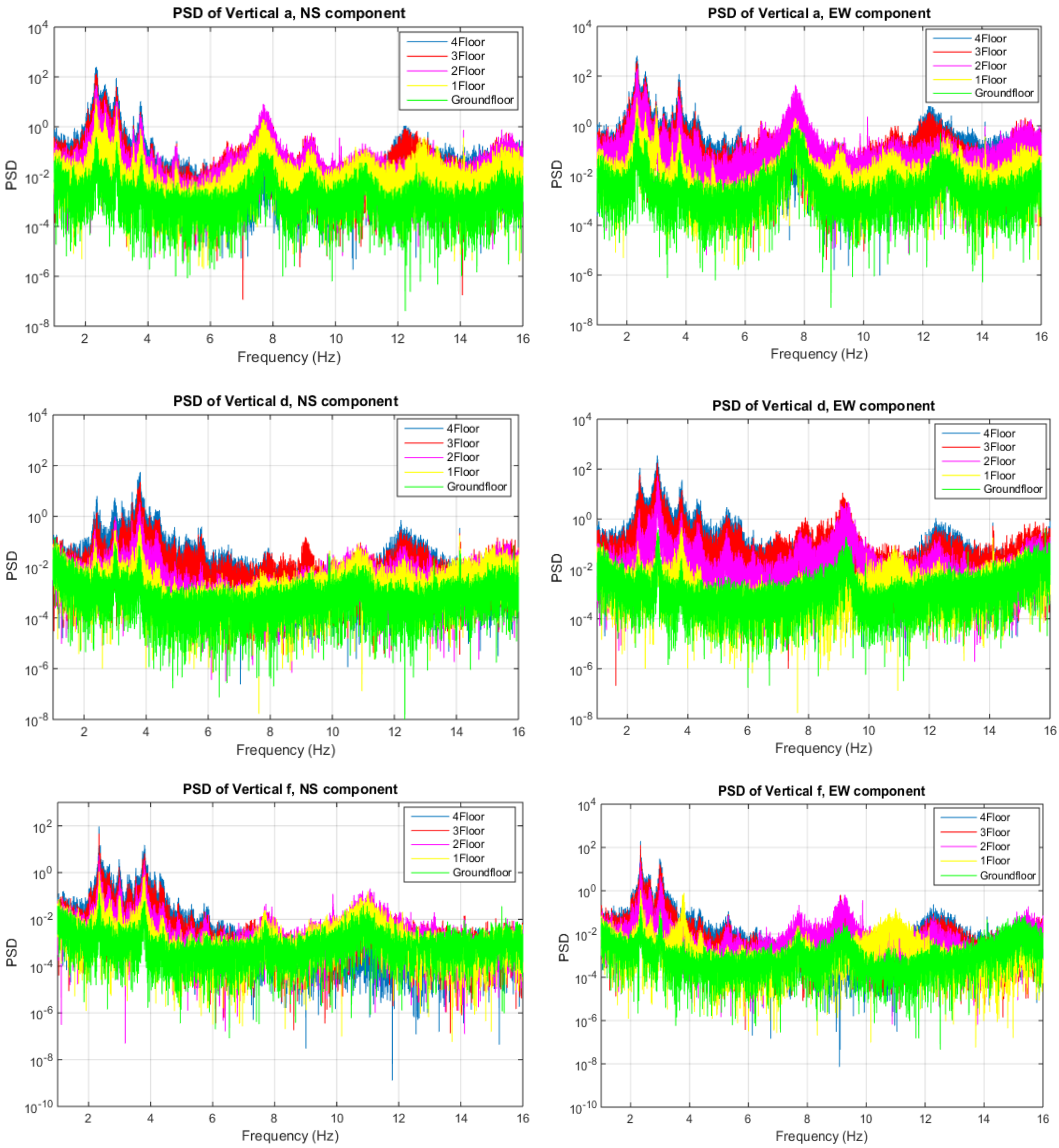

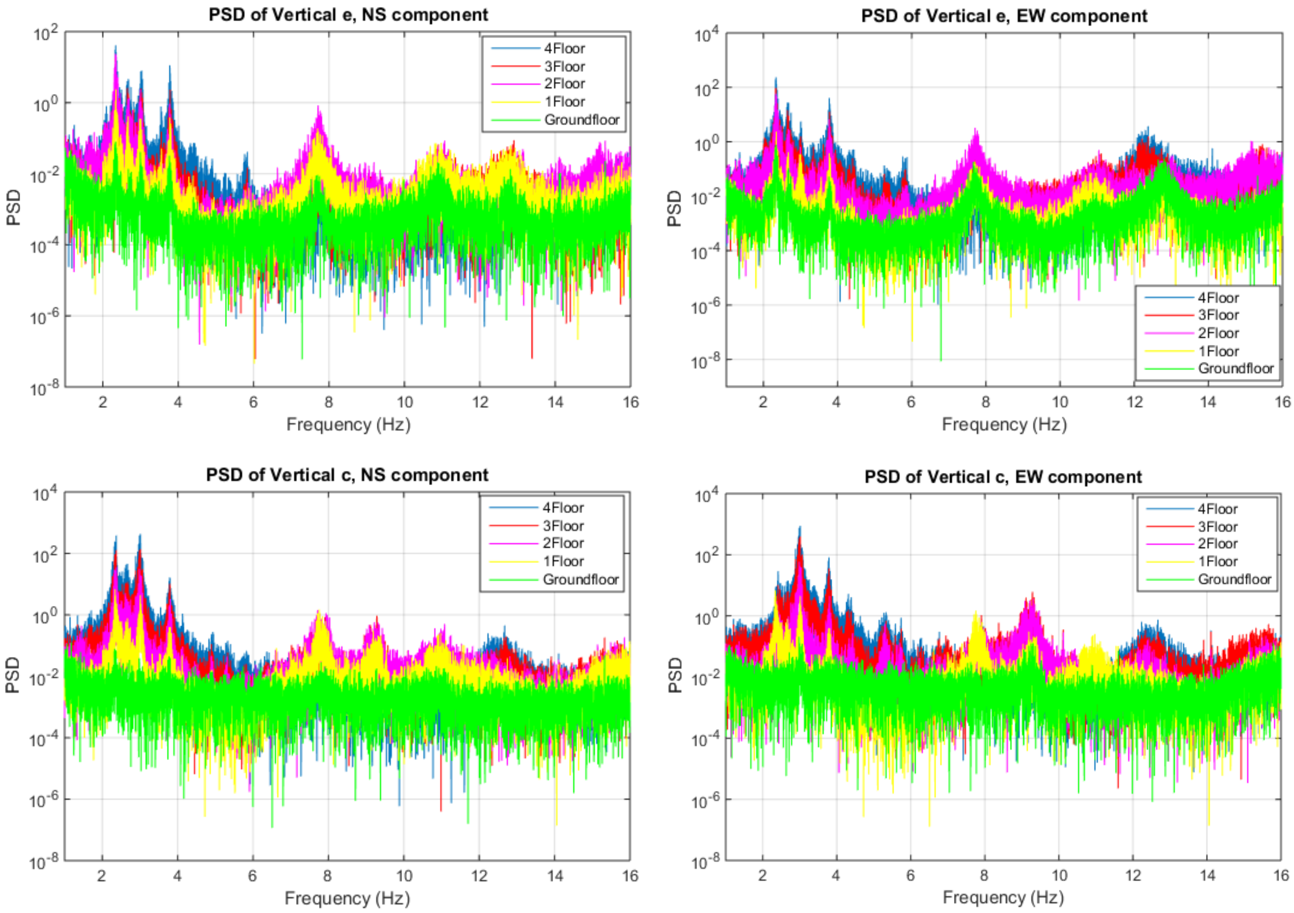

Figure 6.41 *Graphics of PSD in function of frequency for the measures in 'Vertical a', 'Vertical d', 'Vertical f', 'Vertical e' and 'Vertical c' of the building*

The peaks in frequency at all verticals are shown in the Table 6.15. The first three frequency present in all verticals are respectively at 2.3 Hz, 3.0 Hz and 3.8 Hz. The first three frequency corresponds to those identify from spectrum in frequency (see Table 6.15). In the 'Vertical a' is present also a peak in 2.63 Hz frequency.

Frequencies estimated from PSD spectrum and SVD differ not significant between one another, considering that the second decimal is not significant.

Table 6.15 *Frequency value from Spectrum and SVD in different verticals*

Frequency (Hz)	**Vertical a**			**Vertical d**			**Vertical f**			**Vertical e**			**Vertical c**		
	Spectrum		SVD	Spectrum		SVD	Spectrum		SVD	Spectrum		SVD	Spectrum		SVD
	ns	ew		ns	ew		ns	ew		ns	ew		ns	ew	
Mode 1	**2,34**	**2,34**	**2,36**	**2,32**	**2,42**	**2,41**	**2,33**	**2,33**	**2,33**	**2,34**	**2,33**	**2,33**	**2,37**	**2,41**	**2,37**
Mode 2	2,63	**2,63**	**2,63**	-	-	-	2,67	**2,61**	**2,63**	2,68	**2,68**	**2,65**	**2,63**	-	-
Mode 3	**2,99**	**2,99**	2,98	**2,99**	**2,99**	**2,99**	**2,99**	**2,99**	**2,98**	**3,03**	3,01	3,01	**2,99**	**3,01**	**3,01**
Mode 4	**3,76**	3,76	**3,79**	**3,80**	**3,81**	**3,77**	**3,80**	3,81	3,79	**3,78**	**3,78**	**3,78**	3,79	**3,79**	**3,78**

blue - first peak in amplitude; red - second peak in amplitude; black - third peak in amplitude.

In the Figure 6.42 are presented the graphics of the singular value decomposition of PSD matrixes in all verticals.

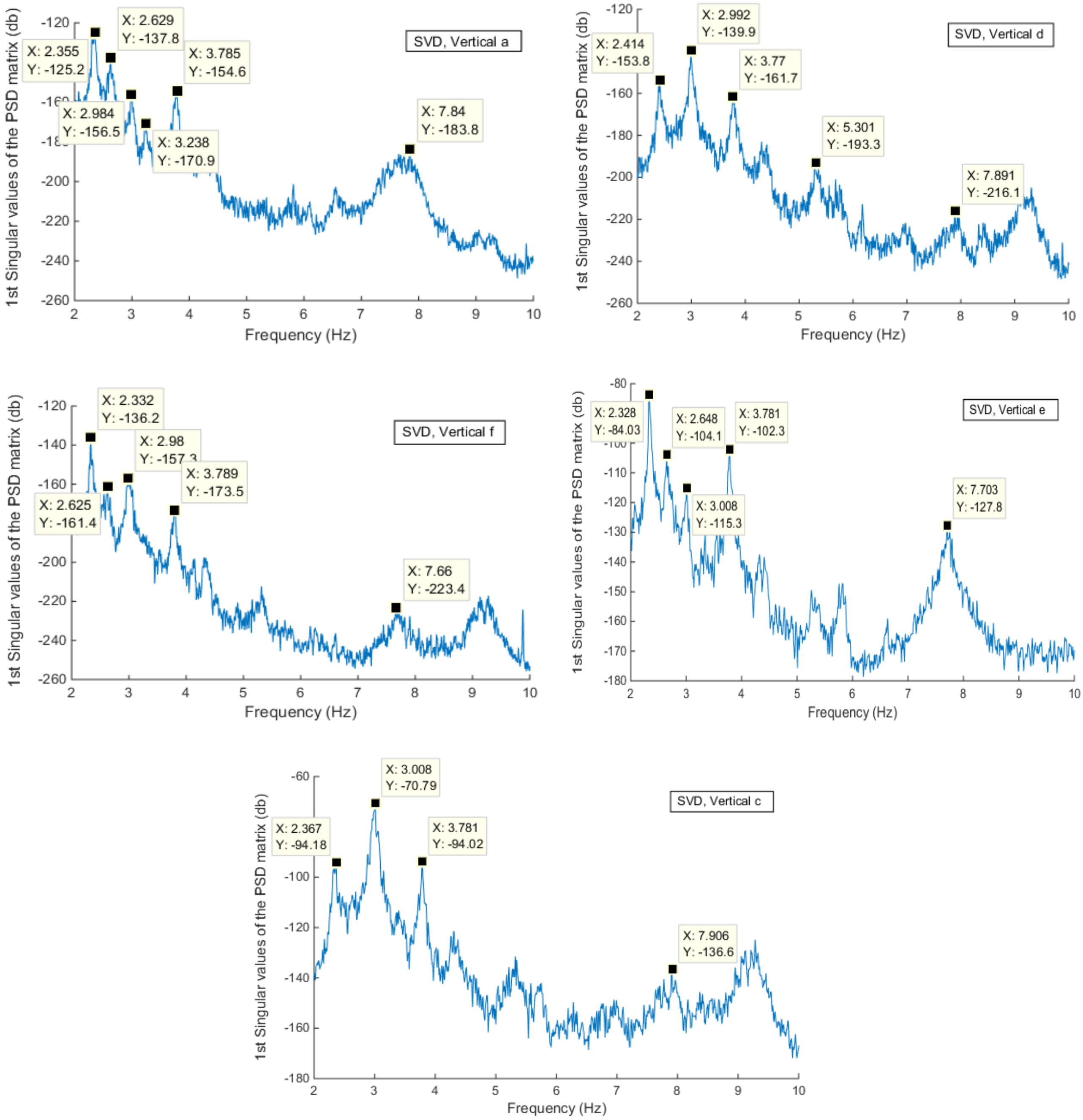

Figure 6.42 *Graphics of Singular Value Decomposition of PSD matrix for 'Vertical a', 'Vertical d', 'Vertical f', 'Vertical e' and 'Vertical c'*

Natural frequencies estimated from two operational modal analysis method differ between each other about 2%, while are about 50% higher than those obtained by the initial finite element model 'FE Model 0' of the project (Table 6.16). This last leads to calibration of the model.

Table 6.16 *Frequency values in all verticals due to OMA methods, using second ambient vibration measurements*

Frequency (Hz), in 'Vertical a'	**OMA**		**Frequency (Hz), in 'Vertical d'**	**OMA**		**FE Model 0**
	Method OMA1	Method OMA2		Method OMA1	Method OMA2	
Mode 1	2,36	2,38	Mode 1	2,41	2,41	1,16
Mode 2	2,98	2,99	Mode 2	2,99	3,01	1,59
Mode 3	3,79	3,80	Mode 3	3,77	3,79	2,05
Mode 4	7,84	7,86	Mode 4	7,89	7,91	4,56

Frequency (Hz), in 'Vertical f'	OMA		Frequency (Hz), in 'Vertical e'	OMA		Frequency (Hz), in 'Vertical c'	OMA	
	Method OMA1	Method OMA2		Method OMA1	Method OMA2		Method OMA1	Method OMA2
Mode 1	2,33	2,34	Mode 1	2,33	2,35	Mode 1	2,37	2,38
Mode 2	2,98	2,99	Mode 2	3,01	3,02	Mode 2	3,01	3,02
Mode 3	3,79	3,80	Mode 3	3,78	3,79	Mode 3	3,78	3,79
Mode 4	7,66	7,69	Mode 4	7,70	7,73	Mode 4	7,91	7,92

The first three mode shapes in the 'Vertical a', 'Vertical d', 'Vertical f', 'Vertical e' and 'Vertical c' due to OMA1 method and calibrated 'FE Model 2' model, are shown in the Figure 6.43, in the Figure 6.44 and in the Figure 6.45.

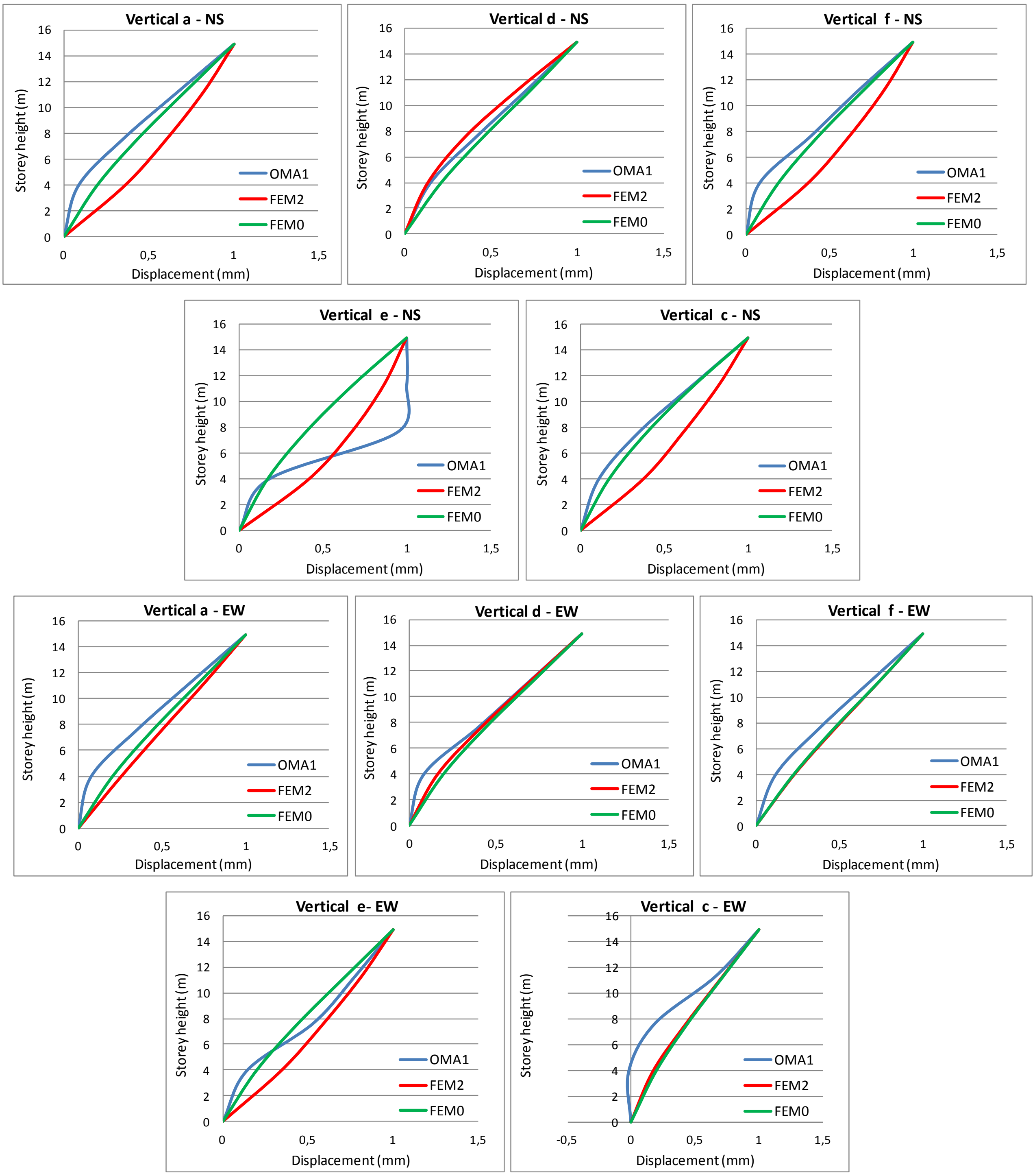

Figure 6.43 *Graphics of the first mode shape from 'FE Model 2', 'FE Model 0' and OMA1 methods, in 'Vertical a', 'Vertical d', 'Vertical f', 'Vertical e' and 'Vertical c' in both direction NS-EW*

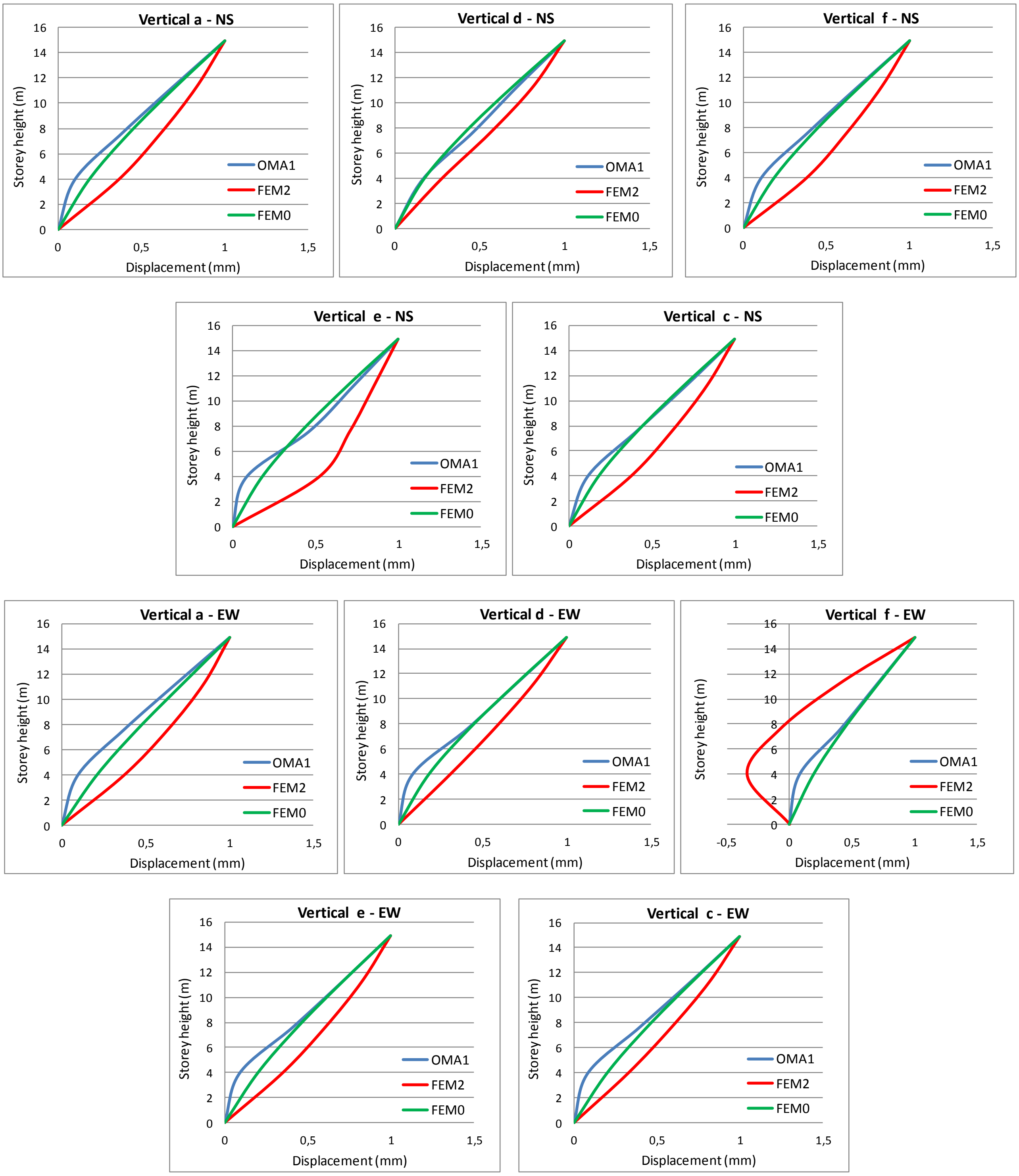

Figure 6.44 *Graphics of the second mode shape from 'FE Model 2', 'FE Model 0' and OMA1 methods, in 'Vertical a', 'Vertical d', 'Vertical f', 'Vertical e' and 'Vertical c' in both direction NS-EW*

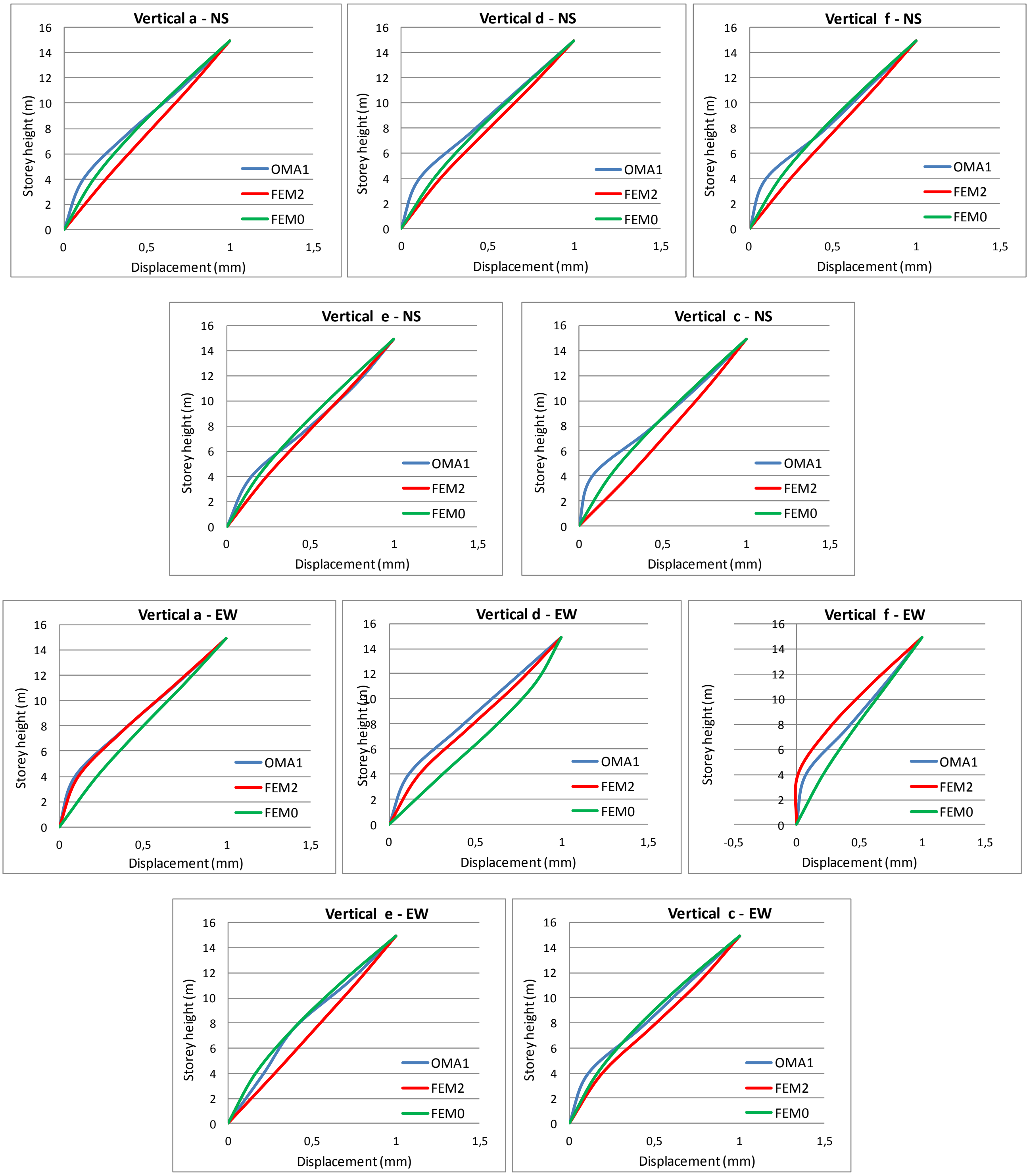

Figure 6.45 *Graphics of the third mode shape from 'FE Model 2', 'FE Model 0' and OMA1 methods, in 'Vertical a', 'Vertical d', 'Vertical f', 'Vertical e' and 'Vertical c' in both direction NS-EW*

The third mode shape has more similarities between the various methods by which it is identified. The peaks in amplitude (the corresponding PSD values at each natural frequencies) of the first three mode are different at the various verticals (see Table 6.15). This probably explain the variation of similarities of mode shapes estimated from different methods (Figure 6.43, Figure 6.44 and Figure 6.45). In other words, some frequencies can be identified better in some verticals and worse on the other locations of the building.

Those measurement have been acquired also one day before the first one, in the 'Vertical a' and in the 'Vertical d', to evaluate the causality of the ambient noise in the structure response. The frequency values estimated this time are presented in the Table 6.17. As one can see, the second decimal of frequencies varies in both cases. Therefore, the frequencies doesn't vary from the values estimated previously (see Table 6.15).

Table 6.17 *Frequency values in the 'Vertical a' and in the 'Vertical d'*

Mode / Frequency (Hz)	**Vertical a**			**Vertical d**		
	Spectrum		SVD	Spectrum		SVD
	ns	ew		ns	ew	
Mode 1	**2,35**	**2,35**	**2,33**	**2,34**	**2,40**	**2,38**
Mode 2	**2,69**	**2,69**	**2,68**	**-**	**-**	**-**
Mode 3	**3,00**	3,00	3,02	**2,99**	**2,99**	**2,99**
Mode 4	3,79	**3,79**	**3,80**	**3,77**	**3,77**	**3,77**

blue **-** first peak in amplitude; red **-** second peak in amplitude; black **-** third peak in amplitude.

The spectrums in frequency in both direction EW and NS are shown in the Figure 6.46. Singular value decomposition graphics, identified using OMA1 method, are shown in the Figure 6.47. The frequencies of the first three mode shapes are respectively 2.3 Hz, 3.0 Hz and 3.8 Hz, which are present in both verticals of the building.

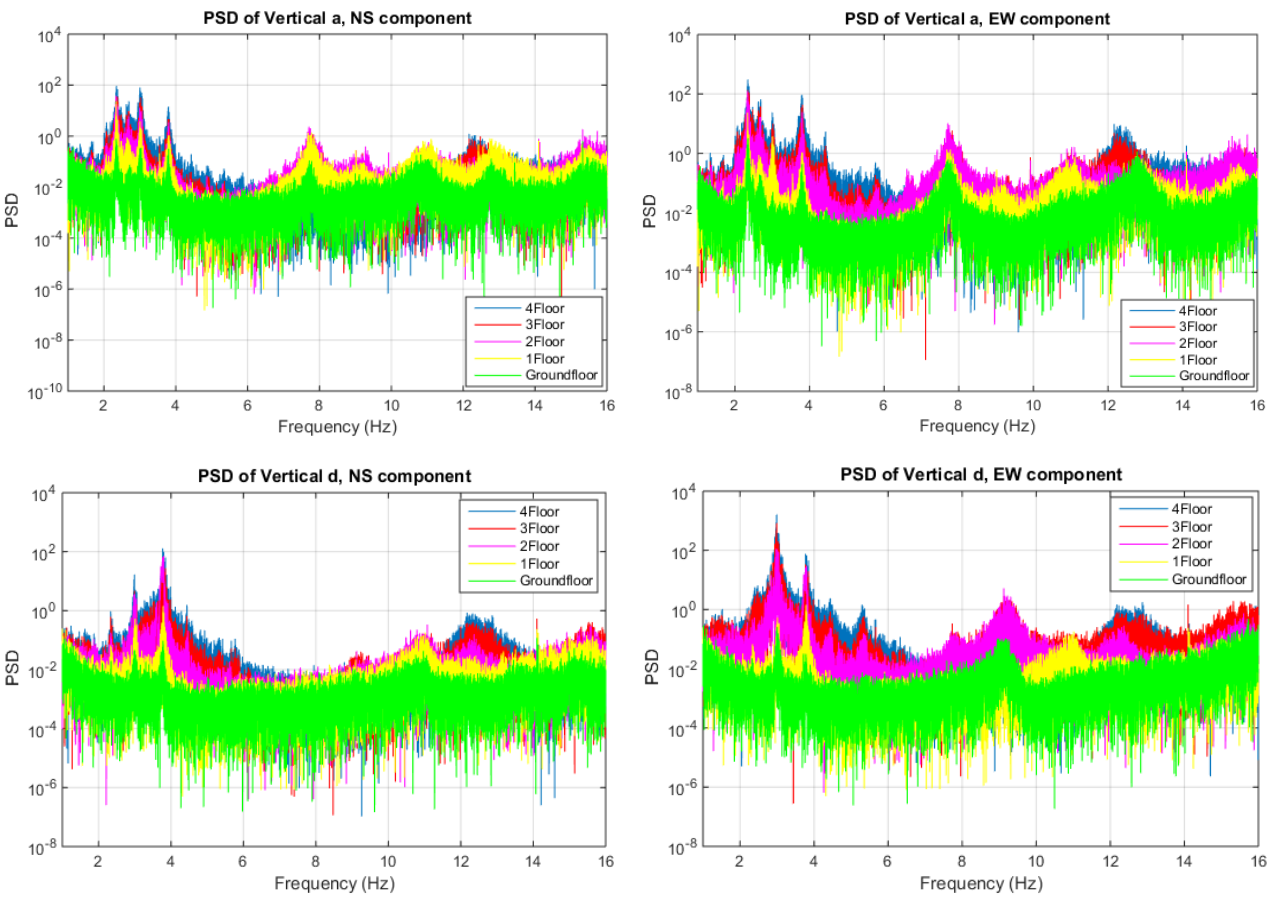

Figure 6.46 *Graphics of PSD in function of frequency of measures in 'Vertical a' and in 'Vertical d'*

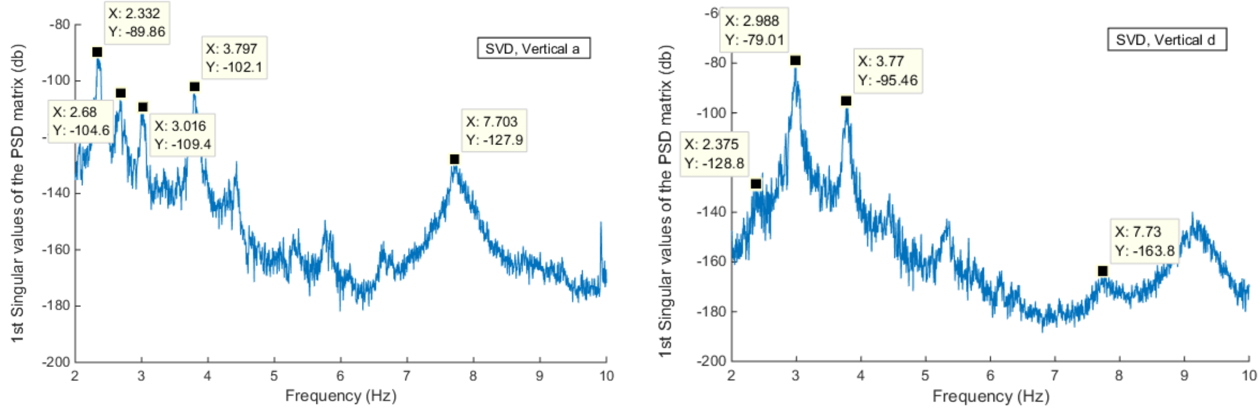

Figure 6.47 *Graphic of Singular value of PSD matrix in the 'Vertical a' and in the 'Vertical d'*

The mode shape identified are shown in the following graphics (see Figure 6.48, Figure 6.49 and Figure 6.50). As one can see, the mode shape estimates by OMA1 method in two different days (OMA1 and OMA1-later) are similar with one another.

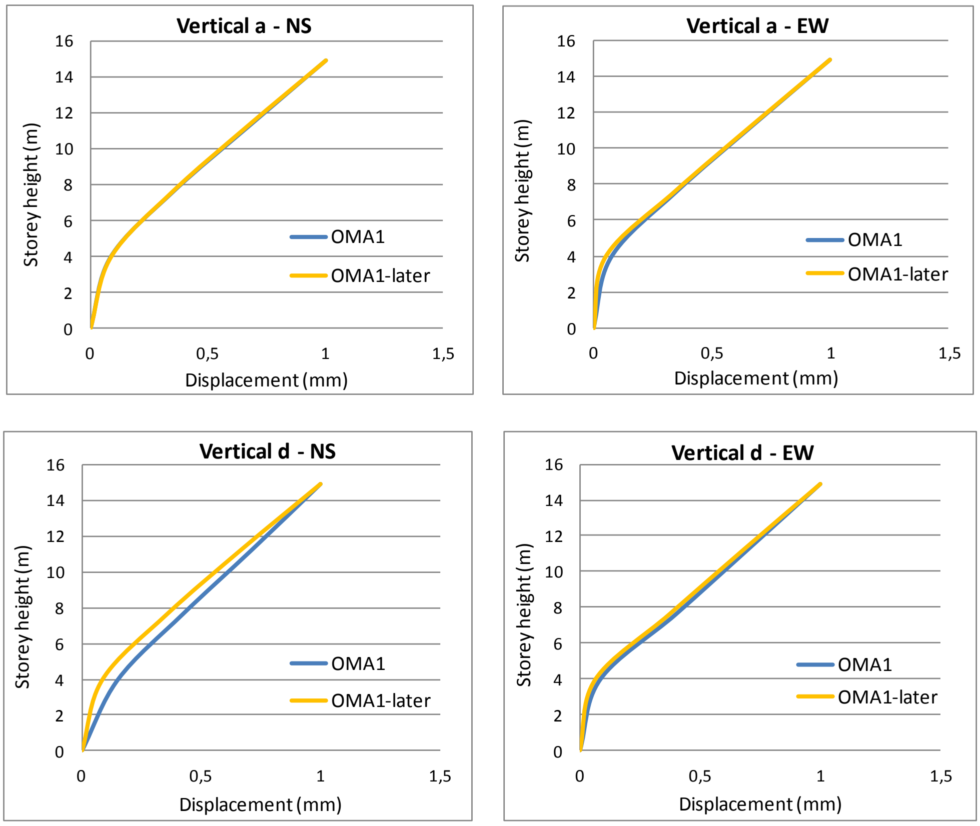

Figure 6.48 *First mode shape in 'Vertical a' and in 'Vertical d' from measures acquired in two different times*

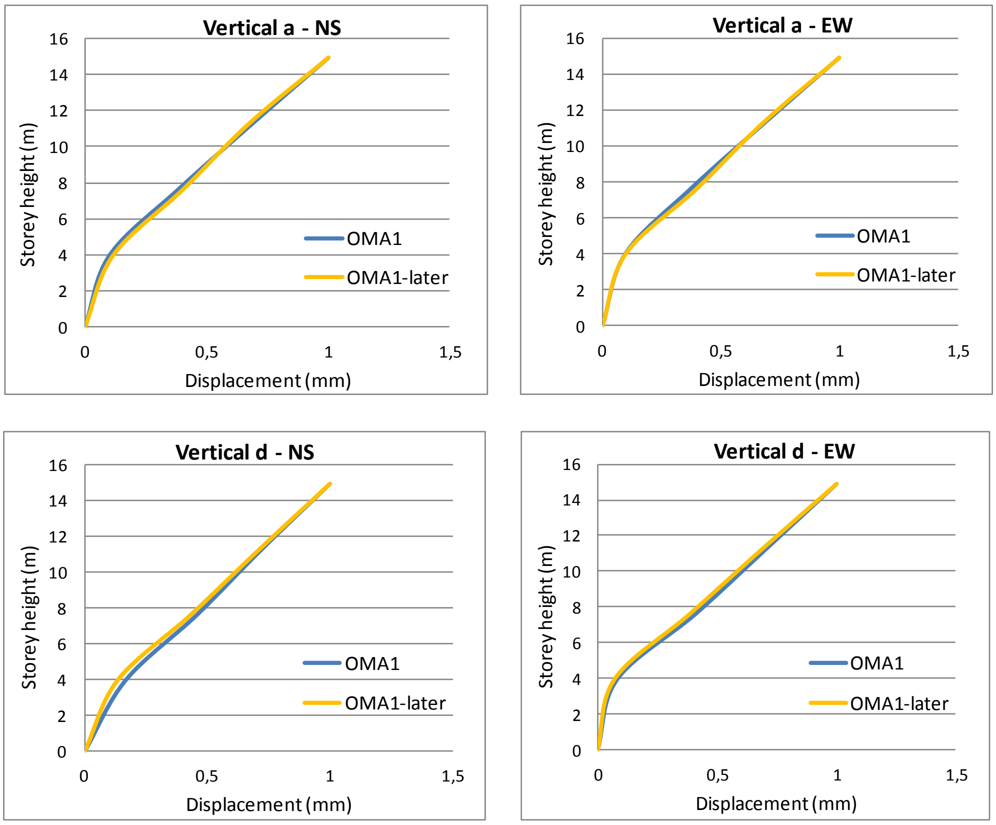

__Figure 6.49__ Second mode shape in 'Vertical a' and in 'Vertical d' from measures acquired in two different times

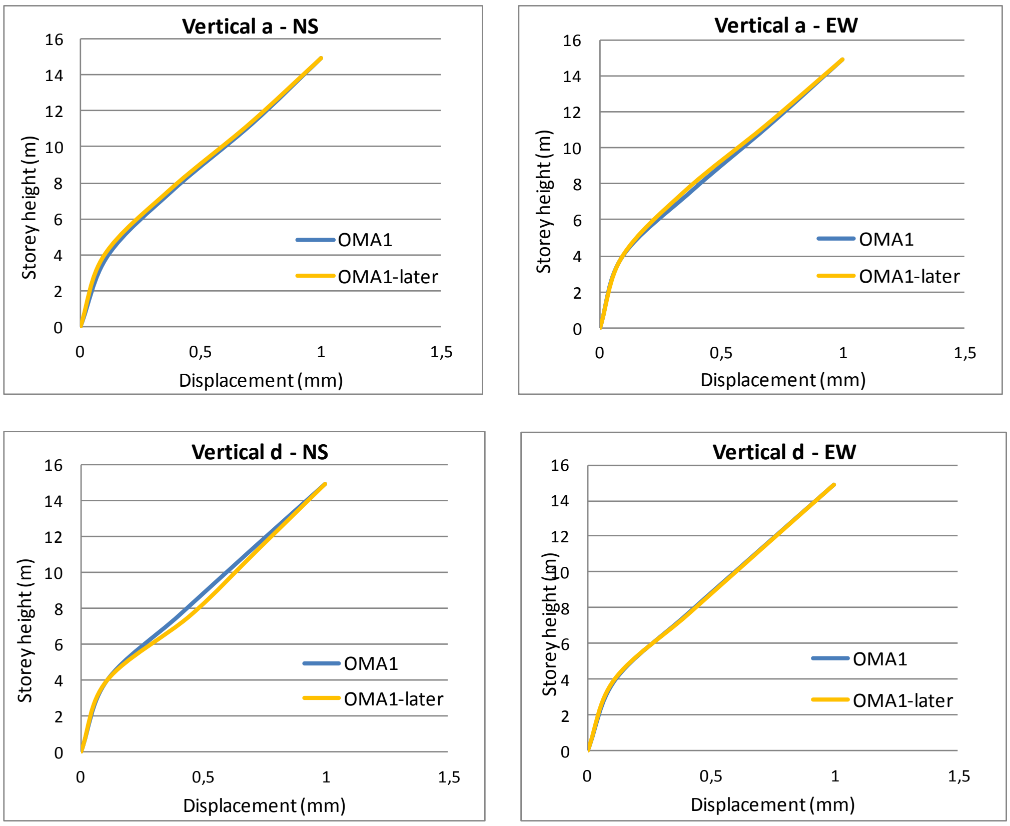

__Figure 6.50__ Third mode shape in 'Vertical a' and in 'Vertical d' from measures acquired in two different times

6.4.3 Comparison between experimental and theoretical structural response

The modal frequencies and the mode shape estimated from experimental data and from finite element model have been confronted with each other. Graphics of the first mode shapes, identified from the first ambient noise measurements and from FEM, are shown in the Figure 6.35, Figure 6.36 and Figure 6.37. Graphics of the first mode shapes, estimated from the second ambient noise measurements and from FEM are shown in the Figure 6.51, Figure 6.52, Figure 6.53, Figure 6.54, Figure 6.55 and Figure 6.56.

Mode shapes from 'FE Model 1' and 'FE Model 2', when modeling the external wall panels, are similar (Figure 6.51, Figure 6.52 and Figure 6.53). Therefore, the rigidity added to the structure doesn't influence significantly the mode shapes, but has a significant influence in frequencies values.

The frequencies estimated from the first ambient noise measurements have been confronted with ones obtained from finite element model. The percentage variation of frequencies estimated due to OMA/EMA method and initial FEM (FE Model 0) are shown in the Table 6.18. As one can see, the frequencies estimated from all ambient noise measurements differ about 50% from those obtained by the finite element model of the project (FE Model 0). At this aim, the finite element model of the project need to be calibrated to receive the same structural response with that obtained from experimental data.

Table 6.18 *Percentage variation of frequencies from the first ambient noise measurements and FEM of the project (FE Model 0)*

Frequency (Hz), in 'Vertical a'	**OMA**		**EMA**		**FE Model**	**Percentage variation (%)**			
	Method OMA1	Method OMA2	Method EMA1	Method EMA2	**0**	Method OMA1	Method OMA2	Method EMA1	Method EMA2
Mode 1	2,35	2,38	2,35	2,33	1,16	50,6	51,3	50,6	50,2
Mode 2	2,70	2,71	2,69	2,68	1,59	41,1	41,3	40,9	40,7
Mode 3	3,45	3,45	3,47	3,45	2,05	40,6	40,6	40,9	40,6
Mode 4	7,68	7,70	7,64	7,65	4,56	40,6	40,8	40,3	40,4

Frequency (Hz), in 'Vertical d'	**OMA**		**EMA**		**FE Model**	**Percentage variation (%)**			
	Method OMA1	Method OMA2	Method EMA1	Method EMA2	**0**	Method OMA1	Method OMA2	Method EMA1	Method EMA2
Mode 1	2,33	2,37	2,35	-	1,16	50,2	51,1	50,6	-
Mode 2	2,71	2,72	2,68	2,67	1,59	41,3	41,5	40,7	40,4
Mode 3	3,44	3,45	3,47	3,44	2,05	40,4	40,6	40,9	40,4
Mode 4	7,61	7,66	7,64	7,62	4,56	40,1	40,5	40,3	40,2

Frequency (Hz), in 'Vertical f'	**OMA**		**EMA**		**FE Model**	**Percentage variation (%)**			
	Method OMA1	Method OMA2	Method EMA1	Method EMA2	**0**	Method OMA1	Method OMA2	Method EMA1	Method EMA2
Mode 1	2,34	2,37	2,35	2,36	1,16	50,4	51,1	50,6	50,8
Mode 2	2,69	2,69	2,68	2,66	1,59	40,9	40,9	40,7	40,2
Mode 3	3,43	3,45	3,46	3,44	2,05	40,2	40,6	40,8	40,4
Mode 4	7,68	7,65	7,61	7,62	4,56	40,6	40,4	40,1	40,2

Frequency (Hz), in 'Vertical e'	**OMA**		**EMA**		**FE Model**	**Percentage variation (%)**			
	Method OMA1	Method OMA2	Method EMA1	Method EMA2	**0**	Method OMA1	Method OMA2	Method EMA1	Method EMA2
Mode 1	2,35	2,37	2,38	2,39	1,16	50,6	51,1	51,3	51,5
Mode 2	2,67	2,69	2,73	2,74	1,59	40,4	40,9	41,8	42,0
Mode 3	3,41	3,45	3,48	3,50	2,05	39,9	40,6	41,1	41,4
Mode 4	7,68	7,65	7,69	7,71	4,56	40,6	40,4	40,7	40,9

The frequencies estimated from the second ambient noise measurements have been confronted with those obtained from finite element model. The percentage variation of frequencies estimated due to OMA method and initial FEM (FE Model 0) are shown in the Table 6.19. Also in this case, the frequencies estimated from the second ambient noise measurements differ about 50% from those obtained by the initial finite element model (FE Model 0).

Table 6.19 *Percentage variation of frequencies from the second ambient noise measurements and FEM of the project (FE Model 0)*

Frequency	Vertical a		Vertical d		Vertical f		**FEM**	**Percentage variation (%)**					
	OMA		**OMA**		**OMA**		FE	Vertical a		Vertical d		Vertical f	
(Hz)	Method OMA1	Method OMA2	Method OMA1	Method OMA2	Method OMA1	Method OMA2	Model 0	Method OMA1	Method OMA2	Method OMA1	Method OMA2	Method OMA1	Method OMA2
Mode 1	2,36	2,38	2,41	2,41	2,33	2,34	1,16	50,8	51,3	51,9	51,9	50,2	50,4
Mode 2	2,98	2,99	2,99	3,01	2,98	2,99	1,59	46,6	46,8	46,8	47,2	46,6	46,8
Mode 3	3,79	3,80	3,77	3,79	3,79	3,80	2,05	45,9	46,1	45,6	45,9	45,9	46,1
Mode 4	7,84	7,86	7,89	7,91	7,66	7,69	4,56	41,8	42,0	42,2	42,4	40,5	40,7

Frequency	Vertical e		Vertical c		**FEM**	**Percentage variation (%)**			
	OMA		**OMA**		FE	Vertical e		Vertical c	
(Hz)	Method OMA1	Method OMA2	Method OMA1	Method OMA2	Model 0	Method OMA1	Method OMA2	Method OMA1	Method OMA2
Mode 1	2,33	2,35	2,37	2,38	1,16	50,2	50,6	51,1	51,3
Mode 2	3,01	3,02	3,01	3,02	1,59	47,2	47,4	47,2	47,4
Mode 3	3,78	3,79	3,78	3,79	2,05	45,8	45,9	45,8	45,9
Mode 4	7,70	7,73	7,91	7,92	4,56	40,8	41,0	42,4	42,4

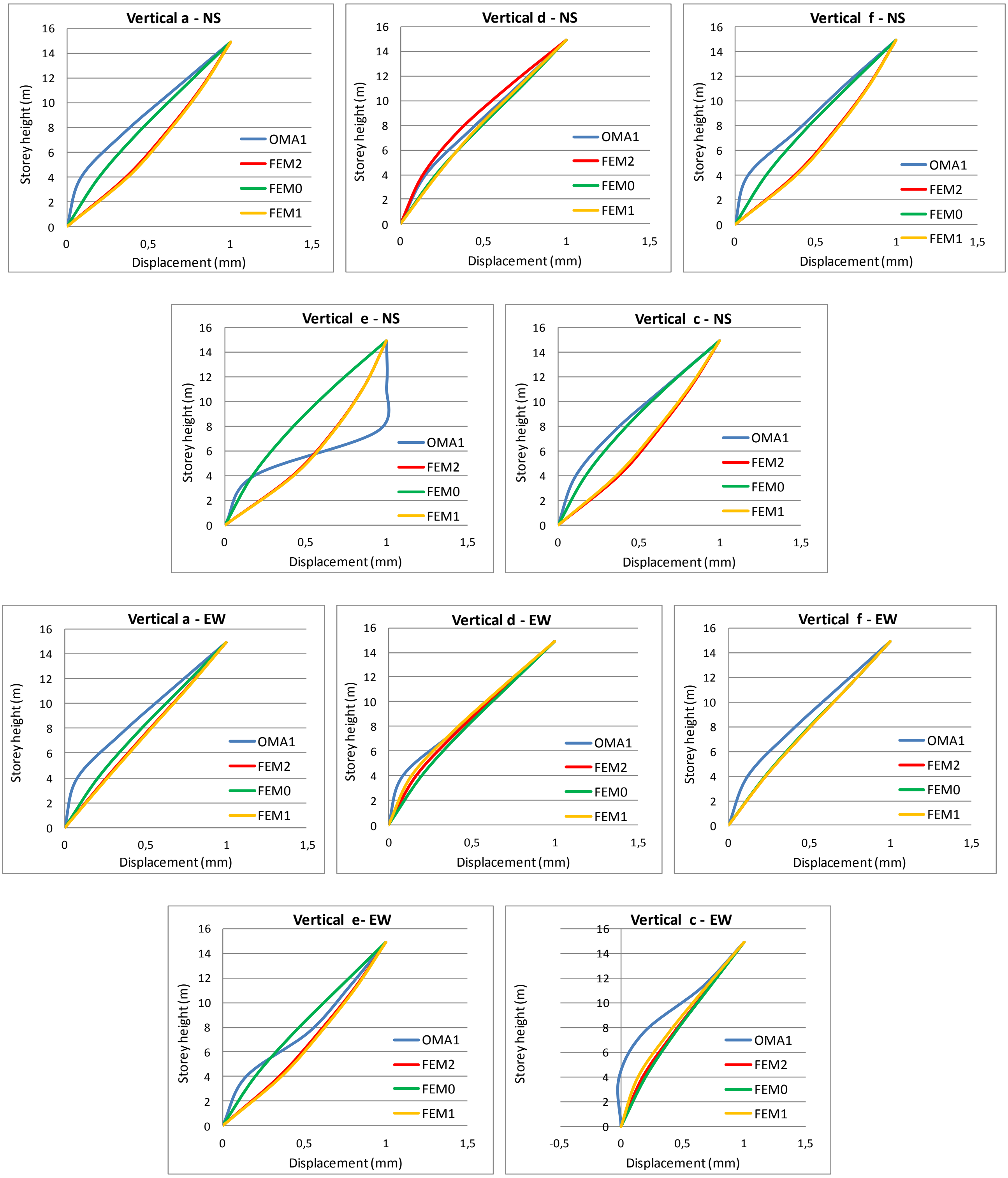

Figure 6.51 *Graphics of the first mode shape in 'Vertical a', in 'Vertical d', in 'Vertical f', in 'Vertical e' and in 'Vertical c' in both direction NS-EW, from 'FE Model 2', 'FE Model 0', 'FE Model 1' and OMA1 method*

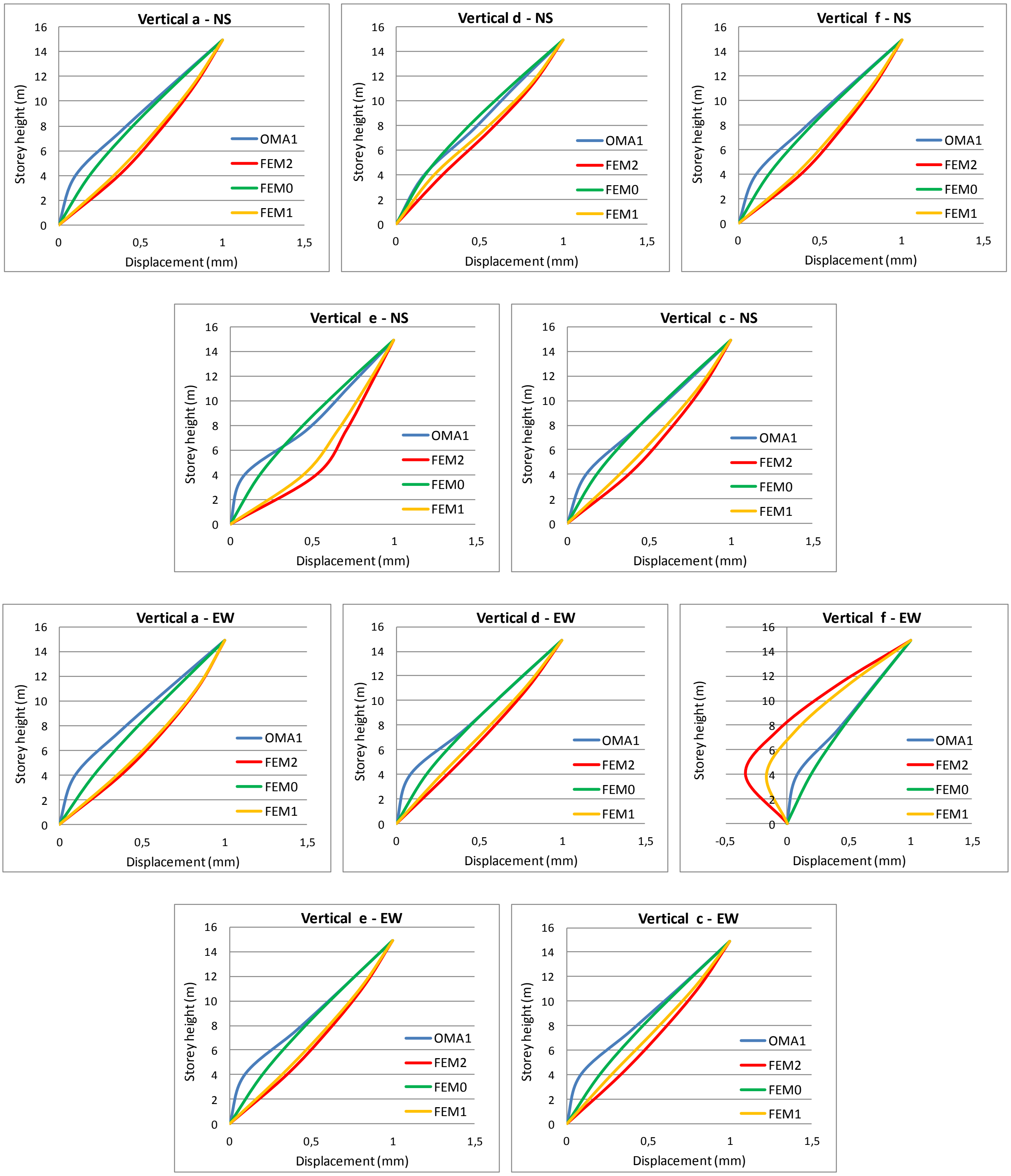

Figure 6.52 *Graphics of the second mode shape in 'Vertical a', in 'Vertical d', in 'Vertical f', in 'Vertical e' and in 'Vertical c' in both direction NS-EW, from 'FE Model 2', 'FE Model 0', 'FE Model 1' and OMA1 method*

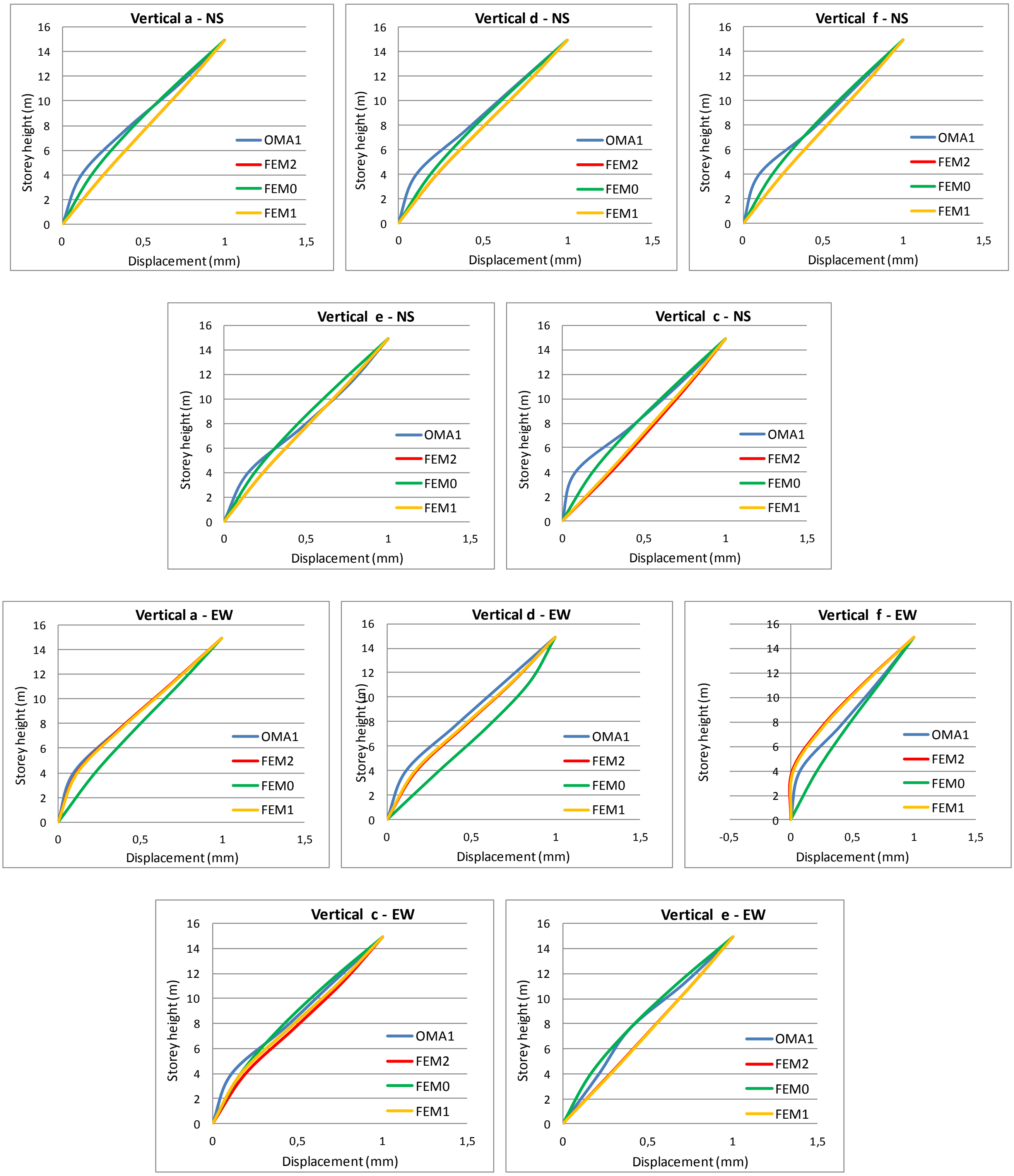

Figure 6.53 *Graphics of the third mode shape in 'Vertical a', in 'Vertical d', in 'Vertical f', in 'Vertical e' and in 'Vertical c' in both direction NS-EW, from 'FE Model 2', 'FE Model 0', 'FE Model 1' and OMA1 method*

The mode shape graphics estimated from ambient vibration measures acquired in two different days in the 'Vertical a' and in the 'Vertical d' are shown in the Figure 6.54, Figure 6.55 and Figure 6.56, respectively for the first three mode shapes.

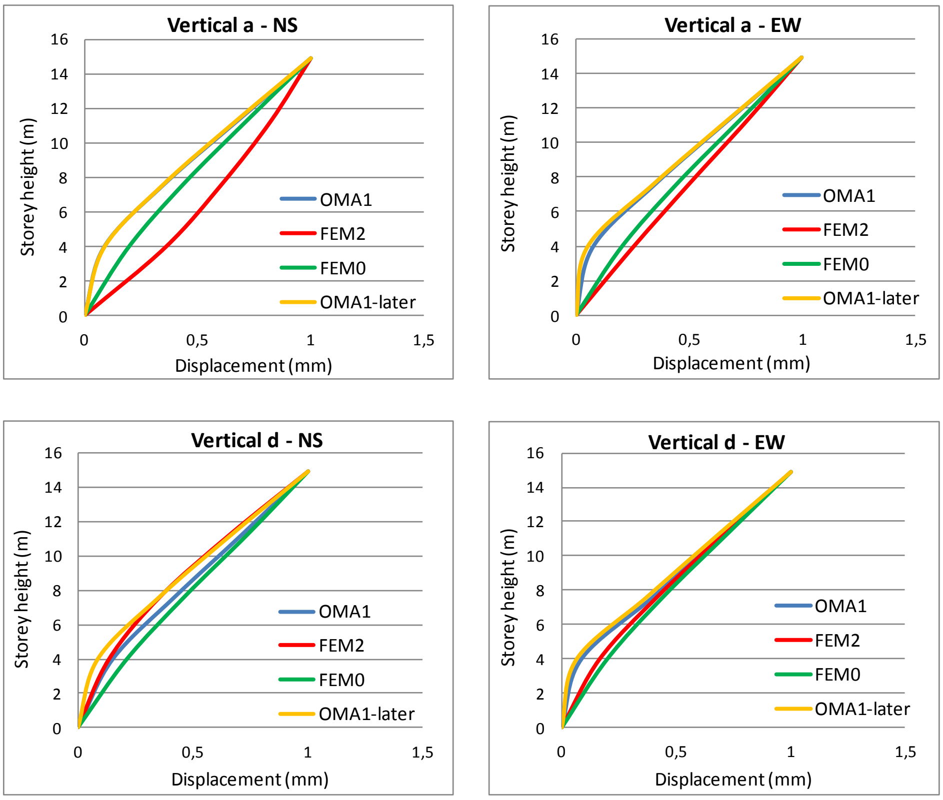

Figure 6.54 *Graphics of the first mode shape in 'Vertical a' and in 'Vertical d' in both direction NS-EW, from 'FE Model 0', 'FE Model 2' and OMA1 method*

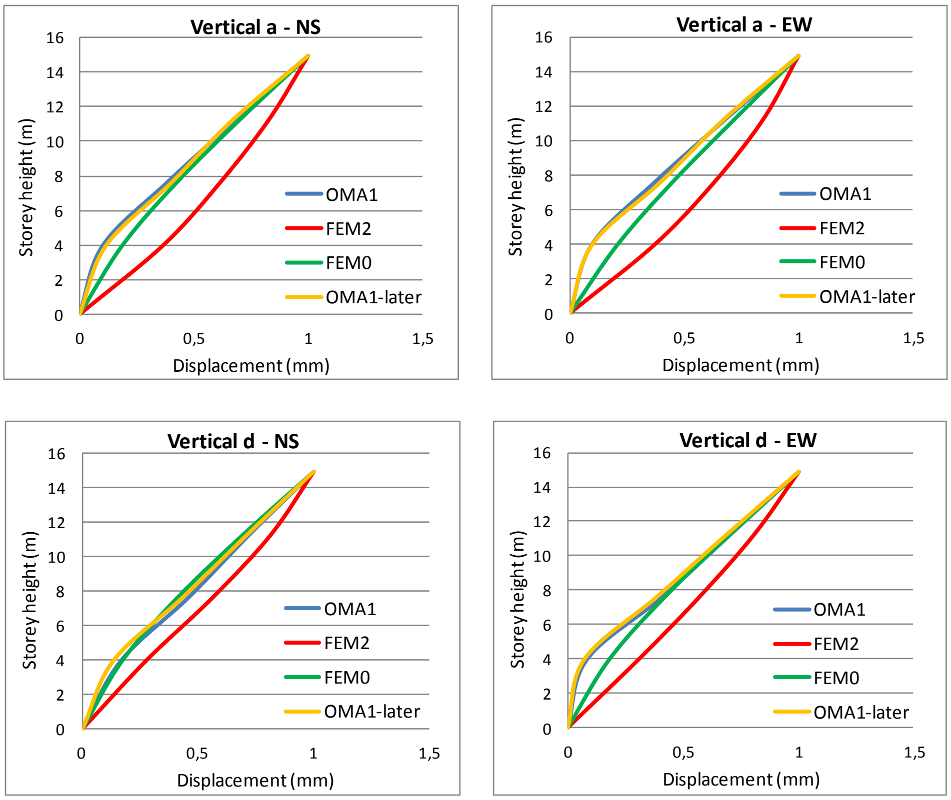

Figure 6.55 *Graphics of the second mode shape in 'Vertical a' and in 'Vertical d' in both direction NS-EW, from 'FE Model 0', 'FE Model 2' and OMA1 method*

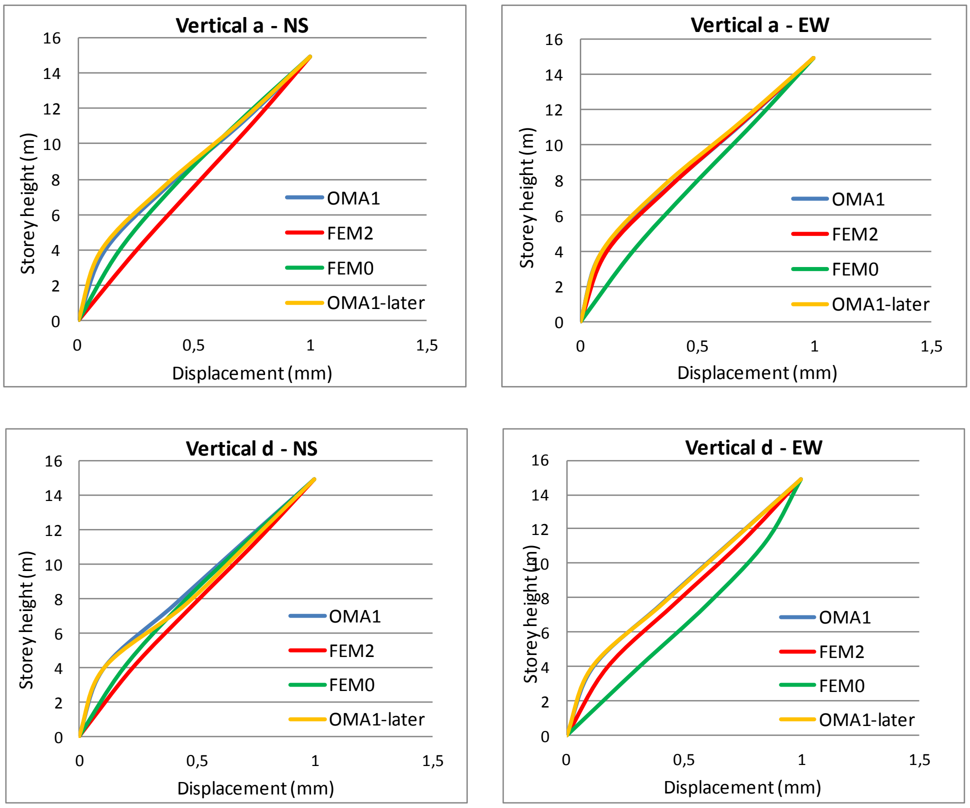

Figure 6.56 *Graphics of the third mode shape in 'Vertical a' and in 'Vertical d' in both direction NS-EW, from 'FE Model 0', 'FE Model 2' and OMA1 method*

6.5 Calibrated FEM

Finite element model of the project 'FE Model 0' has been calibrated to achieve the same structure response with the estimated one from ambient vibration measurements. Software SAP2000 has been used to create the finite element models. Two calibrated finite element model have been realized by using the first and the second ambient noise measures. As mentioned in the above paragraphs the ambient noise measures have been acquired in two different periods during the construction of the building, so as to evaluate the influence of the added mass and rigidity in the structure response. During the second ambient noise measurements the mass and stiffness added to the structure consist on the internal walls, the mechanical ventilation plant with associated machinery placed on the terrace, the windows, the layers of floor pavements and the external walls panels, that were finished. The external walls have been modeled as frame elements to considered its stiffness in addition to the mass while the other elements mentioned are modeled only as mass.
'FE Model 1' and 'FE Model 2' are the calibrated models by using respectively the structural response estimated from the first and the second ambient noise measurements acquired during the construction of the building.
In all finite element models the pillars and beams have been modeled with frame elements while the staircase and lift cores with shell elements. The horizontal structures at all levels have been modeled as rigid diaphragms (by the help of joint constraints), considering the stiffening effect of the completion reinforced slab of 5 cm thick. The pillars are wedge in the base while beams are stuck with pillars. Also, the staircase and lift cores are wedge in the base. The concrete class has been set as described by the project for each structural elements, i.e. in 'FE Model 0'. The mass has been defined from elements and loads which are applied on beams referred to the direction of slabs. The equivalent connecting rod theory has been used to model the external walls by frame elements in the calibrated models.

The external wall panels have been modeled by frame element in 'FE Model 1', while the remaining load (difference between the weight of the connecting rods and the walls) has been modeled as mass. The windows opening in the external wall panels have been considered by reducing the dimension of frame elements used to model the external walls. The modulus of elasticity of the concrete has been modified (25% higher) up to reach the same structure response with those estimated from the first ambient vibration measurements. Moreover, various elements which weren't taken into account before, have been modeled. The beams added to the model 'Cordoli 40x15cm' and 'T20x5cm', where the floor slab are connected with one another, are shown in the Figure 6.59.

In the 'FE Model 2' the external walls have been also modeled with frame elements dimensioned due to the equivalent rod theory. In this case, the windows opening in the external wall panels are considered by reducing the difference of the load between the weight of the connecting rods and the walls. Moreover, various elements and loads which weren't taken into account before, have been modeled. Also in this case, beams where the floor slab are connected with one another, have been modeled (see Figure 6.59, beams named 'Cordoli 40x15cm' and 'T20x5cm'). The modulus of elasticity of the concrete has been increased (25% higher) to reach the same structure response with those estimated from the second ambient noise measurements.

The 'FE Model 3' is the calibrated one 'FE Model 2' without modeling the rigidity of the external walls. Being in the field of environmental measures, the rigidity of external walls panels influence significantly in the dynamic response of the structure but they are not designed to withstand the earthquake. Therefore, the calibrated model without modeled the rigidity of wall panels, should be used for seismic response controls of the structures. In this case, only the mass of walls have been considered.

In the Figure 6.57 is shown the calibrated 'FE Model 1' from the first ambient noise measurements, the staircase and elevator cores. In the Figure 6.58 is shown the calibrated 'FE Model 2', the staircase and elevator cores, calibrated from the second ambient vibration measurements. In the Figure 6.60 is shown the calibrated 'FE Model 3', from the second measurements without taking into account the external wall rigidity, therefore, without modeling external walls as frame element but only as mass.

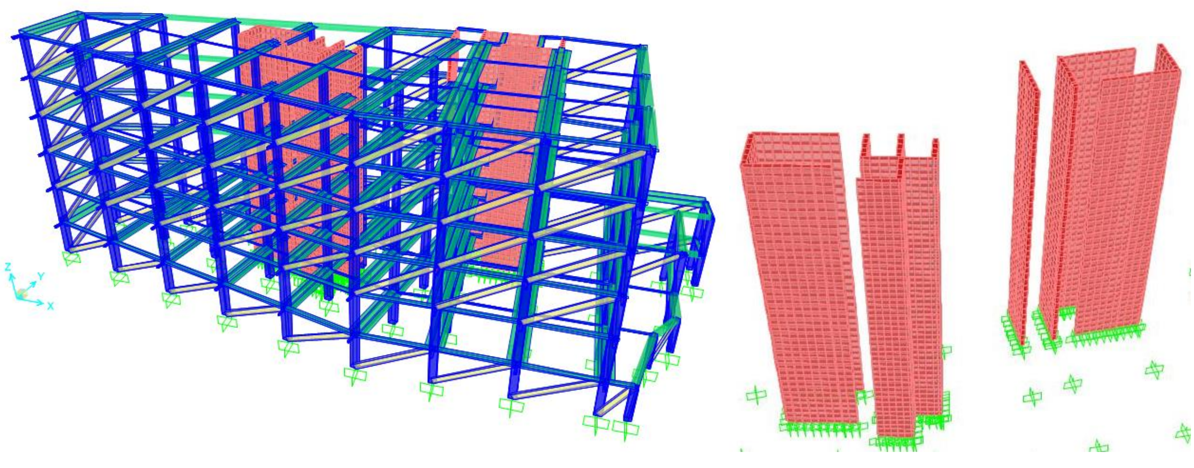

Figure 6.57 *Calibrated 'FE Model 1' of the building (left), staircase and lift cores (right)*

In the Figure 6.59 is shown the distribution in plan of the added beams ('Cordoli 40x15cm' and 'T20x5cm').

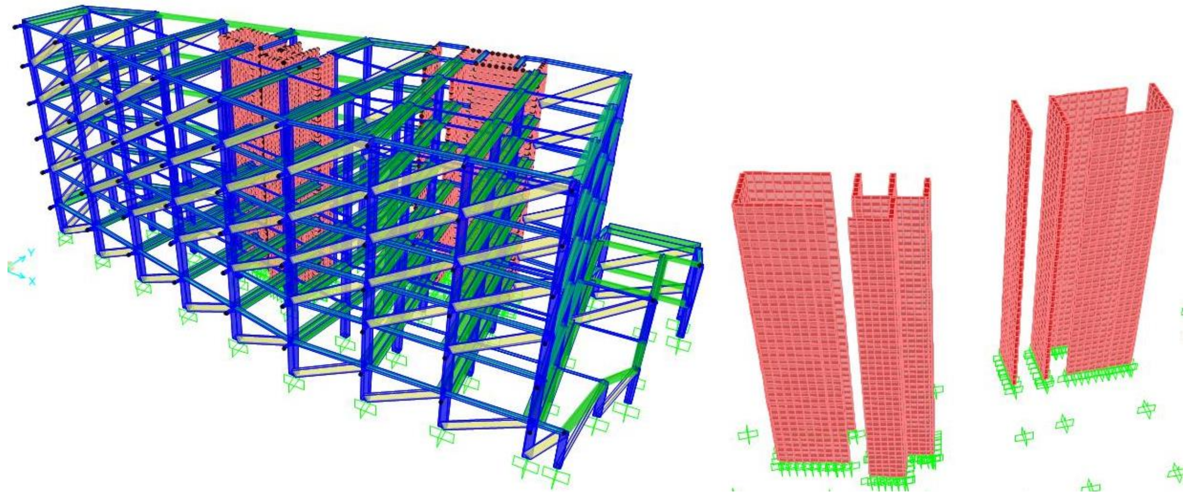

Figure 6.58 *Calibrated 'FE Model 2' of the building (left), staircase and lift cores (right)*

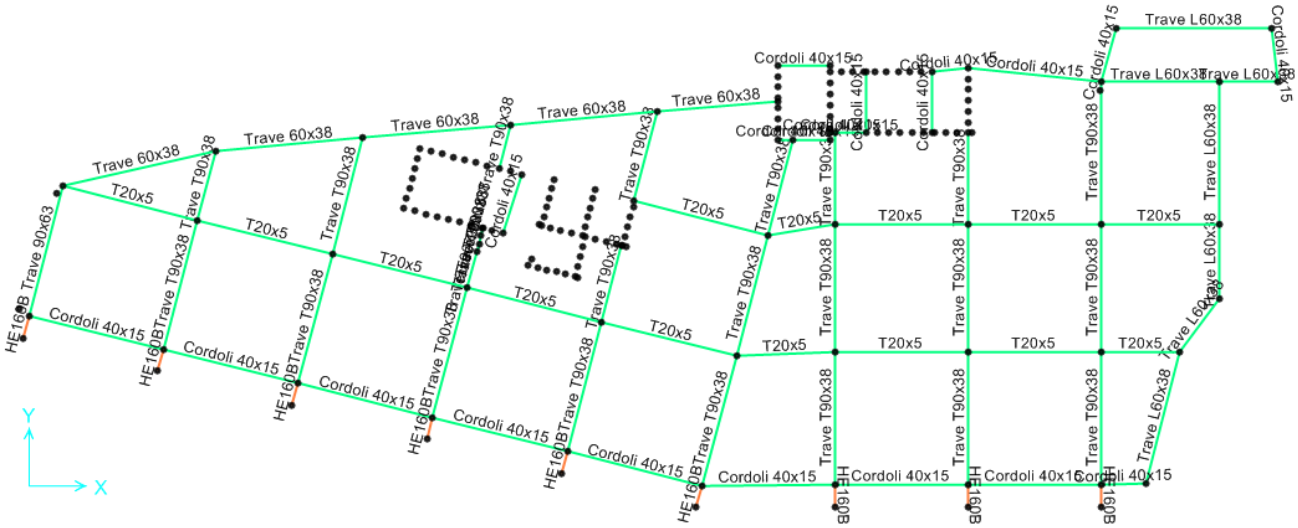

Figure 6.59 *Plan of beams 'Cordoli 40x15cm' and 'T20x5cm' added in the calibrated models*

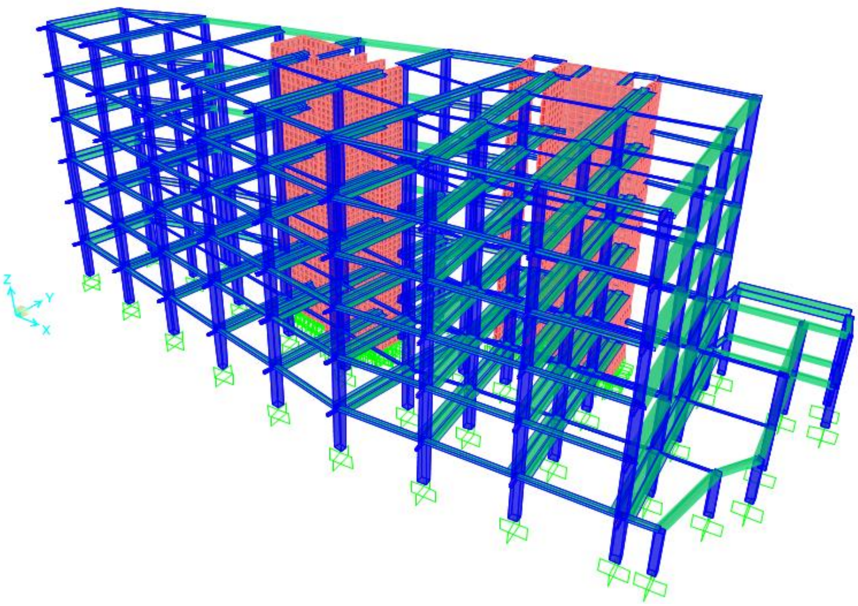

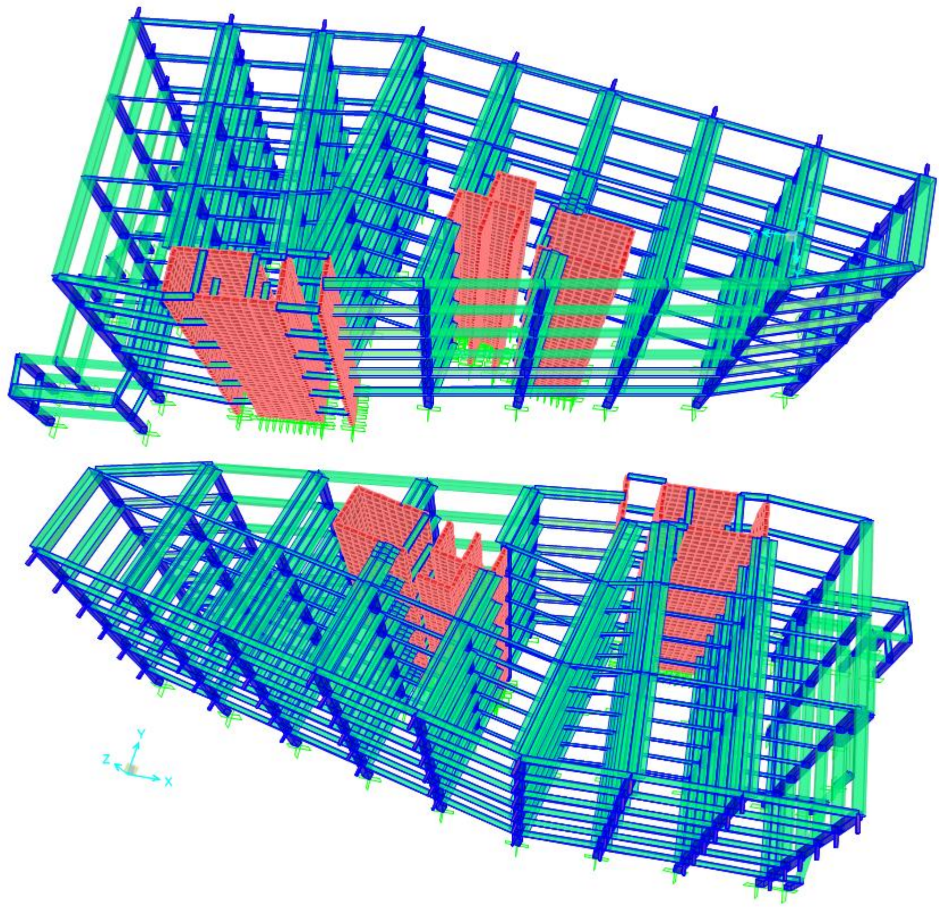

Figure 6.60 *Views from calibrated 'FE Model 3'*

6.5.1 Modified parameters or elements

Different elements and loads have been added to the initial finite element model of the project to achieve the same dynamic response of the structure with that obtained from operational modal analysis. Furthermore, material parameters as concrete class and elastic modulus of concrete have been modified.

6.5.1.1 Modeling of the external cover panels

The external cover panels have been modeled with frame elements dimensioned referred to the theory of equivalent rod of Circolare n.65, 10/4/1997) and studies of various authors. The frame elements used have the same concrete class as the walls panels C32/40.

The external wall panels can be modeled with frame elements with rigidity equal to that of the panels and dimensioned by the Equation 6.1, referred to the 'Circolare n.65'. In this case the thickness of the equivalent rod is equal to the thickness of the wall panel, while the width is about 10% of the diagonal length (L). The surface estimated by the equation (A) is the transversal section of the equivalent rod and is expressed as a product of width and thickness.

$$k_{eq} = \frac{E \cdot A}{L} = 0{,}1 \cdot E_m \cdot t \qquad \text{(Eq. 6.1)}$$

where *E* is the Young modulus of the equivalent rod, *A* is the transversal section of the equivalent rod, *L* is the length of the rod, *E* is the Young modulus of the wall panel and *t* is the thickness of the wall panel.

Stafford Smith and Carter (1969) proposed the Equation 6.2 for the equivalent rod dimensioning. The width of the equivalent rod depends on the relative flexural stiffness between the panel and the pillars. In the Figure 6.61 is shown the schema of the equivalent beam elements for its modeling. The width of the connecting rod can be calculated by the relationship proposed by Mainstone (1974) (Equation 6.3).

$$\lambda_1 \cdot \mathrm{H} = \mathrm{H} \cdot \sqrt[4]{\frac{\mathrm{E_m} \cdot \mathrm{t} \cdot \sin(2\theta)}{4 \cdot \mathrm{E_c} \cdot \mathrm{I_c} \cdot \mathrm{h}}} \qquad \text{(Eq. 6.2)}$$

$$\theta = \arctan\left(\frac{\mathrm{h}}{\mathrm{l}}\right)$$

$$\mathrm{a} = 0{,}175 \cdot \mathrm{D} \cdot (\lambda_1 \cdot \mathrm{H})^{-0{,}4} \qquad \text{(Eq. 6.3)}$$

where λ_1 is the relative rigidity of the rod, *a* is the width of the rod, *H* is the pillar height up to axis of the beam, *h* is the panel height, θ is the inclination of the diagonal with respect to the horizontal axis, I_c is the moment of inertia of the pillar, E_c is the elastic modulus of concrete, *D* is the diagonal of the panel and *t* is the thickness of the panel.

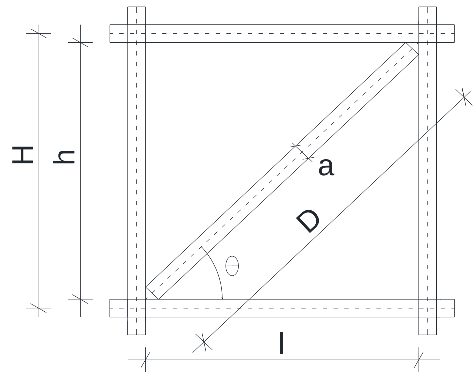

Figure 6.61 *Equivalent connecting rod dimensioning*

The reductive factor of the width (R_1) of the equivalent rod can be calculated by the relationship proposed by Al-Chaar (2002), applicable for surface of opening lower than 60% of the window surface.

$$R_1 = 0.6 \cdot \left(\frac{A_{open}}{A_{panel}}\right)^2 - 1.6 \cdot \left(\frac{A_{open}}{A_{panel}}\right) + 1$$

The width of the equivalent rod can be also calculated due to the relationship proposed by Pagano as follows:

$$\mathrm{a} = 0.5 \cdot \left(\frac{\mathrm{A_p}}{\mathrm{d}}\right) = \frac{\mathrm{l_a} \cdot \mathrm{h_1}}{2\mathrm{d}}$$

where l_a and h_1 are the axial dimension of the wall panel, *d* is the diagonal of the panel.

The calculated values of the equivalent connecting rod width are presented in the Table 6.20. As one can see, the values estimated (the last column) from relationships proposed by different authors, doesn’t vary significantly. In this study the width values calculated from Circolare nr.65, have been used. The window opening have been taken into account by using the reduction factor (R1) on the rod width.

Table 6.20 *Width value of equivalent connecting rod estimated from relationships of different authors*

Circolare n.65												Pagano		
Rod position	**Storey height (m)**	**L (m)**	**D (m)**	**A**	**s (m)**	**t (m)**	**A1**	**si (m)**	**t1 (m)**	**Reduction factor, R1**	**s (m)**	**si**	si/2	**s (m)**
Groundfloor	3,20	6,50	7,25	0,14	0,72	0,16	0,07	**0,72**	0,16	0,704	**0,51**	1,44	0,72	**0,51**
Groundfloor	3,20	6,20	6,98	0,14	0,70	0,16	0,07	**0,70**	0,16	0,704	**0,49**	1,42	0,71	**0,50**
Groundfloor	3,20	6,22	7,00	0,14	0,70	0,16	0,07	**0,70**	0,16	0,704	**0,49**	1,42	0,71	**0,50**
Groundfloor	3,20	6,56	7,30	0,15	0,73	0,16	0,07	**0,73**	0,16	0,704	**0,51**	1,44	0,72	**0,51**
Groundfloor	3,20	6,64	7,37	0,15	0,74	0,16	0,07	**0,74**	0,16	0,704	**0,52**	1,44	0,72	**0,51**
Groundfloor	3,20	6,26	7,03	0,14	0,70	0,16	0,07	**0,70**	0,16	0,704	**0,49**	1,42	0,71	**0,50**
Groundfloor	3,20	6,00	6,80	0,14	0,68	0,16	0,07	**0,68**	0,16	0,704	**0,48**	1,41	0,71	**0,50**
1Floor	3,97	6,50	7,62	0,15	0,76	0,16	0,08	**0,76**	0,16	0,704	**0,54**	1,69	0,85	**0,60**
1Floor	3,97	6,20	7,36	0,15	0,74	0,16	0,07	**0,74**	0,16	0,704	**0,52**	1,67	0,84	**0,59**
1Floor	3,97	6,22	7,38	0,15	0,74	0,16	0,07	**0,74**	0,16	0,704	**0,52**	1,67	0,84	**0,59**
1Floor	3,97	6,56	7,67	0,15	0,77	0,16	0,08	**0,77**	0,16	0,704	**0,54**	1,70	0,85	**0,60**
1Floor	3,97	6,00	7,20	0,14	0,72	0,16	0,07	**0,72**	0,16	0,704	**0,51**	1,66	0,83	**0,58**
1Floor	3,97	6,64	7,74	0,15	0,77	0,16	0,08	**0,77**	0,16	0,704	**0,54**	1,70	0,85	**0,60**
1Floor	3,97	6,26	7,42	0,15	0,74	0,16	0,07	**0,74**	0,16	0,704	**0,52**	1,68	0,84	**0,59**
1Floor	3,97	6,90	7,96	0,16	0,80	0,16	0,08	**0,80**	0,16	0,704	**0,56**	1,72	0,86	**0,61**
1Floor	3,97	7,36	8,36	0,17	0,84	0,16	0,08	**0,84**	0,16	0,704	**0,59**	1,75	0,87	**0,62**
1Floor	3,97	5,70	6,95	0,14	0,69	0,16	0,07	**0,69**	0,16	0,704	**0,49**	1,63	0,81	**0,57**
Other floors	3,65	6,50	7,46	0,15	0,75	0,16	0,07	**0,75**	0,16	0,704	**0,52**	1,59	0,80	**0,56**
Other floors	3,65	6,20	7,20	0,14	0,72	0,16	0,07	**0,72**	0,16	0,704	**0,51**	1,57	0,79	**0,55**
Other floors	3,65	6,22	7,21	0,14	0,72	0,16	0,07	**0,72**	0,16	0,704	**0,51**	1,57	0,79	**0,55**
Other floors	3,65	6,56	7,51	0,15	0,75	0,16	0,08	**0,75**	0,16	0,704	**0,53**	1,60	0,80	**0,56**
Other floors	3,65	6,64	7,58	0,15	0,76	0,16	0,08	**0,76**	0,16	0,704	**0,53**	1,60	0,80	**0,56**
Other floors	3,65	6,00	7,03	0,14	0,70	0,16	0,07	**0,70**	0,16	0,704	**0,49**	1,56	0,78	**0,55**
Other floors	3,65	6,26	7,25	0,14	0,72	0,16	0,07	**0,72**	0,16	0,704	**0,51**	1,58	0,79	**0,56**
Other floors	3,65	6,90	7,81	0,16	0,78	0,16	0,08	**0,78**	0,16	0,704	**0,55**	1,61	0,81	**0,57**
Other floors	3,65	7,36	8,22	0,16	0,82	0,16	0,08	**0,82**	0,16	0,704	**0,58**	1,64	0,82	**0,58**
Other floors	3,65	5,70	6,77	0,14	0,68	0,16	0,07	**0,68**	0,16	0,704	**0,48**	1,54	0,77	**0,54**

Pavia Cavaleri and Fossetti																		
Rod position	**Storey height (m)**	**L (m)**	**D (m)**	**A**	**s (m)**	**t (m)**	**c**	**β**	**z**	**λ**	**Ac**	**Ab**	**w/d**	**w**	**l/h**	**r**	**wr**	**wr/2**
Groundfloor	3,20	6,50	7,25	0,14	0,72	0,16	0,269	0,153	1,258	1,17	0,30	0,34	0,21	1,51	2,03	0,82	1,23	**0,62**
Groundfloor	3,20	6,20	6,98	0,14	0,70	0,16	0,269	0,153	1,234	1,18	0,30	0,34	0,21	1,48	1,94	0,82	1,21	**0,60**
Groundfloor	3,20	6,22	7,00	0,14	0,70	0,16	0,269	0,153	1,236	1,18	0,30	0,34	0,21	1,49	1,94	0,82	1,21	**0,61**
Groundfloor	3,20	6,56	7,30	0,15	0,73	0,16	0,269	0,153	1,263	1,17	0,30	0,34	0,21	1,52	2,05	0,82	1,24	**0,62**
Groundfloor	3,20	6,64	7,37	0,15	0,74	0,16	0,269	0,153	1,269	1,17	0,30	0,34	0,21	1,53	2,08	0,82	1,24	**0,62**
Groundfloor	3,20	6,26	7,03	0,14	0,70	0,16	0,269	0,153	1,239	1,18	0,30	0,34	0,21	1,49	1,96	0,82	1,21	**0,61**
Groundfloor	3,20	6,00	6,80	0,14	0,68	0,16	0,269	0,153	1,219	1,19	0,30	0,34	0,22	1,46	1,88	0,82	1,19	**0,60**
1Floor	3,97	6,50	7,62	0,15	0,76	0,16	0,269	0,153	1,159	1,55	0,30	0,34	0,22	1,65	1,64	0,82	1,35	**0,67**
1Floor	3,97	6,20	7,36	0,15	0,74	0,16	0,269	0,153	1,140	1,59	0,30	0,34	0,22	1,62	1,56	0,82	1,32	**0,66**
1Floor	3,97	6,22	7,38	0,15	0,74	0,16	0,269	0,153	1,142	1,59	0,30	0,34	0,22	1,62	1,57	0,82	1,32	**0,66**
1Floor	3,97	6,56	7,67	0,15	0,77	0,16	0,269	0,153	1,163	1,54	0,30	0,34	0,22	1,66	1,65	0,82	1,36	**0,68**
1Floor	3,97	6,00	7,20	0,14	0,72	0,16	0,269	0,153	1,128	1,63	0,30	0,34	0,22	1,60	1,51	0,82	1,30	**0,65**
1Floor	3,97	6,64	7,74	0,15	0,77	0,16	0,269	0,153	1,168	1,53	0,30	0,34	0,22	1,67	1,67	0,82	1,36	**0,68**
1Floor	3,97	6,26	7,42	0,15	0,74	0,16	0,269	0,153	1,144	1,58	0,30	0,34	0,22	1,63	1,58	0,82	1,33	**0,66**
1Floor	3,97	6,90	7,96	0,16	0,80	0,16	0,269	0,153	1,185	1,51	0,30	0,34	0,21	1,70	1,74	0,82	1,39	**0,69**
1Floor	3,97	7,36	8,36	0,17	0,84	0,16	0,269	0,153	1,213	1,48	0,30	0,34	0,21	1,75	1,85	0,82	1,43	**0,71**
1Floor	3,97	5,70	6,95	0,14	0,69	0,16	0,269	0,153	1,109	1,69	0,30	0,34	0,22	1,56	1,44	0,82	1,27	**0,63**
Other floors	3,65	6,50	7,46	0,15	0,75	0,16	0,269	0,153	1,195	1,37	0,30	0,34	0,21	1,60	1,78	0,82	1,30	**0,65**
Other floors	3,65	6,20	7,20	0,14	0,72	0,16	0,269	0,153	1,175	1,40	0,30	0,34	0,22	1,57	1,70	0,82	1,28	**0,64**
Other floors	3,65	6,22	7,21	0,14	0,72	0,16	0,269	0,153	1,176	1,40	0,30	0,34	0,22	1,57	1,70	0,82	1,28	**0,64**
Other floors	3,65	6,56	7,51	0,15	0,75	0,16	0,269	0,153	1,199	1,37	0,30	0,34	0,21	1,61	1,80	0,82	1,31	**0,65**
Other floors	3,65	6,64	7,58	0,15	0,76	0,16	0,269	0,153	1,205	1,36	0,30	0,34	0,21	1,62	1,82	0,82	1,32	**0,66**
Other floors	3,65	6,00	7,03	0,14	0,70	0,16	0,269	0,153	1,161	1,42	0,30	0,34	0,22	1,54	1,64	0,82	1,26	**0,63**
Other floors	3,65	6,26	7,25	0,14	0,72	0,16	0,269	0,153	1,179	1,39	0,30	0,34	0,22	1,57	1,72	0,82	1,28	**0,64**
Other floors	3,65	6,90	7,81	0,16	0,78	0,16	0,269	0,153	1,223	1,35	0,30	0,34	0,21	1,64	1,89	0,82	1,34	**0,67**
Other floors	3,65	7,36	8,22	0,16	0,82	0,16	0,269	0,153	1,254	1,34	0,30	0,34	0,21	1,69	2,02	0,82	1,38	**0,69**
Other floors	3,65	5,70	6,77	0,14	0,68	0,16	0,269	0,153	1,140	1,46	0,30	0,34	0,22	1,51	1,56	0,82	1,23	**0,61**

Stafford Smith and Carter														
Rod position	Pillar	Beam	Ic(m4)	Ø (°)	h (m)	H (m)	t (m)	D (m)	Ec	Em	λ1*H	Width, a=ai (m)	R1	**a (m)**
2 Floor	P60x50	L60x38	0,0090	27,9	3,27	3,65	0,16	7,81	36416,1	33642,8	3,68	0,81	0,704	**0,57**
2 Floor	P50x40	L60x38	0,0042	26,4	3,27	3,65	0,16	8,22	36416,1	33642,8	4,43	0,79	0,704	**0,56**
2 Floor	P50x50	L60x38	0,0052	30,2	3,27	3,65	0,16	7,25	36416,1	33642,8	4,28	0,71	0,704	**0,50**

6.5.1.2 Elastic modulus and class of concrete

The general characteristics of the concrete class used to model the structural elements of the building are presented in the Table 6.1. Different classes of concrete were used for the construction of the building as described by the computing project. In the finite element model of the project the same concrete class C25/30 for all structural elements, has been used. Therefore, the initial model has been modified by using concrete class as described by the project: pillars and beams with C45/55; external infill panels with concrete C32/40; stairwells and lift shaft with C28/35 and added beams 'Cordoli 40x15cm' and 'T20x5cm' with C28/35.

The influence of the concrete class in the structural response has been evaluated by comparing the frequencies from the calibrated 'FE Model 2' when using the same concrete class for all elements: first C25x30 and second C45/55. At this aim, two calibrated FEM have been created ones using concrete class C25x30 for all elements and ones using C45x55 for all elements. The frequency and modal participation mass ratio are shown respectively for both models in the Table 6.21 and Table 6.22. The first four modal frequencies achieved from both finite element models differ less than 4% from one another, and are higher in the case of FE model with C25/30 concrete class which are also more similar with the initial model (with different concrete class). Modal participation mass ratio doesn't differ significantly in case of FE model with C25/30 concrete class, while has a higher variation for the model with C45/55 concrete class.

Table 6.21 *Frequencies from 'FE Model 2' using the same concrete class for all elements C25x30*

FE Model 2, with		**Period**	**Frequency**	**UX**	**UY**	**RZ**	**SumUX**	**SumUY**	**SumRZ**
C25x30	**No.**	Sec	Hz	Unitless	Unitless	Unitless	Unitless	Unitless	Unitless
Mode	1	0,42	**2,38**	0,00742	**0,62370**	**0,32303**	0,00742	0,62370	0,32303
Mode	2	0,31	**3,23**	0,09451	0,05018	**0,20386**	0,10193	0,67388	0,52689
Mode	3	0,26	**3,86**	**0,60438**	0,00016	**0,14172**	0,70631	0,67404	0,66861
Mode	4	0,11	**8,76**	0,00046	**0,14649**	0,06310	0,70677	0,82053	0,73172
Mode	5	0,10	9,83	0,00173	0,04131	0,09080	0,70851	0,86183	0,82252
Mode	6	0,09	11,04	0,00002	0,00000	0,00000	0,70852	0,86184	0,82252
Mode	7	0,09	11,04	0,00005	0,00000	0,00002	0,70858	0,86184	0,82254
Mode	8	0,09	11,56	0,01825	0,00012	0,00367	0,72683	0,86196	0,82621
Mode	9	0,09	11,72	0,00012	0,00001	0,00001	0,72695	0,86196	0,82622
Mode	10	0,08	11,80	0,00017	0,00001	0,00002	0,72712	0,86197	0,82624
Mode	11	0,08	12,26	0,00028	0,00000	0,00006	0,72741	0,86197	0,82630
Mode	12	0,08	12,26	0,00300	0,00016	0,00021	0,73041	0,86213	0,82651
Mode	13	0,08	12,50	0,03991	0,00095	0,00444	0,77032	0,86308	0,83095
Mode	14	0,08	12,88	0,01940	0,00006	0,00272	0,78972	0,86314	0,83367
Mode	15	0,07	13,37	0,00781	0,00000	0,00114	0,79753	0,86314	0,83481
Mode	16	0,07	13,38	0,04338	0,00009	0,00589	0,84091	0,86323	0,84070
Mode	17	0,07	13,43	0,00728	0,00000	0,00108	0,84819	0,86323	0,84178
Mode	18	0,07	13,52	0,00010	0,00000	0,00001	0,84828	0,86323	0,84179
Mode	19	0,07	13,86	0,01973	0,00000	0,00436	0,86802	0,86324	0,84615
Mode	20	0,07	13,93	0,00100	0,00005	0,00051	0,86901	0,86328	0,84666
Mode	21	0,07	14,79	0,00045	0,00008	0,00004	0,86946	0,86337	0,84670
Mode	22	0,07	15,01	0,00089	0,00046	0,00110	0,87035	0,86383	0,84780
Mode	23	0,06	15,63	0,00432	0,00015	0,00019	0,87467	0,86398	0,84798
Mode	24	0,06	15,74	0,00015	0,00001	0,00000	0,87482	0,86399	0,84799
Mode	25	0,06	15,99	0,00000	0,00007	0,00010	0,87482	0,86406	0,84809
Mode	26	0,06	16,11	0,00000	0,00017	0,00019	0,87482	0,86424	0,84828
Mode	27	0,06	16,17	0,00002	0,00080	0,00132	0,87484	0,86504	0,84960
Mode	28	0,06	16,28	0,00030	0,00055	0,00011	0,87514	0,86559	0,84971
Mode	29	0,06	16,82	0,00109	0,00611	0,00086	0,87623	0,87170	0,85058

Table 6.22 *Frequencies from 'FE Model 2' using the same concrete class for all elements C45x55*

FE Model 2, with		**Period**	**Frequency**	**UX**	**UY**	**RZ**	**SumUX**	**SumUY**	**SumRZ**
C45x55	**No.**	Sec	Hz	Unitless	Unitless	Unitless	Unitless	Unitless	Unitless
Mode	1	0,43	**2,31**	0,00610	**0,63194**	**0,33488**	0,00610	0,63194	0,33488
Mode	2	0,32	**3,15**	0,07597	0,04449	**0,20385**	0,08208	0,67644	0,53873
Mode	3	0,27	**3,70**	**0,62582**	0,00004	**0,13338**	0,70790	0,67648	0,67211
Mode	4	0,12	**8,50**	0,00022	**0,15386**	0,07103	0,70812	0,83034	0,74313
Mode	5	0,10	9,53	0,00085	0,03185	0,08234	0,70896	0,86218	0,82547
Mode	6	0,09	11,18	0,00017	0,00001	0,00001	0,70913	0,86219	0,82548
Mode	7	0,09	11,19	0,00196	0,00001	0,00036	0,71108	0,86220	0,82584
Mode	8	0,09	11,35	0,02660	0,00024	0,00437	0,73769	0,86244	0,83021
Mode	9	0,08	11,79	0,00024	0,00001	0,00002	0,73793	0,86245	0,83023
Mode	10	0,08	11,86	0,00033	0,00001	0,00003	0,73826	0,86246	0,83026
Mode	11	0,08	12,26	0,05891	0,00103	0,00631	0,79717	0,86349	0,83657
Mode	12	0,08	12,39	0,00004	0,00001	0,00000	0,79721	0,86349	0,83657
Mode	13	0,08	12,44	0,00920	0,00007	0,00118	0,80641	0,86356	0,83775
Mode	14	0,08	12,82	0,03039	0,00001	0,00436	0,83680	0,86357	0,84211
Mode	15	0,08	13,22	0,02182	0,00000	0,00311	0,85862	0,86357	0,84522
Mode	16	0,07	13,37	0,00024	0,00000	0,00005	0,85886	0,86358	0,84527
Mode	17	0,07	13,48	0,00008	0,00000	0,00001	0,85894	0,86358	0,84528
Mode	18	0,07	13,50	0,00050	0,00001	0,00009	0,85944	0,86359	0,84538
Mode	19	0,07	13,69	0,01129	0,00000	0,00276	0,87073	0,86359	0,84814
Mode	20	0,07	14,22	0,00002	0,00002	0,00005	0,87074	0,86362	0,84819
Mode	21	0,07	14,47	0,00024	0,00008	0,00002	0,87099	0,86370	0,84821
Mode	22	0,07	14,99	0,00107	0,00035	0,00094	0,87206	0,86405	0,84915
Mode	23	0,07	15,24	0,00300	0,00026	0,00000	0,87505	0,86431	0,84915
Mode	24	0,06	15,78	0,00001	0,00001	0,00000	0,87506	0,86432	0,84916
Mode	25	0,06	15,99	0,00012	0,00070	0,00002	0,87519	0,86502	0,84917
Mode	26	0,06	16,11	0,00001	0,00014	0,00015	0,87519	0,86516	0,84933
Mode	27	0,06	16,24	0,00000	0,00041	0,00048	0,87519	0,86557	0,84980
Mode	28	0,06	16,30	0,00001342	0,00085	0,00188	0,87521	0,86642	0,85168

Elastic modulus of concrete has been increased up to reach satisfying results. In the Table 6.23 are presented the values of elastic modulus of concrete for different percentages of increase.

Table 6.23 *Elastic modulus of concrete for different percentages of increment*

Concrete Class	**E (N/mm^2)**	**1,1·E (N/mm^2)**	**1,2·E (N/mm^2)**	**1,25·E (N/mm^2)**	**1,30·E (N/mm^2)**
C25/30	31476	34623	37771	39345	40919
C28/35	32308	35539	38770	40385	42001
C32/40	33346	36680	40015	41682	43349
C45/55	36283	39912	43540	45354	47168

In the Table 6.24 is presented the percentage variation of frequencies and modal participation mass ratios for different increment values of elastic modulus of concrete. The percentage variation of frequencies increase by 4.7%, 8.7%, 10.6 % and 12.3 % when increase the elastic modulus of concrete respectively by 10%, 20%, 25% and 30%. The modal participation mass ratio doesn't vary significantly, therefore, the mode shape are almost the same.

Table 6.24 *Frequencies and modal participation mass ratio from FEM with different elastic modulus of concrete*

Mode	FE Model 3								Percentage variation (%)			
	E				1.1 E				between E and 1.1 E			
No.	Frq. (Hz)	UX (%)	UY (%)	RZ (%)	Frq. (Hz)	UX (%)	UY (%)	RZ (%)	Frq. (%)	UX (%)	UY (%)	RZ (%)
1	1,09	6,71	0,61	11,22	1,14	6,71	0,61	11,22	4,7	0,0	0,0	0,0
2	1,49	8,14	55,51	48,42	1,56	8,14	55,51	48,42	4,7	0,0	0,0	0,0
3	1,92	47,98	7,88	1,09	2,02	47,98	7,88	1,09	4,7	0,0	0,0	0,0
4	4,28	1,57	0,18	4,23	4,49	1,57	0,18	4,23	4,7	0,0	0,0	0,0

Mode	FE Model 3								Percentage variation (%)			
	E				1.20 E				between E and 1.2 E			
No.	Frq. (Hz)	UX (%)	UY (%)	RZ (%)	Frq. (Hz)	UX (%)	UY (%)	RZ (%)	Frq. (%)	UX (%)	UY (%)	RZ (%)
1	1,09	6,71	0,61	11,22	1,19	6,71	0,61	11,22	8,7	0,0	0,0	0,0
2	1,49	8,14	55,51	48,42	1,63	8,14	55,51	48,42	8,7	0,0	0,0	0,0
3	1,92	47,98	7,88	1,09	2,11	47,98	7,88	1,09	8,7	0,0	0,0	0,0
4	4,28	1,57	0,18	4,23	4,69	1,57	0,18	4,23	8,7	0,0	0,0	0,0

Mode	FE Model 3								Percentage variation (%)			
	E				1.25 E				between E and 1.25 E			
No.	Frq. (Hz)	UX (%)	UY (%)	RZ (%)	Frq. (Hz)	UX (%)	UY (%)	RZ (%)	Frq. (%)	UX (%)	UY (%)	RZ (%)
1	1,09	6,71	0,61	11,22	1,22	6,71	0,61	11,22	10,6	0,0	0,0	0,0
2	1,49	8,14	55,51	48,42	1,66	8,14	55,51	48,42	10,6	0,0	0,0	0,0
3	1,92	47,98	7,88	1,09	2,15	47,98	7,88	1,09	10,6	0,0	0,0	0,0
4	4,28	1,57	0,18	4,23	4,79	1,57	0,18	4,23	10,6	0,0	0,0	0,0

Mode	FE Model 3								Percentage variation (%)			
	E				1.30 E				between E and 1.30 E			
No.	Frq. (Hz)	UX (%)	UY (%)	RZ (%)	Frq. (Hz)	UX (%)	UY (%)	RZ (%)	Frq. (%)	UX (%)	UY (%)	RZ (%)
1	1,09	6,71	0,61	11,22	1,24	6,71	0,61	11,22	12,3	0,0	0,0	0,0
2	1,49	8,14	55,51	48,42	1,70	8,14	55,51	48,42	12,3	0,0	0,0	0,0
3	1,92	47,98	7,88	1,09	2,19	47,98	7,88	1,09	12,3	0,0	0,0	0,0
4	4,28	1,57	0,18	4,23	4,88	1,57	0,18	4,23	12,3	0,0	0,0	0,0

6.5.1.3 Elements and mass added

The ambient noise measures have been acquired in two different periods during the construction of the building, so as to evaluate the influence of the added mass and rigidity in the structure response. The mass and stiffness added to the structure consist mainly on the internal walls, the mechanical ventilation plant on the terrace with the associated machinery, the windows, the layers of floor pavements and the external walls that were completed during the second ambient noise measurements. The permanent load added in the terrace is about 0,8 kN/m^2, at the ‘FE Model 2’.

The external wall panels have been modeled as frame elements, dimensioned due to the equivalent rod theory, in the calibrated models, while the remaining load (difference between the weight of the connecting rods and the walls) is modeled as mass. The load from the external wall panels is 8.58 kN/m. The windows opening in the external wall panels have been considered by reducing the dimension of frame elements used to model the external walls in ‘FE Model 1’. In the 'FE Model 2' the windows opening have been considered by reducing the load applied on the beams where the wall discharge, by the difference of the load between the weight of the connecting rods and the walls. The concrete class used in both cases to model the external wall panels by frame elements is C32/40, equal to the concrete class used to construct the external cover panels.

Element which were not taken into consideration in the FEM of the project design, are beams 'Cordoli 40x15cm' and 'T20x5cm', where the floor slab are connected with one another. Those beams have been model by frame elements with concrete class C28/35. Also, the internal walls were constructed all during the second measurements, so as their load of 3.5 kN/m has been applied on all beams where the wall are supported.

6.5.2 Structure response of calibrated FEM

Finite element model of the project design 'FE Model 0' need to be calibrated as the frequencies differ significantly from the estimated one using ambient noise measurements acquired in two different periods during the construction of the building. As described before, the ambient noise measurements have been carried out in two different periods at the aim to evaluate the evolution of the structure response. The windows mounted the second time helps on the reduction of the noise due to wind and traffic. The progresses of the construction works consist in plants placed in terrace, the internal walls and pavement layer which are modeled as mass. The opening of windows in the external walls has been taken into account by reducing the load of infill panels or the dimension of frame elements used to model the walls. At this way, the rigidity of external walls added has been considered. Furthermore, the section of those frame elements has been modified up to reach the desired structure response.

The finite element model 'FE Model 1' has been calibrated using the first ambient vibration measurements. The modulus of elasticity of concrete has been increased up to 25%, as we are in the field of ambient noise measurements, therefore, the building works in elastic field. The external wall panels have been modeled as frame element, while the remaining load (difference between the weight of the connecting rods and the walls) has been modeled as mass. The windows opening in the external walls have been considered by reducing the dimension of frame elements used to model the external walls. Also, elements and loads (beams 'Cordoli 40x15cm' and 'T20x5cm), which were not taken into account in the FEM of the project design, have been modeled.

In the 'FE Model 2' the external walls have been also modeled with frame elements dimensioned due to the equivalent rod theory. In this case, the windows opening in the external wall panels have been considered by reducing the difference of the load between the weight of the connecting rods and the walls. Moreover, various elements and loads which weren't taken into account initially, have been modeled. The modulus of elasticity of concrete has been increased up to 25%, as we are in the field of ambient noise measurements.

The frequencies from the initial finite element model 'FE Model 0' and the calibrated models ('FE Model 1' and 'FE Model 2') are shown in the Table 6.25. As one can see, the frequencies from the initial FEM differ significantly from the one derived from the calibrated models and furthermore, from those achieved by the ambient noise measurements (see Table 6.27). The same conclusion is also observed for the mode shapes (modal participation mass ratio).

The first mode of 'FE Model 0' is a rotational mode with modal participation mass ratio of about 11%. The second mode shape can be considered as a combination of a translational mode in the *y* direction (modal participation mass ratio 55%) with a rotational mode (modal participation mass ratio 48%). The third mode shape is a translational mode in *x* direction with mass ratio of about 48%. This mode can also be considered as a first translational mode in *x* direction. The frequency value of the first three modes shape are respectively 1.16 Hz, 1.59 Hz and 2.05 Hz.

The first mode of 'FE Model 1' can be considered as a combination of a translational mode in the *y* direction (modal participation mass ratio 60%) with a rotational mode (modal participation mass ratio 29%). The second mode shape is a rotational mode with modal participation mass ratio of about 24%. The third mode shape is a translational mode in *x* direction with mass ratio of about 61% and has a rotational mode component of 13% mass ratio. This mode can also be considered as a first translational mode in *x* direction. The frequency value of the first three modes shape are respectively 2.06 Hz, 2.74 Hz and 3.22 Hz.

The first mode of 'FE Model 2' can be considered as a combination of a translational mode in the *y* direction (modal participation mass ratio 63%) with a rotational mode (modal participation mass ratio 32%). The second mode shape is a rotational mode with modal participation mass ratio of about 21%. The third mode shape is a translational mode in *x* direction with mass ratio of about 61% and has a rotational mode component of 14% mass ratio. This mode can also be considered as a first translational mode in *x* direction. The frequency value of the first three modes shape are respectively 2.30 Hz, 3.11 Hz and 3.70 Hz.

The modal participation mass ratio doesn't vary significantly between two calibrated models. The frequencies increase with about 10% from 'FE Model 1' to 'FE Model 2', with about 43% from 'FE Model 0' to 'FE Model 1', and with about 50% from 'FE Model 0' to 'FE Model 2'.

Table 6.25 *Modal frequencies from 'FE Model 0', 'FE Model 1' and 'FE Model 2'*

Model 0		**Period**	**Frequency**	**UX**	**UY**	**RZ**	**SumUX**	**SumUY**	**SumRZ**
	No.	Sec	(Hz)	Unitless	Unitless	Unitless	Unitless	Unitless	Unitless
Mode	1	0,87	**1,16**	0,06537	0,00534	**0,11154**	0,06537	0,00534	0,11154
Mode	2	0,63	**1,59**	0,08071	**0,55487**	**0,48434**	0,14609	0,56021	0,59589
Mode	3	0,49	**2,05**	**0,48141**	0,07906	0,01082	0,6275	0,63926	0,60671
Mode	4	0,22	**4,56**	0,01514	0,00158	0,04228	0,64264	0,64085	0,64898
Mode	5	0,14	7,13	0,00853	**0,20827**	0,16799	0,65118	0,84912	0,81697
Mode	6	0,11	9,34	0,1681	0,00494	0,02736	0,81928	0,85406	0,84433
Mode	7	0,10	9,62	0,04928	0,00325	0,00721	**0,86856**	**0,85731**	**0,85153**

Model 1		**Period**	**Frequency**	**UX**	**UY**	**RZ**	**SumUX**	**SumUY**	**SumRZ**
	No.	Sec	Hz	Unitless	Unitless	Unitless	Unitless	Unitless	Unitless
Mode	1	0,48	**2,06**	0,01248	**0,59892**	**0,29196**	0,01248	0,59892	0,29196
Mode	2	0,37	**2,74**	0,08088	0,07083	**0,23664**	0,09336	0,66976	0,52859
Mode	3	0,31	**3,22**	**0,60901**	0,0000221	**0,12778**	0,70237	0,66978	0,65637
Mode	4	0,13	**7,60**	0,00165	0,09616	0,02415	0,70402	0,76594	0,68052
Mode	5	0,12	8,38	0,00081	0,09811	**0,14901**	0,70484	0,86405	0,82953
Mode	6	0,10	10,52	0,00013	0,000005131	0,000009325	0,70497	0,86405	0,82954
Mode	7	0,09	10,67	0,04936	0,0006	0,00676	0,75433	0,86465	0,8363
Mode	8	0,09	10,80	0,00792	0,0000938	0,00104	0,76225	0,86474	0,83733
Mode	9	0,09	11,18	0,0007	0,00001157	0,0000672	0,76295	0,86475	0,8374
Mode	10	0,09	11,28	0,00423	0,00005137	0,00045	0,76718	0,8648	0,83786
Mode	11	0,09	11,35	0,09268	0,0008	0,0107	0,85986	0,86561	0,84856
Mode	12	0,09	11,73	0,00081	1,846E-07	0,00009437	0,86067	0,86561	0,84865
Mode	13	0,09	11,73	0,00215	0,000003775	0,00044	0,86282	0,86561	0,8491
Mode	14	0,08	11,93	0,00493	0,000053	0,00101	**0,86775**	**0,86566**	**0,85011**

Model 2		**Period**	**Frequency**	**UX**	**UY**	**RZ**	**SumUX**	**SumUY**	**SumRZ**
	No.	Sec	Hz	Unitless	Unitless	Unitless	Unitless	Unitless	Unitless
Mode	1	0,44	**2,30**	0,00735	**0,62514**	**0,31979**	0,00735	0,62514	0,31979
Mode	2	0,32	**3,11**	0,08915	0,05191	**0,21117**	0,09650	0,67704	0,53097
Mode	3	0,27	**3,70**	**0,61322**	0,00015	**0,14029**	0,70973	0,67719	0,67126
Mode	4	0,12	**8,39**	0,00025	**0,14789**	0,06395	0,70998	0,82508	0,73521
Mode	5	0,11	9,42	0,00120	0,03850	**0,09000**	0,71118	0,86358	0,82521
Mode	6	0,09	11,19	0,00007	0,00000	0,00000	0,71125	0,86358	0,82521
Mode	7	0,09	11,21	0,00064	0,00000	0,00012	0,71189	0,86359	0,82533
Mode	8	0,09	11,46	0,03543	0,00029	0,00583	0,74732	0,86388	0,83116
Mode	9	0,08	11,80	0,00011	0,00000	0,00001	0,74743	0,86388	0,83117
Mode	10	0,08	11,88	0,00016	0,00000	0,00002	0,74759	0,86389	0,83119
Mode	11	0,08	12,34	0,05508	0,00068	0,00642	0,80268	0,86457	0,83761
Mode	12	0,08	12,40	0,00000	0,00000	0,00000	0,80268	0,86457	0,83761
Mode	13	0,08	12,46	0,02995	0,00020	0,00394	0,83263	0,86477	0,84155
Mode	14	0,08	12,88	0,01405	0,00001	0,00232	0,84667	0,86478	0,84387
Mode	15	0,08	13,24	0,01759	0,00000	0,00265	0,86427	0,86478	0,84651
Mode	16	0,07	13,38	0,00054	0,00000	0,00012	0,86480	0,86478	0,84663
Mode	17	0,07	13,49	0,00003	0,00001	0,00000	0,86483	0,86479	0,84663
Mode	18	0,07	13,50	0,00003	0,00001	0,00000	0,86487	0,86480	0,84663
Mode	19	0,07	13,57	0,00000	0,00004	0,00006	0,86487	0,86484	0,84669
Mode	20	0,07	13,83	0,00790	0,00000	0,00224	0,87278	0,86484	0,84893
Mode	21	0,07	14,38	0,00041	0,00026	0,00080	0,87318	0,86510	0,84973
Mode	22	0,07	14,58	0,00035	0,00030	0,00019	0,87353	0,86540	0,84992
Mode	23	0,07	15,12	0,00061	0,00001	0,00002	0,87414	0,86541	0,84994
Mode	24	0,07	15,29	0,00235	0,00008	0,00004	0,87649	0,86550	0,84998
Mode	25	0,06	15,39	0,00001	0,00007	0,00011	**0,87650**	**0,86557**	**0,85009**

Table 6.26 *Frequencies and modal participation mass ratio of FEM of the project and the calibrated ones*

Mode No.	**FE Model 0**				**FE Model 1**				**FE Model 2**			
	Frequency (Hz)	UX (%)	UY (%)	RZ (%)	Frequency (Hz)	UX (%)	UY (%)	RZ (%)	Frequency (Hz)	UX (%)	UY (%)	RZ (%)
1	1,16	6,5	0,5	11,2	2,06	1,2	59,9	29,2	2,30	0,7	62,5	32,0
3	1,59	8,1	55,5	48,4	2,74	8,1	7,1	23,7	3,11	8,9	5,2	21,1
2	2,05	48,1	7,9	1,1	3,22	60,9	0,0	12,8	3,70	61,3	0,0	14,0
4	4,56	1,5	0,2	4,2	7,60	0,2	9,6	2,4	8,39	0,0	14,8	6,4

Table 6.27 *Modal frequencies from FEM and from ambient noise measurements*

Mode\	FEM	**First ambient noise measures**					FEM	**Second ambient noise measures**				
Frequency	**FE**	**FE**	Vertical a	Vertical d	Vertical f	Vertical e	**FE**	Vertical a	Vertical d	Vertical f	Vertical e	Vertical c
(Hz)	**Model 0**	**Model 1**	OMA				**Model 2**	OMA				
1	**1,16**	**2,06**	2,35	2,33	2,34	2,35	**2,30**	2,36	2,41	2,33	2,33	2,37
3	**1,59**	**2,74**	2,70	2,71	2,69	2,67	**3,11**	2,63	-	2,63	2,65	-
2	**2,05**	**3,22**	3,45	3,44	3,43	3,41	**3,70**	2,98	2,99	2,98	3,01	3,01
4	**4,56**	**7,60**	7,68	7,61	7,68	7,68	**8,39**	3,79	3,77	3,79	3,78	3,78

Mode shapes of the initial finite element model 'FE Model 0' and the calibrated models 'FE Model 1' and 'FE Model 2' are presented respectively in the Figure 6.62, Figure 6.63 and Figure 6.64. Mode shapes identified in different verticals, when the ambient vibration measures were acquired, are shown in the paragraph 6.4.

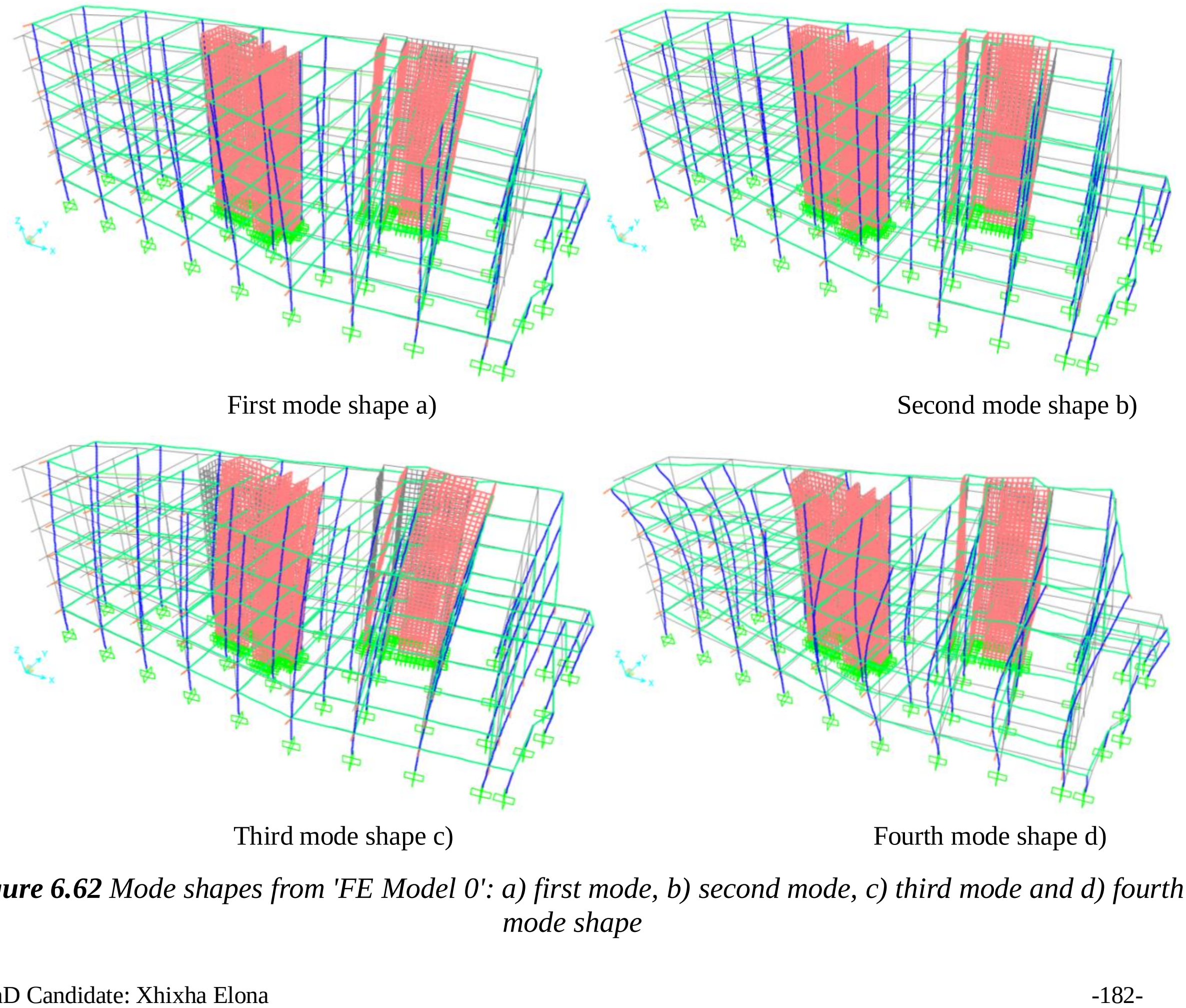

First mode shape a)

Second mode shape b)

Third mode shape c)

Fourth mode shape d)

Figure 6.62 *Mode shapes from 'FE Model 0': a) first mode, b) second mode, c) third mode and d) fourth mode shape*

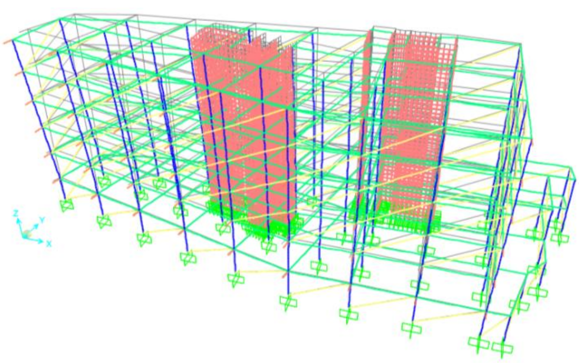
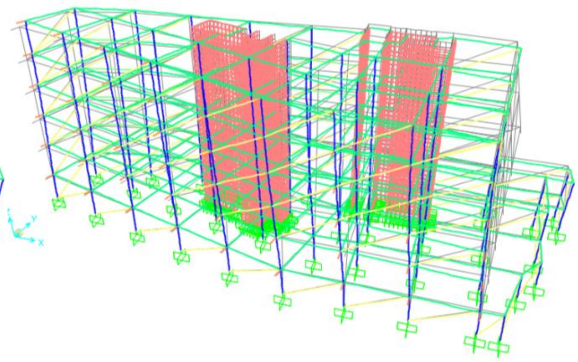

First mode shape a) Second mode shape b)

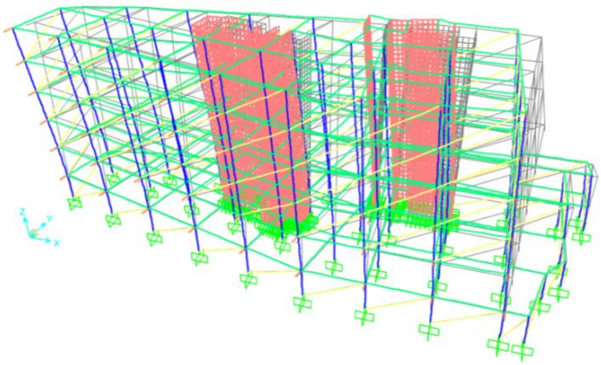
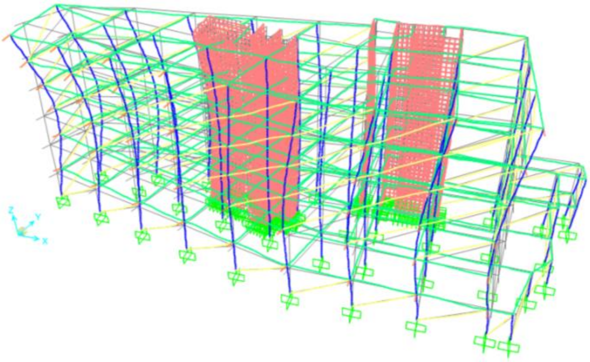

Third mode shape c) Fourth mode shape d)

Figure 6.63 *Mode shapes from 'FE Model 1': a) first mode, b) second mode, c) third mode and d) fourth mode shape*

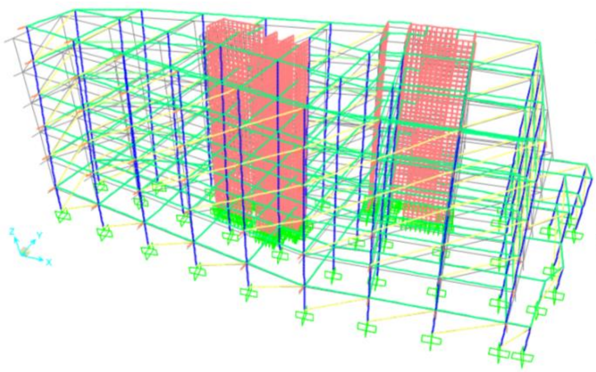
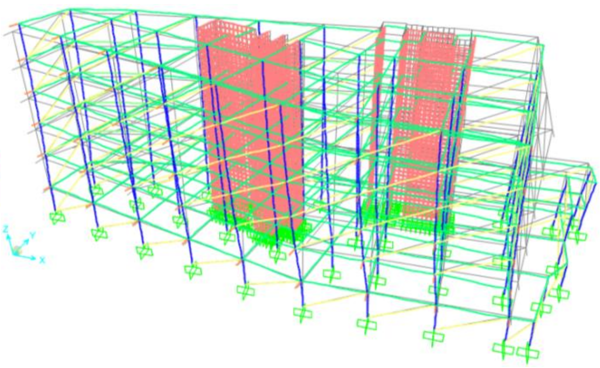

First mode shape a) Second mode shape b)

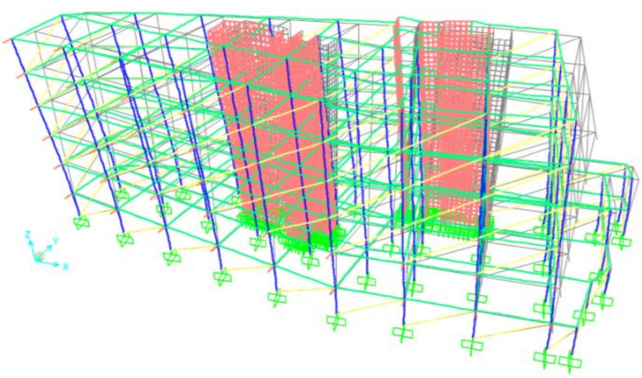
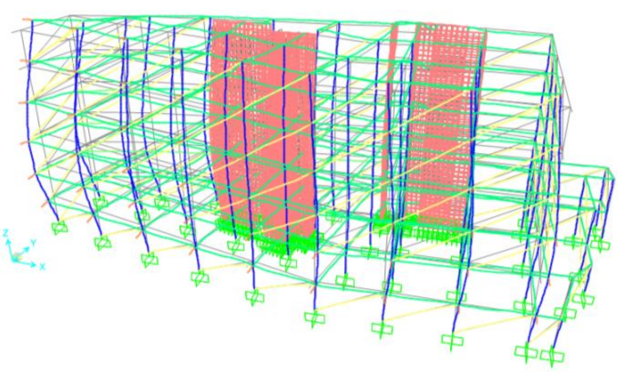

Third mode shape c) Fourth mode shape d)

Figure 6.64 *Mode shapes from 'FE Model 2': a) first mode, b) second mode, c) third mode and d) fourth mode shape*

The frequencies and the modal participation mass ratio of 'FE Model 3' (without modeling the external wall panels rigidity), are shown in the Table 6.28. As one can see, those frequencies are similar with those from the initial FEM (about 5% higher). In the Figure 6.65 are shown the first four mode shapes of this finite element model.

Table 6.28 *Frequencies and modal participation mass ratio of calibrated 'FE Model 3'*

Model 3		**Period**	**Frequency**	**UX**	**UY**	**RZ**	**SumUX**	**SumUY**	**SumRZ**
	No.	Sec	Hz	Unitless	Unitless	Unitless	Unitless	Unitless	Unitless
Mode	1	0,82	**1,21**	0,06704	0,00613	**0,55431**	0,06704	0,00613	0,55431
Mode	2	0,60	**1,66**	0,08145	**0,55505**	0,00051	0,14849	0,56118	0,55482
Mode	3	0,46	**2,15**	**0,4798**	0,07885	0,07809	0,62829	0,64003	0,63291
Mode	4	0,21	**4,79**	0,0157	0,0018	**0,19864**	0,64399	0,64183	0,83154
Mode	5	0,13	7,45	0,00869	**0,20771**	1,576E-05	0,65267	0,84954	0,83156
Mode	6	0,10	9,77	**0,17292**	0,00511	0,04349	0,82559	0,85465	0,87505
Mode	7	0,10	10,08	0,04395	0,00323	0,05257	**0,86954**	**0,85788**	**0,92761**

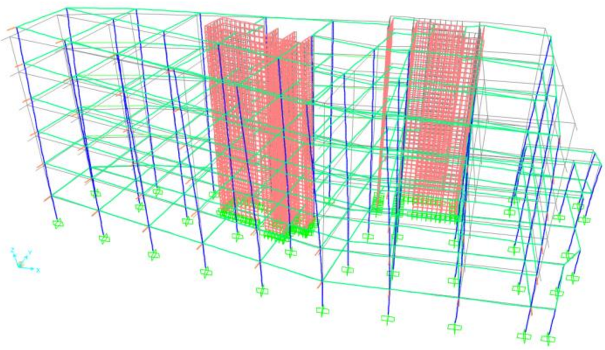

First mode shape a)

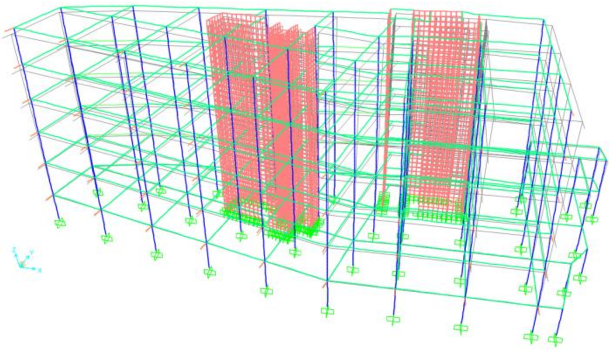

Second mode shape b)

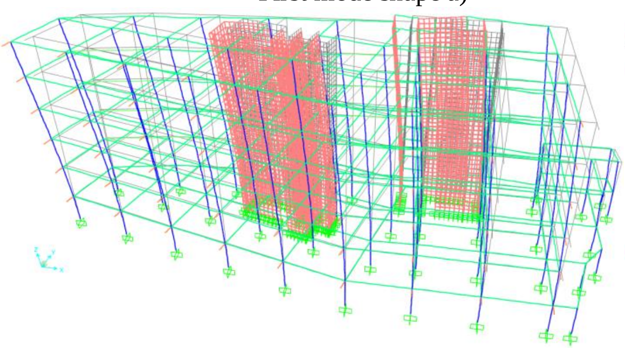

Third mode shape c)

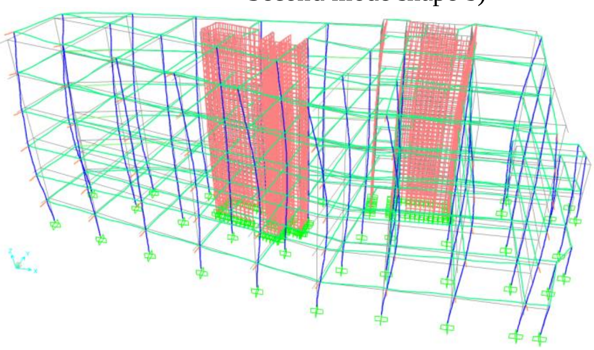

Fourth mode shape d)

Figure 6.65 *Mode shapes from 'FE Model 3': a) first mode, b) second mode, c) third mode and d) fourth mode shape*

6.5.3 Influence of external wall panels on the structural response

External cover panels have a significant influence in the response of the structure. Their rigidity is to be considered in the FEM. At this aim, the external walls have been modeled using frame element with a concrete class C32/40 (as the cover panel) while the rest of their weight has been applied as load. As can be seen in the Table 6.27, the frequencies estimated from ambient noise measurements and from FEM vary significantly between them. Therefore, the calibration of 'FE Model 0' was indispensable to be realized at the aim to receive the same structure response both from experimental and theoretical analysis. In the Table 6.29 are shown the frequencies and modal participation mass ration of all finite element models.

The percentage variation between the results from calibrated finite element models with and without modeling cover panels, have been calculated. The first modal frequency has a percentage variation of 44% for the model calibrated by the first ambient noise measurements, and about 47% for the model calibrated by the second ambient noise measurements (see Table 6.30). The comparison between ‘FE Model 1’ and ‘FE Model 2’, that have different frame sections for the equivalent connecting rods, shows a variation of about 11% for frequencies.

Table 6.29 *Results from calibrated FEM (by first and second ambient noise measures) with and without modeling the external wall panels rigidity*

Mode	**FE Model 0**				**FE Model 1**				**FE Model 1 without wall panels**			
No.	Frequency (Hz)	UX (%)	UY (%)	RZ (%)	Frequency (Hz)	UX (%)	UY (%)	RZ (%)	Frequency (Hz)	UX (%)	UY (%)	RZ (%)
1	1,16	6,5	0,5	11,2	2,06	1,2	59,9	29,2	1,15	6,5	0,5	11,2
3	1,59	8,1	55,5	48,4	2,74	8,1	7,1	23,7	1,59	8,1	55,5	48,3
2	2,05	48,1	7,9	1,1	3,22	60,9	0,0	12,8	2,05	48,1	7,9	1,1
4	4,56	1,5	0,2	4,2	7,60	0,2	9,6	2,4	4,55	1,5	0,2	4,3

Mode	**FE Model 0**				**FE Model 2**				**FE Model 3**			
No.	Frequency (Hz)	UX (%)	UY (%)	RZ (%)	Frequency (Hz)	UX (%)	UY (%)	RZ (%)	Frequency (Hz)	UX (%)	UY (%)	RZ (%)
1	1,16	6,5	0,5	11,2	2,30	0,7	62,5	32,0	1,21	6,7	0,6	55,4
3	1,59	8,1	55,5	48,4	3,11	8,9	5,2	21,1	1,66	8,1	55,5	0,1
2	2,05	48,1	7,9	1,1	3,70	61,3	0,0	14,0	2,15	48,0	7,9	7,8
4	4,56	1,5	0,2	4,2	8,39	0,0	14,8	6,4	4,79	1,6	0,2	19,9

Table 6.30 *Percentage variation between the results from calibrated ‘FE Model 1’ with and without modeling cover panels, from calibrated ‘FE Model 2’ with and without modeling cover panels, and from ‘FE Model 1’ and ‘FE Model 2’ with different frame section*

Mode\ Frequency (Hz)	FEM	First ambient noise measure		Second ambient noise measure		Percentage variation (%)		
	FE Model 0	**FE Model 1**	**FE Model 1** without wall	**FE Model 2**	**FE Model 3**	Model 1 with and without wall	Model 2 with and without wall	Model 1 and Model 2
1	1,16	2,06	1,15	2,30	1,22	44	47	10
3	1,59	2,74	1,59	3,11	1,66	42	47	12
2	2,05	3,22	2,05	3,70	2,15	36	42	13
4	4,56	7,60	4,55	8,39	4,79	40	43	9

Mode shapes identified in several verticals are shown in the following section 6.6, from theoretical analysis (initial finite element model and the calibrated ones) and from experimental analysis (EMA and OMA).

6.6 Comparison of results

The comparison of modal parameters, identified by experimental and operational modal analysis, has been realized, so as to evaluate their applicability in the ambient noise field measures. Another confront consist on the comparison of experimental and theoretical analysis (OMA and FEM), with the finality the calibration of finite element model from the ambient vibration measures.

6.6.1 Comparison of results from EMA/OMA methods

EMA and OMA methods have been applied to identify model parameters. As described above, ambient vibration measurements have been acquired in two different procedures: first living the fixed portable seismograph in the free field and second living the fixed instrument on the top floor. The first acquisition procedure is realized during the first measurement while the second one during the second measurements. Therefore, the influence of mass and rigidity added is presented when applying OMA method from the second ambient noise measurement. To confront EMA and OMA methods they have been applied both using the first ambient noise measurements.

In the Table 6.31 are shown the percentage variation of frequencies estimated in various verticals of the building by using different methods. The results from operational modal analysis (OMA1), which are used also to calibrate the finite element model, are taken as reference to calculate the percentage variations. As one can see from the table below, the maximum variation is about 1.7%, therefore, all methods presents satisfying results for frequencies.

Table 6.31 *Percentage variation of frequencies from different methods used, first ambient noise measurements*

Frequency (Hz), in 'Vertical a'	**OMA**		**EMA**		**Percentage variation (%)**		
	Method OMA1	Method OMA2	Method EMA1	Method EMA2	OMA2-OMA1	EMA1-OMA1	EMA2-OMA1
Mode 1	2,35	2,38	2,35	2,33	1,3	0,0	-0,9
Mode 2	2,70	2,71	2,69	2,68	0,4	-0,4	-0,7
Mode 3	3,45	3,45	3,47	3,45	0,0	0,6	0,0
Mode 4	7,68	7,70	7,64	7,65	0,3	-0,5	-0,4

Frequency (Hz), in 'Vertical d'	**OMA**		**EMA**		**Percentage variation (%)**		
	Method OMA1	Method OMA2	Method EMA1	Method EMA2	OMA2-OMA1	EMA1-OMA1	EMA2-OMA1
Mode 1	2,33	2,37	2,35	-	1,7	0,9	-
Mode 2	2,71	2,72	2,68	2,67	0,4	-1,1	-1,5
Mode 3	3,44	3,45	3,47	3,44	0,3	0,9	0,0
Mode 4	7,61	7,66	7,64	7,62	0,7	0,4	0,1

Frequency (Hz), in 'Vertical f'	**OMA**		**EMA**		**Percentage variation (%)**		
	Method OMA1	Method OMA2	Method EMA1	Method EMA2	OMA2-OMA1	EMA1-OMA1	EMA2-OMA1
Mode 1	2,34	2,37	2,35	2,36	1,3	0,4	0,8
Mode 2	2,69	2,69	2,68	2,66	0,0	-0,4	-1,1
Mode 3	3,43	3,45	3,46	3,44	0,6	0,9	0,3
Mode 4	7,68	7,65	7,61	7,62	-0,4	-0,9	-0,8

Frequency (Hz), in 'Vertical e'	**OMA**		**EMA**		**Percentage variation (%)**		
	Method OMA1	Method OMA2	Method EMA1	Method EMA2	OMA2-OMA1	EMA1-OMA1	EMA2-OMA1
Mode 1	2,35	2,37	2,38	2,39	0,8	1,3	1,7
Mode 2	2,67	2,69	2,73	2,74	0,7	2,2	2,6
Mode 3	3,41	3,45	3,48	3,50	1,2	2,0	2,6
Mode 4	7,68	7,65	7,69	7,71	-0,4	0,1	0,4

The comparison between results achieved from OMA methods is also realized using the second measurements of ambient noise (see Table 6.32). In this case, the percentage variation is lower than 1% for frequencies.

__Table 6.32__ Percentage variation of frequencies from OMA methods used, second ambient noise measurements

Frequency (Hz)	Vertical a OMA		Vertical d OMA		Vertical f OMA		Percentage variation (%)		
	Method OMA1	Method OMA2	Method OMA1	Method OMA2	Method OMA1	Method OMA2	Vertical a OMA2 - OMA1	Vertical d OMA2 - OMA1	Vertical f OMA2 - OMA1
Mode 1	2,36	2,38	2,41	2,41	2,33	2,34	0,8	0,0	0,4
Mode 2	2,98	2,99	2,99	3,01	2,98	2,99	0,3	0,7	0,3
Mode 3	3,79	3,80	3,77	3,79	3,79	3,80	0,3	0,5	0,3
Mode 4	7,84	7,86	7,89	7,91	7,66	7,69	0,3	0,3	0,4

Frequency (Hz)	Vertical e OMA		Vertical c OMA		Percentage variation (%)	
	Method OMA1	Method OMA2	Method OMA1	Method OMA2	Vertical e OMA2 - OMA1	Vertical c OMA2 - OMA1
Mode 1	2,33	2,35	2,37	2,38	0,9	0,4
Mode 2	3,01	3,02	3,01	3,02	0,3	0,3
Mode 3	3,78	3,79	3,78	3,79	0,3	0,3
Mode 4	7,70	7,73	7,91	7,92	0,4	0,1

Mode shapes identified in the ‘Vertical a’ and in the 'Vertical f' from EMA and OMA methods, using the first ambient noise measurements, are shown in the Figure 6.66, Figure 6.67 and Figure 6.68. Mode shapes identified shows high similarity.

Furthermore, mode shapes from finite element model with and without modeling the rigidity of external wall panels (respectively FEM2 and FEM0 line) are plotted on those graphics.

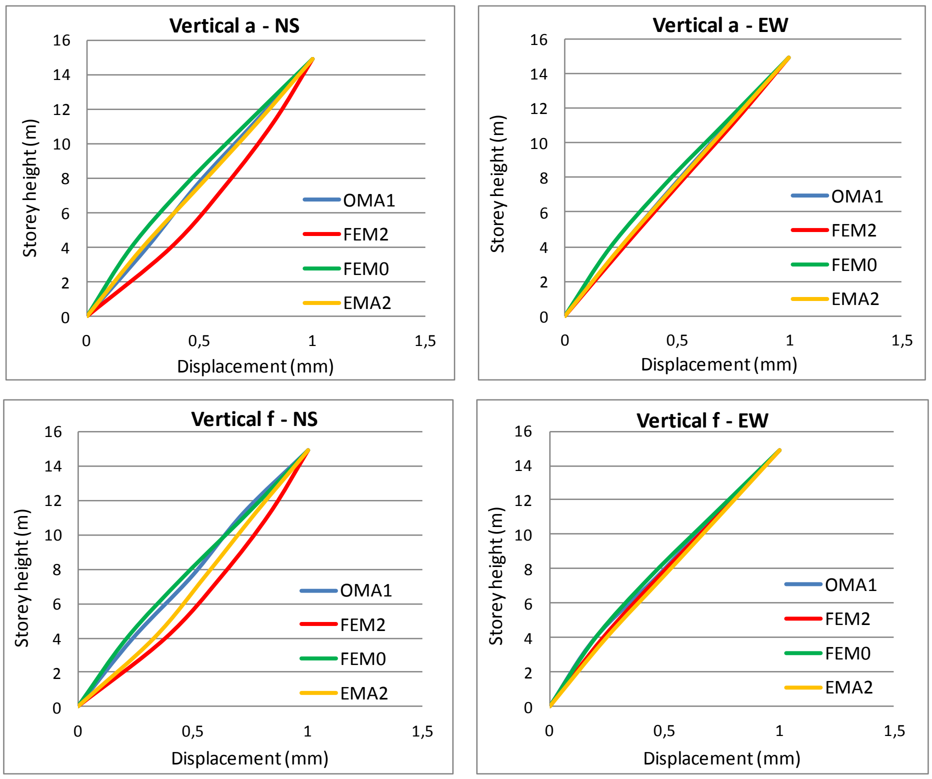

__Figure 6.66__ First mode shapes in the 'Vertical a' and 'Vertical f' from both methods EMA and OMA

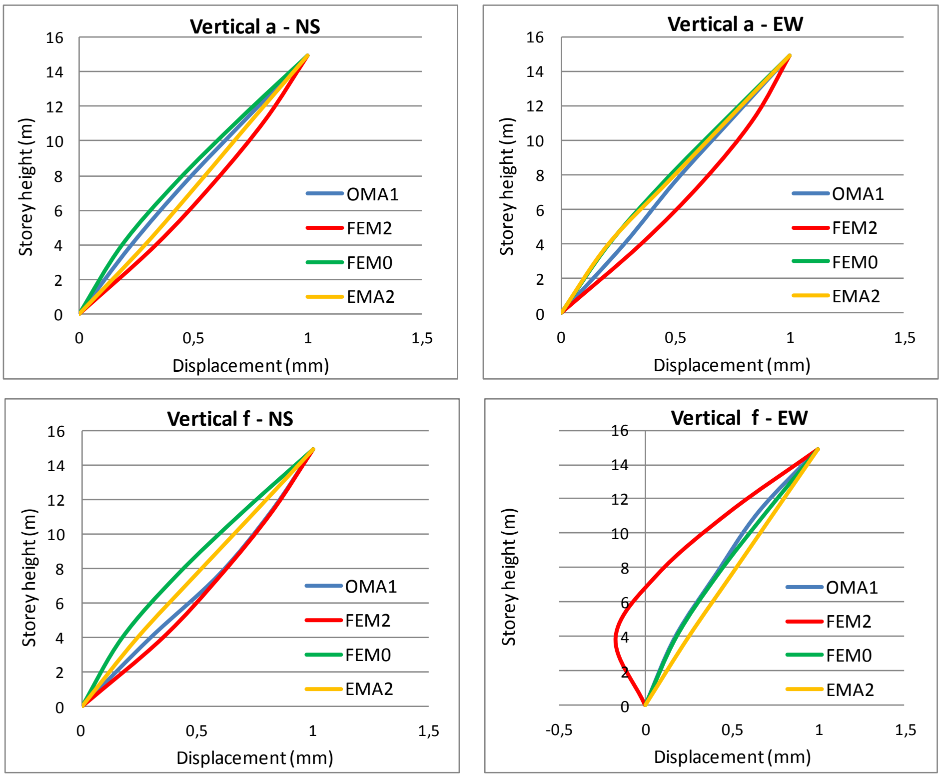

Figure 6.67 *Second mode shapes in the 'Vertical a' and 'Vertical f' from both methods EMA and OMA*

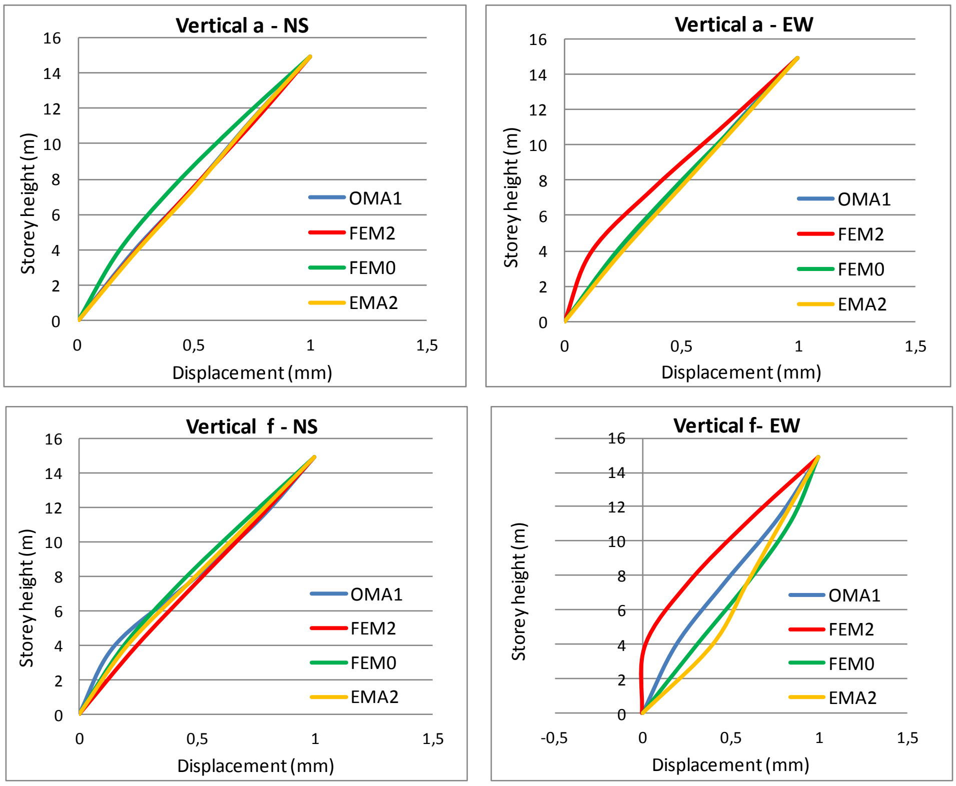

Figure 6.68 *Third mode shapes in the 'Vertical a' and 'Vertical f' from both methods EMA and OMA*

6.6.2 Comparison of structure response from experimental and theoretical analysis

The comparison of frequencies and mode shapes between the operational modal analysis and the finite element model results, has been realized. Two calibrated finite element model, from ambient noise measurements acquired in two different periods during the construction of the

building, have been used for this comparison. As mentioned in the above paragraphs, ‘FE Model 1’ has been calibrated by using as reference the experimental structure response estimated from the first ambient noise measurements acquired inside the building. The ‘FE Model 2’ has been calibrated by using as reference the experimental structure response estimated from the second ambient noise measurements acquired inside the building.
In the Table 6.33 and in the Table 6.34 the percentage variations of modal frequencies between ‘FE Model 1’ and OMA and between ‘FE Model 2’ and OMA in different verticals of the building, are presented.
The second finite element modal is much similar with the current response of the building as was calibrated after the construction of structural and nonstructural elements. The experimental and theoretical results vary less than 5%.
In the case of ‘FE Model 1’, the percentage variation is less than 6.7% for the second and the third mode shape and about 12% for the first mode shape.
The first mode shape is a rotational mode referred to the finite element model without modeling the external cover panels ‘FE Model 3’, and has a modal participation mass ratio of 11%, therefore, the second and the third frequencies are taken as referenced to be reached during the calibration of the model.

***Table 6.33** Results from FEM and OMA realized by the first ambient noise measures*

Mode\ Frequency (Hz)	FE Model 1	First ambient noise measures				Percentage variation (%)			
		Vertical a	Vertical d	Vertical f	Vertical e	Vertical a	Vertical d	Vertical f	Vertical e
		OMA				between OMA and FE Model 1			
1	**2,06**	2,35	2,33	2,34	2,35	12,3	11,5	11,9	12,3
3	**2,74**	2,70	2,71	2,69	2,67	-1,4	-1,0	-1,7	-2,5
2	**3,22**	3,45	3,44	3,43	3,41	6,7	6,5	6,2	5,6
4	**7,60**	7,68	7,61	7,68	7,68	1,0	0,1	1,0	1,0

***Table 6.34** Results from FEM and OMA realized by the second ambient noise measures*

Mode\ Frequency (Hz)	FEM FE Model 2	Second ambient noise measures					Percentage variation (%)				
		Vertical a	Vertical d	Vertical f	Vertical e	Vertical c	Vertical a	Vertical d	Vertical f	Vertical e	Vertical c
		OMA					between OMA and FE Model 2				
1	**2,30**	2,36	2,41	2,33	2,33	2,37	2,7	4,7	1,4	1,4	3,1
3	**3,11**	2,98	2,99	2,98	3,01	3,01	-4,5	-4,2	-4,5	-3,5	-3,5
2	**3,70**	3,79	3,77	3,79	3,78	3,78	2,3	1,7	2,3	2,0	2,0
4	**8,39**	7,84	7,89	7,66	7,70	7,91	-7,1	-6,4	-9,6	-9,0	-6,1

The first three mode shapes from experimental (OMA1) and theoretical 'FE Model 2' method are shown in the Figure 6.43, Figure 6.44 and Figure 6.45. The first three mode shapes from experimental (OMA1) and theoretical 'FE Model 1' method are shown in the Figure 6.31, Figure 6.32 and Figure 6.33. Mode shapes are almost similar in all cases.

6.6.3 Comparison between the initial FEM response and the calibrated one

'FE Model 3' is the calibrated model without modeling the rigidity of external wall panels but only their mass. The modal response of this model has been compared with the response of the initial finite element model 'FE Model 0'. In the Table 6.35 are presented the percentage variation of frequencies and modal participation mass ratio between both FE models. The response of 'FE Model 3' was also evaluated by using the initial values of modulus of elasticity of concretes (E initial). The frequencies varies less than 5% or less than 2% (in the second case), while the mode shapes are almost identical (see Figure 6.69, Figure 6.70 and Figure 6.71). This, due to the variation of modal participation mass ratio in such a way that the first three modes of vibration remains the first mode shape type.

***Table 6.35** Percentage variation between the frequencies from 'FE Model 0' and 'FE Model 3'*

Mode	*FE Model 0*				*FE Model 3*					*Percentage variation (%)*				
	Frequency	UX	UY	RZ	E, 25% higher	E initial	UX	UY	RZ	E, 25% higher	E initial	UX	UY	RZ
No.	(Hz)	Unitless	Unitless	Unitless	Frequency (Hz)	Frequency (Hz)	Unitless	Unitless	Unitless	Frequency (Hz)	Frequency (Hz)	Unitless	Unitless	Unitless
1	1,16	0,065	0,005	**0,112**	1,21	1,14	0,067	0,006	**0,554**	4,9	1,3	2,5	12,9	**79,9**
2	1,59	0,081	**0,555**	**0,484**	1,66	1,56	0,081	**0,555**	0,001	4,6	1,7	0,9	**0,0**	**inf.**
3	2,05	**0,481**	0,079	0,011	2,15	2,02	**0,480**	0,079	0,078	4,7	1,5	**-0,3**	-0,3	86,1
4	4,56	0,015	0,002	0,042	4,79	4,49	0,016	0,002	**0,199**	4,7	1,5	3,6	12,2	78,7
5	7,13	0,009	**0,208**	**0,168**	7,45	6,99	0,009	**0,208**	0,000	4,3	2,0	1,8	**-0,3**	**inf.**
6	9,34	**0,168**	0,005	0,027	9,77	9,17	**0,173**	0,005	0,043	4,5	1,8	**2,8**	3,3	37,1
7	9,62	0,049	0,003	0,007	10,08	9,45	0,044	0,003	0,053	4,5	1,7	-12,1	-0,6	86,3

Note: 'inf' means high value of the percentage variation.

In the Figure 6.69, Figure 6.70 and Figure 6.71 are shown the three mode shapes in various verticals of the building identified both from 'FE Model 0' and 'FE Model 3'. Also, mode shapes identified from experimental data are plotted in those graphics: from OMA method (OMA1 curve) and from the simplified method which use pairs of synchronized measures separately on analysis (OMA1_1 curve).

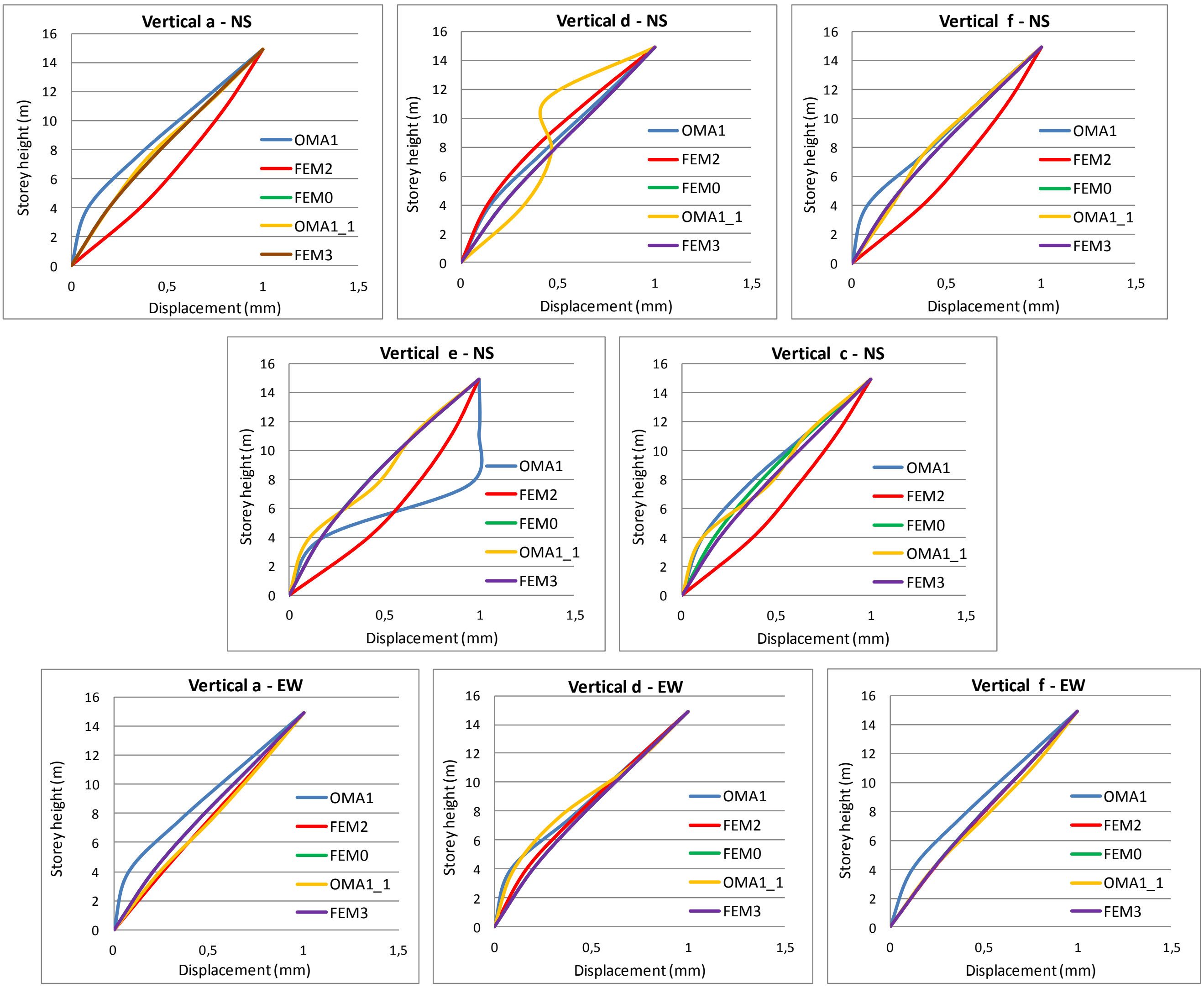

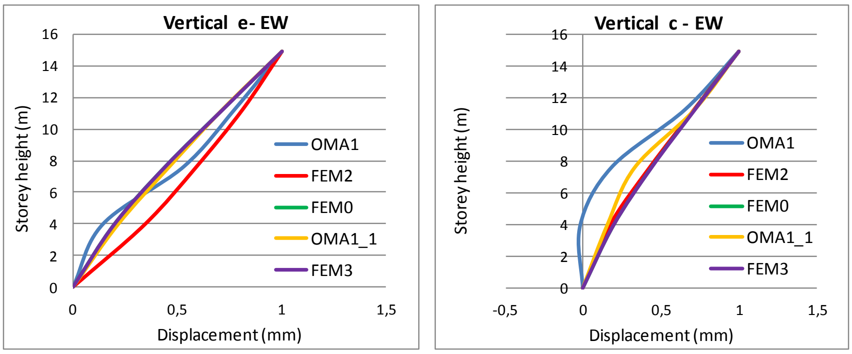

Figure 6.69 *First mode shape from 'FE Model 0' and 'FE Model 3', in both directions NS and EW*

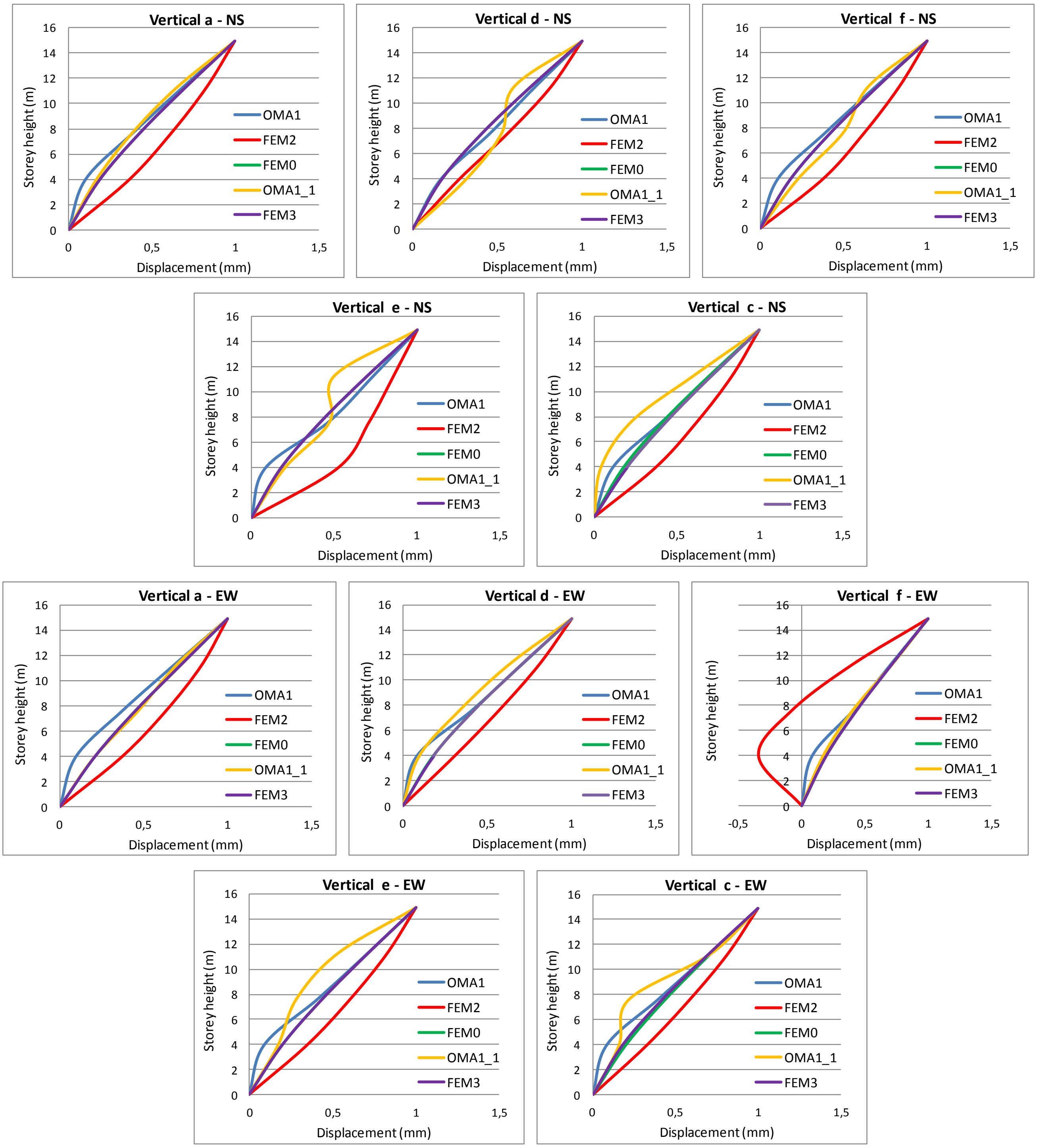

Figure 6.70 *Second mode shape from 'FE Model 0' and 'FE Model 3', in both directions NS and EW*

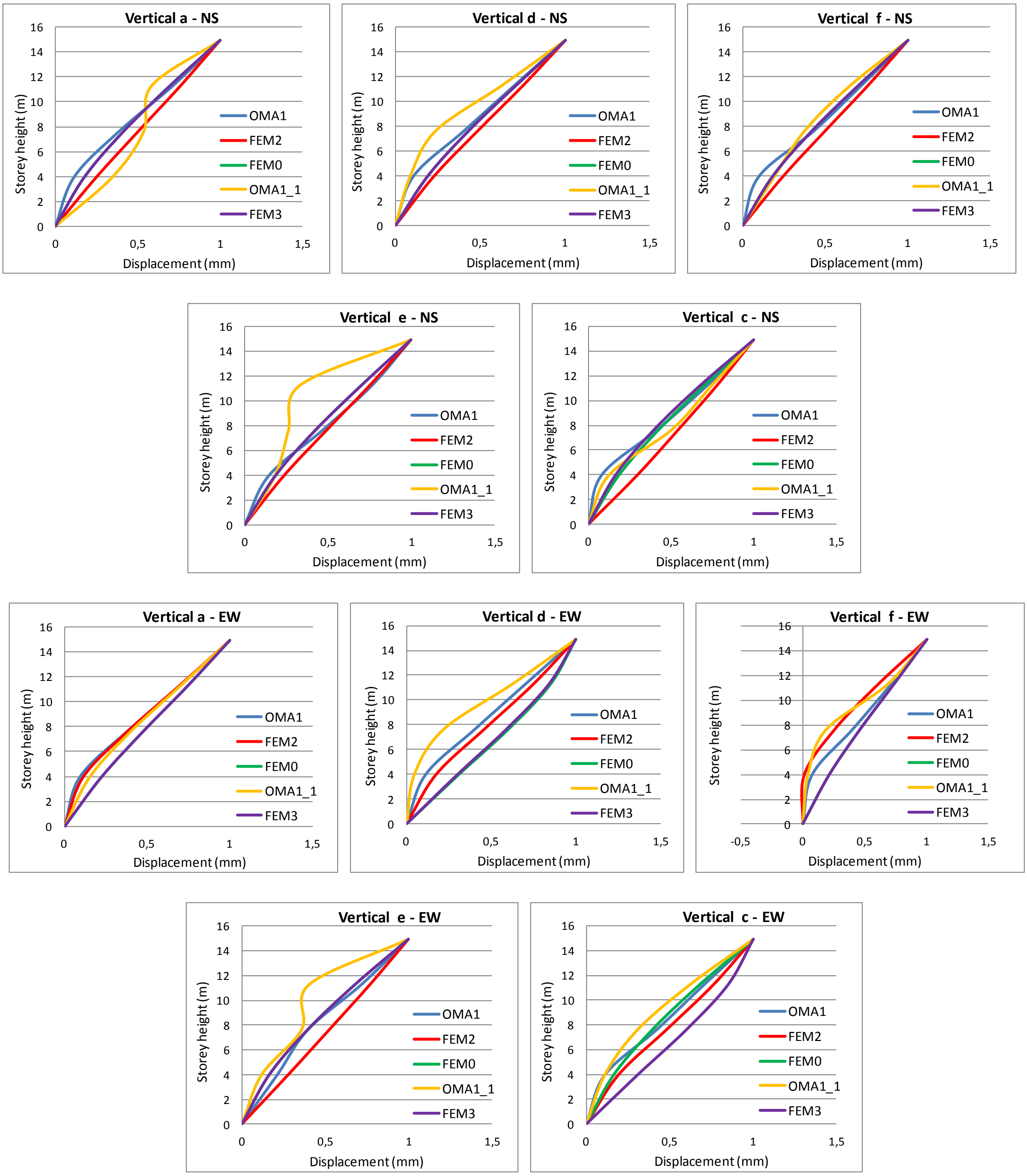

Figure 6.71 *Third mode shape from 'FE Model 0' and 'FE Model 3', in both directions NS and EW*

VII.THE UTILITY OF CALIBRATED FE MODEL

Calibrated FEM model can be used in the future for seismic vulnerability assessment or structural monitoring after an important seismic events or when the building exceeds the expected useful life of the project and needs to be controlled for possible maintenance. FEM contains useful information to evaluate the effects of post-earthquake. According to Italian standard ‘NTC 2008’ or European standard ‘Eurocode 8’, the seismic analysis of existing reinforced concrete buildings can be performed by one of the established procedure (i.e. Linear Static Analysis, Linear Dynamic Analysis, Nonlinear Static Pushover Analysis, Nonlinear Dynamic Analysis) depending on the achieved knowledge level about the structural system and materials.

The response of buildings to earthquakes is a complex, three dimensional, nonlinear, dynamic problem. Limitations in technology and the depth of our understanding of this problem have led to the development of a number of simplified methods for representing it, most of which disregard one or more of its fundamental aspects: the Linear Dynamic procedure ignores nonlinearity; the Nonlinear Static procedure ignores dynamic effects; the Linear Static procedure ignores both. In contrast, the Nonlinear Dynamic procedure attempts to fully represent the seismic response of buildings without any of these major simplifying assumptions.

The seismic effects and the effects of the other actions included in the seismic design situation, may be determined on the basis of a linear-elastic behavior of the structure. Therefore, the reference method suggested from the standard for determining seismic effects is the modal response spectrum analysis, using a linear-elastic model of the structure and the design spectrum. In alternative, a non-linear methods may also be used.

In this study, the aim of structural verifications consist in comparing the building behavior from response spectrum estimated on site and from standard. Therefore, structural verification have been realized for reinforced concrete building in Sanremo, using the response spectrum estimated both from standard and local seismic response of the construction site.

Linear and nonlinear analysis have been performed to evaluate structure response under seismic action.

7.1 Structural verifications using calibrated FEM

A Linear dynamic analysis and a Nonlinear static Pushover analysis have been performed in this study. Also, modal analysis and verification of interstory drift for SLD limit have been realized.

Structural verifications have been realized using the response spectrum estimated on site and also the response spectrum defined from NTC 2008, at the aim to evaluate the differences on the structural response.

As mentioned above, structural verifications carried out in this study have the objective the comparison of structure response under seismic action defined both from the response spectrum on site and from standard. Therefore, the global structure response has been evaluated from both analysis.

Calibrated finite element model 'FE Model 3', without modeling the rigidity of external wall panels, has been used for structural verifications.

7.1.1 Response spectrums used for analysis

Horizontal component of the response spectrum estimated from local seismic response is shown in the Figure 5.22. The reference spectrum of site was also estimated from NTC2008 by using 'Spettri NTC ver.1.0.3' sheet which calculate spectrum due to relationship proposed by technical standard. A *soil class A* was estimated initially from the seismic surveys carried out in

the vicinity of the construction area and from penetrometric test carried out in the area of interest (see paragraph 5.2.3). In addition, a *class B* resulted from the local seismic response (see paragraph 5.3), which has been considered to estimate the response spectrum from the standard.
In the Figure 7.1 are plotted response spectrums in logarithmic scale, identified both from experimental analysis and from empirically formulations. Furthermore, in the Figure 7.2 are shown the response spectrums, identified from local seismic response and from standard.
The response spectrums estimated on site have not been standardized (due to spectrum from standard), to have a real spectrum.

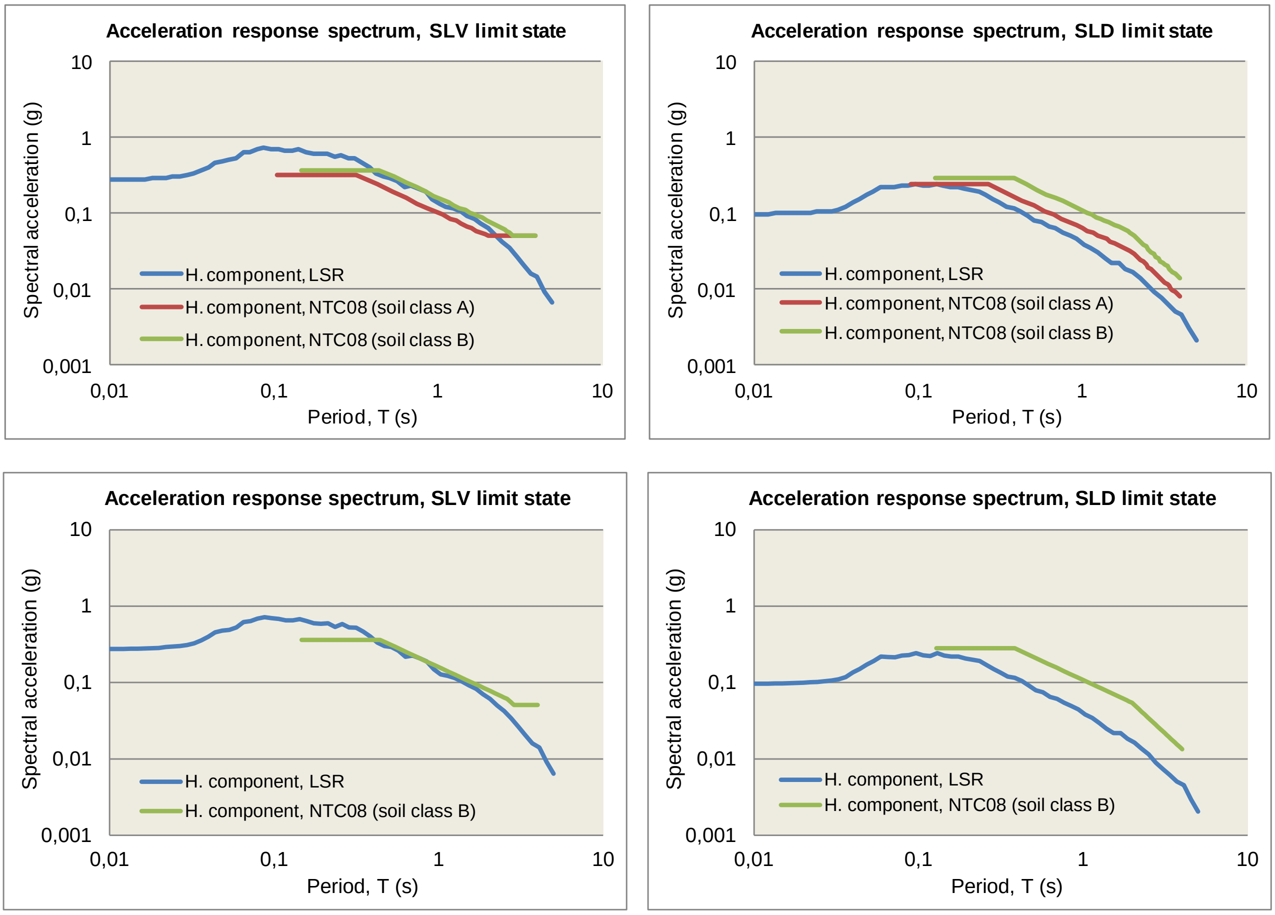

Figure 7.1 *Horizontal response spectrum from NTC2008 and local seismic response, for SLV and SLD limit state, in logarithmic scale*

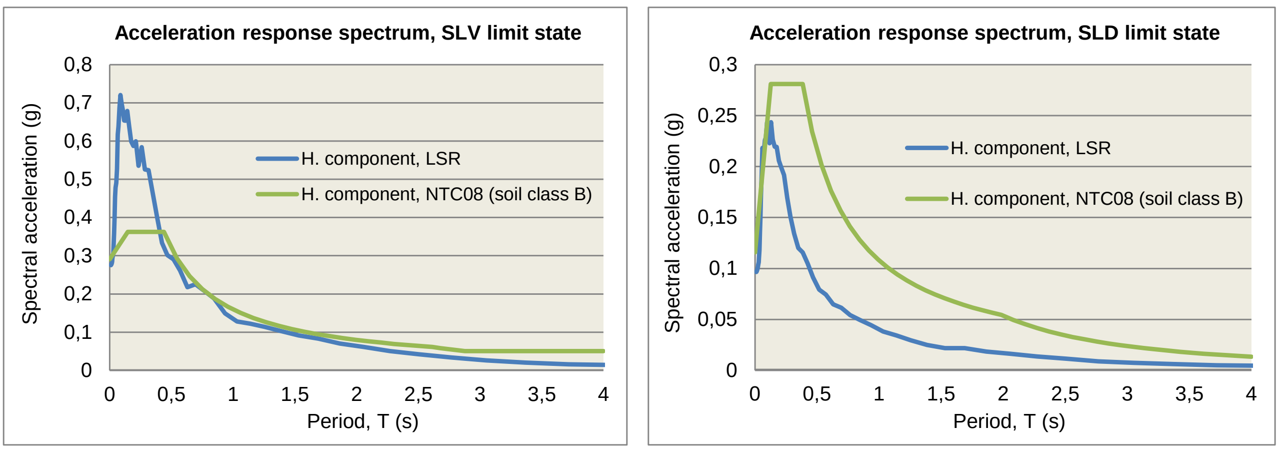

Figure 7.2 *Horizontal response spectrum from NTC2008 and local seismic response, for SLV and SLD limit state*

7.1.2 Interstory drift, damage limitation

The reinforced concrete building under exam falls into the class of use IV, therefore, the standard indicate to check that the design seismic action does not produce damage to the non-construction elements such as to make the construction temporarily not operational. For this purpose, the response spectrum from SLD limit state has been used to estimate the interstory drifts.

Generally, verifications against SLE limit states of structural and non-structural elements are performed in terms of strength, containment of the damage and the functional capability. In this study, the verification of structural elements in terms of containment damage to the non-structural elements, from the analysis of seismic action relating to SLD limit state (§7.3.7.2, NTC 2008), has been realized. Load combination used for SLD limit state is described in the Section 6.1.5.

Interstory drifts have been estimated from the analysis of seismic action relating to SLD once from the response spectrum due to NTC2008 and once from the local seismic response.

Calibrated model 'FE Model 3' (without modeling the rigidity of external walls panels) and also the calibrated model 'FE Model2' (modeling the rigidity of external walls), have been used to check the limits for interstory drifts. Interstorey displacements *dr* ‘drifts’ obtained from analysis of seismic action relating to the SLD limit state must be lower than 0.5% of the floor height *h* ($dr < 0.005\ h$), referred to the standard.

Interstory drifts have been estimated as a modal combination of the product between the delta nodal displacement achieved from modal analysis and the amplification factors from SLD combination (U1amp and U2amp) (Table 7.1). Furthermore, drifts have been estimated directly from SAP2000 as the nodal joint displacement (Table 7.2 and Table 7.3).

In the Table 7.2 and in the Table 7.3 are shown respectively the interstory drifts estimated by using the response spectrum from NTC08 and from local seismic response.

The limits condition of drifts must be satisfied also for fissured model. Flexural rigidity and shear stiffness of beams and columns have been decreases by 50% to achieve the fissured model from the calibrated model ‘FE Model 3’ without modeling the external walls. At this aim, the moment of inertia of section and the shear area on both directions (in plan and out of plan) of beams and pillars have been reduced with a coefficient 0.5 (which means 50%). In alternative, flexural rigidity can be deceased by halving the Young modulus of concrete. Reducing stiffness simulates the phenomenon of cracking of concrete. In this case, the interstory drifts of the fissured model differ not significantly (Table 7.6): about 0.1% higher than for the non-fissured model. Therefore, shell elements (lift and scale core) have been released out of shear plan, by modify f_{12} and m_{22} factors (membrane modifier in plan-shear, bending modifiers for shell element) applying a low multiplayer value (10^{-4}). In this way, the concrete wall works only as bearing walls. The results obtained in this case are shown in the Table 7.4 and in the Table 7.5, for reference spectrum identified both from NTC2008 and local seismic response.

Interstory drifts estimated from analysis with standard spectrum NTC2008 result higher than those achieved by using the response spectrum of site: about 57% and 62% higher respectively for U1 and U2 component. In case of fissured model, interstory drifts differ about 61% for U1 component and 63% for U2 component. Standard response spectrum NTC08 for SLD limit state result more severe than the spectrum estimated on site.

Interstory drifts are also estimated in the case of 'FE Model2', when the rigidity of external walls has been modeled (Table 7.7). Modeling the rigidity of the wall panels reduce the interstory drift by 0.4% in case of response spectrum from NTC08, and about 0.25% in the case of local seismic response.

Furthermore, interstory drifts are also estimated from the local response spectrum for SLV limit state decreased by a factor 2 (*q* structural factor). In this case the interstory drifts are verified and have lower value of about 27% in the center of mass (34% in the vertical A) than those estimated from local seismic response spectrum for SLD limit state.

Table 7.1 *Interstory drift in several verticals of the building estimated manually (response spectrum NTC2008)*

Height Floor (m)	0,005h (m)	Vertical A		Verification		
		U1 (m)	U2 (m)			
0	0	0,0000	0,0000	drx/h	dry/h	<0,005
3,21	0,01605	0,0007	0,0012	0,0002	0,0004	ok
3,97	0,01985	0,0019	0,0029	0,0005	0,0007	ok
3,65	0,01825	0,0025	0,0033	0,0007	0,0009	ok
3,65	0,01825	0,0029	0,0037	0,0008	0,0010	ok
3,65	0,01825	0,0031	0,0038	0,0009	0,0010	ok
3,65	0,01825	0,0032	0,0037	0,0009	0,0010	ok

Height Floor (m)	0,005h (m)	Vertical C		Verification		
		U1 (m)	U2 (m)			
0	0	0	0	drx/h	dry/h	<0,005
3,21	0,01605	0,0007	0,0009	0,0002	0,0003	ok
3,97	0,01985	0,0018	0,0029	0,0005	0,0007	ok
3,65	0,01825	0,0024	0,0038	0,0007	0,0010	ok
3,65	0,01825	0,0029	0,0045	0,0008	0,0012	ok
3,65	0,01825	0,0031	0,0047	0,0009	0,0013	ok
3,65	0,01825	0,0032	0,0048	0,0009	0,0013	ok

Height Floor (m)	0,005h (m)	Vertical D		Verification		
		U1 (m)	U2 (m)			
0	0	0,0000	0,0000	drx/h	dry/h	<0,005
3,21	0,01605	0,0009	0,0009	0,0003	0,0003	ok
3,97	0,01985	0,0024	0,0029	0,0006	0,0007	ok
3,65	0,01825	0,0030	0,0038	0,0008	0,0010	ok
3,65	0,01825	0,0035	0,0045	0,0010	0,0012	ok
3,65	0,01825	0,0037	0,0047	0,0010	0,0013	ok
3,65	0,01825	0,0037	0,0048	0,0010	0,0013	ok

Height Floor (m)	0,005h (m)	Vertical E		Verification		
		U1 (m)	U2 (m)			
0	0	0,0000	0,0000	drx/h	dry/h	<0,005
3,21	0,01605	0,0007	0,0013	0,0002	0,0004	ok
3,97	0,01985	0,0021	0,0032	0,0005	0,0008	ok
3,65	0,01825	0,0027	0,0037	0,0007	0,0010	ok
3,65	0,01825	0,0032	0,0041	0,0009	0,0011	ok
3,65	0,01825	0,0034	0,0042	0,0009	0,0012	ok
3,65	0,01825	0,0034	0,0041	0,0009	0,0011	ok

Height Floor (m)	0,005h (m)	Center of mass		Verification		
		U1 (m)	U2 (m)			
0	0	0,0000	0,0000	drx/h	dry/h	<0,005
3,21	0,01605	0,0006	0,0010	0,0002	0,0003	ok
3,97	0,01985	0,0018	0,0028	0,0005	0,0007	ok
3,65	0,01825	0,0023	0,0035	0,0006	0,0010	ok
3,65	0,01825	0,0028	0,0041	0,0008	0,0011	ok
3,65	0,01825	0,0030	0,0043	0,0008	0,0012	ok
3,65	0,01825	0,0031	0,0042	0,0008	0,0012	ok

Table 7.2 *Interstory drift in several verticals of the building estimated from seismic combinations (response spectrum NTC2008)*

Vertical A	U1 (m)	U2 (m)	ΔU1 (m)	ΔU2 (m)	Height floor (m)	Verification		
						drx/h	**dry/h**	<0,005
SVL1 combination	0,0009	0,0017	0,0000	0,0000	3,21	0,0000	0,0000	ok
	0,0033	0,0060	0,0024	0,0043	3,97	0,0006	0,0011	ok
	0,0064	0,0109	0,0031	0,0049	3,65	0,0009	0,0014	ok
	0,0101	0,0164	0,0037	0,0054	3,65	0,0010	0,0015	ok
	0,0141	0,0218	0,0040	0,0054	3,65	0,0011	0,0015	ok
	0,0181	0,0269	0,0041	0,0051	3,65	0,0011	0,0014	ok

Vertical A	U1 (m)	U2 (m)	ΔU1 (m)	ΔU2 (m)	Height floor (m)	Verification		
						drx/h	**dry/h**	<0,005
SVL2 combination	0,0007	0,0016	0,0000	0,0000	3,21	0,0000	0,0000	ok
	0,0027	0,0055	0,0020	0,0039	3,97	0,0005	0,0010	ok
	0,0052	0,0100	0,0026	0,0045	3,65	0,0007	0,0012	ok
	0,0083	0,0149	0,0030	0,0049	3,65	0,0008	0,0014	ok
	0,0115	0,0199	0,0033	0,0050	3,65	0,0009	0,0014	ok
	0,0148	0,0247	0,0033	0,0048	3,65	0,0009	0,0013	ok

Vertical C	U1 (m)	U2 (m)	ΔU1 (m)	ΔU2 (m)	Height floor (m)	Verification		
						drx/h	**dry/h**	<0,005
SVL1 combination	0,0009	0,0011	0,0000	0,0000	3,21	0,0000	0,0000	ok
	0,0033	0,0043	0,0024	0,0032	3,97	0,0006	0,0008	ok
	0,0064	0,0083	0,0031	0,0040	3,65	0,0009	0,0011	ok
	0,0101	0,0129	0,0037	0,0046	3,65	0,0010	0,0013	ok
	0,0140	0,0176	0,0039	0,0047	3,65	0,0011	0,0013	ok
	0,0180	0,0222	0,0040	0,0046	3,65	0,0011	0,0013	ok

Vertical C	U1 (m)	U2 (m)	ΔU1 (m)	ΔU2 (m)	Height floor (m)	Verification		
						drx/h	**dry/h**	<0,005
SVL2 combination	0,0007	0,0012	0,0000	0,0000	3,21	0,0000	0,0000	ok
	0,0026	0,0049	0,0019	0,0037	3,97	0,0005	0,0009	ok
	0,0049	0,0097	0,0024	0,0048	3,65	0,0006	0,0013	ok
	0,0077	0,0152	0,0028	0,0056	3,65	0,0008	0,0015	ok
	0,0107	0,0210	0,0030	0,0058	3,65	0,0008	0,0016	ok
	0,0138	0,0268	0,0031	0,0058	3,65	0,0008	0,0016	ok

Vertical D	U1 (m)	U2 (m)	ΔU1 (m)	ΔU2 (m)	Height floor (m)	Verification		
						drx/h	**dry/h**	<0,005
SVL1 combination	0,0010	0,0011	0,0000	0,0000	3,21	0,0000	0,0000	ok
	0,0039	0,0043	0,0029	0,0032	3,97	0,0007	0,0008	ok
	0,0077	0,0083	0,0037	0,0040	3,65	0,0010	0,0011	ok
	0,0120	0,0129	0,0043	0,0046	3,65	0,0012	0,0013	ok
	0,0165	0,0176	0,0046	0,0047	3,65	0,0012	0,0013	ok
	0,0211	0,0222	0,0046	0,0046	3,65	0,0013	0,0013	ok

Vertical D	U1 (m)	U2 (m)	ΔU1 (m)	ΔU2 (m)	Height floor (m)	Verification		
						drx/h	**dry/h**	<0,005
SVL2 combination	0,0008	0,0012	0,0000	0,0000	3,21	0,0000	0,0000	ok
	0,0031	0,0049	0,0023	0,0037	3,97	0,0006	0,0009	ok
	0,0062	0,0097	0,0030	0,0048	3,65	0,0008	0,0013	ok
	0,0097	0,0152	0,0036	0,0056	3,65	0,0010	0,0015	ok
	0,0135	0,0210	0,0038	0,0058	3,65	0,0010	0,0016	ok
	0,0174	0,0268	0,0038	0,0058	3,65	0,0011	0,0016	ok

Vertical E	U1 (m)	U2 (m)	ΔU1 (m)	ΔU2 (m)	Height floor (m)	Verification		
						drx/h	**dry/h**	<0,005
SVL1 combination	0,0009	0,0017	0,0000	0,0000	3,21	0,0000	0,0000	ok
	0,0035	0,0058	0,0026	0,0041	3,97	0,0007	0,0010	ok
	0,0069	0,0106	0,0034	0,0048	3,65	0,0009	0,0013	ok
	0,0109	0,0158	0,0040	0,0053	3,65	0,0011	0,0014	ok
	0,0151	0,0210	0,0042	0,0052	3,65	0,0012	0,0014	ok
	0,0194	0,0260	0,0043	0,0049	3,65	0,0012	0,0014	ok

Vertical E	U1 (m)	U2 (m)	ΔU1 (m)	ΔU2 (m)	Height floor (m)	Verification		
						drx/h	**dry/h**	<0,005
SVL2 combination	0,0007	0,0016	0,0000	0,0000	3,21	0,0000	0,0000	ok
	0,0029	0,0054	0,0021	0,0038	3,97	0,0005	0,0010	ok
	0,0057	0,0098	0,0028	0,0044	3,65	0,0008	0,0012	ok
	0,0090	0,0147	0,0033	0,0049	3,65	0,0009	0,0013	ok
	0,0125	0,0197	0,0035	0,0050	3,65	0,0010	0,0014	ok
	0,0161	0,0245	0,0036	0,0048	3,65	0,0010	0,0013	ok

Center mass	U1 (m)	U2 (m)	ΔU1 (m)	ΔU2 (m)	Height floor (m)	Verification		
						drx/h	**dry/h**	<0,005
SVL1 combination	0,0009	0,0008	0,0000	0,0000	3,21	0,0000	0,0000	ok
	0,0033	0,0030	0,0025	0,0022	3,97	0,0006	0,0006	ok
	0,0065	0,0058	0,0031	0,0028	3,65	0,0009	0,0008	ok
	0,0102	0,0089	0,0037	0,0031	3,65	0,0010	0,0009	ok
	0,0143	0,0122	0,0040	0,0032	3,65	0,0011	0,0009	ok
	0,0184	0,0154	0,0041	0,0032	3,65	0,0011	0,0009	ok

Center mass	U1 (m)	U2 (m)	ΔU1 (m)	ΔU2 (m)	Height floor (m)	Verification		
						drx/h	**dry/h**	<0,005
SVL2 combination	0,0007	0,0011	0,0000	0,0000	3,21	0,0000	0,0000	ok
	0,0027	0,0044	0,0020	0,0032	3,97	0,0005	0,0008	ok
	0,0053	0,0084	0,0026	0,0041	3,65	0,0007	0,0011	ok
	0,0084	0,0131	0,0031	0,0046	3,65	0,0008	0,0013	ok
	0,0117	0,0179	0,0033	0,0048	3,65	0,0009	0,0013	ok
	0,0151	0,0226	0,0034	0,0048	3,65	0,0009	0,0013	ok

Table 7.3 *Interstory drift in several verticals of the building, from seismic combinations (from response spectrum estimated on site)*

Vertical A	U1 (m)	U2 (m)	ΔU1 (m)	ΔU2 (m)	Height floor (m)	Verification		
						drx/h	**dry/h**	<0,005
SVL1 combination	0,0004	0,0007	0,0000	0,0000	3,21	0,0000	0,0000	ok
	0,0014	0,0024	0,0010	0,0017	3,97	0,0003	0,0004	ok
	0,0028	0,0043	0,0013	0,0019	3,65	0,0004	0,0005	ok
	0,0043	0,0064	0,0016	0,0021	3,65	0,0004	0,0006	ok
	0,0060	0,0085	0,0017	0,0021	3,65	0,0005	0,0006	ok
	0,0078	0,0105	0,0018	0,0020	3,65	0,0005	0,0006	ok

Vertical A	U1 (m)	U2 (m)	ΔU1 (m)	ΔU2 (m)	Height floor (m)	Verification		
						drx/h	**dry/h**	<0,005
SVL2 combination	0,0003	0,0007	0,0000	0,0000	3,21	0,0000	0,0000	ok
	0,0012	0,0022	0,0009	0,0015	3,97	0,0002	0,0004	ok
	0,0023	0,0039	0,0011	0,0017	3,65	0,0003	0,0005	ok
	0,0036	0,0058	0,0013	0,0019	3,65	0,0004	0,0005	ok
	0,0050	0,0077	0,0014	0,0019	3,65	0,0004	0,0005	ok
	0,0064	0,0096	0,0015	0,0019	3,65	0,0004	0,0005	ok

Vertical C	U1 (m)	U2 (m)	ΔU1 (m)	ΔU2 (m)	Height floor (m)	Verification		
						drx/h	**dry/h**	<0,005
SVL1 combination	0,0004	0,0005	0,0000	0,0000	3,21	0,0000	0,0000	ok
	0,0014	0,0017	0,0010	0,0012	3,97	0,0003	0,0003	ok
	0,0027	0,0032	0,0013	0,0015	3,65	0,0004	0,0004	ok
	0,0043	0,0048	0,0015	0,0017	3,65	0,0004	0,0005	ok
	0,0059	0,0066	0,0017	0,0017	3,65	0,0005	0,0005	ok
	0,0077	0,0083	0,0017	0,0017	3,65	0,0005	0,0005	ok

Vertical C	U1 (m)	U2 (m)	ΔU1 (m)	ΔU2 (m)	Height floor (m)	Verification		
						drx/h	**dry/h**	<0,005
SVL2 combination	0,0003	0,0005	0,0000	0,0000	3,21	0,0000	0,0000	ok
	0,0011	0,0019	0,0008	0,0014	3,97	0,0002	0,0004	ok
	0,0021	0,0037	0,0010	0,0018	3,65	0,0003	0,0005	ok
	0,0033	0,0058	0,0012	0,0020	3,65	0,0003	0,0006	ok
	0,0046	0,0079	0,0013	0,0022	3,65	0,0004	0,0006	ok
	0,0060	0,0101	0,0014	0,0022	3,65	0,0004	0,0006	ok

Vertical D	U1 (m)	U2 (m)	ΔU1 (m)	ΔU2 (m)	Height floor (m)	Verification		
						drx/h	**dry/h**	<0,005
SVL1 combination	0,0005	0,0005	0,0000	0,0000	3,21	0,0000	0,0000	ok
	0,0017	0,0017	0,0012	0,0012	3,97	0,0003	0,0003	ok
	0,0033	0,0032	0,0016	0,0015	3,65	0,0004	0,0004	ok
	0,0051	0,0048	0,0018	0,0017	3,65	0,0005	0,0005	ok
	0,0071	0,0066	0,0020	0,0017	3,65	0,0005	0,0005	ok
	0,0091	0,0083	0,0020	0,0017	3,65	0,0005	0,0005	ok

Vertical D	U1 (m)	U2 (m)	ΔU1 (m)	ΔU2 (m)	Height floor (m)	Verification		
						drx/h	**dry/h**	<0,005
SVL2 combination	0,0003	0,0005	0,0000	0,0000	3,21	0,0000	0,0000	ok
	0,0013	0,0019	0,0010	0,0014	3,97	0,0003	0,0004	ok
	0,0026	0,0037	0,0013	0,0018	3,65	0,0004	0,0005	ok
	0,0042	0,0058	0,0015	0,0020	3,65	0,0004	0,0006	ok
	0,0058	0,0079	0,0016	0,0022	3,65	0,0004	0,0006	ok
	0,0075	0,0101	0,0017	0,0022	3,65	0,0005	0,0006	ok

Vertical E	U1 (m)	U2 (m)	ΔU1 (m)	ΔU2 (m)	Height floor (m)	Verification		
						drx/h	**dry/h**	<0,005
SVL1 combination	0,0004	0,0007	0,0000	0,0000	3,21	0,0000	0,0000	ok
	0,0016	0,0023	0,0011	0,0016	3,97	0,0003	0,0004	ok
	0,0030	0,0042	0,0014	0,0018	3,65	0,0004	0,0005	ok
	0,0047	0,0062	0,0017	0,0020	3,65	0,0005	0,0005	ok
	0,0065	0,0082	0,0018	0,0020	3,65	0,0005	0,0006	ok
	0,0084	0,0101	0,0019	0,0019	3,65	0,0005	0,0005	ok

Vertical E	U1 (m)	U2 (m)	ΔU1 (m)	ΔU2 (m)	Height floor (m)	Verification		
						drx/h	**dry/h**	<0,005
SVL2 combination	0,0003	0,0007	0,0000	0,0000	3,21	0,0000	0,0000	ok
	0,0013	0,0022	0,0009	0,0015	3,97	0,0002	0,0004	ok
	0,0024	0,0039	0,0012	0,0017	3,65	0,0003	0,0005	ok
	0,0039	0,0057	0,0014	0,0018	3,65	0,0004	0,0005	ok
	0,0054	0,0076	0,0015	0,0019	3,65	0,0004	0,0005	ok
	0,0070	0,0095	0,0016	0,0019	3,65	0,0004	0,0005	ok

Center mass	U1 (m)	U2 (m)	ΔU1 (m)	ΔU2 (m)	Height floor (m)	Verification		
						drx/h	**dry/h**	<0,005
SVL1 combination	0,0004	0,0003	0,0000	0,0000	3,21	0,0000	0,0000	ok
	0,0015	0,0012	0,0011	0,0009	3,97	0,0003	0,0002	ok
	0,0028	0,0022	0,0013	0,0011	3,65	0,0004	0,0003	ok
	0,0044	0,0034	0,0016	0,0012	3,65	0,0004	0,0003	ok
	0,0061	0,0046	0,0017	0,0012	3,65	0,0005	0,0003	ok
	0,0079	0,0058	0,0018	0,0012	3,65	0,0005	0,0003	ok

Center mass	U1 (m)	U2 (m)	ΔU1 (m)	ΔU2 (m)	Height floor (m)	Verification		
						drx/h	**dry/h**	<0,005
SVL2 combination	0,0003	0,0005	0,0000	0,0000	3,21	0,0000	0,0000	ok
	0,0012	0,0018	0,0009	0,0013	3,97	0,0002	0,0003	ok
	0,0023	0,0033	0,0011	0,0015	3,65	0,0003	0,0004	ok
	0,0036	0,0050	0,0013	0,0017	3,65	0,0004	0,0005	ok
	0,0051	0,0068	0,0014	0,0018	3,65	0,0004	0,0005	ok
	0,0066	0,0086	0,0015	0,0018	3,65	0,0004	0,0005	ok

Interstory drifts for fissured 'FE Model 3' are shown in the Table 7.4 and in the Table 7.5 from reference spectrum identified both from NTC2008 and local seismic response. Interstory drifts are about 65% higher when using NTC08 spectrum, and are not satisfied in some cases.

Table 7.4 *Interstory drift in several verticals of the building estimated by the fissured model, from response spectrum of NTC2008*

Vertical A	U1 (m)	U2 (m)	ΔU1 (m)	ΔU2 (m)	Height floor (m)	Verification		
						drx/h	**dry/h**	<0,005
SVL1 combination	0,0037	0,0045	0,0000	0,0000	3,21	0,0000	0,0000	ok
	0,0159	0,0168	0,0122	0,0123	3,97	0,0031	0,0031	ok
	0,0319	0,0292	0,0159	0,0124	3,65	0,0044	0,0034	ok
	0,0501	0,0427	0,0183	0,0135	3,65	0,0050	0,0037	ok
	0,0673	0,0538	0,0171	0,0110	3,65	0,0047	0,0030	ok
	0,0817	0,0615	0,0145	0,0077	3,65	0,0040	0,0021	ok

Vertical A	U1 (m)	U2 (m)	ΔU1 (m)	ΔU2 (m)	Height floor (m)	Verification		
						drx/h	**dry/h**	<0,005
SVL2 combination	0,0023	0,0065	0,0000	0,0000	3,21	0,0000	0,0000	ok
	0,0094	0,0225	0,0072	0,0161	3,97	0,0018	0,0040	ok
	0,0186	0,0376	0,0091	0,0150	3,65	0,0025	0,0041	ok
	0,0292	0,0536	0,0106	0,0160	3,65	0,0029	0,0044	ok
	0,0390	0,0655	0,0098	0,0119	3,65	0,0027	0,0033	ok
	0,0471	0,0724	0,0081	0,0069	3,65	0,0022	0,0019	ok

Vertical C	U1 (m)	U2 (m)	ΔU1 (m)	ΔU2 (m)	Height floor (m)	Verification		
						drx/h	**dry/h**	<0,005
SVL1 combination	0,0041	0,0031	0,0000	0,0000	3,21	0,0000	0,0000	ok
	0,0176	0,0124	0,0135	0,0093	3,97	0,0034	0,0023	ok
	0,0350	0,0226	0,0174	0,0103	3,65	0,0048	0,0028	ok
	0,0549	0,0337	0,0199	0,0111	3,65	0,0055	0,0030	no
	0,0736	0,0421	0,0187	0,0084	3,65	0,0051	0,0023	no
	0,0893	0,0472	0,0157	0,0051	3,65	0,0043	0,0014	ok

Vertical C	U1 (m)	U2 (m)	ΔU1 (m)	ΔU2 (m)	Height floor (m)	Verification		
						drx/h	**dry/h**	<0,005
SVL2 combination	0,0024	0,0060	0,0000	0,0000	3,21	0,0000	0,0000	ok
	0,0104	0,0236	0,0081	0,0176	3,97	0,0020	0,0044	ok
	0,0208	0,0430	0,0104	0,0194	3,65	0,0028	0,0053	no
	0,0327	0,0636	0,0119	0,0206	3,65	0,0033	0,0056	no
	0,0437	0,0788	0,0109	0,0152	3,65	0,0030	0,0042	ok
	0,0526	0,0874	0,0090	0,0087	3,65	0,0025	0,0024	ok

Vertical D	U1 (m)	U2 (m)	ΔU1 (m)	ΔU2 (m)	Height floor (m)	Verification		
						drx/h	**dry/h**	<0,005
SVL1 combination	0,0034	0,0031	0,0000	0,0000	3,21	0,0000	0,0000	ok
	0,0140	0,0124	0,0106	0,0093	3,97	0,0027	0,0023	ok
	0,0280	0,0226	0,0140	0,0103	3,65	0,0038	0,0028	ok
	0,0442	0,0337	0,0162	0,0111	3,65	0,0044	0,0030	ok
	0,0593	0,0421	0,0151	0,0084	3,65	0,0041	0,0023	ok
	0,0720	0,0472	0,0127	0,0051	3,65	0,0035	0,0014	ok

Vertical D	U1 (m)	U2 (m)	ΔU1 (m)	ΔU2 (m)	Height floor (m)	Verification		
						drx/h	**dry/h**	<0,005
SVL2 combination	0,0021	0,0060	0,0000	0,0000	3,21	0,0000	0,0000	ok
	0,0082	0,0236	0,0061	0,0176	3,97	0,0015	0,0044	ok
	0,0158	0,0430	0,0076	0,0194	3,65	0,0021	0,0053	no
	0,0247	0,0636	0,0089	0,0206	3,65	0,0024	0,0056	no
	0,0330	0,0788	0,0083	0,0152	3,65	0,0023	0,0042	ok
	0,0400	0,0874	0,0070	0,0087	3,65	0,0019	0,0024	ok

Vertical E	U1 (m)	U2 (m)	ΔU1 (m)	ΔU2 (m)	Height floor (m)	Verification		
						drx/h	**dry/h**	<0,005
SVL1 combination	0,0035	0,0044	0,0000	0,0000	3,21	0,0000	0,0000	ok
	0,0148	0,0165	0,0113	0,0121	3,97	0,0028	0,0030	ok
	0,0296	0,0287	0,0148	0,0122	3,65	0,0041	0,0033	ok
	0,0467	0,0419	0,0171	0,0132	3,65	0,0047	0,0036	ok
	0,0627	0,0527	0,0160	0,0108	3,65	0,0044	0,0030	ok
	0,0762	0,0603	0,0135	0,0075	3,65	0,0037	0,0021	ok

Vertical E	U1 (m)	U2 (m)	ΔU1 (m)	ΔU2 (m)	Height floor (m)	Verification		
						drx/h	**dry/h**	<0,005
SVL2 combination	0,0022	0,0065	0,0000	0,0000	3,21	0,0000	0,0000	ok
	0,0087	0,0225	0,0066	0,0161	3,97	0,0017	0,0040	ok
	0,0170	0,0376	0,0082	0,0151	3,65	0,0023	0,0041	ok
	0,0266	0,0537	0,0096	0,0161	3,65	0,0026	0,0044	ok
	0,0356	0,0657	0,0090	0,0120	3,65	0,0025	0,0033	ok
	0,0431	0,0726	0,0075	0,0069	3,65	0,0021	0,0019	ok

Center mass	U1 (m)	U2 (m)	ΔU1 (m)	ΔU2 (m)	Height floor (m)	Verification		
						drx/h	**dry/h**	<0,005
SVL1 combination	0,0037	0,0031	0,0000	0,0000	3,21	0,0000	0,0000	ok
	0,0155	0,0116	0,0118	0,0086	3,97	0,0030	0,0022	ok
	0,0313	0,0209	0,0158	0,0093	3,65	0,0043	0,0025	ok
	0,0492	0,0307	0,0180	0,0098	3,65	0,0049	0,0027	ok
	0,0661	0,0384	0,0169	0,0077	3,65	0,0046	0,0021	ok
	0,0804	0,0435	0,0143	0,0051	3,65	0,0039	0,0014	ok

Center mass	U1 (m)	U2 (m)	ΔU1 (m)	ΔU2 (m)	Height floor (m)	Verification		
						drx/h	**dry/h**	<0,005
SVL2 combination	0,0022	0,0060	0,0000	0,0000	3,21	0,0000	0,0000	ok
	0,0092	0,0223	0,0069	0,0164	3,97	0,0017	0,0041	ok
	0,0182	0,0390	0,0090	0,0167	3,65	0,0025	0,0046	ok
	0,0285	0,0568	0,0103	0,0177	3,65	0,0028	0,0049	ok
	0,0381	0,0698	0,0096	0,0131	3,65	0,0026	0,0036	ok
	0,0461	0,0772	0,0080	0,0074	3,65	0,0022	0,0020	ok

Table 7.5 *Interstory drift in several verticals of the building estimated by the fissured model, from response spectrum estimated on site*

Vertical A	U1 (m)	U2 (m)	ΔU1 (m)	ΔU2 (m)	Height floor (m)	Verification		
						drx/h	**dry/h**	<0,005
SVL1 combination	0,0014	0,0016	0,0000	0,0000	3,21	0,0000	0,0000	ok
	0,0058	0,0058	0,0045	0,0042	3,97	0,0011	0,0011	ok
	0,0116	0,0101	0,0058	0,0042	3,65	0,0016	0,0012	ok
	0,0184	0,0146	0,0068	0,0046	3,65	0,0019	0,0013	ok
	0,0249	0,0184	0,0065	0,0038	3,65	0,0018	0,0010	ok
	0,0306	0,0211	0,0057	0,0027	3,65	0,0016	0,0007	ok

Vertical A	U1 (m)	U2 (m)	ΔU1 (m)	ΔU2 (m)	Height floor (m)	Verification		
						drx/h	**dry/h**	<0,005
SVL2 combination	0,0009	0,0022	0,0000	0,0000	3,21	0,0000	0,0000	ok
	0,0036	0,0075	0,0028	0,0054	3,97	0,0007	0,0013	ok
	0,0072	0,0125	0,0035	0,0050	3,65	0,0010	0,0014	ok
	0,0113	0,0178	0,0042	0,0053	3,65	0,0011	0,0014	ok
	0,0154	0,0217	0,0040	0,0039	3,65	0,0011	0,0011	ok
	0,0190	0,0241	0,0036	0,0024	3,65	0,0010	0,0007	ok

Vertical C	U1 (m)	U2 (m)	ΔU1 (m)	ΔU2 (m)	Height floor (m)	Verification		
						drx/h	**dry/h**	<0,005
SVL1 combination	0,0015	0,0012	0,0000	0,0000	3,21	0,0000	0,0000	ok
	0,0064	0,0048	0,0049	0,0036	3,97	0,0012	0,0009	ok
	0,0129	0,0088	0,0064	0,0040	3,65	0,0018	0,0011	ok
	0,0203	0,0131	0,0074	0,0044	3,65	0,0020	0,0012	ok
	0,0274	0,0167	0,0071	0,0035	3,65	0,0020	0,0010	ok
	0,0337	0,0192	0,0063	0,0025	3,65	0,0017	0,0007	ok

Vertical C	U1 (m)	U2 (m)	ΔU1 (m)	ΔU2 (m)	Height floor (m)	Verification		
						drx/h	**dry/h**	<0,005
SVL2 combination	0,0009	0,0021	0,0000	0,0000	3,21	0,0000	0,0000	ok
	0,0040	0,0083	0,0031	0,0062	3,97	0,0008	0,0016	ok
	0,0081	0,0152	0,0040	0,0069	3,65	0,0011	0,0019	ok
	0,0128	0,0225	0,0047	0,0074	3,65	0,0013	0,0020	ok
	0,0173	0,0282	0,0045	0,0057	3,65	0,0012	0,0016	ok
	0,0213	0,0318	0,0040	0,0036	3,65	0,0011	0,0010	ok

Vertical D	U1 (m)	U2 (m)	ΔU1 (m)	ΔU2 (m)	Height floor (m)	Verification		
						drx/h	**dry/h**	<0,005
SVL1 combination	0,0012	0,0012	0,0000	0,0000	3,21	0,0000	0,0000	ok
	0,0051	0,0048	0,0038	0,0036	3,97	0,0010	0,0009	ok
	0,0102	0,0088	0,0051	0,0040	3,65	0,0014	0,0011	ok
	0,0161	0,0131	0,0059	0,0044	3,65	0,0016	0,0012	ok
	0,0218	0,0167	0,0057	0,0035	3,65	0,0016	0,0010	ok
	0,0268	0,0192	0,0050	0,0025	3,65	0,0014	0,0007	ok

Vertical D	U1 (m)	U2 (m)	ΔU1 (m)	ΔU2 (m)	Height floor (m)	Verification		
						drx/h	**dry/h**	<0,005
SVL2 combination	0,0008	0,0021	0,0000	0,0000	3,21	0,0000	0,0000	ok
	0,0031	0,0083	0,0023	0,0062	3,97	0,0006	0,0016	ok
	0,0060	0,0152	0,0029	0,0069	3,65	0,0008	0,0019	ok
	0,0095	0,0225	0,0035	0,0074	3,65	0,0010	0,0020	ok
	0,0129	0,0282	0,0034	0,0057	3,65	0,0009	0,0016	ok
	0,0160	0,0318	0,0031	0,0036	3,65	0,0008	0,0010	ok

Vertical E	U1 (m)	U2 (m)	ΔU1 (m)	ΔU2 (m)	Height floor (m)	Verification		
						drx/h	**dry/h**	<0,005
SVL1 combination	0,0013	0,0016	0,0000	0,0000	3,21	0,0000	0,0000	ok
	0,0054	0,0057	0,0041	0,0042	3,97	0,0010	0,0010	ok
	0,0108	0,0099	0,0054	0,0042	3,65	0,0015	0,0011	ok
	0,0171	0,0144	0,0063	0,0045	3,65	0,0017	0,0012	ok
	0,0231	0,0181	0,0061	0,0037	3,65	0,0017	0,0010	ok
	0,0285	0,0208	0,0053	0,0027	3,65	0,0015	0,0007	ok

Vertical E	U1 (m)	U2 (m)	ΔU1 (m)	ΔU2 (m)	Height floor (m)	Verification		
						drx/h	**dry/h**	<0,005
SVL2 combination	0,0008	0,0022	0,0000	0,0000	3,21	0,0000	0,0000	ok
	0,0033	0,0075	0,0025	0,0054	3,97	0,0006	0,0014	ok
	0,0065	0,0125	0,0032	0,0050	3,65	0,0009	0,0014	ok
	0,0103	0,0179	0,0038	0,0053	3,65	0,0010	0,0015	ok
	0,0140	0,0219	0,0037	0,0040	3,65	0,0010	0,0011	ok
	0,0173	0,0243	0,0033	0,0024	3,65	0,0009	0,0007	ok

Center mass	U1 (m)	U2 (m)	ΔU1 (m)	ΔU2 (m)	Height floor (m)	Verification		
						drx/h	**dry/h**	<0,005
SVL1 combination	0,0013	0,0011	0,0000	0,0000	3,21	0,0000	0,0000	ok
	0,0056	0,0043	0,0043	0,0032	3,97	0,0011	0,0008	ok
	0,0114	0,0077	0,0058	0,0034	3,65	0,0016	0,0009	ok
	0,0181	0,0114	0,0066	0,0036	3,65	0,0018	0,0010	ok
	0,0245	0,0144	0,0064	0,0030	3,65	0,0018	0,0008	ok
	0,0301	0,0165	0,0056	0,0022	3,65	0,0015	0,0006	ok

Center mass	U1 (m)	U2 (m)	ΔU1 (m)	ΔU2 (m)	Height floor (m)	Verification		
						drx/h	**dry/h**	<0,005
SVL2 combination	0,0008	0,0021	0,0000	0,0000	3,21	0,0000	0,0000	ok
	0,0035	0,0077	0,0027	0,0056	3,97	0,0007	0,0014	ok
	0,0070	0,0134	0,0035	0,0057	3,65	0,0010	0,0016	ok
	0,0111	0,0196	0,0041	0,0062	3,65	0,0011	0,0017	ok
	0,0150	0,0243	0,0040	0,0047	3,65	0,0011	0,0013	ok
	0,0186	0,0271	0,0035	0,0029	3,65	0,0010	0,0008	ok

***Table 7.6** Interstory drift in the mass center of the building estimated by the fissured model changing only flexural rigidity and shear stiffness of beams and columns (response spectrum NTC2008, Local seismic response)*

Center mass	U1 (m)	U2 (m)	ΔU1 (m)	ΔU2 (m)	Height floor (m)	Verification		
						drx/h	**dry/h**	<0,005
SVL1 combination, LRS	0,0004	0,0003	0,0000	0,0000	3,21	0,0000	0,0000	ok
	0,0015	0,0012	0,0011	0,0008	3,97	0,0003	0,0002	ok
	0,0029	0,0022	0,0014	0,0011	3,65	0,0004	0,0003	ok
	0,0045	0,0034	0,0016	0,0012	3,65	0,0005	0,0003	ok
	0,0063	0,0047	0,0018	0,0012	3,65	0,0005	0,0003	ok
	0,0082	0,0059	0,0019	0,0013	3,65	0,0005	0,0003	ok

Center mass	U1 (m)	U2 (m)	ΔU1 (m)	ΔU2 (m)	Height floor (m)	Verification		
						drx/h	**dry/h**	<0,005
SVL2 combination, LRS	0,0003	0,0005	0,0000	0,0000	3,21	0,0000	0,0000	ok
	0,0012	0,0018	0,0009	0,0013	3,97	0,0002	0,0003	ok
	0,0023	0,0034	0,0011	0,0016	3,65	0,0003	0,0004	ok
	0,0037	0,0051	0,0013	0,0018	3,65	0,0004	0,0005	ok
	0,0051	0,0070	0,0015	0,0019	3,65	0,0004	0,0005	ok
	0,0066	0,0090	0,0015	0,0019	3,65	0,0004	0,0005	ok

Center mass	U1 (m)	U2 (m)	ΔU1 (m)	ΔU2 (m)	Height floor (m)	Verification		
						drx/h	**dry/h**	<0,005
SVL1 combination, NTC08	0,0009	0,0008	0,0000	0,0000	3,21	0,0000	0,0000	ok
	0,0035	0,0030	0,0026	0,0022	3,97	0,0006	0,0006	ok
	0,0068	0,0059	0,0033	0,0029	3,65	0,0009	0,0008	ok
	0,0107	0,0092	0,0039	0,0033	3,65	0,0011	0,0009	ok
	0,0149	0,0126	0,0042	0,0034	3,65	0,0012	0,0009	ok
	0,0192	0,0161	0,0043	0,0034	3,65	0,0012	0,0009	ok

Center mass	U1 (m)	U2 (m)	ΔU1 (m)	ΔU2 (m)	Height floor (m)	Verification		
						drx/h	**dry/h**	<0,005
SVL2 combination, NTC08	0,0007	0,0012	0,0000	0,0000	3,21	0,0000	0,0000	ok
	0,0028	0,0045	0,0021	0,0034	3,97	0,0005	0,0009	ok
	0,0055	0,0089	0,0027	0,0043	3,65	0,0007	0,0012	ok
	0,0087	0,0138	0,0032	0,0049	3,65	0,0009	0,0014	ok
	0,0121	0,0190	0,0034	0,0052	3,65	0,0009	0,0014	ok
	0,0155	0,0242	0,0035	0,0052	3,65	0,0009	0,0014	ok

Table 7.7 *Interstory drift in 'FE Model 2' with external walls modeled (response spectrum NTC2008, Local seismic response)*

Center mass	U1 (m)	U2 (m)	ΔU1 (m)	ΔU2 (m)	Height floor (m)	Verification		
						drx/h	**dry/h**	<0,005
SVL1 combination, NTC08	0,0136	0,0096	0,0000	0,0000	3,21	0,0000	0,0000	ok
	0,0111	0,0077	0,0025	0,0019	3,97	0,0006	0,0005	ok
	0,0085	0,0058	0,0026	0,0019	3,65	0,0007	0,0005	ok
	0,0058	0,0038	0,0027	0,0019	3,65	0,0007	0,0005	ok
	0,0033	0,0020	0,0026	0,0019	3,65	0,0007	0,0005	ok
	0,0009	0,0005	0,0023	0,0014	3,65	0,0006	0,0004	ok

Center mass	U1 (m)	U2 (m)	ΔU1 (m)	ΔU2 (m)	Height floor (m)	Verification		
						drx/h	**dry/h**	<0,005
SVL2 combination, NTC08	0,0081	0,0192	0,0000	0,0000	3,21	0,0000	0,0000	ok
	0,0067	0,0154	0,0014	0,0038	3,97	0,0004	0,0010	ok
	0,0052	0,0116	0,0015	0,0039	3,65	0,0004	0,0011	ok
	0,0037	0,0077	0,0016	0,0039	3,65	0,0004	0,0011	ok
	0,0020	0,0041	0,0016	0,0037	3,65	0,0004	0,0010	ok
	0,0006	0,0011	0,0015	0,0030	3,65	0,0004	0,0008	ok

Center mass	U1 (m)	U2 (m)	ΔU1 (m)	ΔU2 (m)	Height floor (m)	Verification		
						drx/h	**dry/h**	<0,005
SVL1 combination, LSR	0,0060	0,0036	0,0000	0,0000	3,21	0,0000	0,0000	ok
	0,0049	0,0029	0,0011	0,0007	3,97	0,0003	0,0002	ok
	0,0037	0,0022	0,0012	0,0007	3,65	0,0003	0,0002	ok
	0,0026	0,0015	0,0012	0,0007	3,65	0,0003	0,0002	ok
	0,0015	0,0008	0,0011	0,0007	3,65	0,0003	0,0002	ok
	0,0004	0,0002	0,0010	0,0006	3,65	0,0003	0,0002	ok

Center mass	U1 (m)	U2 (m)	ΔU1 (m)	ΔU2 (m)	Height floor (m)	Verification		
						drx/h	**dry/h**	<0,005
SVL2 combination, LSR	0,0036	0,0073	0,0000	0,0000	3,21	0,0000	0,0000	ok
	0,0030	0,0059	0,0007	0,0014	3,97	0,0002	0,0004	ok
	0,0023	0,0044	0,0007	0,0014	3,65	0,0002	0,0004	ok
	0,0016	0,0030	0,0007	0,0014	3,65	0,0002	0,0004	ok
	0,0009	0,0016	0,0007	0,0014	3,65	0,0002	0,0004	ok
	0,0003	0,0005	0,0006	0,0012	3,65	0,0002	0,0003	ok

Vertical A	U1 (m)	U2 (m)	ΔU1 (m)	ΔU2 (m)	Height floor (m)	Verification		
						drx/h	**dry/h**	<0,005
SVL1 combination, NTC08	0,0009	0,0015	0,0000	0,0000	3,21	0,0000	0,0000	ok
	0,0033	0,0049	0,0024	0,0035	3,97	0,0006	0,0009	ok
	0,0058	0,0085	0,0025	0,0036	3,65	0,0007	0,0010	ok
	0,0085	0,0123	0,0026	0,0038	3,65	0,0007	0,0010	ok
	0,0110	0,0160	0,0026	0,0036	3,65	0,0007	0,0010	ok
	0,0135	0,0193	0,0024	0,0033	3,65	0,0007	0,0009	ok

Vertical A	U1 (m)	U2 (m)	ΔU1 (m)	ΔU2 (m)	Height floor (m)	Verification		
						drx/h	**dry/h**	<0,005
SVL2 combination, NTC08	0,0007	0,0022	0,0000	0,0000	3,21	0,0000	0,0000	ok
	0,0023	0,0076	0,0017	0,0054	3,97	0,0004	0,0014	ok
	0,0039	0,0130	0,0016	0,0054	3,65	0,0004	0,0015	ok
	0,0056	0,0185	0,0016	0,0056	3,65	0,0005	0,0015	ok
	0,0071	0,0239	0,0016	0,0053	3,65	0,0004	0,0015	ok
	0,0086	0,0287	0,0014	0,0049	3,65	0,0004	0,0013	ok

Vertical A	U1 (m)	U2 (m)	ΔU1 (m)	ΔU2 (m)	Height floor (m)	Verification		
						drx/h	**dry/h**	<0,005
SVL1 combination, LSR	0,0004	0,0006	0,0000	0,0000	3,21	0,0000	0,0000	ok
	0,0015	0,0020	0,0010	0,0014	3,97	0,0003	0,0003	ok
	0,0026	0,0034	0,0011	0,0014	3,65	0,0003	0,0004	ok
	0,0037	0,0048	0,0012	0,0015	3,65	0,0003	0,0004	ok
	0,0049	0,0063	0,0011	0,0015	3,65	0,0003	0,0004	ok
	0,0060	0,0076	0,0011	0,0014	3,65	0,0003	0,0004	ok

Vertical A	U1 (m)	U2 (m)	ΔU1 (m)	ΔU2 (m)	Height floor (m)	Verification		
						drx/h	**dry/h**	<0,005
SVL2combination, LSR	0,0003	0,0009	0,0000	0,0000	3,21	0,0000	0,0000	ok
	0,0010	0,0029	0,0007	0,0021	3,97	0,0002	0,0005	ok
	0,0017	0,0050	0,0007	0,0021	3,65	0,0002	0,0006	ok
	0,0024	0,0071	0,0007	0,0021	3,65	0,0002	0,0006	ok
	0,0031	0,0092	0,0007	0,0021	3,65	0,0002	0,0006	ok
	0,0038	0,0111	0,0007	0,0019	3,65	0,0002	0,0005	ok

Finally, verifications at serviceability limit states SLE for horizontal displacement (4.2.4.2 of NTC2008), using the calibrating FE model, have been realized. The lateral displacements at the top of the building has been estimated both from response spectrum estimated on site and by the technical standards for construction. Deformability limits for ordinary multistory buildings subjected to horizontal actions (Table 4.2.XI of the standard) can be estimated by the ratio between relative storey displacement δ and storey height h ($\delta/h = 1/300$ in this case) or by the ratio between displacement at the top Δ and total building height H ($\Delta/H = 1/500$ in this case). As one can see from the Table 7.8, the ratio Δ/H does not satisfy the limits set by the standard only for the fissured model when using the spectrum from NTC08 for analysis. Also, δ/h is not satisfy for this case (see tables above).

Table 7.8 *Storey displacement at the top of the building*

Analisi	Δ top floor (m)		Verification	
	U1 (m)	U2 (m)	Δ/H	< 0,002
NTC08	0,0184	0,0226	0,0010	ok
RSL	0,0079	0,0086	0,0004	ok
NTC08, fissured	0,0804	0,0772	0,0037	no
RSL, fissured	0,0301	0,0271	0,0014	ok
NTC08, wall modeled	0,0136	0,0192	0,0009	ok
RSL, wall modeled	0,0060	0,0073	0,0003	ok

7.1.3 Linear dynamic analysis

Response spectrum analysis has been performed to confront the global structure response both for NTC08 spectrum and local seismic response spectrum. Differences in amplitude of both spectrums are shown in the Table 7.13. To evaluate their influence on the structure response, base shear reaction, floor actions, displacement, also maximum shear forces and bending moment at columns, have been estimated.

Generally, the linear dynamic analysis (§7.3.3.1 NTC 2008) consist in:

- determining the vibration modes of the building (modal analysis);
- calculating the effects of the seismic design spectra for the ultimate limit states (SLV) for each vibration modes calculated;
- and combination of these effects.

Base shear forces and resultant of the force acting on each floor have been determined for SLV combination described in the Section 6.1.5.

Those results are confronted with those obtained from a linear static analysis in which, the seismic base shear force F_h, for each horizontal direction, is determined as follows:

$$\mathrm{F_h} = \mathrm{S_d}(\mathrm{T_1}) \cdot \lambda \cdot \mathrm{W/g}$$

where $W/g = m$ is the total mass of the building, above the foundation or above the top of a rigid basement, λ is the correction factor equal to 0.85 if $T_1 < 2\ T_C$ and the building has more than two floors, or λ = 1,0 otherwise, $S_d(T_1)$ is the amplitude spectrum related to the first period T_1.

The seismic action effects shall be determined by applying, horizontal forces F_i to all floors:

$$\mathrm{F_i} = \frac{\mathrm{F_h} \cdot \mathrm{z_i} \cdot \mathrm{W_i}}{\sum_j \mathrm{z_j}.\mathrm{W_j}}$$

where F_i horizontal force acting on storey i, F_h is the seismic base shear, z_i and z_j are displacements of masses W_i/g and W_j/g in the fundamental mode shape, W_i/g and W_j/g are masses of each storey.

All vibration modes with significant modal participating mass ratio have been used in analysis. It is appropriate in this respect to consider all modes with more than 5% participating mass and still a number of ways of which the total participating mass is greater than 85%. For the combination of the effects from individual modes it has been used the complete quadratic combination (CQC) and also, the square root of the sum of squares (SRSS), of effects relating to each mode.

Referred to the standard, actions calculated to various modes of vibration must be appropriately combined by using a complete quadratic combination (CQC), if the oscillation periods differ from each other less than 10%, or the square root of the sum of squares SRSS in cases of clear distinguished periods from each other (§7.3.3.1 NTC2008).

$$E = \sqrt{\sum_i \sum_j \rho_{ij} E_i E_j} \qquad \text{(CQC)}$$

$$E = \sqrt{\sum_i E_i^2} \qquad \text{(SRSS)}$$

$$\rho_{ij} = \frac{8\xi^2 \beta_{ij}^{3/2}}{(1+\beta_{ij})\left[(1-\beta_{ij})^2 + 4\xi^2\beta_{ij}\right]}$$

where E is the global action value (u, T or M), E_i is the action value at mode i, ρ_{ij} is the correlation coefficient between mode i and j, ξ is the viscous damping of mode i and mode j, β_{ij} is the inverse ratio of the periods of each of i-j pair of vibration modes (β_{ij} = T_j/T_i) (§C7.3.3.1 NTC2008).

The accidental eccentricity effects of the center of mass have been considered by the application of static loads constituted by torques, of value equal to the horizontal resultant of the force acting on the floor, determined as described above, multiplied by the 'accidental eccentricity' of the center of gravity of the masses (Table 7.9).

Table 7.9 *Torques value*

Building floors	Floor actions		Floor dimentions		Eccentricity		Torques value				Variation
	Fi (kN)	Fi (kN)	Lx (m)	L(y)	ex (m)	ey (m)	Mx (kN*m)	My (kN*m)	Mx (kN*m)	My (kN*m)	%
Groundfloor	853,1	851,1	62,00	23,74	1,19	3,10	2644,7	1012,6	2638,5	1010,3	0,23
1 Floor	1471,3	1467,9	62,00	23,74	1,19	3,10	4561,1	1746,4	4550,4	1742,4	0,23
2 Floor	1941,0	1936,5	53,21	20,82	1,04	2,66	5164,1	2020,6	5152,0	2015,9	0,23
3 Floor	2538,5	2532,6	53,21	20,82	1,04	2,66	6753,7	2642,6	6737,9	2636,4	0,23
4 Floor	3179,8	3172,3	53,21	20,82	1,04	2,66	8459,8	3310,2	8440,0	3302,4	0,23
5 Floor	3382,6	3374,7	53,21	20,82	1,04	2,66	8999,4	3521,3	8978,3	3513,0	0,23

Floor actions estimated from linear static analysis, by using response spectrum from NTC08 and from local seismic response analysis, are shown in the Table 7.10. As can be seen, floor actions estimated by using the response spectrum from NTC08 are slightly higher about 0.23% than those estimated by using local response spectrum. This due to the lower variation of the amplitude of the spectrums for the first mode of about 0.23% (Table 7.13). As can be known, linear static analysis take into account only the first mode shape. The same results is observed for the base reaction.

Table 7.10 *Seismic lateral actions estimated from linear static analysis*

Linear static analysis					NTC spectrum		LSR spectrum		Variation
Building floors	**Wi (kN)**	**Mass (kN*s2/m)**	**zi (m)**	**Wi *Zi**	**Fh (kN)**	**Fi (kN)**	**Fh (kN)**	**Fi (kN)**	**(%)**
Groundfloor	15629,4	1593,2	3,2	50170,5	13366,4	853,1	13335,1	851,1	0,23
1 Floor	12050,9	1228,4	7,2	86525,6		1471,3		1467,9	0,23
2 Floor	10540,2	1074,4	10,8	114150,1		1941,0		1936,5	0,23
3 Floor	10309,8	1051,0	14,5	149286,4		2538,5		2532,6	0,23
4 Floor	10314,4	1051,4	18,1	186999,5		3179,8		3172,3	0,23
5 Floor	9133,4	931,0	21,8	198926,2		3382,6		3374,7	0,23
	Σ	6929,47741	∑Wi *Zi	786058,4		13366,4		13335,1	

Floor actions have been estimated by the relationship below using both spectrums: from NTC08 and LSR (Table 7.14):

$F_j = \Gamma_j * S_d(T_j) * mi * \phi_j$

where $S_d(T_j)$ is the amplitude spectrum at each j-mode, Γ_j is modal participation factor of each j-mode, m_i is the mass of floor, ϕ_j is the modal displacement of the center of mass for each j-mode.

Amplitude spectrum $S_d(T_j)$ for seven modes with total participating mass 85%, has been selected by the response spectrum for SLV limit state both from NTC08 and local seismic analysis (Table 7.12, Table 7.13). The amplitude of local response spectrum, at periods lower than 0.2 s, is higher than the amplitude of the spectrum from NTC08, making at this way modes from the fourth to the seventh more important than the other (Table 7.13).

Floor actions calculated to various modes of vibration have been combined by using a complete quadratic combination (Table 7.15) and the square root of the sum of squares combination (Table 7.16). As one can see, floor actions are higher when using the local response spectrum and show different percentage variations at various levels of the building.

Maximum and minimum shear forces and bending moment on columns estimated from both response spectrums are confronted and presented in the Table 7.18. Those parameters are higher (not more than 10%) when using the response spectrum from NTC08.

Table 7.11 *Interstory drifts in the center of mass*

Mode	LSR		NTC08		Variation (%)	
	U1Amp (m)	U2Amp (m)	U1Amp (m)	U2Amp (m)	U1Amp	U2Amp
1	0,7425	0,2246	0,7449	0,2253	-0,3	-0,3
2	-0,5369	1,4016	-0,6016	1,5704	-12,0	-12,0
3	0,9912	0,4019	1,1283	0,4574	-13,8	-13,8
4	-0,0711	-0,0241	-0,0431	-0,0146	39,3	39,3
5	0,0242	-0,1183	0,0130	-0,0637	46,2	46,2
6	-0,0653	-0,0112	-0,0323	-0,0056	50,5	50,5
7	-0,0312	-0,0085	-0,0152	-0,0041	51,1	51,1

Height Floor (m)	LSR		NTC08		Variation (%)	
	Center of mass		Center of mass		Center of mass	
	ΔU1 (m)	ΔU2 (m)	ΔU1 (m)	ΔU2 (m)	ΔU1	ΔU2
0	0,00	0,00	0,00	0,00	0,0	0,0
3,21	0,00094	0,00148	0,00104	0,00153	-10,8	-3,7
7,18	0,00269	0,00405	0,00301	0,00443	-11,8	-9,5
10,83	0,00346	0,00497	0,00387	0,00556	-11,8	-12,0
14,48	0,00409	0,00571	0,00461	0,00637	-12,5	-11,5
18,13	0,00444	0,00605	0,00495	0,00664	-11,5	-9,8
21,78	0,00456	0,00602	0,00503	0,00655	-10,4	-8,9

Note: U1Amp and U2Amp are the multipliers of the mode shapes that contribute to the displaced shape for the each direction of acceleration load from the response spectrum modal amplitude.

Interstory drifts in the vertical that pass on mass center are about 9% (mean value) higher when using NTC08 spectrum (Table 7.11). The mean variation of the interstory drifts in the other verticals of the building is about 8.3%.

Table 7.12 *Modal Participation Factors, Modal Participating Mass Ratios*

StepType	**StepNum**	**Period**	**UX**	**UY**
Text	Unitless	Sec	KN-s2	KN-s2
Mode	1	0,82	21,49	4,92
Mode	2	0,60	-27,33	64,23
Mode	3	0,45	-60,29	-27,74
Mode	4	0,21	-10,71	-3,24
Mode	5	0,13	-10,08	39,57
Mode	6	0,10	-31,95	-7,14
Mode	7	0,10	-24,74	-6,85

StepType	**StepNum**	**Period**	**UX**	**UY**	**RZ**
Text	Unitless	Sec	Unitless	Unitless	Unitless
Mode	1	0,82	0,060	0,003	0,566
Mode	2	0,60	0,097	0,536	0,000
Mode	3	0,45	0,473	0,100	0,066
Mode	4	0,21	0,015	0,001	0,200
Mode	5	0,13	0,013	0,204	0,000
Mode	6	0,10	0,133	0,007	0,060
Mode	7	0,10	0,080	0,006	0,035

Table 7.13 *Response spectrum amplitude corresponding to modal frequencies of the building*

Period (s)	Sd (Ti), g		Variation (%)	
	LSR	NTC08	higher NTC08	higher LSR
0,82	0,196	0,197	0,23	−
0,60	0,241	0,269	10,36	−
0,45	0,316	0,357	11,56	−
0,21	0,597	0,362	−	39,27
0,13	0,658	0,355	−	45,99
0,10	0,691	0,340	−	50,78
0,10	0,694	0,339	−	51,15

Table 7.14 *Modal floor actions*

	Building floors	Tj (s)	mx,i (KN-s2/m)	ϕi,j (m), x direction	ϕi,j (m), y direction	Γx,j (KN-s2)	Γy,j (KN-s2)	Sa(Tj), g	NTC08		LRS	
									Vbx,j (kN)	**Vby,j (kN)**	**Vbx,j (kN)**	**Vby,j (kN)**
Mode 1	Groundfloor	0,82	1593,2	-0,00030	-0,00021	21,49	4,92	0,197	20,01	3,14	19,97	3,13
	1 Floor		1228,4	-0,00117	-0,00057				59,38	6,59	59,24	6,58
	2 Floor		1074,4	-0,00264	-0,00032				117,46	3,26	117,19	3,25
	3 Floor		1051,0	-0,00407	-0,00057				177,38	5,66	176,96	5,65
	4 Floor		1051,4	-0,00555	-0,00085				241,88	8,50	241,31	8,48
	Terrace		931,0	-0,00707	-0,00082				272,97	7,19	272,33	7,18

Mode 2	Building floors	Tj (s)	mx,i (KN-s2/m)	φi,j (m), x direction	φi,j (m), y direction	Γx,j (KN-s2)	Γy,j (KN-s2)	Sa(Tj), g	**Vbx,j (kN)**	**Vby,j (kN)**	**Vbx,j (kN)**	**Vby,j (kN)**
	Groundfloor	0,60	1593,2	0,00038	-0,00091	-27,33	64,23	0,269	43,35	246,20	38,86	220,68
	1 Floor		1228,4	0,00149	-0,00360				132,02	750,55	118,34	672,77
	2 Floor		1074,4	0,00292	-0,00699				226,14	1273,56	202,70	1141,57
	3 Floor		1051,0	0,00459	-0,01089				347,87	1942,03	311,82	1740,77
	4 Floor		1051,4	0,00637	-0,01496				483,03	2667,86	432,97	2391,37
	Terrace		931,0	0,00816	-0,01895				548,42	2993,32	491,58	2683,10

Mode 3	Building floors	Tj (s)	mx,i (KN-s2/m)	φi,j (m), x direction	φi,j (m), y direction	Γx,j (KN-s2)	Γy,j (KN-s2)	Sa(Tj), g	**Vbx,j (kN)**	**Vby,j (kN)**	**Vbx,j (kN)**	**Vby,j (kN)**
	Groundfloor	0,45	1593,2	0,00086	0,00041	-60,29	-27,74	0,357	288,63	63,38	255,26	56,05
	1 Floor		1228,4	0,00329	0,00156				854,09	186,14	755,34	164,62
	2 Floor		1074,4	0,00632	0,00319				1436,35	333,34	1270,27	294,80
	3 Floor		1051,0	0,01000	0,00482				2221,63	492,67	1964,75	435,70
	4 Floor		1051,4	0,01394	0,00646				3098,32	660,89	2740,07	584,47
	Terrace		931,0	0,01792	0,00814				3526,90	736,99	3119,09	651,77

Mode 4	Building floors	Tj (s)	mx,i (KN-s2/m)	φi,j (m), x direction	φi,j (m), y direction	Γx,j (KN-s2)	Γy,j (KN-s2)	Sa(Tj), g	**Vbx,j (kN)**	**Vby,j (kN)**	**Vbx,j (kN)**	**Vby,j (kN)**
	Groundfloor	0,21	1593,2	0,00140	0,00071	-10,71	-3,24	0,362	84,63	13,11	139,35	21,58
	1 Floor		1228,4	0,00348	0,00102				162,60	14,45	267,72	23,79
	2 Floor		1074,4	0,00479	-0,00035				196,01	-4,37	322,74	-7,20
	3 Floor		1051,0	0,00312	-0,00006				124,70	-0,68	205,32	-1,12
	4 Floor		1051,4	-0,00028	0,00022				-11,09	2,67	-18,26	4,39
	Terrace		931,0	-0,00423	0,00054				-149,89	5,81	-246,80	9,57

Mode 5	Building floors	Tj (s)	mx,i (KN-s2/m)	φi,j (m), x direction	φi,j (m), y direction	Γx,j (KN-s2)	Γy,j (KN-s2)	Sa(Tj), g	**Vbx,j (kN)**	**Vby,j (kN)**	**Vbx,j (kN)**	**Vby,j (kN)**
	Groundfloor	0,13	1593,2	0,00128	-0,00530	-10,08	39,57	0,355	71,54	1164,57	132,47	2156,27
	1 Floor		1228,4	0,00318	-0,01337				137,39	2264,05	254,38	4192,02
	2 Floor		1074,4	0,00370	-0,01535				139,76	2274,75	258,77	4211,83
	3 Floor		1051,0	0,00242	-0,00975				89,25	1412,21	165,26	2614,78
	4 Floor		1051,4	-0,00029	0,00191				-10,53	-276,77	-19,49	-512,45
	Terrace		931,0	-0,00349	0,01571				-114,30	-2016,34	-211,64	-3733,38

Mode 6	Building floors	Tj (s)	mx,i (KN-s2/m)	φi,j (m), x direction	φi,j (m), y direction	Γx,j (KN-s2)	Γy,j (KN-s2)	Sa(Tj), g	**Vbx,j (kN)**	**Vby,j (kN)**	**Vbx,j (kN)**	**Vby,j (kN)**
	Groundfloor	0,10	1593,2	0,00355	0,00082	-31,95	-7,14	0,340	601,84	31,14	1222,77	63,27
	1 Floor		1228,4	0,00958	0,00276				1254,29	80,72	2548,37	164,00
	2 Floor		1074,4	0,01266	0,00329				1449,45	84,21	2944,88	171,09
	3 Floor		1051,0	0,01000	0,00128				1119,44	31,98	2274,39	64,97
	4 Floor		1051,4	-0,00031	-0,00088				-34,84	-22,00	-70,79	-44,70
	Terrace		931,0	-0,01438	-0,00262				-1426,94	-57,99	-2899,15	-117,81

Mode 7	Building floors	Tj (s)	mx,i (KN-s2/m)	φi,j (m), x direction	φi,j (m), y direction	Γx,j (KN-s2)	Γy,j (KN-s2)	Sa(Tj), g	**Vbx,j (kN)**	**Vby,j (kN)**	**Vbx,j (kN)**	**Vby,j (kN)**
	Groundfloor	0,10	1593,2	0,00540	0,00162	-24,74	-6,85	0,339	708,25	58,72	1449,87	120,20
	1 Floor		1228,4	0,00974	0,00177				984,32	49,42	2015,00	101,16
	2 Floor		1074,4	0,00708	0,00184				626,17	44,91	1281,84	91,93
	3 Floor		1051,0	0,00095	0,00199				82,42	47,54	168,72	97,33
	4 Floor		1051,4	-0,00290	0,00012				-250,92	2,90	-513,65	5,93
	Terrace		931,0	-0,00420	-0,00272				-321,64	-57,58	-658,43	-117,87

Table 7.15 *Floor actions from linear dynamic analysis, CQC comb*

Building floors	NTC08		RSL		Variation (%)	
	Vbx (kN)	**Vby (kN)**	**Vbx (kN)**	**Vby (kN)**	**Vbx**	**Vby**
Groundfloor	1332,9	1197,1	2663,0	2177,8	49,9	45,0
1' floor	2381,7	2399,2	4592,1	4253,8	48,1	43,6
2' floor	2512,0	2646,0	4395,4	4383,7	42,8	39,6
3' floor	2496,6	2493,5	3127,3	3199,5	20,2	22,1
4' floor	3047,4	2825,3	2749,6	2568,7	-10,8	-10,0
Terraze	3863,6	3735,1	4674,0	4670,6	17,3	20,0

Table 7.16 *Floor actions from linear dynamic analysis, SRSS comb*

Building floors	NTC08		RSL		Variation (%)	
	Vbx (kN)	**Vby (kN)**	**Vbx (kN)**	**Vby (kN)**	**Vbx**	**Vby**
Groundfloor	980,7	1193,9	1923,9	2172,6	49,0	45,0
1' floor	1827,0	2394,4	3358,4	4253,3	45,6	43,7
2' floor	2163,1	2630,0	3486,4	4378,1	38,0	39,9
3' floor	2524,2	2451,9	3043,0	3173,5	17,0	22,7
4' floor	3155,3	2762,5	2832,5	2515,0	-11,4	-9,8
Terraze	3871,6	3684,5	4357,6	4646,5	11,2	20,7

Base reaction has been estimated for two combination of SLV limit state, by using spectrum from NTC08 and from locals seismic response, and the results are shown in the Table 7.17. In case of local response spectrum, base reactions are 10% higher. Also, total forces and moment about the global co-ordinates (Fx, Fy, Mx & My) are shown in Table 7.17.

Table 7.17 *Base reactions*

	Base reaction for SLV limit state, Sap2000					
	from NTC08 spectrum		from RSL spectrum		**Variation (%)**	
	Vbx (kN)	**Vby (kN)**	**Vbx (kN)**	**Vby (kN)**	Vbx	Vby
SLV1 comb	16463,5	11130,0	18325,7	11556,5	10,2	3,7
SLV2 comb	11580,6	14961,3	12048,8	16684,6	3,9	10,3

Note: ‘SLV1 comb’ seismic action E=Ex+0,3Ey; ‘SLV2 comb’ seismic action E=0,3Ex+Ey.

	from NTC08 spectrum		from RSL spectrum		**Variation (%)**	
	Mx (kN m)	**My (kN m)**	**Mx (kN m)**	**My (kN m)**	Mx	My
SLV1 comb	631373,2	1101330,2	613871,5	1128059,4	-2,9	2,4
	284402,4	1614348,1	301904,0	1587618,9	5,8	-1,7
SLV2 comb	681357,9	-1172211,7	661281,7	-1192026,0	-3,0	1,7
	234417,7	-1543466,6	254493,9	-1523652,3	7,9	-1,3

Table 7.18 *Maximum and minimum shear forces and bending moment on columns*

		P	V2	V3	T	M2	M3
		KN	KN	KN	KN-m	KN-m	KN-m
LSR	min	-5600,01	-92,01	-489,04	-15,49	-393,18	-240,72
	max	5068,13	114,34	300,70	13,54	403,15	197,26
NTC08	min	-6172,61	-96,80	-523,43	-15,88	-417,50	-254,66
	max	5640,73	120,89	315,19	14,06	426,84	214,92
Variation (%)		9,28	4,95	6,57	2,40	5,83	5,47
		10,15	5,42	4,60	3,66	5,55	8,22

7.1.4 Nonlinear static Pushover analysis

Nonlinear static pushover analysis provides the capacity of the structure, and does not give directly the demands associated with a particular level of seismic action. Pushover analysis is a non-linear static analysis under constant gravity loads and monotonically increasing horizontal loads. In the case of non-linear static analysis, the safety check consists of a comparison between the ultimate displacement capacity of the construction and the displacement demand obtained by applying the method described in §7.3.4.1 of the standard NTC2008. Pushover analysis assumes that the response is governed by a single mode of vibration which is constant during the analysis. The distribution of lateral forces (applied at the center of mass of each floors) is uniform with lateral forces proportional to story masses and consider usually the first mode (inverted triangle), and also can be applied at the mass center. The lateral forces can be then monotonically increased in constant proportion with a displacement control at the top of the building until a certain level of deformation is reached. The target of the top displacement may be the deformation expected in the design earthquake in case of designing a new structure, or the drift corresponding to structural collapse for assessment purposes.

Target displacement can be estimated from the response spectrum, referred to 'Annex B' of Eurocode8. The displacement at the top of the building (Table 7.19) has been estimated from the response spectrum analysis performed previously and then the target displacement at the top of the building has been estimated by the relationship:

$d_t = S_a \cdot T^2/4\cdot\pi^2$ (as $T > T_C$)

where S_a (m/s^2) is the spectral acceleration corresponding to the period T (s).

The relation between the base shear force and the control displacement (the “capacity curve”) have been determined by pushover analysis, for values of the control displacement that ranging between 0% and 150% of the target displacement. The control displacement has been checked at the center of mass and in the 'Vertical a' at the roof of the building.

The nonlinear properties of structure elements have been determined first by applying hinges on beams (M3 shear hinge, modeled to account for inelastic shear behavior applied to link beams) and columns (P-M2-M3 hinge). The moment-rotation curve of a P-M2-M3 hinge is a monotonic backbone relationship used to describe the post-yield behavior of a column element subjected to combined axial and biaxial-bending conditions (FEMA 356, 2000).

Demand curve is plotted once for response spectrum due to NTC08 and once from local seismic response (Figure 7.3). Scale factor has been changed up to intersect the demand curve with the capacity curve in the so called 'performance point', which represent the global behavior of the building. This scale factor has been set first 9.81 as the spectrum is in *g*. In this way, it is avoided to perform various Pushover analyzes by changing hinge properties.

Table 7.19 Target displacement at the top of the building

Height	Displacement at the top								Target displacement (T > Tc)		Max.displacement	
	LSR		NTC08		LSR		NTC08		LSR	NTC08	LSR	NTC08
	Center of mass		Center of mass		Vertical A		Vertical A		Center of mass	Vertical A	Center of mass	Vertical A
Floor (m)	U1 (m)	U2 (m)	U1 (m)	U2 (m)	U1 (m)	U2 (m)	U1 (m)	U2 (m)	dt (m)	dt (m)	dmax (m)	dmax (m)
0	0,0000	0,0000	0,0000	0,0000	0,0000	0,0000	0,0000	0,0000	–	–	–	–
3,21	0,0009	0,0015	0,0010	0,0015	0,0009	0,0016	0,0010	0,0017	–	–	–	–
7,18	0,0036	0,0055	0,0041	0,0060	0,0035	0,0054	0,0037	0,0057	–	–	–	–
10,83	0,0071	0,0105	0,0079	0,0115	0,0067	0,0096	0,0073	0,0104	–	–	–	–
14,48	0,0112	0,0162	0,0125	0,0179	0,0105	0,0144	0,0116	0,0157	–	–	–	–
18,13	0,0156	0,0223	0,0175	0,0245	0,0146	0,0193	0,0162	0,0211	–	–	–	–
21,78	0,0202	0,0283	0,0225	**0,0311**	0,0189	0,0242	0,0208	0,0263	**0,0328**	**0,0329**	**0,0492**	**0,0493**

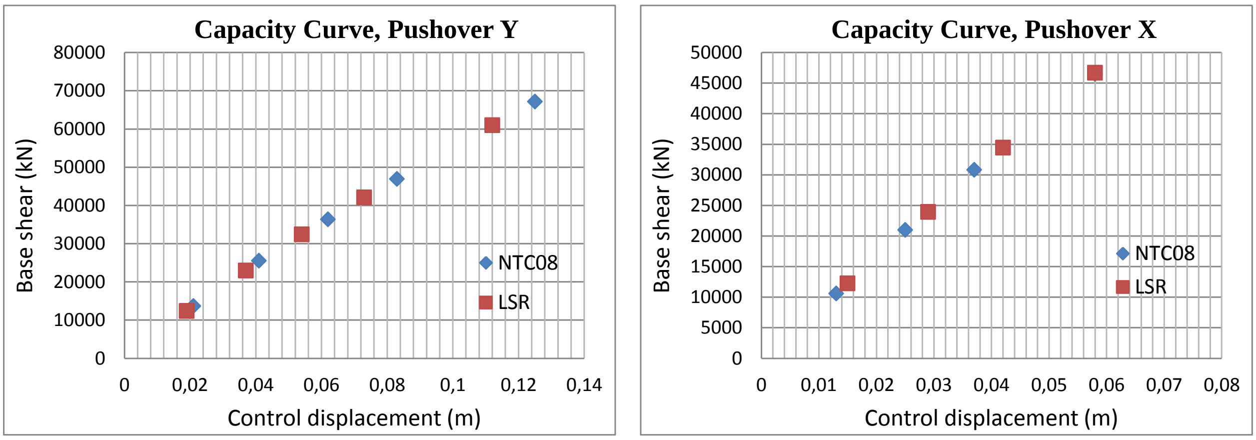

Figure 7.3 *Demand curve*

The maximum displacement estimated (Table 7.19), was also an objective to be reached during this analysis. In the Figure 7.4 and in the Figure 7.5 are shown the spectral displacement to spectral acceleration curves in case of Pushover analysis for seismic action in the *Y* direction and for scale factor respectively 9.81 and 20. In those figures, the blue lines show the demand spectra for damping ratios 0.02, 0.05, 0.1 and 1.5, the red line shows single demand spectrum, the grey line shows the constant period line, while the green line shows the capacity curve.

Parameters of the 'performance points' achieved from analysis are shown in the Table 7.20.

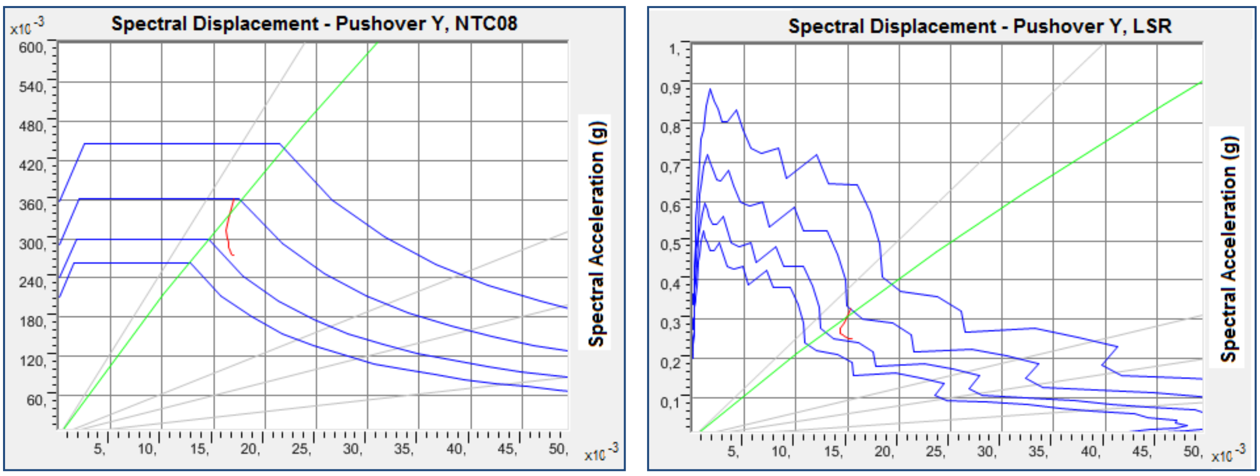

Figure 7.4 *Spectral displacement – Spectral Acceleration curve for LSR and NTC08 spectrum in case of scale factor 9.8*

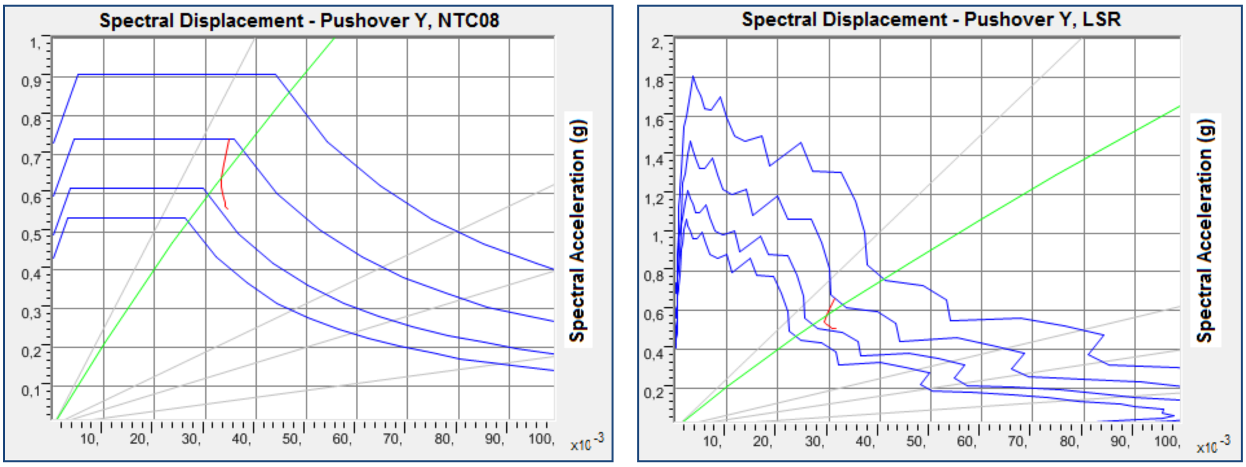

Figure 7.5 *Spectral displacement – Spectral Acceleration for LSR and NTC08 spectrum in case of scale factor 20*

Table 7.20 *Performance point data at the roof, in the center of mass and in the 'Vertical a'*

Control point: 'Vertical a' at the roof								
Spectrum name	Performance point	V (kN)	D (m)	Sa (m/s²)	Sd (m/s²)	Teff (s)	Beff	SF
NTC08	Pushover_X	10599,8	0,013	0,362	0,013	0,374	0,05	9,81
LSR	Pushover_X	12268	0,015	0,419	0,015	0,374	0,05	9,81
NTC08	Pushover_X	20986,2	0,026	0,73	0,026	0,376	0,052	20
LSR	Pushover_X	23953,4	0,03	0,837	0,029	0,376	0,052	20
NTC08	Pushover_X	30769,7	0,039	1,084	0,038	0,377	0,054	30
LSR	Pushover_X	34429,5	0,044	1,223	0,044	0,378	0,056	30
NTC08	Pushover_X	39534	0,051	1,417	0,051	0,38	0,058	40
LSR	Pushover_X	43900	0,057	1,583	0,057	0,381	0,06	40
NTC08	Pushover_X	46464,2	0,061	1,682	0,061	0,382	0,061	48
LSR	Pushover_X	46671,8	0,061	1,69	0,061	0,382	0,061	43
Spectrum name	Performance point	V (kN)	D (m)	Sa (m/s²)	Sd (m/s²)	Teff (s)	Beff	SF
NTC08	Pushover_Y	13558,7	0,017	0,34	0,017	0,441	0,056	9,81
LSR	Pushover_Y	12282,6	0,015	0,308	0,015	0,44	0,055	9,81
NTC08	Pushover_Y	24305,5	0,029	0,607	0,031	0,456	0,07	18,5
LSR	Pushover_Y	23295,4	0,028	0,582	0,03	0,455	0,069	20
LSR	Pushover_Y	24865	0,03	0,621	0,032	0,457	0,071	21,5
Control point: 'Center of mass' at the roof								
Spectrum name	Performance point	V (kN)	D (m)	Sa (m/s²)	Sd (m/s²)	Teff (s)	Beff	SF
NTC08	Pushover_X	10599,8	0,013	0,362	0,013	0,374	0,05	9,81
LSR	Pushover_X	12268	0,015	0,419	0,015	0,374	0,05	9,81
NTC08	Pushover_X	20971,2	0,025	0,73	0,026	0,376	0,052	20
LSR	Pushover_X	23929,7	0,029	0,837	0,029	0,376	0,052	20
NTC08	Pushover_X	30800,1	0,037	1,085	0,038	0,377	0,054	30
LSR	Pushover_X	34453,6	0,042	1,224	0,044	0,378	0,056	30
NTC08	Pushover_X	46476	0,058	1,682	0,061	0,382	0,061	48
LSR	Pushover_X	46682,7	0,058	1,69	0,061	0,382	0,061	43
Spectrum name	Performance point	V (kN)	D (m)	Sa (m/s²)	Sd (m/s²)	Teff (s)	Beff	SF
NTC08	Pushover_Y	13659	0,021	0,342	0,017	0,441	0,059	9,81
LSR	Pushover_Y	12348,7	0,019	0,31	0,015	0,44	0,056	9,81
NTC08	Pushover_Y	25506,3	0,041	0,637	0,033	0,457	0,078	20
LSR	Pushover_Y	22948,4	0,037	0,573	0,029	0,454	0,074	20
NTC08	Pushover_Y	36365,7	0,062	0,913	0,05	0,469	0,084	30
LSR	Pushover_Y	32434,4	0,054	0,813	0,044	0,465	0,083	30
NTC08	Pushover_Y	46891,3	0,083	1,184	0,067	0,478	0,088	40
LSR	Pushover_Y	42081,4	0,073	1,06	0,059	0,474	0,086	40
NTC08	Pushover_Y	67149,3	0,125	1,7	0,102	0,492	0,093	60
LSR	Pushover_Y	60984,7	0,112	1,544	0,091	0,488	0,092	60

where V is the base shear, D is the displacement at the point of control, S_a is spectral acceleration, S_d is spectral displacement, T_{eff} is period and D_{eff} is damping.

VIII. Case study 2 – MASONRY CONSTRUCTION

Three important historic towers ('Guaita' Tower, 'Cesta' Tower, 'Montale' Tower) in Republic of San Marino, have been studied. The town center of San Marino interest Epiligure succession referable to the Miocene. In the eastern part of the town with major morphological relief, outcrop the limestone of San Marino formation. Generally, are gray organogenic limestone and grayish white calcite limestone in bioclasts with disseminated fragments of corals and bryozoans. There are also present limestone intensely bioturbated, with convex-concave, parallel, wavy, and crossed stratification. The thickness of the formation is variable, it can reach 200 meters. In CARG 267 sheet of San Marino (see Figure 8.1) (Cornamusini et al., 2009) the age of the San Marino formation refers to Burdigalian Sup.- Langhian Inf. The stratigraphy dips to the south west and the average slope is about 30°. At the west to the roof of the formation described above, outcrop sandstones of Monte Funaiolo formation referable to the Burdigalian Sup. - Serravallian. In this area, the Epiligure succession of Inferior-Middle Miocene rests on discordance in succession Cretaceous-Paleocene of Ligurian Unit. The latter rests in tectonic contact (overthrust with kinematics towards north east) on Pliocene Succession pre and post blanket.

TECTONIC SCHEME **Scale 1: 200.000**

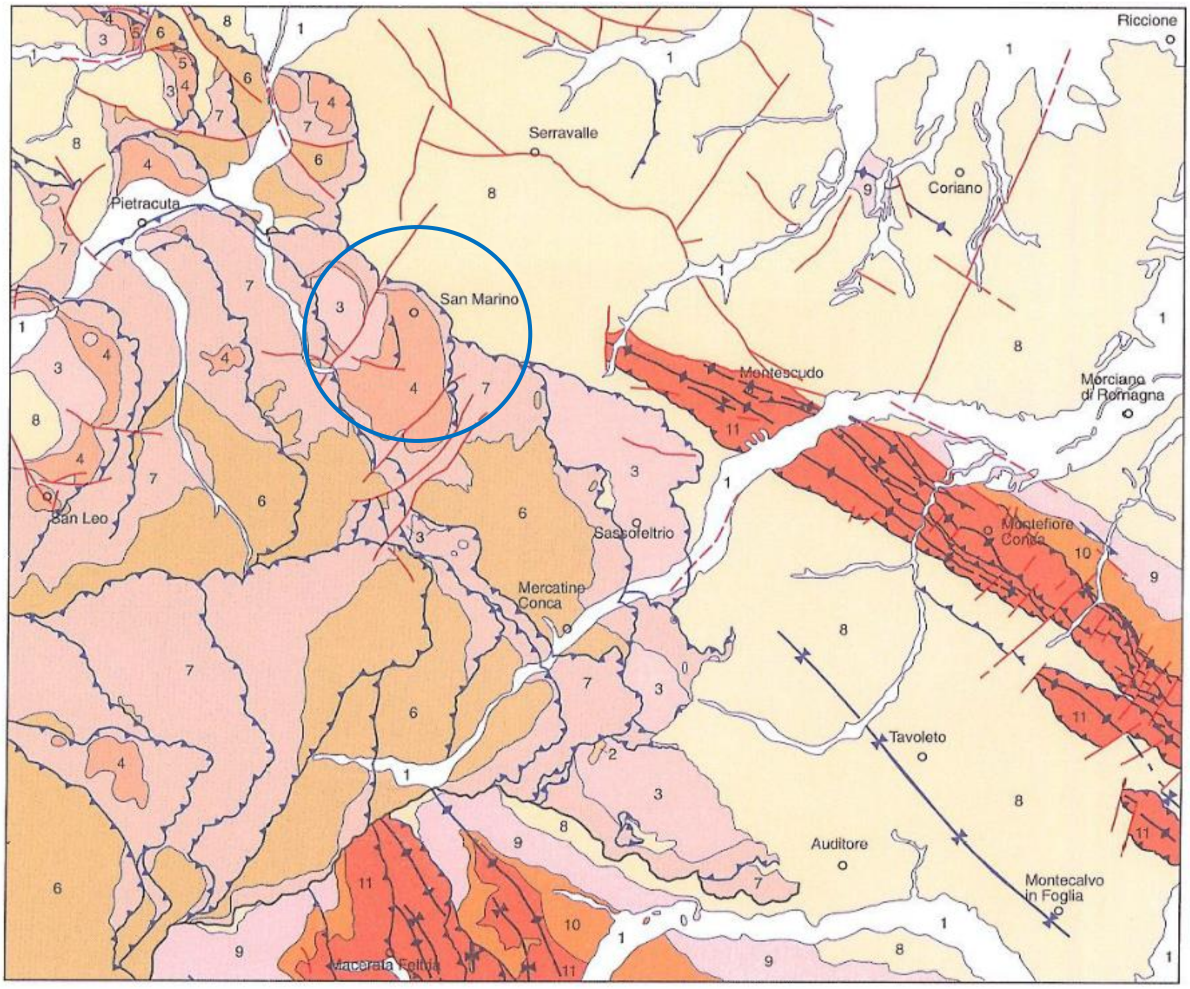

1 Continental and coastal deposits post-evaporitic quaternary
EPILIGURE SUCCESSION
2 Post-evaporitic Miocene succession
3 Succession of Upp Miocene
4 Succession of Low-Mid. Miocene
5 Oligo-Aquitanian succession
LIGURIAN UNITS
6 Eocene succession
7 Cretaceous-Paleocene succession
POST-EVAPORITIC SUCCESSION OF PADANO-ADRIATICO BORDER
8 Pliocene succession pre and post cover
9 Messinian succession of lake-sea
10 Messinian succession of pre lake-sea
UMBRIO-MARCHIGIANO-ROMAGNOLO succession
11 Pre-evaporitic Miocene succession
Fault
Base of cover of Val Marecchia
Overthrust
Axial surface of syncline
Axial surface of anticline

Figure 8.1 *Geologic Map of San Marino (Cornamusini et al., 2009)*

The historic center of the Republic of San Marino was included in UNESCO world heritage list in 2008, furthermore, is located in a region characterized by medium level of seismic hazard that make important the evaluation of seismic hazard. The ambient noise measurements have been acquired by two synchronized three directional portable seismographs in three towers in San Marino.
The towers are masonry construction documented for the first time in 1253. Numerous restoration and reinforcement changed the structure of the towers, however, without removing the primitive crudeness of the same.

In the 'Montale' Tower has been realized a more detailed study. University of San Marino, has realized the FE model of the 'Montale' Tower using 3D mapping and the bibliography for the material properties (Guerra et. al). 3D laser scanner technology was applied in order to have the complete survey of the building with 2D data (floor plants and section) and 3D data (point cloud of the tower) in the faster and easier way. A difficulty of the project was the total absence of data and certain plans of many of the historical buildings of the Republic of San Marino and particularly the third tower. This model has been calibrated then by using OMA method.

8.1 Ambient vibration measure acquired

Ambient vibration measurements have been acquired at every accessible floor of the buildings and in correspondence with the ground, outside the buildings. In the 'Montale Tower' the seismic noise measurements have been acquired in two different ways: first leaving the fixed seismograph in the top floor and second living one seismograph fixed in the free field, to evaluate the applicability of both EMA and OMA method. In the other towers, the ambient vibration measures have been acquired by living one seismograph fixed in the top floor.

Two portable seismographs called Tromino™, by Micromed S.p.a., have been used to acquire the ambient noise measurements. The devices have been oriented in order to have their principle axes parallel with the buildings facades. Ambient vibration measurements has a duration of 26 minutes and a sampling frequency of 128 Hz.

In the Figure 8.2 are shown the vertical positions in the three towers in the Republic of San Marino, where the environmental seismic noise have been acquired (see yellow line).

Figure 8.2 *Towers in San Marino: 'Guaita' Tower, 'Cesta' Tower and 'Montale' Tower*

In the Figure 8.3 is shown the position in plan and in elevation of measurements acquired in '*Guaita' Tower*. The ambient vibration measurements have been acquired in two verticals leaving one of the instrument fixed on the top floor and moving the other one in the various levels. The duration of the acquisition is 26 minutes for the first vertical and 20 min for the second vertical. The seismograph has been placed over the floors near the edges of the tower. The frequencies and the mode shapes have been estimated using the OMA1 method.
The pairs of measurements synchronized vertically are:

- 1' Vertical: 4'Floor-3'Floor; 4'Floor-2'Floor; 4'Floor-1'Floor; 4'Floor - Ground Floor;
- 2' Vertical: 4'Floor-3'Floor; 4'Floor-2'Floor; 4'Floor-1'Floor.

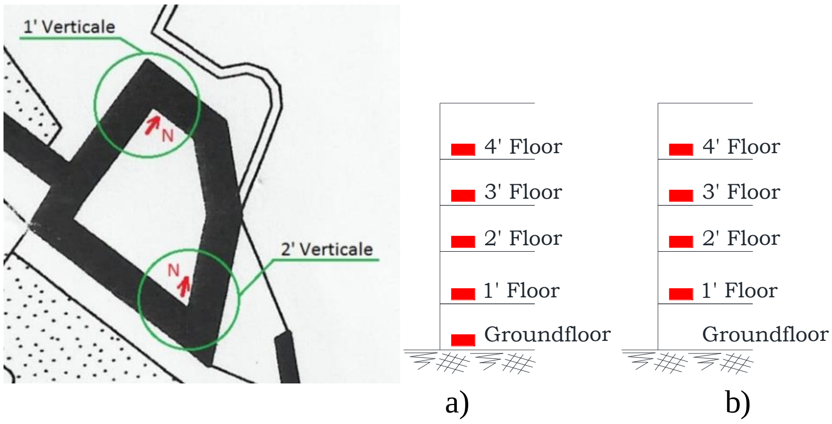

***Figure 8.3** Measurements position in plan and in elevation in 'Guaita' Tower: a) first vertical, b) second vertical*

In the Figure 8.4 are presented the measurements position in elevation in '*Cesta' Tower.* The synchronized ambient vibration measurements have been acquired in one vertical by leaving one of the seismograph fixed on the top floor and moving the other one in the various levels. The duration of the acquisition is 26 minutes. The pairs of measurements synchronized vertically are:

- 4'Floor-3'Floor; 4'Floor-2'Floor; 4'Floor-1'Floor; 4'Floor - Ground Floor.

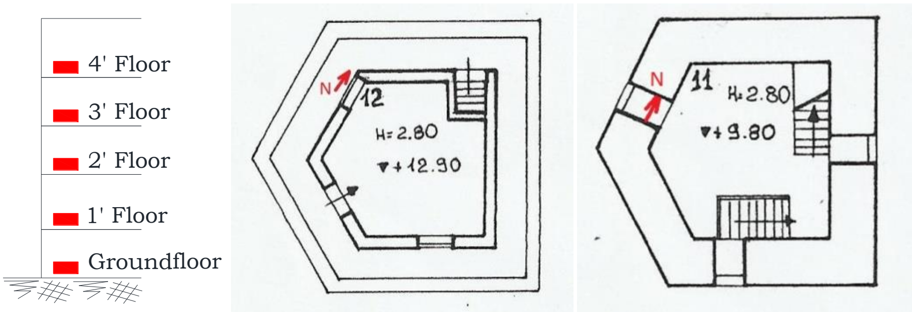

***Figure 8.4** Measurements position in elevation in 'Cesta' Tower*

In the Figure 8.5 is shown the position in vertical of synchronized measurements acquired in '*Montale' Tower* for both procedures: first living the fixed seismograph in the top floor and second living the fixed seismograph outside in the free field. The ambient vibration measurement has not been acquired in the first floor, because has been not possible to access it. The instrument has been placed above the windows sills or windows openings. The duration of the acquisition has been 26 minutes. The pairs of measurements synchronized vertically are:
-first case: 4'Floor-3'Floor; 4'Floor-2'Floor; 4'Floor-Ground Floor,
-second case: 4'Floor-Free field; 3'Floor-Free field; 2'Floor-Free field; Ground Floor-Free field.

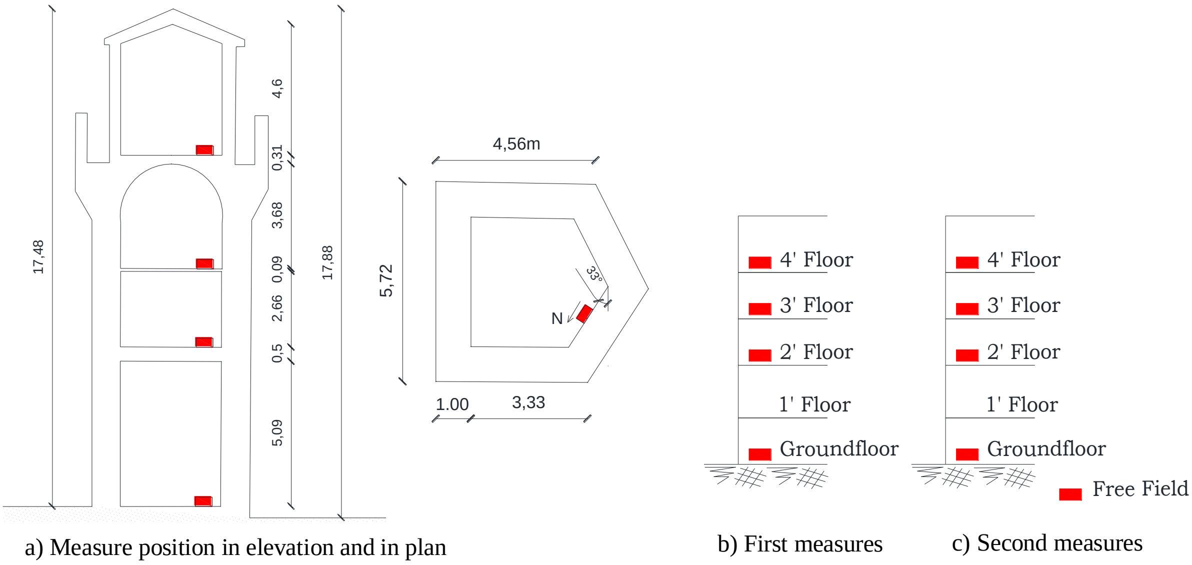

Figure 8.5 *Position of measures synchronized in vertical in 'Montale' Tower: a) fixed instrument in the top floor, b) fixed instrument in the free field*

8.2 Structure response

Natural frequencies and mode shapes have been identified in all towers by using operational modal analysis. Peaks in frequency have been first identified from the cross power spectrum density and then have been used to estimate the relative mode shapes by peak picking method in the SVD graphic. In this case, all ambient noise measurement have been analyzed simultaneously. In fact, pairs of synchronized measures have been acquired by the help of two seismographs movable to the various floors, maintaining one fixed on the top floor. Furthermore, another method has been applied for the 'Montale' Tower to identify modal parameters at the aim to achieve an accurate calibrated FEM. This consist mainly on the analysis of measures separately. Therefore, peak picking method has been implemented simply by analyzing each pairs of synchronized measures separately, at the aim to evaluate the accuracy of OMA method using PSD matrix of all measurements although they have not been synchronized all at the same time (see Figure 4.21).

8.2.1 Modal frequencies

Modal frequencies have been estimated first by selecting the peaks in power spectrum density graphics. Those peaks in frequency have been used as reference values to identify the mode shapes by the peak picking method in the SVD graphics. The spectrum in frequency in all Towers are shown in the Figure 8.6.
Natural frequencies of the Towers estimated from PSD graphics, are shown in the Table 8.1. It 'should be noted that the second decimal of the frequency is not significant because it depends on the techniques and functions used (filters, svd etc).

Table 8.1 *Frequencies identified from the power spectrum density*

Frequency (Hz) from PSD					
Cesta Tower		**Guaita Tower**		**Montale Tower**	
NS Component	EW Component	NS Component	EW Component	NS Component	EW Component
4,82	4,82	4,46	4,46	4,02	3,85
5,27	5,27	5,71	5,71	6,19	6,18
8,04	8,04	7,93	7,93	8,93	8,93
9,28	9,30	8,87	8,81	9,62	9,86
9,97	9,75	11,13	11,13	15,2	14,96

In cases of the 'Montale' Tower the natural frequencies have been estimated using several methods (Table 8.2). Standard Spectral Ratios (SSR), Operational Modal Analysis (OMA) and Peak picking method (see Figure 4.21), have been applied to estimation modal parameters of the tower based on ambient vibration measures. OMA method allows to identify the second modal frequency, which was not possible to identify it from SSR method. Other frequencies are quite similar from all methods.

Table 8.2 *Natural frequencies identify from different methods at 'Montale' Tower*

Frequency	SSR		OMA - FDD		OMA -	OMA - Peak Picking		FEM (shell
	N-S	E-W	N-S	E-W	FDD	N-S	E-W	element)
1^{st}	3,95	3,89	3,90	3.83	3,83	3,93	3,85	3,48
2^{nd}	-	-	4,02	3,85	3,95	4,02	3,99	4,06
3^{rd}	-	6,20	6.19	6.18	6,19	6,17	6,19	-
4^{th}	8,85	8,95	8.93	8.82	8,93	8,93	8,93	10,66
5^{th}	-	-	9.62	9.71	9,60	9,59	10,40	14,94
6^{th}	15,11	14,67	14,97	14.71	14,99	14,9	14,68	15,49

OMA1 method has been applied to identify the modal frequencies and the mode shapes of the towers. From the peak picking method has been identified the modal freqeuncies in the SVD graphics of the PSD matrix. Then, the SVD on the selected peaks has been calculated to identify the mode shapes. The frequencies identified by the SVD are presented in the Table 8.3. As one can see, result a similarity between the modal frequencies of the three towers.

Table 8.3 *Natural frequencies from SVD*

Frequency (Hz) from SVD			
Cesta Tower	**Guaita Tower**		**Montale Tower**
	1' Vertical	2' Vertical	
4,82	4,46	4,44	4,02
5,27	5,71	5,71	6,21
9,28	7,93	7,97	8,95
14,74	8,81	8,81	9,62
15,90	11,13	11,18	14,97
–	14,57	14,74	–
–	15,74	15,56	–

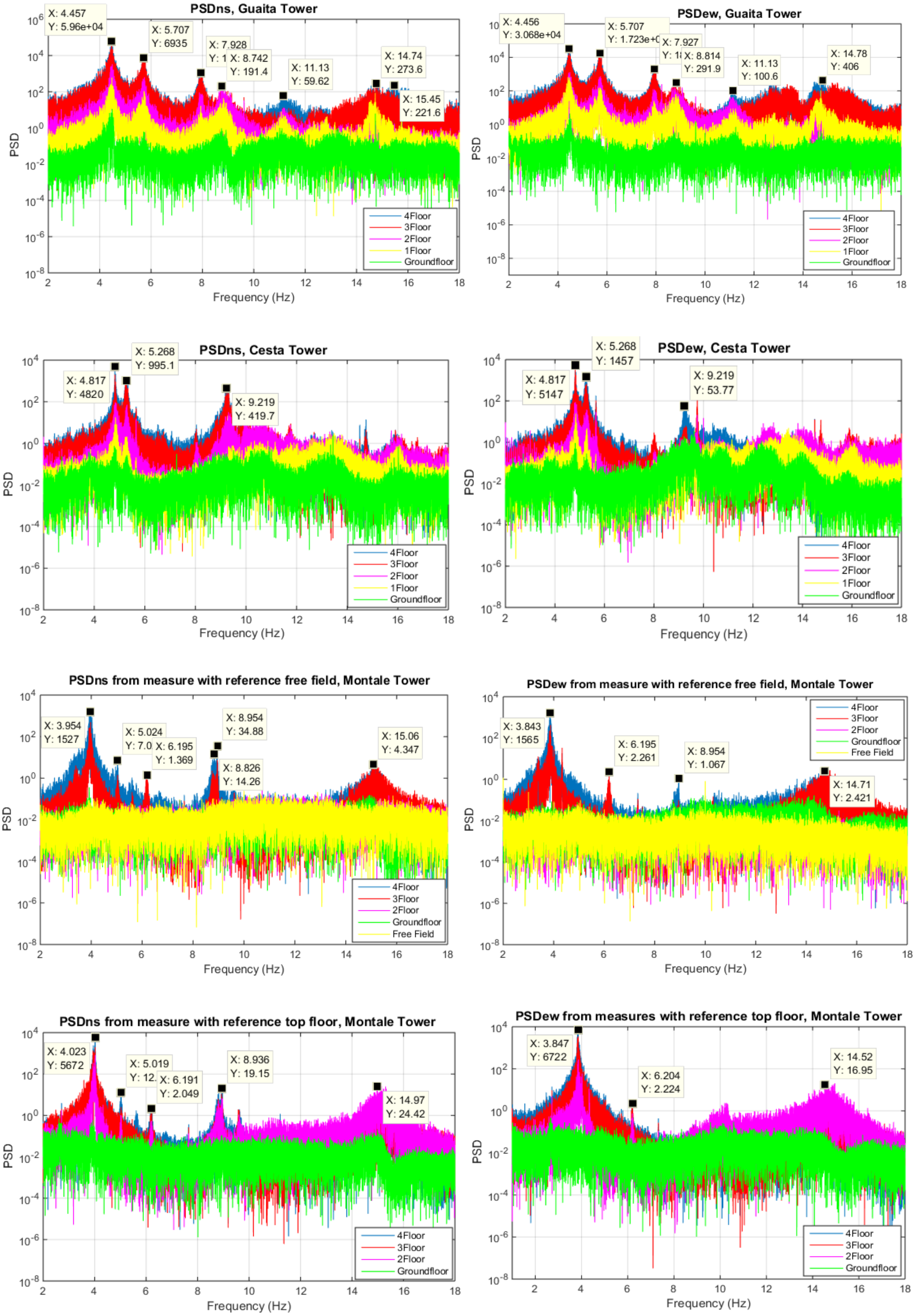

Figure 8.6 *PSD spectrum as a function of frequencies at 'Guaita' Tower, 'Cesta' Tower and 'Montale' Tower*

At mentioned above, another method has been applied for the 'Montale' Tower (right diagram in the Figure 4.21). CPSD graphics, used to identify modal parameters for the 'Montale' Tower, are shown in the Figure 8.7. NS and EW components have been used simultaneously or separately in analysis, at the aim to verify the presence of the first two peaks in all cases (see Figure 8.7). Also, peak picking method has been implemented simply by analyzing each pairs of synchronized measures separately, at the aim to evaluate the accuracy of OMA method using PSD matrix of all measurements although they are not all synchronized at the same time. Peak picking method on PSD or SVD graphics allows to identify the second modal frequency which wasn't possible from SRR method, as the peaks in frequency are close to each other (see Table 8.2). The first two mode shapes are translational, due to FEM, with almost the same modal participation mass ratio (in one of the direction in the floor), making so difficult their estimation as probably has the same energy in the spectrum.

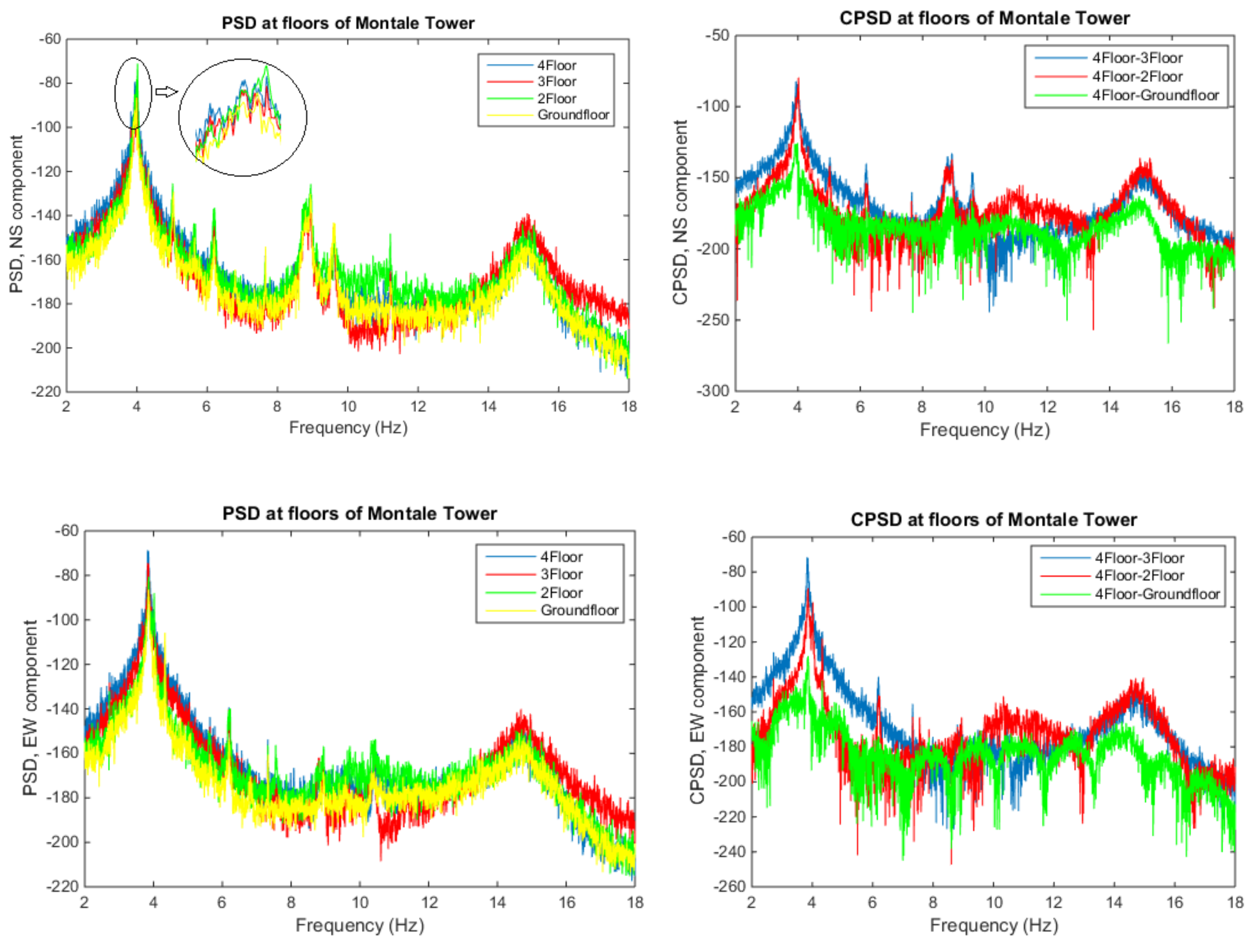

Figure 8.7 *CPSD of NS and EW components, 'Montale' Tower*

Singular value decomposition graphics of PSD matrix, are shown in the Figure 8.8.

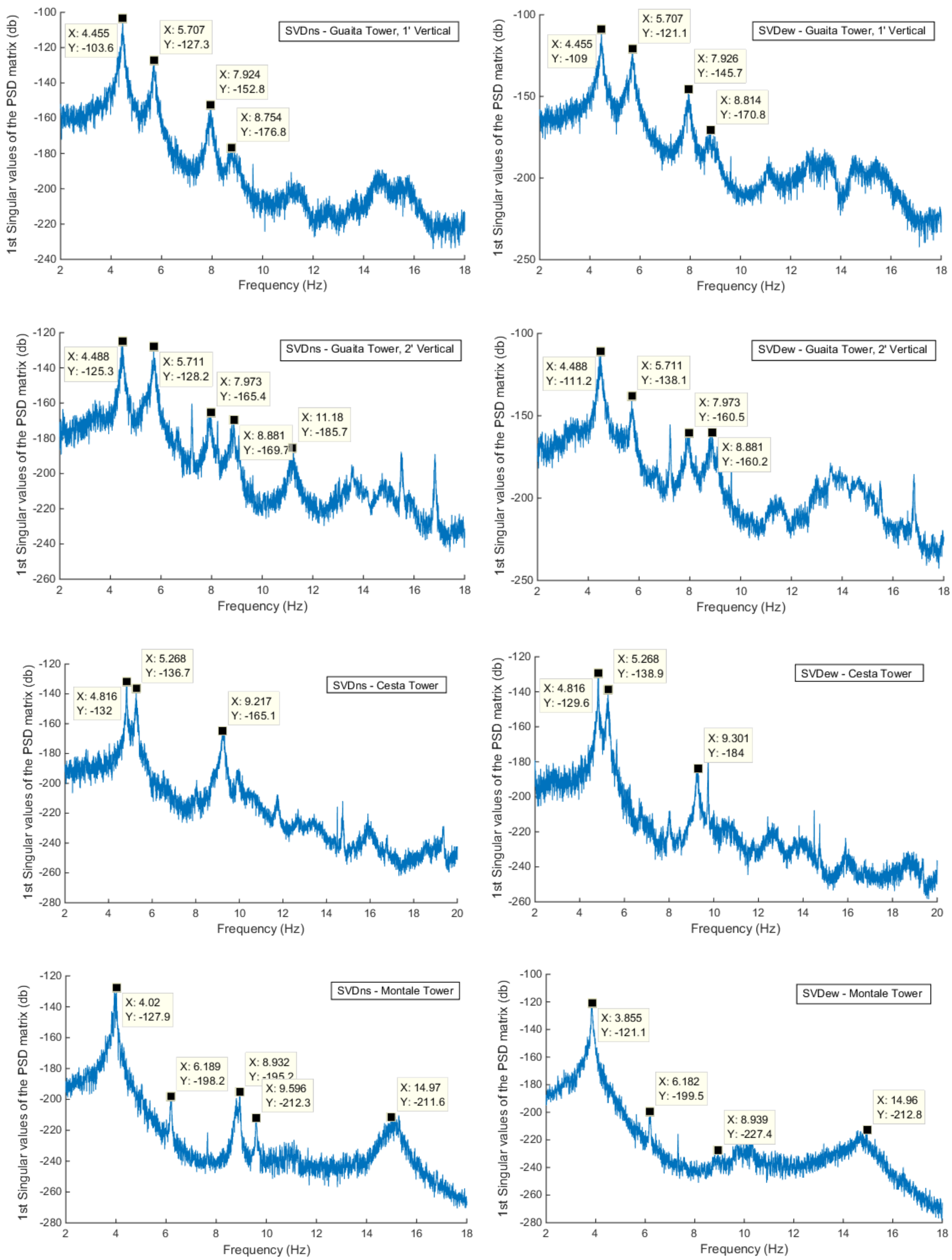

Figure 8.8 *Singular value decomposition graphics of measures at 'Guaita' Tower, 'Cesta' Tower and 'Montale' Tower*

8.2.2 Mode shape

The identification of the mode shapes has been possible thanks to the use of synchronized seismographs, oriented in such a way to have their principle axes parallel with the buildings facades.

In case of 'Montale' Tower another method has been used, which estimate the ration between the amplitude of the cross power spectrum density (of two synchronized pairs of measures) in their corresponding natural frequencies identified (see the right diagram in the Figure 4.21). Mode shapes of the 'Montale' tower, identified from experimental and theoretical analysis, are shown in the Figure 8.12.

The first two mode shapes of 'Cesta' Tower and 'Guaita' Tower are shown respectively in the Figure 8.9 and in the Figure 8.10.

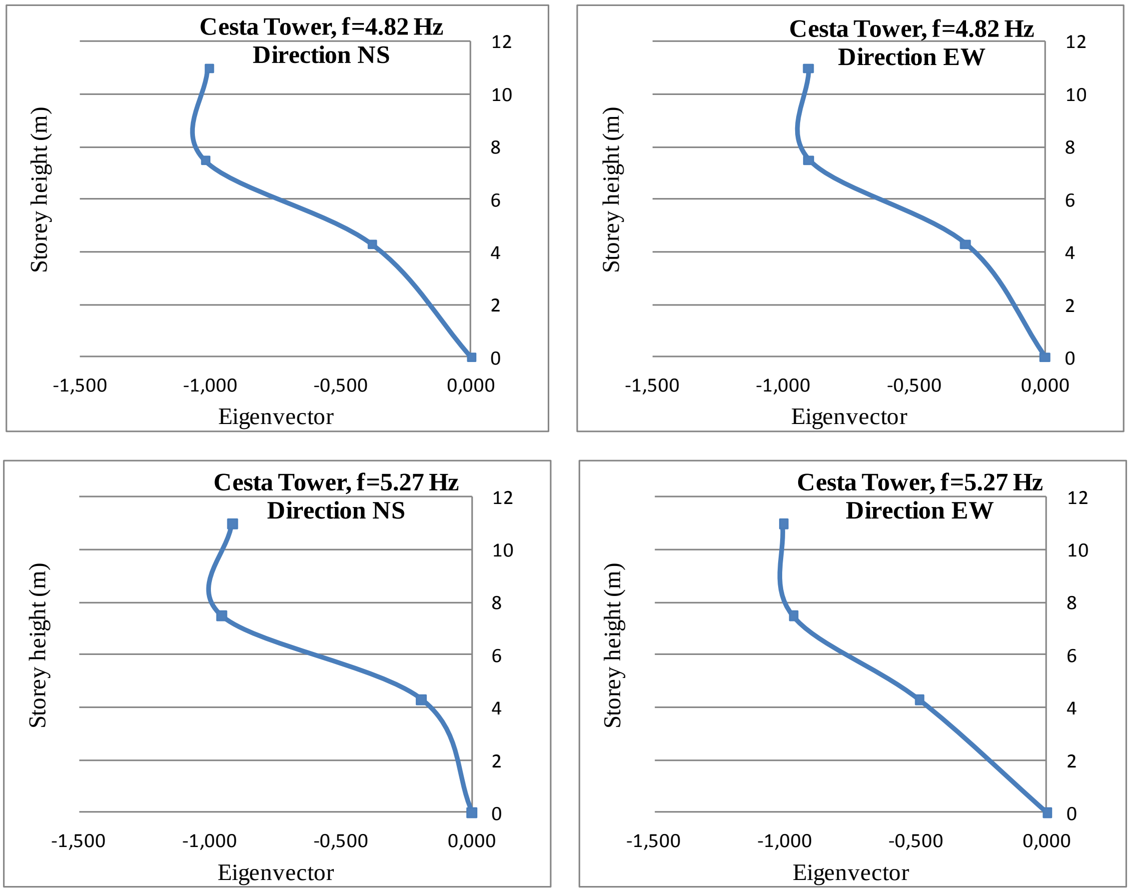

Figure 8.9 *Mode shapes of 'Cesta' Tower*

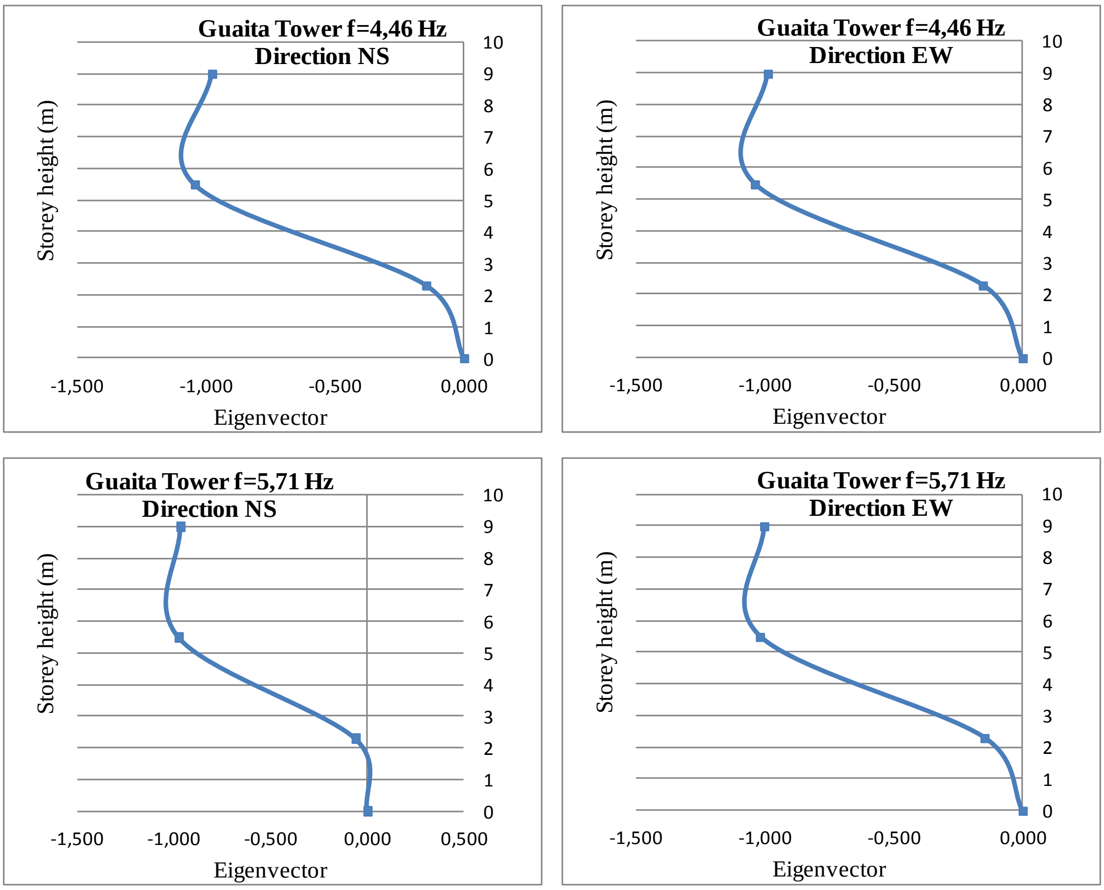

Figure 8.10 *Mode shapes of 'Guaita' Tower*

8.3 Calibrated FEM

Finite element model has been calibrated using the results achieved from ambient noise measurements acquired inside the 'Montale' Tower. This study has been realized in collaboration with University of San Marino (Guerra et. al). Two main finite element model have been created by using different type of element and materials. In the first model ‘FEMsolid’ have been used solid and shell elements to model respectively the external walls and various floors of the tower. In the second model ‘FEMshell’ have been used shell elements to model the external walls and the floors of the tower. Characteristics of the materials and the dimension of elements, are presented in the Table 8.4 for both finite element models. The tower height is about 17.7 m. Finite element models with solid and shell elements are shown in the Figure 8.11.

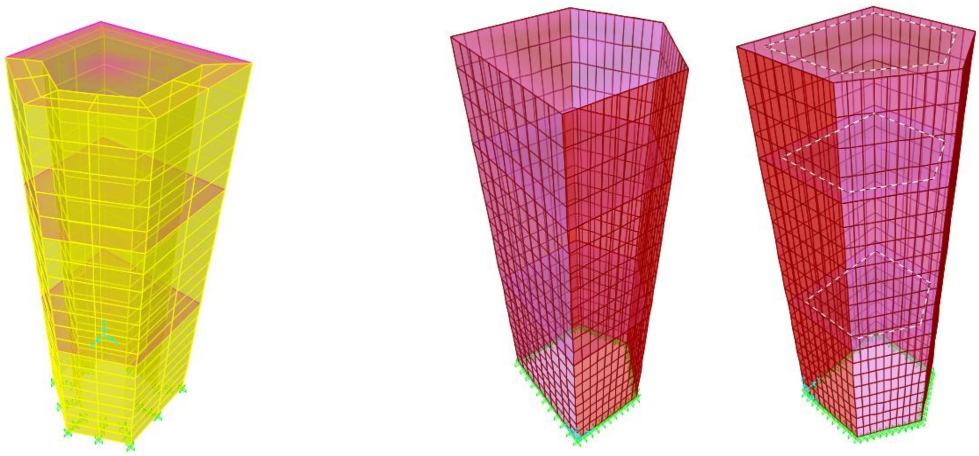

Figure 8.11 *Finite element model using solid elements (left 3D view, in yellow colour) or shell elements (right 3D view, in red colour)*

Two type of materals have been used on the first model with solid elements, while in the FEM with shell elements three different materials have been used (see Table 8.4).

***Table 8.4** Material and element characteristics for FEMsolid and FEMshell*

Material\Element property of **FEMsolid**	Material used for floor	Material used for walls		Material used for roof
		various levels	roof	
Thickness of shell elements (cm)	25	–	25	–
Weight per unit volume, γ (kN/m3)	21	21	15	15
Modulus of elasticity, E (kN/m2)	3585557	3585557	1285557	1285557
Poisson coefficient , υ	0,2	0,2	0,2	0,2
Shear modulus, G (kN/m2)	1493982	1493982	535649	535649
Expected concrete compressive strength (kN)	27579	27579	27579	27579

Material property of **FEMshell**	Material used for floors		Material used for walls	Material used for the roof
	2' floor	4' floor		
Thickness of shell elements (cm)	25	50	100	25
Weight per unit volume, γ (kN/m3)	20	21	21	8
Modulus of elasticity, E (kN/m2)	3500000	3500000	3500000	1200000
Poisson coefficient , υ	0,2	0,2	0,2	0,2
Shear modulus, G (kN/m2)	1458333	1458333	1458333	500000
Expected concrete compressive strength (kN)	2759	2759	2759	2759

***Table 8.5** Frequencies and modal participation mass ratio of FEMsolid and FEMshell*

FEMsolid		**Period**	**Frequency**	**UX**	**UY**	**RZ**	**SumUX**	**SumUY**	**SumRZ**
Mode No.		Sec	Hz	Unitless	Unitless	Unitless	Unitless	Unitless	Unitless
Mode	1	0,26	**3,79**	**0,64845**	0,00666	0,00000	0,64845	0,00666	0,00000
Mode	2	0,26	**3,85**	0,00662	**0,64805**	0,00000	0,65507	0,65471	0,00000
Mode	3	0,09	**11,69**	0,00000	0,00000	**0,84039**	0,65507	0,65471	0,84039
Mode	4	0,06	**15,55**	**0,21373**	0,00180	0,00000	0,86880	0,65651	0,84040
Mode	5	0,06	15,74	0,00185	**0,21420**	0,00000	0,87064	0,87071	0,84040
Mode	6	0,06	17,50	0,00000	0,00000	0,00000	0,87064	0,87072	0,84040
Mode	7	0,03	30,49	0,00001	0,00000	0,00000	0,87065	0,87072	0,84040
Mode	8	0,03	32,56	0,00022	0,00001	0,08166	0,87087	0,87072	0,92206

FEMshell		**Period**	**Frequency**	**UX**	**UY**	**RZ**	**SumUX**	**SumUY**	**SumRZ**
Mode No.		Sec	Hz	Unitless	Unitless	Unitless	Unitless	Unitless	Unitless
Mode	1	0,29	**3,48**	**0,55902**	0,00296	0,00011	0,55902	0,00296	0,00011
Mode	2	0,25	**4,06**	0,00255	**0,66584**	0,00010	0,56156	0,66880	0,00020
Mode	3	0,09	**10,66**	0,00755	0,00007	**0,81004**	0,56911	0,66887	0,81024
Mode	4	0,07	**14,93**	**0,22237**	0,01185	0,00022	0,79148	0,68073	0,81046
Mode	5	0,06	15,49	0,01442	**0,12713**	0,00096	0,80589	0,80786	0,81142
Mode	6	0,06	15,82	0,00062	0,07240	0,00029	0,80652	0,88026	0,81171
Mode	7	0,06	16,84	0,00002	0,00121	0,00000	0,80654	0,88148	0,81171
Mode	8	0,06	17,78	0,00001	0,00079	0,00000	0,80655	0,88227	0,81171
Mode	9	0,04	27,84	0,01997	0,00060	0,00576	0,82651	0,88287	0,81747
Mode	10	0,04	28,17	0,01627	0,00019	0,00010	0,84278	0,88305	0,81757
Mode	11	0,03	29,55	0,01929	0,00009	0,00000	0,86207	0,88315	0,81757
Mode	12	0,03	30,85	0,00000	0,02841	0,00641	0,86207	0,91155	0,82398
Mode	13	0,03	31,52	0,00005	0,00378	0,00348	0,86212	0,91533	0,82745
Mode	14	0,03	32,19	0,00173	0,00611	0,07109	0,86385	0,92144	0,89855

Modal analysis results are shown in the Table 8.5, for both models. The fourth mode shapes in both models are respectively: translational mode in *x* direction; translational mode in *y* direction; rotational mode and translational mode in *x* direction. The modal participation mass ratio of the first mode differ by 14% (Ux) between two models, while, the frequency differ by 8%.

The finite element model with shell element (FEMshell) has been calibrated modifying the modulus of elasticity of the concrete, which was increased by 10%, 17% and 20% (Table 8.6).

***Table 8.6** Modulus of elasticity for different FEM*

<table>
<tr><th colspan="2" rowspan="2">FEM of Montale Tower</th><th colspan="3">Modulus of elasticity, E (kN/m2)</th><th colspan="3">Percentage variation (%)</th></tr>
<tr><th>floor</th><th>roof</th><th>wall</th><th>floor</th><th>roof</th><th>wall</th></tr>
<tr><td></td><td>FEMshell</td><td>3500000</td><td>1200000</td><td>3500000</td><td>–</td><td>–</td><td>–</td></tr>
<tr><td rowspan="3">Calibrated FEM</td><td>FEMshell_mod 1</td><td>4200000</td><td>1440000</td><td>4200000</td><td>17</td><td>17</td><td>17</td></tr>
<tr><td>FEMshell_mod 2</td><td>4400000</td><td>1500000</td><td>4400000</td><td>20</td><td>20</td><td>20</td></tr>
<tr><td>FEMshell_mod 3</td><td>3900000</td><td>1340000</td><td>3900000</td><td>10</td><td>10</td><td>10</td></tr>
</table>

The modal analysis results for all calibrated models are presented in the Table 8.7. The second FEM ('FEMshell_mod2') shows higher values of frequencies, while the modal participation mass ratio does not vary between models.

The comparison of experimental and theoretical frequencies respectively from ambient noise measurements (SVD) and from FEM, are presented in the Table 8.8. 'FEMshell mod 2' show better results which means lower percentage variation values between experimental and theoretical analysis.

In the Figure 8.12 are shown the graphics of the three mode shapes identified from experimental (SVD and Peak Picking) and theoretical (FEM) analysis, normalized with the maximum value. The first two modal shapes achieved from FEM analysis are comparable with those identified from OMA method, while the third modal shape is more similar for the Peak Picking method.

Table 8.7 *Frequencies and modal participation mass ratio of calibrated finite element models*

FEMshell_mod 1		**Period**	**Frequency**	**UX**	**UY**	**RZ**	**SumUX**	**SumUY**	**SumRZ**
Mode No.		Sec	Hz	Unitless	Unitless	Unitless	Unitless	Unitless	Unitless
Mode	1	0,26	**3,82**	**0,55902**	0,00296	0,00011	0,55902	0,00296	0,00011
Mode	2	0,22	**4,45**	0,00255	**0,66584**	0,00010	0,56156	0,66880	0,00020
Mode	3	0,09	**11,67**	0,00755	0,00007	**0,81004**	0,56911	0,66887	0,81024
Mode	4	0,06	**16,36**	**0,22237**	0,01185	0,00022	0,79148	0,68073	0,81046
Mode	5	0,06	16,97	0,01442	**0,12713**	0,00096	0,80589	0,80786	0,81142
Mode	6	0,06	17,33	0,00062	0,07240	0,00029	0,80652	0,88026	0,81171
Mode	7	0,05	18,45	0,00002	0,00121	0,00000	0,80654	0,88148	0,81171
Mode	8	0,05	19,48	0,00001	0,00079	0,00000	0,80655	0,88227	0,81171
Mode	9	0,03	30,49	0,01997	0,00060	0,00576	0,82651	0,88287	0,81747
Mode	10	0,03	30,86	0,01627	0,00019	0,00010	0,84278	0,88305	0,81757
Mode	11	0,03	32,37	0,01929	0,00009	0,00000	0,86207	0,88315	0,81757
Mode	12	0,03	33,80	0,00000	0,02841	0,00641	0,86207	0,91155	0,82398

FEMshell_mod 2		**Period**	**Frequency**	**UX**	**UY**	**RZ**	**SumUX**	**SumUY**	**SumRZ**
Mode No.		Sec	Hz	Unitless	Unitless	Unitless	Unitless	Unitless	Unitless
Mode	1	0,26	**3,91**	**0,55902**	0,00296	0,00011	0,55902	0,00296	0,00011
Mode	2	0,22	**4,55**	0,00255	**0,66584**	0,00010	0,56156	0,66880	0,00020
Mode	3	0,08	**11,95**	0,00755	0,00007	**0,81004**	0,56911	0,66887	0,81024
Mode	4	0,06	**16,74**	**0,22226**	0,01187	0,00022	0,79137	0,68075	0,81046
Mode	5	0,06	17,36	0,01442	**0,12322**	0,00094	0,80580	0,80396	0,81140
Mode	6	0,06	17,72	0,00072	0,07612	0,00031	0,80651	0,88009	0,81171
Mode	7	0,05	18,85	0,00002	0,00139	0,00000	0,80653	0,88148	0,81171
Mode	8	0,05	19,93	0,00001	0,00079	0,00000	0,80654	0,88227	0,81171
Mode	9	0,03	31,21	0,01999	0,00060	0,00576	0,82654	0,88287	0,81747
Mode	10	0,03	31,59	0,01625	0,00019	0,00010	0,84279	0,88305	0,81757
Mode	11	0,03	33,13	0,01928	0,00009	0,00000	0,86208	0,88315	0,81757
Mode	12	0,03	34,58	0,00000	0,02728	0,00602	0,86208	0,91043	0,82359
Mode	13	0,03	35,26	0,00004	0,00494	0,00366	0,86212	0,91538	0,82725
Mode	14	0,03	36,09	0,00173	0,00606	0,07129	0,86385	0,92144	0,89854

FEMshell_mod 3		**Period**	**Frequency**	**UX**	**UY**	**RZ**	**SumUX**	**SumUY**	**SumRZ**
Mode No.		Sec	Hz	Unitless	Unitless	Unitless	Unitless	Unitless	Unitless
Mode	1	0,27	**3,68**	**0,55902**	0,00296	0,00011	0,55902	0,00296	0,00011
Mode	2	0,23	**4,28**	0,00255	**0,66584**	0,00010	0,56156	0,66880	0,00020
Mode	3	0,09	**11,25**	0,00755	0,00007	**0,81004**	0,56911	0,66887	0,81024
Mode	4	0,06	**15,76**	**0,22241**	0,01185	0,00022	0,79152	0,68072	0,81046
Mode	5	0,06	16,35	0,01441	**0,12849**	0,00097	0,80593	0,80921	0,81143
Mode	6	0,06	16,70	0,00059	0,07111	0,00028	0,80652	0,88032	0,81171
Mode	7	0,06	17,79	0,00002	0,00115	0,00000	0,80654	0,88147	0,81171
Mode	8	0,05	18,77	0,00001	0,00079	0,00000	0,80655	0,88227	0,81171
Mode	9	0,03	29,38	0,01996	0,00060	0,00576	0,82651	0,88287	0,81747
Mode	10	0,03	29,74	0,01627	0,00019	0,00010	0,84278	0,88305	0,81757
Mode	11	0,03	31,19	0,01929	0,00009	0,00000	0,86207	0,88315	0,81757
Mode	12	0,03	32,57	0,00000	0,02875	0,00653	0,86207	0,91190	0,82410
Mode	13	0,03	33,31	0,00005	0,00342	0,00344	0,86212	0,91531	0,82755
Mode	14	0,03	33,98	0,00172	0,00612	0,07100	0,86384	0,92144	0,89855

Table 8.8 *Percentage variation of frequencies estimated from SVD and FEM*

Frequency (Hz) from SVD and FEM, Montale Tower					Percentage variation (%)			
SVD	FEMshell	FEMshell_ mod 1	FEMshell_ mod 2	FEMshell_ mod 3	FEMshell	FEMshell_ mod 1	FEMshell_ mod 2	FEMshell_ mod 3
4,02	3,48	3,82	**3,91**	3,68	13,3	5,1	2,8	8,5
6,21	4,06	4,45	**4,55**	4,28	34,7	28,4	26,7	31,0
9,62	10,66	11,67	**11,95**	11,25	-10,8	-21,4	-24,2	-16,9
14,97	14,93	16,36	**16,74**	15,76	0,2	-9,3	-11,9	-5,3

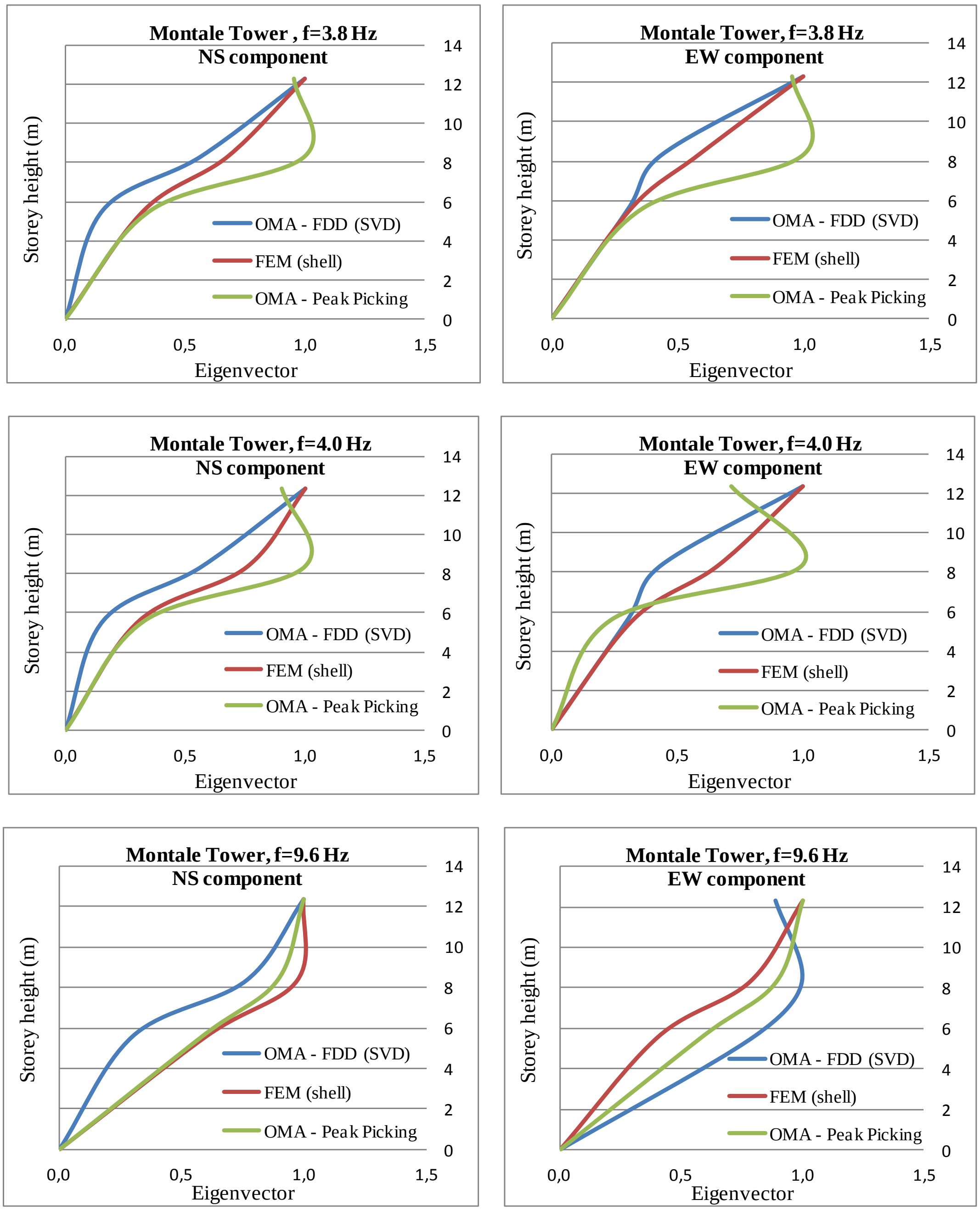

Figure 8.12 *Mode shapes from OMA and FEM method, Montale Tower*

IX. CONCLUSIONS

In this study, feasibility of ambient vibration measurements for the Dynamic characterization of soil and building has been tested. Local seismic response of soil and calibration of finite element model of the building demonstrate the effectiveness of the approach here adopted. This allowed to compare the expected structural response of a real building by considering ground motion predicted by considering the local seismic response with those expected by considering standard loads deduced from NTC08.

The research methodology in this thesis mainly consists in the use of synchronized ambient vibration measures for estimation of the dispersion curves of soil and mode shapes of the building. Two portable seismographs, synchronized by the GPS signal, have been used to acquire ambient vibration measures inside the building and in the free field near the construction area. Ambient vibration measures have been acquired in the free field near the construction area to estimate the dispersion curve, using vertical components of synchronized pairs of ambient vibration measures acquired with the same portable seismographs. Generally, the directionality of the signal may be a problem when using two-station method. Therefore, the knowledge of the location, the use of previous investigations and detailed stratigraphic sections are important parameter to be considered at the aim to identify the correct dispersion curve. ESAC2015 code based on the SPatial AutoCorrelation zero crossing method has been used to achieve the Rayleigh phase velocity dispersion curve between two sensors (two synchronized portable seismographs). This method is based on the spatial autocorrelation analysis and derived from SPAC method. Seismic stratigraphic profile (1D model) has been then estimated by solving the inversion problem with 'GAinvers6 code'. Finally, the response spectra and 1D-Vs model have been estimated performing an one-dimensional linear equivalent analysis on 'STRATA' software.

Frequencies and mode shapes of the reinforced concrete building located in Sanremo, have been identified from experimental and operational analysis (EMA and OMA method). Furthermore, Peak Picking method has been implemented simply by analyzing each pairs of synchronized measures separately, at the aim to evaluate the accuracy of OMA method which use PSD matrix of all measurements although they are not all synchronized at the same time (see Figure 4.21). Those methods have been also applied in historic masonry structures to check their efficiency, being in this case in the luck of the project design. At this aim, the second case study concerns the three historic Tower of San Marino.

Frequencies and modal shapes estimated experimentally have been used to calibrate the FEM of the buildings, by using the sensitivity of parameters that directly affect the dynamic properties. Finally, structural verification have been realized for the reinforced concrete building, by using both estimated response spectrums on site and from NTC08.

A summary of results and conclusions are described in the following paragraphs.

9.1 Local seismic response from ambient vibration measurements

Local seismic response of the construction site has been estimated. Synchronized pairs of ambient vibrations measurements have been acquired to estimate the Rayleigh waves dispersion curves of soil. Those measurements have been acquired in the vicinity of the building as it was difficult to find free area (not built up). Furthermore, ambient vibration measures acquired in the vicinity of the interest area have been confronted with single station measures acquired outside the building under exam, at the aim to evaluate their comparability in the interest interval of frequencies from 0 Hz to 10 Hz. HVSR curve selected to estimate the dispersion curve, shows a discrete similarity with the HVSR curve of the construction site (Figure 5.17). HVSR curve chosen for analysis is shown in the Figure 5.19. A peak in frequency around 3.8 Hz, present in all HVSR curves, can be considered as a natural frequency of site.

The dispersion curve has been estimated from experimental data, i.e. from synchronized pairs of ambient vibration measures acquired by two portable seismographs. Spatial autocorrelation analysis which is based on zero crossing method (ESAC 2015 code), has been used. Vertical components of a pair of synchronized ambient vibration measures, located at a distance of 75 m (or of 50 m) from each other, have been used as input to estimate the dispersion curves (Figure 5.18). The dispersion curves estimated from synchronized ambient vibration measures placed at a distance of 50 m or 75 m from each other shows similarities in their results (see third graphic in the Figure 5.18). It is worth to note that, the use of two sensors only for assessing the dispersion curve represents an important novelty with respect the common practice based on the deployment of seismic antennas including a number of sensors (16-24).

Seismic stratigraphic profile has been identified then by the inversion procedure which use as input the dispersion curve estimated on site and the respective HVSR curve of ambient vibration measures. Seismic stratigraphic profile, which has the lower misfit, have been selected. In the Figure 5.20 is shown the best Vs seismic stratigraphic profile estimated by varying some parameters (limits of Vs, HVSR and VR percentage participation on analysis, i.e. their weights) up to reach available result.

The decay curves have been chosen from the bibliography for each soil type (Table 5.8). In the Table 5.7 are presented the G/Gmax model and damping model value. The last data on those graphics have been added to reach a valid analysis in STRATA. Also, the decay curve presented in bibliography of STRATA have been used to estimate the influence of the decay curve in the response spectrum estimation. Spectrum amplitude does not vary significantly (see blue and red line in the Figure 5.21 and in the Figure 5.22) when used diverse decay curves of layers selected from different bibliography as described in the paragraph 5.2.2. The uncertainty of nonlinear soil properties (G/Gmax and D) have been taken into account during the equivalent linear analysis, by the variation of those parameters due to the Darendeli (2001) model. Nonlinear soil properties variation (shear modulus reduction curve, damping ratio curve and damping of the bedrock) has been realized to all layers.

The reference accelerograms of the area of interest has been selected from 'Rexel v3.5' database which contain natural accelerograms recorded in the word. Seismic hazard of the construction site has been first defined from National Institute of Geophysics and Volcanology website (*http://esse1-gis.mi.ingv.it/)*, in which can be identified the interactive seismic hazard map of the interest area. In the Figure 5.9 are shown the disaggregation of a(g) values, near the area of interest, with probability of exceedance 10% in 50 years. The magnitude of events, happened in an epicentral distance between 0 km and 30 km, is between 4 and 6.5 Richter. Those parameters have been used as input data when checking the reference accelerograms of site in 'Rexel v3.5' database. Horizontal accelerograms have been extracted from European database, selecting a set of input data for Sanremo at a given return period (100 years), for different limit states (SLV and SLD).

Equivalent linear analysis of the subsoil has been computed by STRATA software, where the subsoil model consist of a finite number of flat and parallel layers equivalent to an elastic material placed on a viscous-elastic half-space representing the bedrock. Each layer has been considered homogeneous and isotropic, with thickness, density, stiffness modulus and transverse damping factor defined from the bibliography and existent geological report. For each layer, the profiles of the normalized shear modulus *G* and the damping ratio *D*, as a function of the level of deformation, have been selected from the bibliography (see section 5.2.4). Stochastic variation of the site properties (shear-wave velocity, layer thicknesses, depth to bedrock, shear modulus reduction and material damping curves) has been realized on STRATA software. Spectrum amplitude does not vary significantly (see blue and red line in the Figure 5.21 and in the Figure 5.22) when used diverse decay curves of layers selected from the bibliography. Horizontal spectral acceleration components generated from 7 accelerograms (selected for SLV limit state) by varying nonlinear properties of layers (shear modulus, damping ration curves, damping of the bedrock) and site profile parameters (shear wave velocity, layer thickness, depth to bedrock) are shown in the Figure 5.23. The mean values of those results (graphics with continue blue line) has been used then for seismic structural verifications of the building.

Acceleration response spectra estimated on site, which has been used for seismic structural verifications, is shown in the Figure 5.22, for SLV limit state and for nominal life 100 years. In the Figure 7.1 are plotted the response spectrums in logarithmic scale, identified both from experimental analysis and from empirically formulations. The amplitude of local response spectrum, at periods lower than 0.2 s, is higher than the amplitude of the spectrum from NTC08. This means that the response spectrum estimated on site is more severe for lower periods than 0.2 s. Differences in amplitude of both spectrums are shown in the Table 7.13. The response spectrum estimated on site has not been standardized (due to spectrum from the technical standard), to have a real spectrum of the construction site.

Finally, V_{s30} has been estimated to identify the soil class due to standards classifications. V_{s30} estimated from the seismic stratigraphic profile is about 577 m/s. Therefore, the subsoil has a *class B* referred to the standards (Table 5.13).

9.2 Calibrated finite element model from ambient vibration measurements

The building under exam (in the first case study) is a prefabricated reinforced concrete construction consisting of five floors above ground and one underground, with a total height of about 18.5 m in view, and about 23 m in elevation considering the basement. This building is located in the municipality of Sanremo, province of Imperia in Italy, and has a sanitary use. The building falls in the class of use IV (with coefficient CU equal to 2), according to Eurocode 8 and NTC 2008. Being an ordinary construction the study of local seismic response becomes even more important to be realized for the seismic prevention of the building.

Modal parameters have been identified from ambient noise measurements using experimental and operational modal analysis. Especially, the frequencies and mode shapes have been estimated in this study. Referred to the bibliography Gallipoli et al. (2008) (see section 6.2.2) the damping estimated from ambient vibration measures result about 4.8%, which can justify the standard assumption of an average 5%.

Natural frequencies and the associated mode shapes have been identified from ambient vibration measures using several operational and experimental method analysis (OMA and EMA). Two operation modal analysis methods have been implemented OMA1 and OMA2 which differ between them mainly on the truncated signal in the case of OMA 2 (Figure 4.21). Operational modal analysis OMA1 presents better results for the mode shapes. Truncating the signal does not give a higher resolution in frequency and in the mode shapes identification as was expected for OMA2 method. Furthermore, another method has been applied by analyzing separately each synchronized pair of measures (see diagram on the right in the Figure 4.21) at the aim to evaluate the influence in modal parameter results of the non-simultaneously acquisition of measures in all floors. The experimental modal analysis EMA has been applied by using two algorithms (EMA1 and EMA2) which differ between them mainly on the use of FFT or PSD (see Figure 4.18). The FFT gives a high resolution in frequency and a slightly smooth spectrum of the signal making so difficult the final resolution in frequency. A script code has been written in Matlab for each method (see Appendix).

So as to apply those methods, ambient vibrations have been acquired in several verticals near the corners of the structure, in two different procedures: first leaving the fixed seismograph on the top floor and second leaving the fixed one in the free field. Two portable seismographs have been synchronized with each other by GPS signal, to identify the mode shapes by acquiring velocimetric measurements at all floors of the buildings. Furthermore, the ambient vibration inside the building have been acquired in two different periods during the construction of the building, to evaluate the influence in the structure response of the mass and stiffness added during its construction. The major measures have an acquisition length of about 20 min and a sampling frequency 128 Hz.

In the Table 6.31 are shown the percentage variation of frequencies estimated in various verticals of the building from the first ambient noise measures, by using experimental and operational analysis methods. The maximum variation is about 1.7%, therefore, all methods presents satisfying results for frequencies. The comparison between results achieved from OMA methods has been also realized using the second measurements of ambient noise (see Table 6.32). In this case, the percentage variation for frequencies is lower than 1%. It should be noted that the second decimal of the frequency is not significant because it depends on the techniques and functions used (SVD, PSD, FRF, filters, etc). Mode shapes identified in the ‘Vertical a’ and in the 'Vertical f' from EMA and OMA methods, using the first ambient noise measurements are almost similar with one another (see Figure 6.66, Figure 6.67 and Figure 6.68).

Calibration of finite element model of the building has been realized by an iterative parameter method which use the sensitivity of parameters that directly affect the dynamic properties. Different elements and loads have been added to the initial finite element model of the project to achieve the same dynamic response of the structure with that obtained from operational modal analysis. Also, material parameters as concrete class and elastic modulus of concrete have been modified. Those modifications can be summarized as:

- different classes of concrete used for the construction of the building as described by the computing project. Therefore, pillars and beams have been modeled with concrete class C45/55, external infill panels with concrete C32/40, stairwells and lift shaft C28/35 and added beams ‘Cordoli 40x15cm’ and ‘T20x5cm’ with C28/35. In the finite element model of the project design it was used the same class of concrete C25/30 for all structural elements;
- modulus of elasticity of concrete has been increased up to 25%, as we are in the field with the ambient vibration measurements, therefore, the building works in the elastic field;
- external wall panels have been modeled with frame elements dimensioned referred to the theory of equivalent rod of Circolare n.65, 10/4/1997) and studies of various authors, while the remaining load (difference between the weight of the connecting rods and the walls) has been modeled as mass. The frame elements used have the same concrete class as the walls panels C32/40;
- the windows opening in the external wall panels has been considered by reducing the dimension of frame elements (in ‘FE Model 1’) or by reducing the load applied on the beams where the wall discharge, by the difference of the load between the weight of the connecting rods and the walls (in the 'FE Model 2');
- elements which have not been taken into consideration before (beams 'Cordoli 40x15cm' and 'T20x5cm', in the Figure 6.59), beams where the floor slab are connected with one another, have been modeled by frame elements with concrete class C28/35;
- the load of the internal walls (3.5 kN/m) has been applied in the beams where the wall are supported, and also were the wall were constructed (in case of the FEM calibrated by the first ambient noise measures) or in all building (in FEM calibrated by the second ambient noise measures);
- mass and rigidity added: the internal walls, the mechanical ventilation plant on the terrace with the associated machinery, the windows, the layers of floor pavements and the external walls, which have been completed during the second ambient noise measurements.

The influence of the concrete class in the structural response has been evaluated by comparing the frequencies and modal shapes achieved from the calibrated ‘FE Model 2’ and the identical one, by using the same concrete class for all elements: once C25x30 and once C45/55. The first four modal frequencies achieved from both models differ less than 4% from one another, and are higher in the case of FE model with C25/30 concrete class, which is by itself more similar with the initial model (with different concrete class). Modal participation mass ratio does not differ significantly in case of FE model with C25/30 concrete class, while has a higher variation for the model with C45/55 concrete class.

Furthermore, the influence of Young modulus of the concrete in the modal parameters results, has been estimated before the calibration of the FE model. At this aim, different elastic modulus of concrete have been used (Table 6.24). The percentage variation of frequencies increase by 4.7%, 8.7%, 10.6% and 12.3%, when the elastic modulus of concretes is increased respectively by 10%, 20%, 25% and 30%. In this case, the modal participation mass ratio does not vary, therefore, the modal shapes are the same.

The first mode shape is a rotational mode, referred to the finite element model without modeling the external cover panels, and has a modal participation mass ratio of 11%. Therefore, the second and the third frequencies have been taken as references to be reached during the calibration of the model.

Four main finite element model have been realized in this Thesis with software SAP2000. The first one is the FEM of the project 'FE Model 0' realized by using the computing project data and verifying in site the presence and dimension of structural elements. This finite element model has been calibrated twice 'FE Model 1' and 'FE Model 2', by using respectively the structural response estimated from ambient noise measurements acquired in two different periods during the construction of the building. The latest model 'FE Model 3' is the calibrated one 'FE Model 2' without modeling the rigidity of the external walls. Being in the field of ambient vibration measures, the rigidity of external walls panels influence significantly in the dynamic response of the structure, therefore has been modeled to reach the same structural response experimentally and theoretically. The external walls are not designed to withstand the earthquake, therefore, the calibrated model without wall panels should be used for seismic response controls of the structures. In all finite element models the pillars and beams have been modeled with frame elements, while the staircase and lift cores with shell elements. The horizontal structures at all levels have been modeled as rigid diaphragms (by the help of joint constraints), considering the stiffening effect of the completion reinforced slab of 5 cm thick. The pillars are wedge in the base while beams are stuck with pillars. Also, the staircase and lift cores are wedge in the base. The mass has been defined from elements and loads which have been applied on beams where the slabs discharge.

During the calibration process, modal parameters estimated from experimental (OMA1) and theoretical analysis (FEM), have been confronted. The percentage variations of modal frequencies between ‘FE Model 1’ and OMA and between ‘FE Model 2’ and OMA in different verticals of the building, are presented in the Table 6.33 and in the Table 6.34. As one can see, the second finite element modal is much similar with the experimental response of the building as has been calibrated after the construction of structural and nonstructural elements. The experimental and theoretical results in this case vary less than 5%. For ‘FE Model 1’, the percentage variation is less than 6.7% for the second and the third mode shape and about 12% for the first mode shape. The first three mode shapes achieved from theoretical ('FE Model 2', 'FE Model 1') and from experimental methods (OMA1) (see Figure 6.43, Figure 6.44, Figure 6.45 and Figure 6.31, Figure 6.32, Figure 6.33), has a discrete similarities.

The influence of the rigidity of external walls in the modal response of the building, has been estimated. The percentage variation between the results from calibrated finite element models with and without modeling external walls, are shown in the Table 6.30. The first modal frequency is about 44% higher for FE model calibrated from the first ambient vibration measurements by modeling the external walls, and about 47% higher for FE model calibrated from the second ambient noise measurements by modeling external walls.

Furthermore, the modal response of FE model without modeling the rigidity of external wall panels 'FE Model 3', has been compared with the response of the initial model 'FE Model 0'. The frequencies varies less than 5% while the mode shapes are almost identical (see Figure 9.1, Figure 9.2 and Figure 9.3), probably due to the variation of modal participation mass ratio in such a way that the first three modes of vibration remains in all cases similar to the first modal shape type. This confirms the influence of the external wall panels in the structure response. Therefore, the rigidity of the external wall panels is to be considered in the complex stiffness of the building.

The natural frequencies, estimated from the project and from ambient noise measurement carried out inside the building, have been compared with bibliographic values obtained by various studies using seismic noise, empirical relationships of numerous authors and technical standard. The height of the reinforced concrete building taken in this study is about 22 m and has a first period of about 0.8 s referred to the FEM of the project 'FE Model 0', 1.4 s referred to the initial FEM of the project, and a period 0.43 s referred to the ambient noise measurement results and the calibrated FEM ('FE Model 2'). As can see from the reported studies, the periods estimated theoretically (0.76 s referred to the Italian and European standards and 0.8 s by the FEM) is overestimated comparing to experimental data results (0.40 s, see paragraph 6.4), which is compatible with values estimated from various authors for similar structures height and building type.

This methodology, applied in 'Montale' Tower, San Marino (second case study), show also satisfying results. Frequencies differ about 1% from one method to another (EMA, OMA, Peak Picking, SSR). The first two modal shapes achieved from FEM analysis are comparable with those identified from OMA method, while the third modal shape is more similar for the Peak Picking method (see Figure 8.12). The finite element model (with shell element) has been calibrated by modifying the modulus of elasticity of the concrete, which has been increased by 10%, 17% and 20% (see Table 8.6). The FE model, achieved by increasing the modulus of elasticity of the concrete by 20%, shows better results, which means lower percentage variation values between experimental and theoretical analysis.

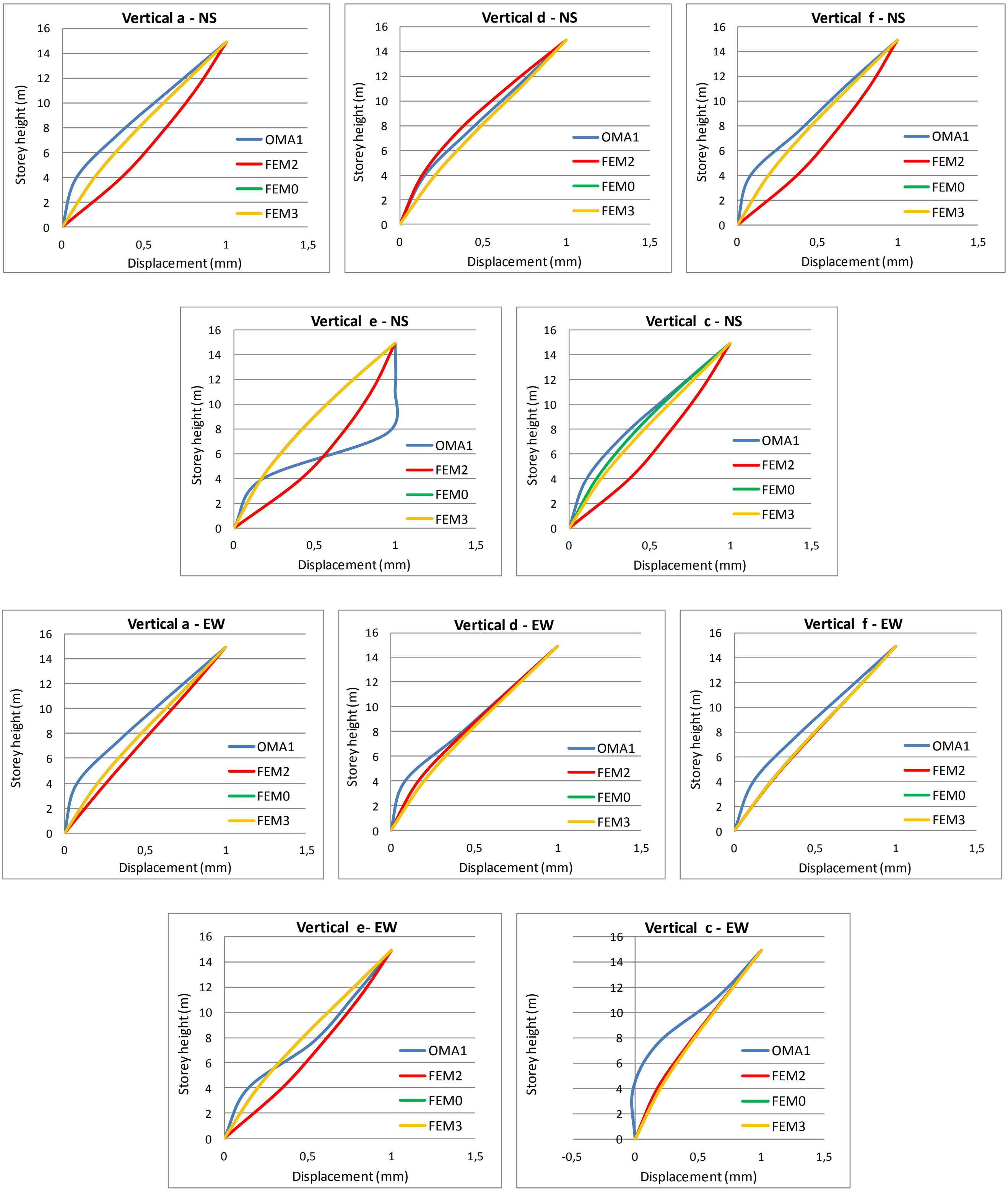

Figure 9.1 *First mode shape from experimental (OMA1 curve) and theoretical analysis (FEM0, FEM2, FEM3)*

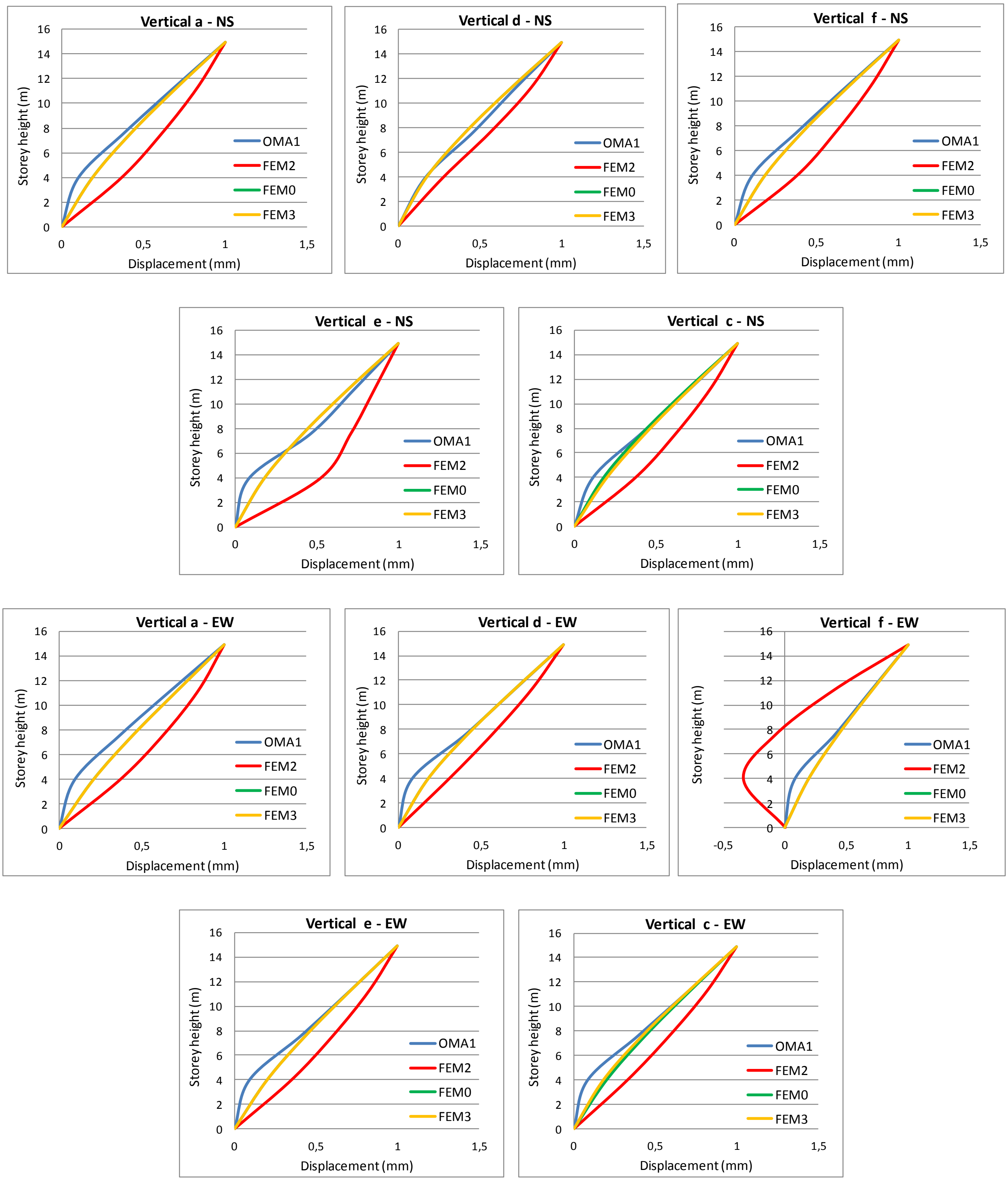

***Figure 9.2** Second mode shape from experimental (OMA1 curve) and theoretical analysis (FEM0, FEM2, FEM3)*

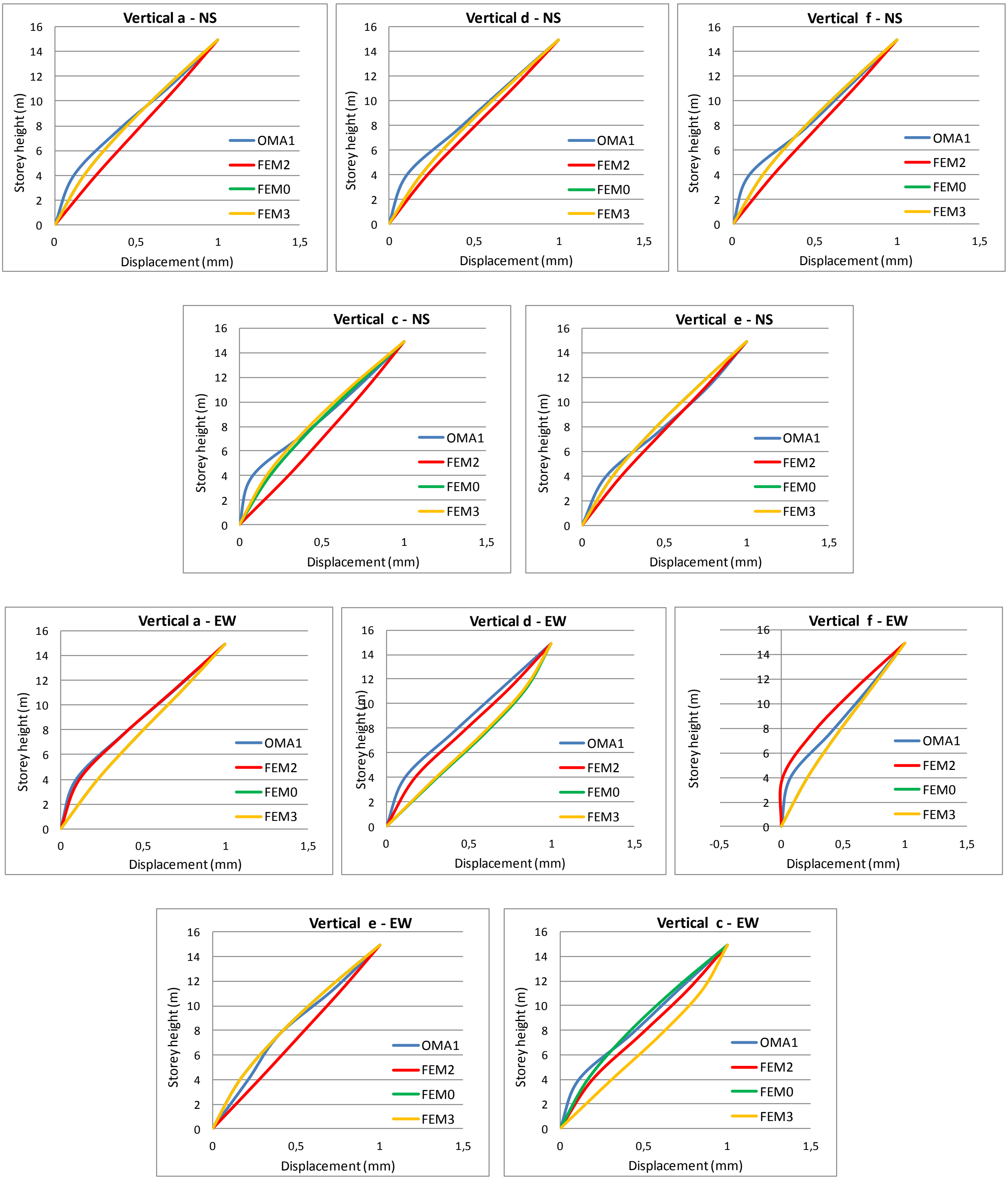

Figure 9.3 *Third mode shape from experimental (OMA1 curve) and theoretical analysis (FEM0, FEM2, FEM3)*

9.3 Structural verification using the response spectrum estimated

The main objective of structural verifications carried out in this study regards the confront of structure response under seismic action defined both from the response spectrum estimated on site and from technical standards. Therefore, global structure response has been evaluated. At this aim, a Linear dynamic analysis and a Nonlinear static Pushover analysis have been performed in this study. Also, modal analysis and verification of interstory drift for SLD limit have been realized. Calibrated finite element model 'FE Model 3', without modeling the rigidity of external wall panels, has been used for structural verifications.

Response spectrum analysis, shows that LSR spectrum can be more severe that NTC08 spectrum (both estimated for SLV limit state) for some parameter results and vice versa. It is worth to note that, the response spectrum estimated on site has not been standardized (due to spectrum from standard), at the aim to have a real spectrum and consequently a real structure response. Differences in amplitude of both spectrums are shown in the Table 7.13. The amplitudes of the first three vibration modes are higher in case of NTC08 spectrum (about 11% in case of the second and the third mode), and are lower for the other modes of about 50%. This affect the structure response, taking into account also the modal participation mass ratio (Table 7.12) and the amplification factors (see Table 7.11, on the left). As one can see in the Table 7.13, the first amplitudes are similar from both spectrum which leads to similar results of floor actions estimated by the linear static analysis, which are slightly higher about 0.23% when using response spectrum from NTC08. As can be known, linear static analysis take into account only the first mode shape. The same result is observed also for the base reaction, when performed a linear static analysis. Base shear reactions, floor actions and demand curve, in case of linear dynamic analysis with seismic action in *x* direction, shows higher value when using LSR spectrum. Instead, the displacement, the maximum shear forces and the bending moment at columns and demand curve for seismic action in *y* direction of the building, shows higher value when using NTC08 spectrum.

Floor actions estimated from the linear dynamic analysis by using LSR spectrum, have higher values (about 45% for the first three floors and about 17% for the other floors) than those from NTC08 spectrum (Table 7.15, Table 7.16).

The amplitude of local response spectrum, at periods lower than 0.2 s, is higher than the amplitude of the spectrum from NTC08, making at this way modes from the fourth to the seventh more important than the other (Table 7.12). This influence the base reaction results which are higher of about 10% in case of local response spectrum. Maximum and minimum shear forces and bending moment on columns are about 5% higher from NTC08 spectrums (see Table 7.18).

Interstory drifts in the center of mass are about 9% higher (mean value) when using NTC08 spectrum, for SLV limit state. This due to the influence of the multipliers of the mode shapes U1Amp and U2 Amp due to the response spectrum modal amplitude (Table 7.11). The mean variation of the interstory drifts in the other verticals of the building is about 8.3%.

Parameters of the 'performance points' achieved from Pushover analysis, are shown in the Table 7.20. Response spectrum estimated on site result more severe than the spectrum from NTC08, when performing response seismic analysis with *x* seismic component. Base shear reaction and displacement at the roof of the building are respectively about 12% and about 13% higher when using Pushover analysis in *x* direction (with LSR spectrum), and are about 10% and 11% lower when using Pushover analysis in *y* direction (LSR spectrum).

Interstory drifts are estimated using the response spectrum from SLD limit state. Interstory drifts estimated from analysis with standard spectrum NTC2008 result higher than those achieved by using the response spectrum on site for SLD limit state: about 57% and 62% higher respectively for U1 and U2 component. In case of fissured model, interstory drifts differ about 61% for U1 component and 63% for U2 component. Standard response spectrum NTC08 for SLD limit state result more severe than the spectrum estimated on site. Interstory drifts are also estimated in the case of 'FE Model2' when the rigidity of external walls has been modeled (Table 7.7). Modeling the rigidity of the wall panels reduce the interstory drift by 0.4% in case of response spectrum from NTC08 and 0.25% in the case of local seismic response.

Lateral displacements at the top of the building results also higher when using response spectrum from NTC08 and are not satisfied only for the fissured model (Table 7.8).

APPENDIX

Script code for Operational Modal Analysis - OMA (OMA 1 method)

```
% Read measures acquired in all floors in one vertical
Pew=dlmread('SynchronizedNSpt.dat',' ',0,0);   % composed by two column, first one measured in the ground floor ,
% and second one measured in 4'floor, ns component;
pew=dlmread('SynchronizedEWpt.dat',' ',0,0);
Pew1=dlmread('SynchronizedNS1p.dat',' ',0,0);
pew1=dlmread('SynchronizedEW1p.dat',' ',0,0);
Pew2=dlmread('SynchronizedNS2p.dat',' ',0,0);
pew2=dlmread('SynchronizedEW2p.dat',' ',0,0);
Pew3=dlmread('SynchronizedNS3p.dat',' ',0,0);
pew3=dlmread('SynchronizedEW3p.dat',' ',0,0);

nspt=Pew(:,[1]);  % Ground floor, ns
ns40=Pew(:,[2]);  % 4 floor, ns
ewpt=pew(:,[1]);  % Ground floor, ew
ew40=pew(:,[2]);  % 4 floor, ew
ns1=Pew1(:,[1]);  % 1 floor, ns
ns41=Pew1(:,[2]);  % 4 floor, ns
ew1=pew1(:,[1]);  % 1 floor, ew
ew41=pew1(:,[2]);  % 4 floor, ew
ns2=Pew2(:,[1]);  % 2 floor, ns
ns42=Pew2(:,[2]);  % 4 floor, ns
ew2=pew2(:,[1]);  % 2 floor, ew
ew42=pew2(:,[2]);  % 4 floor, ew
ns3=Pew3(:,[1]);  % 3 floor, ns
ns43=Pew3(:,[2]);  % 4 floor, ns
ew3=pew3(:,[1]);  % 3 floor, ew
ew43=pew3(:,[2]);  % 4 floor, ew

% Check the noise in measures by plot the signals as function of times and then remove the segments with noise
n=length(ew43);
fs=128;
dt=1/fs;
tf=dt*n; % Length of signal in sec
t=dt:dt:tf;
plot(t,ew43)
xlabel('Time (s)')
ylabel('Signal in velocity (mm/s)')
legend('ew43, Vertical a')

% Truncate the segments with noise,  for example the first 30 seconds (30 second * 128Hz=3840);
n=length(ew43);
ew43=ew43(3840:(n));
ns43=ns43(3840:(n));
ew3=ew3(3840:(n));
ns3=ns3(3840:(n));

% Matrix of measures
M1=[nspt ns1 ns2 ns3 ns43];
M2=[ewpt ew1 ew2 ew3 ew43];

% Align in the ns-ew direction of FEM
n4=length(ns1);
n5=length(M1(1,:));
for i=1:n4;
for j=1:n5;
M1(i,j)=M1(i,j).*(cos(14*pi/180))+M2(i,j).*sin(14*pi/180);
end
end
for i=1:n4;
for j=1:n5;
```

```
M2(i,j)=M2(i,j).*(cos(14*pi/180))+M1(i,j).*sin(14*pi/180);
end
end

% Matrix of measures
V=[M1 M2];

% Butterworth pass band filter
fs=128;
dt=1/fs;
f3=0.6; % cutoff frequency (Hz)
f4=10; % cutoff frequency (Hz)
fs=1/dt; % sample rate (Hz)
fN=f3/(fs/2);  % frequency normalyzer
fN1=f4/(fs/2); % frequency normalyzer
[b,a]=butter(1,[fN fN1],'bandpass');
Vel=filtfilt(b,a,V);

for I=1:size(Vel,2)
   for J=1:size(Vel,2)
      [psd(I,J,:),F(I,J,:)]=cpsd(Vel(:,I),Vel(:,J),[],[],[],fs);
   end
end

Frequencies(:,1)=F(1,1,:);
f=Frequencies;

% Integration of the signals if needed
for I=1:size(Vel,2)
   for J=1:size(Vel,2)
if (F(I,J,:))==0;
  PSD(I,J,:)=0;
else
  PSD(I,J,:)=psd(I,J,:)./((F(I,J,:)*2*pi).^2);
  end
end
end
PSD(isinf(PSD)) = 0;

% Compute SVD of the PSD at each frequency
for I=1:size(PSD,3)
   [u,s,v] = svd(PSD(:,:,I));
   s1(I) = s(1);              % First eigen values
   s2(I) = s(2,2);            % Second eigen values
   ms(:,I)=u(:,1);            % Mode shape
end

% Plot first singular values of the PSD matrix
figure
hold on
plot(f,20*log10(s1))
xlabel('Frequency (Hz)')
ylabel('1st Singular values of the PSD matrix (db)')

% Select peaks in frequency
Fp=[];% Frequencies related to selected peaks
NumPeaks=input('Enter the number of desired peaks:');

k=0;
while k~=NumPeaks
   A=getrect;                    % Draw a rectangle around the peak
   [a,P1]=min(abs(f-A(1)));
   [b,P2]=min(abs(f-(A(1)+A(3))));
```

```
    [c,B]=max(s1(P1:P2));
    Max=B+P1-1;              % Frequency at the selected peak
    scatter(f(Max),mag2db(s1(Max)),'MarkerEdgeColor','b','MarkerFaceColor','b')        % Mark this peak
    pause;key=get(gcf,'CurrentKey');
    Fp(end+1,:)=[Max,f(Max)];
    if strcmp(key,'space')
          % Press space to continue peak selection
           k=k+1;
           scatter(f(Max),mag2db(s1(Max)),'MarkerEdgeColor','g','MarkerFaceColor','g')      % Mark this peak as green
    else
          % Press any other key to ignore this peak
          Fp(end,:)=[];
          scatter(f(Max),mag2db(s1(Max)),'MarkerEdgeColor','r','MarkerFaceColor','r')      % Mark this peak as red
    end
end

% Number the selected peaks
[nr,Sr]=sort(Fp(:,2));
Fp=Fp(Sr,:);
clf
plot(f,mag2db(s1))
hold on
xlabel('Frequency (Hz)')
ylabel('1st Singular values of the PSD matrix (db)')
for I=1:size(Fp,1)
    scatter(Fp(I,2),mag2db(s1(Fp(I,1))),'MarkerEdgeColor','g','MarkerFaceColor','g')
    text(Fp(I,2), mag2db(s1(Fp(I,1)))*1.05, mat2str(I))
end

% Identify mode shapes
Frq=Fp(:,2);
% Compute mode shapes for each selected peak
for J=1:size(Fp,1)
    [ug, g, vg] = svd(PSD(:,:,Fp(J,1)));
    phi(:,J) = ug(:,5);
end

% Print frequencies
display('Identified frequencies')
for I=1:size(Frq,1)
    fprintf('Mode: %d; Modal Frequency: %6.4g (Hz)\n',I,Frq(I));
end

% Print Mode shapes
display('Related mode shapes')
for I=1:size(Frq,1)
    fprintf('Mode shape # %d:\n\n',I);
    disp(phi(:,I))
end

MODE=[phi(:,1),phi(:,2),phi(:,3),phi(:,4),phi(:,5),phi(:,6),phi(:,7)];

% Save results in excel format
xlswrite('file.xlsx', Frq);    % Frequencies values
xlswrite('file2.xlsx', MODE);   % Eigenvectors
```

Script code for Operational Modal Analysis - OMA (OMA 2 method)

The initial three steps of the script code 'Read signals', 'Check the noise' and 'Select the same length of signals to be analyzed with reference the zero center' are similar to the steps of the codes described above. After those steps, the signal is truncated in segments of 30 seconds and then the cross covariance is calculated. The PSD matrix is estimated by the FFT of the cross covariance means estimated. An example of one measures is presented below.

```
n=length(ew3);
```

```
fs=128;
dt=1/fs;
tf=dt*n; %
t=dt:dt:tf;
t=t';
ts=n/fs; % length of signal in second
t1=30; % length of segments, 30 second
b=ts/t1;% Segment number
a=n/b; % Number of element in one segment
 for i=1:17;
m(i)=(i-1)*(a+1);
k(i)=i*(a+1)-1;
end
A=[m' k'];
A(1,1)=1;
A(17,2)=62580;
x=A(:,1);
y=A(:,2);

for i=1:17;
   x(i,1);
   y(i,1);
   EWi=ew3(x(i,1):y(i,1));  % measure inside the building in various floors
   EW1=ew3(x(1,1):y(1,1));
   EW2=ew3(x(2,1):y(2,1));
   EW3=ew3(x(3,1):y(3,1));
   …
   EW17=ew3(x(17,1):y(17,1));
end

for i=1:17;
   x(i,1);
   y(i,1);
   ewi=ew(x(i,1):y(i,1));  % measure in the free field or in the top floor
   ew1=ew(x(1,1):y(1,1));
   ew2=ew(x(2,1):y(2,1));
   ew3=ew(x(3,1):y(3,1));
   …
   ew17=ew(x(17,1):y(17,1));
end

% Cross-Covariance by xcov not normalized function
for i=1:17;
   [vewi,lags]=xcov(EWi,ewi,3841);    % xcov of the measure inside the building and in the free field or the top floor
end
for i=1;
   [vew1,lags]=xcov(EW1,ew1,3841);
end
for i=2;
   [vew2,lags]=xcov(EW2,ew2,3841);
end
for i=3;
   [vew3,lags]=xcov(EW3,ew3,3841);
end
…
for i=17;
   [vew17,lags]=xcov(EW17,ew17,3841);
end

% The mean of cross-cov of segments
V1p=(vew1+vew2+vew3+vew4+vew5+vew6+vew7+vew8+vew9+vew10+vew11+vew12+vew13+vew14+vew15+v
ew16+vew17)/.17;
```

```
l=length(EW3);
fs=128;
dtt=1/fs;
tff=dtt*l; % lunghezza del segnale in secondi
tt=dtt:dtt:tff;
tt=tt';

% Auto-Covariance, of measure inside the building
for i=1:17;
   [vewi,lags]=xcov(EWi,EWi,3841);
end
for i=1;
   [vew1,lags]=xcov(EW1,EW1,3841);
end
for i=2;
   [vew2,lags]=xcov(EW2,EW2,3841);
end
for i=3;
   [vew3,lags]=xcov(EW3,EW3,3841);
end
…
for i=17;
   [vew17,lags]=xcov(EW17,EW17,3841);
end

% The mean of the xcov
V1=(vew1+vew2+vew3+vew4+vew5+vew6+vew7+vew8+vew9+vew10+vew11+vew12+vew13+vew14+vew15+ve
w16+vew17)/.17;

% Auto-Covariance of the measure in the free field or in the top floor
for i=1:17;
   [vewi,lags]=xcov(ewi,ewi,3841);
end
for i=1;
   [vew1,lags]=xcov(ew1,ew1,3841);
end
for i=2;
   [vew2,lags]=xcov(ew2,ew2,3841);
end
for i=3;
   [vew3,lags]=xcov(ew3,ew3,3841);
end
…
for i=17;
   [vew17,lags]=xcov(ew17,ew17,3841);
end

% The mean of the xcov
V1f=(vew1+vew2+vew3+vew4+vew5+vew6+vew7+vew8+vew9+vew10+vew11+vew12+vew13+vew14+vew15+v
ew16+vew17)/.17;

% PSD
n=length(V1p);
fs=128;
dt=1/fs;
tf=dt*n; % Length of signal in sec
t=dt:dt:tf;
t=t';
Be=1/tf; % Step frequency (df)
fmax=Be*n/2; % maximum frequency in Hz
ff=Be:Be:fmax; % Vector of frequency
fs=1/dt;
f=fs/n*(1:((n+1)/2));
```

```
%PSD using FFT
    Zns1p=fft(V1p,n); % Fourier transformation of random variables
    format long
    mm1p=Zns1p.*(conj(Zns1p))/(n*fmax);
    psdew1p=mm1p(1:((n+1)/2));      % PSD
    PSDew1p=Zns1p;

    Znsp1=fft(Vp1,n); % Fourier transformation of random variables
    format long
    mmp1=Znsp1.*(conj(Znsp1))/(n*fmax);
    psdewp1=mmp1(1:((n+1)/2));      % PSD
    PSDewp1=Znsp1;

    Zns1=fft(V1,n); % Fourier transformation of random variables
    format long
    mm1=Zns1.*(conj(Zns1))/(n*fmax);
    psdew1=mm1(1:((n+1)/2));
    PSDew1=Zns1;

    Zns1f=fft(V1f,n); % Fourier transformation of random variables
    format long
    mm1f=Zns1f.*(conj(Zns1f))/(n*fmax); % squared Fourier amplitude spectrum
    psdew1f=mm1f(1:((n+1)/2));
    PSDew1f=Zns1f;

P11=PSDew1;
P10=PSDew1p;
P00=PSDew1f;

 % The same procedure for all measures in one vertical

% PSD Matrix with Maxwell rule
P01=P10;
P02=P20;
P03=P30;
P04=P40;
P05=P50;
P51=(P50.*P01)./P00;
P52=(P50.*P02)./P00;
P53=(P50.*P03)./P00;
P54=(P50.*P04)./P00;
P15=P51;
P25=P52;
P35=P53;
P45=P54;
P21=(P20.*P01)./P00;
P31=(P30.*P01)./P00;
P41=(P40.*P01)./P00;
P32=(P30.*P02)./P00;
P42=(P40.*P02)./P00;
P43=(P40.*P03)./P00;
P12=P21;
P13=P31;
P14=P41;
P23=P32;
P24=P42;
P34=P43;

for i=1:size(P00,1);
    PSD(:,:,i)=[P00(i,1) P01(i,1) P02(i,1) P03(i,1) P04(i,1) P05(i,1);P10(i,1) P11(i,1) P12(i,1) P13(i,1) P14(i,1)
P15(i,1);P20(i,1) P21(i,1) P22(i,1) P23(i,1) P24(i,1) P25(i,1);P30(i,1) P31(i,1) P32(i,1) P33(i,1) P34(i,1)
P35(i,1);P40(i,1) P41(i,1) P42(i,1) P43(i,1) P44(i,1) P45(i,1);P50(i,1) P51(i,1) P52(i,1) P53(i,1) P54(i,1) P55(i,1)];
```

```
end

f=fs/n*(1:n);

% function [Frq,phi,Fp,s1] = Identifier(PSD,F)
% Compute SVD of the PSD at each frequency
for I=1:size(PSD,3)
   [u,s,v] = svd(PSD(:,:,I));
   s1(I) = s(1);              % First eigen values
   s2(I) = s(2,2);            % Second eigen values
   ms(:,I)=u(:,1);            % Mode shape
end

% Plot first singular values of the PSD matrix
figure
hold on
plot(f,20*log10(s1))
xlabel('Frequency (Hz)')
ylabel('1st Singular values of the PSD matrix (db)')
% Select peaks in frequency
Fp=[];% Frequencies related to selected peaks
NumPeaks=input('Enter the number of desired peaks:');

k=0;
while k~=NumPeaks
   A=getrect;                 % Draw a rectangle around the peak
   [a,P1]=min(abs(f-A(1)));
   [b,P2]=min(abs(f-(A(1)+A(3))));
   [c,B]=max(s1(P1:P2));
   Max=B+P1-1;                % Frequency at the selected peak
   scatter(f(Max),mag2db(s1(Max)),'MarkerEdgeColor','b','MarkerFaceColor','b')      % Mark this peak
   pause;key=get(gcf,'CurrentKey');
   Fp(end+1,:)=[Max,f(Max)];
   if strcmp(key,'space')
      % Press space to continue peak selection
       k=k+1;
       scatter(f(Max),mag2db(s1(Max)),'MarkerEdgeColor','g','MarkerFaceColor','g')    % Mark this peak as green
   else
      % Press any other key to ignore this peak
      Fp(end,:)=[];
      scatter(f(Max),mag2db(s1(Max)),'MarkerEdgeColor','r','MarkerFaceColor','r')    % Mark this peak as red
   end
end

% Number the selected peaks
[nr,Sr]=sort(Fp(:,2));
Fp=Fp(Sr,:);
clf
plot(f,mag2db(s1))
hold on
xlabel('Frequency (Hz)')
ylabel('1st Singular values of the PSD matrix (db)')
for I=1:size(Fp,1)
   scatter(Fp(I,2),mag2db(s1(Fp(I,1))),'MarkerEdgeColor','g','MarkerFaceColor','g')
   text(Fp(I,2), mag2db(s1(Fp(I,1)))*1.05, mat2str(I))
end

% Identify mode shapes
Frq=Fp(:,2);
% Compute mode shapes for each selected peak
for J=1:size(Fp,1)
   [ug, g, vg] = svd(PSD(:,:,Fp(J,1)));
   phi(:,J) = ug(:,5);
```

```
end

% Print frequencies
display('Identified frequencies')
for I=1:size(Frq,1)
    fprintf('Mode: %d; Modal Frequency: %6.4g (Hz)\n',I,Frq(I));
end

% Print Mode shapes
display('Related mode shapes')
for I=1:size(Frq,1)
    fprintf('Mode shape # %d:\n\n',I);
    disp(phi(:,I))
end

MODE=[phi(:,1),phi(:,2),phi(:,3),phi(:,4),phi(:,5),phi(:,6),phi(:,7)];

% Save results in excel format
xlswrite('file.xlsx', Frq);    % Frequencies values
xlswrite('file2.xlsx', MODE);   % Eigenvectors
```

Script code for Experimental Modal Analysis – EMA (EMA 2 method)

```
% Read measures acquired in all floors in one vertical
Pew=dlmread('Synchronized2NSpf.dat',' ',0,0);
pew=dlmread('Synchronized2EWpf.dat',' ',0,0);
Pew1=dlmread('Synchronized2NS1.dat',' ',0,0);
pew1=dlmread('Synchronized2EW1.dat',' ',0,0);
Pew2=dlmread('Synchronized2NS2.dat',' ',0,0);
pew2=dlmread('Synchronized2EW2.dat',' ',0,0);
Pew3=dlmread('Synchronized2NS3.dat',' ',0,0);
pew3=dlmread('Synchronized2EW3.dat',' ',0,0);
Pew4=dlmread('Synchronized2NS4.dat',' ',0,0);
pew4=dlmread('Synchronized2EW4.dat',' ',0,0);

nspt=Pew(:,[2]);  % fuori, ns
ns40=Pew(:,[1]);  % pterra ns
ewpt=pew(:,[2]);  % fuori, ew
ew40=pew(:,[1]);  % pterra ew
ns1=Pew1(:,[2]);  % fuori, ns
ns41=Pew1(:,[1]);  % 1 piano ns
ew1=pew1(:,[2]);  % fuori, ew
ew41=pew1(:,[1]);  % 1 piano ew
ns2=Pew2(:,[2]);  % fuori, ns
ns42=Pew2(:,[1]);  % 2 piano ns
ew2=pew2(:,[2]);  % fuori, ew
ew42=pew2(:,[1]);  % 2 piano ew
ns3=Pew3(:,[2]);  % fuori, ns
ns43=Pew3(:,[1]);  % 3 piano ns
ew3=pew3(:,[2]);  % fuori, ew
ew43=pew3(:,[1]);  % 3 piano ew
ns4=Pew4(:,[2]);  % fuori, ns
ns44=Pew4(:,[1]);  % 4 piano ns
ew4=pew4(:,[2]);  % fuori, ew
ew44=pew4(:,[1]);  % 4 piano ew

% Check the noise in measures by plot the signals as function of times
n=length(ew43);
fs=128;
dt=1/fs;
tf=dt*n; % Length of signal in sec
t=dt:dt:tf;
plot(t,ew43)
```

```
xlabel('Time (s)')
ylabel('Signal in velocity (mm/s)')
legend('ew43, Vertical a')

% Truncate the segments with noise,  for example the first 30 seconds (30 second * 128Hz=3840);
n=length(ew43);
ew43=ew43(3840:(n));
ns43=ns43(3840:(n));
ew3=ew3(3840:(n));
ns3=ns3(3840:(n));

% Analyze the same signal length for all measures, selected by the center of the signals
l=length(ns42);
g=138240;
r=(l-g)/2;
r=ceil(r);
ns42=ns42(r:(l-r));
ns2=ns2(r:(l-r));

l0=length(ns41);
g0=138240;
r0=(l0-g0)/2;
r0=ceil(r0);
ns41=ns41(r0:(l0-r0));
ns1=ns1(r0:(l0-r0));
…
l2=length(ewpt);
g2=138240;
r2=(l2-g2)/2;
r2=ceil(r2);
ewpt=ewpt(r2:(l2-r2));
ew40=ew40(r2:(l2-r2));

% Fast Fourier transform and FRF function
n=length(ns42);
fs=128;
dt=1/fs;
tf=dt*n; % Length of signal in sec
t=dt:dt:tf;
t=t';
Be=1/tf; % Step frequency (df)
fmax=Be*n/2; % maximum frequency in Hz
ff=Be:Be:fmax; % Vector of frequency
fs=1/dt;
f=fs/n*(1:((n+1)/2));

%PSD using FFT
   Zns4f=fft(ew4,n); % Fourier transformation of random variables
   format long
   mm4f=Zns4f.*(conj(Zns4f))/(n*fmax);
   psdew4f=mm4f(1:((n+1)/2));      % PSD
   PSDew4f=Zns4f;
m4f=(Zns4f.*(conj(Zns4f))).^0.5;
   FAS4f=m4f(1:((n+1)/2));        % FAS Fourier amplitude spectrum
   Sfas4f=FAS4f.^2;               % Squared Fourier amplitude spectrum

   Zns4=fft(ew44,n); % Fourier transformation of random variables
   format long
   mm4=Zns4.*(conj(Zns4))/(n*fmax);
   psdew4=mm4(1:((n+1)/2));
   PSDew4=Zns4;
m4=(Zns4.*(conj(Zns4))).^0.5;
   FAS4=m4(1:((n+1)/2));       % FAS Fourier amplitude spectrum
```

```
   Sfas4=FAS4.^2;              % Squared Fourier amplitude spectrum
Zns44=Zns4;
Zns04=Zns4f;
P40=Zns44./Zns04;

clear Zns4; clear PSDew4; clear psdew4; clear mm4;

   Zns4f=fft(ew3,n); % Fourier transformation of random variables
   format long
   mm4f=Zns4f.*(conj(Zns4f))/(n*fmax);
   psdew4f=mm4f(1:((n+1)/2));      % PSD
   PSDew4f=Zns4f;
m4f=(Zns4f.*(conj(Zns4f))).^0.5;
   FAS4f=m4f(1:((n+1)/2));       % FAS Fourier amplitude spectrum
   Sfas4f=FAS4f.^2;              % Squared Fourier amplitude spectrum

   Zns4=fft(ew43,n); % Fourier transformation of random variables
   format long
   mm4=Zns4.*(conj(Zns4))/(n*fmax);
   psdew4=mm4(1:((n+1)/2));
   PSDew4=Zns4;
m4=(Zns4.*(conj(Zns4))).^0.5;
   FAS4=m4(1:((n+1)/2));       % FAS Fourier amplitude spectrum
   Sfas4=FAS4.^2;              % Squared Fourier amplitude spectrum

Zns33=Zns4;
Zns03=Zns4f;
P30=Zns33./Zns03;

clear Zns4; clear PSDew4; clear psdew4; clear mm4;

   Zns4f=fft(ew2,n); % Fourier transformation of random variables
   format long
   mm4f=Zns4f.*(conj(Zns4f))/(n*fmax);
   psdew4f=mm4f(1:((n+1)/2));      % PSD
   PSDew4f=Zns4f;
m4f=(Zns4f.*(conj(Zns4f))).^0.5;
   FAS4f=m4f(1:((n+1)/2));       % FAS Fourier amplitude spectrum
   Sfas4f=FAS4f.^2;              % Squared Fourier amplitude spectrum

   Zns4=fft(ew42,n); % Fourier transformation of random variables
   format long
   mm4=Zns4.*(conj(Zns4))/(n*fmax);
   psdew4=mm4(1:((n+1)/2));
   PSDew4=Zns4;
m4=(Zns4.*(conj(Zns4))).^0.5;
   FAS4=m4(1:((n+1)/2));       % FAS Fourier amplitude spectrum
   Sfas4=FAS4.^2;              % Squared Fourier amplitude spectrum

Zns22=Zns4;
Zns02=Zns4f;
P20=Zns22./Zns02;

clear Zns4; clear PSDew4; clear psdew4; clear mm4;

   Zns4f=fft(ew1,n); % Fourier transformation of random variables
   format long
   mm4f=Zns4f.*(conj(Zns4f))/(n*fmax);
   psdew4f=mm4f(1:((n+1)/2));      % PSD
   PSDew4f=Zns4f;
m4f=(Zns4f.*(conj(Zns4f))).^0.5;
   FAS4f=m4f(1:((n+1)/2));       % FAS Fourier amplitude spectrum
   Sfas4f=FAS4f.^2;              % Squared Fourier amplitude spectrum
```

```
   Zns4=fft(ew41,n); % Fourier transformation of random variables
   format long
   mm4=Zns4.*(conj(Zns4))/(n*fmax);
   psdew4=mm4(1:((n+1)/2));
   PSDew4=Zns4;
m4=(Zns4.*(conj(Zns4))).^0.5;
   FAS4=m4(1:((n+1)/2));       % FAS Fourier amplitude spectrum
   Sfas4=FAS4.^2;              % Squared Fourier amplitude spectrum

Zns11=Zns4;
Zns01=Zns4f;
P10=Zns11./Zns01;

clear Zns4; clear PSDew4; clear psdew4; clear mm4;

   Zns4f=fft(ewpt,n); % Fourier transformation of random variables
   format long
   mm4f=Zns4f.*(conj(Zns4f))/(n*fmax);
   psdew4f=mm4f(1:((n+1)/2));      % PSD
   PSDew4f=Zns4f;
m4f=(Zns4f.*(conj(Zns4f))).^0.5;
   FAS4f=m4f(1:((n+1)/2));       % FAS Fourier amplitude spectrum
   Sfas4f=FAS4f.^2;              % Squared Fourier amplitude spectrum

   Zns4=fft(ew40,n); % Fourier transformation of random variables
   format long
   mm4=Zns4.*(conj(Zns4))/(n*fmax);
   psdew4=mm4(1:((n+1)/2));
   PSDew4=Zns4;
m4=(Zns4.*(conj(Zns4))).^0.5;
   FAS4=m4(1:((n+1)/2));       % FAS Fourier amplitude spectrum
   Sfas4=FAS4.^2;              % Squared Fourier amplitude spectrum

Znspt=Zns4;
Zns0t=Zns4f;
Pt0=Znspt./Zns0t;
clear Zns4; clear PSDew4; clear psdew4; clear mm4;

P00=Zns0t;
P001=Zns01;
P002=Zns02;
P003=Zns03;
P004=Zns04;

% PSD matrix using Maxwell rule
P0t=Pt0;
P01=P10;
P02=P20;
P03=P30;
P04=P40;
P1t=(P10.*P0t)./P001;
P2t=(P20.*P0t)./P002;
P3t=(P30.*P0t)./P003;
P4t=(P40.*P0t)./P004;
Ptt=(Pt0.*P0t)./P00;
Pt3=P3t;
Pt2=P2t;
Pt1=P1t;
Pt4=P4t;
P21=(P20.*P01)./P001;
P31=(P30.*P01)./P001;
P41=(P40.*P01)./P001;
```

```
P32=(P30.*P02)./P002;
P42=(P40.*P02)./P002;
P43=(P40.*P03)./P003;
P12=P21;
P13=P31;
P14=P41;
P23=P32;
P24=P42;
P34=P43;
P11=(P10.*P01)./P00;
P22=(P20.*P02)./P00;
P33=(P30.*P03)./P00;
P44=(P40.*P04)./P00;

% PSD Matrix
for i=1:size(P00,1);
    PSD(:,:,i)=[P00(i,1) P0t(i,1) P01(i,1) P02(i,1) P03(i,1) P04(i,1);Pt0(i,1) Ptt(i,1) Pt1(i,1) Pt2(i,1) Pt3(i,1)
Pt4(i,1);P10(i,1) P1t(i,1) P11(i,1) P12(i,1) P13(i,1) P14(i,1);P20(i,1) P2t(i,1) P21(i,1) P22(i,1) P23(i,1)
P24(i,1);P30(i,1) P3t(i,1) P31(i,1) P32(i,1) P33(i,1) P34(i,1);P40(i,1) P4t(i,1) P41(i,1) P42(i,1) P43(i,1) P44(i,1)];
end

f1=fs/n*(1:n);
f=f1';

% Compute SVD of the PSD at each frequency
for I=1:size(PSD,3)
    [u,s,v] = svd(PSD(:,:,I));
    s1(I) = s(1);                 % First eigen values
    s2(I) = s(2,2);               % Second eigen values
    ms(:,I)=u(:,1);               % Mode shape
end

% Plot first singular values of the PSD matrix
figure
hold on
plot(f,20*log10(s1))
xlabel('Frequency (Hz)')
ylabel('1st Singular values of the PSD matrix (db)')

% Select peaks in frequency
Fp=[];% Frequencies related to selected peaks
NumPeaks=input('Enter the number of desired peaks:');

k=0;
while k~=NumPeaks
    A=getrect;                          % Draw a rectangle around the peak
    [a,P1]=min(abs(f-A(1)));
    [b,P2]=min(abs(f-(A(1)+A(3))));
    [c,B]=max(s1(P1:P2));
    Max=B+P1-1;                % Frequency at the selected peak
    scatter(f(Max),mag2db(s1(Max)),'MarkerEdgeColor','b','MarkerFaceColor','b')        % Mark this peak
    pause;key=get(gcf,'CurrentKey');
    Fp(end+1,:)=[Max,f(Max)];
    if strcmp(key,'space')
         % Press space to continue peak selection
          k=k+1;
          scatter(f(Max),mag2db(s1(Max)),'MarkerEdgeColor','g','MarkerFaceColor','g')      % Mark this peak as green
    else
         % Press any other key to ignore this peak
         Fp(end,:)=[];
         scatter(f(Max),mag2db(s1(Max)),'MarkerEdgeColor','r','MarkerFaceColor','r')      % Mark this peak as red
    end
end
```

```
% Number the selected peaks
[nr,Sr]=sort(Fp(:,2));
Fp=Fp(Sr,:);
clf
plot(f,mag2db(s1))
hold on
xlabel('Frequency (Hz)')
ylabel('1st Singular values of the PSD matrix (db)')
for I=1:size(Fp,1)
    scatter(Fp(I,2),mag2db(s1(Fp(I,1))),'MarkerEdgeColor','g','MarkerFaceColor','g')
    text(Fp(I,2), mag2db(s1(Fp(I,1)))*1.05, mat2str(I))
end

% Identify mode shapes
Frq=Fp(:,2);
% Compute mode shapes for each selected peak
for J=1:size(Fp,1)
    [ug, g, vg] = svd(PSD(:,:,Fp(J,1)));
    phi(:,J) = ug(:,5);
end

% Print frequencies
display('Identified frequencies')
for I=1:size(Frq,1)
    fprintf('Mode: %d; Modal Frequency: %6.4g (Hz)\n',I,Frq(I));
end

% Print Mode shapes
display('Related mode shapes')
for I=1:size(Frq,1)
    fprintf('Mode shape # %d:\n\n',I);
    disp(phi(:,I))
end
MODE=[phi(:,1),phi(:,2),phi(:,3),phi(:,4),phi(:,5),phi(:,6),phi(:,7)];
% Save results in excel format
xlswrite('file.xlsx', Frq);    % Frequencies values
xlswrite('file2.xlsx', MODE);   % Eigenvectors
```

Script code for Experimental Modal Analysis – EMA (EMA 1 method)

This code differ from the EMA 2 method as the signal is truncated in segments of 30 seconds before starting the analysis. Then with the CPSD function is used as in the other cases.

Script code for Power spectral density function - PSD

The initial three steps of the script code 'Read signals', 'Check the noise' and 'Select the same length of signals to be analyzed with reference the zero center' are similar to the steps of the codes described above. Then the PSD and FRF graphic are estimated.

```
n=length(ns42);
fs=128;
dt=1/fs;
tf=dt*n; % Length of signal in sec
t=dt:dt:tf;
t=t';
Be=1/tf; % Step frequency (df)
fmax=Be*n/2; % maximum frequency in Hz
ff=Be:Be:fmax; % Vector of frequency
fs=1/dt;
f=fs/n*(1:((n+1)/2));

%PSD using FFT at all measures in one vertical
   Zns4f=fft(ns4,n); % Fourier transformation of random variables
   format long
```

```
   mm4f=Zns4f.*(conj(Zns4f))/(n*fmax);
   psdew4f=mm4f(1:((n+1)/2));      % PSD
   PSDew4f=Zns4f;
m4f=(Zns4f.*(conj(Zns4f))).^0.5;
   FAS4f=m4f(1:((n+1)/2));       % FAS Fourier amplitude spectrum
   Sfas4f=FAS4f.^2;              % Squared Fourier amplitude spectrum

   Zns4=fft(ns44,n); % Fourier transformation of random variables
   format long
   mm4=Zns4.*(conj(Zns4))/(n*fmax);
   psdew4=mm4(1:((n+1)/2));
   PSDew4=Zns4;
m4=(Zns4.*(conj(Zns4))).^0.5;
   FAS4=m4(1:((n+1)/2));       % FAS Fourier amplitude spectrum
   Sfas4=FAS4.^2;              % Squared Fourier amplitude spectrum

P44=Sfas4;
P004=Sfas4f;
P4=P44./P004;
clear Zns4; clear PSDew4; clear psdew4; clear mm4;

   Zns4f=fft(ns3,n); % Fourier transformation of random variables
   format long
   mm4f=Zns4f.*(conj(Zns4f))/(n*fmax);
   psdew4f=mm4f(1:((n+1)/2));      % PSD
   PSDew4f=Zns4f;
m4f=(Zns4f.*(conj(Zns4f))).^0.5;
   FAS4f=m4f(1:((n+1)/2));       % FAS Fourier amplitude spectrum
   Sfas4f=FAS4f.^2;              % Squared Fourier amplitude spectrum

   Zns4=fft(ns43,n); % Fourier transformation of random variables
   format long
   mm4=Zns4.*(conj(Zns4))/(n*fmax);
   psdew4=mm4(1:((n+1)/2));
   PSDew4=Zns4;
m4=(Zns4.*(conj(Zns4))).^0.5;
   FAS4=m4(1:((n+1)/2));       % FAS Fourier amplitude spectrum
   Sfas4=FAS4.^2;              % Squared Fourier amplitude spectrum

P33=Sfas4;
P003=Sfas4f;
P3=P33./P003;

clear Zns4; clear PSDew4; clear psdew4; clear mm4;

   Zns4f=fft(ns2,n); % Fourier transformation of random variables
   format long
   mm4f=Zns4f.*(conj(Zns4f))/(n*fmax);
   psdew4f=mm4f(1:((n+1)/2));      % PSD
   PSDew4f=Zns4f;
m4f=(Zns4f.*(conj(Zns4f))).^0.5;
   FAS4f=m4f(1:((n+1)/2));       % FAS Fourier amplitude spectrum
   Sfas4f=FAS4f.^2;              % Squared Fourier amplitude spectrum

   Zns4=fft(ns42,n); % Fourier transformation of random variables
   format long
   mm4=Zns4.*(conj(Zns4))/(n*fmax);
   psdew4=mm4(1:((n+1)/2));
   PSDew4=Zns4;
m4=(Zns4.*(conj(Zns4))).^0.5;
   FAS4=m4(1:((n+1)/2));       % FAS Fourier amplitude spectrum
   Sfas4=FAS4.^2;              % Squared Fourier amplitude spectrum
```

```
P22=Sfas4;
P002=Sfas4f;
P2=P22./P002;

clear Zns4; clear PSDew4; clear psdew4; clear mm4;

   Zns4f=fft(ns1,n); % Fourier transformation of random variables
   format long
   mm4f=Zns4f.*(conj(Zns4f))/(n*fmax);
   psdew4f=mm4f(1:((n+1)/2));      % PSD
   PSDew4f=Zns4f;
m4f=(Zns4f.*(conj(Zns4f))).^0.5;
   FAS4f=m4f(1:((n+1)/2));       % FAS Fourier amplitude spectrum
   Sfas4f=FAS4f.^2;              % Squared Fourier amplitude spectrum

   Zns4=fft(ns41,n); % Fourier transformation of random variables
   format long
   mm4=Zns4.*(conj(Zns4))/(n*fmax);
   psdew4=mm4(1:((n+1)/2));
   PSDew4=Zns4;
m4=(Zns4.*(conj(Zns4))).^0.5;
   FAS4=m4(1:((n+1)/2));       % FAS Fourier amplitude spectrum
   Sfas4=FAS4.^2;              % Squared Fourier amplitude spectrum

P11=Sfas4;
P001=Sfas4f;
P1=P11./P001;
clear Zns4; clear PSDew4; clear psdew4; clear mm4;

   Zns4f=fft(nspt,n); % Fourier transformation of random variables
   format long
   mm4f=Zns4f.*(conj(Zns4f))/(n*fmax);
   psdew4f=mm4f(1:((n+1)/2));      % PSD
   PSDew4f=Zns4f;
m4f=(Zns4f.*(conj(Zns4f))).^0.5;
   FAS4f=m4f(1:((n+1)/2));       % FAS Fourier amplitude spectrum
   Sfas4f=FAS4f.^2;              % Squared Fourier amplitude spectrum

   Zns4=fft(ns40,n); % Fourier transformation of random variables
   format long
   mm4=Zns4.*(conj(Zns4))/(n*fmax);
   psdew4=mm4(1:((n+1)/2));
   PSDew4=Zns4;
m4=(Zns4.*(conj(Zns4))).^0.5;
   FAS4=m4(1:((n+1)/2));       % FAS Fourier amplitude spectrum
   Sfas4=FAS4.^2;              % Squared Fourier amplitude spectrum

P00=Sfas4;
P000=Sfas4f;
P0=P00./P000;
clear Zns4; clear PSDew4; clear psdew4; clear mm4;

n=2*length(P4);
f=fs/n*(1:((n+1)/2));

% Plot FRF and PSD function of all measures in one vertical

figure(1);
plot(f,P4)
grid on
hold on
plot(f,P3,'r')
plot(f,P2,'m')
```

```
plot(f,P1,'y')
plot(f,P0,'g')
xlabel('Frequency (Hz)')
ylabel('FRF')
title('Transfer Function, NS')
legend('4Floor','3Floor','2Floor','1Floor','Underground Floor')

figure(2);
plot(f,P44)
grid on
hold on
plot(f,P33,'r')
plot(f,P22,'m')
plot(f,P11,'y')
plot(f,P00,'g')
xlabel('Frequency (Hz)')
ylabel('PSD')
title('PSD of Vertical a, NS component')
legend('4Floor','3Floor','2Floor','1Floor','Underground Floor')
```

REFERENCES

Adel M.E. Mohamed, A.S.A. Abu El Ata, F. Abdel Azim and M.A. Taha (2013). ‘Site-specific shear wave velocity investigation for geotechnical engineering applications using seismic refraction and 2D multi-channel analysis of surface waves’. NRIAG Journal of Astronomy and Geophysics Volume 2, Issue 1, Pages 88–101.

Aki K. (1957). ‘Space and time spectra of stationary stochastic waves, with special reference to microtremors’. Bull Earthq Res Inst 35:415–456.

Aki K. (1965). ‘A note on the use of microseisms in determining the shallow structure of the Earth’s crust’. Geophysics 30:665–666.

Aki K. and P. G. Richards (2002). ‘Quantitative Seismology: University Science Books’.

Albarello D. and Lunedei E. (2010). ‘Alternative interpretations of Horizontal to Vertical Spectral Ratios of ambient vibrations: new insights from theoretical modeling’. Bull Earthq Eng 8(3):519–534.

Albarello D. and Lunedei E. (2011). ‘Structure of an ambient vibration wavefield in the frequency range of engineering interest ([0.5, 20] Hz): insights from numerical modelling’. Near Surface Geophys 9:543–559.

Albarello D., Cesi C., Eulilli V., Guerrini F., Lunedei E., Paolucci E., Pileggi D., Puzzilli L.M. (2011). ‘The contribution of the ambient vibration prospecting in seismic microzoning: an example from the area damaged by the 26th April 2009 L’Aquila (Italy) earthquake’. Boll. Geofis. Teor. Appl., 52 (3), 513-538.

Albarello D. and Lunedei E. (2013). ‘Combining horizontal ambient vibration components for HVSR spectral ratio estimates’. Geophys J Int 194:936–951.

Ali Ismet Kanlı, Pèter Tildy, Zsolt Prònay, Ali Pınar and Làszlò Hermann (2006). ‘Vs30 mapping and soil classification for seismic site effect evaluation in Dinar region, SW Turkey’. Geophys. J. Int. 165, 223–235.

American Society Of Civil Engineers (2000). ‘FEMA 356 - Prestandard and commentary for the seismic rehabilitation of buildings’. Federal Emergency Management Agency, Washington, D.C.

Anderson J. G. (1991). ‘Strong motion seismology’. Reviews of Geophysics 29, 700-720.

Arai H. and Tokimatsu K. (2004). ‘S-wave velocity profiling by inversion of microtremor HVSR spectrum’. Bull Seism Soc Am 94:53–63.

Asten M. W. and Henstridge J. D. (1984). Array estimators and use of microseisms for reconnaissance of sedimentary basins. Geophysics, 49, 1828-1837.

Asten M. W. (1978). Geological control of the three-component spectra of rayleigh-wave microseisms. Bulletin of Seismological Society of America, 68, 1623-1636.

Au S. K., Zhang F. L. and To P. (2012). ‘Field observations on modal properties of two tall buildings under strong wind’. Journal of Wind Engineering and Industrial Aerodynamics, 101, 12-23.

Bard PY. (1998). ‘Microtremor measurement: a tool for site effect estimation’. Second international symposium on the effects of the surface geology on seismic motion ESG98, Japan.

Beskhyroun S., Wotherspoon L., Ma Q. T. and Popli B. (2013). ‘Ambient and Forced Vibration Testing of a 13-Story Reinforced Concrete Building’. NZSEE Conference.

Bindi D., Parolai S., Spallarossa D. and Cattaneo M. (2000). ‘Site effects by HVSR ratio: comparison of two different procedures’. Journal of Earthquake Engineering, 4, 1, 97-113.

Bonnefoy-Claudet S., Cornou C., Kristek J., Ohrnberger M., Wathelet M., Bard P.Y., Moczo P., Fäh D., Cotton F. (2004). ‘Simulation of seismic ambient noise: I. Results of HVSR and array techniques on canonical models’. In: Proceedings of the 13th world conferences on earthquake engineering (WCEE), Vancouver.

Bonnefoy-Claudet S., Cotton F. and Bard P. Y. (2006, a). The nature of noise wavefield and its applications for site effects studies: A literature review. Earth Science Review 79, 205–227.

Bonnefoy-Claudet S., C. Cornou, P. Bard, F. Cotton, P. Moczo, J. Kristek and D. Fah (2006, b). ‘HVSR ratios; a tool for site effects evaluation; results from 1-D noise simulations’. Geophysical Journal International 167, 827-837.

Bonnefoy-Claudet S., Kohler A., Cornou C., Wathelet M., Bard P.Y. (2008). ‘Effects of Love waves on microtremor HVSR ratio’. Bull Seismol Soc Am 98(1):288–300.

Brekhovskikh L.M. (1960). ‘Waves in Layered Media’. Academic Press, NewYork, NY.

Brincker R., Zhang L. and Anderson P. (2000). 'Output-Only Modal Analysis by Frequency Domain Decomposition.' International Seminar on Modal Analysis (ISMA25), Katholieke Universiteit Leuven, Belgium.

Brincker R., Zhang LM., Andersen P. (2000). 'Modal identification of output-only systems using frequency domain decomposition'. Smart Materials and Structures 2000; 10:441–445.

Brincker R., Ventura C. E. and Andersen P. (2003). ‘Why output-only modal testing is a desirable tool for a wide range of practical applications’. In Proceedings of IMAC-21: A Conference on Structural Dynamics. Society for Experimental Mechanics. The Hyatt Orlando, Kissimmee, Florida. USA. s. 265-272.

Brownjohn J. M. W. (2003). ‘Ambient vibration studies for system identification of tall buildings’. Earthquake Engineering & Structural Dynamics, 32, 71-95.

Campillo M. and A. Paul (2003). ‘Long-range correlations in the diffuse seismic coda’. Science 299, 547–549.

Castellaro S., Mulargia F. and Bianconi L. (2005). ‘Passive seismic stratigraphy: a new efficient, fast and economic technique’. Geologia Tecnica e Ambientale, 3, 76-102.

Chatfield C. (1996). ‘The Analysis of Time Series’. Chapman & Hall/CRC.

Chung D. H. and Bernreuter D. L. (1981). 'The effect of regional variation of seismic wave attenuation on the strong ground motion from earthquakes'. NRC publications.

Clarence W. de Silva (2007). Second edition of book ‘Vibration, Fundamentals and Practice’.

Comina C., Foti S., Boiero D. and Socco LV. (2011). ‘Reliability of VS,30 evaluation from surface waves tests’. J Geotech Geoenviron Eng ASCE 137(6).

Cooley J.W. and Tukey J.W. (1965). ‘An algorithm for the machine calculation of complex Fourier series’. Math. Comput., 19, 297–301.

Cornamusini G., Conti P., Bonciani F., Callegari I., Carmignani L., Martelli L. and Quagliere S. (2009). 'Foglio 267 San Marino, Note illustrative della Carta Geologica d'Italia alla scala 1/50.000'. ISPRA (Istituto Superiore per la Protezione e la Ricerca Ambientale).

Çelebi M. (2009). ‘Comparison of recorded dynamic characteristics of structures and ground during strong and weak shaking’. Increasing Seismic Safety by Combining Engineering Technologies and Seismological Data, 99-115.

Çelebi M., Bazzurro P., Chiaraluce L., Clemente P., Decanini L., DeSortis A., Ellsworth W., Gorini A., Kalkan E., Marcucci S., Milana G., Mollaioli F., Olivieri M., Paolucci R., Rinaldis D., Rovelli A., Sabetta F. and Stephens C. (2010). ‘Recorded motions of the 6 April 2009 MW 6.3 L'aquila, Italy’. Earthquake and implications for building structural damage: Overview. Earthquake Spectra, 26, 651-684.

Delgado J., Lopez Casado C., Estevez AC., Giner J., Cuenca A. and Molina S. (2000a). ‘Mapping soft soils in the Segura river valley (SE Spain): a case study of microtremors as an exploration tool’. J Appl Geophys 45:19–32.

Delgado J., Lopez Casado C., Giner J., Estevez A., Cuenca A. and Molina S. (2000b). ‘Microtremors as a geophysical exploration tool: applications and limitations’. Pure Appl Geophys 157:1445–1462.

D’Amico V., Picozzi M., Baliva F. and Albarello D. (2008). ‘Ambient noise measurements for preliminary site effects characterization in the urban area of Florence’. Bull Seism Soc Am 98(3):1373–1388.

Di Giulio G., Savvaidis A., Ohrnberger M., Wathelet M., Cornou C., Knapmeyer-Endrun B., Renalier F., Theodoulidis N. and Bard P.Y. (2012). ‘Exploring the model space and ranking a best class of models in surface wave dispersion inversion: Application at European strong-motion sites’. Geophysics, 77, 3, B147-B166.

Di Giulio Giuseppe, Gaudiosi Iolanda, Cara Fabrizio, Milana Giuliano and Tallini Marco (2014). ‘Shear-wave velocity profile and seismic input derived from ambient vibration array measurements: the case study of downtown l’Aquila’. Geophysical Journal International, 198 (2): 848-866.

Dorman J. and Ewing M. (1962). ‘Numerical Inversion of seismic surface waves dispersion data and crust-mantle structure in the New York-Pennsylvania area’. J. of Geophysical Research, 67, 5227-5241.

Eiben A.E. and Smith J.E. (2003). ‘Introduction to Evolutionary Computing’. Sprinter, 3-540-40184-9.

Ekstrom G., Abers G.A. and Webb S.C. (2009). ‘Determination of surface-wave phase velocities across USArray from noise and Aki’s spectral formulation’. Geophys. Res. Lett., 36, L18301.

Endrun B., Ohrnberger M. and Savvaidis A. (2010). ‘On the repeatability and consistency of three-component ambient vibration array measurements’. Bulletin of Earthquake Engineering, 8, 535-570.

Escobar J.A., Sosa J.J. and Gomez R. (2001). ‘Damage Detection in Framed Buildings’. Canadian Journal of Civil Engineering, 28(1), 35-47.

European Committee for Standardization, CEN (2003). Eurocode 8: ‘Design of structures for earthquake resistance’.

Farrar C.R. and Sohn H. (2001). ‘Condition/Damage Monitoring Methodologies’. Invited Talk, The Consortium of Organizations for Strong Motion Observation Systems (COSMOS) Workshop, Emeryville, CA, November 14-15, 2001.

Fäh D. (1997). ‘Microzonation of the city of Basel’. Journal of Seismology 1 (1), 87–102.

Fäh D., Kind F. and Giardini D. (2001). ‘A theoretical investigation of average HVSR ratios’. Geophys J Int 145:535–549.

Fäh D., Kind F. and Giardini D. (2003). ‘Inversion of local S-wave velocity structures from average HVSR ratios, and their use for the estimation of site-effects’. J Seismol 7:449–467.

Forbriger T. (2006). ‘Low-frequency limit for HVSR studies due to tilt’. Sitzung der Arbeitsgruppe Seismologie des FKPE. Haidhof, Germany, Extended Abstract, 32.

Foti S. (2000). ‘Multistation methods for geotechnical characterization using surface waves’. PhD dissertation, Politecnico di Torino, Italy.

Foti S. (2003). ‘Small strain stiffness and damping ratio of Pisa Clay from surface wave tests’. Geotechnique 53(5):455–461.

Foti S., Comina C., Boiero D. and Socco LV. (2009). ‘Non uniqueness in surface wave inversion and consequences
on seismic site response analyses’. Soil Dyn Earthq Eng 29(6):982–993.

Foti Sebastiano, Parolai Stefano, Albarello Dario and Picozzi Matteo (2011). ‘Application of Surface-wave methods for seismic site characterization’. Surveys in Geophysics (ISSN 1084-0702), Volume 32, Issue. 6, pp. 777-825.

Gallagher K. and Sambridge M. (1994). ‘Genetic algorithms: A powerful tool for large-scale non-linear optimization problems’. Comput. Geosci., 20(7/8), 1229–1236.

Gallipoli M. R., Mucciarelli M. and Vona M. (2008). 'Empirical estimate of fundamental frequencies and damping for Italian buildings'. Earthquake Engineering Structural Dynamic 38:973–988.

Gallipoli M. R., Mucciarelli M., Šket-Motnikar B., Zupancic P., Gosar A., Prevolnik S., Herak M., Stipcevic J., Herak D., Milutinovic Z. and Olumceva T. (2009). 'Empirical estimates of dynamic parameters on a large set of European buildings'. Bull Earthquake Eng (2009) 8:593–607.

Gallipoli M.R. and Mucciarelli M. (2009). ‘Comparison of site classification from VS30, VS10, and HVSR in Italy’. Bulletin of the Seismological Society of America, 99, 340-351.

Gallipoli M.R., Albarello D., Mucciarelli M. and Bianca M. (2011). ‘Ambient noise measurements to support emergency seismic microzonation: the Abruzzo 2009 earthquake experience’. Boll.Geofis.Teor Appl., 52 (3), 539-559.

George A. Papagiannopoulosa and George D. Hatzigeorgiou (2011). ' On the use of the half-power bandwidth method to estimate damping in building structures'. Soil Dynamics and Earthquake Engineering, 31, 1075 - 1079.

Goldberg D.E. (1989). ‘Genetic Algorithms in Search, Optimization, and Machine Learning’. Addison-Wesley, Reading, Mass.

Green M.F. (1995). 'Modal Test Methods For Bridges’. Proceedings of the 13th International Modal Analysis Conference, Nashville, Tennessee, 1, 552-558.

Guerra G., Forcellini D., Xhixha E., Peruzzi G., Albarello D., Lo E., Mayer D.E., Trinh S., Zheng E. and Kuester F. (2017). '3D numerical simulations of the San Marino third tower (Montale) based on 3d mapping'. Ingenio.

Gutenberg B. (1958). Microseisms. Advanced Geophysics, 5, 53-93.

Herrmann R. B. (2002). 'Computer Programs in Seismology. Surface waves, receiver functions and crustal structure'. Version 3.25, Saint Louis University (Missouri, USA).

Hobiger M., Bard P-Y., Cornou C. and Le Bihan N. (2009). 'Single station determination of rayleigh wave ellipticity by using the random decrement technique (RayDec)'. Geophys Res Lett 36:14.

Hobiger M, Cornou C., Wathelet M., Di Giulio G., Knapmeyer-Endrun B., Renalier F., Bard P.Y., Savvaidis A., Hailemikael S., Le Bihan N., Ohrnberger M. and Theodoulidis N. (2013). 'Ground structure imaging by inversions of Rayleigh wave ellipticity: sensitivity analysis and application to European strong-motion sites'. Geophys. J. Int., 192, 207-229.

Holland J.H. (1975). 'Adaptation in Natural and Artificial Systems'. Univ. of Mich. Press, Ann Arbor, Mich.

Horike M. (1985). 'Inversion of phase velocity of long period microtremors to the S-wave-velocity structure down to the basement in urbanized areas'. J. Phys. Earth, 33, 59-96.

Iervolino I., Galasso C. and Cosenza E. (2010). 'REXEL: computer aided record selection for code-based seismic structural analysis'. Bulletin of Earthquake Engineering, 8:339-362.

James III G. H., Came T. G. and Lauffer J. P. (1993). 'The Natural Excitation Technique (NExT) for Modal Parameter Extraction From Operating Wind Turbines'. Sandia National Laboratories, Albuquerque, New Mexico, USA.

Karbhari Vistasp M. and Ansari F. (2009). 'Structural Health Monitoring of Civil Infrastructure Systems'. Woodhead Publishing.

Kawase H., Sanchez-Sesma F.J. and Matsushima S. (2011). 'The optimal use of horizontal-to-vertical spectral ratios of earthquake motions for velocity inversions based on diffuse-field theory for plane waves'. Bull Seismol Soc Am 101(5):2001–2014.

Kottke AR. and Rathje EM. (2008). 'Technical manual for strata'. Pacific Earthquake Engineering Research Center Report 2008/10, University of California, Berkeley, California.

Konno K. and Ohmachi T. (1998). 'Ground-motion characteristics estimated from spectral ratio between horizontal and vertical components of microtremor'. Bulletin of Seismological Society of America, 88, 1, 228-241.

Kudo K. (1995). 'Practical estimates of site response. State-of-art report'. Proceedings of the fifth International Conference on Seismic Zonation, Nice (France).

Lamarche C. P., Paultre P., Proulx J. and Mousseau S. (2008). 'Assessment of the frequency domain decomposition technique by forced-vibration tests of a full-scale structure'. Earthquake Engineering and Structural Dynamics, 37:487-494.

Lachet C. and Bard P.Y. (1994). 'Numerical and theoretical investigations on the possibilities and limitations of Nakamura's technique'. J. Phys. Earth 42:377–397.

Lai C. G. (1998). 'Simultaneous inversion of Rayleigh phase velocity and attenuation for near-surface site characterization'. PhD Thesis, Georgia Inst. Technology, Atlanta (Georgia, USA).

Lay T. and Wallace T.C. (1995). 'Modern global seismology'. Academic Press.

Lermo J. and Chavez-Garcia FJ. (1993). 'Site effect evaluation using spectral ratios with only one station'. Bull Seism Soc Am 85(5):1574–1594.

Lermo J. and Chavez-Garcia FJ. (1994). 'Are microtremors useful in site response evaluation'. Bull Seism Soc Am 84(135):1364.

Liu Y., Luke B, Pullammanappallil S., Louie J. N. and Bay J. (2005). 'Combining active- and passive-source measurements to profile shear wave velocities for seismic microzonation'. Congress proceedings of Geo-Frontiers 2005, Austin, Texas (USA).

Lunedei E. and Albarello D., (2009). 'On the seismic noise wave field in a weakly dissipative layered Earth'. Geophys J Int.

Lunedei E. and Albarello D. (2010). 'Theoretical HVSR from the full wave field modelling of ambient vibrations in a weakly dissipative layered Earth'. Geophys J Int 181:1093–1108.

Lunedei E. and Malischewsky P. (2015). ‘A review and some new issues on the theory of the HVSR technique for ambient vibrations’. A. Ansal (ed.), Perspectives on European Earthquake Engineering and Seismology, Geotechnical, Geological and Earthquake Engineering 39.

Malagnini L., Rovelli A., Hough SE. and Seeber L. (1993). ‘Site amplification estimates in the Garigliano Valley, Central Italy, based on dense array measurements of ambient noise’. Bull Seism Soc Am 83:1744–1755.

Maia N. M. M., Montalvao and Silva J. M. (1997). ‘Theoretical and experimental modal analysis, Research Studies Press’. Wiley, Hertfordshire, England / New York.

Marco Pilz, Tanatkan Abakanov, Kanatbek Abdrakhmatov, Dino Bindi, Tobias Boxberger, Bolot Moldobekov, Sagynbek Orunbaev, Natalya Silacheva, Shahid Ullah, Sheyshenaly Usupaev, Pulat Yasunov and Stefano Parolai (2015). 'An overview on the seismic Microzonation and site effect studies in Central Asia'. Annals of Geophysics, 58.

Martinez M. D., Lana X., Badal J., Canas J. A. and Pujades L. (1999). ‘Simulated annealing in 3-D seismic modelling and elastic structure of the Mediterranean basin’. Phys. Chem. Earth, 24, 3, 253–260.

Martinez M. D., Lana X., Olarte J., Badal J. and Canas J. A. (2000). ‘Inversion of Rayleigh wave phase and group velocity by simulated annealing’. Physics of the Earth and planetary interiors, 122, 3-17.

Marinos V., Marinos P. and Hoek E. (2005). ‘The geological strength index: applications and limitations’. Bull Eng Geol Environ (2005) 64: 55–65.

Marinos V., Marinos P. and Hoek E. (2007). ‘The Geological Strength Index (GSI): A characterization tool for assessing engineering properties of rock masses’. Underground works under special conditions, Publisher: Taylor and Francis, Editors: Romana, Perucho, Olalla, pp.13-21.

Menke W. (1989). ‘Geophysical data analysis: discrete inverse theory’. International Geophysical Series, Academic Press, Inc., vol. 45, pp. 289.

Metropolis N. and Ulam S. M. (1949). ‘The Monte Carlo method’. J. Am. Stat. Ass., 44, 335-341.

Miller G. F. and Pursey H. (1955). ‘On the Partition of Energy between Elastic Waves in a Semi-Infinite Solid’. Royal Society’s physical sciences research journal. Volume 233, issue 1192.

Ministry of infrastructure and transport (2008). NTC 08 ‘Technical standard for the construction’.

Moss RES (2008). ‘Quantifying measurement uncertainty of thirty-meter shear-wave velocity’. Bull Seism Soc Am 98(3):1399–1411.

Mucciarelli M. (1998). ‘Reliability and applicability of Nakamura’s technique using microtremors: an experimental approach’. J. Earthquake Engin., 2, 4, 625-638.

Mucciarelli M., Herak M. and Cassidy J. (2007). Book: ‘Increasing Seismic Safety by Combining Engineering Technologies and Seismological Data’. The NATO Science for Peace and Security Programme.

Mucciarelli M., Other C.D., Gosar Andrej, Herak Marjan, Albarello Dario (2008). 'Assessment of seismic site amplification and of seismic building vulnerability in the republic of Macedonia, Croatia And Slovenia'. The 14th World Conference on Earthquake Engineering October 12-17, Beijing, China.

Navarro M., Vidal F., Enomoto T., Alcalá FJ., García-Jerez A., Sánchez FJ. and Abeki N (2007). 'Analysis of the weightiness of site effects on reinforced concrete (RC) building seismic behaviour: The Adra town example (SE Spain)'. Earthquake Engineering Structural Dynamic 36:1363–1383.

Nazarian S. and Stokoe II KH. (1984). ‘In situ shear wave velocities from spectral analysis of surface waves’. Proceedings of the 8th conference on earthquake engineering, S. Francisco, vol. 3. Prentice-Hall, pp 31–38.

Nakamura Y. (1989). ‘A method for dynamic characteristics estimation of subsurface using microtremor on the ground surface’. QR Railway Technical Research Institute, 30, 25 - 33.

Nakamura Y. (1996). ‘Real-time information systems for hazards mitigation’. Proceedings of the XI World Conference on Earthquake Engineering, Acapulco (Mexico).

Nakamura Y. (2000). ‘Clear identification of fundamental idea of Nakamura's technique and its applications’. Proceedings of the XII World Conference on Earthquake Engineering, Auckland (New Zealand).

Nogoshi M. and Igarashi T. (1970). ‘On the amplitude characteristics of microtremor (part 1)’. Journ. Seism. Soc. Japan, 23, 281-303.

Nogoshi M. and Igarashi T. (1971). ‘On the amplitude characteristics of microtremor (part 2)’. Journ. Seism. Soc. Japan, 24, 26-40.

OPCM-Ordinance of President of the Council of Ministers 3274 (2003). ‘The first items regarding the general criteria for seismic classification of the national territory and technical standards for construction in seismic zone’.

OPCM-Ordinance of President of the Council of Ministers 3519 (2006). ‘Criteri generali per l'individuazione delle zone sismiche e per la formazione e l'aggiornamento degli elenchi delle medesime zone’.

Okada H. (2003). ‘The microtremor survey method, Geophysical Monograph Series, no. 12’. Society of Exploration Geophysicists.

Ohori M., Nobata A. and Wakamatsu K. (2002). ‘A comparison of ESAC and FK methods of estimating phase velocity using arbitrarily shaped microtremor analysis’. Bull Seism Soc Am 92:2323–2332.

Park CB., Miller RD. and Xia J. (1999). ‘Multichannel analysis of surface waves’. Geophysics 64:800–808.

Parker R. L. (1994). ‘Geophysical Inverse Theory’. Princeton University Press, New Jersey, pp. 386.

Paolucci Enrico (2016). 'Dynamic characterization of soils by means seismic passive measures and their utility in Seismic Microzonation studies'. PhD thesis, University of Pisa.

Parolai S., Bormann P. and Milkereit C. (2001). ‘Assessment of the natural frequency of the sedimentary cover in the Cologne area (Germany) using noise measurements’. J Earthq Eng 5:541–564.

Parolai S., Richwalski S. M., Milkereit C. and Bormann P. (2004). ‘Assessment of the stability of HVSR spectral ratios from ambient noise and comparison with earthquake data in the Cologne area (Germany)’. Tectonophysics, 390, 57-73.

Parolai S., Picozzi M., Richwalski S.M. and Milkereit C. (2005). ‘Joint inversion of phase velocity dispersion and HVSR ratio curves from seismic noise recordings using a genetic algorithm considering higher modes’. Geophys. Res. Lett., 32, L01303.

Parolai S., Richwalski SM., Milkereit C. and Faeh D. (2006). ‘S-wave velocity profile for earthquake engineering
purposes for the Cologne area (Germany)’. Bull Earthq Eng 65–94.

Pei Donghong (2007). Dissertation Title ' Modeling and Inversion of Dispersion Curves of Surface Waves in Shallow Site Investigations'. University of Nevada, Reno.

Picozzi M., Parolai S. and Albarello D. (2005a). ‘Statistical analysis of noise Horizontal to Vertical Spectral Ratios (HVSR)’. Bull. Seism. Soc. Am., 95, 5, 1779-1786.

Picozzi M., Parolai S. and Richwalski S. M. (2005b). ‘Joint inversion of HVSR ratios and dispersion curves from seismic noise: estimating the S-wave velocity of bedrock’. Geoph. Res. Lett., 32, 11.

Picozzi M. and Albarello D. (2007). ‘Combining genetic and linearized algorithms for a two-step joint inversion of Rayleigh wave dispersion and HVSR spectral ratio curves’. Geophys. J. Int., 169, 189-200.

Pilz M., Parolai S., Picozzi M. and Bindi D. (2012). ‘Three-dimensional shear wave velocity imaging by ambient seismic noise tomography’. Geophys. J. Int., 189, 501–512.

Pilz M., Parolai S., and Bindi D. (2013). ‘Three-dimensional passive imaging of complex seismic fault systems: evidence of surface traces of the Issyk-Ata fault (Kyrgyzstan)’. Geophys. J. Int., 194, 1955–1965.

Pradel D., and G. Raad (1993). ‘Effect of permeability on surficial stability of homogeneous slopes’. J. Geotech. Eng., 119, 315–332.

Press F. (1968). ‘Earth models obtained by Monte Carlo inversion’. J. Geophys. Res., 73, 5223–5234.

Priolo E., Romanelli M., Barnaba C., Mucciarelli M., Laurenzano G., Dall’Olio L., Abu Zeid N., Caputo R., Santarato G., Vignola L., Lizza C. and Di Bartolomeo P. (2012). ‘The Ferrara thrust earthquakes of May–June 2012: preliminary site response analysis at the sites of the OGS temporary network’. Ann. Geophys. 55(4):591–597.

Rhie J. and B. Romanowicz (2004). ‘Excitation of Earth's continuous free oscillations by atmosphere-ocean-seafloor coupling’. Nature 431, 552-556.

Richart F.E., Hall J.R. and Woods R.D. (1970). ‘Vibrations of soils and foundations’. Prentice-Hall, Inc., New Jersey, 414 pp.

Salawu O.S. and Williams C. (1995). ‘Review of Full-Scale Dynamic Testing of Bridge Structures’. Engineering Structures, 17(2), 113-121.

Sakaji K. (1998). ‘Temporal variation of the power spectra of microtremors observed at soil and rock sites’. Graduation Thesis, Hokkaido University.

Sanchez-Sesma F.J. and Campillo M. (2006). ‘Retrieval of the Green’s function from cross correlation: the canonical elastic problem’. Bull. Seismol. Soc. Am. 96(3):1182–1191.

Sanchez-Sesma F.J., Rodrıguez M., Iturraran-Viveros U., Luzon F., Campillo M., Margerin L., Garcıa Jerez A., Suarez M., Santoyo M.A., Rodrıguez-Castellanos A. (2011). ‘A theory for microtremor HVSR spectral ratio: application for a layered medium’. Geophys J Int 186:221–225.

Sambridge M. and Drijkoningen G.G. (1992). ‘Genetic algorithms in seismic waveform inversion’. Geophys. J. Int., 109, 323–342.

Sambridge M. and Mosegaard K. (2002). ‘Monte Carlo methods in geophysical inverse problems’. Review of Geophysics, 40, 3, 1-27.

Schnabel PB., Lysmer J. and Seed HB. (1972). ‘SHAKE: a computer program for earthquake response analysis of horizontally layered sites’. Rep. No. EERC/72–12, Earthquake Engineering Research Center. University of California, Berkeley.

Scherbaum F., Hinzen K-G. and Ohrnberger M. (2003). ‘Determination of shallow shearwave velocity profiles in Cologne, Germany area using ambient vibrations’. Geophys J Int 152:597–612.

SESAME (2004). ‘Guidelines for the implementation of the HVSR spectral ratio technique on ambient vibrations Measurements, processing and interpretation’. SESAME European research project WP12 – Deliverable D23.12, http://sesame-fp5.obs.ujfgrenoble.fr/SES_Reports.htm.

Sen M.K. and Stoffa P.L. (1992). ‘Rapid sampling of model space using genetic algorithms’. Geophys. J. Int., 108, 281–292.

Stoffa P.L. and Sen M.K. (1991). ‘Nonlinear multiparameter optimization using genetic algorithms: Inversion of plane wave seismograms’. Geophys, 56, 1794–1810.

Suhairy Sinan Al (2000). 'Prediction of ground vibration from railways'. SP Swedish National Testing and Research Institute, SP Report 2000:25.

Shearer P. (1999). ‘Introduction to seismology’. Cambridge University Press.

Shapiro N.M., Camillo M., Stehly L. and Ritzwoller M.H. (2005). ‘High resolution surface wave tomography from ambient seismic noise’. Science, 307, 1615-1618.

Taleb R., Bouriche F., Remas A., Boukri M. and Kehila F. (2012). 'Use of Ambient and Forced Vibration Tests to Evaluate Seismic Properties of an Unreinforced Masonry Building Rehabilitated by Dampers'. 15 WCEE Lisbona.

Tanimoto T. and Alvizuri C. (2006). ‘Inversion of the HZ ratio of microsisms fopr S-wave velocity in the crust’. Geophys J Int 165:323–335.

Tarantola A. (2005). ‘Inverse problem theory and methods for model parameter estimation’. SIAM, Philadelphia, pp. 342.

Tuan TT., Scherbaum F. and Malischewsky PG. (2011). ‘On the relationship of peaks and troughs of the ellipticity (HVSR) of Rayleigh waves and the transmission response of single layer over half-space models’. Geophys J Int 184:793–800.

Tokimatsu K. (1997). ‘Geotechnical site characterization using surface waves’. Earthquake Geotechnical Engin., ed. Ishihara, Balkema, Rotterdam, 1333-1368.

Tokimatsu K., Shinzawa K. and Kuwayama S. (1992). ‘Use of short-period microtremors for Vs profiling'. Journal of Geotechnical Engineering, 118, 10, 1544-1558.

Ventura Carlos E., Lord Jean-François and Simpson Robert D. (2002). ‘Effective use of ambient vibration measurements for modal updating of a 48 storey building in Vancouver, Canada’. Research Gate.

Ventura, C.E. and Horyna, T. (2000). ‘Measured and Calculated Modal Characteristics of the Heritage Court Tower in Vancouver, B.C.’. International modal analysis conference-XVIII: A Conference on Structural Dynamics, pp. 1070-1074.

Wathelet M., Jongmans D. and Ohrnberger M. (2004). ‘Surface-wave inversion using a direct search algorithm and its application to ambient vibration measurements’. Near Surface Geophys 2:211–221.

Wathelet M. (2005). ‘Array recordings of ambient vibrations: surface wave inversion’. PhD Thesis, University of Liege (Belgium).

Wathelet M., Jongmans D. and Ohrnberger M. (2005). ‘Direct Inversion of Spatial Autocorrelation Curves with the Neighborhood Algorithm’. Bulletin of the Seismological Society of America, 95, 5, 1787-1800.

Yamanaka H., Takemura M., Ishida H. and Niwa M. (1994). ‘Characteristics of long-period microtremors and their applicability in the exploration of deep sedimentary layers’. Bull Seism Soc Am 84:1831–1841.

Yamanaka H. and Ishida H. (1996). ‘Application of Genetic Algorithms to an inversion of surface-wave dispersion data’. Bull. Seism. Soc. America, 86, 2, 436-444.

Xia J., Miller R.D. and Park C.B. (1999). ‘Estimation of near surface shear wave velocity by inversion of Rayleigh waves’. Geophysics, 64, 3, 691-700.